Polymers for Tissue Engineering

VSP

Utrecht, The Netherlands, 1998

Polymers for Tissue Engineering

This page intentionally left blank

Polymers for Tissue Engineering

Editors:
M.S. Shoichet and J.A. Hubbell

VSP
Utrecht, The Netherlands, 1998

VSP BV
P.O. Box 346
3700 AH Zeist
The Netherlands

Tel: +31 30 692 5790
Fax: +31 30 693 2081
E-mail: vsppub@compuserve.com
Home Page: http://www.vsppub.com

First published in 1998

ISBN 90-6764-289-4

Printed in The Netherlands by Ridderprint bv, Ridderkerk.

Contents

This page intentionally left blank

Polymers for Tissue Engineering, pp. ix–xi
Molly S. Shoichet and Jeffrey A. Hubbell (Eds)

Foreword

Tissue Engineering thrives on collaboration across traditional disciplines, combining polymer science and drug delivery with cell biology, immunology and surgery. A wealth of knowledge has been gained from both the materials science and the cell and molecular biology communities in the development of new or modified biomaterials for implantation. For example, the biomaterials community has provided insight into the host tissue response to implanted materials, particularly in relation to blood-material interactions or bone substitute materials. A greater understanding of the biology of cell adhesion and differentiation has facilitated the synthesis of both bio-inert and bio-responsive polymers. These new materials often have a biological component incorporated in their design by any of several techniques: surface modification to incorporate synthetic biomimetic molecules, surface immobilization of biological molecules, incorporation of biological molecules for local delivery, or harnessing biological methods of synthesis, such as recombinant DNA techniques, for the production of fully biological polymers with total control over design. The incorporation of the biological component is performed with the aim of achieving a specific response from the host.

While we have a greater foundation today for the development of new implantable materials for tissue engineered devices, we still have a significant amount to learn. For example, most of our knowledge of cell biology, and thus of cellular interactions with these materials, is based on *in vitro* research in cell culture models that are at best only partially relevant to the implant situation. Indeed, often the tissue engineering approach provides a platform for cell biological studies *in vivo*, and we find the opportunity to develop polymers specifically to test biological hypotheses, thus yielding new biological insight for the design of better biomedical polymers for tissue engineering and other purposes. Furthermore, much work remains to be done to translate the new foundational approaches into engineering systems that are sufficiently practical to be used in treating patients. This is to say, the initially conceived embodiment for bioactive polymers may be sufficient to demonstrate the concept and to understand the level of control that can be obtained over biological

interactions, but translation of that initial embodiment to one that is clinically practicable may be a difficult process requiring great creativity. Moreover, in many cases the pieces of a complex tissue engineering puzzle have been developed in different laboratories, and the fitting together of those pieces to create the intact puzzle of a new therapeutic method may be non-trivial.

The articles included in this book highlight the important advances in polymer science that impact tissue engineering. The breadth of polymer science is well represented with the relevance of both polymer chemistry and morphology emphasized in terms of cell and tissue response. While not a comprehensive book on all the advances in polymer science that impact tissue engineering, the book includes contributions from leaders in the field that are representative of current research endeavors. The book is organized in four sections: (1) New Polymers, (2) Polymer Modification, (3) Scaffolds, and (4) Hydrogels.

In section 1, New Polymers, exciting new developments are described that build either upon biological or synthetic approaches to creating novel materials for tissue engineering applications. Biologically synthesized polypeptides are described in terms of their mechanical properties (Chapter 1.1.) and cellular responses (Chapter 1.2.), while traditionally synthesized polymers are described that incorporate peptides into their design (Chapters 1.3. and 1.4.). Polyesters have been used for several years in medical applications, relying on hydrolysis for their biodegradation: a new polyester-functionalized polymer si described (Chapter 1.5.) as is a review on recent advances in synthetic polymers for tissue engineering (Chapter 1.6.).

In section 2, Polymer Modification, chemical techniques are used to create well-defined surfaces. Two distinctly different methods are described to surface modify fluoropolymers, which are known to be chemically inert (Chapters 2.1. and 2.2.). Poly(ethylene glycol), which is known to render a polymer both less protein adsorptive and cell-adhesive, is used as a surface modifier (Chapters 2.3. and 2.4.). Protein adsorption as an alternative method to control the cellular response is demonstrated in the last chapter of this section (Chapter 2.5.).

Section 3, Scaffolds, builds on some of the scientific issues described in previous sections. For example, Chapter 3.1. highlights the use of a poly(ethylene glycol)-based scaffold with biodegradable ester linkages. Scaffolds are described for cell encapsulation (Chapter 3.2.) and skeletal myogenesis (Chapter 3.3.). Hepatocyte cell culture is described for ultimate use as an artificial liver (Chapters 3.4. and 3.5.). Scaffolds are further described as synthetic extracellular matrices for use in tissue engineering of dental pulp (Chapter 3.6.) and cartilage (Chapter 3.7.). Novel adhesion proteins are characterized and refined for pre-treatment of scaffold materials for more efficient attachment of cells (Chapter 3.8.).

Section 4, Hydrogels, further builds on the previous sections, taking advantage of new polymers, surface modification and scaffolds. The first two chapters describe hydrogel scaffolds used for neural applications (Chapters 4.1. and 4.2.). The last

two chapters include growth factors in their design for improved cellular responses in tissue regeneration (Chapters 4.3. and 4.4.).

The possibilities for polymers to influence tissue engineering are great, leaving the door open for inventiveness, collaboration and synergism across traditional boundaries of research. It is clear that advances are required that span from materials synthesis, to the understanding of materials degradation and clearance, to the manipulation of cellular behavior by the incorporation of biological signals, to the integration of multiple approaches to develop functional therapies, to the demonstration in patients to improve quality of life. The chapters in this book provide examples of some of these issues and we hope that they will serve to stimulate further work, to move the approaches of tissue engineering with biomedical polymers closer toward widespread clinical impact.

Molly S. Shoichet
University of Toronto
Toronto, Canada

Jeffrey A. Hubbell
ETH and University of Zurich
Zurich, Switzerland

This page intentionally left blank

Section 1

New Polymers

This page intentionally left blank

Polymers for Tissue Engineering, pp. 3–18
Molly S. Shoichet and Jeffrey A. Hubbell (Eds)

Mechanical properties of a self-assembling oligopeptide matrix

ERASMO J. LEON, NEETA VERMA, SHUGUANG ZHANG, DOUGLAS A. LAUFFENBURGER and ROGER D. KAMM*

Center for Biomedical Engineering, Massachusetts Institute of Technology, Canbridge, MA 02139, USA

Received 3 June 1997; accepted 6 October 1997

Abstract—We have begun studies of a novel type of biomaterial derived from a recently-discovered class of ionic self-complementary oligopeptides. These short peptides (typically 8, 16, 24, or 32 amino acid residues with internally-repeating sequences) self-assemble in aqueous salt solution into three-dimensional matrices capable of favorable interactions with cells, and offer promise for useful bioengineering design based on rational changes in sequence. In this paper we present preliminary results on mechanical properties, combining experimental and theoretical approaches, of one particular example of these peptide materials, EFK8. The static elastic modulus was measured using an apparatus designed to allow sample fabrication and mechanical testing in the same system with the sample in aqueous solution. The material microstructure was examined by SEM and the measurements interpreted with the aid of a model for cellular solids. Values for the elastic modulus increased from 1.59 ± 0.06 to 14.7 ± 1.0 kPa for peptide concentrations increasing from 2.7 to 10 mg ml^{-1}. SEM photographs showed the microstructure to consist of a relatively homogeneous lattice with fiber thickness of $10 - 30$ nm independent of peptide concentration, but with fiber density increasing with peptide concentration. This behavior is consistent with scaling predictions from the cellular solids model and yields an estimate for the individual fiber elastic modulus in the range of 1–20 MPa. We therefore have provided some initial physical principles for guiding improvement of the mechanical properties of these new materials.

Key words: Biomaterial; self-assembling peptides; elastic modulus; model; tensile test; microstructure.

INTRODUCTION

It is widely recognized that the current repertoire of biomaterials will not be adequate for the vast range of applications in drug delivery, artificial organs, and tissue engineering technologies (e.g. [1–4]). Issues that must be resolved satisfactorily for development of new biomaterials suitable for particular applications include: (a) capability for providing molecularly-specific interactions with cells; (b) capability for minimization of immune and inflammatory responses; (c) capability for controlled

*To whom correspondence should be addressed. E-mail: rdkamm@mit.edu

degradation into harmless constituent products on appropriate time scales; (d) capability for offering proper permeabilities to diffusible nutrients, regulatory factors, and cell products; (e) capability for exhibiting necessary mechanical properties; (f) capability for reproducible GMP synthesis and fabrication; and, (g) capability for flexibility in molecular-level design. While diverse approaches to development of new materials are being pursued energetically in numerous laboratories, it is highly improbable that a single class of materials will resolve all these issues optimally for the entire range of applications. Thus, innovative directions with the potential for success in even a subset of applications need to continue to be strongly encouraged.

Recently, a new class of ionic, self-complementary oligopeptides has been discovered [5] and its potential value as a biomaterial is currently being explored. These short (8-, 16-, 24-, and 32-amino acid residue monomers) oligopeptides consist of regular repeats of alternating ionic hydrophilic and hydrophobic amino acids and associate to form stable β-sheet structures in water [5, 6]. The addition of buffers containing millimolar amounts of monovalent salts results in the spontaneous assembly of the oligopeptides into a stable, macroscopic membranous matrix; this assembly is facilitated by ionic side chain interactions in addition to conventional β-sheet backbone hydrogen bonding.

This class of peptide biomaterials has several attractive features. Because they are short oligomers, they can be readily synthesized *in vitro* from entirely *de novo* design, and subsequently, purified, manipulated and modified. The twenty natural amino acids — as well as numerous 'non-natural' amino acids — potentially allow a wide range of physico-chemical properties, such as mechanical strength, permeability, and degradation rates, to be custom-generated for particular applications. Since they arise via self-assembly in aqueous salt solutions, they can be produced using fabrication processes that introduce no toxic solvents.

In terms of biologically-relevant features, the natural pore size arising in these matrices — roughly 100 nm — is appropriate for diffusive transport of regulatory molecules. Furthermore, a diverse spectrum of cells has been demonstrated to interact favorably with the materials in terms of attachment, spreading, and migration [7]. At the same time, their strongly ionic character [5, 7] minimizes their immunogenicity. In matrices for which their constituent monomers are all natural L-amino acids, their degradation will yield normal amino acids which can then be reused by the host tissue. They are resistant to heat, to many chemical denaturation agents, and to degradation by proteolytic enzymes *in vitro*, nonetheless appear to resorb *in vivo* [5, 6].

Although these peptide materials possess many desirable properties, our initial experience has shown that they are rather fragile and somewhat difficult to handle. Since problematic structural integrity could limit the range of usefulness of these materials, we are now focusing on the structural characteristics of the materials, with an aim toward developing a more fundamental understanding of those factors that influence them and to identifying methods by which materials with appropriate strength can be designed.

In this paper, we explore the mechanical properties of one particular peptide from this class, EFK8. Methods are developed for measuring the elastic modulus and fracture strength using minute specimens. The microstructure is examined by SEM

and an existing theory for cellular solids is used as one framework within which the microstructure and measurements might be related.

METHODS

Mechanical testing

To allow the testing of samples under uniaxial stress, cylindrical threads were produced. These are fabricated using the apparatus shown in Fig. 1, consisting of a micrometer-controlled translating stage with the extrusion needle attached, a syringe pump to control the flow rate of peptide solution, and a cuvette containing salt solution placed on an electronic balance. The specimen is visually recorded by means of a high resolution CCD camera (Pulnix TM-9700). Both the video signal and the signal from the electronic balance (Denver Instruments) are fed into a data acquisition system (Macintosh Power PC, Model 8500).

Cylindrical threads of peptide biomaterial are formed vertically in the cuvette which contains salt solution with density matched to that of the injected peptide to eliminate buoyancy effects. Initially a small amount of peptide is injected to produce a base that adheres to the bottom of the cuvette. The needle is then raised at a speed commensurate with the ejection flow rate to produce a cylindrical thread approximately the same diameter as the needle. The values used were 65 μm s^{-1} for the needle withdrawal speed and 0.097 mm^3 s^{-1} for the flow rate.

Using this method, specimens of the type shown in Fig. 2 are readily produced. The test specimens typically had bottom and top anchors 2 mm in length and 1.6 mm in diameter. At their narrowest point, the neck had an approximate length and diameter

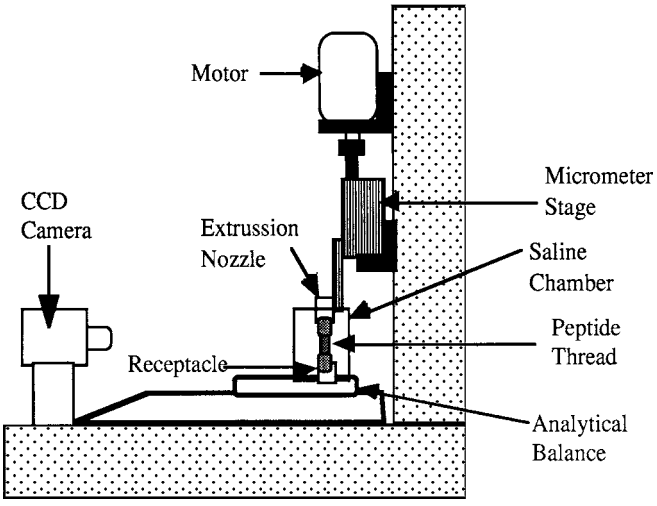

Figure 1. Schematic of tensile testing system.

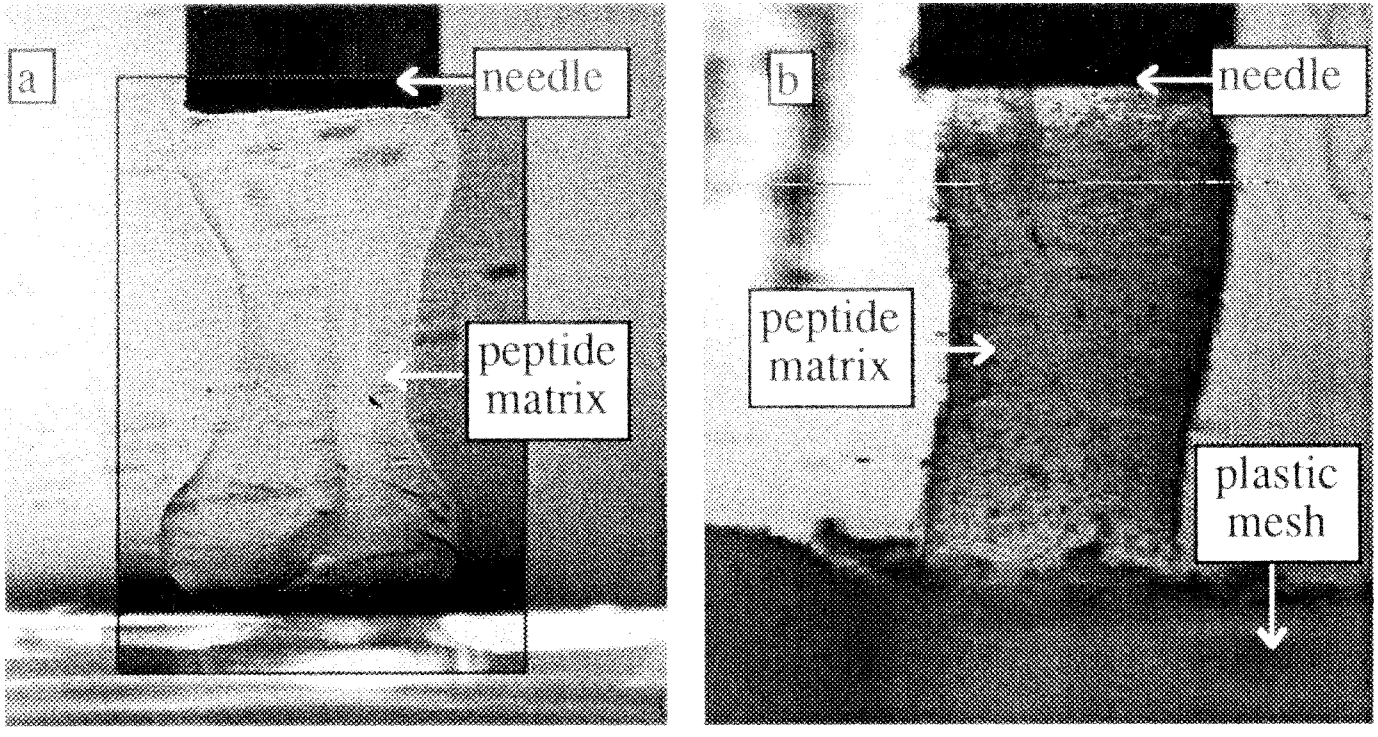

Figure 2. Photographs of tensile test specimens: (a) specimen after fabrication (shaded box shows enhanced contrast to allow observation of colorless specimen); (b) specimen anchored to plastic mesh (Congo red stain added to enhance specimen visibility).

of 8 mm and 1.4 mm, respectively. The images used to measure lengths and displacements can resolve 7.3 μm. Since the length monitored for strain measurements is approximately 0.8 mm, the uncertainty introduced in strain measurements is about 0.9% elongation compared to measured strains of up to 8%. The effect of this error can be reduced by making multiple measurements from a given test as discussed below. The balance used to measure resulting forces on the specimen has a resolution of 0.1 mg corresponding to a force of 9.8×10^{-7} N. The forces measured in the experiments ranged from 9.8×10^{-6} to 2×10^{-4} N (stresses from 6 to 127 Pa).

Once formed, the peptide biomaterial solidifies on a diffusional time scale ($\sim$ minutes for samples as shown in the figure). When solid, the specimen can be immediately subjected to mechanical tests without removal from the fabrication apparatus. Small increments (~ 0.01 mm) are made in the micrometer stage while the video and force signals are recorded. After a short transient (< 1 min) the force stabilizes and the next increment is imposed. Stress can be computed as the change from baseline force, divided by the cross-sectional area, determined from the diameter measured from the video signal. Strain in the central region (away from the ends of the specimen) can be calculated as the change in distance between two identifiable points on the surface of the peptide thread. Ultimately, the specimen fractures, usually near its midpoint (tests in which the fracture occurs near one of the ends are discarded).

Scanning electron microscopy

After self-assembly of the peptides into macroscopic matrices, we examined the detailed material structure with scanning electron microscopy (SEM). The oligopeptide matrices were prepared for SEM by incubating the matrices in 5% glutaraldehyde at 4°C for 2 h, followed by slow sequential dehydration steps in 10% increments of ethanol in PBS for 5 min each. The sample was then placed in pressurized liquid CO_2/syphon for 1 h. The sample was next sputter-coated with gold–palladium particles, mounted on a grid and examined using a JEOL JSM-6320FV field emission SEM at between 2000 and 100 000 $\times$ magnification [7].

The SEMs were analyzed to quantify the structural parameters relevant to the mechanical properties. The public domain software package, NIH Image (ver. 1.60) was used to identify the diameter of the fibers, and their junction-to-junction distance. Length measurements were corrected to account for the three-dimensionality of the structure. On the assumption that the material is isotropic (so that every orientation is equally likely), the mean length determined from the two-dimensional image was multiplied by $4/\pi$ to give the true mean length. This correction is not necessary for fiber diameters assuming them to be circular in cross-section. The mean values thus obtained were used to determine the density of the fiber matrix.

Peptide

This study concentrates on a single peptide, EFK8 (N-KFEFKFEF-C), the chemical structure of which is shown in Fig. 3. The negative and positive charged amino acids are glutamate (E) and lysine (K), respectively. The hydrophobic R-group is provided

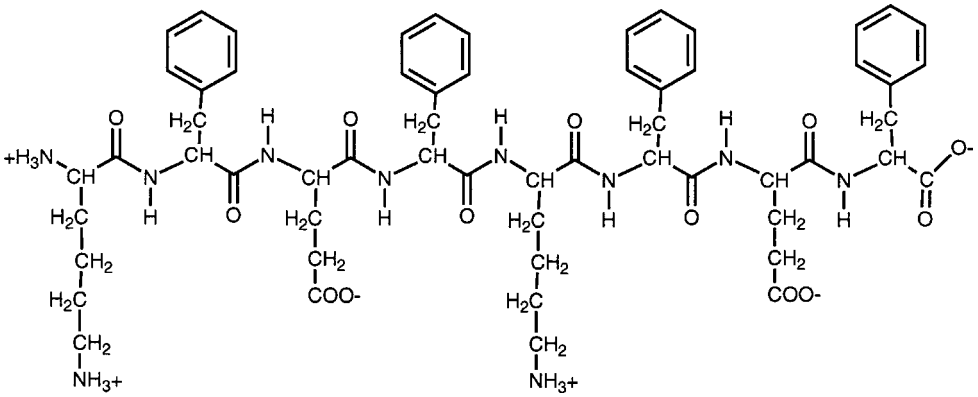

Figure 3. Molecular structure of the oligopeptide, EFK8.

by the aromatic amino acid phenylalanine (F). A molecular model of EFK8 produced with Molecules 3-D (ver. 2.1), is included in the figure. This model clearly shows the bulky hydrophobic phenylalanine R groups lying on one side of the β-sheet and the charged glutamate and lysine R groups lying on the opposite side.

EFK8 is one of the smallest peptides in the family of ionic self-complementary oligopeptide biomaterials. Presently, 8-mers are the smallest peptides that form part of this class of materials. Previous studies suggest that longer peptides are more stable than shorter ones and show greater tendency for self-assembly. However, the shortest peptides offer the advantage of lower cost, greater ease of synthesis, and higher solubility and purity. Also, shorter peptides show lesser structural and chemical complexity, which facilitate their study. Therefore, the study of small peptides provides the starting point towards greater comprehension of the self-assembling oligopeptide biomaterials and their material properties.

Cellular solids model

The theory of cellular solids relates the mechanical properties of low density cellular materials to their structural characteristics [8] and has been successfully used to characterize materials ranging from cotton to the F-actin intracellular matrix [9]. The analysis is based on the concept that the material can be thought of as being comprised of many 'unit cells', one representation of which is shown in Fig. 4. These unit cells are staggered with struts meeting at their midpoints. It should be noted that the following analysis, while developed with the structure of Fig. 4 in mind, has been shown to be applicable to a variety of fibrous materials with different microstructures. When a cellular solid is stressed under tension or compression, the fibers act like struts and beams that deform under stress as illustrated in Fig. 4b. At loads exceeding the linear–elastic regime, the struts can buckle and plastic hinges are created [8]. This leads to plastic collapse of the structure. If the constitutive material is brittle, brittle crushing or brittle fracture are the cause of collapse [8].

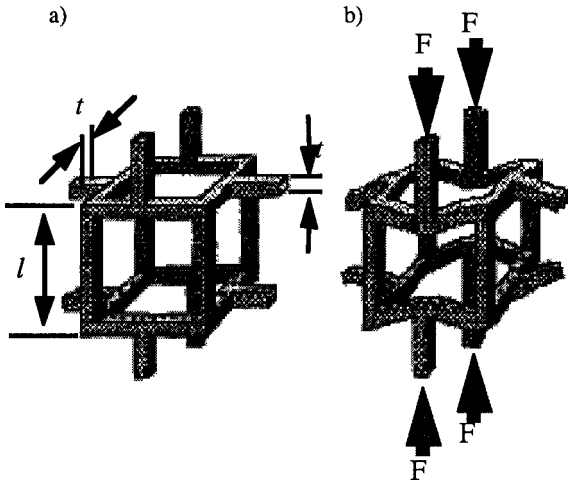

Figure 4. Unit cell model used in theoretical model of mechanical strength: (a) undeformed; and (b) loaded and deformed by element bending (adapted from Gibson and Ashby, 1988).

The unit cell model in Fig. 4 has struts or fiber elements of length l and thickness t. The relative density of the material is defined as the density of the network, ρ^*, divided by the density of the fibers ρ_s. This ratio depends on the geometry of the matrix structure. It is related to the cell dimensions t and l [8].

$$\frac{\rho^*}{\rho_s} \propto \left(\frac{t}{l}\right)^2. \tag{1}$$

Beam theory [10] gives the deflection δ of a beam of length l to a force F acting at its midpoint as

$$\delta \propto \frac{Fl^3}{E_s I}, \tag{2}$$

where E_s is the stiffness of the beam constitutive material and I is the beam's second moment of area. The moment of area for a beam of thickness t is given by

$$I \propto t^4. \tag{3}$$

The stress σ is the force per unit area, or

$$\sigma \propto \frac{F}{l^2}. \tag{4}$$

The strain is related to beam deflection δ by

$$\varepsilon \propto \frac{\delta}{l}. \tag{5}$$

Using the results from Eqs (2), (4), and (5), the network Young's modulus or elastic modulus can be expressed as

$$E^* = \frac{\sigma}{\varepsilon} = \frac{kE_s I}{l^4}, \tag{6}$$

where k is a constant of proportionality. Substituting Eqs (1) and (3) into (6) gives [8]:

$$\frac{E^*}{E_s} = k_1 \left(\frac{\rho^*}{\rho_s}\right)^2. \tag{7}$$

Data from a wide range of materials and cell geometries give a value for k_1 of approximately 1. A similar analysis for cellular materials subjected to shear stresses results in an expression for the network shear modulus G^* given by [8]:

$$\frac{G^*}{E_s} = k_2 \left(\frac{\rho^*}{\rho_s}\right)^2, \tag{8}$$

where $k_2 \sim 3/8$. If the material is linear-elastic and isotropic, elasticity theory [10] provides the following relationship

$$G = \frac{E}{2(1+\nu)}, \tag{9}$$

which, when solved for the Poisson ratio ν, gives a value of $1/3$.

Brittle materials in tension fail by propagation of cracks. The scaling analysis of this deformation mechanism is done using the results of linear elastic fracture mechanics. It relates the network fracture toughness K^* to the solid toughness K_s by

$$\frac{K^*}{K_s} = k_3 \left(\frac{\rho^*}{\rho_s}\right)^{3/2}. \tag{10}$$

Extensive data dictate the value of k_3 to be approximately 0.65 [8].

Finally, it should be noted that each of these expressions involving a density ratio (ρ^*/ρ_s) can also be expressed in terms of a concentration in the form:

$$\frac{\rho^*}{\rho_s} = \frac{k_4}{C}, \tag{11}$$

where k_4 can be taken to be a constant on the assumption that the peptide concentration within the fibers is independent of bulk concentration. Substituting Eq. (11) into (7), (8), or (10) provides a scaling relation for the dependence of elastic, shear and toughness moduli on peptide concentration.

RESULTS

Characterization of microstructure using SEM

Micrographs obtained from critical-point dried samples of EFK8 are shown in Figs 5 and 6 at 3.3 and 10.0 mg ml^{-1}, respectively. The macroscopic membrane formed by the peptides is seen to consist of a low density fibrous material At the lower magnifications, namely, 2000 and 4000 $\times$, the specimen has the appearance of a

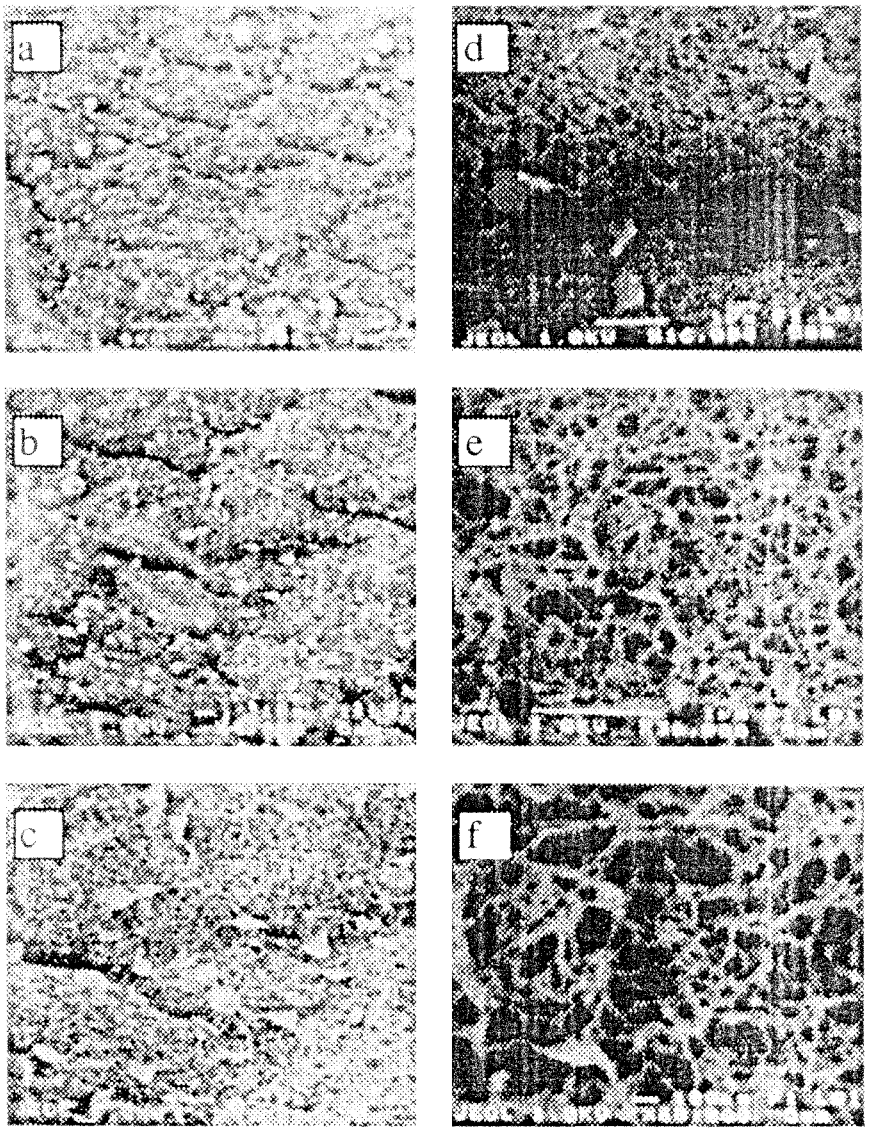

Figure 5. Scanning electron micrographs of EFK8 at 3.3 mg ml^{-1}. Magnifications of: (a) 2000; (b) 4000; (c) 8000; (d) 16 000; (e) 32 000; and (f) 60 000.

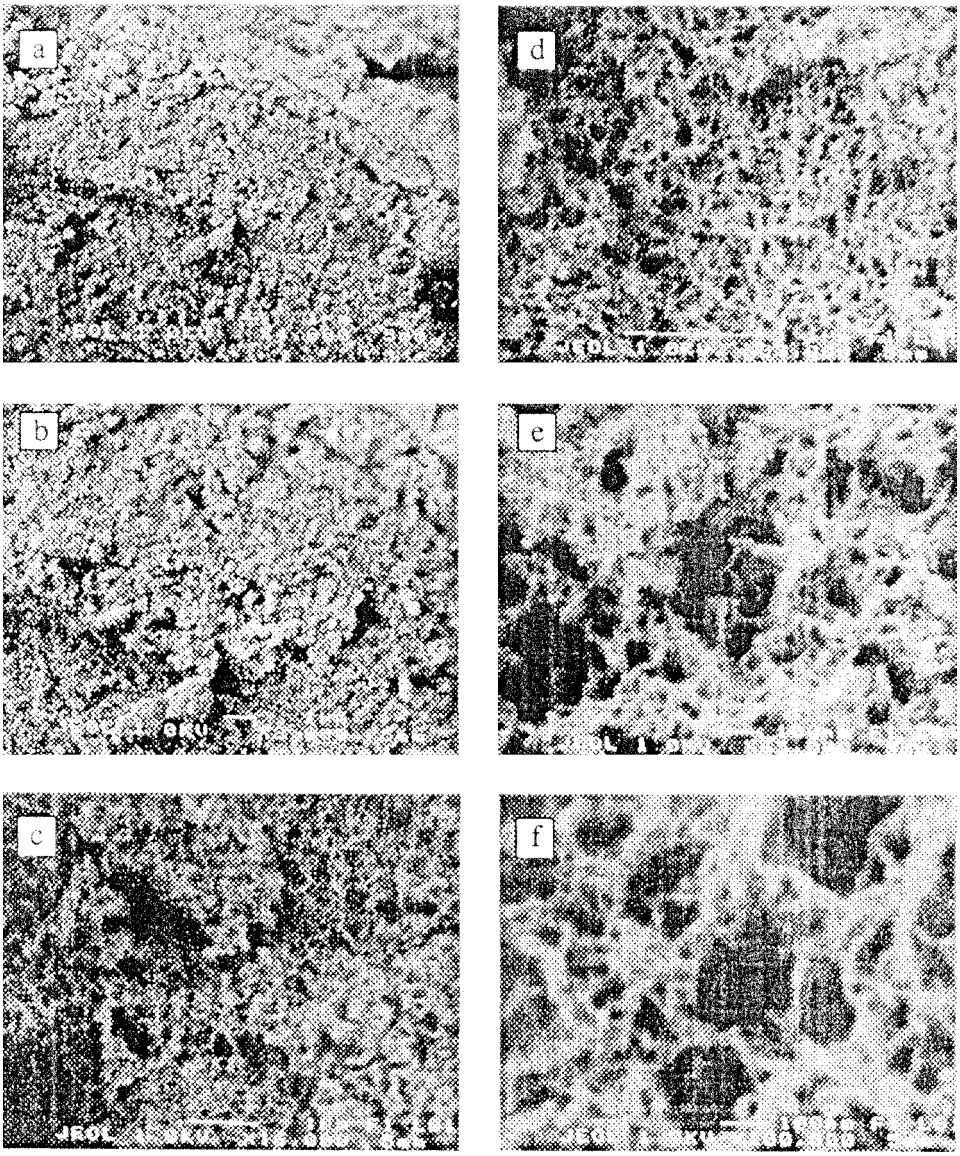

Figure 6. Scanning electron micrographs of EFK8 at 10 mg ml^{-1}. Magnifications of: (a) 4000; (b) 8000; (c) 16 000; (d) 33 000; (e) 65 000; and (f) 100 000.

continuous solid with a rough surface. At the higher magnifications of 16 000 $\times$ and 32 000 $\times$ the material's porous structure becomes discernible.

At a concentration of 3.3 mg ml^{-1}, the material can be described as a mesh of randomly interconnected fibers. These filaments are interwoven forming a macroscopic porous matrix [5, 7]. The fibers show no apparent preferred orientation, nor are there any systematic variations in fiber thickness or edge-connectivity. These fibrous networks have a fairly uniform appearance compared to those formed at higher

concentrations with fiber thicknesses 10–30 nm (after correction for the thickness of the gold coating) and distance between fiber junctions of 100–250 nm.

The high magnification micrographs of EFK8 at 10 mg ml^{-1} revealed that the detailed microstructure differs somewhat from that of the same peptide at 3.3 mg ml^{-1}. Comparison of their respective pictures clearly illustrate that the 10 mg ml^{-1} peptide dilution resulted in a denser matrix. The fibers have similar thickness (10–30 nm), however, the 10 mg ml^{-1} sample has a larger number of fibers per volume and a correspondingly shorter fiber length of 50–100 nm. Notably, the network of the 10 mg ml^{-1} sample is less uniform than that observed at 3.3 mg ml^{-1}. These inhomogeneities are especially evident in the 65 000 and 100 000 × magnifications of Fig. 6e and f, respectively.

Tensile tests

Tensile tests were performed on EFK8 specimens at concentrations of 2.7, 3.3, 5.4, and 10 mg ml^{-1}. Figure 7 illustrates the averaging method used to determine the stress–strain curve for a single experiment. Four curves are shown; the solid curves correspond to strain measurements obtained using three different paired points near the center of the specimen. The dashed curve depicts the stress–strain behavior that resulted from averaging the three individual curves.

The three curves in Fig. 8, each obtained from the averaging procedure just described, suggest that the stress–strain behavior of the peptide material at 2.7 mg ml^{-1}

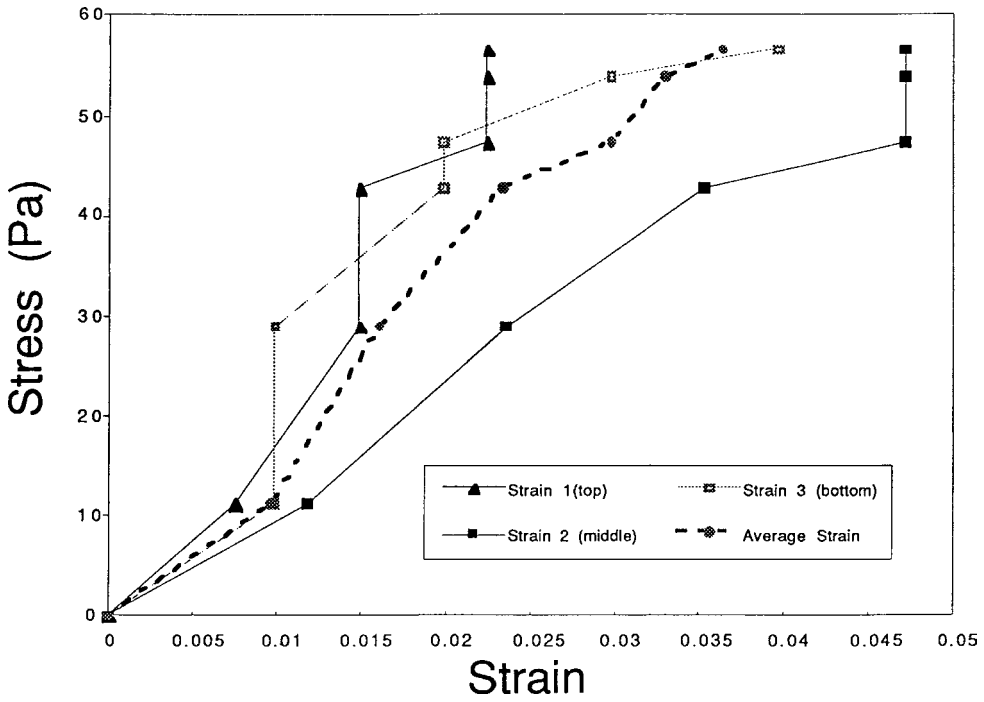

Figure 7. Averaging strain technique for stress–strain curves. Individual curves correspond to different pairs of reference points on specimen. Tensile test of EFK8 at 2.7 mg ml^{-1}.

Table 1.
Tensile tests data for EFK8

Concentration ($mg\,ml^{-1}$)	Modulus (kPa)		Strength (Pa)		Max. elongation (%)	
	Range	Average	Range	Average	Range	Average
2.7	1.52 – 1.63	1.59 ($n = 3$)	44 – 57	50.5 ($n = 2$)	3.0 – 3.6	3.3 ($n = 2$)
3.3	2.67 – 3.32	2.90 ($n = 4$)	119 – 218	176.3 ($n = 4$)	4.4 – 7.8	5.9 ($n = 4$)
5.4	5.0 – 7.3	6.23 ($n = 3$)	123	123 ($n = 1$)	1.7	1.7 ($n = 1$)
10	14.0 – 15.4	14.7 ($n = 2$)	162 – 231	196.5 ($n = 2$)	1.1 – 1.3	1.2 ($n = 2$)

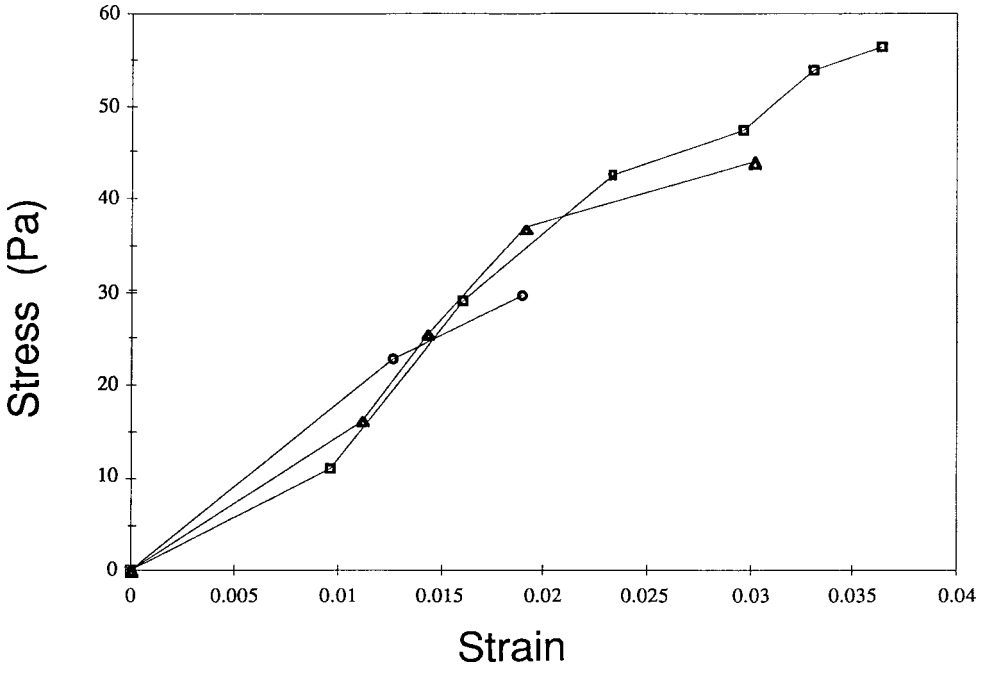

Figure 8. Tensile stress–strain curves for EFK8 at 2.7 $mg\,ml^{-1}$. Each curve is averaged as in Fig. 7.

is essentially linear all the way to fracture. The Young's modulus (values reported in Table 1 and Fig. 9) was obtained from the slope of the least squares linear regression for stress vs strain. Two of the three curves include data all the way to fracture. In both cases, fracture occurred near the middle of the specimen.

The data for all four concentrations exhibited similar linearity, although the experimental noise, primarily due to limitations imposed by the spatial resolution of the imaging set-up, cause increasing scatter at higher concentrations as the total strain before fracture decreases.

The mechanical measurements are summarized in Table 1. This table presents the elastic modulus, fracture strength, and strain to fracture at the four concentrations, presented as a range and an average. These data demonstrate a trend of increasing Young's modulus with increasing concentration. The fracture strength also exhibits

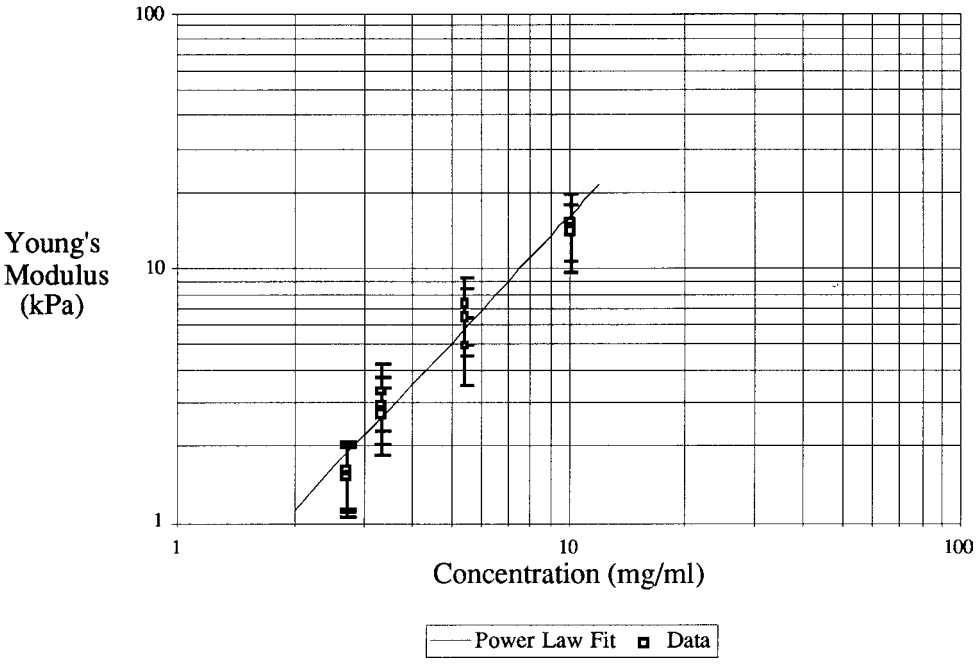

Figure 9. Dependence of Young's modulus on peptide concentration for EFK8. Solid line is best logarithmic fit to the data.

some tendency to increase with concentration although this tendency is masked by the high degree of scatter in the fracture results and the mean values are not significantly different. The elongation, however tends to decrease with increasing material concentration.

The Poisson ratio was determined from a ratio of the diametrical strain to the axial strain, measured near the midpoint of the specimen. The value determined from these measurements was 0.47 ± 0.16.

Cellular solids analysis

The cellular solid analysis suggests that the elastic or Young's modulus should vary as C^2. Although the values for elastic modulus plotted in Fig. 9 show a clear tendency to increase with increasing concentration, when the experimental data are fit to a power law relationship, the dependence of concentration is found to be somewhat weaker than predicted by the scaling analysis, satisfying

$$E^* \cong 0.36C^{1.6}, \tag{12}$$

where E^* is in kPa and C is in mg ml^{-1}. This regression line is also shown in the figure.

An estimate for the elastic modulus of the individual fibers comprising the matrix can be obtained from Eq. (7), using the value of the constant found from other studies ($k_1 \sim 1$). Using a fiber dimension in the range of 10–30 nm, the measured values of

matrix stiffness, and values for fiber length obtained by image analysis, fiber elastic modulus is estimated to be in the range 0.6–23 MPa.

DISCUSSION

Earlier studies have demonstrated that the self-complimentary ionic oligopeptides may have considerable potential for use as biomaterials in drug delivery, wound healing, and tissue regeneration [5–7]. Practical application, however, will require further investigation of key properties of the materials and their interactions with a biological environment. An initial question concerns the ability of these materials to respond in satisfactory manner to mechanical stresses likely to be imposed. Hence, the primary purpose of this study was to measure the static elastic properties of one member of this new class of peptide biomaterials and interpret these measurements with the aid of scanning electron microscopy complimented by analysis.

For the purpose of measuring the mechanical properties of these materials, it was necessary to design a new test apparatus that met several stringent requirements. Because of the high cost of synthesizing new oligopeptides, the specimen volume needed to be as small as possible. Due to the fragility of such small samples, and because of the need to maintain an aqueous environment, it was decided that fabrication and testing should be done in the same system. The use of an electronic balance in this setting simultaneously provided the required accuracy in load measurement and the capability of taring the system, including cuvette and aqueous solution, just prior to testing. In order to avoid artifacts associated with end regions, the image analysis method was selected for strain measurement. This also precluded the need for direct contact with the specimen. The main limitation of this system was the resolution of the strain measurements. Before performing the experiments it was felt that $\sim 10\ \mu$m resolution would be adequate; it was not until measurements were made with the high concentration samples that the limitations of the constrain were evident. The use of a lens with higher magnification would obviously improve the accuracy of the strain measurements.

The microstructure as seen in the SEMs consists of an isotropic lattice with fibers of nearly uniform thickness. It is interesting to note that the fiber thickness is comparable to the length of the oligopeptide molecule, suggesting a possible link. The fiber length between junctions (and therefore the pore size) is somewhat more variable, to an increasing degree as the peptide concentration is increased. These inhomogeneities may, however, have been more accentuated on the surface of the gelled thread where the SEMs were obtained. More study is needed to determine the extent to which the sample is spatially uniform. It is apparent from these results, that extrusion of the solution into the aqueous bath at these rates did not produce a preferred fiber orientation.

The elastic modulus exhibited by these preliminary measurements on EFK8 (of approximately 10 kPa at easily practicable peptide concentrations), compares favorably with that of soft tissues, for example, young male thigh and forearm skin with respective moduli of 1.99 and 1.51 kPa [11]. It is also comparable to the elastic modulus of

biomaterials considered as potential candidates for scaffolds in engineered soft tissue. Collagen sponge, for example, has an elastic modulus of 5 kPa at a concentration of 0.5–2.0%, but this can be increased to 20 kPa by cross-linking with glutaraldehyde [12, 13]. All these values, however, lie far below those used in the repair of bone or connective tissue which are in the range of 400 to 10 000 MPa [14–16].

The matrix modulus is low primarily because of the low volume fraction of the gel rather than because the individual fibers lack sufficient strength. This can be seen from a comparison of our estimate of the fiber modulus (0.6–23 MPa) to the fiber modulus for other polymers such as latex rubber and polybutadiene with moduli of 2.6 MPa and 1–50 MPa [8], respectively.

There are several approaches that could be considered to increase this material's strength and modulus. According to the scaling predictions of the cellular solids theory, the elastic modulus will increase roughly as the square of the peptide volume fraction, and the fracture strength by the 3/2 power. This suggests that one promising approach would be to investigate methods for increasing the solubility of peptide in water. Concentrations of up to 10 mg ml^{-1}, as used in the present tests, are easily achieved; higher concentrations, with EFK8 or another oligopeptide, are readily produced. The samples tested, however, exhibited a less strong dependence on concentration than predicted by the theory. One likely cause for this is the increasing degree of inhomogeneity observed as peptide concentration was increased. It remains to be seen, therefore, whether the increases suggested by the theory will actually be attainable. A second means of increasing the elastic modulus is through cross-linking, or otherwise increasing the strength of the intermolecular bonds. Cross-linking, for instance, can be accomplished by introducing multiple cysteine residues into the oligopeptide to allow for disulfide linkage via thiol groups. This approach is especially attractive because mechanical properties could then be controlled by biochemical kinetics. One example candidate peptide would be RADSRADC, based on one of the originally synthesized peptides RADn with $n = 8$, 16, 24, or 32. According to some preliminary molecular modeling, the alternating substitution of cysteine for serine does not affect the backbone geometry of the peptide so should not interfere with the self-assembly process.

The cellular solids model has also been used to analyze the elasticity of the intracellular F-actin matrix which exhibits close similarity to our peptide biomaterial in terms of microstructure and dimensions. In that work [9], the value for the elastic modulus predicted by the theory was roughly consistent with independent measurements. It should be noted, though, that while the present results lend some credence to the applicability of the cellular solids model for these materials, this approach neglects Brownian or entropic effects that could be important on these length scales. Indeed, one recent study [17] of tape-like structures ~ 0.7 nm thick and ~ 8 nm wide produced by gelation of a 24-residue oligopeptide used an entropic rubber elasticity model in their interpretation of the observed rheological properties. It is interesting to observe that the elastic modulus of a material characterized by rubber elasticity also exhibits a power law dependence on concentration, to a power of ~ 1.5–2.25 [18].

Acknowledgements

We would like to acknowledge the support of an Engineering/Biology Seed Grant from the MIT Center for Biomedical Engineering.

REFERENCES

1. A. S. Hoffman, *Artificial Organs* **16**, 43 (1992).
2. B. D. Ratner, *J. Biomed. Mat. Res.* **27**, 837 (1993).
3. J. G. Tirrell, M. J. Fournier, T. L. Mason and D. A. Tirrell, *Chem. Eng. News* 40 (19 December 1994).
4. R. Langer, *Ann. Biomed. Eng.* **23**, 101 (1995).
5. S. Zhang, T. Holmes, C. Lockshin and A. Rich, *Proceedings From the National Academy of Science USA* **90**, 3332 (1993).
6. S. Zhang, C. Lockshin, R. Cook and A. Rich, *Biopolymers* **34**, 663 (1994).
7. S. Zhang, T. C. Holmes, C. M. DiPersio, R. O. Hynes, X. Su and A. Rich, *Biomaterials* **16**, 1385 (1995).
8. L. J. Gibson and M. F. Ashby, *Cellular Solids*. Pergamon Press (1988).
9. R. L. Satcher and C. F. Dewey, *Biophys. J.* **71**, 109 (1996).
10. S. P. Timoshenko and J. N. Godier, *Theory of Elasticity*, 3rd edn. McGraw-Hill, New York (1970).
11. D. L. Bader and P. Bowker, *Biomaterials* **11**, 721 (1983).
12. M. Chvapil, *J. Biomed. Mater. Res.* **11**, 721 (1977).
13. M. Chvapil, *J. Biomed. Mater. Res.* **16**, 245 (1982).
14. J. Lawrence-Katz, L. L. Latta, S. Singh and H. S. Yoon, in: *Handbook of Biomedical Engineering*, J. Kline (Ed.), p. 460. Harcourt Brace Jovanovich, New York (1985).
15. K. James and J. Kohn, *MRS Bull.* (20 November 1996).
16. I. Engelberg and J. Kohn, *Biomaterials* **12**, 292 (1991).
17. D. A. Evans, N. J. Beukes and J. L. Kirschvink, *Nature* **386**, 262 (1997).
18. M. Doi and S. E. Edwards, *The Theory of Polymer Dynamics*. Clarendon, Oxford (1961).

Polymers for Tissue Engineering, pp. 19–52
Molly S. Shoichet and Jeffrey A. Hubbell (Eds)

Elastic protein-based polymers in soft tissue augmentation and generation *

DAN W. URRY [1,2,†], ASIMA PATTANAIK [1], JIE XU [1], T. COOPER WOODS [1], DAVID T. McPHERSON [1] and TIMOTHY M. PARKER [1]

[1] *Bioelastic Research, Ltd., OADI Technology Center, 2800 Milan Court, Suite 386, Birmingham, AL 35211-6912, USA*
[2] *Department of Chemical Engineering and Materials Science, 151 Amundson Hall, 421 Washington Avenue SE, University of Minnesota, Minneapolis, MN 55455-0132, USA and the Biological Process Technology Institute, 240 Gortner Laboratories, 1479 Gortner Avenue, University of Minnesota, St. Paul, MN 55108, USA*

Received 22 September 1997; accepted 6 February 1998

Abstract—Five elastic protein-based polymers, designed as variations of polymer **I**, $(GVGVP)_{251}$, elicited different responses when injected as subcutaneous implants in the guinea pig, a preclinical test used to evaluate materials for soft tissue augmentation and specifically for correction of urinary incontinence. All six polymers, prepared using recombinant DNA technology, expressed at good levels using transformed *E. coli* fermentation. These *E. coli*-produced polymers were purified for the first time to the exacting levels required for use as biomaterials where a large quantity could disperse into the tissues in a few days. Time periods of 2 and 4 weeks were used.

Polymer **I** functioned as a bulking agent around which a fine fibrous capsule formed. Inclusion of $(GVGVAP)_8$, a chemoattractant toward monocytes and elastin-synthesizing fibroblasts in the sequence of polymer **I**, resulted in an appropriate tissue response of invasion of macrophages. Inclusion of lysine residues, for lysyl oxidase cross-linking, suggested a possible remodeling of the implant toward fibers. Most promising however, when the cell attachment sequence, GRGDSP, was added to polymer **I**, the implant elicited tissue generation with a normal complement of collagen and elastic fibers, spindle-shaped histiocytes and angiogenesis. If this response is retained over time, the desired soft tissue augmentation and generation will have been achieved. Our working hypothesis is that on formation of elastin, with a half-life of the order of 70 years, a long lasting soft tissue augmentation would result rather than scar tissue as occurs with Contigen®, the currently approved injectable implant for soft tissue augmentation.

---

*This manuscript was initially written while the corresponding author was at the Laboratory of Molecular Biophysics, UAB School of Medicine, University of Alabama at Birmingham but was revised and completed after relocation of his academic efforts to the University of Minnesota, Twin Cities Campus. The work was performed at Bioelastics Research, Ltd.

†To whom correspondence should be addressed at Bioelastic Research, Ltd., 2800 Milan Court, Suite 386, Birmingham, AL 35211, USA.

Key words: Guinea pig model for soft tissue augmentation; elastic protein-based polymers; recombinant DNA technology, injectable implants; cell attachment sequences; chemoattractant peptide sequences; elastic fiber generation; long-lasting tissue reconstruction.

INTRODUCTION

Within the broad discipline of Biomaterials Science, the area of soft tissue augmentation and generation is one of enormous economic impact. Setting aside the aesthetic and often elective elements relating to improvement of facial and body contours and considering the more limited subspecialty involving urinary incontinence (UI), the impact is yet staggering. The prevalence of UI among 1.5 million nursing facility residents is reported to be 50%, and for the population at large over the age of 60 years, it ranges from 15% for men to 30% for women [1]. A "highly conservative estimate" of the medical care costs "for persons of all ages with incontinence is $7 billion annually in the community and $3.3 billion in nursing homes (based on 1987 dollars)" [1, 2].

The following report is presented and discussed with a focus on the correction of stress urinary incontinence (SUI), but its relevance is to the entire area of soft tissue augmentation, generation and reconstruction. The approach utilizes certain compositions of bioelastic materials, elastic protein-based polymers, produced by means of recombinant DNA technology. Depending on composition protein-based polymers can be inert periurethral bulking agents to provide sphincter support by enhancing urethral compression, or they can contain tissue active sequences with the potential for generation of stable, long lasting, and loose connective tissue. The combination of histology and the macroscopic appearance of a 'bump' under the skin constitute evaluations.

To the best of our knowledge, there is no animal model for establishing efficacy of a particular material in alleviating SUI. The approach is to perform subcutaneous injections in the chosen animal (commonly the rat or guinea pig) and to determine if there results a lasting 'bump', constituting a bulking effect. Clearly, the most desirable result would be for the injected material to induce a lasting generation of natural tissue without the retention of any foreign material. This report provides initial data on such a promising protein-based polymer composition, and on a range of protein-based polymer compositions and an associated spectrum of results. The challenge, that must be met in order properly to observe and characterize such a spectrum of results, is the demonstration of success in purification of the microbially-prepared protein-based polymers.

The challenge of purification

The elastic protein-based polymers are produced by *E. coli* fermentation [3]. Critically, it is essential to demonstrate success in purification with an elastic protein-based polymer comprised of an innocuous repeating peptide sequence that is imperceptible (stealth) in the tissues, that is, the polymer can be injected into

the tissue and disappear within two weeks time leaving no sign of its having been present, e.g. leaving no inflammatory response.

We begin with a particular composition of a *chemically-synthesized* elastic protein-based polymer which was neither seen as a foreign material by the tissues [4] nor by human monocytes *in vitro* [5], and was incapable of eliciting a significant immune response [6]. The next critical step is to demonstrate that the microbial product of the same composition can be purified to the same innocuous level. As will be shown in the present report, this challenge of purification is extreme, because it requires removal of trace amounts of *E. coli* contaminants to levels substantially less than 5 ppb. The strategy is then to introduce biologically active peptide sequences into the elastic protein-based polymers that can elicit different, desirable tissue responses. To make meaningful progress, the observed tissue response must be correctly ascribed to the added biologically active peptide sequence and not be the result of one or another microbial contaminant.

Purification of insulin for human use is reported to require a purity of 10 ppm [7]. When the microbially-produced protein product is used in large quantities as a biomaterial, however, the required purities become much greater. In fact, a purity of 5 ppb is still insufficient to prevent an inflammatory response to trace *E. coli* contaminants. When using subcutaneous injection of several tens of milligrams of polymer as the test for impurities, a determined purity of 5 ppb (on the basis of the immunological Western dot blot technique to detect impurities) still effects a significant inflammatory response using the microbially-prepared product whereas their is no inflammatory response for the same composition and dose of the chemically-prepared protein-based polymer. This exacting purification challenge, nonetheless, has been met for the basic composition, $(GVGVP)_{251}$. Furthermore, a microbially-prepared and subsequently purified elastic protein-based polymer is identified, here, which simply disperses without a trace in the histological sections at 2 weeks; this polymer becomes the gold standard for purity as, by dispersing in 2 weeks, it releases to the tissues its complete load of impurities with which to elicit inflammatory and pyrogenic responses. As the immunoblot technique is not sufficiently sensitive, the level of purity required for such an absence of inflammatory response in the *in vivo* subcutaneous test is to be established by radioactive labeling.

Previously considered materials

Biomaterials, previously given serious consideration as periurethral bulking agents for prevention of SUI, are polytetrafluoroethylene (PTFE) [8, 9], and a connective tissue component, bovine dermal collagen, treated to decrease immunogenicity [10, 11]. Autologous fat [12], sodium morrhuate [13], and paraffin [14] injected as bulking agents elicited unsatisfactory results. Additional materials have been reviewed by Canning [15]. Finally, injectable bioglass is being considered, but a 16 to 18 gauge needle appears to be required for injection [16].

While the initial use of PTFE indicated a 73% improvement rate for SUI [8], that initial promise was tempered by subsequent findings of distant particle migration to the lungs, liver, spleen, and brain with formation of foreign body granulomas [9]. Following extensive study and development of collagen, the product known as Contigen®, a glyceraldehyde cross-linked bovine dermal collagen, with reduced antigenicity and increased resistance to fibroblast-secreted collagenases, emerged as a promising material. The initial reports on Contigen® seemed promising with about 80% of the patients being either cured, greatly improved or improved after injection of Contigen® [10, 17]. While this report at the outset seemed impressive, a growing number of significant limitations require continued search for and development of additional materials. Some patients exhibit a hypersensitivity reaction following the required intradermal skin test [18], and are not suitable candidates for this therapy. The injection is reported to function as the result of a mild inflammatory response in which the injected collagen is joined by near equal amounts of host collagen over a period of about six months to result in formation of permanent scarring [17], which could complicate further efforts at treatment. Furthermore, as Contigen® "begins to degrade in 12 weeks and is completely degraded in 9 to 19 months," there is the need for repeated injections in about 20% of the successful cases within 2 years [19].

More current studies demonstrate more severe limitations of Contigen®. In a recent study of 187 women with SUI, Contigen®, the only FDA approved periurethral bulking agent for the correction of this problem, resulted in a 'cure' for only 25% of female patients, and the 'durability of cure of incontinence' decreased to 46% at 3 years [20]. This is a cure rate of 15% at 3 years. Similar limited success rates are reported for men following post-radical prostatectomy [21] and in the pediatric population [22]. A 25% cure rate at the outset and a 10–15% cure rate at 3 years clearly requires a new therapy for the great majority of patients troubled with SUI.

Desired properties of elastic protein-based polymeric materials

A relatively new family of biomaterials, elastic protein-based polymers, derives from a repeating sequence of mammalian elastins, $(GVGVP)_{11}$, which occurs as the longest sequence between cross-links of bovine elastin [23, 24]. Another interesting repeating sequence of elastin is the non-elastic sequence, $(GVGVAP)_n$, where n is 8 in human elastin with but three isomorphous substitutions [25]. The several desirable properties of a biomaterial for soft tissue augmentation are considered below.

Biocompatibility. Extensive biocompatibility studies have been carried out on the chemically synthesized protein-based polymers: poly (GVGVP) and its 20 Mrad γ-irradiation cross-linked matrix, X^{20}-poly(GVGVP) [4], on poly(AVGVP) and X^{20}-poly(AVGVP) [26], and on poly(GGAP) [27]. Poly(GVGVP) and poly(GGAP)

were found to exhibit extraordinary biocompatibility [4, 27] and poly(AVGVP) was found to exhibit good biocompatibility [26].

Perhaps most remarkably, using sensitive and sensitized Balb/c mice, a primary immunization using 200 μg of poly(GVGVP) in emulsion with complete Freund's adjuvant, followed by a secondary immunization using 200 μg of poly(GVGVP) in emulsified incomplete Freund's adjuvant, and finally boosted with a third immunization repeating the conditions of the second, failed to produce antigen-specific hybridomas. The use of two additional strains of mice (DBA and CB6 F1) similarly failed. As stated in the report of the results, "The preceding results suggest that certain protein-based (bioelastic) polymers, such as the elastic poly(GVGVP), appear to be incapable of eliciting a significant immune response" [6].

Also at the cellular level poly(GVGVP) appears to subdue cellular response of human macrophages indicating that this bioelastic material is not recognized as a foreign substance by these scavenger cells. Picciolo *et al*. [5] studied the responses of elutriated human monocytes to a series of biomaterials and found the background level of oxidative bursts to be decreased in the presence of poly(GVGVP) with and without the fibronectin GRGDSP cell attachment sequence whereas the usual response to a biomaterial was effectively to attack the material as a foreign substance with enhancement of oxidative bursts. The elastic protein-based polymers were not seen as a foreign material by the human macrophages, but rather they muted the background response exhibited in the test chamber.

Extrusibility. The polypentapeptides, such as the microbially prepared $(GVGVP)_{251}$, and the polytetrapeptides, such as the chemically synthesized poly-[0.6(GGVP), 0.4(GGFP)], are extrusible through 22 and even 27 gauge needles at 37°C immediately after having been dissolved at concentrations of 500 mg ml^{-1} and at 4°C. On standing at a temperature above that of a hydrophobic folding and assembly transition, e.g. at 37°C, for a period of time, of the order of hours, the polypentapeptide became too viscous for extrusion whereas the polytetrapeptide remained extrusible indefinitely. Obviously, an injectable implant must be extrusible.

Control of volume change after injection. The elastic protein-based polymers of interest here are soluble in water at all proportions at a sufficiently low temperature. On raising the temperature above a critical value, designated as T_t, they fold, assemble and phase separate into a more-ordered state of predetermined composition, of the order of 50% peptide/50% water by weight. This phase separation is an inverse temperature transition and the more-dense phase is called a coacervate. Thus as long as T_t is below 37°C, as it is for both of the polymers noted immediately above, the concentration of a solution can be prepared such that the volume will not change on injection as a periurethral bulking agent. When the injectable implant is functioning to induce tissue formation, then the entire tissue response must be followed to assess effect of resulting volume.

Potential to design for staying in place after injection. Chemically synthesized X^{20}-poly(GVGVP), when pure, appears to be ignored by the host and does not elicit fibrous capsule formation [28–30]. On the addition of phenylalanine (Phe, F) residues, however, fibrous capsule formation, without the development of inflammation, does occur for X^{20}-poly[0.75(GVGVP),0.25(GFGVP)] after implantation under the ocular conjunctiva of the rabbit eye [30]. Also, subcutaneous injections of poly[0.6(GGVP),0.4(GGFP)] elicit fibrous capsule formation. Thus, fibrous capsule formation could be used to fix the tissue augmentation at the injection site. With bioelastic polymers additional approaches may be considered for maintaining the material at the injection site; these include *in situ* cross-linking [31] and the inclusion of cell attachment sequences [32]. Both aspects are considered in the studies reported here.

Potential for long lasting augmentation. The issue of long-lasting soft tissue augmentation can only be determined by following the implants over sufficient time periods. What can be considered with elastic protein-based polymeric materials goes beyond the usual considerations of periurethral bulking agents and even of soft tissue augmentation and becomes tissue generation, or tissue reconstruction [6, 33]. In general, tissue reconstruction comes into play with an implant having the correct elastic modulus of the natural tissue and an implant that can induce the natural cells to enter and to function naturally at the site of planned reconstruction. If there is an elastic material of the proper elastic modulus that can become cross-linked to the surrounding tissues, into which the natural tissue cells can invade and attach and thereby sense the forces to which the tissue is subjected, then there is the potential for the natural cells to regenerate the tissue to sustain the forces required for the tissue to function appropriately. This draws on the principle of cellular tensegrity wherein the tensional forces sensed by the appropriate cells can induce the cells to elaborate an extracellular matrix sufficient to sustain those forces and can result in tissue reconstruction [6, 33, 34]. In short, fibroblasts do not attach and spread on X^{20}-poly(GVGVP), but they do attach, spread and grow to confluence when there are cell attachment sequences included in the polymer as previously found for the chemically synthesized polymer, poly[20(GVGVP),(GRGDSP)] [31, 34]. In the present report, the protein-based polymer, $[(GVGVP)_{10}GVGVPGRGDSP(GVGVP)_{10}]_{18}(GVGVP)$, has been prepared using recombinant DNA technology and subsequently cross-linked (see below). Such elastic matrices have been shown to support attachment, spreading and division of human uroepithelial cells with further elaboration of extracellular matrix (Pattanaik & Urry unpublished research).

The physical properties of bioelastic materials

Physical properties of bioelastic materials have been extensively reviewed at more [36, 37] and less [38] technical levels. Those reviews should be sought for a more fundamental understanding of the materials.

Present report

In the present report, six elastic protein-based polymers have been prepared using recombinant DNA technology, expressed at good levels by *E. coli* fermentation, and examined in the guinea pig model for the purposes of developing purification control standards and evaluating potential efficacy for correction of SUI in terms of 'bump' retention resulting from the injectable implant. The initial reference (or control) polymer, $(GVGVP)_{251}$, of these six compositions is known to be extraordinarily biocompatible based on extensive toxicity testing of the chemically synthesized polymer, poly(GVGVP) [4–6]. Four other polymers each contain an added compositional feature designed to elicit different specific tissue responses of interest in soft tissue augmentation. The roles of $(GVGVP)_{251}$, as the initial reference protein-based polymer, are several: (1) it is the interim standard against which our purification procedures for the microbial product are measured in order to approach the same innocuous state as found for the chemically prepared polymer; (2) it provides an initial reference for tissue response such that newly observed tissue responses may be ascribed to the added compositional feature of a new polymer; and (3) it serves as a possible periurethral bulking agent in its own right. The sixth polymer, because of its stealth character, i.e. its apparent total lack of eliciting an inflammatory tissue response, becomes the new purification standard against which future purifications of whatever composition can be measured without having always to rely upon expensive and time consuming animal model testing.

METHODS AND MATERIALS

Protein-based polymers to be considered in this report and their roles in the developing soft tissue augmentation approaches will be listed, as will be the methodology for their production, their physical and chemical characterization, and their *in vivo* testing procedures.

Protein-based polymers to be examined

*Polymer **I**. $(GVGVP)_{251}$.* This is the innocuous reference or initial control protein-based polymer for which extensive toxicity data has been obtained demonstrating extraordinary biocompatibility of the chemically synthesized polymer [4–6], i.e. poly(GVGVP) with a mean molecular weight of approximately 100 000 Da. The molecular weight of the microbial product, $(GVGVP)_{251}$, is 102 500 Da.

*Polymer **II**. (GVGVP-GVGVP-GVGVP-G<u>K</u>GVP-GVGVP-GVGVP)$_n$(GVGVP).* This sequence adds one enzymatically cross-linkable Lys(K) residue per thirty residues in a sequence for which the natural extracellular cross-linking enzyme, lysyl oxidase, is active [31].

Polymer ***III****. (GVGVP-GVGVP-GKGVP-GVGVP-GVGFP-GFGFP)*$_n$*(GVGVP).* This adds, in addition to the Lys(K) of polymer **II**, the hydrophobic Phe(F) residue, three per 30mer, which has been shown to induce fibrous capsule formation without significant inflammation when under the ocular conjunctiva of the rabbit eye [30]. Thus, enzymatic cross-linking *in situ* and fibrous capsule formation could function to keep such a bulking agent in place.

Polymer ***IV****. [(GVGVP)*$_{10}$*GVGVPGRGDSP(GVGVP)*$_{10}$*]*$_n$*(GVGVP).* This polymer adds the fibronectin GRGDSP sequence to polymer **I** with its well known RGD cell attachment sequence [6, 32, 39] and which has also been reported to be a chemoattractant toward fibroblasts [40].

Polymer ***V****. [(GVGVP)*$_{10}$*(GVGVAP)*$_8$*(GVGVP)*$_{10}$*]*$_n$*(GVGVP).* This polymer contains the repeating VGVAPG sequence and is a reported chemoattractant for fibroblasts and for monocytes [41] which on entering the tissues from the blood stream become macrophages. This repeat which recurs eight times in man [25] has been proposed *in vivo* to induce elastic fiber repair. Thus, it could add elastic fiber synthesis to the tissue response. Elastogenesis is considered important in achieving reconstruction of a loose connective tissue rather than dense scar tissue which has little or no elastic fiber [42].

Polymer ***VI****. (GVGVP-GVGVP-GVGVP-GEGVP-GVGVP-GVGVP)*$_n$*(GVGVP).* This polymer contains the Glu(E) residue with its ionizable carboxyl function to control the inverse temperature transition. Polymer **VI** can be purified to a level that makes it a gold standard for purity against which all other microbially prepared polymers can be compared.

Preparation of the elastic protein-based polymers

The preparation of the elastic protein-based polymers utilized gene construction, development of an expression system [43], fermentation and purification [3] as described below.

Gene construction. The basic monomer genes were first prepared to have appropriate cohesive ends, and then polymerization of the basic gene was carried out through the compatible cohesive ends generated by restriction endonuclease *Pfl*M1 digestion, and by subsequent ligation using DNA ligase to form multimers of the basic gene. This protocol was used when producing the six basic monomer gene sequences. The monomers were then concatemerized (polymerized) to form multimer genes with many different numbers of repeats, and many of the multimer genes have been expressed at high levels as will be briefly reported below. The gene for polymer **IV**, for example, encoding for eighteen repeats with a chain of 2003 residues has expressed with good yields.

The basic monomer gene for polymer **I** has been previously described [3]. Polymers **II**, **III** and **VI** are closely similar to polymer **I**. Accordingly, polymer **IV** will be given as the example of gene construction as described below.

Construction of the basic monomer gene for polymer **IV**, [$(GVGVP)_{10}$-GVGVP-GRGDSP-$(GVGVP)_{10}$], was a little more involved. First, the basic gene for $(GVGVP)_{10}$ was constructed such that a sequence containing the cell attachment site, G*RGD*SP, could be flanked on both sides by the basic $(GVGVP)_{10}$ gene. This was done as follows: The plasmid consisting of pUC118 containing the basic gene of $(GVGVP)_{10}$ was cleaved with restriction endonuclease *Pfl*M1 to release the gene fragments for purification. In addition, the resulting pUC118 plasmid with *Pfl*M1 ends, pUC-*Pfl*M1, was purified and used as the cloning vector for the subsequent gene constructs. For this polymer, a ligation reaction was performed including the *Pfl*M1 gene fragment and a synthetic double-stranded oligonucleotide encoding the GRGDSP cell attachment sequence. As illustrated with the sequence information below,

```
(PflM1)       Kpn1              Hinf1 (PflM1)
         TAGGGGTACCGGGTCGTGGTGACTCTCCGGGCG
      CGCATCCCCATGGCCCAGCACCACTGAGAGGCC
     G  V  G  V  P  G  R  G  D  S  P  G  ,
```

the GRGDSP oligo has 3-base 3′ extensions that are complimentary to the *Pfl*M1 ends of the gene fragments; however, upon ligation with the *Pfl*M1 ends, the *Pfl*M1 site is not restored at this junction. Notice also that the GRGDSP oligo provides one additional GVGVP coding sequence to the pentamer repeats. The above ligation mix was then digested with *Pfl*M1 to resolve the concatenated ligation products to the smallest units spanning the enzyme recognition sites. The digestion mix was then electrophoresed through a polyacrylamide gel where fragments of the appropriate size (333 bp) were purified by excision and electroelution. These *Pfl*M1 fragments were then cloned by ligating to pUC-*Pfl*M1. Clones representing the catemer gene for $(GVGVP)_{11}$GRGDSP$(GVGVP)_{10}$ were isolated and characterized. This catemer gene also has the *Pfl*M1 ends that allow their subsequent purification and concatenation as described below. DNA sequencing was performed to verify the sequence of the basic catemer genes that were constructed utilizing synthetic oligonucleotides. This was done, as has become our routine, using standard methodology of the 'Sequenase' kit from Amersham Life Science, Inc.

For the concatemer gene construction to produce polymer **IV**, the required large amount of the catemer (monomer) gene fragment was prepared by releasing the gene from plasmid pUC118 by cleavage with *Pfl*M1, separation by electrophoresis through a polyacrylamide gel, followed by electroelution from the gel. The gene fragments were then concatenated by ligation through the *Pfl*M1 ends in the presence of double-stranded oligonucleotide adaptors. These adaptors terminate further polymer growth from the ends that they adjoin and provide the terminal restriction endonuclease sites required for cloning the gene polymers, as follows:

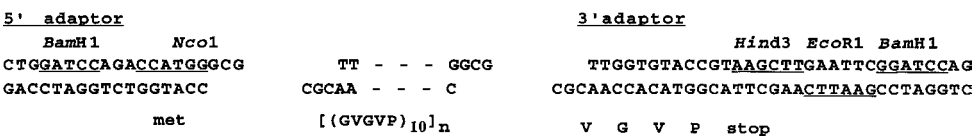

In this case, the concatenation ligation product was digested with *Bam*H1, mixed with *Bam*H1-cleaved pUC118 and ligase, and was inserted into *E. coli* by transformation. Concatemer clones were analyzed by restriction endonuclease digestion and electrophoresis versus known size standards, including a concatemer ligation ladder where it was possible to count from the basic gene in multiples of this gene right up to the particular isolated concatemer size. Following this protocol, the gene for polymer **IV** was successfully constructed, with an n as large as 18, i.e. $[(GVGVP)_{10}GVGVPGRGDSP(GVGVP)_{10}]_{18}(GVGVP)$ with 2003 residues and expressed in good levels. The polymer **IV**, used for the injectable implant studies, however, had an n of 7.

Gene expression. The pET plasmids (Novagen, Inc., Madison, WI, USA), for instance pET-11d, were used for expression of the concatemer genes described above. These plasmids are part of the T_7 expression system [41] that utilize the T_7 phage RNA polymerase in conjunction with a T_7 promoter to drive recombinant gene expression. This system has been used extensively by this laboratory, and in particular to express the concatemer genes of some one hundred polymers. For each of the concatemer genes, the gene fragment was released from the pUC118 plasmid by cleavage with *Nco*1 and *Bam*H1 and purified. It was then cloned into the pET plasmid at the *Nco*1 and *Bam*H1 sites placing the initiator ATG codon of the concatemer gene immediately adjacent to the T_7 promoter and ribosome binding sequences.

Expression of the concatemer genes was analyzed following bench-scale culture and induction with or without the inducer IPTG. Crude culture cell lysates, taken pre- and post-induction, were electrophoresed on an SDS-polyacrylamide gel (SDS-PAGE) and viewed following staining of the gels with $CuCl_2$. In addition, the proteins expressed from these small-scale cultures were purified following the procedures described below and included in the SDS-PAGE analysis.

Fermentation. Fermentations were performed, as required, to obtain adequate quantities of the elastic protein-based polymers for characterization as injectable implants in the guinea pig. Basically, either Luria broth (LB) or Terrific Broth (TB) media was used, and the production of the protein-based polymers was induced with the addition of the inducing agent, IPTG. After the appropriate number of hours of growth, the culture was harvested by centrifugation and cells disrupted by means of a French press to release the cell contents. Using favorable conditions, $(GVGVP)_n$ polymers have been expressed to the extent that 80% of the *E. coli* cell volume is occupied by bioelastic polymer inclusion bodies [44].

The fermentations were done in either a 28-l or a 500-l New Brunswick fermentor (wherein the latter has a working volume of 375 l) with appropriate air flow, agitation rate and temperature controls. The 28-l fermentor was used for polymers **II**, **III**, **IV**, **V** and **VI**, and the 500-l fermentor was used for polymer **I**. In all cases, yeast extract and tryptone based media were used in the presence of 100 $mg\,l^{-1}$ ampicillin, and the cultures were grown for about 36 h before harvesting by centrifugation. After resuspension in deionized H_2O, cells were disrupted either by French press for polymers **I**, **II**, **IV**, **V** and **VI**, or guanidine hydrochloride for polymer **III** to release the cellular contents. The polymers were conveniently purified from cell lysate employing their inverse temperature transitional properties.

Purification. The purifications utilized the class 10 000 clean room facilities of Bioelastics Research Ltd. and followed GLP protocols under development. They were carried out utilizing the methodology whereby the protein-based polymers can be conveniently purified from the culture lysate based on their fundamental inverse temperature transitional properties [3]. The cell lysate was cooled to 4°C and centrifuged at high speed to remove the insoluble material. The protein-based polymers form large aggregates and undergo the phase separation (coacervation) when the supernatant fraction is either warmed to 37°C, or exposed to high concentration of salt (NaCl) or subjected to a pH change, depending upon their composition. The protein-based polymer was then removed by centrifugation and brought back into solution under the appropriate conditions. Repeating this process several times results in a protein-based polymer with no apparent evidence of other proteins, when using the Western blot technique with a sensitivity of 1 ppm. As will be seen below on injection in the guinea pig model, however, this stage of the preparation, called the bulk preparation, gives a substantial inflammatory reaction. Several steps of purification are yet required to have the stage of purification desired. For the Lys(K)-, Glu(E)-, and G<u>RGDS</u>P-containing polymers, **II**, **III**, **IV**, and **VI**, of interest here, the variable of pH was used to achieve the differential phase separations that are central to the purification process.

Endotoxins, removal and determination of levels. Several gram quantities of protein-based polymer of different compositions were prepared as follows. After centrifugation, the samples were dialyzed to remove any residual salts and then lyophilized to determine initial yield. The solution was then passed under pressure through a 0.2-μm membrane as a pre-filtration step and then through a sterile bench-top Amicon ProFlux M12 tangential flow ultrafiltration apparatus employing a 100-kDa spiral wound cartridge, passing polymer and retaining larger membrane-containing endotoxin. The solutions were then lyophilized and the protein-based polymers tested at concentrations of 20 $mg\,ml^{-1}$ for endotoxin levels using the Associates of Cape Cod, Inc. Pyrotell Limulus Amebocyte Lysate (LAL) test.

The endotoxin levels for the polymers as used for the *in vivo* testing for the two week and the four week studies are given in Table 1 both on a per mg and a per

Table 1.
Endotoxin levels for 2-week and 4-week studies

Polymer	Endotoxin levels 2-week study (Eu/mg)	Endotoxin levels 2-week study (Eu/injection site)	Endotoxin levels 4-week study (Eu/mg)	Endotoxin levels 4-week study (Eu/injection site)
I	< 0.0125	< 0.27	< 0.0015	< 0.05
II	< 0.003	< 0.10	< 0.0125	< 0.38
III	< 0.06	< 1.45	< 0.003	< 0.08
IV	< 0.0125	< 0.44	< 0.25	< 8.75
V	< 0.003	< 0.07	< 0.0125	< 0.38
VI	< 0.003	< 0.08	< 0.0015	< 0.05

Concentration of 1736: 300 mg ml^{-1}, extrusible through 23 gauge needle.

100 μl injection basis, i.e. for the specific quantity of polymer injected. All but polymer **III** of the 2-week study and polymer **IV** of the 4-week study were purified to acceptable endotoxin levels.

Acceptable endotoxin unit (EU) levels are due to the *Guideline on Validation of the Limulus Amebocyte Lysate as an End Product Endotoxin Test for Human and Animal Parenteral Drugs, Biological Products, and Medical Devices*, from the Centers for Drug Evaluation & Research, Biological Evaluation & Research, Devices & Radiological Health and Veterinary Medicine.

Trace impurities of E. coli *protein, removal and determination.* The issue of removal of trace amounts of *E. coli* proteins was approached by a series of steps with the purpose of determining those procedures that would be sufficient for adequate lowering of reactivity to protein impurities. Utilizing a series of purification steps beyond the bulk preparation level, the effectiveness of five purification steps of all the polymers was determined by two methods: Western dot blotting and animal implant studies.

Western blotting. Using the supernatants of lysed *E. coli* strain BL21(DE3) as the positive control, polymers **I**, **II**, **IV**, and **V** (5 μg per well) were resolved on a 12.5% SDS-PAGE gel followed by transfer to the nitrocellulose membrane. After blocking with 5% non-fat milk followed by three washes with buffer, the membranes were incubated with polyclonal rabbit anti-*E. coli*-IgG (primary antibody) followed by three washes. Then the membranes were incubated with biotinylated anti-rabbit-IgG (secondary antibody) followed by three washes. The highly sensitive amplified alkaline phosphatase detection procedure (BioRad) was followed to detect the antigens (i.e. the trace *E. coli* protein). With the detection limit of 5 pg, it was not possible to detect the antigen on any of the polymer lanes (3–10) although the detection of the positive control (lane 1) and the molecular weight markers (lane 2) were demonstrated to be satisfactory (see Fig. 1A). Following the same protocol, a strong band for polymer **III** was detected (Fig. 1B). The molecular weight of this band overlaps to the size of polymer **III**. This positive response to polymer **III** in

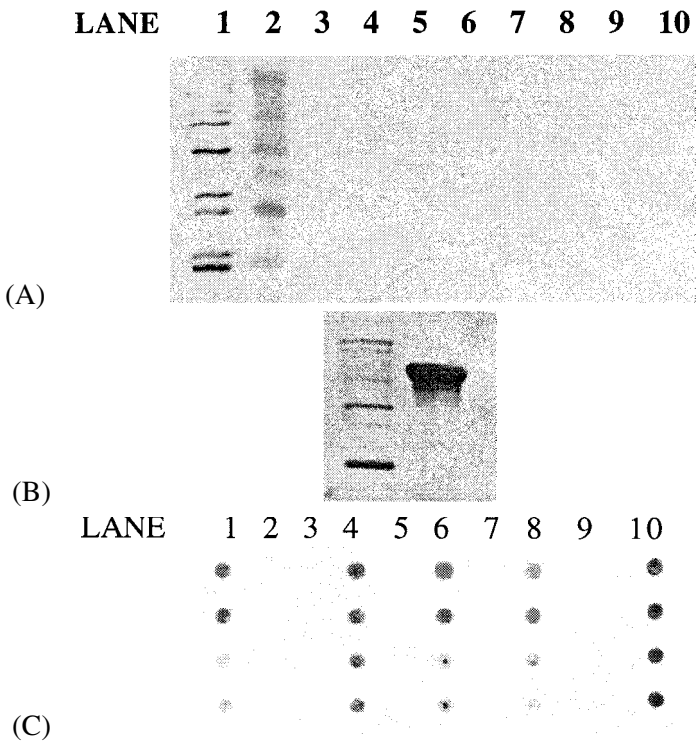

Figure 1. (A) Western blot assay — lane 1: positive control; lane 2: molecular weight marker; lanes 3–6: polymers **I**, **II**, **IV**, and **V** (5 μg per well), respectively. (B) Western blot assay — lane 1: positive control; lane 2: polymer **III** (5 μg per well). (C) Dot blot assay — lanes 1, 4, 6 and 8: polymers **I**, **IV**, **V**, **II** (1 mg per well), respectively; lane 10: positive control; lane 2: negative control; lanes 3, 5, 7 and 9: further purified polymers **I**, **IV**, **V** and **II** (1 mg per spot), respectively.

Fig. 1B could be due to cross-reactivity of the polymer with antibody or due to *E. coli* antigen bound to the polymer.

In order to gain more sensitivity, the BioRad dot-blot assay was followed so that more polymer could be loaded at a single spot with all of the trace protein impurities located at that spot. In Fig. 1C, by using 1 mg of sample per well, the antigens on the polymer lane 1 (polymer **I**), lane 4 (polymer **IV**), lane 6 (polymer **V**), lane 8 (polymer **II**), and lane 10 (positive control) were detected to a reasonable amount. However, the antigens were undetectable on addition of a single further purification step as demonstrated in lane 3 (polymer **I**), lane 5 (polymer **IV**), lane 7 (polymer **V**) and lane 9 (polymer **II**) similar to the negative control (lane 2). This demonstrates a level of purification to better than 5 ppb.

The detection of trace amounts of *E. coli* protein contaminant (below 5 pg per 1 mg of polymer, i.e. less than 5 ppb), or any other cellular components (DNA, carbohydrates, lipids, etc.) is not possible by Western blotting. Yet further purifications are required for polymer **I** based on the tissue responses observed in the injection implant sites of the guinea pig (see below).

Physical and chemical characterization

Proton nuclear magnetic resonance data (NMR, one- and two-dimensional). The one-dimensional proton nuclear magnetic resonance data for four (polymers **I**, **II**, **IV** and **V**) of the six elastic protein-based polymers are given in Fig. 2, where purity is demonstrated to the 1% level capable by this methodology. Due to the limitations on space, only the two-dimensional map given for polymer **III** is seen in Fig. 3, where the complete sequence of the basic repeating unit is verified. Thus, two-dimensional proton NMR provides for verification of the sequences of the basic repeating unit. The number of repeating units is then determined by mass spectrometry at the protein product level as a backup to the gene ladder which derives from the recombinant DNA technology.

Mass spectrometry. As determined by MALDI-TOF (matrix assisted laser desorption ionization – time of flight) mass spectrometry, the molecular weights of the microbially prepared polymers are:

I: $(GVGVP)_{251}$, 102 500 Da;

II: (GVGVP-GVGVP-GVGVP-G<u>K</u>GVP-GVGVP-GVGVP)$_{36}$(GVGVP), 90 800 Da

III: (GVGVP-GVGVP-GVGVP-G<u>K</u>GVP-GVG<u>F</u>P-G<u>F</u>G<u>F</u>P)$_{22}$(GVGVP), 55 400 Da

IV: [(GVGVP)$_{10}$GVGVPG<u>RGD</u>SP(GVGVP)$_{10}$]$_7$(GVGVP), 64 300 Da

V: [(GVGVP)$_{10}$(<u>GVGVAP</u>)$_8$(GVGVP)$_{10}$]$_5$(GVGVP), 60 300 Da

VI: (GVGVP-GVGVP-GVGVP-G<u>E</u>GVP-GVGVP-GVGVP)$_{36}$(GVGVP), $\sim$ 89 000 Da

Representative mass spectra are given for polymers **IV** and **V** in Fig. 4.

T_t *in physiological saline.* The values of T_t were determined using 40 mg ml^{-1} solutions of polymer, and the temperature was scanned at the rate of 30°C h^{-1} from 0 to 20 or 30°C above the onset of turbidity. The value of T_t is then defined as the temperature at which half-maximal turbidity is obtained. The value for the polymers are the following: polymer **I**, 25°C; polymer **II**, 39°C; polymer **III**, 4°C; polymer **IV**, 29°C; polymer **V**, 28°C; and polymer **VI**, 58°C at pH 7.3 in phosphate buffered saline and 20°C at pH 3.

Coacervate concentration and extrusibility. Coacervate concentrations (the natural concentrations of the polymers under physiological conditions) of all of the polymers, **I** through **V**, are of the order of 400 mg ml^{-1}. The concentrations that were extrusible through 23 gauge hypodermic needles after the 2.5 Mrad sterilization to prevent bioburden were: **I** 214; **II** 322; **III** 242; **IV** 350; **V** 233; and

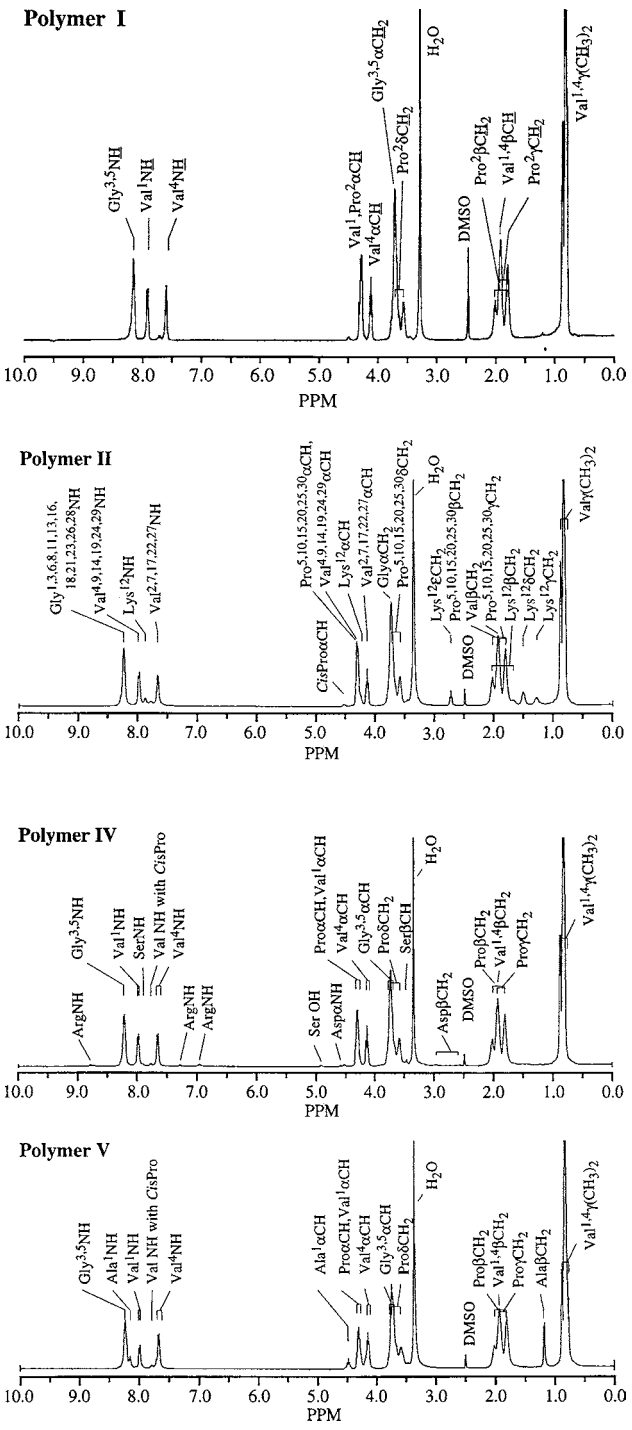

Figure 2. 1D NMR map of polymers **I**, **II**, **IV** and **V**.

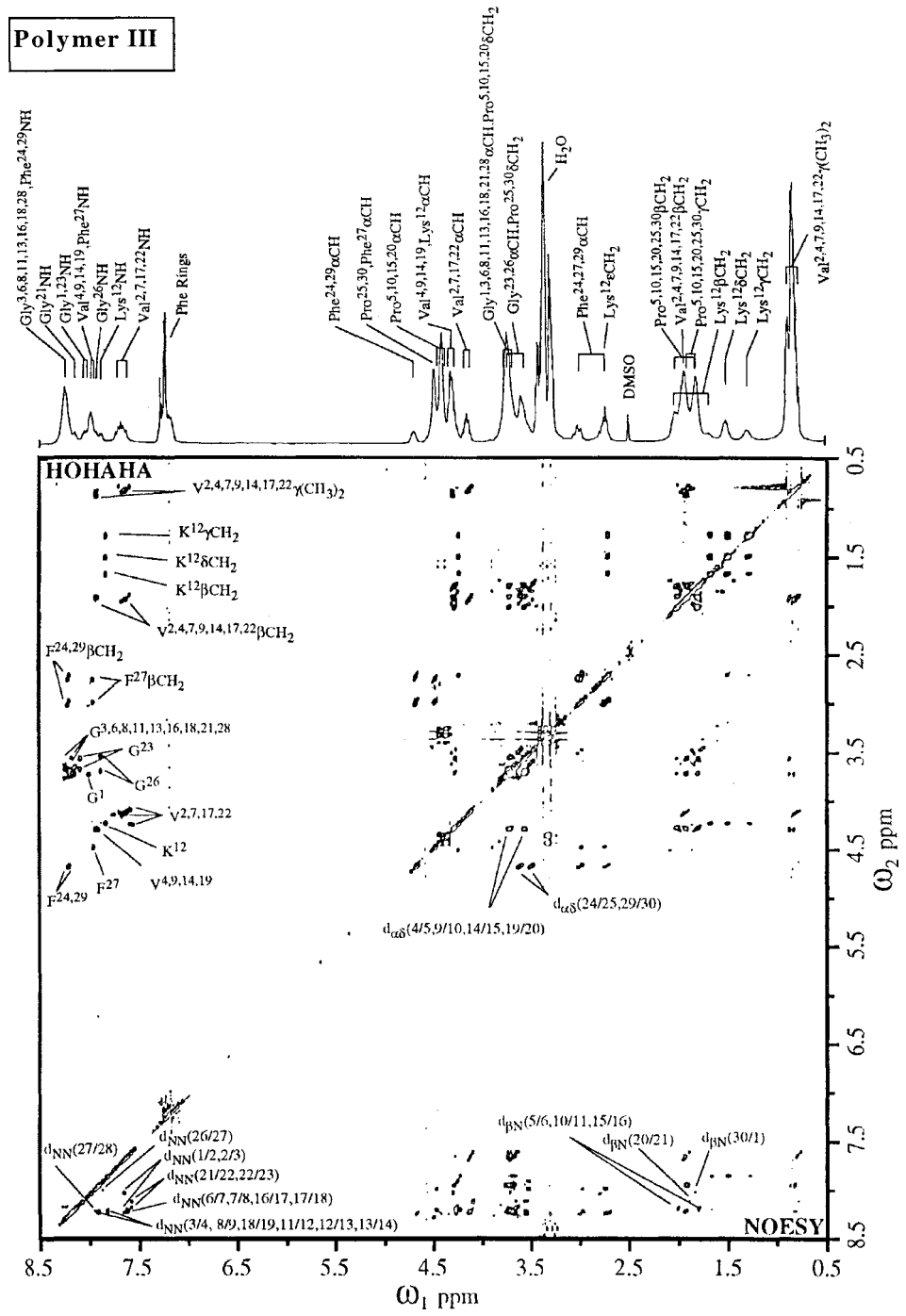

Figure 3. Two dimensional NMR map of polymer **III**.

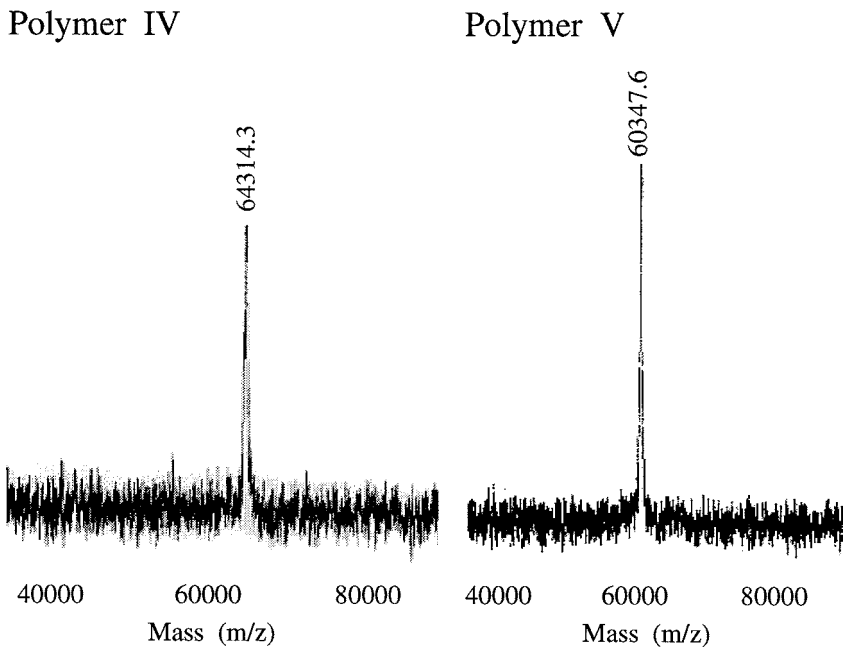

Figure 4. Mass spectra of polymers **IV** and **V**.

VI 300 mg ml^{-1}. The advantage of extrusibility of these high concentrations is that the volume filling result of the injectable implant would exhibit a more limited volume change due to water removal into the tissues in the short term following injection. The collagen injections are commonly at concentrations of less than 50 mg ml^{-1} where substantial volume loss due to water uptake occurs.

*Acid–base titrations to determine p*K$_a$ *values as relevant.* For the methodology for carrying out the acid–base titrations please refer to previously published data on related polymers [45]. The three polymers with potentially interesting pK_a values are polymers **II**, **III** and **IV**; these values are 9.8, 9.1, and, 4.4, respectively.

In vivo *evaluation of elastic protein-based polymers as injectable implants*

In vivo evaluation of the designed and microbially-prepared elastic protein-based polymers involves a two stage procedure. The first stage is to determine what purification steps are required of the microbially-prepared $(GVGVP)_{251}$ to reach the same innocuous level of tissue response as previously obtained for the extensively characterized, chemically-prepared poly(GVGVP). This was done with a series of stepwise purified microbial $(GVGVP)_{251}$ preparations. The essential result is that it is possible to purify the microbial product to the level of purity of the chemical product. Significantly, however, the required purity goes beyond that which can be followed by Western blot techniques. Accordingly, at this stage the animal response to the injected implant was the final determinant of purity.

The second stage in the evaluation of the microbially-prepared elastic protein-based polymers utilized the same steps to purify the other five polymers as required for purification of the parent polymer **I**, $(GVGVP)_{251}$. This is complicated by the added functionalities which alter to variable extents the ease of employing the same steps as for polymer **I**. As we will see, the approach has been fruitful.

The *in vivo* testing was carried out by NAmSA® of Northwood, OH, USA. The injectable implant animal model was the guinea pig, strain Crl:(HA)BR from the Charles River Laboratories. The fur was clipped free along the left and right flanks to provide for three injection sites on each side of the animal, and six different materials were used with each animal. The control was cottonseed oil and the injection volumes for each test material and control were 100 μl. For both the 2- and 4-week studies, all sites were examined at 4 and 8 h and every 24 h thereafter for erythema and edema. In no case for the 2-week study was edema apparent, and the numerical scale for erythema was 0, no erythema; 1, very slight (barely perceptible); 2 well-defined (pink); 3, moderate to severe (red); and 4, severe (beet redness) to slight eschar formation (injuries in depth). At the 2- and 4-week termination times, all sites were examined for histopathology.

*Injectable implants to develop polymer **I** purification procedures.* The polymer preparations for the development of purification procedures utilized five different progressive steps of purification of polymer **I**, $(GVGVP)_{251}$. The protein-based polymer samples were seven in total: six samples of the same microbially-prepared protein-based polymer, $(GVGVP)_{251}$, at different stages of purification; these are designated as A, B, C, D, and E, and the so-called bulk sample, F, which was at the stage of Fig. 1A above, and the seventh sample was the chemically-synthesized poly(GVGVP), sample G. The rating of the histopathology from greatest to the least degree of inflammation (panniculitis) was $F \gg B > A > C = D > E = G$. This evaluation was carried by the NAmSA® pathologist who had no knowledge of the nature of the samples and their purpose. Quoting from the pathologist's report "Test articles E and G were, therefore, the least likely to produce an inflammatory response". As test article E was the most purified microbially-prepared polymer **I**: $(GVGVP)_{251}$ and G was the chemically-synthesized and purified poly(GVGVP) which had been shown by extensive toxicity testing to exhibit an extraordinary biocompatibility, purification of the microbially-prepared $(GVGVP)_{251}$ reached a level of purity comparable to that of the chemically-prepared poly(GVGVP). This methodology development was considered necessary for use as an injectable implant for the correction of SUI. Instead of simply inducing scarring, our approach is to achieve the desired tissue response by introducing sequences with special interactional capacities with the cells and cell products of the extracellular matrix.

It is useful to recall here on the basis of the Western dot blot technique discussed above with a sensitivity of 5 pg mg^{-1} of protein-based polymer that no differences were detectable in the levels of purification among samples A, B, C, D, and

E, and yet there occur crucial differences in the tissue responses (i.e. in the biocompatibility) of the samples as judged by the inflammatory responses to the injectable implants.

RESULTS

Injectable implants for the comparison of the six test compositions at 2 weeks

Before describing in some detail the 2-week results of three of the six protein-based polymers (**I** through **IV**), a few general comments and comparisons should be made. In all cases there was no edema reported; the rating for erythema never exceeded 1 for any of the test compositions, i.e. a very slight (barely perceptible) erythema, and the results were similar for the Control, cottonseed oil. Polymer **III** which exhibited a detectable impurity at the Western blot level of characterization for the 2-week sample (see Fig. 1B) presented with the most marked acanthosis and dermatitis, yet with no significant neofibrosis, because of this a purer sample of polymer **III** was selected for characterization after 4 weeks of implantation (see below).

To quote from the pathologist's report, "Reactive fibrosis was not particularly prominent within any of the sites but was present to the greatest degree in the Group E (polymer **IV**) injection sites", and further, "Group C (polymer **I**) injection sites were relatively non-inflamed, and the Group G (polymer **VI**) injection sites were less inflamed than the Control (cottonseed oil) injection sites". Polymer **VI** is the least reactive, most innocuous of the microbially-prepared protein-based polymers. Polymer **VI**, therefore, becomes the purification standard for microbially-prepared protein-based polymers. Radiolabeling studies are planned to detect trace *E. coli* impurities in the preparation of polymer **VI**; these results will set the standard for the acceptable levels of impurities in the other purifications.

For the necessary brevity of this report, only representative histological prints (at low and higher power) of four of the thirty sites will be included as Figs 5–9. These will be Fig. 5 for the original Control, cottonseed oil; Fig. 6 for polymer **I**; Fig. 7 for polymer **IV**; Fig. 8 for polymer **V**; and Fig. 9 for **VI**. All tissue sections at the two week study were stained with hematoxylin and eosin, and the following descriptions are taken in major part from the NAmSA® pathologist's report.

Another element central to the efficacy for soft tissue augmentation is 'bump' size visible under the skin, and particularly, the retention of 'bump' size with time. Accordingly, greater comparison will be given 'bump' size in discussion of results for the 4-week time period.

Control. Figure 5A is a medium power (× 108) photomicrograph of the deep dermis and subcutis of a control (cottonseed oil) injection site. Most of the clear spaces are fat cells. Those spaces which are slightly larger in size and have slightly thicker walls represent injection site cysts containing cottonseed oil (e.g. the largest being seen left of center). Figure 5B is a high power (× 430) photomicrograph

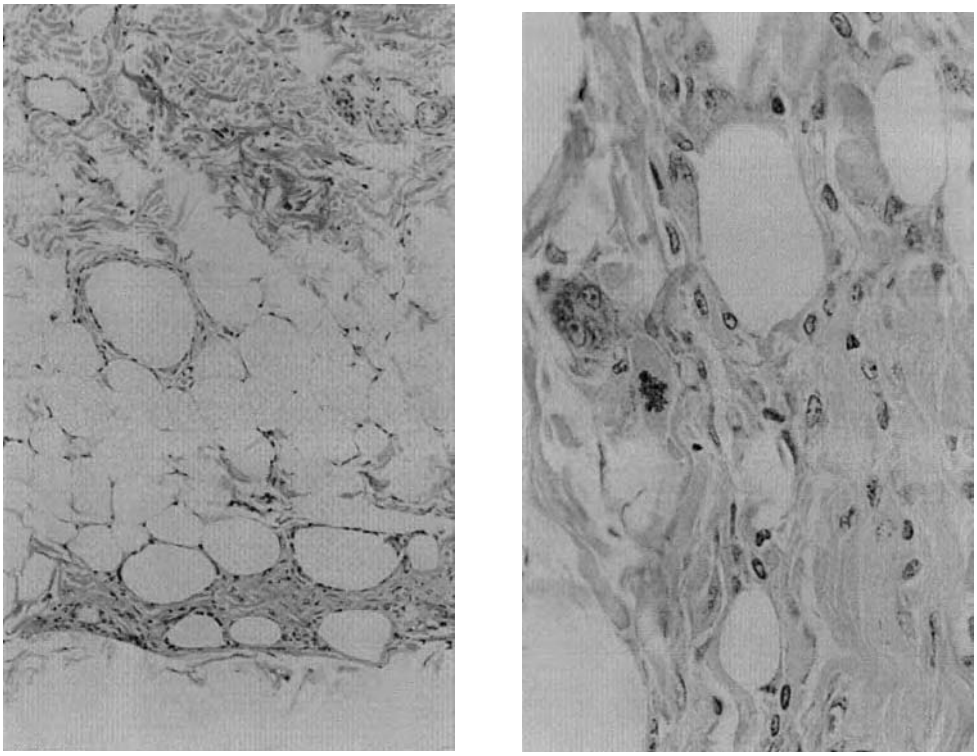

(A) (B)

Figure 5. Hematoxylin and Eosin stained photomicrograph of deep dermis of control site: (A) medium power (× 108); and (B) high power (× 430).

of the subcutis of the same control site as depicted in Fig. 5A. The newly formed collagenous connective tissue is moderately cellular and characterized by thinner collagen fibers than those seen in mature collagenous connective tissue. A mitotic figure, probably within a fibroblast or histiocyte, is present to the left of center.

*Polymer **I**.* Figure 6A is a low power (× 43) photomicrograph of the dermis in an area injected with polymer **I**, the parent polymer. Even at this lower magnification the polymer-containing cyst is too large to fit into the field. The entire polymer cyst is surrounded by a fine fibrous capsule. Figure 6B is a high power (× 430) photomicrograph of the thickest portion of the wall of the cyst shown in Fig. 6A. Only a narrow zone of elongated cells, either flattened histiocytes or fibrocytic cells, forms the wall of this cyst with little evidence for inflammation. Particles and/or air bubbles of variable size are seen within the cyst.

*Polymer **IV**.* Figure 7A is a low power (× 43) photomicrograph of the deep subcutis, deep to the panniculus carnosus. Note the band of muscle fibers on

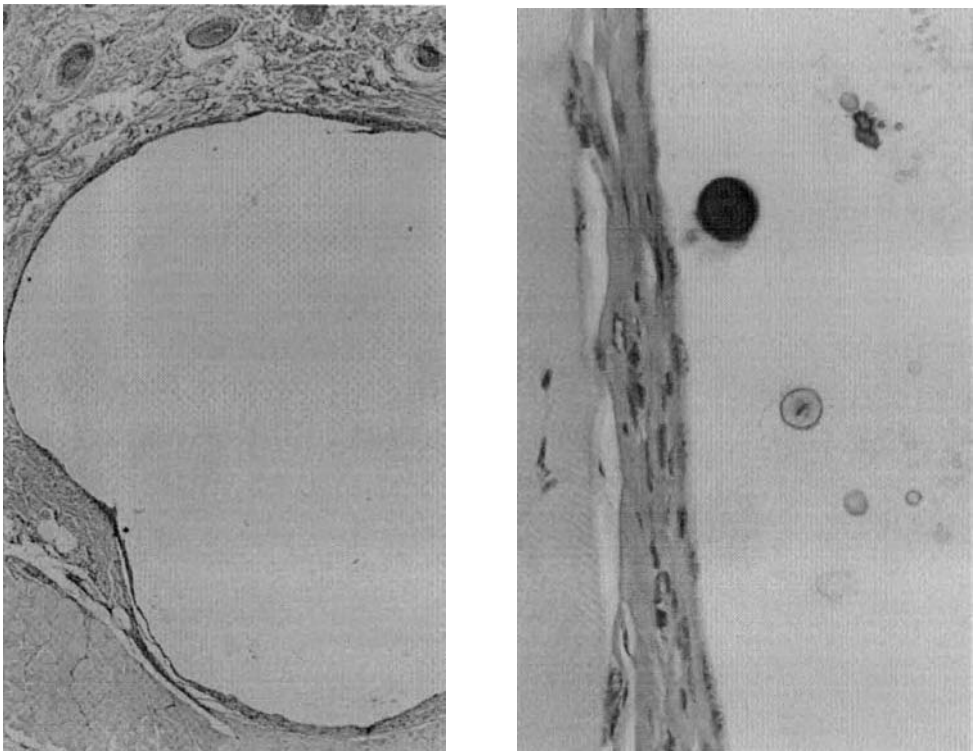

(A) (B)

Figure 6. Hematoxylin and Eosin stained photomicrograph of dermis of the site injected with polymer **I** (A) low power (× 43); and (B) high power (× 430).

the right side of the photomicrograph. As the result of injection of polymer **IV**, the subcutaneous fatty tissue is replaced by multifocal to confluent infiltrates of inflammatory cells and spindle-shaped fibroblasts or fibrocytic cells. Figure 7B is a high power (× 430) photomicrograph of another area of the panniculus from the same injection site as shown in Fig. 7A. In this area only a minimal degree of inflammation is present, but moderate numbers of spindle-shaped cells consistent with fibroblasts are evident. At this time only small amounts of collagen have been formed, and this collagen is rather pale in staining character. Note also the small capillary representing angiogenesis at the bottom center of the photomicrograph. Remarkably, the only compositional difference between the polymer **I** of Fig. 6A and B and the polymer **IV** of Fig. 7A and B is the addition of a peptide sequence toward which fibroblasts are chemotactic and to which fibroblasts attach, spread and grow to confluence, and the dramatic difference in the tissue response is consistent with the introduction of such a biologically active peptide sequence.

The injection sites of polymer **IV**exhibit the largest 'bumps' even though there is minimal residual material apparent as cysts in Fig. 7A and none in Fig. 7B. The entire field of Fig. 7A represents the development of new tissue with an apparent

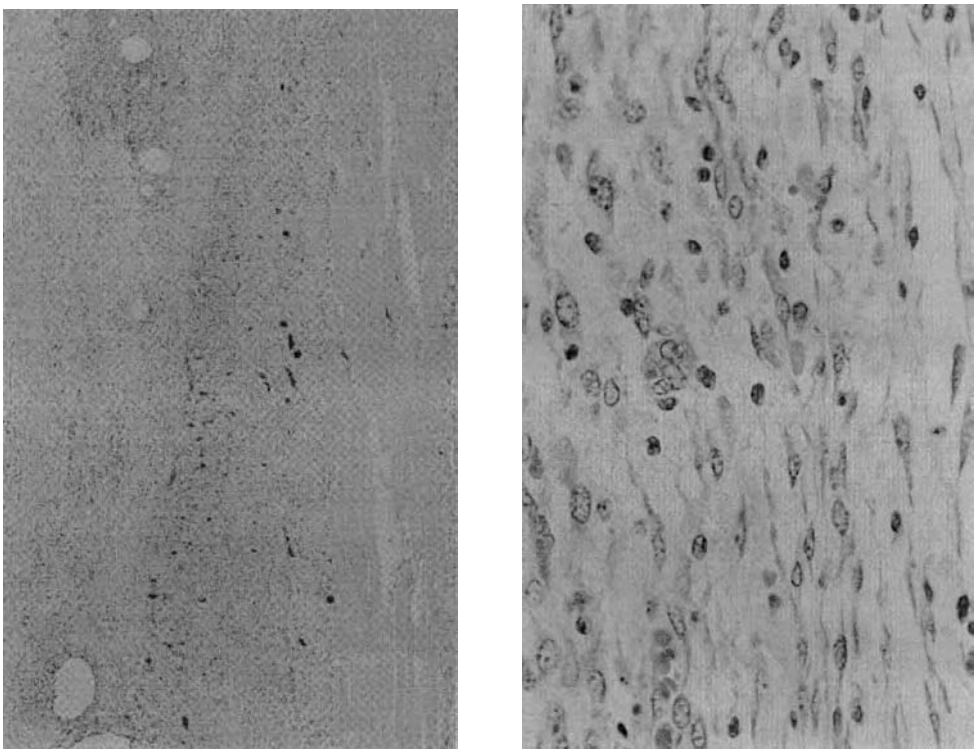

(A) (B)

Figure 7. Hematoxylin and Eosin stained photomicrograph of dermis of the site injected with polymer **IV** (A) lower power (× 43); and (B) high power (× 430).

normal distribution of elastin and collagen fibers. This indicates the preferred result of significant soft tissue generation.

Polymer V. Figure 8A is a low power (× 43) photomicrograph of the dermis and subcutis showing numerous irregularly-shaped cysts and rather diffuse inflammation within both the subcutis and dermis, yet neutrophils are limited in number. The skeletal muscle layer present deep to the subcutis is at the bottom of the micrograph. Figure 8B is a high power (× 430) photomicrograph of the deep subcutis characterized by inflammatory cell infiltrates and by scattered spindle-shaped cells and fine strands of collagen indicative of a possible early neofibrotic reaction. This polymer **V** differs from polymer **I** by the addition of a sequence that repeats eight times in human elastin, that has been shown to be a chemoattractant toward monocytes (which on leaving the blood and entering the tissues become macrophages) and toward fibroblasts differentiated for elastin synthesis, and that is thought to function in inducing fibroblasts into areas of injured elastic fibers to begin repair. Again, the tissue appears to be responding selectively to the compositional variation introduced into the elastic protein-based polymer.

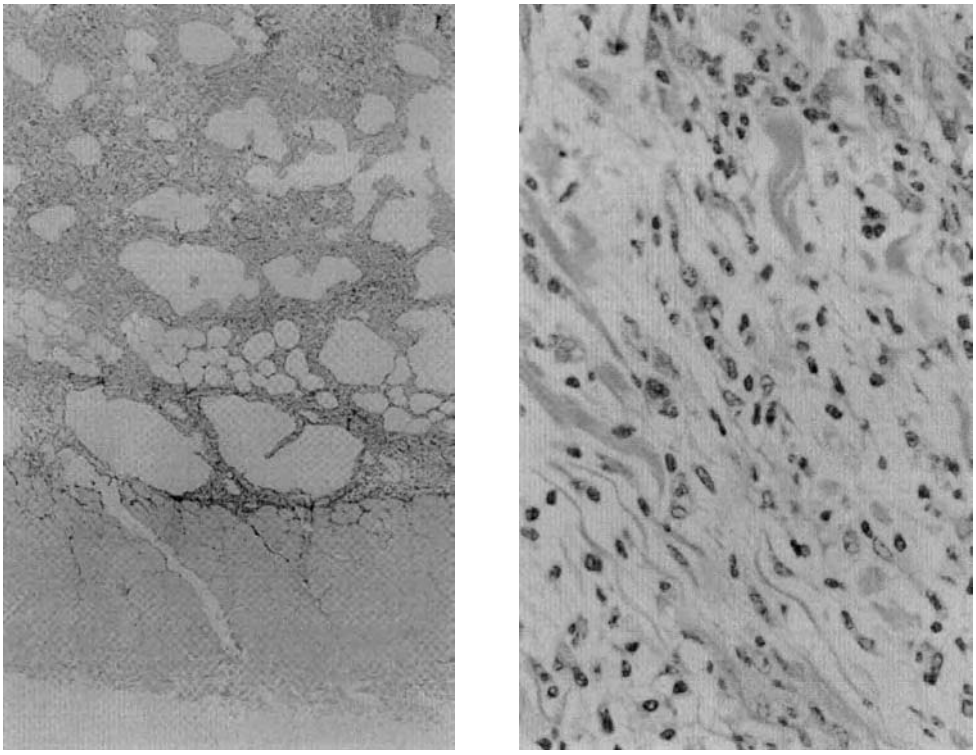

(A) (B)

Figure 8. Hematoxylin and Eosin stained photomicrograph of dermis of the site injected with polymer **V** (A) lower power (× 43); and (B) high power (× 430).

As will be discussed below, the synthesis of elastin can be the key factor in the generation or reconstruction of stable loose connective tissue rather than scar tissue where there are few if any elastic fibers.

*Polymer **VI***. Figure 9 contains medium power (× 108) photomicrographs of the dermis and subcutis of four different sites injected with approximately 30 mg each of the elastic protein-based polymer (GVGVP-GVGVP-GVGVP-GEGVP-GVGVP-GVGVP)$_n$(GVGVP). The sections of Fig. 9 were selected to show the most inflammatory regions of each site. In all of the sites there was no remaining trace of the implant, and normal tissue was observed. In two of the sites no inflammatory cells could be found (Fig. 9B and D). In another two sites, the most inflammation that could be found was the extremely limited reaction of Fig. 9A and C.

Of the approximately 30 mg injected per site, all of the material with its entire load of endotoxin and trace *E. coli* impurities were released to the tissue and yet there resulted no significant inflammatory response. This represents perhaps the most stringent test of purification, and, therefore, this sample becomes the target

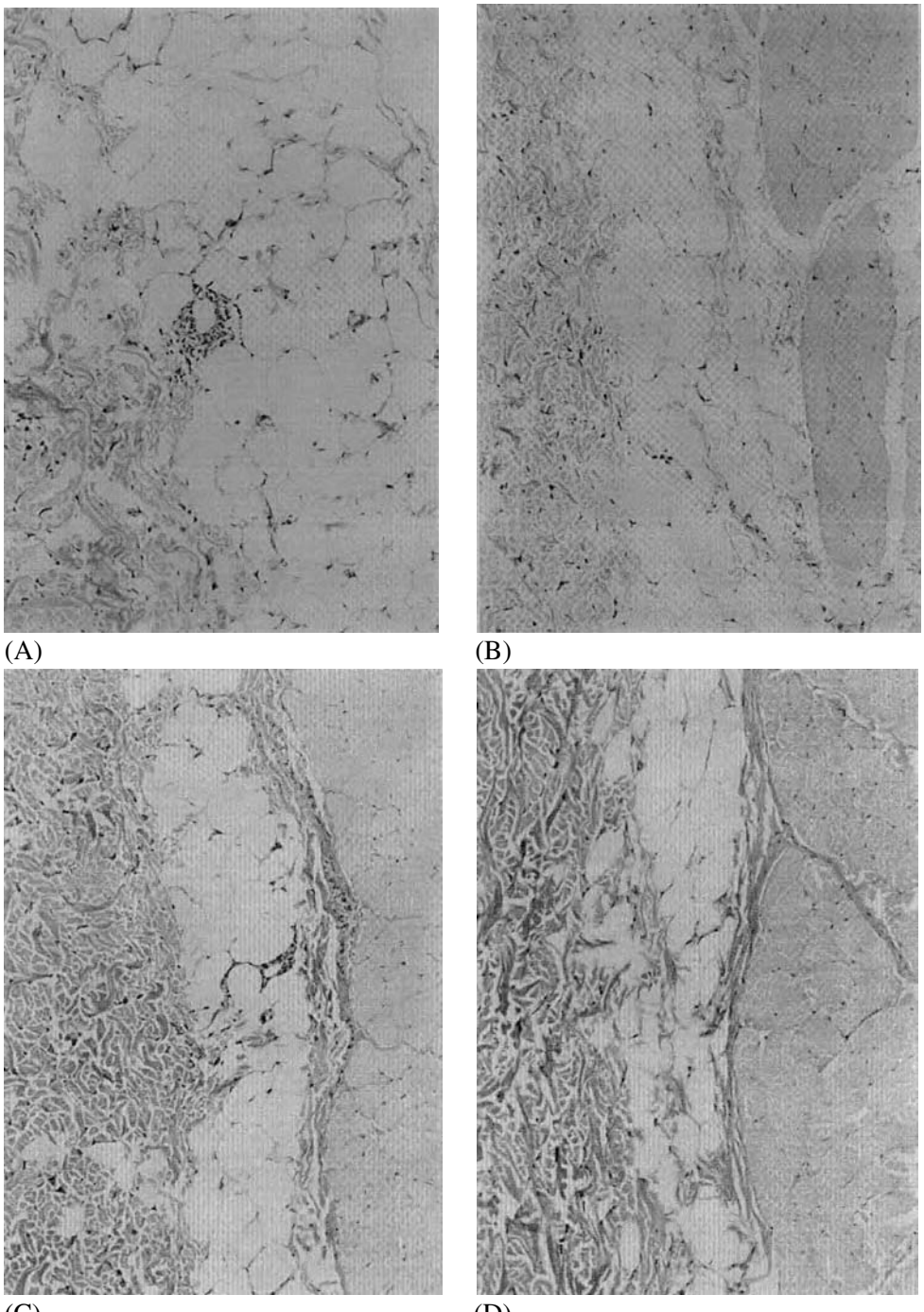

Figure 9. (A)–(D) Hematoxylin and Eosin stained photomicrograph of dermis of four different sites injected with polymer **VI** ($\times$ 108).

level for purification for each of the elastic protein-based polymers of different compositions designed for eliciting selected tissue responses. It is essential to know that the tissue response is due to the particular composition and not due to a different impurity resulting from a modified purification procedure required of a varied composition.

General comparison of 'bump' size at 2 weeks

As the objective of any soft tissue augmentation effort is a volume filling effect, an important piece of information can simply be referred to as the size of a 'bump' resulting from the injected material. First, it may be recalled that at two weeks there was no edema reported at any sites. No bumps were observed at 2 weeks at any of the sites of the control and polymer **VI**. In terms of size, the most significant bumps observed at 2 weeks were at the injection sites for polymers **IV** and **V**. The principal issue for the bump size of a biocompatible injection is retention with time. Accordingly, the results at 4 weeks (discussed below) are of greater significance.

Injectable implants for evaluation of two test compositions at 4 weeks

In addition to the hematoxylin and eosin stain of the 2-week study, samples examined at 4 weeks used trichrome and Verhoeff–van Gieson stains to assess connective tissue development. Due to efforts to limit the length of this report, only the 4-week data for the Control and Polymers **II** and **III** will be considered in comparable detail to the 2-week data.

Control. Figure 10 represents several control sites of cottonseed oil injection at four weeks. Figure 10A (upper left) is a low power ($\times$ 43) photomicrograph of the full thickness of the skin stained with hematoxylin and eosin. No lesions are present. Figure 10B (upper right) is a medium power ($\times$ 108) photomicrograph of microscopically normal skin stained with a trichrome stain. Figure 10C (lower left) is a medium-high power photomicrograph ($\times$ 216) of dermis showing the normal pattern of slender elastic fibers as demonstrated with the Verhoeff–van Gieson technique. Figure 10D (lower right) is another medium-high power photomicrograph of the deep dermis and subcutis showing a paucity of elastic fibers in this region using Verhoeff–van Gieson stain for elastic fibers. In general, therefore, the sites injected with cottonseed oil have recovered to exhibit essentially normal tissue by four weeks.

*Polymer **II**.* Figure 11 includes four photomicrographs of sites injected with lysine-containing polymer **II** using two different stains, hematoxylin and eosin, and Verhoeff–van Gieson with the purpose of the latter being to assess elastic fiber or elastic fiber-like activity. Figure 11A (upper left) is representative of a medium power photomicrograph ($\times$ 108) of the subcutis of a site injected with polymer **II**. A marked degree of pyogranulomatous panniculitis is associated with

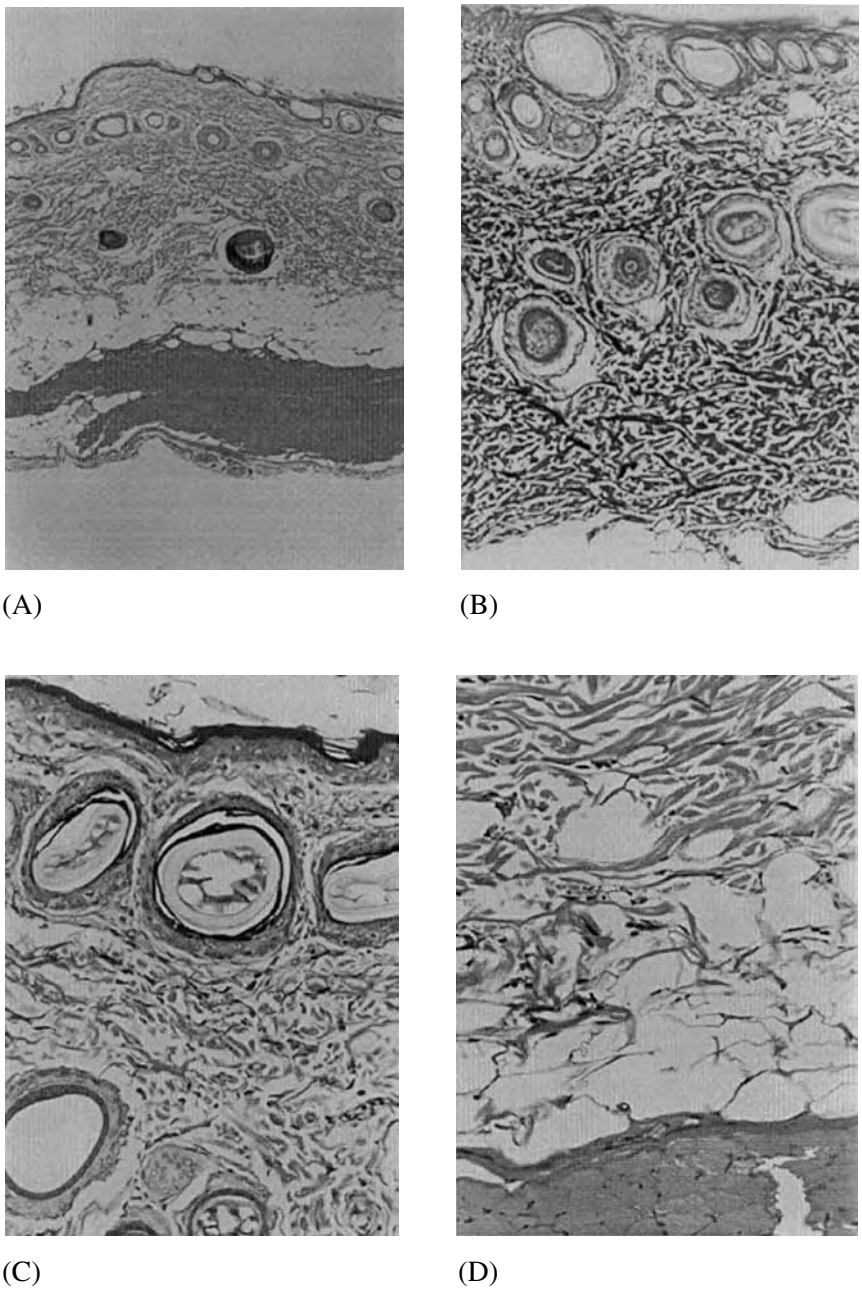

Figure 10. (A) Hematoxylin and Eosin stained photomicrograph of deep dermis of control site (× 43). (B) Trichrome stained photomicrograph of deep dermis of control site (× 108). (C)–(D) Verhoeff–van Gieson stained photomicrograph of deep dermis of control site (× 216).

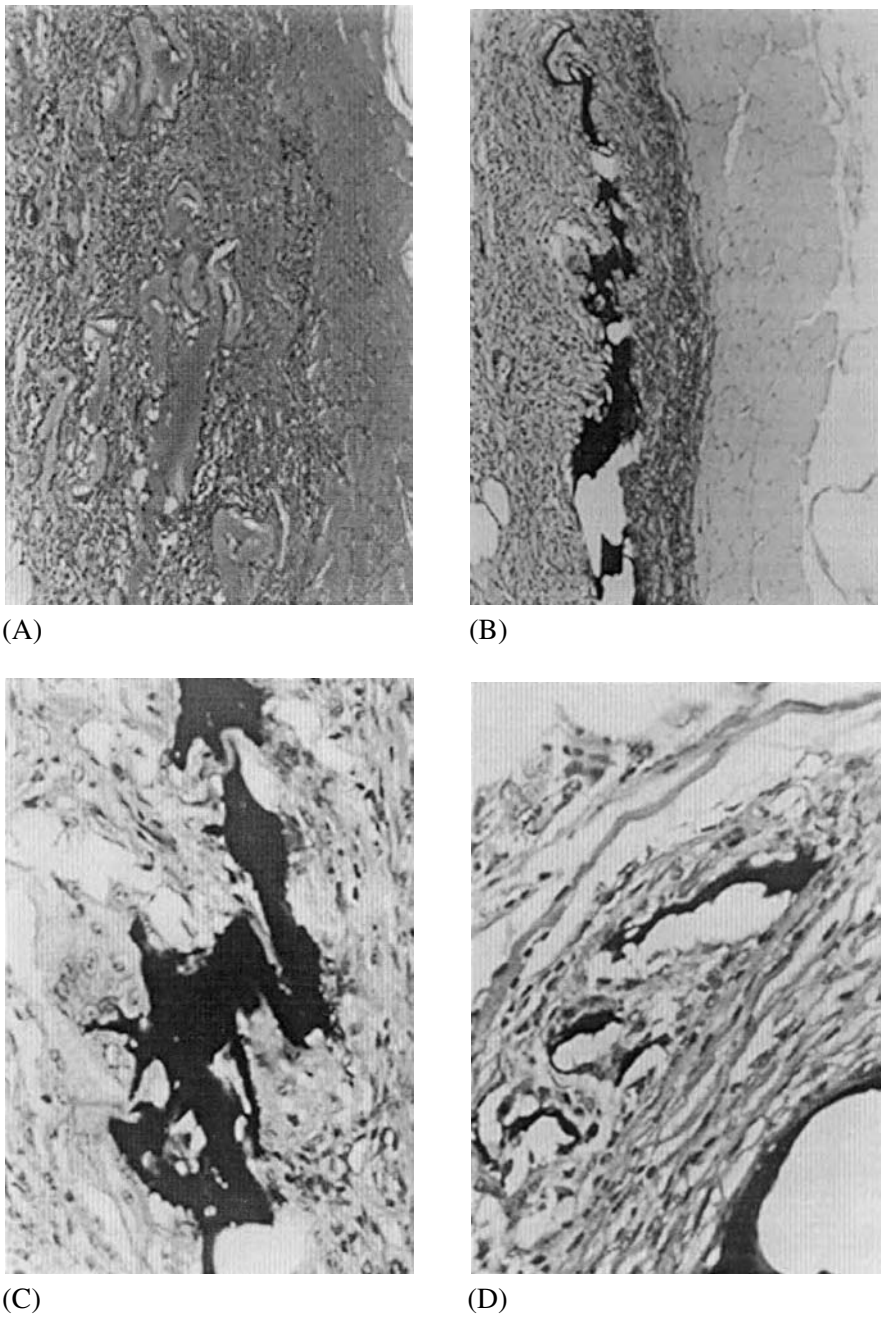

Figure 11. (A) Hematoxylin and Eosin stained photomicrograph of deep dermis of the site injected with polymer **II** (× 108). (B) Verhoeff–van Gieson stained photomicrograph of deep dermis of the site injected with polymer **II** (× 108). (C)–(D) Verhoeff–van Gieson stained photomicrograph of deep dermis of two different sites injected with polymer **II** (× 430).

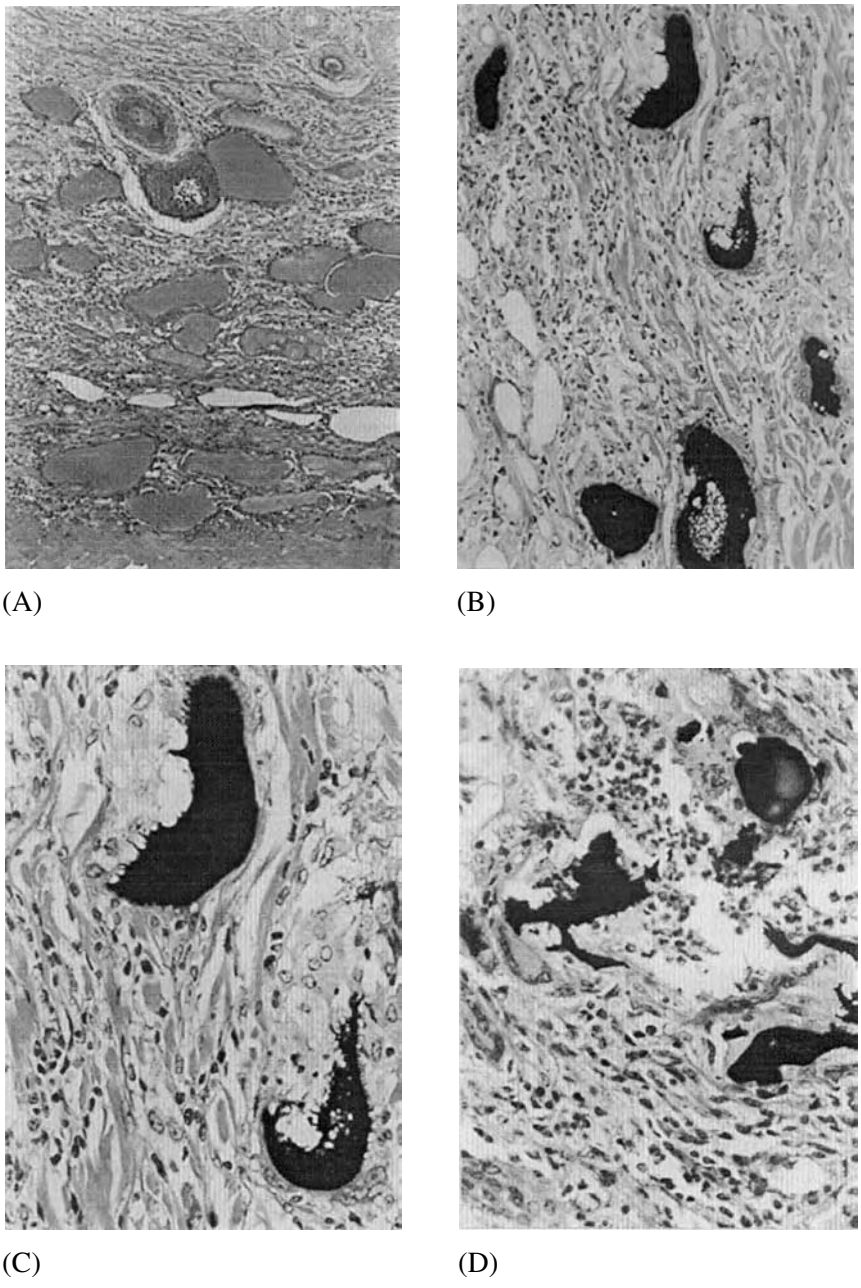

Figure 12. (A) Hematoxylin and Eosin stained photomicrograph of deep dermis of the site injected with polymer **III** (× 108). (B) Verhoeff–van Gieson stained photomicrograph of deep dermis of the site injected with polymer **III** (× 108). (C)–(D) Verhoeff–van Gieson stained photomicrograph of deep dermis of two different sites injected with polymer **III** (× 430).

large irregularly-shaped eosinophilic deposits (presumably representing the injected material). The origin of the eosinophilic granules is verified by means of the Verhoeff–van Gieson staining of the additional three sections. Figure 11B (upper right) is a photomicrograph at medium power (× 108) of the same area of the subcutis as shown in Fig. 11A, but stained with the Verhoeff–van Gieson technique. As expected above, the material which was eosinophilic in the H&E-stained sections appear as black bodies using the Verhoeff–van Gieson stain. Figure 11C (lower left) represents a photomicrograph at high power (× 430) of the same area of the subcutis as shown in Fig. 11B. Note the giant cell which appears to be digesting/remodeling the black material. Figure 11D (lower right) represents another high power photomicrograph (× 430) of the subcutis of a Verhoeff–van Gieson-stained section from the same site as shown in Figs 11A–C. Note that some of the black-staining material is being remodeled into long broad fiber.

*Polymer **III**.* Figure 12 provides four histological sections of the lysine/phenylalanine-containing polymer **III**. Figure 12A (upper left) is a (× 108) medium power photomicrograph of the deep dermis and subcutis of a site injected with polymer **III** stained with hematoxylin and eosin. Large eosinophilic deposits are present which are surrounded by granulomatous and pyogranulomatous inflammatory cell infiltrates. Figure 12B (upper right) is a medium-high power photomicrograph (× 108) of the dermis/subcutis of the same injection site as in Fig. 12A. The injected material is black when stained with the Verhoeff–van Gieson technique. Most of the deposits are surrounded by giant cells, and there is evidence of remodeling of this material at the perimeter of the deposits, i.e. at the interface between the material and the giant cell cytoplasm. Figure 12C (lower left) demonstrates at high power (× 430) the same field as in Fig. 12B, showing that the black deposits are being remodeled into slender fibers which stain similarly to elastic fibers when using the Verhoeff–van Gieson stain. Figure 12D (lower right) shows a similar high power micrograph to that of Fig. 12C of the subcutis of another site injected with polymer **III**. Note that the Verhoeff–van Gieson stain shows some of the black deposits present within giant cells becoming elongated and convoluted in configuration.

General comparison of 'bump' size at 4 weeks

Again at 4 weeks, there were no measurable bumps observed for the control and polymer **VI** sites. Only a trace of a bump (about 10% of the more prominent bumps) was observed for polymer **II**. The size of the bumps for polymers **I**, **IV**, and **V** were comparable with the most prominent diameter being found for polymer **IV**. The size of the bump for polymer **III** injection sites was about half of that observed for polymer **IV**.

DISCUSSION

> "In a scar, where there are few elastic fibers and where collagen fibers become oriented primarily along lines of tension, there is little 'give', and stretching and relaxation are not possible. This accounts for the rigidity of scar tissue and inability to undergo repeated deformation and recovery as needed in skin covering a joint or other moving part. Failure to include new elastic fibers in repair tissue until long after collagen fibers are formed is another example of the inferiority of scar tissue to normal tissue and has obvious implications in the repair of skin defects, ligamentous structures and large arteries" [42].

In developing a periurethral support volume for the correction of SUI, as in any tissue repair process, the ultimate objective is regeneration of the natural tissue. That is the objective of this effort utilizing elastic protein-based polymers for soft tissue augmentation and generation, and it considers effective introduction of elastic fibers into the repair process as a stabilizing factor.

At present, the only FDA approved material for the correction of SUI is the injectable collagen product called Contigen®. The result of Contigen® injection is the formation of a dense scar tissue comprised of collagen without significant amounts of elastin and with a disappointing 'cure' rate for urinary incontinence of less than 15% at 3 years [20].

The half-life of elastin in the body is 70 years or more [46, 47]. Accordingly, our working hypothesis is that tissue regeneration induced by the injection of specific elastic protein-based polymers in which there results a normal distribution of elastin and collagen fibers would effect a stable, long-lasting cure for urinary incontinence due to intrinsic sphincter deficiency. The role of the elastic fibers would be, by their lasting presence, to prevent the collagen from condensing or remodeling into a dense scar tissue.

The design of bioelastic polymers for control of stress urinary incontinence

Two extracellular enzymes, prolyl hydroxylase (PH) and lysyl oxidase (LO), play key roles in both the formation of collagen and elastic fibers, that is, in the formation of connective tissue. The cross-linking essential for quality fibers of both collagen and elastin is the result of LO. (It may be noted here that the first synthetic peptide found to be a substrate for lysyl oxidase was the chemically synthesized counterpart to polymer **II** [31].) On the one hand prolyl hydroxylation of collagen facilitates the release of collagen from the cell [48], is required to form strong collagen fibers [49–52], and provides resistance to non-specific proteolytic degradation [49, 50]. On the other hand, hydroxylation of the prolines of elastin has been shown to raise the temperature of the fiber assembly transition sufficiently to interfere with fiber formation [53, 54]. Indeed in cell culture, enhancing the PH activity results in little elastic fiber being formed and the observation of a hydroxylated tropoelastin remaining in the supernatant [55].

As high prolyl hydroxylase activity is key to scar formation, this activity needs to be moderated for our purposes. Our hypothesis is that the formation, regeneration, or reconstruction of a stable loose connective tissue can be achieved by the appropriate signaling to induce those fibroblasts into the injection site that are active in elastin synthesis. The repeating sequence most prominent in human elastin, VGVAPG, has been shown to be a chemoattractant toward those fibroblasts that have differentiated for elastin synthesis [41], and has been proposed to induce migration of fibroblasts competent for elastogenesis into sites for elastic fiber repair [56, 57]. This is one putative role of the $(GVGVAP)_8$ sequence of polymer **V**. Accordingly, the elastic protein-based polymers of our focus are for the purpose of finding the appropriate balance of collagen and elastic fiber synthesis that will result in the formation of a stable, loose connective tissue on injection into the periurethral region of patients suffering from stress urinary incontinence.

The purpose of the animal model studies for soft tissue augmentation is to assess the different tissue responses resulting from injection of elastic protein-based polymers of different compositions. In order to do this, one must be certain that the observed differences are not the result of differences of purity wherein the purifications themselves depend on the different chemical and physical properties resulting from the different compositions. Accordingly, it is necessary to have an independent and more sensitive methodology with which to detect impurities arising from *E. coli*. A measure other than *in vivo* tissue reactivity would be preferred for more effective and simpler quality control. In the present report the stage is set for an alternate method in which, at the fermentation step, ^{14}C-glucose can be introduced into in the culture medium. By using the radiolabelled glucose, the cellular components will become labeled with ^{14}C. The purification stage at which the microbially-prepared $(GVGVP)_{251}$ is as innocuous as the chemically-prepared poly(GVGVP) defines the level of contaminant that is acceptable. Beyond this, an even more effective standard for purity, polymer **VI**, emerges from the present studies.

The range of tissue responses to the six elastic protein-based polymers examined in this report show differential responses to changes in composition. At present the most promising materials are polymers **I**, **IV**, and **V** with polymer **I** being of the traditional inert type. The interesting responses to polymers **IV** and **V** (for example, see Figs 7 and 8 above) containing different tissue active peptide sequences indicate differentiable cellular invasion and extracellular matrix formation. Accordingly, these compositions hold the potential for the most favorable results of the formation a long-lasting, stable, and loose connective tissue volume. Animal model studies currently underway involving more sites and longer times will determine if the compositional variations already tested can, in fact, result in formation of a stable, loose connective tissue.

There is reason for optimism that a more favorable result, than is currently obtained using Contigen®, will be available for the many whose lifestyles and productivity have been severely curtailed due to the prevalent problem of urinary

incontinence. It is expected to occur with a dramatic reduction in cost of material, as compared to Contigen®, and without the contamination concerns that currently attend obtaining collagen from cows (e.g. BSE).

Acknowledgements

The authors wish to acknowledge the support of the National Institutes of Health — Nat. Inst. of Child Health & Human Development under Grant No. 1 R43 HD34659-01 and the Office of Naval Research under the grant No. N00014-89-J-1970, and thank Shao-Qing Peng for obtaining the proton NMR spectra and Larry Hayes for obtaining the mass spectra.

REFERENCES

1. Urinary Incontinence Guideline Panel. *Urinary Incontinence in Adults: Clinical Practice Guideline*. AHCPR Pub. No. 92-0038. Rockville, MD (1992).
2. T. W. Hu, *J. Am.Geriatrics Soc.* **38**, 292 (1990).
3. D. T. McPherson, J. Xu and D. W. Urry, *Protein Expression Purification* **7**, 51 (1996).
4. Dan W. Urry, Timothy M. Parker, Michael C. Reid and D. Channe Gowda, *J. Bioactive Compatible Polym.* **6**, 263 (1991).
5. G. L. Picciolo, D. S. Kaplan, K. F. Batchelder, R. Kapur and R. M. Kotz, Biotechnology-derived biomaterials modulate host cell reactive oxygen production as measured by chemiluminescence, 19th Annual Meeting, Society for Biomaterials, Birmingham, AL (1993).
6. D. W. Urry, A. Pattanaik, M. A. Accavitti, C.-X. Luan, D. T. McPherson, J. Xu, D. C. Gowda, T. M. Parker, C. M. Harris and N. Jing, in: *Handbook of Biodegradable Polymers*, A. J. Domb, J. Kost and D. M. Wiseman (Eds), p. 367. Harwood Academic Publishers, Chur, Switzerland (1997).
7. A. F. Bristow, in: *Protein Purification Applications*, E. L. V. Harris and S. Angal (Eds), p. 29. IRL Press, New York (1990).
8. J. G. Blaivas and B. Z. Jacobs, *J. Urol.* **145**, 1214 (1991).
9. A. A. Malizia, Jr., H. M. Reiman, R. P. Myers, J. R. Sande, S. S. Barham, R. C. Benson, Jr., M. K. Dewanjee and W. J. Utz, *JAMA* **251**, 3277 (1984).
10. T. D. Richardson, M. J. Kennelly and G. J. Faerber, *Adult Urol.* **46**, 378 (1995).
11. D. H. Frank, L. Vakassian, J. C. Fisher and N. Ozkan, *Plastic Reconstruct. Surg.* **87**, 1080 (1991).
12. R. P. Santarosa and J. G. Blaivas, *J. Urol.* **151**, 607 (1994).
13. B. C. Murless, *J. Obstet. Gynaecol.* **45**, 67 (1938).
14. R. Quackels, *Acta Urol. Belg.* **23**, 259 (1955).
15. D. A. Canning, *Dial. Ped. Urol.* **14**, 6 (1991).
16. R. D. Walker, J. Wilson and A. E. Clark, *J. Urol.* **148**, 645 (1992).
17. P. Stricker and B. Haylen, *Med. J. Austral.* **158**, 89 (1993).
18. R. J. Siegle, J. P. McCoy, W. Schade and N. A. Swanson, *Arch. Dermatol.* **120**, 183 (1984).
19. R. A. Appell, *Craft Urologic Surg.* **21**, 177 (1994).
20. S. Herschorn, D. J. Steele and S. B. Radomski, *J. Urol.* **156**, 1305 (1996).
21. J. M. Cummings, J. A. Boullier and R. O. Parra, *J. Urol.* **155**, 1011 (1996).
22. L. M. Perez, E. A. Smith, T. S. Parrott, B. H. Broecker, C. A. Massad and J. R. Woodard, *J. Urol.* **156**, 633 (1996).
23. H. Yeh, G. N. Ornstein, Z. Indik, P. Sheppard, N. Anderson, J. C. Rosenbloom, G. Cicila, K. Yoon and J. Rosenbloom, *Collagen Related Res.* **7**, 235 (1987).

24. L. B. Sandberg, J. G. Leslie, C. T. Leach, V. L. Alvarez, A. R. Torres and D. W. Smith, *Pathol. Biol.* **33**, 266 (1985).
25. Z. Indik, H. Yeh, G. N. Ornstein, P. Sheppard, N. Anderson, J. C. Rosenbloom, L. Peltonen and J. Rosenbloom, *Proc. Natl Acad. Sci. USA* **84**, 5680 (1987).
26. D. W. Urry, D. T. McPherson, J. Xu, D. C. Gowda and T. M. Parker, in: *Industrial Biotechnological Polymers*, C. Gebelein and C. E. Carraher, Jr. (Eds), p. 259. Technomic Publishing Co., Lancaster, PA (1995).
27. D. W. Urry, A. Nicol, D. T. McPherson, J. Xu, P. R. Shewry, C. M. Harris, T. M. Parker and D. C. Gowda, in: *Encyclopedic Handbook of Biomaterials and Bioengineering — Part A — Materials,* Vol. 2, p. 1619. Marcel Dekker, Inc., New York (1995).
28. D. W. Urry, D. C. Gowda, B. A. Cox, L. D. Hoban, A. McKee and T. Williams, *Mat. Res. Soc. Symp. Proc.* **292**, 253 (1993).
29. L. D. Hoban, M. Pierce, J. Quance, I. Hayward, A. McKee, D. C. Gowda, D. W. Urry and T. Williams, *J. Surgical Res.* **56**, 179 (1994).
30. F. J. Elsas, D. C. Gowda and D. W. Urry, *J. Pediatr. Ophthalmol. Strabismus* **29**, 284 (1992).
31. H. M. Kagan, L. Tseng, P. C. Trackman, K. Okamoto, R. S. Rapaka and D. W. Urry, *J. Biol. Chem.* **255**, 3656 (1980).
32. A. Nicol, D. C. Gowda and D. W. Urry, *J. Biomed. Mater. Res.* **26**, 393 (1992).
33. D. W. Urry, in: *Tissue Engineering: Current Perspectives*, Eugene Bell (Ed.), p. 199. Birkhäuser Boston, Div. Springer-Verlag, New York (1993).
34. D. Ingber, *Current Opinion Cell Biol.* **3**, 841 (1991).
35. A. Nicol, D. C. Gowda, T. M. Parker and D. W. Urry, in: *Biotechnology and Bioactive Polymers*, C. G. Gebelein and C. E. Carraher, Jr. (Eds), p. 95. Plenum Press, New York (1994).
36. D. W. Urry, *Angew. Chem.* (German) **105**, 859 (1993);
Angew. Chem. Int. Ed. Engl. **32**, 819 (1993).
37. D. W. Urry, *J. Phys. Chem. B* **101**, 11007 (1997).
38. D. W. Urry, *Scient. Am.* 64 (January 1995).
39. A. Nicol, D. C. Gowda, T. M. Parker and D. W. Urry, *J. Biomed. Mater. Res.* **27**, 801 (1993).
40. M. M. Long, V. J. King, K. U. Prasad and D. W. Urry, *Biochim. Biophys. Acta* **928**, 114 (1987).
41. R. M. Senior, G. L. Griffin, R. P. Mecham, D. S. Wrenn, K. U. Prasad and D. W. Urry, *J. Cell Biol.* **99**, 870 (1984).
42. E. R. Peacock, Jr., in: *Wound Repair*, p. 56. W. B. Saunders, Philadelphia, PA (1984).
43. F. W. Studier, A. H. Rosenberg, J. J. Dunn and J. W. Dubendorff, *Meth. Enzymol.* **185**, 60 (1990).
44. H. Daniell, C. Guda, D. T. McPherson, X. Zhang and D. W. Urry, in: *Methods in Molecular Biology, Vol. 63: Recombinant Proteins: Protocol Detection and Isolation*, R. Tuan (Ed.), Ch. 27, p. 359. Humana Press Inc., Totowa, NJ (1996).
45. D. W. Urry, S. Q. Peng, D. C. Gowda, T. M. Parker, N. Jing and R. D. Harris, *Chem. Phys. Lett.* **225**, 97 (1994).
46. J. T. Powell, in: *The Cause and Management of Aneurysms*, R. M. Greenhalgh and J. A. Marrick (Eds), p. 89. W. B. Saunders, London (1990).
47. R. B. Rucker and D. Tinker, *Int. Rev. Exp. Pathol.* **17**, 1 (1977).
48. J. Uitto, J.-P. Hoffmann and D. J. Prockop, *Arch. Biochem. Biophys.* **173**, 187 (1976).
49. R. A. Berg and D. J. Prockop, *Biochem. Biophys. Res. Commun.* **52**, 115 (1973).
50. J. Rosenbloom, M. Harsch and S. Jiminez, *Arch. Biochem. Biophys.* **158**, 478 (1973).
51. G. N. Ramachandran, M. Bansal and R. S. Bhatnagar, *Biochim. Biophys. Acta* **322**, 166 (1973).
52. G. N. Ramachandran, M. Bansal and C. Ramakrishnan, *Curr. Sci.* **44**, 1 (1975).
53. D. W. Urry, R. S. Bhatnagar, H. Sugano, K. U. Prasad and R. S. Rapaka, in: *Molecular Basis of Environmental Toxicity*, R. S. Bhatnagar (Ed.), p. 515. Ann Arbor Scientific Publishers Inc., Ann Arbor, MI (1980).
54. D. W. Urry, H. Sugano, K. U. Prasad, M. M. Long and R. S. Bhatnagar, *Biochem. Biophys. Res. Commun.* **90**, 194 (1979).

55. L. Barone, B. Faris, S. Chipman, P. Toselli, B. Oakes and C. Franzblau, *Biochim. Biophys. Acta* **840**, 245 (1985).
56. D. W. Urry, C.-H. Luan and S. Q. Peng, in: *Proceedings of The Ciba Foundation Symposium No. 192, The Molecular Biology and Pathology of Elastic Tissues*, p. 4. John Wiley & Sons, Ltd., Sussex (1995).
57. D. W. Urry, *J. Protein Chem.* **7**, 81 (1988).

Polymers for Tissue Engineering, pp. 53–72
Molly S. Shoichet and Jeffrey A. Hubbell (Eds)

Synthesis and characterization of polymer–(multi)-peptide conjugates for control of specific cell aggregation

NADYA BELCHEVA, SAMUEL P. BALDWIN and W. MARK SALTZMAN*
School of Chemical Engineering, Cornell University, Ithaca, NY 14853, USA

Received 10 June 1997; accepted 28 August 1997

Abstract—A new synthetic approach has been applied to obtain novel di-, tetra-, and (multi)-peptide containing polymer conjugates in quantitative yields with a high degree of conjugation. Bis-(*N*-hydroxysuccinimidyl) esters of PEG (M_w = 200, 600, 1400, 2000, and 3400) were synthesized and studied in a condensation reaction with synthetic peptides: glycine–glycine–tyrosine–arginine (GGYR), a model peptide, and glycine–arginine–glycine–aspartic acid–tyrosine (GRGDY), a sequence known to promote cell adhesion and aggregation. Tetra-substituted derivatives of PEG-based conjugates were synthesized by coupling L-aspartic acid and L-aspartyl-L-phenylalanine through a condensation procedure in organic media. Poly(acrylic acid) and co-polymers (M_w = 2000 and 5000) were studied as a model of multifunctional linear polymers in the reaction with L-tryptophan and GGYR. Alternative polymer–(multi)-peptide conjugates were successfully synthesized using Starburst® dendrimer PAMAM (G = 3), 'short' and 'long'-chain PEG-based active esters and GRGDY. The structure of the intermediate precursors and peptide-conjugates was confirmed by spectral (UV-Vis, FTIR, ^{1}H-NMR) and chromatographic (RP-HPLC and SEC) methods. By varying the properties of the interconnecting polymer — such as hydrophobicity, molecular weight, and functionality — a set of polymer–GRGDY conjugates was synthesized.

Key words: GRGDY; GGYR; PEG; PAMAM; dendrimer; polymer–peptide conjugate, active esters.

LIST OF ABBREVIATIONS

ACA	6-aminocaproic acid
APhA or AspPhA	dipeptide (L-aspartyl-phenylalanine)
DCC	*N*,*N*′-dicyclohexylcarbodiimide
DCU	*N*,*N*′-dicyclohexylurea
EDC	1-ethyl-3-(3-dimethyl aminopropyl)-carbodiimide
GGYR	tetrapeptide (glycine–glycine–tyrosine–arginine)

*To whom correspondence should be addressed.

GRGDY	pentapeptide (glycine–arginine–glycine–aspartic acid–tyrosine)
$Jeff_{600}$ or $Jeffamine_{600}$	O,O'-bis-(2-aminipropyl)-polyethylene glycol 500, $M_r \sim 600$
$Jeff_{600}$-$(PEG_{600}$-GRGDY$)_2$	O,O'-bis-(PEG_{600}-GRGDY)-polyethylene glycol 500
$Jeff_{600}$-(TEG-GRGDY$)_2$	O,O'-bis-(TEG-GRGDY)-polyethylene glycol 500
NHS	N-hydroxysuccinimide
PAAc	poly(acrylic acid)
$PAAc_{2000}$-(multi)-NHS	multi-(N-hydroxysuccinimidyl) ester of PAAc with $M_w = 2000$
PAMAM (G = 3)	polyamidoamine dendrimer; 3rd generation
PAMAM-(G = 3)$(PEG_{600}$-GRGDY$)_m$	PAMAM-PEG_{600}–multi-GRGDY conjugate
PAMAM-(G = 3)$(PEG_{3400}$-GRGDY$)_n$	PAMAM-PEG_{3400}–multi-GRGDY conjugate
PAMAM-(PEG-NHS$)_n$	multi-(N-hydroxysuccinimidyl) ester of PAMAM-PEG
PEG	poly(ethylene glycol)
PEG_{3400}-$(ACA)_2$	poly(ethylene glycol)-(3400)-bis-(ACA)
PEG_{3400}-[APhA$(GRGDY)_2]_2$	poly(ethylene glycol)-(3400)-bis-[APhA$(GRGDY)_2$]
PEG_{3400}-$(Asp)_2$ or PEG_{3400}-$(Aspartic\ acid)_2$	poly(ethylene glycol)-(3400)-bis-(aspartate)
PEG_{3400}-[Asp$(GRGDY)_2]_2$	poly(ethylene glycol)-(3400)-bis-[aspartate$(GRGDY)_2$]
PEG_{600}-COOH	poly(ethylene glycol)-bis-(carboxymethyl) ether
PEG_{600}-$(GGYR)_2$	poly(ethylene glycol)-(600)-bis-(GGYR)
PEG_{3400}-$(GGYR)_2$	poly(ethylene glycol)-(3400)-bis-(GGYR)
PEG_{600}-$(GRGDY)_2$	poly(ethylene glycol)-(600)-bis-(GRGDY)
PEG_{3400}-$(GRGDY)_2$	poly(ethylene glycol)-(3400)-bis-(GRGDY)
PEG_{600}-$(NHS)_2$	bis-(N-hydroxysuccinimidyl) ester of PEG_{600}-COOH
PEG_{3400}-(tetra)-NHS	tetra-(N-hydroxysuccinimidyl) ester of PEG_{3400}-$(Asp)_2$
$(SPA)_2$-PEG_{3400}	poly(ethylene glycol)-(3400)-bis-(succinimidyl propionate)
TEG-COOH	3,6,9-trioxaundecanedicarboxylic acid
TEG-$(GGYR)_2$	triethylene glycol-bis-(GGYR)
TEG-$(GRGDY)_2$	triethylene glycol-bis-(GRGDY)

INTRODUCTION

Cell aggregation is a complex phenomenon of importance in embryonic development, tissue engineering, wound healing, and bioprocessing technology. In previous work, cell aggregation has been enhanced through the use of polymer–(di)-peptide conjugates consisting of a biocompatible, water-soluble poly(ethylene glycol) 'bridge' and peptides containing the cell adhesion sequence, RGD (arginine–glycine–aspartic acid), derived from fibronectin [1, 2]. Since poly(ethylene glycol) (PEG) is a stable and bioinert synthetic polymer, it seems to be a promising candidate for synthesis of a variety of hybrids.

A vast body of literature describes the advantages of pegylated peptides and proteins, which include their increased proteolytic resistance and circulation time, improved solubility, decreased antigenicity and immunogenicity [3, 4]. A number of proteins, enzymes, and cytokines — including Cytochrome P450 1A2 [5], interleukin-8, granulocyte-colony stimulating factor, interleukin-1 receptor antagonist [6], and BSA [7] — have been covalently modified with varying sizes of PEG as monomethoxy-poly(ethylene glycol)s, carrying a reactive electrophile group, or activated diester- or diamino-terminated PEGs [8, 9]. An improved coupling method has been reported for tresylated methoxy-PEG reacting with recombinant chimeric F(ab′) fragment (F9) under mild conditions [10]. Cyclic peptides with large incorporated PEG loops have been designed and synthesized *de novo* for binding to class I MHC (major histocompatibility complex) [11]. Tumor necrosis factor receptor was attached to 20-kDa PEG linker by reaction with bis(vinyl sulfone)-PEG, yielding a 'dumbbell' conjugate, which was found to be effective as a drug delivery system without a deleterious antigenic response [12].

PEG–oligopeptide hybrids have been produced as pharmaceuticals; pegylation may potentiate and prolong the activity of peptides. Kawasaki *et al.* [13] studied the inhibitory effect of methoxy-PEG–RGD and methoxy-PEG–RGDS on experimental metastasis in mice, and reported on their increased stability in the bloodstream. Conjugates with defined repetitive or cyclic structures of RGDT and PEG enhanced the inhibition of lung metastasis in proportion to the degree of RGDT repetition and dose [14].

Another important group of polymers, poly-*N*-(2-hydroxypropyl)methacrylamide (PHPMA) and co-polymers, have been explored for a broad range of polymer-conjugates [15]. A model peptide, the b-chain of insulin, and the peptide VP2 (human rhinovirus antigenic determinant), were covalently bound to PHPMA in a content of approximately 25 wt% [16]. HPMA copolymer conjugates are prospective candidates for oral vaccines; conjugation reduced the rate of degradation for both peptides during *in vitro* incubation with small intestinal brush border and luminal enzymes. Recently, semitelechelic poly-HPMAs with carboxyl end groups were synthesized and conjugated to enzymes, α-chymotrypsin and bovine seminal ribonuclese, via single polymer end chain linkage as an alternative approach for increased proteolytic stability [17]. A similar end linking reaction was performed for the synthesis of trypsin conjugates with oligomers of *N*-isopropylacrylamide for thermal recycling [18].

A variety of natural and synthetic polymers have been tested for biomedical applications, including situations in which the polymer remains in intimate contact with

cells and tissues for prolonged periods [19]. Some of the most promising candidates for tissue engineering are described in reviews by Peppas and Langer [20] and Marchant [21]. Understanding the role of polymers in cellular adhesion and aggregation is one of the challenges in current biomaterials research [22]. Synthetic materials can be modified to interact with cell surface receptors called integrins, many of which bind with reasonable affinity to the cell adhesive sequence, RGD. The importance of the adhesive motif RGD [23, 24] has motivated many studies with RGD-containing peptides immobilized onto synthetic polymers like PTFE [25], PET [25], polyacrylamide [26], PLA [27], etc., as well as in a soluble PEG–peptide conjugate form [1, 2].

In this report we synthesized a variety of new compounds for testing the hypothesis that cell aggregation can be controlled by means of novel polymer–(multi)-peptide conjugates. By varying the type of the interconnecting polymer, i.e. its hydrophobicity, molecular weight, and functionality, a set of novel active polymer–(multi)-GRGDY conjugates was synthesized. To achieve higher yields and conjugate purity, condensation reactions were performed in organic media, when possible, in the presence of carbodiimides. Intermediate products and the polymer–peptide conjugates were isolated, purified, and characterized by spectral and chromatographic methods.

EXPERIMENTAL PROCEDURES

Materials and methods

All starting compounds were used as received without additional purification. All solvents were distilled prior to use. Carboxylic groups were determined by titration with aqueous 0.1 N NaOH. The UV spectra were measured on a Hitachi U-2010 UV-Vis Spectrophotometer equipped with WI and D2 lamps using UV Solutions software under Windows NT (version 4) operating system. The FT-IR spectra were recorded on a Mattson 2020 Galaxy series instrument at a resolution of 3.0 cm^{-1} in KBr, neat or nujol. ^{1}H-NMR spectra were measured on a Bruker AF-300 spectrometer with Tecmag Update at 300 MHz in D_2O using Mac NMR 5.4. The $\overline{M}_w$, $\overline{M}_n$ and $\overline{M}_w/\overline{M}_n$ values were determined on Proteinpak KW801.5 and Proteinpak KW803 (Shodex®) columns using a Waters gel-permeation chromatograph equipped with a differential refractive index detector Refractometer IV Milton Roy and UV detector M486 at 254 nm. Water/methanol, in a ratio of 1 : 1 v/v, was used as eluent with flow rate 1 ml min^{-1} at 40 °C. Calibration was performed with poly(ethylene glycol) and poly(ethylene oxide) standards with narrow molecular weight distributions. Gradient reverse-phase chromatography (RP-HPLC) was performed on a Waters 2690 Alliance Separations Module including Waters 996 Photodiode Array Detector and Waters 410 Differential Refractometer on a Waters column μBondapak™ C_{18} (3.9 × 150 mm, Part. No. WAT086684).

Synthesis of N-*hydroxysuccinimide active diesters*

(i) Carboxylated PEG derivatives, 3,6,9-trioxaundecanedicarboxylic acid, M_r 222.2 (Fluka) (TEG-COOH) and poly(ethylene glycol)-bis-(carboxymethyl) ether, M_n

c. 600 (Aldrich) (PEG_{600}-COOH) were activated via *N*-hydroxysuccinimide (Aldrich) (NHS) using *N*,*N*′-dicyclohexylcarbodiimide (DCC) [28–30]. In a typical preparation, the carboxylic component (TEG-COOH) (8.25×10^{-3} mol COOH groups, 1 g) was dissolved in 5 ml of a mixed solvent DMF/CH_2Cl_2 in a 1 : 1 v/v ratio at 0°C under stirring. To this solution NHS (18.25×10^{-3} mol, 2.09 g) was added in a molar ratio of NHS/TEG-COOH equal to 2.2 and one to two drops of pyridine as a catalyst. After 5–10 min, DCC (18.25×10^{-3} mol, 3.77 g) was added to the homogeneous reaction mixture dissolved in a minimal amount of solvent in a molar ratio of DCC/TEG-COOH equal to 2.2. The reaction was carried out at 0°C for 2 h and kept overnight at room temperature for a total reaction time of 20 h. *N*,*N*′-Dicyclohexylurea (DCU) was filtered under suction and the filtrate was evaporated to dryness under vacuum. The yellowish residue was dissolved in a large excess of acetone, cooled for several hours at −70°C, filtered, and then the filtrate was reduced to 3–5 ml by rotary evaporation under vacuum. TEG-$(NHS)_2$ was isolated in 75–80 wt% yield by precipitation in cold ether. The precipitation procedure was repeated twice to achieve higher purity of the activated NHS-esters.

(ii) The synthesized TEG-$(NHS)_2$ and PEG_{600}-$(NHS)_2$ were used in a condensation reaction with NH_2-terminated PEG, *O*,*O*′-bis(2-aminopropyl)-polyethylene glycol 500, $M_r \sim 600$ (Fluka), or Jeffamine 600 ($Jeff_{600}$). Thus, TEG-$(NHS)_2$ (19.6×10^{-4} mol, 0.8164 g) and $Jeff_{600}$ (2.45×10^{-4} mol, 0.148 g) in a molar ratio of 8 : 1 were dissolved in 20 ml of tetrahydrofuran (THF) at 0°C. The reaction was maintained overnight under stirring at room temperature. After dilution with distilled water, the reaction mixture was dialyzed with distilled water using a Cellulose Ester Membrane (Spectra/Por®, Spectrum) type MWCO:1000 D for 24 h. The yield of $Jeff_{600}$-(TEG-$NHS)_2$ after lyophilization was 20 wt%. When PEG_{600}-$(NHS)_2$ was used, the yields of $Jeff_{600}$-(PEG_{600}-$NHS)_2$ were up to 65 wt%.

(iii) Tetra-NHS active esters of PEG with $M_w \sim 3400$ were synthesized by two-step condensation reaction using activated PEG, PEG succinimidyl propionate, $(SPA)_2$-PEG_{3400}, (SPA-3400, Shearwater Polymers, Inc.). First, L-aspartic acid (Sigma) (2.65×10^{-4} mol, 0.035 g) was dissolved in 2–3 ml of 0.1 M MES monohydrate (4-morpholineethanesulfonic acid) (Aldrich) at 0°C by adding one to two drops of pyridine keeping neutral pH ∼ 7. $(SPA)_2$-PEG_{3400} (8.82×10^{-5} mol, 0.3 g) dissolved in 5 ml of DMF was added dropwise to the reaction mixture under stirring and kept overnight at room temperature. After dilution with distilled water (1 : 1 v/v), the reaction mixture was dialysed in distilled water for 24 h using a Cellulose Ester Membrane (Spectra/Por®, Spectrum) type MWCO:2000 D for 24 h. PEG_{3400}-$(Asp)_2$ was obtained in a yield of 57–60 wt% after lyophilization. When the condensation reaction was carried out with L-aspartyl-phenylalanine (Sigma) instead of L-aspartic acid, the yield was 45 wt%. PEG_{3400}-(tetra)-NHS esters were obtained in quantitative yields up to 60 wt% following the procedure described in (i).

(iv) Multi-NHS esters were synthesized using poly(acrylic acid) (PAAc) (Aldrich) with average M_w *c*. 2000 (GPC), 65 wt% solution in water, and average M_w

c. 5000 (GPC), 50 wt% solution in water. In a typical preparation, PAAc 2000 (0.7×10^{-3} mol COOH, based on titration, 0.106 g) and NHS (1.05×10^{-4} mol, 0.121 g) were dissolved in 5 ml of 0.1 M MES at 0°C. 1-Ethyl-3-(3-dimethyl aminopropyl)-carbodiimide (EDC), (Sigma) (1.05×10^{-3} mol, 0.202 g) was added under stirring. The reaction temperature was increased slightly to room temperature, and the reaction allowed to proceed to completion for 5 h. After dialysis with a membrane MWCO:1000 D in distilled water for 24 h and lyophilization, $PAAc_{2000}$-(multi)-NHS ester was obtained in yield of 45 wt%.

(v) Multi-NHS esters of poly(acrylic acid-*co*-aminocaproylacrylic acid) were obtained using procedure (iv). Co-polymers of acrylic acid and aminocaproylacrylic acid in a ratio of 1 : 1 were synthesized as follows [31]: PAAc average M_w 5000 (2.5×10^{-3} mol, 0.416 g) was partially neutralized by 0.1015 N NaOH (1.25×10^{-3} mol, 12.3 ml) in 10 ml of 0.1 M MES solution and cooled to 0°C. NHS (1.88×10^{-3} mol, 0.216 g) and EDC (1.88×10^{-3} mol, 0.361 g) were added under stirring. The condensation reaction was carried out for 2 h at 0°C and 3 h at room temperature. Then, 6-aminocaproic acid (Aldrich) (2.13×10^{-3} mol, 0.28 g) was added and the reaction mixture was stirred at room temperature overnight. COOH groups of the aminocaproylacrylic acid residues were activated in MES using NHS and EDC, according to the procedure described in (iv). The final (multi)-NHS active esters of poly(acrylic acid-*co*-aminocaproylacrylic acid) were purified by dialysis and lyophilized. The yields were up to 50–60 wt%.

(vi) Synthesis of dendrimer-based (multi)-NHS active esters — PAMAM — $(PEG\text{-}NHS)_n$. Starburst polyamidoamine dendrimer, PAMAM (G = 3), $M_w = 6909$, 20–30% aqueous solution, was kindly supplied as a gift from Dendritech, Inc. PAMAM (theoretical number of NH_2 surface groups equal to 32) was lyophilized prior to use. A solution of PAMAM (1.44×10^{-5} mol of NH_2, 0.1 g) in 20 ml of 0.1 M MES, was added dropwise to a solution of PEG_{600}-$(NHS)_2$ (1.44×10^{-3} mol, 0.864 g) dissolved in 30–40 ml of DMF at 0°C under stirring. The reaction was carried out for 24 h at room temperature and then the solvent was evaporated under vacuum. The residue was dissolved in distilled water and dialyzed for 24 h using MWCO:2000 D membrane. The yield of PAMAM-$(PEG_{600}\text{-}NHS)_n$ after lyophilization was 60 wt%. The average functionality was estimated as moles COOH resp. NHS groups per 1 g of PAMAM-$(PEG_{600}\text{-}NHS)_n$ by titration with 0.1 N NaOH. A similar procedure was applied for the synthesis of PAMAM-$(PEG_{3400}\text{-}SPA)_n$. In this case two types of active esters were isolated differing in the average functionality: PAMAM-$(PEG_{3400}\text{-}NHS)_n$, isolated as a soluble fraction in absolute ethanol, (type I), yield up to 10 wt%, and PAMAM-$(PEG_{3400}\text{-}NHS)_n$, obtained after dialysis with MWCO:5000 D membrane (type II), yield up to 60 wt%.

Synthesis of polymer–peptide conjugates

A condensation reaction between the activated electrophile (NHS-esters) and NH_2-terminus of L-tryptophan (Sigma), GGYR (glycine–glycine–tyrosine–arginine) (Sigma) or GRGDY (glycine–arginine–glycine–aspartic acid–tyrosine) was performed

in a mixed solvent DMF/MES at 0–10°C. In a general procedure, GRGDY (3.5×10^{-5} mol, 0.020 g) was dissolved in 3 ml of 0.1 M MES at 0°C. SPA_2-PEG_{3400} (1.17×10^{-5} mol, 0.0397 g) was dissolved in 2 ml of DMF and added dropwise to the peptide solution under stirring. The reaction was performed for 1 h at 0°C and 4 h at room temperature. The reaction mixture was dialyzed for 24 h in distilled water using MWCO:2000 D membrane, then lyophilized. The yields of the conjugates varied from 60 to 90 wt% depending on the type of the electrophile and the nucleophile.

UV-spectrophotometric measurments

UV spectra of the polymer–peptide conjugates were obtained in distilled water. Extinction coefficients for L-tryptophan, GGYR, and GRGDY were determined in distilled water at 25°C as follow: L-tryptophan $-\varepsilon = 5400\ \text{M}^{-1}\,\text{cm}^{-1}$ at $\lambda = 279$ nm; GGYR $-\varepsilon = 920\ \text{M}^{-1}\,\text{cm}^{-1}$ at $\lambda = 275$ nm; GRGDY $-\varepsilon = 1110\ \text{M}^{-1}\,\text{cm}^{-1}$ at $\lambda = 275$ nm. The peptide content (conjugation yield) in the peptide-conjugates was estimated using these extinction coeficients: i.e. assuming that the conjugation to the polymer does not affect the spectral characteristics of the chromophore.

Reverse phase-high performance liquid chromatography analysis

Gradient RP-HPLC methods were used for separation and identification of the polymer precursors and polymer–peptide conjugates using a Waters column μBondapak^{TM} C_{18} (3.9 × 150 mm). For polymer–(di)-peptide conjugates an appropriate aqueous mobile phase was found to be a gradient 0–40% acetonitrile (0.1% trifluoroacetic acid) at flow rate 1 ml min^{-1} and column temperature 30°C: (A) water; (B) acetonitrile; (C) 0.5% trifluoroacetic acid: A/B/C = 80/0/20 → 40/40/20 (0′ → 40′). For the dendrimer-based derivatives, successful separation was achieved by a similar method with a combination of isocratic mode: (A) water; (B) acetonitrile; (C) 0.5% trifluoroacetic acid: A/B/C = 80/0/20 → 71/9/20 → 71/9/20 → 40/40/20 (0′ → 9′ → 14′ → 45′).

RESULTS AND DISCUSSION

In previous studies [1, 2] where PEG–peptide conjugates were designed to promote cell aggregation, a correlation between the length of the poly(ethylene oxide) chain of the polymer–(di)-peptide was identified. Since polymer properties influenced aggregation and subsequent aggregate function, we sought to extend the group of available polymer–peptide conjugates by producing materials in which chemical structure, molecular weight, conformation and functionality, were controlled. Four models of polymer–(multi)-peptide conjugates were considered (Fig. 1): (a) ‘dumbbell’ or dipeptide with an adjustable length of poly(ethylene oxide) chain; (b) ‘double-fork’ or PEG–tetra-peptide; (c) ‘ladder’ or linear (multi)-peptide-poly(acrylic acid); and (d) ‘star-dendrimer’ or dendrimer-PEG-based (multi)-peptide conjugate. In this work,

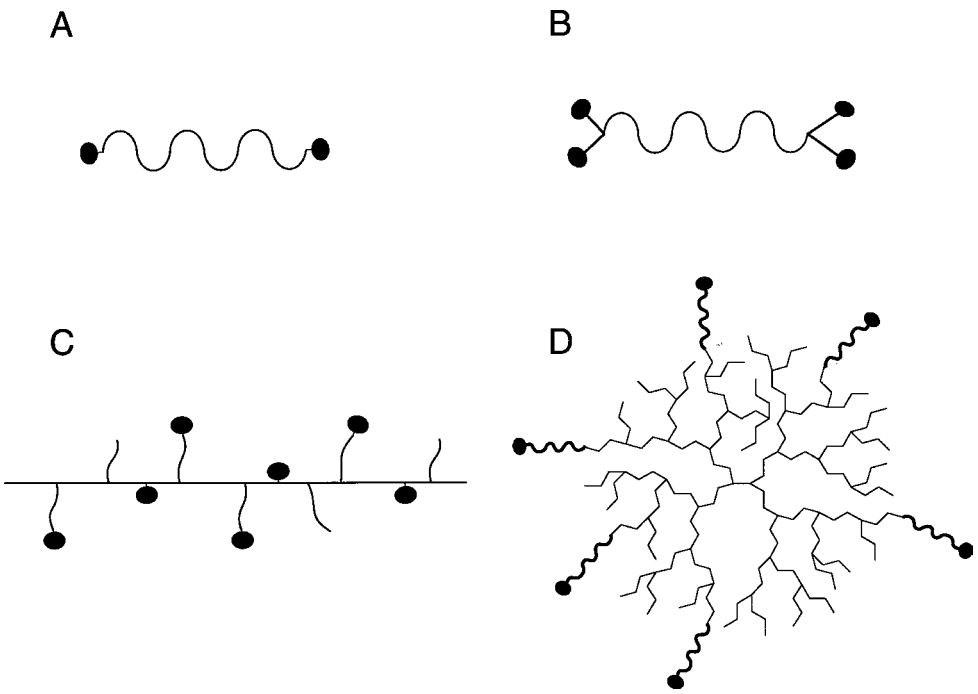

Figure 1. This cartoon shows the hypothesized structures of the polymer–peptide conjugates synthesized in the course of this study. (A) 'dumbbell': linear, di-functional PEG–peptide conjugates; (B) 'double-fork': linear, tetra-functional PEG–peptide conjugates; (C) 'ladder': linear, multi-functional poly(acrylic acid)–peptide conjugates; (D) 'star-dendrimer': PAMAM-PEG–peptide conjugates.

we describe synthetic procedures leading to high yields of polymer–(multi)-peptide conjugates as well as methods for their characterization, isolation, and purification.

N-Hydroxysuccinimidyl esters of PEGs are widely employed as highly reactive acylating reagents in organic synthesis and peptide chemistry. However, some precautions considering their hydrolytic instability are always required. On the other hand, buffered aqueous media is the only appropriate solvent for most of the peptides. To reduce solubility and stability problems, we modified the condensation procedure for synthesis of PEG_{3400}–peptide conjugates by changing the solvent system and the order of reactant addition. GGYR was dissolved in a minimal quantity of 0.1 M MES while the activated electrophile $(SPA)_2$-PEG_{3400}, dissolved in DMF, was added dropwise. No changes in pH (pH $\sim$ 6.5–7) of the media were found. The yield of the conjugate PEG_{3400}-$(GGYR)_2$ increased from 50 wt%, when the reaction was carried out only in MES, to 70–75 wt% (Table 1) even at reduced stoichiometry ratio of peptide/active ester = 1.5/1 molar ratio. By comparison of the UV spectra of the PEG_{3400}-$(GGYR)_2$ conjugates (Fig. 2), the advantages of using organic media rather than aqueous media became more obvious: the mass yield was increased as well as the conjugation yield, which was almost 10% higher based on the total content of GGYR. Aqueous SEC (Fig. 3) confirmed the higher degree of conversion achieved in DMF/MES media. Both chromatograms

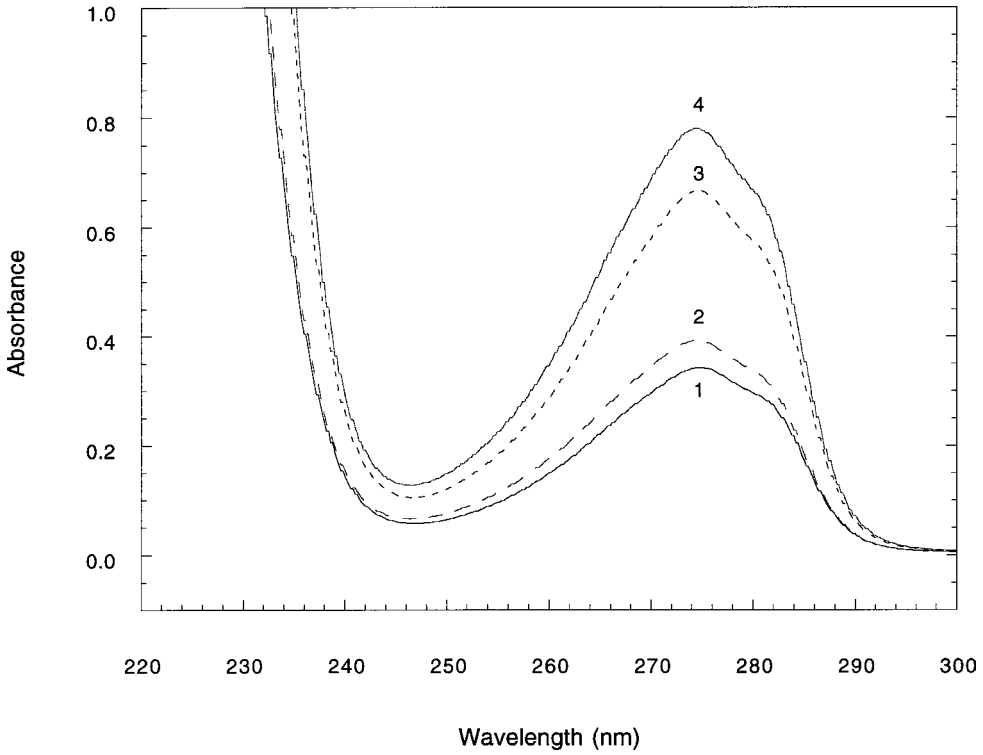

Figure 2. UV spectra of PEG_{3400}-$(GGYR)_2$ conjugates in distilled water. Curves 1 and 3 correspond to PEG_{3400}-$(GGYR)_2$ synthesized in MES; curves 2 and 4 — PEG_{3400}-$(GGYR)_2$ synthesized in DFM/MES. Curves 1 and 2 — concentration of 1 mg ml^{-1}; curves 3 and 4 concentration of 2 mg ml^{-1}.

Table 1.
PEG-based 'dumbbell' and 'double-fork' type precursors and peptide-conjugates obtained in DMF/MES media

Product name	Molecular weight of PEG (theoretical)	Theoretical peptide content (wt%)	Yield (wt%)
PEG_{3400}-$(GGYR)_2$	3400	21	70–75
PEG_{3400}-$(GRGDY)_2$	3400	25 (23*)	90
PEG_{3400}-$(ACA)_2$	3400	N/A	75
PEG_{600}-$(GGYR)_2$	600	60	25–30
PEG_{600}-$(GRGDY)_2$	600	65	35–40
TEG-$(GGYR)_2$	150	86	85
TEG-$(GRGDY)_2$	150	88 (70*)	75–80
$Jeff_{600}$-(TEG-$GRGDY)_2$	1400	49	20
$Jeff_{600}$-(PEG_{600}-$GRGDY)_2$	1400	36	35–40
PEG_{3400}-(Aspartic acid)$_2$	3400	N/A	60–70
PEG_{3400}-[Asp$(GRGDY)_2]_2$	3400	38 (28*)	45
PEG_{3400}-[APhA$(GRGDY)_2]_2$	3400	36 (17*)	70

*Values in brackets were experimentaly determined by UV-Vis spectrophotometry, see Fig. 4.

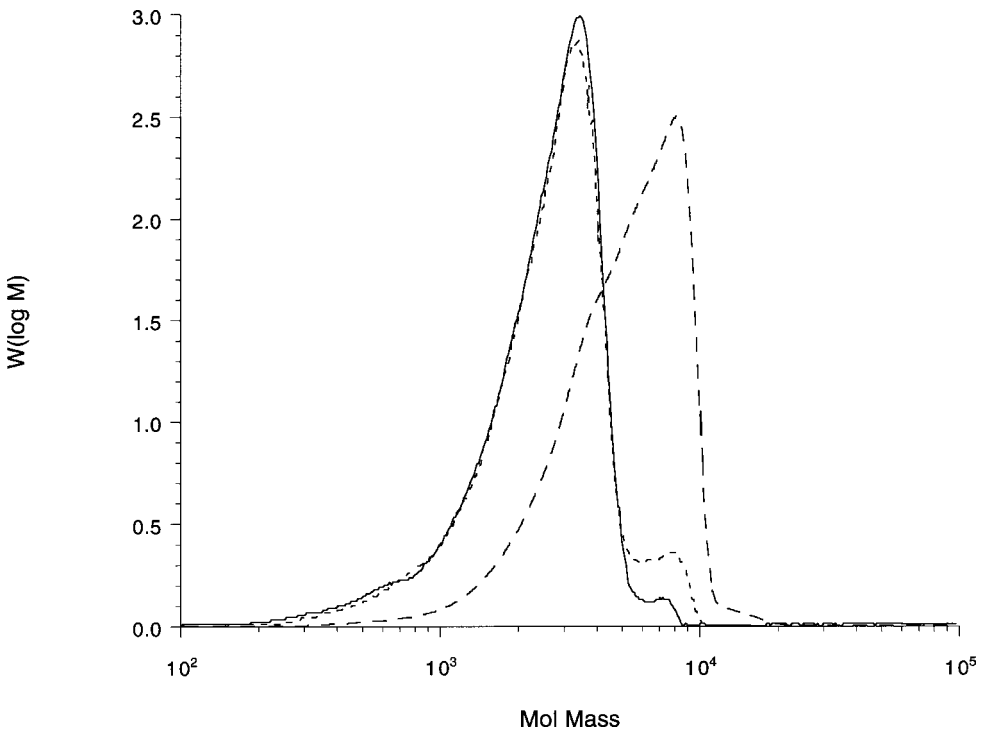

Figure 3. SEC of PEG_{3400}-$(GGYR)_2$ conjugates obtained in MES (- - -), and DMF/MES (—). The spectrum of the starting active ester $(SPA)_2$-PEG (– –) is shown as reference.

displayed M_{peak} at 4030 and $\overline{M}_w/\overline{M}_n = 1.25$. The peak for the starting polymer, $(SPA)_2$-PEG_{3400}, has an anomalously high M_{peak} of 8050, probably due to an interaction of the succinimidyl end groups with the stationary phase (Proteinpak) making comparison with the activated precursors difficult. Still, the chromatograms of both conjugates indicated some impurities (hydrolyzed $(SPA)_2$-PEG_{3400}) as small peaks at $M_w = 8050$, which were more pronounced for the conjugate obtained in MES.

Based on the results with the model peptide GGYR, the conjugation reaction was performed with GRGDY. In this case PEG_{3400}-$(GRGDY)_2$ conjugate was obtained in yield of 90 wt% (Table 1).

$(SPA)_2$-PEG_{3400} was examined in condensation reactions with amino carboxylic acid (6-aminocaproic acid, ACA) and amino-dicarboxy compounds (L-aspartic acid, Asp, and L-aspartyl-phenylalanine, AspPhA). ACA coupling was tested as end hydrophobization of the PEG chain, because it may be desirable to modify polymer character to influence ligand–receptor interaction. Asp and AspPhA, reacting through their amino-groups with the NHS-active ends, introduce two terminal carboxylic groups leading to a precursor of tetra-peptide 'double-fork' PEG-conjugate (Fig. 1B). By this procedure the content of the active residues can be increased by up to two-fold, while retaining an equivalent length of interconnecting PEG.

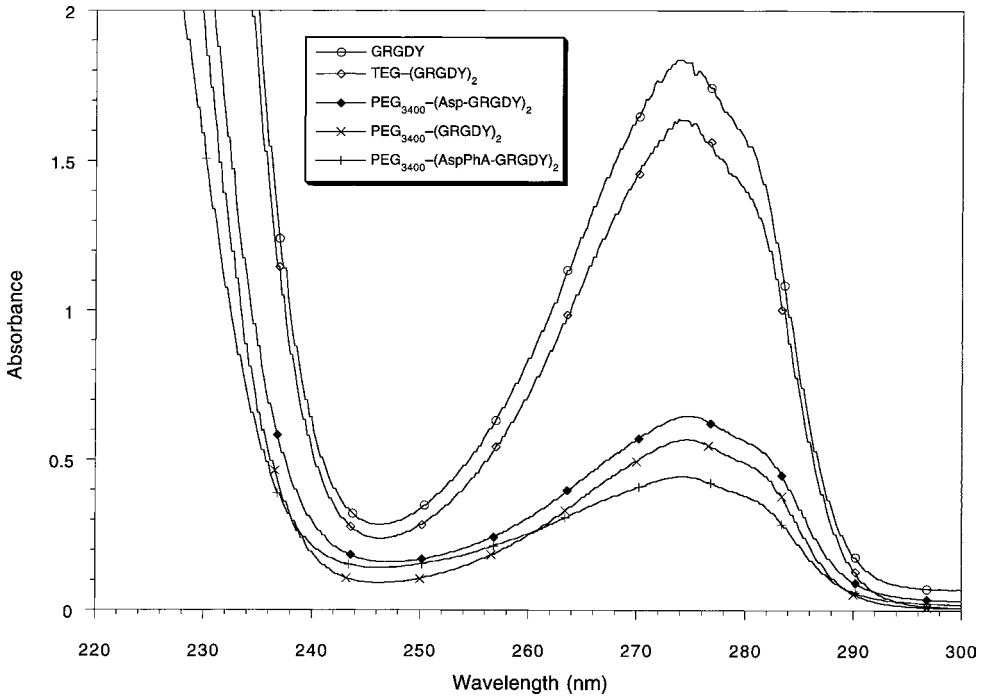

Figure 4. UV-spectra of 'dumbbell' and 'double-fork' PEG-based GRGDY conjugates in distilled water. All concentrations equal to 1.2 mg ml^{-1}.

Since the length of the poly(ethylene oxide) chain affected the aggregation in previous studies (i.e. an increase in the MW of PEG reflected in a lower activity), we synthesized (di)-peptide conjugates using low molecular PEGs such as 3,6,9-trioxaundecanedicarboxylic acid, M_r 222.2 (TEG-COOH) and PEG-bis-(carboxymethyl) ether, M_r *c*. 600 (PEG_{600}-COOH). After activation of the carboxylic groups with *N*-hydroxysuccinimide in the presence of carbodiimides in organic media, the resulting TEG-$(NHS)_2$ and PEG-$(NHS)_2$ were used as precursors for two types of reactions: (1) direct condensation reactions with peptides; and (2) condensation reactions with amino-terminated PEG (Jeffamine or $Jeff_{600}$), for a graded extention of the poly(ethylene oxide) chain, and subsequent conjugation with peptides. In this way, a set of 'dumbell' type conjugates were synthesized with a wide range of MW of PEG — 150, 600, 1400, 2000, and 3400 (Table 1).

The structure of the synthesized PEG-based precursors, 'dumbbell', and 'double-fork' conjugates were confirmed by spectral and chromatographic methods. Figure 4 summarizes the UV spectra of conjugates containing GRGDY; all conjugates were dissolved in distilled water at a concentration of 1.2 mg ml^{-1}. Comparison of the absorption at $\lambda = 275$ nm demonstrates that the decrease in the length of PEO chain and the increase in the functionality leads to a set of conjugates with different content of the active residue, i.e. GRGDY.

Formation of active esters and peptide bonds was studied by FT-IR. Unfortunately, due to the ionic nature of the peptide, FT-IR was not an appropriate method to follow

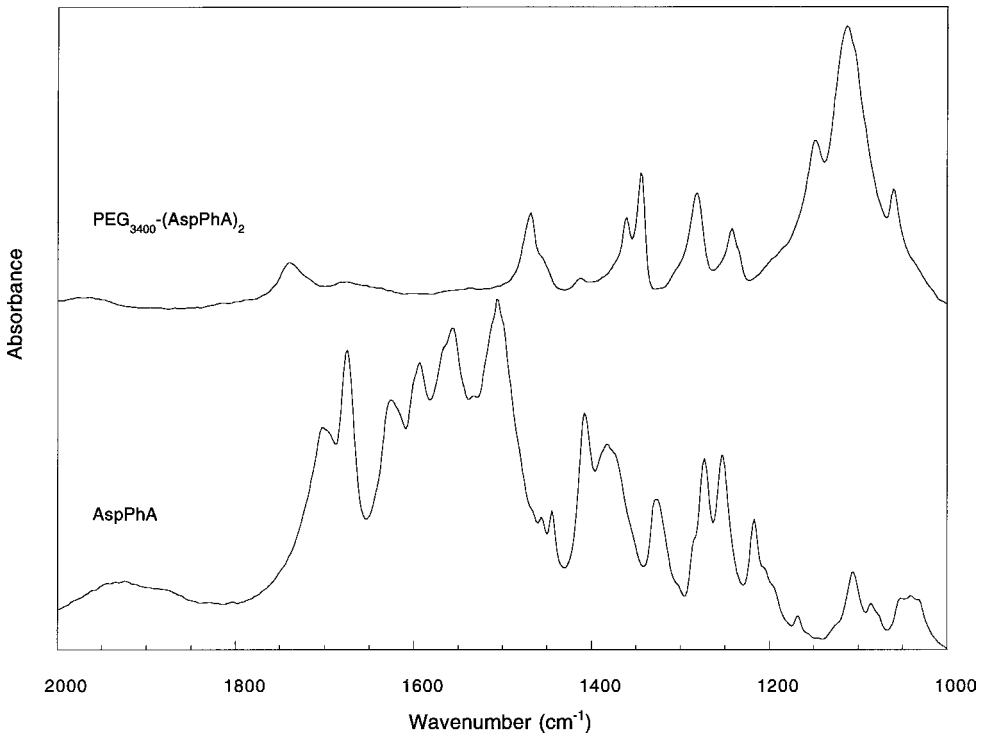

Figure 5. FT-IR spectra of AspPhA and PEG_{3400}-$(AspPhA)_2$ in KBr.

peptide bond formation with GGYR and GRGDY. Therefore, a peptide with more hydrophobic nature, AspPhA, was studied as a model (Fig. 5). Although typical amide peaks at $\nu = 1650$ and 1520 cm^{-1} were poorly resolved for PEG_{3400}-$(AspPhA)_2$, peaks for the ethylene oxide ether bonds at $\nu = 1230$ and 1120 cm^{-1} indicated successful formation of the conjugate. FT-IR spectra also confirmed the formation of the *N*-hydroxysuccinimidyl esters (Fig. 6). The disappearance of the intensive peak for free carboxylic groups at $\nu = 1750$ cm^{-1} in the PEG_{600}-COOH spectrum and appearance of new peaks at $\nu = 1800$, 1790, 1740, and 1550 cm^{-1} (typical for *N*-hydroxysuccinimide esters) in PEG_{600}-$(NHS)_2$ spectrum indicated the active ester formation.

Active esters and the respective peptide derivatives were also characterized by ^{1}H-NMR (Fig. 7) in D_2O. Conjugation yields for 'dumbbell' and 'double-fork' conjugates were estimated by assignment of Tyr aromatic protons at 6.8 ppm and 7.12 ppm. The integral value for ethylene oxide protons at 3.65 ppm was arbitrarily assigned 320, a value corresponding to the number of protons in the ethylene oxide chain based on the $(SPA)_2$-PEG_{3400} spectrum. The spectra of PEG_{3400}-$(GRGDY)_2$ and PEG_{3400}-$[(AspGRGDY_2)]_2$ clearly indicate an increase in the peptide content as demonstrated by an increase in the integral for Tyr aromatic protons from 8.31 to 12.43. Moreover, a value of 8.31 for PEG_{3400}-$(GRGDY)_2$ implies successful formation of a di-peptide since each Tyr residue has four aromatic protons. If a mono-peptide fraction is present,

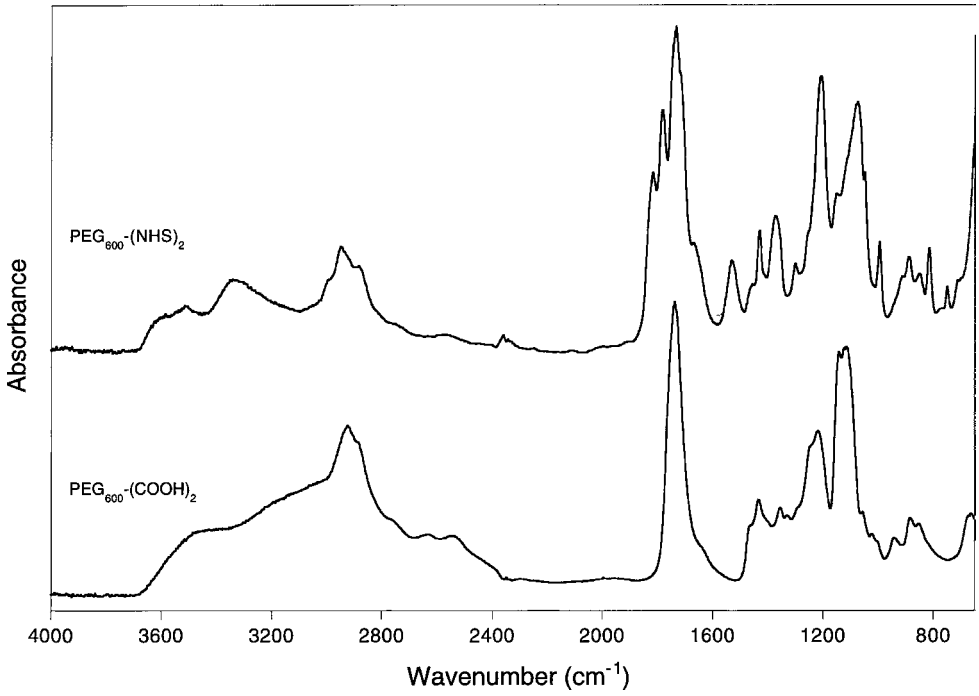

Figure 6. FT-IR spectra of PEG_{600}-$(COOH)_2$ and PEG_{600}-$(NHS)_2$ (neat).

it must be in negligible quantity (1–2 wt%). An integration of the peaks for Tyr aromatic protons in the PEG_{3400}-$[(AspGRGDY_2)]_2$ spectrum resulted in a value of 12.43 indicating that the final product has $\sim$ three peptides per conjugate.

Reverse-phase HPLC was performed with TEG-$(GGYR)_2$ to develop a method for separation of the di-peptide from other components in the final conjugation product. Successful separation was achieved using an Alliance — Waters HPLC system on μBondapak^{TM} C_{18} (3.9×150 mm) column under gradient 0–40% acetonitrile (0.1% TFA) as aqueous mobile phase at flow rate 1 ml min^{-1} and column temperature 30°C: (A) water; (B) acetonitrile; (C) 0.5% trifluoroacetic acid: A/B/C = 80/0/20 $\rightarrow$ 40/40/20 ($0' \rightarrow 40'$). The retention time (RT) for GGYR was found to be 9.28 min. Figure 8A shows the chromatogram of TEG-$(GGYR)_2$ where at least six peaks are resolved. Using PDA 996 UV detection (Fig. 8B) it was possible to distinguish peptide–polymer conjugates from the other components. The peak at RT = 9.448 min appears to be TEG-$(GGYR)_2$ (being more polar) while the peak at RT = 18.015 min is the mono-peptide.

Linear multi-conjugate 'ladder' type conjugates were based on poly(acrylic acid) polymers and co-polymers. Acrylic acid polymers are the simplest model for linear polymers with a pendant carboxylic group at each monomer unit. Also, by condensation reaction of NHS-activated esters of poly(acrylic acid) with 6-aminocaproic acid (ACA), (acrylic acid-*co*-aminocaproylacrylic acid) polymers were synthesised. ACA spacers were added to overcome possible steric hindrance in the further con-

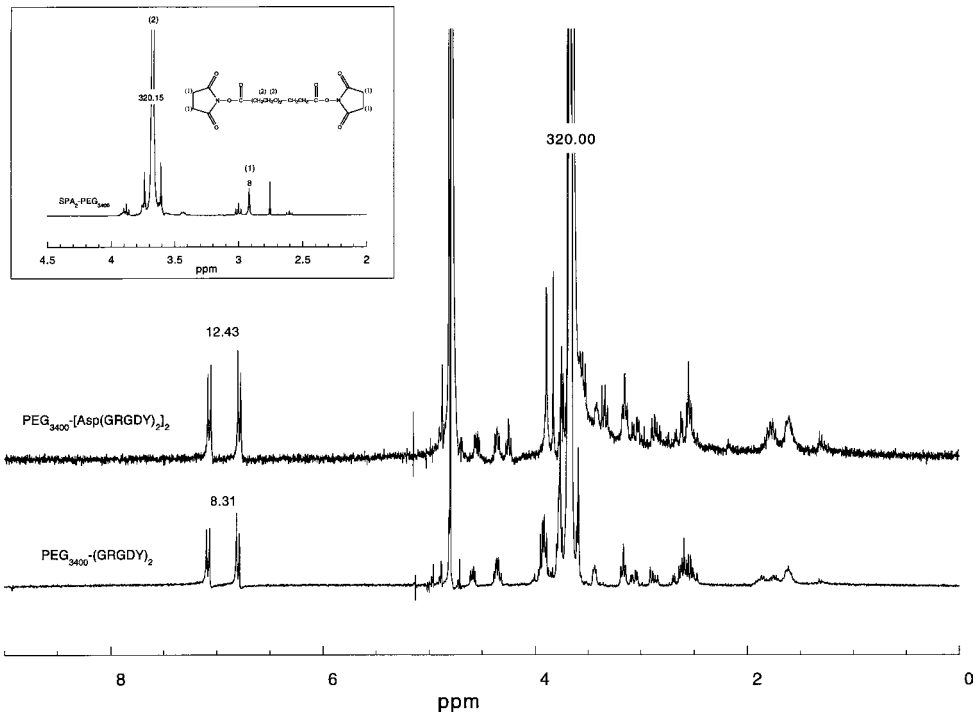

Figure 7. ^{1}H-NMR spectra of PEG_{3400}-$(GRGDY)_2$ and PEG_{3400}-$[Asp(GRGDY)_2]_2$ in D_2O are shown in this figure. The inset shows the ^{1}H-NMR spectrum of the starting material, $(SPA)_2$-PEG_{3400} as a reference.

densation reaction with the peptides; the spacers can be used for tailoring the number of the activated COOH groups as well. L-Tryptophan was used as a model nucleophile and the condensation reactions were carried out in aqueous media. Figure 9 shows UV-spectra of two different L-tryptophan conjugates — poly(acrylic acid)–(L-tryptophan)$_n$ and poly(acrylic-*co*-aminocaproylacrylic acid)(1 : 1)–(L-tryptophan)$_{n/2}$ in distilled water at concentration 1.2 mg ml^{-1}. An increase in the number of pendent peptides from $n/2$ to n was found to reflect in an adequate absorption increase.

Dendritic (multi)-peptide conjugates were synthesized from the water soluble Starburst® dendrimer polyamidoamine PAMAM (G = 3), MW = 6909. We designed 'star-dendrimer' where the core was the dendrimer and the arms were PEG fragments with MW = 600 and 3400. The flexibility of the PEO chain was considered a prerequisite for promoting effective multiple ligand–cell receptor interactions. To achieve successful coupling of PEG in the condensation reaction with PAMAM (G = 3), while avoiding some possible cross-linking, a 100-fold molar excess of PEG_{600}-$(NHS)_2$ or $(SPA)_2$-PEG_{3400} was used. After reaction the basic nature of PAMAM (G = 3) (pH > 11) was reduced to acidic, an indication of a successful coupling of PEG-active esters. Titration with 0.1 N NaOH suggested $1.6–1.7 \times 10^{-3}$ mol NHS per 1 g of PAMAM(G = 3)-PEG_{600}-(NHS). It was difficult to estimate the number of NHS groups per molecule, since PEG_{600}-$(NHS)_2$was not fractionated and the presence of

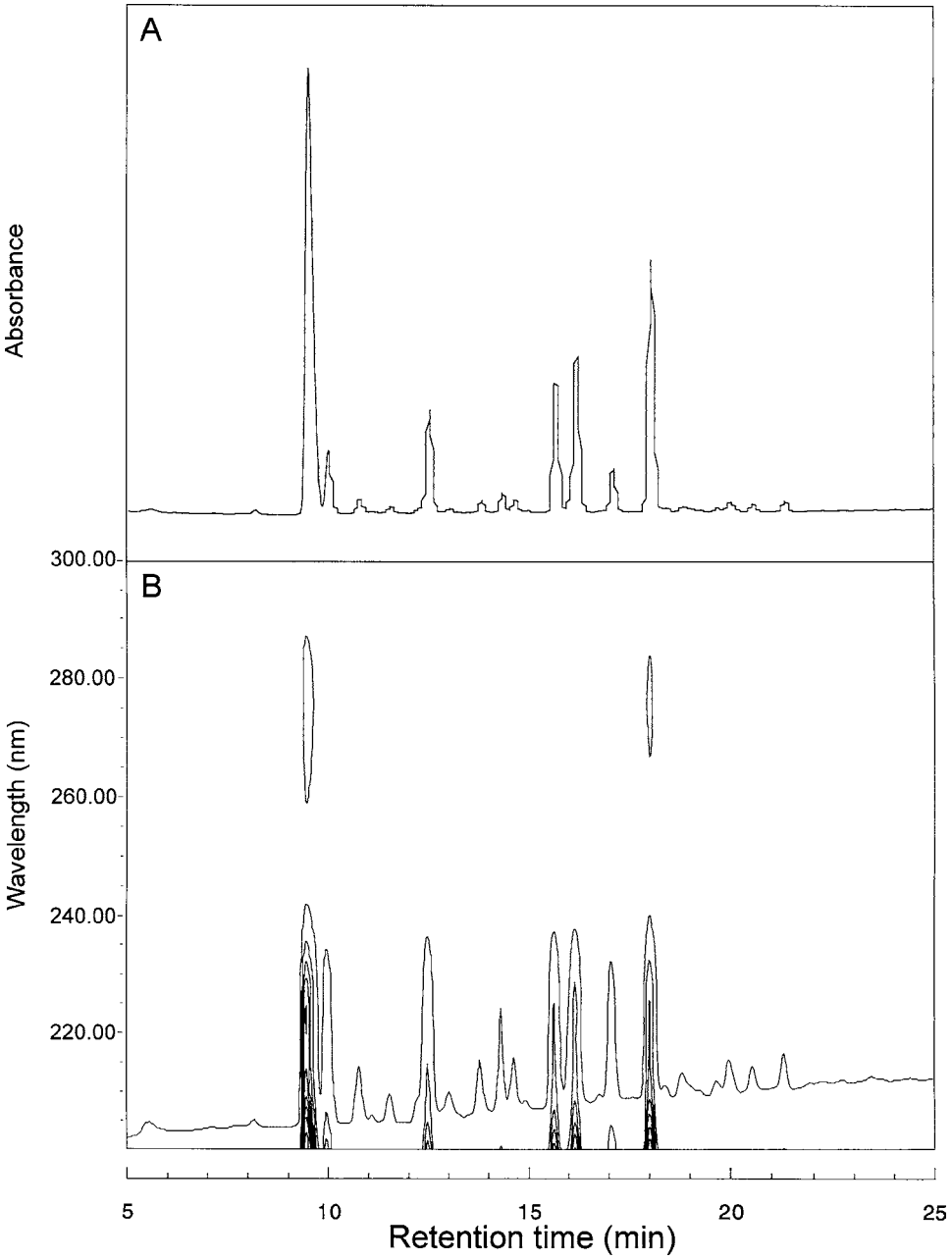

Figure 8. RP-HPLC of TEG-$(GGYR)_2$. Gradient: (A) water, (B) acetonitrole, (C) 0.5% trifluoroacetic acid: $A/B/C = 80/0/20 \rightarrow 40/40/20$ ($0' \rightarrow 40'$). Column: Waters μBondapak^{TM} C_{18} (3.9×150 mm). (A) shows the chromatogram registered at $\lambda = 237$ nm, while (B) shows the corresponding PDA contour plot.

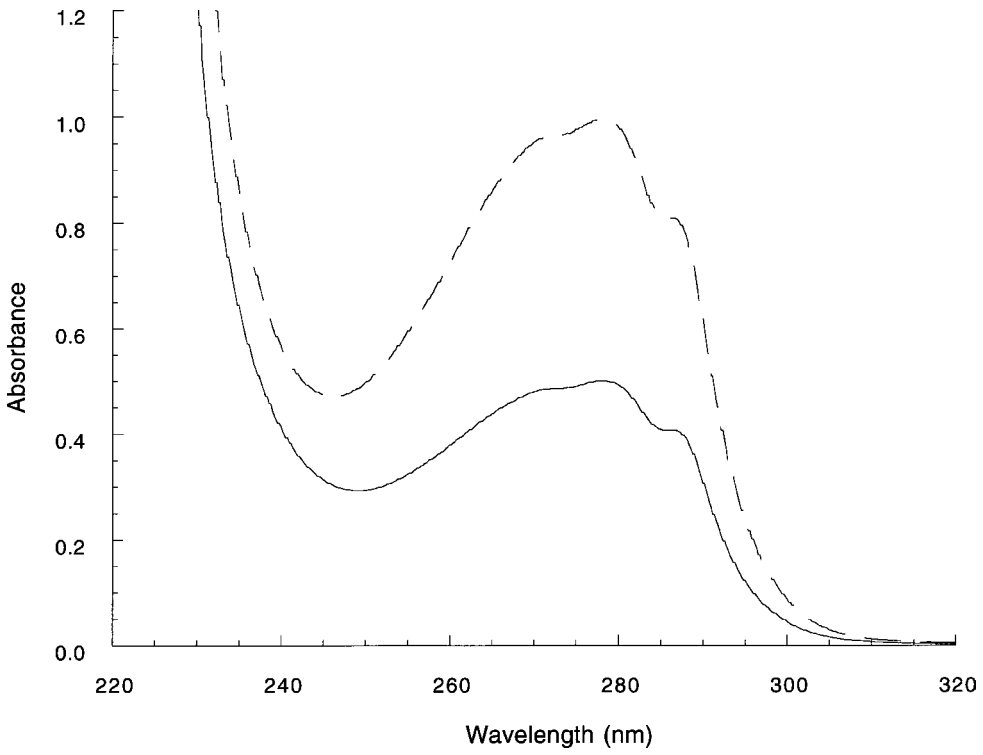

Figure 9. UV spectra of L-tryptophan conjugates: poly(acrylic acid)–(L-tryptophan)$_n$ (– –), and poly-(acrylic-*co*-aminocaproylacrylic acid)–(L-tryptophan)$_{n/2}$ (—) in distilled water at a concentration of 1.2 mg ml^{-1}.

some mono-ester fraction can not be excluded. Thus, using GRGDY as a nucleophile, two 'star-dendrimer' conjugates were synthesized and isolated: PAMAM(G = 3)-(PEG$_{600}$-GRGDY)$_m$ and PAMAM(G = 3)-(PEG$_{3400}$-GRGDY)$_n$.

The number of active peptide residues that were successfully attached was estimated by spectral methods. UV spectra of both conjugates were performed in 0.2 N HCl where ε at $\lambda = 275$ for GRGDY was found to be 1280 M^{-1} cm^{-1}. Acidic media was used because neutral aqueous solutions of PAMAM(G = 3)-(PEG$_{600}$-GRGDY)$_m$ displayed turbidity even at low concentrations. An increase in the length of PEO chain from PEG$_{600}$ to PEG$_{3400}$ resulted in a more soluble conjugate; aqueous solutions were transparent over a broad concentration range. For PAMAM(G = 3)-(PEG$_{600}$-GRGDY)$_m$ the average GRGDY content was 38.7 wt% (for 'dumbbell' PEG$_{3400}$-(GRGDY)$_2$ it was found 23 wt%). In the reaction with PEG$_{3400}$ two fractions of conjugates were isolated, differing in GRGDY content: type A — 31.7 wt% and type B — 8.7 wt%. This finding was confirmed with ^{1}H-NMR spectra in D_2O by estimating the ratio between Tyr aromatic protons (7.20–6.65 ppm) and ethylene oxide protons (3.80–3.50 ppm) (Fig. 10). A high GRGDY content for type A conjugates (average 3.5 peptide units per PEG$_{3400}$) suggests that two types of peptide binding are possible: covalent end binding to the PEG$_{3400}$-active ester, and salt formation

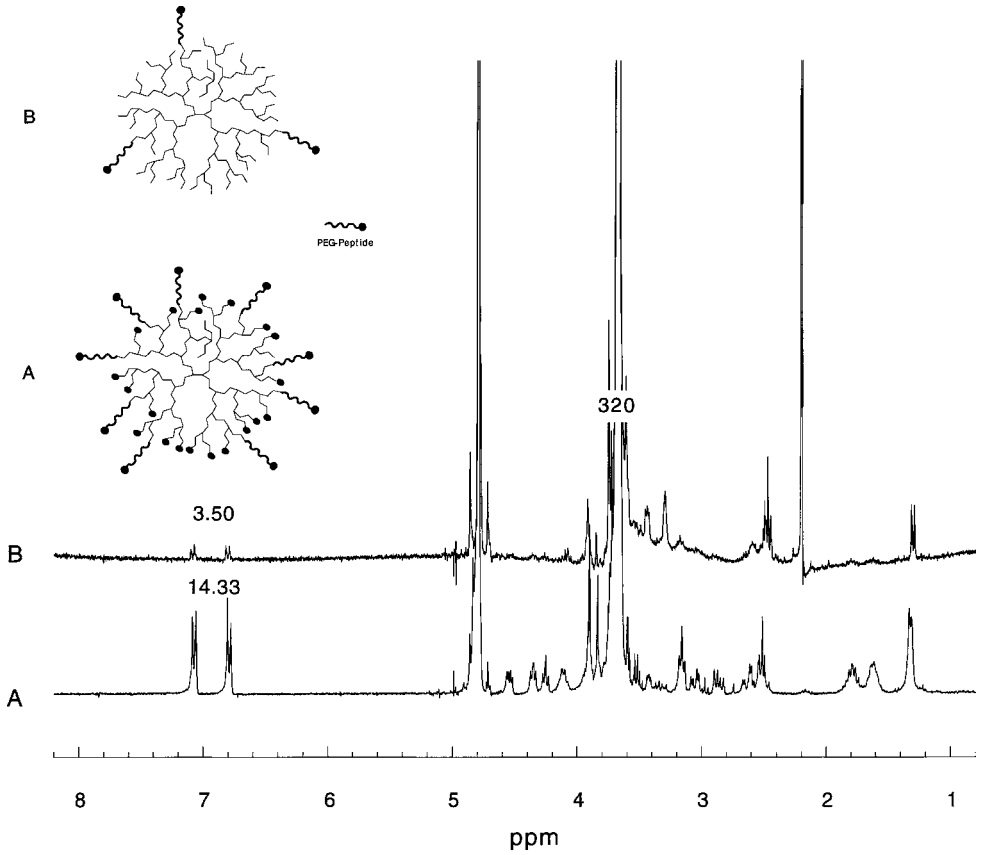

Figure 10. ^{1}H-NMR spectra of PAMAM-(PEG$_{3400}$-GRGDY)$_n$ 'star-dendrimer' conjugates in D_2O; type (A) $n = 31.5$; type (B) $n = 3$.

between PAMAM tertiary amino groups and peptide carboxylic groups. For type B, ^{1}H-NMR confirmed the content of one peptide molecule per PEG$_{3400}$; the same ratio of peptide/PEG$_{600}$ = 1/1 was found for PAMAM(G = 3)-(PEG$_{600}$-GRGDY)$_m$, also. Based on the results from the spectral methods, the average functionality (i.e. number of GRGDY residues) was estimated as follows: (i) for PAMAM(G = 3)-(PEG$_{600}$-GRGDY)$_m$ — 11 GRGDY residues; (ii) for PAMAM(G = 3)-(PEG$_{3400}$-GRGDY)$_n$ type A — an incredibly high content of peptide — 31.5 (theoretical numbers equal to 32) where 9 of them are bound through PEG$_{3400}$; (iii) for PAMAM(G = 3)-(PEG$_{3400}$-GRGDY)$_n$ type B — 3 GRGDY residues covalently bound.

Some preliminary RP-HPLC data also confirmed the successful formation of PAMAM(G = 3)-(PEG$_{600}$-GRGDY)$_m$ (m = 11) conjugate. Applying a gradient method water/acetonitrile/0.5% trifluoroacetic acid: 80/0/20 → 71/9/20 → 71/9/20 → 40/40/20 (0′ → 9′ → 14′ → 45′) on Waters column μBondapak^{TM} C$_{18}$ (3.9 × 150 mm) at flow rate 1 ml min^{-1} and column temperature 30°C, one peak at RT = 10.040 min was registered (Fig. 11). The peak for GRGDY appeared at RT = 9.758 min under the same conditions. A more detailed study is in progress.

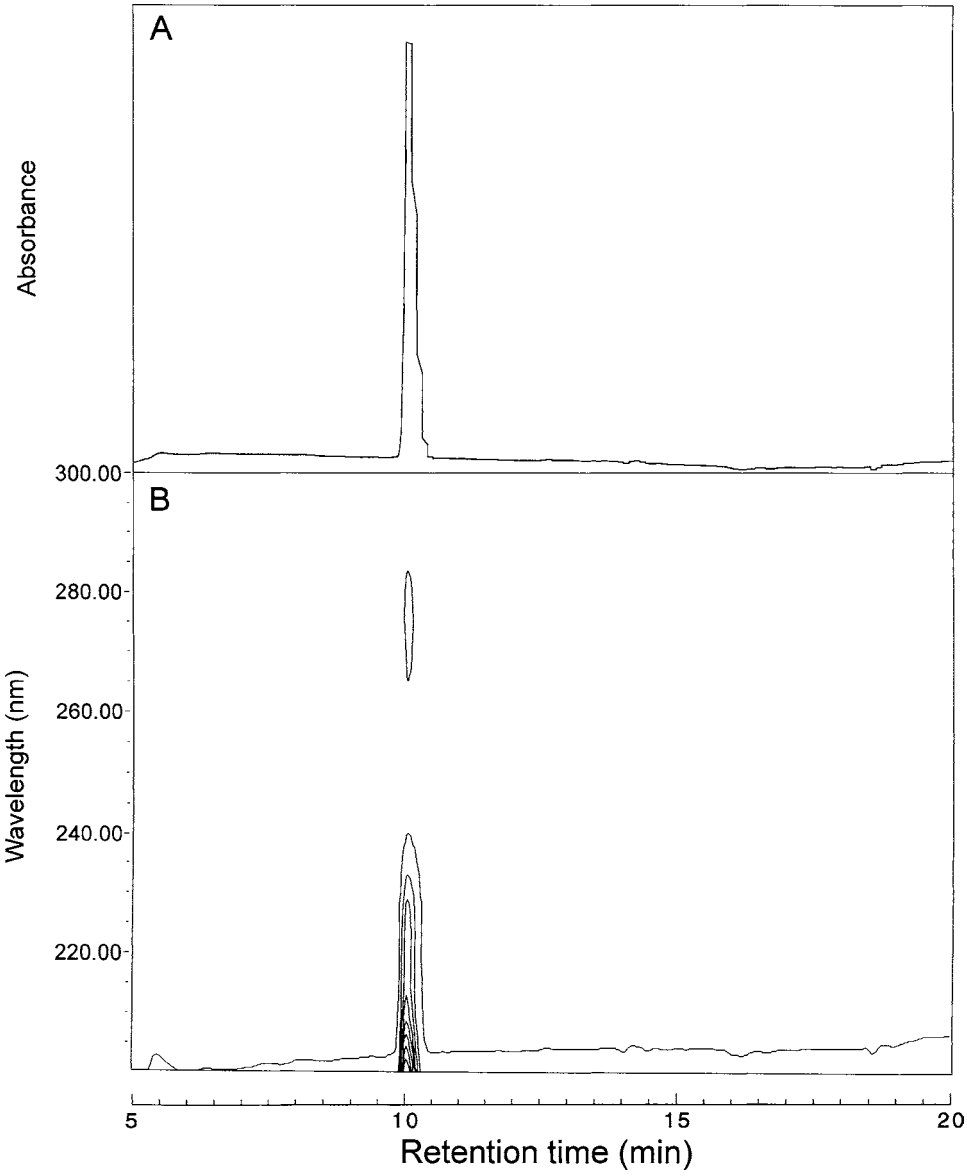

Figure 11. RP-HPLC of PAMAM-(PEG$_{600}$-GRGDY)$_m$ ($m = 11$) under gradient of water/acetonitrile/0.5% trifluoroacetic acid: 80/0/20 → 71/9/20 → 71/9/20 → 40/40/20 (0′ → 9′ → 14′ → 45′). (A) shows the chromatogram registered at $\lambda = 237$ nm, while (B) shows the corresponding PDA contour plot.

CONCLUSIONS

A condensation method in the presence of carbodiimides was performed using *N*-hydroxysuccinimidyl active esters for synthesis of novel polymer–(multi)-peptide conjugates. We believe that these materials will be useful for cell aggregation. Four

types of conjugates were obtained: (a) 'dumbbell' or polymer–di-peptide conjugates with different length of poly(ethylene oxide) chain, MW = 150, 600, 1400, 2000, and 3400, and content of GRGDY up to 70 wt%; (b) 'double-fork' or PEG–tetra-peptide conjugate, where functionality of PEG was increased prior to conjugation with GRGDY by end-linking of L-aspartic acid or L-aspartyl-phenylalanine, resulting in a higher peptide content (up to 28 wt% for PEG_{3400}-$[Asp(GRGDY)_2]_2$ keeping the same length of PEO as 'dumbbell' type); (c) acrylic acid polymers or copolymers were used for synthesis of 'ladder' type conjugates by developing a strategy for linear polymer–(multi)-peptide conjugates with controlled structure and functionality; (d) 'star–dendrimer' type conjugates were obtained as a model of hyperbranched macromolecules combining the multifunctional nature of PAMAM (G = 3) with the flexibility of PEG, MW = 600 and 3400 and resulting in conjugates with high content of GRGDY ($n = 32$) up to 38 wt%.

Acknowledgements

The authors are thankful to: Dr. Ivan Gitsov for the SEC analysis; Dr. Vladimir Benin and Dr. Ralph Spindler for useful suggestions and discussions. Financial support was provided by a grant from NASA (NAG-9-654).

REFERENCES

1. W. Dai, J. Belt and W. M. Saltzman, *Bio/Technology* **12**, 797 (1994).
2. W. Dai and W. M. Saltzman, *Biotechnol. Bioeng.* **50**, 349 (1996).
3. T. Sakane and W. Pardridge, *Pharmaceutical Res.* **14** (8), 1085 (1997).
4. A. Felix, Y.-A. Lu and R. Campbell, *Int. J. Peptide Protein Res.* **46**, 253 (1995).
5. R. Nakhgevany, O. Bonsu, J. Barber, P. Mabrouk, Y.-F. Ueng, L. C. Bell and F. P. Guengerich, *Biochem. Biophys. Res. Commun.* **222**, 406 (1996).
6. H. Gaertner and R. Offord, *Bioconjugate Chem.* **7**, 38 (1996).
7. A. Nag, G. Mitra and P. Ghosh, *Anal. Biochem.* **237**, 224 (1996).
8. S. Zalipsky, F. Albericio, U. Slomczynska and G. Barany, *Int. J. Peptide Protein Res.* **30**, 740 (1987).
9. S. Zalipsky, *Bioconjugate Chem.* **6**, 150 (1995).
10. C. Delgado, R. Pedley, A. Herraez, R. Boden, P. Keep, K. Chester, D. Fisher, R. Begent and G. Francis, *Br. J. Cancer* **73**, 175 (1996).
11. M. Bouvier and D. Wiley, *Proc. Natl Acad. Sci. USA* **93**, 4583 (1996).
12. R. Tuma, M. Russell, M. Rosendahl and G. Thomas, Jr., *Biochemistry* **34**, 15 150 (1995).
13. K. Kawasaki, M. Namikawa, Y. Yamashiro, Y. Iwai, T. Hama, Y. Tsutsumi, S. Yamamoto, S. Nakagawa and T. Mayumi, *Chem. Pharm. Bull.* **43**, 2133 (1995).
14. I. Saiki, J. Yoneda, Y. Igarashi, M. Aoki, N. Kusunose, K.-I. Ono and I. Azuma, *Jpn. J. Cancer Res.* **84**, 558 (1993).
15. D. Putnam and J. Kopecek, *Adv. Polym. Sci.* **122**, 57 (1995).
16. S. Morgan, V. Subr, K. Ulbrich, J. Woodley and R. Duncan, *Int. J. Pharmaceutics* **128**, 99 (1996).
17. K. Ulbrich and D. Oupicky, in: *Abstracts of the Eighth International Symposium on Recent Advances in Drug Delivery Systems*, Salt Lake City, Utah, February 24–27, 1997, p. 215.
18. Z. Ding, G. Chen and A. Hoffman, *Bioconjugate Chem.* **7**, 121 (1996).
19. W. M. Saltzman, in: *Textbook of Tissue Engineering*, R. P. Lanza, W. L. Chick and R. Langer (Eds), p. 227. Springer, New York (1996).
20. N. Peppas and R. Langer, *Science* **263**, 1715 (1994).
21. R. Marchant and I. Wang, in: *Implantation Biology*, R. S. Greco (Ed.), p. 13. CRC Press, Boca Raton, FL (1994).

22. J. Smith, in: *Integrins — Molecular and Biological Responces of the Extracellular Matrix*, D. Cheresh and R. Mecham (Eds), p. 1. Academic Press (1994).
23. M. D. Piershbacher, E. Hagman and E. Ruoslahti, *Cell* **26**, 259 (1981).
24. M. D. Piershbacher and E. Ruoslahti, *Nature* **309**, 30 (1984).
25. S. Massia and J. Hubbell, *J. Biomed. Mater. Res.* **25**, 223 (1991).
26. B. Brandley and R. Schnaar, *Anal. Biochem.* **172**, 270 (1988).
27. D. Barrera, E. Zylstra, P. Lansbury and R. Langer, *J. Am. Chem. Soc.* **115**, 11 010 (1993).
28. Y. Lu and A. Felix, *Int. J. Peptide Protein Res.* **43**, 127 (1993).
29. G. Chen and A. Hoffman, *Bioconjugate Chem.* **4**, 509 (1993).
30. N. Belcheva, C. Tsvetanov, I. Panayotov and S. Lazarova, *Makromol. Chem.* **191**, 213 (1990).
31. N. Nakajima and Y. Ikada, *Bioconjugate Chem.* **6**, 123 (1995).

Polymers for Tissue Engineering, pp. 73–97
Molly S. Shoichet and Jeffrey A. Hubbell (Eds)

Synthesis and characterization of degradable polyurethane elastomers containing an amino acid-based chain extender

G. A. SKARJA and K. A. WOODHOUSE*

Department of Chemical Engineering and Applied Chemistry, University of Toronto, 200 College St., Toronto, Ontario, Canada M5S 3E5

Received 10 June 1997; accepted 11 September 1997

Abstract—Degradable polyurethane elastomers were synthesized using a diester chain extender. The chain extender was synthesized by a diesterification reaction between L-phenylalanine and 1,4-cyclohexane dimethanol to yield a diester, diamine. Soft segment chemistry (polycaprolactone diol, PCL and polyethylene oxide, PEO) and molecular weight were varied and the impact on polyurethane physicochemical and degradation characteristics was evaluated. It was found that the PEO containing polyurethanes absorbed large amounts of water while the PCL containing ones did not, indicating a large difference in bulk hydrophilicity. The rate of water vapor permeance (WVP) through the polyurethane films generally followed the water absorption trends. However, soft segment crystallinity, noted by DSC, for the PCL containing polyurethanes served to reduce WVP values with increasing PCL molecular weight. Polyurethane surface characterization was carried out by water contact angles and XPS. The PEO containing polyurethanes exhibited low contact angles in comparison with the PCL ones. In addition, angle-resolved XPS demonstrated soft segment surface enrichment in all cases typical for phase segregated materials. Significant variation in the physicochemical properties of the experimental polyurethanes was observed indicating potential use in a variety of biomaterials applications.

An *in vitro* degradation study was carried out by incubating the polymers in 0.1 M TBS at 37°C, pH 8.0 for up to 56 days. Degradation was followed by measuring mass loss, change in molecular weight by GPC and surface alteration by scanning electron microscopy. The polyurethane containing PEO was found to exhibit substantial mass and molecular weight loss over 56 days resulting in a porous material of little strength. In contrast, the PCL containing polyurethane displayed modest mass and molecular weight loss after 56 days. This polyurethane retained its strength and displayed little surface alteration after 56 days in buffer. It was hypothesized that differences in polyurethane hydrophilicity as well as initial molecular weight may have been responsible for the dramatic difference in degradation rate observed here.

Key words: Biodegradable polyurethanes; tissue engineering; polymer synthesis; amino acids.

INTRODUCTION

There is growing interest in degradable polymers for a variety of biomaterials uses, ranging from tissue engineering scaffolds to drug delivery [1–3]. Polymeric devices

*To whom correspondence should be addressed.

which intentionally degrade and disappear upon completion of their function may mitigate the inevitable, usually negative physiologic responses (e.g., thrombosis, fibrous encapsulation) which may limit long-term device success. Thus, an array of degradable polymers have been developed and studied for many uses [4–6]. However, relatively few of these degradable materials are elastomeric polymers. Rather, the majority of degradable polymers are essentially hard, brittle materials [7], developed for drug delivery uses. With the increasing interest in tissue engineering, degradable materials exhibiting a wide variety of physical properties are necessary to integrate with the various tissues of the body. Degradable elastomers may be envisioned to be specifically applicable to soft tissue engineering (e.g., skin, vasculature, etc.).

Segmented polyurethane elastomers have enjoyed wide use as biomaterials due to their excellent mechanical properties and great chemical versatility [8]. Variations on the chemistry may be employed to produce polyurethanes which display a wide range of physical and chemical properties. Thus, polyurethanes may be easily modified to produce materials specifically tailored for a variety of biomaterials applications. The vast majority of research devoted to the development of biomedical polyurethanes has focused on long-term applications such as vascular grafts and pacemaker lead insulators [8]. Accordingly, a significant amount of research involving the degradation of non-degradable polyurethanes has been undertaken [9–12]. The research here indicates that the urethane, urea and ester groups which may be present in the polyurethane are susceptible to limited hydrolysis (both chemical and enzymatic) in biological media. In addition, ether groups often present in the soft segment are susceptible to oxidative degradation via phagocyte-derived oxidants [13], and this is believed to be a key component of the stress cracking phenomenon noted for pacemaker lead insulation.

In comparison to the above studies, relatively little research has been directed at developing intentionally degradable polyurethanes for temporary implantation. Several papers were published in the early 1980s describing polyurethane/polylactide blends as degradable materials for skin substitutes, vascular prostheses and nerve regeneration guides [14, 15]. However, in these cases the polyurethane portion of the blend was non-degradable and served only to provide favorable mechanical properties. Subsequent work by Bruin *et al*. [16] involved the synthesis of cross-linked polyurethane networks incorporating lactide or glycolide and ε-caprolactone joined by a lysine-based diisocyanate. These polymers displayed good elastomeric properties and were found to degrade within 26 weeks *in vitro* and 12 weeks *in vivo* (subcutaneous implantation in guinea pigs). However, a drawback of this approach is that the highly cross-linked polymer may not be processed by standard techniques such as solution casting or melt processing as is the case for typical linear, segmented polyurethanes. Cohn *et al*. developed and patented a series of elastomeric polyester–polyether–polyurethane block copolymers intended for use as surgical articles [17]. More recently, poly(phosphoester urethanes) have been synthesized by Dahiyat *et al*. [18] for drug delivery applications. However, these polymers are relatively stiff, low tensile strength materials, which may preclude their use as elastomeric biomaterials.

The objective of the work reported here was to synthesize and characterize a series of degradable polyurethane elastomers which could be employed in soft tissue repair applications. An aliphatic diisocyanate (hexamethylene diisocyanate, HDI) was employed as a precursor to the use of an experimental aliphatic diisocyanate which is potentially non-toxic. The HDI-based polyurethanes described here are expected to exhibit similar physical and degradative properties to the ultimate materials.

The degradable polymers were synthesized using an amino acid-based diester chain extender and two soft segments of varying molecular weight. An amino acid-based chain extender was chosen for two reasons. First, it was hypothesized that non-toxic degradation products would be released upon degradation of the polymer, and second, the presence of amino acid groups in the polymer backbone might confer some degree of susceptibility towards enzymatic degradation. In particular, L-phenylalanine was chosen as the amino acid since it is present in the reactive site for chymotrypsin-like enzymes which may be present in the physiological environment and thus may contribute to the degradation of the polyurethanes [19].

Polycaprolactone diol and polyethylene oxide were employed as the soft segments since both of these molecules have been widely employed in biomaterials applications and are generally accepted as non-toxic [20, 21]. By varying the type and molecular weight of the soft segment of the polyurethanes, it was possible to modulate both the polymers physicochemical and degradative properties widely, which are reported here.

MATERIALS AND METHODS

Materials

L-Phenylalanine and 1,4-cyclohexane dimethanol were obtained from Aldrich Chemicals, Milwaukee, WI, USA and used as received. The *p*-toluene sulfonic acid monohydrate was obtained from Sigma Chemical Co., St. Louis, MO, USA. Toluene used to suspend the reactants in the chain extender synthesis reaction was obtained from BDH Chemicals, Mississauga, ON, Canada. Ethanol used in the chain extender purification was obtained from Commercial Alcohols Inc., Brampton, ON, Canada.

Polycaprolactone diol (molecular weights 530, 1250, and 2000) and polyethylene oxide (molecular weights 600, 1000, and 2000) were obtained from Aldrich Chemicals. The soft segment diols were placed in a vacuum oven at 60°C for at least 48 h to remove residual water prior to reaction. Hexamethylene diisocyanate (HDI) was obtained from Fluka Chemie AG, Buchs, Switzerland and was distilled under vacuum prior to use. Stannous octoate, used as a catalyst for the prepolymer reaction, was obtained from Sigma. Polyurethane solvents dimethyl formamide (anhydrous grade DMF) and chloroform were obtained from Aldrich and ACP Chemicals Inc., Montreal, PQ, Canada, respectively.

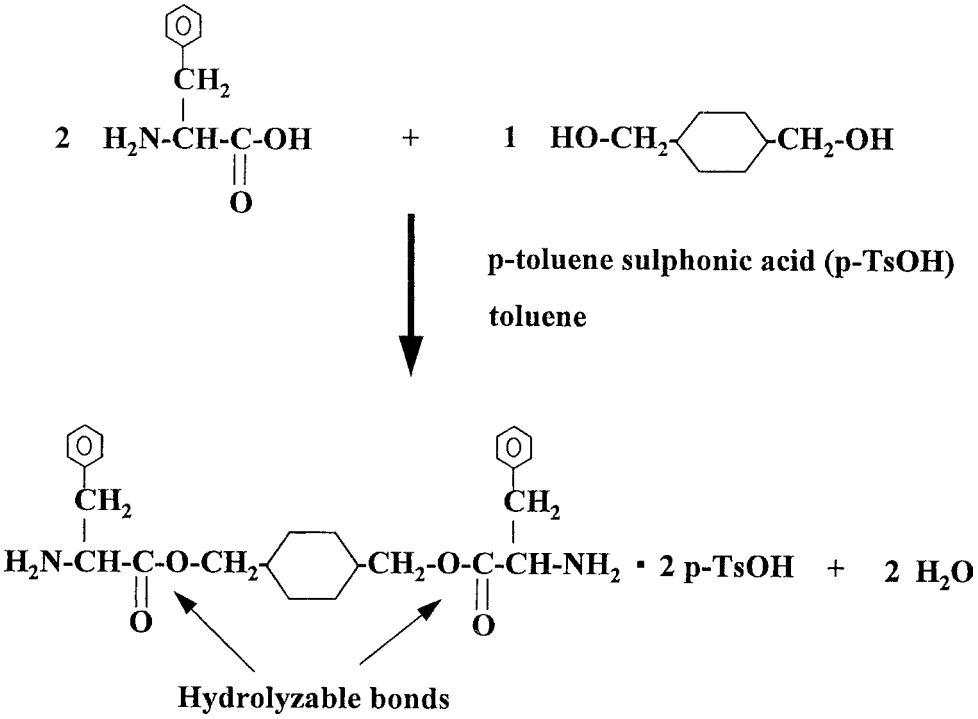

Figure 1. Synthesis of L-phenylalanine-based diester chain extender.

Chain extender synthesis and characterization

The method of Huang *et al.* [22] was employed to carry out the chain extender synthesis. The method utilizes a Fischer esterification reaction between the carboxyl function of 2 mol of L-phenylalanine and the hydroxyl functions of 1 mol of 1,4-cyclohexane dimethanol to produce a diester diamine chain extender (Fig. 1). The reaction was carried out in the presence of *p*-toluene sulfonic acid in toluene under refluxing conditions. The reaction was driven towards completion by trapping the evolved water and is continued until no more water was collected. The crude product (in the form of a tosylate salt) was then dried under vacuum at 80°C for 48 h to remove residual toluene and then ground into a fine powder. The light brown powder was subsequently washed five times by stirring the powder in a $\sim$15% w/v suspension of anhydrous ethanol followed by filtering the purified solid. Finally, the solid was washed with 60°C distilled water and filtered to remove any residual, unreacted phenylalanine. The bright white purified solid was then dried under vacuum at 80°C for 48 h.

The tosylate salt of the chain extender was converted to the free diamine form as follows. The salt was dissolved in distilled water at 90°C and a molar excess of potassium carbonate was added slowly. The diamine formed a yellow oil which solidified to a waxy solid upon cooling. The solid diamine was filtered, washed with distilled water and dried under vacuum at room temperature for 48 h. The dried solid

was then dissolved in chloroform at approximately 20% w/v and filtered to remove any insoluble impurities. Finally, the chloroform was evaporated off and the resulting light yellow solid was stored in a desiccator until use.

The success of the synthesis reaction as well as the purification scheme was monitored by nuclear magnetic resonance (NMR) spectroscopy, Fourier transform infrared spectroscopy (FTIR) and elemental analysis. NMR samples were dissolved in d_6 dimethyl sulfoxide at 1% w/v and analyzed in a 400 MHz Bruker spectrometer. FTIR samples were either analyzed neat or prepared as a mull in paraffin oil and placed between two NaCl crystals and analyzed in a Nicolet Impact 410 spectrometer. Elemental analysis was carried out by Galbraith Laboratories, Knoxville, TN, USA to determine elemental composition and allow comparison to theoretical prediction.

Polymer synthesis and film casting

Polyurethanes were synthesized via the standard, two-step reaction procedure [23]. Briefly, HDI was reacted with either polyethylene oxide (PEO) or polycaprolactone diol (PCL) at a 2 : 1 molar ratio in anhydrous DMF at 85°C. The prepolymer reaction was catalyzed using 0.1% stannous octoate and allowed to proceed for 150 min. The reaction temperature was lowered to 25°C, the chain extender was added at a 1 : 1 molar ratio with the prepolymer and allowed to react for approximately 18 h. The polymers were precipitated in saturated aqueous KCl and vacuum filtered. The polymers were then immersed in distilled water for 48 h, refiltered and dried under vacuum at 60°C for 48 h. Finally, the polymers were stored in a desiccator until use.

Solid films were prepared by solution casting. The PCL-based polyurethanes were dissolved in chloroform at a concentration of 3% w/v and the PEO-based polyurethanes were dissolved in DMF at 3% w/v. The solution (20 ml) was poured into a level 5 cm Teflon casting dish. The DMF solutions were cast in an oven at 55°C while the chloroform solutions were cast at room temperature. The dishes were covered to prevent dust from contaminating the film and excessively fast casting, which can result in surface defects. The cast films were removed from the casting dishes and dried under vacuum at 60°C for 48 h to remove residual solvent.

The polymer nomenclature used here is based on the type and molecular weight of the soft segment and the chain extender. For example, PCL1250/Phe refers to a polyurethane consisting of 1250 molecular weight PCL, chain extended with the novel phenylalanine-based chain extender. All of the polyurethanes employ HDI as the diisocyanate component.

Polyurethane characterization

Gel permeation chromatography (GPC) was employed to determine polyurethane molecular weights. The polymers were dissolved at 0.25% w/v in the GPC carrier solvent (0.1 M LiBr in DMF) and 200 μl samples were injected. The number and weight average molecular weights were determined from the retention time data with Waters Baseline™ software (Waters Chromatography, Mississauga, ON, Canada) using a calibration curve generated with polystyrene standards (Varian, Sunnyvale, CA, USA).

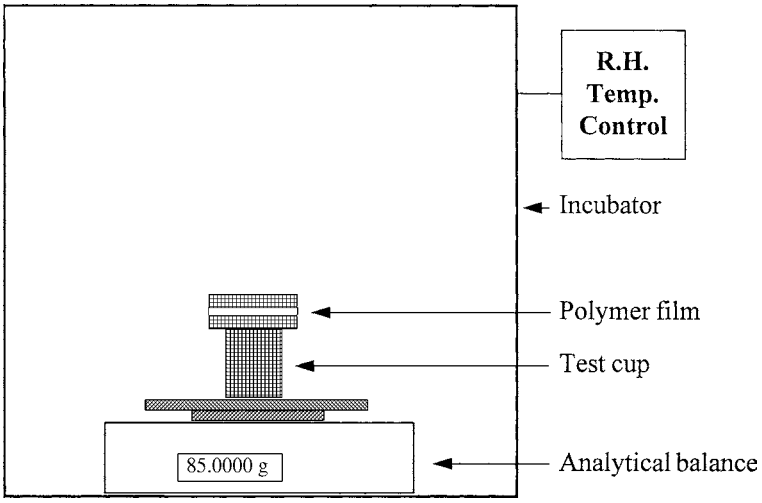

Figure 2. Water vapor permeance testing apparatus.

Differential scanning calorimetry (DSC) was performed using a Thermal Analyst 2100 thermal analyzer at the Institute for Materials Research (McMaster University, Hamilton, ON, Canada) to determine the phase segregated morphology of the polyurethanes. Scan rates of 15°C min^{-1} were employed over a temperature range of −100 to 250°C.

The bulk hydrophilicity of the polyurethanes was quantified by determining the amount of water that each polymer absorbed at room temperature. Films 100 μm thick were cast as described above and four 1×1 cm pieces of each polymer were cut out and weighed. The samples were then placed in 20 ml glass scintillation vials and 20 ml of distilled water were added. After 48 h, the samples were removed, weighed and then dried under vacuum and reweighed. The increase in weight due to water absorption was calculated as the difference between the hydrated and subsequently dried samples since some of the polymers exhibited significant weight loss over the 2-day experiment.

Water vapor permeability of the polyurethane films was determined using a modification of the method of Queen *et al.* [24]. The apparatus (Fig. 2) consists of: an aluminum dish which holds 5 ml of water; an analytical balance used to measure weight loss due to water permeation; an incubator which allows for control of the test environment humidity and temperature; a thermometer/hygrometer; and a sample of thin polymer film which is fastened over the cup surface. The mass readings of the analytical scale are collected every 15 min for 10 h and stored via computer. The rate of weight loss due to water permeation through the polymer film is calculated by linear regression of a plot of weight loss vs time. The value may then be converted to a water vapor permeance (WVP) by the following equation:

$$\text{WVP} = \frac{m}{A \times \Delta P} \ (\text{g m}^{-2}\,\text{h}^{-1}\,\text{kPa}^{-1}), \tag{1}$$

where m is the experimentally determined rate of water transport in $g\,h^{-1}$, A is the area of polymer available for transport in m^2 and ΔP is the water vapor pressure difference across the polymer film in kPa. The water vapor pressure inside the cup is assumed to be 100% while the vapor pressure outside the cup is controlled by the incubator. All of the water vapor permeance tests were performed at 35°C and 60% relative humidity.

Water contact angles were measured on cast films of 100 μm thickness. Prior to measurement the cast films were placed under vacuum at 60°C for 14 h to remove any volatile impurities. The samples were then washed with a 0.1% detergent solution (Alconox Inc., New York, NY, USA), rinsed with distilled water and dried at 55°C for 2 h. The samples were then washed with 1,1,2-trichlorotrifluoroethane (Aldrich) to remove silicon-containing surface contaminants and dried under vacuum at 60°C overnight. The advancing and receding water contact angles were measured by goniometer using the sessile drop technique. Ten measurements of both advancing and receding angles were made.

X-ray photoelectron spectroscopy (XPS) was performed at the Surface Science Laboratory at the University of Toronto. Take-off angles of 90, 30, and 20 deg were employed to obtain a compositional depth profile of the polymer surfaces. Films cast as above were prepared as for the contact angle studies. Low resolution spectra were performed to generate elemental composition data while high resolution analysis of the C 1*s* peak was performed to determine the relative contributions of the urethane, urea, ester and ether groups.

Degradation experiments

An *in vitro* degradation study was carried out over 8 weeks to determine if the synthesized polyurethanes would degrade in buffer and, if so, how fast the degradation would occur. Two polymers (PCL1250/Phe and PEO1000/Phe) were assayed for degradation in 0.1 M TBS, pH 8.0 at 37°C by measuring weight loss and change in molecular weight at various time points over the experiment. The PCL1250/Phe and PEO1000/Phe polyurethanes were chosen for the degradation study because they had relatively good mechanical properties as assessed qualitatively and also had similar soft segment contents to allow for comparison. Buffer pH of 8.0 was employed because subsequent degradation tests employing proteolytic enzymes with maximum activity near pH 8.0 are planned. Films cast as described above were cut into 1×1 cm pieces and weighed (approximately 30 mg). The samples were then placed in a 20 ml glass scintillation vial and immersed in 20 ml of 0.1 M TBS containing 0.02% w/v NaN_3 and placed in a shaking water bath at 37°C. Four samples were removed at each time interval, dried for 14 h under vacuum at 60°C and weighed for mass loss. In addition, three samples per polymer were assayed for molecular weight changes by GPC and one sample per polymer was evaluated for alteration in surface morphology by scanning electron microscopy (SEM). For SEM evaluation, the samples were dehydrated through graded ethanol, dried in a CO_2 critical point dryer, mounted on aluminum specimen stubs, coated with gold and examined in the scanning electron microscope.

RESULTS AND DISCUSSION

Chain extender characterization

The proton NMR spectrum of the chain extender synthesized is shown in Fig. 3. The peak assignments were aided by obtaining spectra of the constituent molecules alone (1,4-cyclohexane dimethanol, L-phenylalanine and *p*-toluene sulfonic acid). The multiplets centered at 3.8 ppm were attributed to the methylene protons of 1,4-cyclohexane dimethanol which are adjacent to the ester functionalities. Two sets of multiplets are observed here because the cyclohexane dimethanol received is a mixture of *cis* and *trans* isomers (60% *cis* and 40% *trans*) and thus the methylene protons are in a slightly different electronic environment in each conformation. Since these protons are adjacent to the reactive site, they may be utilized to assess the success of the synthesis reaction. It was found that these methylene protons yield two multiplets centered at 3.2 ppm for unreacted 1,4-cyclohexane dimethanol when the protons are adjacent to the reactive hydroxyl groups. It appears that the esterification reaction results in a shift of these peaks from 3.2 to 3.8 ppm due to the presence of the ester group which has a greater deshielding effect, in comparison to the hydroxyl group, on the methylene protons. Figure 3 clearly shows the presence of the multiplets at 3.8 ppm indicating the success of the synthesis reaction, however, it appears that some unreacted hydroxyl functionalities remain as indicated by the small peaks centered at 3.2 ppm.

Quantitation of the relative amount of unreacted to reacted hydroxyl groups is complicated by the presence of an overlapping water peak at ~ 3.3 ppm, however, it is apparent that the great majority of the methylene protons of 1,4-cyclohexane dimethanol are adjacent to ester groups as anticipated (rough calculation indicates approximately 8% of the methylene protons are adjacent to unreacted hydroxyl groups). The presence of a small amount of unreacted hydroxyl groups may indicate either the synthesis reaction was incomplete, yielding an amine/hydroxyl molecule rather than a diamine or that limited hydrolysis occurred during the conversion of the tosylate salt to the free diamine, which is carried out in aqueous solution. Comparison of integrated peak areas, in general, indicates close agreement with stoichiometric prediction suggesting that the synthesis reaction and purification technique were successful.

FTIR analysis (Figs 4 and 5) was carried out to determine the presence of specific functional groups in the synthesized chain extender, particularly ester and amine groups. In addition, the success of the reaction to generate the free diamine (Fig. 5) from the tosylate salt (Fig. 4) was followed by FTIR. The spectra of both the tosylate salt and free diamine show a strong peak at 1735 cm^{-1} which is attributed to the presence of ester functionalities indicating the success of the synthesis reaction. In addition, no significant hydroxyl peak is noted in the region of 3000–3500 cm^{-1} in either spectra which would result from the presence of unreacted 1,4-cyclohexane dimethanol hydroxyl groups. However, the presence of a broad double peak centered at ~ 3300 cm^{-1}, in Fig. 4, which was attributed to the amine functional groups of the free diamine would overlap any small hydroxyl peak which may appear as suggested by NMR analysis. Successful generation of the free diamine may be inferred from

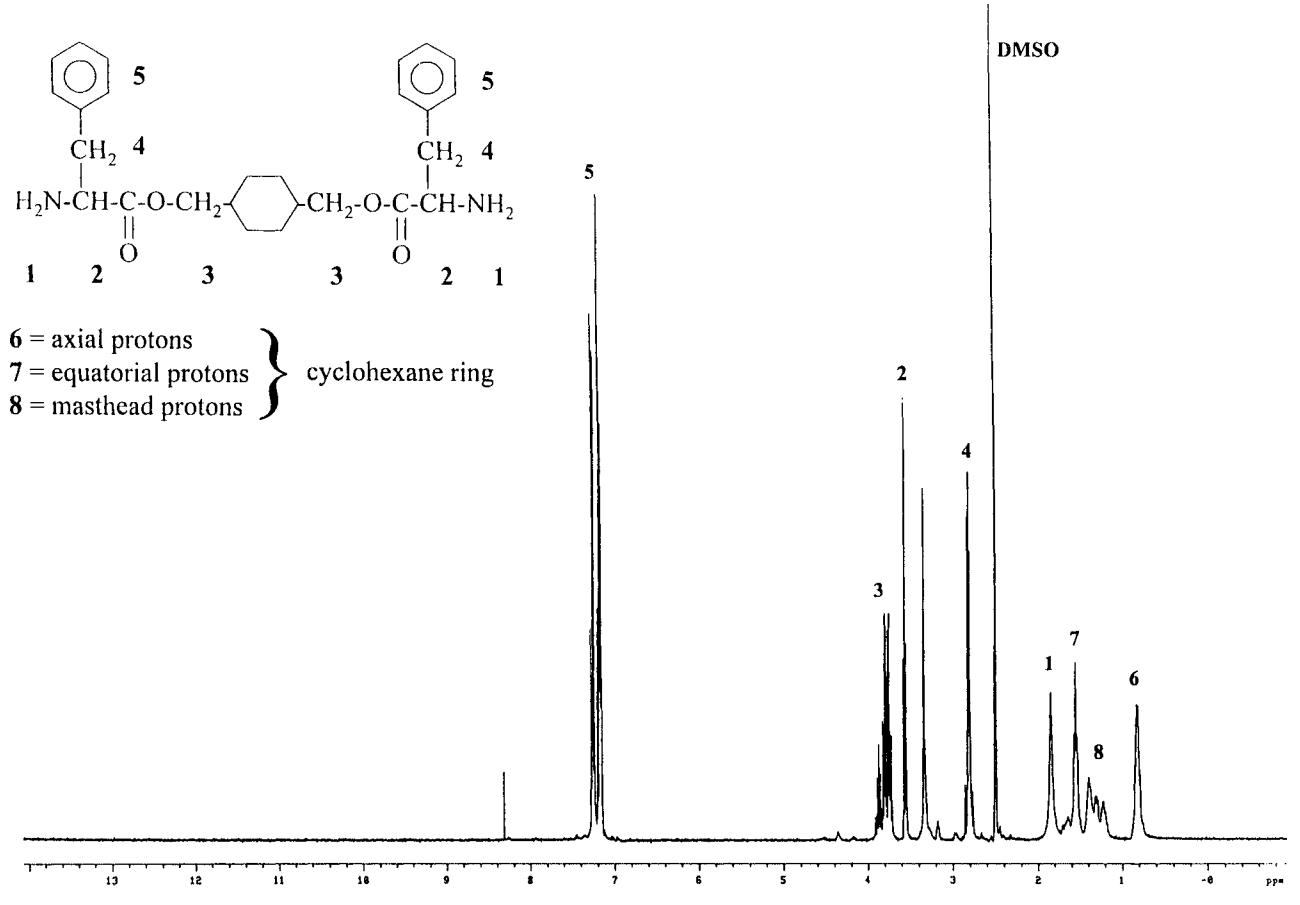

Figure 3. H-NMR spectrum of experimental chain extender.

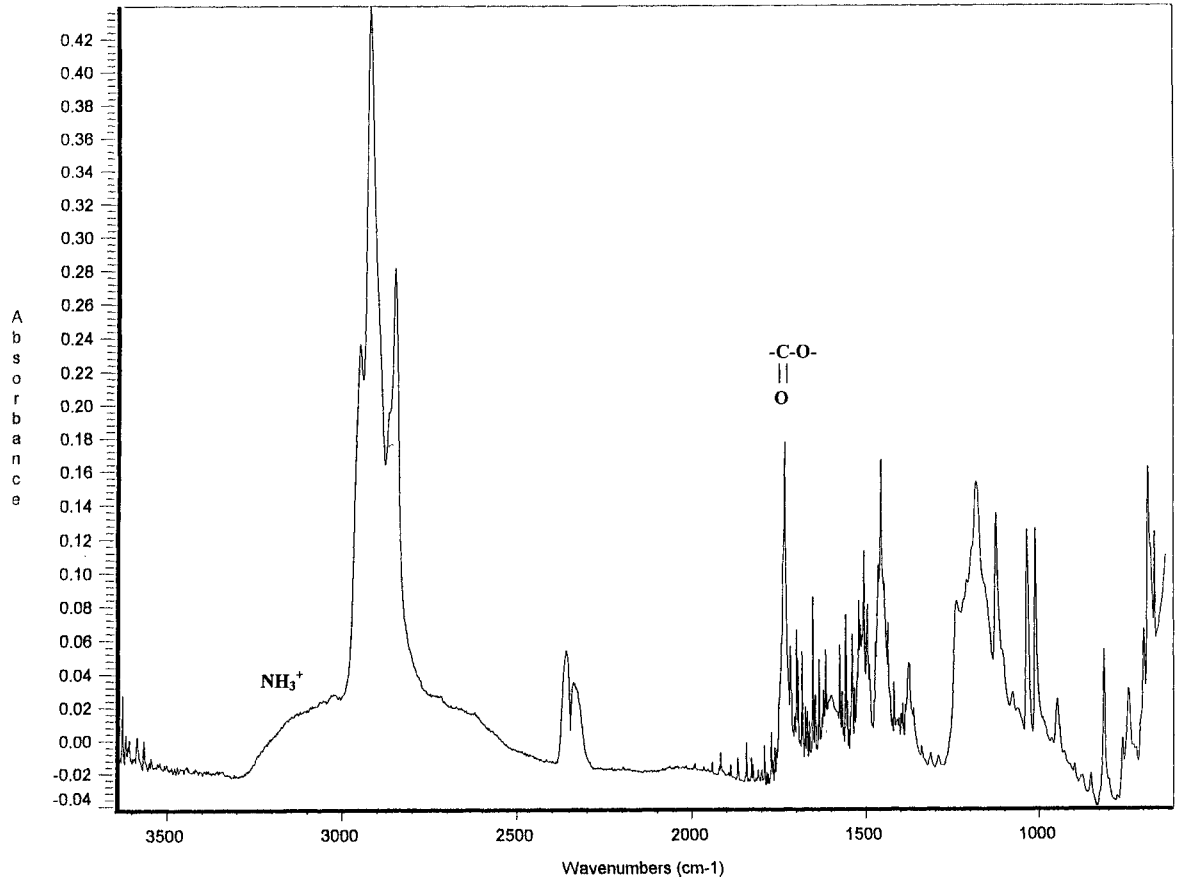

Figure 4. FTIR spectrum of tosylate salt of chain extender.

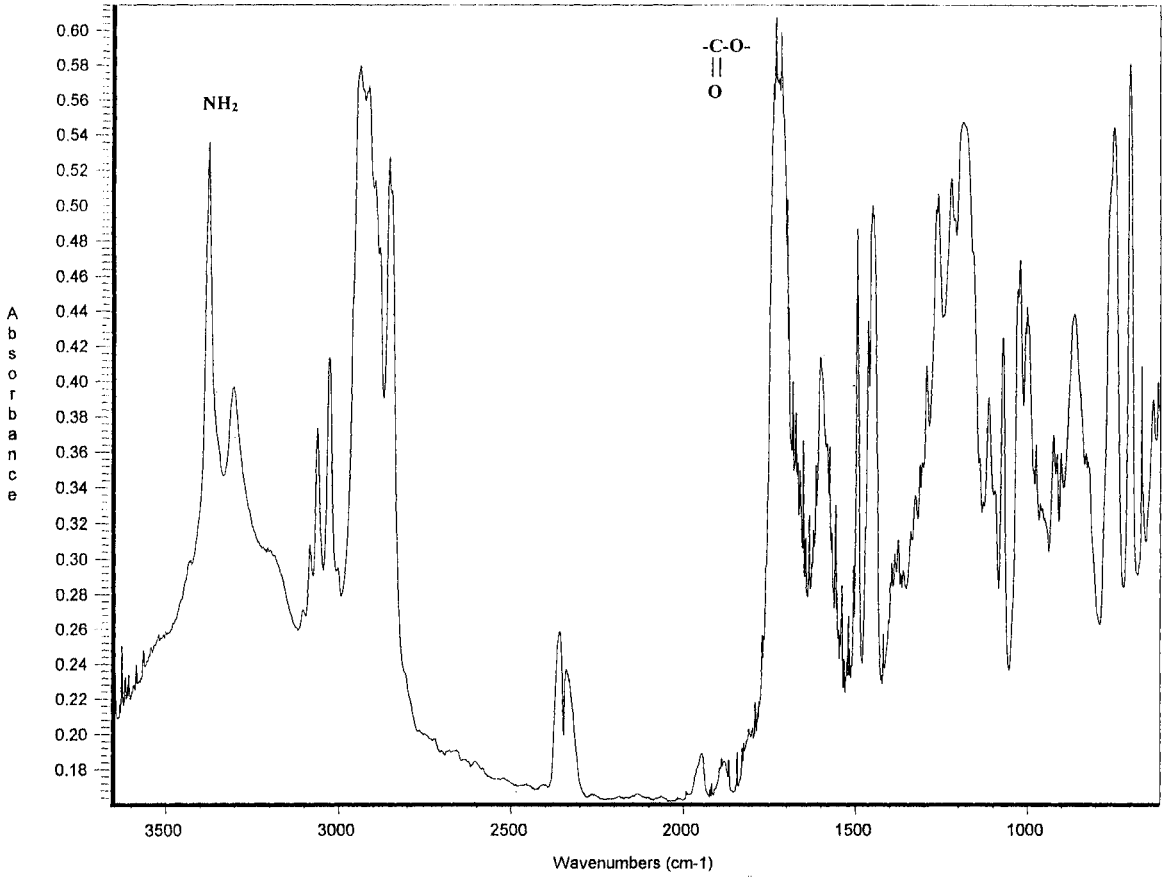

Figure 5. FTIR spectrum of free diamine form of the chain extender.

comparison of Figs 4 and 5. It is evident that the tosylate salt yields a broad peak centered at 2900 cm^{-1} (Fig. 4) which may be attributable to the NH_3^+ group while this peak disappears and the amine peak at 3300 cm^{-1} appears indicating successful conversion (Fig. 5).

Additional evidence of the success of the synthesis reaction and purification procedure was provided by elemental analysis. Table 1 shows the elemental composition data for both the tosylate salt and free diamine forms of the chain extender, compared to theoretical prediction. In both cases the measured and predicted atomic weight percents are within 5% indicating the success of the reaction and that the chain extender was obtained at good purity.

Polyurethane molecular weights

The number average molecular weights of the synthesized polyurethanes are given in Table 2. The molecular weights in all cases are high enough to impart adequate elastomeric behavior for the solid films [8], ranging from approximately 25 000 to 140 000. In general, the PCL-based polyurethanes exhibited higher molecular weights than the PEO-based ones. This difference likely results from the presence of water contamination in the hydrophilic PEO soft segment. Water may react with the isocyanate functionalities of the prepolymer to yield the corresponding amines which are capable of competitively reacting with remaining isocyanate groups [23]. Thus, the water side reaction will alter the synthesis reaction stoichiometry and limit chain extension, limiting molecular weight. The gross difference in molecular weight be-

Table 1.
Atomic weight percents of chain extender by elemental analysis

Atom	Tosylate salt		Free diamine	
	Theory (wt%)	Measured (wt%)	Theory (wt%)	Measured (wt%)
C	61.36	60.85	71.21	68.00
H	6.44	6.45	7.81	7.78
N	3.58	3.58	6.39	6.06
S	8.19	8.64	0.00	0.18

Table 2.
Polyurethane molecular weight data from GPC

Polymer	Number average molecular weight
PCL530/Phe	98 820
PCL1250/Phe	138 980
PCL2000/Phe	102 320
PEO600/Phe	79 020
PEO1000/Phe	24 960

tween the PCL and PEO-based polyurethanes may be expected to impact on both the mechanical and degradation properties of the polymers.

Differential scanning calorimetry (DSC)

The DSC data obtained for the five polyurethanes is shown in Table 3. None of the polymers exhibited detectable hard segment crystallization but rather displayed a distinct hard segment glass transition in the temperature range 67–77.4°C. Thus, the hard segments are in all cases amorphous and glassy at room or body temperature. The mobile aliphatic diisocyanate employed here [25] as well as the presence of bulky sidechains on the chain extender may preclude the efficient chain packing necessary for hard segment crystallization [26]. Polyurethanes containing non-crystalline hard segments, as is generally the case for aliphatics, tend to exhibit reduced tensile strength. However, tensile properties may also be greatly affected by other polymer characteristics such as the microdomain morphology and the ability of the hard segments to hydrogen bond [27]. For example, van Bogart *et al.* [28] observed higher ultimate tensile strength values for a series of aliphatic polyurethanes in comparison to aromatic ones and this was attributed to presence of smaller or more interconnected hard segment domains in the aliphatics as determined by small-angle X-ray scattering (SAXS).

No general trend of hard segment glass transition temperature with soft segment molecular weight was noted for the PCL-based polyurethanes. In contrast, the hard segment T_g does increase with increasing PEO content from 67 to 74.2°C. This trend indicates that increasing phase separation between hard and soft segment occurs with increasing PEO molecular weight. Increased phase separation would be expected to reduce the amount of low T_g soft segment material present in the hard segment domains and thus lead to increased hard segment T_g values.

The soft segment glass transition temperature was observed to decrease consistently with increasing soft segment molecular weight for both the PCL and PEO-based polyurethanes. The trend of decreasing soft segment T_g likely results from increasing phase separation which usually occurs with increasing segment length [29]. In addition, increasing hard segment content, which results from decreasing soft segment molecular weight, leads to decreased mobility of the soft segment domains and thus results in increased soft segment T_g values [30]. Since some degree of phase mixing

Table 3.
Thermal transition temperatures from DSC

Polymer	Soft segment		Hard segment T_g (°C)
	T_g (°C)	T_m (°C)	
PCL530/Phe	−25.5	—	75.2
PCL1250/Phe	−33.1	41.5	77.4
PCL2000/Phe	−51.9	45.3	75.7
PEO600/Phe	−31.3	—	67.0
PEO1000/Phe	−40.7	—	74.2

is inevitable, the pure PCL and PEO T_gs of -62 and -67°C are unobtainable and may be regarded as lower limits.

Interestingly, soft segment crystallization was observed for PCL1250/Phe and PCL2000/Phe, but not for PCL530/Phe or the PEO-based polyurethanes. This result suggests that a minimum chain length is required to facilitate PCL crystallization. The PCL530/Phe polymer soft segment may be interrupted too frequently by hard segments to align into a crystal structure. In addition, increased phase mixing, as inferred by increased soft segment T_g, in PCL530/Phe would also inhibit efficient chain ordering necessary for crystallization. Increasing soft segment crystal melt temperature was observed with increasing PCL molecular weight. Once again, this may be attributed to increased phase separation afforded by increasing soft segment chain length as well as increasing soft segment content. For reference, the crystal melt temperature of pure PCL is approximately 57°C [7], and thus some phase mixing results in a significant depression in soft segment T_m. It is apparent that with relatively minor modifications in chemistry it is possible to greatly vary the resulting polyurethane morphology ranging from completely amorphous to semicrystalline.

Water absorption

Water absorption was measured to determine polyurethane bulk hydrophilicity as this was expected to have a substantial impact on degradation kinetics. The absorption data is shown in Fig. 6. As expected, the polyurethanes containing hydrophilic PEO soft segment exhibited substantially higher levels of water absorption than the PCL-based ones indicating greater bulk hydrophilicity. In addition, increasing PEO molecular weight results in increasing water absorption, likely due to increased PEO content

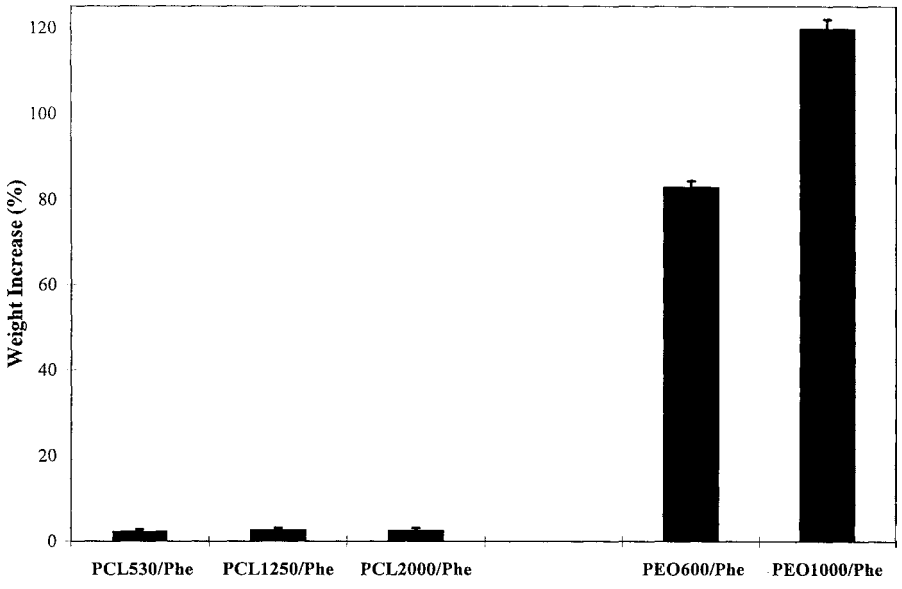

Figure 6. Water absorption values for polyurethanes (mean ± SD, $n = 4$).

in the polyurethane. Increasing the PEO molecular weight beyond 1000, as in the case of PEO2000/Phe, resulted in a water soluble polyurethane indicating that the relative PEO content can dramatically effect the resulting bulk hydrophilicity of the polyurethane.

In contrast, the PCL-based polyurethanes showed no significant dependence of PCL molecular weight on water absorption. Rather, these polymers displayed an essentially constant level of water absorption ($\sim 3\%$) even though their microphase segregated morphology differed quite markedly as measured by DSC. The essentially hydrophobic PCL-based polyurethanes would thus be expected to degrade at a significantly reduced rate in comparison to the hydrophilic PEO-based polymers and would therefore be better suited to longer residence time applications.

Water vapor permeance (*WVP*)

It was anticipated that the synthesized polyurethanes may be useful materials for wound dressing applications, since several non-degradable polyurethane wound dressings are currently commercially available and in wide use [31]. One of the major functions of a wound dressing is to control evaporative water loss from the wound site. Excessive water loss may lead to wound bed dehydration and delayed healing [32]. However, fluid buildup at the wound site may lead to pain, leakage and bacterial infiltration [24]. Therefore, it is desirable to maintain an intermediate level of fluid retention, and a material's ability to do this can be assessed *in vitro*. However, it must be noted that a wide range of water vapor permeances are clinically useful since different types of wounds will generate exudate at different rates and a variety of commercial dressings are available [31]. The water vapor permeabilities of two commercially available polyurethane wound dressings (Opsite™ and Tegaderm™) were measured as a reference for the experimental polyurethanes.

Table 4 lists the measured water vapor permeance values for the experimental polyurethanes as well as Opsite™ and Tegaderm™. As expected, the hydrophilic PEO-based polyurethanes displayed significantly higher WVP values in comparison to the more hydrophobic PCL-based ones. The enhanced WVP for the PEO-based

Table 4.
Water vapor permeance measurements for polyurethanes

Polymer	WVP ($g\,m^{-2}\,h^{-1}\,kPa^{-1}$)
PCL530/Phe	9.6 ± 0.4
PCL1250/Phe	7.6 ± 0.5
PCL2000/Phe	4.4 ± 0.6
PEO600/Phe	14.3 ± 1.5
PEO1000/Phe	21.6 ± 2.3
Opsite™	$7.5 \pm 0.5^*$
Tegaderm™	$7.4 \pm 0.2^*$

Mean $\pm$ SD, $n = 4$, $^*n = 6$.

polyurethanes is presumably a result of the highly hydrophilic nature of these polymers. In addition, increasing PEO molecular weight results in increasing WVP, again due to increasing hydrophilicity as noted by the water absorption experiments. In contrast, increasing PCL molecular weight was observed to result in decreasing WVP, although the bulk hydrophilicity was essentially constant. This behavior may result from increasing soft segment crystallinity with increasing PCL molecular weight as observed by DSC. Increasing polymer crystallinity will result in a less porous and thus less permeable material leading to reduced WVP values. It may be noted that the PCL-based polyurethanes yield WVP values similar to the commercial dressings and thus may find application in cases where Opsite^{TM} and Tegaderm^{TM} are presently employed. The PEO-based polymers exhibit significantly higher WVPs indicating that they may be applicable to highly exudative wounds such as burns [33].

Contact angles

Figure 7 shows the advancing and receding water contact angles for the experimental polyurethanes. The PEO-based polyurethanes exhibit reduced advancing and receding contact angles in comparison to the PCL-based ones, in agreement with the bulk hydrophilicity results obtained from the water absorption studies. Again, increasing PEO molecular weight results in decreasing advancing and receding contact angles suggesting increasing surface hydrophilicity. However, no simple trend can be noted for the PCL-based polyurethanes with PCL molecular weight. In this case, increasing PCL content may be expected to result in decreasing surface hydrophilicity due to depletion of the relative amount of polar hard segment. This is not observed, rather both advancing and receding contact angles increase from PCL530/Phe to PCL1250/Phe

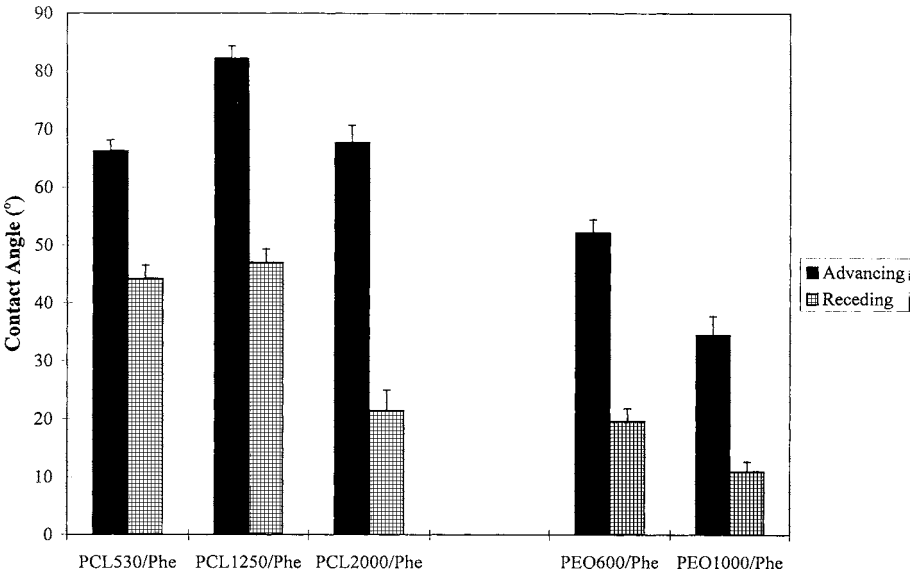

Figure 7. Advancing and receding water contact angle measurements on polyurethanes (mean ± SD, $n = 10$).

but then decrease for PCL2000/Phe. Therefore, it appears that other factors may be involved in determining the polymers' surface energetics. For example, the degree of phase mixing, which may effect the surface distribution of the microdomains, and the level of soft segment crystallinity are two factors that could impact on polymer surface energy. The overall effect of these factors is difficult to predict. However, DSC showed increasing soft segment crystallinity with increasing PCL molecular weight and thus increasing surface tension may be expected to result which would lead to decreasing contact angles. In contrast, increasing phase mixing was noted with decreasing PCL molecular weight and this might be expected to lead to increasing polar hard segment content at the surface and thus increasing surface tension reflected in decreasing contact angles. Thus, the combination of the above effects may result in the observed results. At low PCL content (e.g., PCL530/Phe), the increased phase mixing may lead to relatively low contact angles while at high PCL content (e.g., PCL2000/Phe) the increase in polymer crystallinity dominates and results in decreased contact angles. The intermediate case of PCL1250/Phe could then be expected to yield the highest contact angles reflecting the lowest surface energy.

All of the polymers exhibit significant contact angle hysteresis. The PCL-based polyurethanes display increasing hysteresis with increasing PCL molecular weight while the opposite trend is noted for the PEO-based polyurethanes. Hysteresis has been interpreted to result from rapid reorientation of the surface region to favor the polar hard segment domains in response to the introduction of the water droplet [26]. Minimization of the interfacial free energy of the system using a polar liquid such as water dictates the polar groups of the polymer are preferentially oriented towards the surface. However, contact angle hysteresis may also result from surface roughness and surface absorption during the experiment [34]. Since the measured absorption was essentially constant for the PCL-based polyurethanes, the differences in hysteresis may not be attributed to this effect. In addition, SEM observation of the surfaces showed no qualitatively significant differences in terms of roughness. Therefore, the increasing hysteresis noted with increasing PCL content may be best explained by an increasing ability to reorient in response to the water droplet. Increased phase separation may allow for greater alteration in surface chemistry, however, the increased crystallinity also noted with increased PCL molecular weight would be expected to reduce the conformational mobility of the surface region. Thus, the origin of the trend of increasing hysteresis with increasing PCL content is unclear. The corresponding trend of decreasing hysteresis with increasing PEO content may result from the differences in polymer hydrophilicity in this case since the PEO soft segment is highly hydrophilic and thus the driving force for rearrangement is reduced here. It must be noted however, that the difficulty in measuring contact angle values less than 20 deg, as for the receding angles, makes any definitive evaluations difficult here.

X-ray photoelectron spectroscopy (*XPS*)

The XPS data measured using take-off angles of 90, 30, and 20 deg (relative to the surface) is given in Table 5. Since nitrogen should be present only in the hard segment of the polyurethanes, it can be used to examine the hard segment content of the

Table 5.
Atomic surface composition data from XPS (data precision ± 10%)

Polymer	Take-off angle (deg)	Atomic percent				Percent		
		C 1*s*	C 1*s*	N 1*s*	Si 2*p*	C—C	C—O	O=C—O
PCL530/Phe	90	85.62	11.97	2.41	0.00	76.89	17.89	5.22
	30	90.13	7.58	1.59	0.70	75.73	19.87	4.40
	20	90.38	8.22	1.39	0.01	85.95	12.04	2.01
PCL1250/Phe	90	80.82	17.56	1.51	0.11	69.97	21.65	8.39
	30	86.03	12.80	0.63	0.53	74.75	18.64	6.61
	20	76.87	18.94	0.60	3.59	74.80	19.27	5.93
PCL2000/Phe	90	76.78	22.95	0.26	0.00	61.13	24.73	14.14
	30	77.82	21.33	0.19	0.66	66.74	20.98	12.29
	20	72.77	23.33	0.03	3.87	71.51	18.78	9.71
PEO600/Phe	90	77.88	16.24	5.56	0.32	55.69	37.22	7.09
	30	78.91	15.00	5.00	1.09	57.72	36.22	6.06
	20	80.14	15.05	3.93	0.88	57.14	37.30	5.57
PEO1000/Phe	90	71.79	21.72	5.14	1.35	48.44	42.99	8.57
	30	74.74	19.95	3.12	2.19	54.85	38.78	6.37
	20	75.73	21.35	1.40	1.52	63.89	29.41	6.70

surface regions. All of the polyurethanes show lower nitrogen content as the depth of analysis is reduced, suggesting that the surface regions of the polymers are soft segment enriched. Soft segment surface enrichment in the high vacuum environment of XPS has been well documented for a variety of segmented polyurethanes [35, 36]. It is believed that a predominance of the relatively apolar soft segments at the polymer surface serves to minimize the surface free energy of the system in a vacuum environment. A greater depth dependence of nitrogen is observed with increasing soft segment molecular weight in agreement with the DSC data suggesting increasing phase separation with increasing soft segment molecular weight. Increasing phase separation can be expected to lead to increasingly 'pure' surface soft segment content while phase mixing will result in the inclusion of hard segment 'impurities' in the surface region.

High resolution analysis of the C 1*s* peak showed a decrease in contribution of the ester/urethane/urea component of the C 1*s* peak as the sampling depth decreased for all of the polymers. Thus, the high resolution carbon data provides additional evidence for hard segment depletion at the surface of the polyurethanes *in vacuo*. The prevalence of soft segment domains at the polymer surface may be expected to reduce the rate of hydrolysis of the polyurethanes since the ester containing chain extender is present in the hard domain. This would be particularly important for the relatively hydrophobic PCL-based polyurethanes which may be expected to exhibit surface-limited degradation. However, previous studies have demonstrated that polyurethanes are capable of reorienting in a polar aqueous environment to enhance

hard segment surface distribution [37]. Therefore, since any degradable polymer intended for biomedical use will be placed into an essentially aqueous environment, surface enrichment of hard segment is likely.

Degradation experiments

The mass loss data collected for PEO1000/Phe and PCL1250/Phe is shown in Fig. 8. It is apparent that PEO1000/Phe exhibited substantial and progressive mass loss, while PCL1250/Phe showed only minor mass loss, over the 56-day experimental period. After 56 days exposure to buffer, PEO1000/Phe retained approximately 30% of its initial mass and became extremely fragile and difficult to handle without fragmenting. In contrast, PCL1250/Phe retained approximately 98% of its original mass and also retained its qualitative mechanical stability after 56 days. Since the hard segment chemistry of each polyurethane was identical and the hard segment contents were also similar (PEO1000/Phe 37%, PCL1250/Phe 32%), it can be hypothesized that the substantial difference in weight loss, resulting from buffer incubation, is attributable to the different soft segments.

In discussing the differences in mass loss, it is noted that the process of mass loss will depend not only on hydrolysis of the polymer backbone but also the rate of diffusion or release of the degradation products generated (oligomers and/or monomers). Therefore, several factors may contribute to the difference in mass loss noted here. First, differences in polymer morphology may impact on the degradation rate. DSC measurements indicated that PEO1000/Phe was completely amorphous while

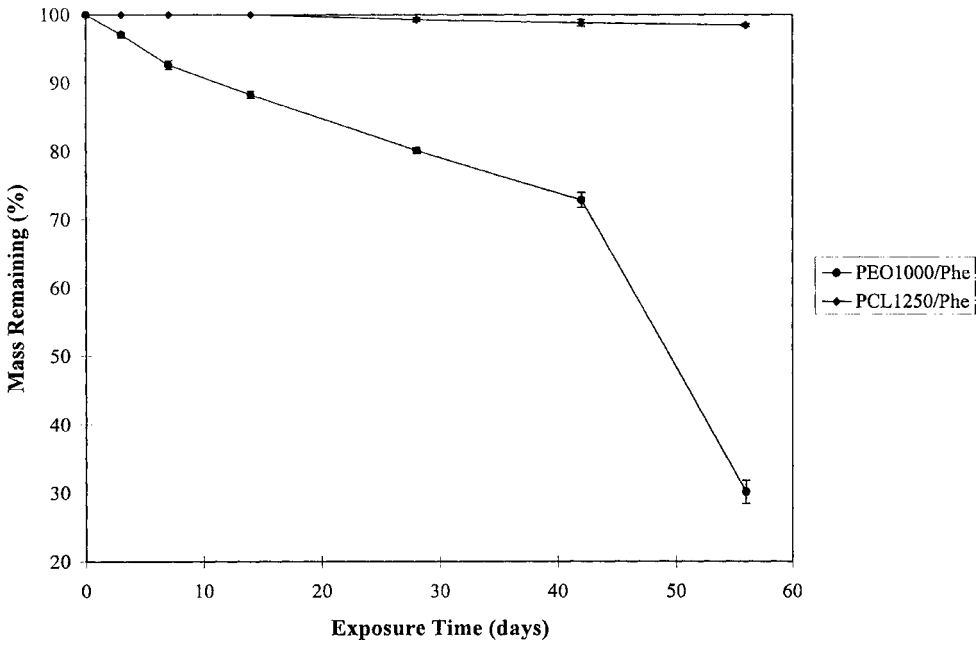

Figure 8. Mass loss data with buffer incubation (mean ± SD, $n = 4$).

PCL1250/Phe was semicrystalline. A greater free volume is associated with the amorphous phase making it more accessible to water than the crystalline phase. Consequently, amorphous polymers generally degrade much more quickly than semicrystalline polymers, as noted here.

For semicrystalline polymers, such as PCL1250/Phe, the amorphous regions degrade first, followed by a progressive erosion of the crystalline regions [38]. However, since neither polymer exhibits hard segment crystallization, and the amorphous hard segment contains the labile ester bonds via the chain extender, the presence of crystalline structure in the soft segment for PCL1250/Phe may not be expected to significantly affect the rate of hydrolysis of the polymer. Rather, other material properties may be of greater importance. For example, the drastic difference in the molecular weights of the two polyurethanes may be expected to affect the relative rates of degradation. The higher molecular weight PCL1250/Phe ($\sim$ 140 000) would be expected to require a greater degree of hydrolytic cleavage to permit the release of oligomeric degradation products, leading to mass loss, than PEO1000/Phe (molecular weight $\sim$ 25 000). In this respect, the solubilities of the respective degradation products will also substantially impact on the mass loss characteristics observed. The degradation products released from the hydrophilic PEO1000/Phe are presumably much more soluble than those liberated from PCL1250/Phe and are thus more easily able to diffuse from the solid, leading to mass loss.

Finally, the dramatic difference in water uptake noted for the two polyurethanes may impact greatly on the rate of mass loss in several ways. Since hydrolysis requires the reaction between water and the labile ester bond, the reaction velocity will depend on the concentrations of both 'reactants' in the polymer matrix. Therefore, polymers capable of absorbing a significant amount of water, such as PEO1000/Phe, generally degrade more rapidly than those which absorb little water (e.g., PCL1250/Phe) [39]. In this case, the water uptake measured for PCL1000/Phe was approximately forty times greater than for PCL1250/Phe, presumably resulting in a substantial difference in the rate of hydrolysis. In addition to the effect on the rate of hydrolysis, the level of water uptake may also be hypothesized to impact on the rate of mass loss through alterations in the swollen polymer matrix. A high degree of water uptake will generally lead to a swollen polymer matrix which contains greater free volume for mass transfer to occur into and out of the solid [39]. This may then lead to high rate of release of soluble degradation products from the bulk of the material. Hydrophobic materials are likely to swell to a lesser degree inhibiting transport of degradation products. Therefore, the difference in mass loss noted in Fig. 8 for the two polyurethanes may be a result of both differences in water uptake and initial molecular weight.

The effect of buffer incubation on polyurethane number average molecular weight is shown in Fig. 9. Both polyurethanes exhibit an initial increase in molecular weight which is hypothesized to result from leaching of low molecular weight polymer. A concurrent drop in the polydispersity of the molecular weight distribution supports this hypothesis. The leaching process appears to be complete within 7 days for PCL1250/Phe and 3 days for PCL1000/Phe. The more rapid leaching process noted for PCL1000/Phe is presumably due to the greater bulk hydrophilicity of this polymer

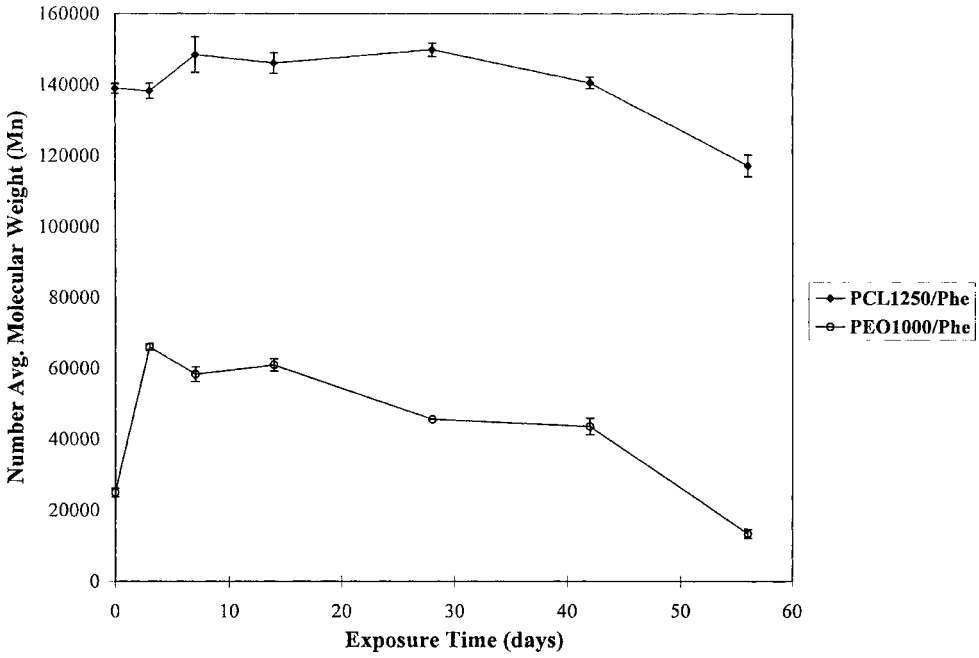

Figure 9. Molecular weight changes with buffer incubation (mean ± SD, $n = 3$).

in comparison to PCL1250/Phe which may lead to more soluble low molecular weight fractions.

After the initial leaching period, PCL1250/Phe exhibits essentially no molecular weight changes up to 4 week buffer exposure times and then displays decreasing molecular weight with exposure time up to 56 days. The delayed and modest reduction in molecular weight for PCL1250/Phe corresponds well with the weight loss data shown in Fig. 8, and is hypothesized to result from the relative hydrophobicity of this polymer. The low level of water uptake noted for PCL1250/Phe may result in relatively slow hydrolysis and thus delayed reduction in molecular weight in comparison to PEO1000/Phe. In contrast, PEO1000/Phe displays immediate and successive decrease in molecular weight subsequent to the initial leaching phase, suggesting relatively rapid bulk hydrolysis. Again, the immediate and substantial loss in molecular weight correlates with the weight loss data and is presumed to result from the substantial bulk hydrophilicity of this polyurethane.

Scanning electron microscopic evaluation of the degraded polyurethane surfaces at 56 days buffer exposure highlights the difference in the degradation behavior of the two polymers. Figure 10 shows the PEO1000/Phe surface after 56 day exposure to buffer. The initial surface was smooth and nonporous while after 56 days in buffer, the polymer displays marked porosity and fracturing. The extremely porous morphology noted by SEM corresponds with the substantial weight loss noted for PEO1000/Phe at 56 days ($\sim$ 70% mass loss) which, in addition to the reduction in molecular weight,

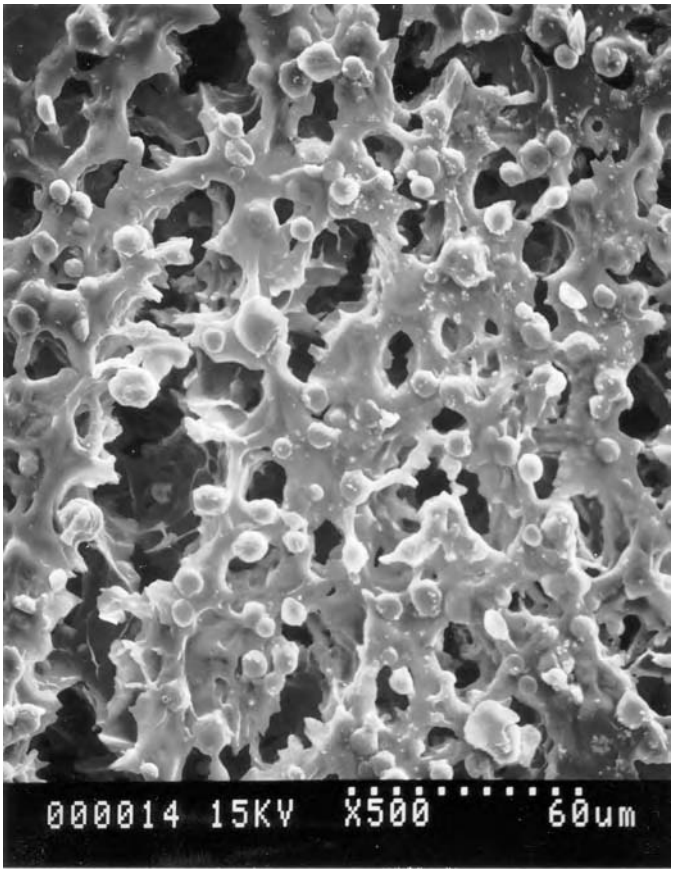

Figure 10. Scanning electron micrograph of PEO1000/Phe after 56 day buffer exposure.

suggests a relatively rapid bulk hydrolysis mechanism is responsible for the polymer degradation.

In comparison, the SEM of PCL1250/Phe after 56 day buffer exposure (Fig. 11) does not exhibit any apparent surface alteration compared to the initially cast film, which was essentially smooth. The PCL1250/Phe samples generally showed little surface structure. The lines apparent on the film sample result from small surface abrasions present on the casting dishes. In addition, a significant number of pores are present in the PCL1250/Phe film which are believed to result from the presence of air bubbles in the casting solution or excessively fast vaporization of the chloroform casting solvent in the final stages of casting. The general lack of surface alteration for PCL1250/Phe is in agreement with the minor mass loss and molecular weight reduction described previously and suggests that little degradation occurs for this polyurethane over the 56 day experimental period.

Further SEM studies of the cross-sectional morphology of the degrading polyurethanes would be of interest to better elucidate the possible formation of bulk pore

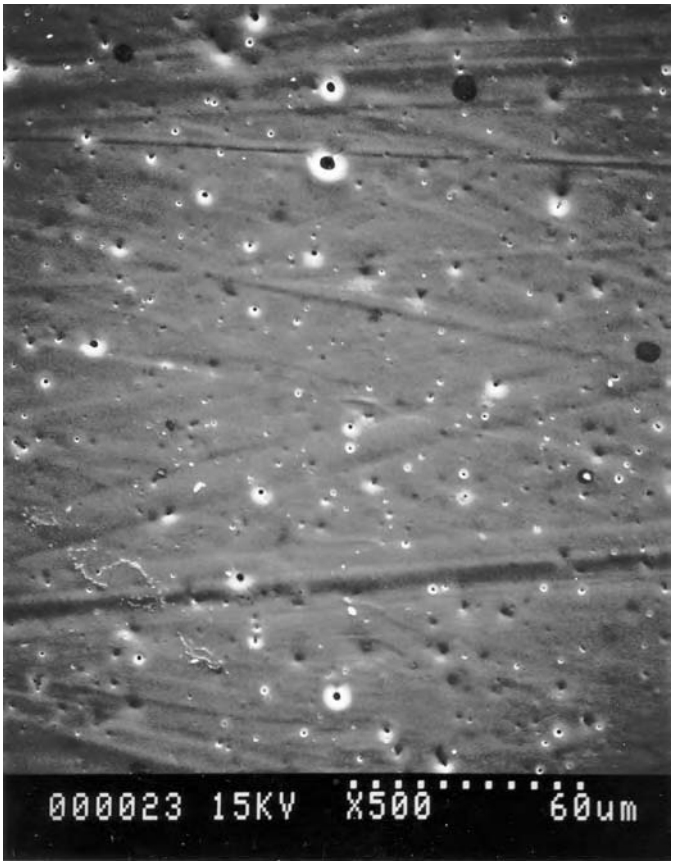

Figure 11. Scanning electron micrograph of PCL1250/Phe after 56 day buffer exposure.

formation due to hydrolysis as has been noted for other degradable polymers [39]. In addition, DSC evaluation of the degrading polyurethanes may be employed to determine possible alterations in the microphase morphology. In particular, DSC may indicate changes in relative crystallinity for the semicrystalline PCL1250/Phe which may be expected as a result of preferential amorphous phase degradation.

In conclusion, a phenylalanine-based chain extender was synthesized and utilized to generate a series of degradable polyurethane elastomers. It was found that alteration of the soft segment type (PCL or PEO) and molecular weight resulted in variable physical and degradation properties for the polyurethanes. Generally, increasing soft segment molecular weight resulted in increasing phase separation and also soft segment crystallinity (PCL-based polyurethanes). The PEO-based polyurethanes exhibited a high degree of hydrophilicity, as noted by water uptake, contact angle and WVP studies, in comparison to the PCL-based polyurethanes. The hydrophilic nature imparted by the PEO soft segment of PEO1000/Phe was hypothesized to promote rapid degradation while the more hydrophobic PCL soft segment of PCL1250/Phe served to reduce the rate of degradation noted.

Acknowledgements

Financial support of this work by the Natural Sciences and Engineering Research Council of Canada and the Ontario Centre for Materials Research is gratefully acknowledged. In addition, the assistance of Professor William Reynolds, Department of Chemistry, in NMR peak assignments and Professor John Brash, McMaster University, for the use of GPC equipment is also acknowledged.

REFERENCES

1. R. Langer, L. G. Cima, J. A. Tamada and E. Wintermantel, *Biomaterials* **11**, 738 (1990).
2. S. W. Shalaby and K. J. L. Burg, *J. Appl. Biomater.* **6**, 219 (1995).
3. M. Sittinger, J. Bujia, N. Rotter, D. Reitzel, W. W. Minuth and G. R. Burmester, *Biomaterials* **17**, 237 (1996).
4. A. S. Sawhney and J. A. Hubbell, *J. Biomed. Mater. Res.* **24**, 1397 (1990).
5. A. M. Radder, H. Leenders and C. A. van Blitterswijk, *J. Biomed. Mater. Res.* **28**, 141 (1994).
6. S. I. Ertel and J. Kohn, *J. Biomed. Mater. Res.* **28**, 919 (1994).
7. I. Engelberg and J. Kohn, *Biomaterials* **12**, 292 (1991).
8. M. D. Lelah and S. L. Cooper, *Polyurethanes in Medicine*. CRC Press Inc., Boca Raton, FL (1986).
9. B. D. Ratner, K. W. Gladhill and T. A. Horbett, *J. Biomed. Mater. Res.* **22**, 509 (1988).
10. M. Bouvier, A. S. Chawla and I. Hinberg, *J. Biomed. Mater. Res.* **25**, 773 (1991).
11. J. P. Santerre, R. S. Labow and G. A. Adams, *J. Biomed. Mater. Res.* **27**, 97 (1993).
12. L. Pinchuk, *J. Biomater. Sci. Polymer Edn* **6**, 225 (1994).
13. K. Sutherland, J. R. Mahoney, A. J. Coury and J. W. Eaton, *J. Clin. Invest.* **92**, 2360 (1993).
14. B. Eling, S. Gogolewski and A. J. Pennings, *Polymer* **23**, 1587 (1982).
15. S. Gogolewski and A. J. Pennings, *Makromol. Chem.*, *Rapid Commun.* **4**, 675 (1983).
16. P. Bruin, G. J. Veenstra, A. J. Nijenhuis and A. J. Pennings, *Makromol. Chem.*, *Rapid Commun.* **9**, 589 (1988).
17. D. Cohn, H. Younes and G. Uretzky, Eur. Pat. Appl. EP295,055, 14 Dec. 1988.
18. B. I. Dahiyat, E. Hostin, E. M. Posadas and K. W. Leong, *J. Biomater. Sci. Polymer Edn* **4**, 529 (1993).
19. J. C. Powers, T. Tanaka, J. W. Harper, Y. Minematsu, L. Barker, D. Lincoln and K. V. Crumley, *Biochemistry* **24**, 2048 (1985).
20. C. G. Pitt, in: *Biodegradable Polymers as Drug Delivery Systems*, R. Langer and M. Chasin (Eds), p. 71. Marcel Dekker, New York, NY (1990).
21. K. E. Bailey and J. V. Koleske, *Polyethylene Oxide*. Academic Press, New York, NY (1976).
22. S. J. Huang, D. A. Bansleben and J. R. Knox, *J. Appl. Polymer Sci.* **23**, 429 (1979).
23. J. H. Saunders and K. C. Frisch, *Polyurethanes: Chemistry and Technology*, *Part I.* Interscience Publishers, New York (1967)
24. D. Queen, J. D. S. Gaylor, J. H. Evans, J. M. Courtney and W. H. Reid, *Biomaterials* **8**, 367 (1987).
25. M. Szycher, V. L. Poirier and D. J. Dempsey, *J. Elastomers Plast.* **15**, 81 (1983).
26. A. Z. Okkema and S. L. Cooper, *Biomaterials* **12**, 668 (1991).
27. G. Woods, *The ICI Polyurethanes Book*, 2nd edn. John Wiley and Sons, New York (1990).
28. J. W. C. van Bogart, P. E. Gibson and S. L. Cooper, *J. Polymer Sci.*, *Polymer Phys. Edn* **21**, 65 (1983).
29. S. Krause, in: *Block and Graft Copolymers*, J. J. Burke and V. Weiss (Eds). Syracuse University, New York (1973).
30. G. Spathis, E. Kontou, V. Kefalas, L. Apekis, C. Christodoulides, P. Pissis, M. Ollivon and S. Quinquenet, *J. Macromol. Sci.-Phys.* **B29**, 31 (1990).
31. D. M. Wiseman, M. R. Pharm, D. T. Rovee and O. M. Alvarez, in: *Wound Healing*, *Biochemical and Clinical Aspects*, I. K. Cohen, R. F. Diegelmann and W. J. Lindblad (Eds), p. 562. W. B. Saunders, Philadelphia, PA (1992).

32. W. H. Eaglstein, *Clin. Dermatol.* **2**, 107 (1984).
33. A. Nangia and C. T. Hung, *Burns* **16**, 358 (1990).
34. S. Wu, *Polymer Interface and Adhesion*. Marcel Dekker Inc., New York (1982).
35. M. D. Lelah, T. G. Grasel, J. A. Pierce and S. L. Cooper, *J. Biomed. Mater. Res.* **20**, 433 (1986).
36. J. H. Silver, K. B. Lewis, B. D. Ratner and S. L. Cooper, *J. Biomed. Mater. Res.* **27**, 735 (1993).
37. J.-H. Chen and E. Ruckenstein, *J. Colloid Interfac. Sci.* **135**, 496 (1990).
38. A. Gopferich and R. Langer, *J. Polym. Sci.* **31**, 2445 (1993).
39. A. Gopferich, *Biomaterials* **17**, 103 (1996).

This page intentionally left blank

Polymers for Tissue Engineering, pp. 99–112
Molly S. Shoichet and Jeffrey A. Hubbell (Eds)

Preparation and characterization of poly(propylene fumarate-*co*-ethylene glycol) hydrogels

LAURA J. SUGGS, EDMUND Y. KAO, LAURIE L. PALOMBO, RAVI S. KRISHNAN, MARKUS S. WIDMER and ANTONIOS G. MIKOS *

Cox Laboratory for Biomedical Engineering, Institute of Biosciences and Bioengineering and Department of Chemical Engineering, Rice University, P.O. Box 1892, Houston, TX 77251-1892, USA

Received 4 August 1997; accepted 12 December 1997

Abstract—We describe the preparation and bulk characterization of a cross-linked poly(propylene fumarate-*co*-ethylene glycol), p(PF-*co*-EG), hydrogel. Eight block copolymer formulations were made varying four different design parameters including: poly(ethylene glycol) (PEG) molecular weight, poly(propylene fumarate) (PPF) molecular weight, copolymer molecular weight, and ratio of PEG to PPF. Two different cross-linking formulations were also tested, one with a cross-linking monomer and one without. The extent of the cross-linking reaction and the degree of swelling in aqueous solution were determined on copolymer formulations made without a cross-linking monomer. The values of molecular weight between cross-links, $\overline{M}_c$ ranged from 300 ± 120 to 1190 ± 320 as determined from swelling data ($n = 3$). The equilibrium volume swelling ratios, Q, varied from 1.5 ± 0.1 to 3.0 ± 0.1. This ratio was found to increase with increasing PEG content in the copolymer and decrease with increasing PPF molecular weight. The values for complex dynamic elastic moduli $|E^*|$, ranged from 0.9 ± 0.2 to 13.1 ± 1.1 MPa for the formulations with the cross-linking monomer, *N*-vinyl pyrrolidinone (VP) ($n = 3$). The ultimate tensile stresses on the formulations made with VP ranged from 0.15 ± 0.03 to 1.44 ± 1.06 MPa, and tensile moduli ranged from 1.11 ± 0.20 to 20.66 ± 2.42 MPa ($n = 5$). All of the mechanical properties increased with increasing PPF molecular weight and decreased with increasing PEG content in the copolymer. These data show that the physical properties of p(PF-*co*-EG) hydrogels can be tailored for specific applications by altering the material composition.

Key words: Poly(ethylene glycol); poly(propylene fumarate); hydrogel; swelling; mechanical properties.

*To whom correspondence should be addressed.

INTRODUCTION

Interventional cardiovascular procedures such as percutaneous transluminal coronary angioplasty (PTCA) are currently used for the treatment of coronary artery diseases. Problems such as restenosis as well as elastic recoil can result in the reocclusion of the treated artery [1]. Mechanical stenting has been used in order to alleviate these difficulties, however, additional damage to the traumatized tissue from implantation as well as the thrombogenic nature of the materials used, typically metals, can cause further complications [1]. We have previously described the synthesis of a block copolymer for use as a vascular stent which consists of poly(propylene fumarate) (PPF) and poly(ethylene glycol) (PEG) blocks in an effort to address these issues [2].

PPF is an unsaturated, linear polyester which has been described for use as an injectable biomaterial for bone replacement [3, 4]. It can be polymerized *in situ* to form a solid composite with mechanical properties similar to that of trabecular bone. PEG has been used in the vasculature in part because, for molecular weights up to 20 000, it has no known toxic side effects [5]. It is nonthrombogenic and has been covalently bound to several different compounds in order to decrease their thrombogenicity [6, 7]. PEG was therefore chosen in an effort to optimize PPF for use in blood-contacting spaces.

The poly(propylene fumarate-*co*-ethylene glycol), p(PF-*co*-EG), copolymer was formed through a transesterification of the terminal hydroxyl groups of PEG with the ester bonds in PPF and consisted primarily of diblock and triblock forms with evidence that the PEG capped the ends of the PPF [2]. This prepolymer could be further polymerized with the appropriate initiators and/or cross-linking agents to form a solid. We proposed an *in situ* polymerizable system which can cross-link in the vascular space, causing minimal damage to the surrounding tissue, while providing a barrier between the vessel wall and the blood space. The concept of this type of blood-vessel barrier has been previously described for use with other polymer systems [8, 9].

The present study focuses on the evaluation of the swelling behavior and mechanical properties of p(PF-*co*-EG) hydrogels. Eight different copolymer compositions were investigated in order to evaluate the effects of four different design parameters: PEG molecular weight, PPF molecular weight, copolymer reaction time, and ratio of PEG to PPF. Two different cross-linking formulations were also tested, one with a cross-linking monomer and one without. We wanted to determine the cross-linking density, the degree of swelling in aqueous solution, the tensile properties, as well as the dynamic mechanical properties of the cross-linked copolymer. We also examined how these properties could be altered in order to optimize this material for its intended use.

MATERIALS AND METHODS

Polymer synthesis

The synthesis of PPF has been previously described [10]. Briefly, fumaryl chloride (Aldrich, Milwaukee, WI, USA) was added dropwise to a three fold molar excess of propylene glycol (Acros, Pittsburgh, PA, USA) at room temperature in the absence of any catalyst. HCl was given off as a gas and trapped in aqueous NaOH. The resulting intermediate fumaric diester was then purified by solution-precipitation in chloroform and petroleum ether, respectively. The second step was a transesterification of the intermediate to form the linear polyester, PPF. Finally, the copolymer was formed by adding PEG (Aldrich, Milwaukee, WI, USA) to the reaction vessel at 160°C under a vacuum of approximately 115 mm Hg [2]. Antimony trioxide was added as a basic catalyst and propylene glycol was removed by condensation. The entire reaction was performed under nitrogen by the use of a sparging apparatus within the reaction vessel. The resulting copolymer was again purified by solution-precipitation as described above. Excess chloroform and petroleum ether were removed by roto-evaporation. Gel permeation chromatography (GPC) was previously performed on the eight different copolymer formulations in order to determine molecular weights and compositions [2].

Fabrication of cross-linked copolymers

Cross-linked copolymer networks were fabricated with two different formulations. The first was made using a vinyl monomer, and the second was made without this agent in order to examine the cross-linked copolymer alone. The proposed reaction scheme with the cross-linking monomer, *N*-vinyl pyrrolidinone (VP) is given in Fig. 1. In the first formulation, we used VP at a 1 : 1 ratio of copolymer to monomer (wt/vol), 20 : 1 ratio of copolymer to benzoyl peroxide (BP) initiator (wt/wt), and catalytic amounts (1–5 μl/g of copolymer) of *N*,*N*-dimethyl-*p*-toluidine (DMT) at 25°C. This formulation was allowed to cross-link overnight prior to testing. The second formulation consisted of a 10 : 1 ratio of copolymer to BP (wt/wt) in enough chloroform to dissolve the mixture and was dried by roto-evaporation. This formulation was then heated at 60°C overnight to cross-link. Heat was used to accelerate the peroxide cleavage in the second formulation due to the insolubility of DMT in the dry copolymer.

Swelling studies

Films of copolymer formulations made without VP were cross-linked in 5 cm diameter glass Petri dishes with Teflon-coated bottoms (Bytac, Akron, OH, USA). These cross-linked samples were 2–3 mm thick depending on the exact amount of copolymer used. They were vacuum-dried at 25°C and 10 μm Hg overnight prior to use to remove any residual solvents. They were then weighed, and their volumes were measured by displacement in a nonsolvent, cyclohexane (Aldrich,

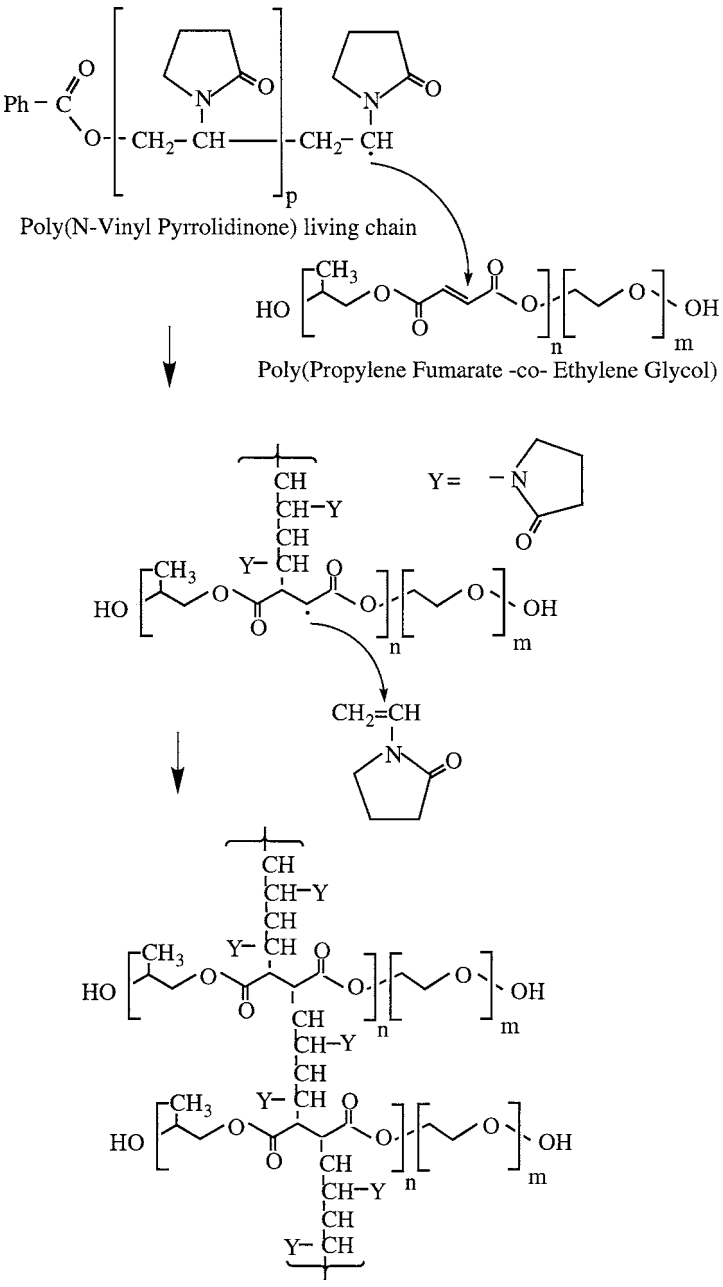

Figure 1. One proposed reaction scheme for the cross-linking of the diblock form of p(PF-*co*-EG) beginning with a poly(*N*-vinyl pyrrolidinone) living chain which has been initiated by the radical initiator, benzoyl peroxide. Initiation and propagation can also occur with double bonds on p(PF-*co*-EG) as in the case of cross-linking without VP.

Milwaukee, WI, USA). This was done by suspending the sample on a hook attached to a hanging pan balance. The nonsolvent was contained in a beaker which did not touch any part of the balance apparatus. Weight and volume measurements were taken after soaking the samples in distilled deionized H_2O (ddH_2O) and again after vacuum-drying until no weight change was observed. In all cases, the films were fully hydrated within one hour.

Using procedures outlined in Peppas and Barr-Howell [11], the swelling data were used to determine the ratio of the final dry weight of the polymer sample after swelling and vacuum-drying to the initial sample weight, gel fraction; the equilibrium volume swelling ratio, Q; as well as the molecular weight between cross-links, $\overline{M}_c$. In this case where cross-links were introduced without the presence of a solvent, the Flory and Rehner equilibrium swelling model was appropriate [11].

$$\frac{1}{\overline{M}_c} = \frac{2}{\overline{M}_n} - \frac{\frac{\overline{v}}{V_1}\left[\ln(1 - v_{2,s}) + v_{2,s} + \chi_1 v_{2,s}^2\right]}{v_{2,s}^{1/3} - \frac{v_{2,s}}{2}}, \tag{1}$$

where $\overline{M}_n$ is the number average molecular weight of the linear polymer, $\overline{v}$ is the specific volume of the polymer, V_1 is the molar volume of the swelling agent and χ_1 is the Flory–Huggins polymer–solvent interaction parameter. The equilibrium polymer volume fraction, $v_{2,s}$, was calculated as shown in Eq. (3) from the following measured weights.

The first measured weight was the initial weight of the cross-linked sample in air, $w_{a,r}$, which was measured after cross-linking and vacuum-drying. The sample was placed in cyclohexane and the initial weight of the cross-linked sample in a nonsolvent, $w_{n,r}$, was measured. The sample was then placed in distilled, deionized water and swollen to equilibrium and then removed to determine $w_{a,s}$, the weight in air of the sample at equilibrium swelling. The sample was then placed in cyclohexane again to get $w_{n,s}$, the weight in a nonsolvent of the sample at equilibrium swelling. Finally, the sample was vacuum-dried and the final dry weight of the sample gel after swelling, $w_{a,d}$, was measured. The density of the polymer, ρ_p, was calculated from the displacement of nonsolvent, given its density, ρ_n, which for cyclohexane is 0.79 g cm^{-3}

$$\rho_p = \frac{w_{a,r}}{w_{a,r} - w_{n,r}}\rho_n. \tag{2}$$

Then the equilibrium polymer volume fraction was calculated using $V_p = w_{a,d}/\rho_p$ and $V_{g,s} = (w_{a,s} - w_{n,s})/\rho_n$ from the following equation:

$$v_{2,s} = \frac{V_p}{V_{g,s}}. \tag{3}$$

Table 1.
Number average molecular weights of eight copolymer formulations as previously determined by gel permeation chromatography[2] and their corresponding tensile testing data

Sample name	Molecular weight, $\overline{M}_n$	Ultimate tensile stress, σ_b (MPa)	Tensile modulus, E (MPa)
Copolymer 1	8200 ± 150	0.23 ± 0.09	2.16 ± 0.34
Copolymer 2	7370 ± 10	0.82 ± 0.37	6.14 ± 2.04
Copolymer 3	8050 ± 20	1.06 ± 0.13	11.02 ± 1.00
Copolymer 4	10060 ± 90	0.56 ± 0.15	4.62 ± 0.77
Copolymer 5	13090 ± 20	0.91 ± 0.08	5.05 ± 1.36
Copolymer 6	13950 ± 40	0.15 ± 0.03	1.11 ± 0.20
Copolymer 7	14200 ± 70	0.32 ± 0.14	1.90 ± 0.67
Copolymer 8	14080 ± 160	1.44 ± 0.06	20.66 ± 2.42

Given the other parameters, such as the polymer molecular weights presented in Table 1 (from GPC analysis) and the molar volume of the solvent (the value for water is 18.152 $cm^3\,mol^{-1}$), the cross-linking density was calculated from an estimate of the Flory–Huggins polymer–solvent interaction parameter, χ_1, for each of the copolymers. The values of χ_1 for pure PEG of nominal molecular weight 5000 were used. These values were 0.5 for copolymer numbers 1, 4, 6, and 7; 0.6 for copolymers 2 and 5; and 0.7 for copolymers 3 and 8 and depended on the volume fraction of polymer in the solvent [12].

Dynamic mechanical testing

Copolymer films were made both with and without VP by injection-molding, and cut into 1 cm × 2 cm × 1 mm films for testing. The injection molding system consisted of a 6-in. long, 20 gauge needle mounted on a syringe and inserted into a mold. The cavity in the Teflon mold was machined to 1 mm depth and, the mold was then clamped to a glass in order to visualize the film formation. A dynamic mechanical analyzer (DMA) (model 983, TA Instruments, Newark, DE, USA) was used to determine complex dynamic flexural moduli, $|E^*|$, and complex dynamic shear moduli, $|G^*|$. The samples were swollen first overnight in ethanol and then in ddH_2O to avoid cracking. The samples were equilibrium swollen and run at 25°C, at a frequency of 1 Hz, and at a strain of approximately 0.1%. The testing was performed in the flexural mode and lasted 15 min. The value of $\overline{M}_c$ was also determined from the shear modulus, $|G^*|$, an approximation for G, using the following equation derived from rubber elasticity theory [13].

$$\frac{1}{\overline{M}_c} = \frac{2}{\overline{M}_n} + \frac{G}{RT\rho}, \tag{4}$$

where R is the ideal gas constant, T is the temperature in Kelvin, and ρ is the density of the wet hydrogel as determined by swelling studies.

Tensile testing

Tensile tests were performed on a Vitrodyne 1000 Universal Materials Tester (Chattilon, Greensboro, NC, USA) at a crosshead speed of 0.1 mm s^{-1}. The cross-linked copolymers were made with VP and injection-molded into dogbone shapes which were 114 mm in total length, 33 mm in length at the narrow section, 6 mm wide at the narrowest point, and 1 mm thick. They conformed to ASTM standard D639-91 for testing tensile properties of plastics. The samples were swollen first overnight in ethanol and then in ddH_2O until equilibrium was reached, and they were subsequently tested to failure. Stress and strain were calculated based on swollen dimensions as calculated from the swelling ratio. Tensile modulus was then determined from the slope of the linear region of the stress/strain graph. The samples were marked 20 mm from each end prior to swelling and then clamped even with the markings after hydration. The swelling ratio was determined from the Vitrodyne output based on the distance between marks both before and after swelling.

Statistical design

Several parameters were varied in order to assess their effects on the properties of the copolymer. This was accomplished through the use of a resolution IV, two level, fractional factorial design [14]. The design is given in Table 2. The parameters were varied as follows: PEG nominal molecular weight was either 2000 or 4600, transesterification time for the PPF homopolymer was either 5 or 10 h, copolymer transesterification time was either 5 or 10 h, and weight percent PEG was either 33 or 66%. For a transesterification reaction, molecular weight of the linear chain increases with increasing reaction time. In total, eight copolymers were made and three repetitions of each of the tests were performed except for the tensile

Table 2.
Resolution IV fractional factorial design showing the eight combinations of high and low values for four different design parameters

Sample name	Nominal molecular weight of PEG	PPF reaction time (h)	Copolymer reaction time (h)	% PEG by weight
Copolymer 1	2000	5	5	66
Copolymer 2	2000	5	10	33
Copolymer 3	2000	10	5	33
Copolymer 4	2000	10	10	66
Copolymer 5	4600	5	5	33
Copolymer 6	4600	5	10	66
Copolymer 7	4600	10	5	66
Copolymer 8	4600	10	10	33

tests in which five samples of each copolymer formulation were tested. Statistical comparisons were made using a student's t-test with a 95% confidence interval.

RESULTS AND DISCUSSION

Swelling studies

The gel fraction was calculated from the swelling properties of the copolymer. This value is a ratio of the final dry weight of the polymer sample after equilibrium swelling and vacuum-drying to the initial sample weight and is a measure of the degree to which the cross-linking reaction has proceeded. The gel fractions ranged from 0.78 ± 0.05 to 0.86 ± 0.01, which show that the reaction is relatively efficient for all copolymer formulations. The equilibrium volume swelling ratio, Q, which is a ratio of the equilibrium swollen volume to the initial sample volume, varied from 1.5 ± 0.1 to 3.0 ± 0.1. This is typical for moderately swollen hydrogels [11]. Figure 2 shows the effects of the design parameters on the resulting value of Q. Increasing the weight percent PEG in the copolymer increases the swelling ratio, while increasing the molecular weight of PPF decreases the ratio.

The approximation of the Flory–Huggins polymer–solvent interaction parameter as described above leads to values of $\overline{M}_c$ which range from 300 ± 120 to 1190 ± 320 (Fig. 3). A reasonable number would fall between about 156 (the minimum possible distance between unsaturated sites in pure PPF) and the molecular weight of a single chain of PPF homopolymer, about 500–1300. The relatively low values of $\overline{M}_c$ suggest that the PEG chains are not involved in the cross-linked section of

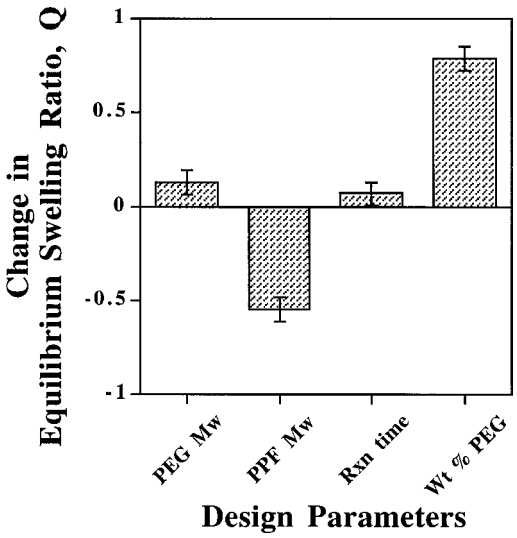

Figure 2. Magnitude of the change in the equilibrium swelling ratio, Q, of the copolymers caused by increasing the values of the four different design parameters. Error bars stand for means ± standard error of the effect ($n = 3$, standard error = 0.06).

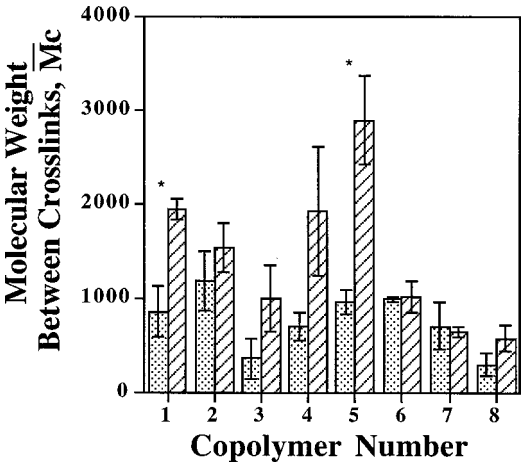

Figure 3. Molecular weight between cross-links, $\overline{M}_c$, for eight different copolymer formulations as determined by both swelling studies and DMA. Dotted bars represent data from swelling studies and hash marked bars represent data from DMA. Error bars stand for means ± standard deviation ($n = 3$, * designates significant difference at 95% confidence limit).

the molecule. This case is supported by the effects of the design parameters on the swelling ratio. With a triblock copolymer of which only the central block is cross-linkable, the primary mode of affecting the cross-linking density would be to change either the molecular weight or the weight percent of the cross-linkable group as described above. As the cross-linking density is increased, the hydrogel is less permeable to water and the degree of swelling is decreased.

Dynamic mechanical analysis

From DMA measurements, the calculated values for $\overline{M}_c$ range from 630 ± 160 to 3150 ± 480. The values are also shown in Fig. 3 and are consistently higher than those determined by swelling studies. However, only copolymers 1 and 5 gave statistically different values for $\overline{M}_c$ as determined by the two methods. One explanation for this difference may be that the estimation of χ_1 based on pure PEG fails for certain PEG copolymer compositions. In an effort to develop an experimentally determined value χ_1 for p(PF-*co*-EG) hydrogels we have plotted χ_1 as determined by DMA versus $v_{2,s}$ as determined by swelling studies. The data were curve-fitted as shown in Fig. 4 and gave the following equation:

$$\chi_1 = 0.232 + 1.016 v_{2,s}. \tag{5}$$

The complex dynamic flexural moduli, $|E^*|$, were also determined by DMA on copolymer formulations fabricated both with and without VP. The values for $|E^*|$ ranged from 0.9 ± 0.2 to 13.1 ± 1.1 MPa for the formulations with VP and 1.6 ± 0.5 to 13.9 ± 3.4 MPa for the formulations without VP. These data, along with the values for $|G^*|$ are given in Table 3. In comparison, the value for dynamic tensile

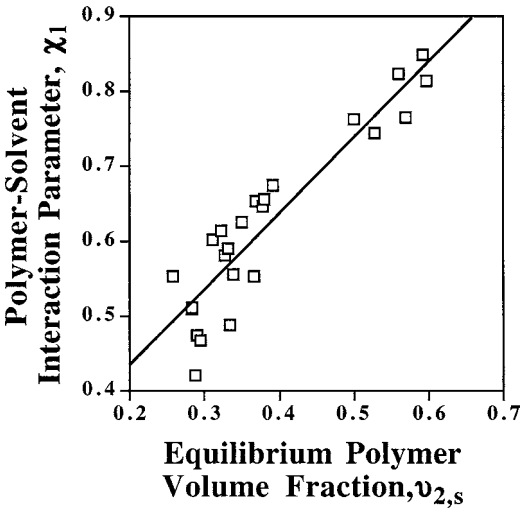

Figure 4. Scatter plot of χ_1 as determined by DMA vs $v_{2,s}$ as determined by swelling (correlation coefficient, $r^2 = 0.847$).

Table 3.
Flexural and shear moduli as determined by DMA for all formulations of the copolymer made both with and without *N*-vinyl pyrrolidinone

Sample name	Flexural modulus, $\|E^*\|$ w/ VP (MPa)	Flexural modulus, $\|E^*\|$ w/o VP (MPa)	Shear modulus, $\|G^*\|$ w/ VP (MPa)	Shear modulus, $\|G^*\|$ w/o VP (MPa)
Copolymer 1	0.87 ± 0.19	2.13 ± 0.19	0.30 ± 0.06	0.73 ± 0.06
Copolymer 2	2.99 ± 0.32	3.21 ± 0.95	1.00 ± 0.07	1.10 ± 0.34
Copolymer 3	1.69 ± 1.43	7.32 ± 2.61	1.95 ± 0.50	0.99 ± 0.76
Copolymer 4	5.64 ± 0.18	2.29 ± 1.26	0.59 ± 0.07	2.53 ± 0.89
Copolymer 5	2.39 ± 0.12	1.57 ± 0.47	0.83 ± 0.04	0.55 ± 0.16
Copolymer 6	2.65 ± 0.12	6.65 ± 1.43	0.92 ± 0.04	2.32 ± 0.50
Copolymer 7	3.87 ± 0.39	11.15 ± 0.95	1.35 ± 0.13	2.16 ± 0.33
Copolymer 8	13.14 ± 1.13	13.88 ± 3.39	4.60 ± 0.40	4.85 ± 1.21

modulus of canine aorta has been measured at 1.55 MPa under the same strain at the same frequency and that of elastin, the primary component of the aortic wall, has been measured at 1.90 MPa [15]. Figure 5 shows the effects of the design parameters on the resulting values of $|E^*|$. Increasing the molecular weight of PPF or the molecular weight of PEG increases the elastic moduli and therefore reduces hydrogel compliance. Conversely, increasing the weight percent of PEG decreases the $|E^*|$ and increases compliance. This result is again due to the fact that the PPF is the only cross-linkable group. As the relative amount of PPF is increased, more cross-links are introduced, and consequently, the material becomes less compliant. Therefore, in order to minimize $|E^*|$ in the resulting cross-linked material, the molecular weight of PPF as well as the molecular weight of PEG should be low

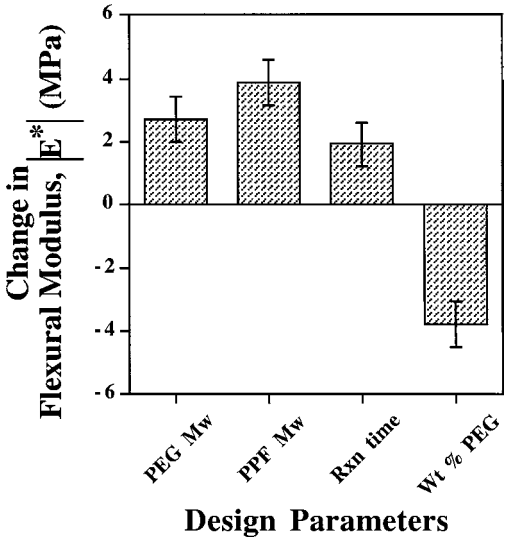

Figure 5. Magnitude of the change in complex dynamic flexural modulus, $|E^*|$, of the copolymers made with VP caused by increasing the values of the four different design parameters. Error bars stand for means $\pm$ standard error of the effect ($n = 3$, standard error $= 0.28$).

and the relative weight percent of PEG should be high. However, it has also been shown that a reduction in thrombogenicity by the presence of covalently bound PEG only occurs for high molecular weights between approximately 10 000 and 20 000 [16].

Tensile testing

The ultimate tensile stress or stress at break, σ_b, on the formulations made with VP ranged from 0.15 ± 0.03 to 1.44 ± 1.06 MPa at typical strains between 10 and 20%. Tensile modulus, E, ranged from 1.11 ± 0.20 to 20.66 ± 2.42 MPa (Table 1). In comparison, these values are significantly lower than those for PEG copolymers with polyurethanes [17] or poly(ethylene terephthalate) [18]. However, they are comparable to PEG copolymers with poly(lactic acid) for which ultimate tensile strengths have been reported in the range of 4–7 MPa [19]. The effects of the four design parameters on the resulting values of σ_b and E are shown in Figs 6 and 7. Both stress and modulus increase with increasing PPF molecular weight and decrease with increasing PEG content. The molecular weight of PEG as well as the copolymer reaction time have little effect on ultimate tensile stress or E. This again shows that changing the cross-linking density by varying the size and amount of PPF is the primary method of affecting the mechanical properties.

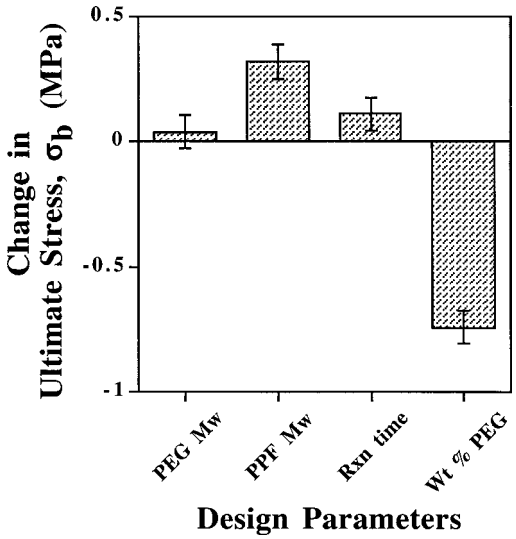

Figure 6. Magnitude of the change in the ultimate tensile stress, σ_b, of the copolymers made with VP caused by increasing the values of the four different design parameters. Error bars stand for means $\pm$ standard error of the effect ($n = 5$, standard error $= 0.07$).

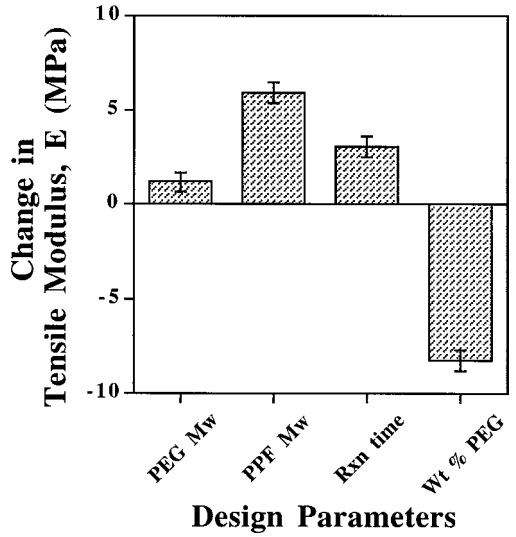

Figure 7. Magnitude of the change in the tensile modulus, E, of the copolymers made with VP caused by increasing the values of the four different design parameters. Error bars stand for means $\pm$ standard error of the effect ($n = 5$, standard error $= 0.54$).

CONCLUSIONS

The equilibrium volume swelling ratios of p(PF-*co*-EG) block copolymer hydrogels are characteristic of moderately swollen hydrogels, and, along with the relatively low values of $\overline{M}_c$, show that the hydrogel is highly cross-linked. The swelling

ratio can be reduced by increasing the relative amount or molecular weight of the PPF block. Copolymer hydrogels made both with and without VP showed similar values for flexural moduli and these values are comparable to those of canine aorta. The moduli can be decreased by increasing the relative amount of PEG or decreasing its molecular weight or the molecular weight of PPF. The ultimate tensile stresses on the hydrogels made with VP were relatively low compared to other PEG copolymers, however, these values can be increased by increasing the relative amount or molecular weight of PPF.

Many applications in tissue engineering require a material which has the biocompatibility and drug delivery potential of a hydrogel. Hydrogels, however, typically have very poor mechanical properties. We have designed a copolymer with relatively high mechanical properties due to the presence of cross-linkable groups along the molecular backbone. We have developed this material for use in the vasculature to protect the vessel wall against restenosis as well as potentially serving a carrier for bioactive molecules. We envision that this material could be optimized for use in other applications and have attempted to give a method for altering physical properties by changing design parameters.

Acknowledgements

This work was performed through funding from the Whitaker Foundation and the National Institutes of Health (R01-AR44381). L. J. Suggs acknowledges financial support by the National Institutes of Health Biotechnology Training Grant (5T32GM08362).

REFERENCES

1. M. Gottsauner-Wolf, D. J. Moliterno, A. M. Lincoff and E. J. Topol, *Clin. Cardiol.* **19**, 347 (1996).
2. L. J. Suggs, R. G. Payne, M. J. Yaszemski, L. B. Alemany and A. G. Mikos, *Macromolecules* **30**, 4318 (1997).
3. M. J. Yaszemski, R. G. Payne, W. C. Hayes, R. S. Langer, T. B. Aufdemorte and A. G. Mikos, *Tissue Eng.* **1**, 41 (1995).
4. A. J. Domb, N. Manor and O. Elmalak, *Biomaterials* **17**, 411 (1996).
5. D. A. Herold, K. Keil and D. E. Bruns, *Biochem. Pharmacol.* **38**, 73 (1989).
6. E. W. Merrill and E. W. Salzman, *ASAIO J.* **6**, 60 (1982).
7. A. Mansoor and K. Park, *Biomaterials* **13**, 682 (1992).
8. J. L. Hill-West, S. M. Chowdhury, M. J. Slepian and J. A. Hubbell, *Proc. Natl Acad. Sci.* **91**, 5967 (1994).
9. J. L. West and J. A. Hubbell, *Proc. Natl Acad. Sci.* **93**, 13 188 (1996).
10. S. J. Peter, M. J. Yaszemski, L. J. Suggs, R. G. Payne, R. Langer, W. C. Hayes, M. R. Unroe, L. B. Alemany, P. S. Engel and A. G. Mikos, *J. Biomater. Sci. Polymer Edn* **8**, 893 (1997).
11. N. A. Peppas and B. D. Barr, in: *Hydrogels in Medicine and Pharmacy, Vol. 1, Fundamentals*, N. A. Peppas (Ed.), pp. 27–56. CRC Press, Boca Raton, FL (1988).
12. A. F. M. Barton, in: *CRC Handbook of Polymer–Liquid Interaction Parameters and Solubility Parameters*, p. 189. CRC Press, Boca Raton, FL (1990).

13. K. S. Anseth, C. N. Bowman and L. Brannon-Peppas, *Biomaterials* **17**, 1647 (1996).
14. G. E. P. Box, W. G. Hunter and J. S. Hunter, *Statistics for Experimenters: An Introduction to Design, Data Analysis, and Model Building*. John Wiley and Sons, New York (1978).
15. J. T. Apter and E. Marquez, *Circul. Res.* **22**, 393 (1968).
16. E. W. Merrill, in: *Poly(Ethylene Glycol) Chemistry*, J. M. Harris (Ed.), pp. 199–200. Plenum Press, New York (1992).
17. J. H. Silver, C. W. Myers, F. Lim and S. L. Cooper, *Biomaterials* **15**, 695 (1994).
18. D. K. Gilding and A. M. Reed, *Polymer* **20**, 1454 (1979).
19. D. Cohn and H. Younes, *J. Biomed. Mater. Res.* **22**, 993 (1988).

Polymers for Tissue Engineering, pp. 113–124
Molly S. Shoichet and Jeffrey A. Hubbell (Eds)

Creating biomimetic micro-environments with synthetic polymer–peptide hybrid molecules

KEVIN M. SHAKESHEFF,[2] SCOTT M. CANNIZZARO[1]
and ROBERT LANGER[1,*]

[1]*Department of Chemical Engineering, Massachusetts Institute of Technology, Cambridge, MA 02139, USA*
[2]*School of Pharmaceutical Sciences, The University of Nottingham, Nottingham, NG7 2RD, UK*

Received 9 June 1997; accepted 13 November 1997

Abstract—In designing polymers that can act as tissue engineering templates it is beneficial to consider methods of mimicking the natural support structures used by the human body to guide the behavior and development of cells within tissues. The well-known RGD cell adhesion ligand provides a simple mechanism of creating polymer surfaces that mimic the extracellular matrix. This paper considers the methods that have been used to attach such motifs to synthetic polymers. In general there are two strategies: the formation of polymer–peptide hybrid molecules, or the immobilization of the ligand on the fabricated surface of the polymer. The three major synthetic strategies of creating polymer–peptide hybrids are reviewed.

Key words: Polymers; tissue engineering; RGD; cell adhesion; integrins; biomimetic materials; extracellular matrix; synthesis.

1. INTRODUCTION

The aim of tissue engineering is to control the growth, differentiation and behavior of cells so they may organize into functional tissue [1–3]. One mechanism of achieving this control is the formation of a defined micro-environment that surrounds the cells and promotes specific cell interactions. Successful micro-environments employed in tissue engineering are often designed to mimic the micro-environments created by the body in natural cell and tissue development.

A promising method of creating biomimetic micro-environments for tissue engineering applications is the employment of synthetic polymers that possess precisely controlled surface properties [4, 5]. The concept of designing polymeric materials with

*To whom correspondence should be addressed.

precisely controlled and complex surface chemistries is often encountered in biomaterial science. For example, the development of implants with improved biocompatibility [6] and of site-specific drug delivery systems is founded on the optimization of surface design [7]. The rapid growth of polymer-based tissue engineering has further stimulated the study of polymer surface engineering because the intimate relationship required between biomimetic polymer surfaces and cells presents new challenges. This paper aims to provide an overview of the current methods of creating synthetic polymers with surface properties that generate biomimetic micro-environments. In the next section the general properties of biomimetic micro-environments are considered. Then, an overview of the methods used to synthesize biomimetic polymers is provided. The final section of this review considers in detail a number of approaches to this synthesis based on the formation of polymer–peptide hybrid molecules.

2. BIOMIMETIC MICRO-ENVIRONMENTS

Two principles guide the design of biomimetic micro-environments using synthetic polymer surfaces, the promotion of receptor-mediated cell adhesion and the elimination of non-specific protein or cell interactions with the polymer.

In aiming to promote receptor-mediated cell adhesion the polymer surface is mimicking the extracellular matrix (ECM) [8]. The ECM provides cells with an interactive construct onto which they can adhere via integrin receptors. Integrin-mediated binding of cells is the foundation for cell growth and differentiation and is the dominant mechanism by which cells communicate with non-cellular surroundings [9]. The creation of polymer surfaces that can adhere cells via integrin receptors has been facilitated by the elucidation of the structure of a number of short peptide motifs that bind to these receptors [10]. The tripeptide RGD is the most utilized example of such motifs. The cell-adhesive function of this peptide was determined in 1984 when Pierschbacher and Ruoslahti demonstrated that it could mimic the cell attachment activity of the extracellular protein, fibronectin [11]. This sequence was determined to be present on the fourth β-turn of the fibronectin molecule. The authors demonstrated that the immobilization of the peptide to Sepharose beads, resulted in the beads inheriting the cell adhesion activity of the extracellular matrix. The potential importance of integrin-mediated cell responses in tissue engineering has been significantly enhanced by the elucidation of the structure and cellular function of a large number of different integrin types. Therefore, a major objective in the design of functionalized polymer surfaces for tissue engineering applications is the attachment of peptides that promote integrin-mediated cell attachment.

The design of microenvironments that bind cells via receptors need not be limited to the targeting of integrin receptors. The structure of short molecular motifs (peptide or carbohydrate based) that bind to other classes of cell adhesion receptors are known [12, 13]. Non-integrin classes of cell adhesion receptors are principally involved in cell-to-cell communications. Stimulating cell development using cadherin, selectins and immunoglobulin superfamily receptors may be necessary as the complexity of the tissue being engineered increases [14]. Major non-integrin-receptor

types used to adhere cells to tissue engineering supports include the asialoglycoprotein (ASGP-R) receptor responsible for hepatocyte binding [15]. Although the ASGP-R is not a cell adhesion receptor, it has been demonstrated that adhesion to surfaces via this receptor promotes the specific spreading of hepatocytes [16].

When designing polymer surfaces so they interact with cells via specific receptors the aim is to stimulate an active interaction between the synthetic polymer and the biological environment. This strategy is dependent on the polymer surface chemistry remaining unchanged during the period of time that elapses between the material being exposed to the biological environment and the receptor-mediated cell adhesion. For *ex vivo* tissue engineering applications the biological environment can be tailored to ensure that this surface chemistry is static for extended periods, e.g. by removal of serum proteins from the media. However, for *in vivo* tissue engineering applications, e.g. accelerated wound healing or *in situ* nerve regeneration, dynamic surface chemistry changes are likely in the first seconds of contact between the polymer surface and the biological environment. The principle change will be caused by non-specific protein adsorption that can mask any desired surface feature. Therefore, in designing micro-environments for tissue engineering applications it is necessary to balance the desire for active biological interactions with the need to prevent detrimental passive interactions.

This balance can be achieved by the inclusion of poly(ethylene glycol) (PEG) in engineered surfaces. Non-specific protein adsorption to PEG surfaces is unfavorable due to a steric stabilization effect in which proteins are repelled by energetic and entropic penalties incurred if a protein molecule compresses PEG chains [17]. It has been demonstrated that protein resistivity can be achieved by surfaces that present density packed PEG oligomers. Mrksich and Whitesides have shown that self-assembled monolayers, prepared from alkane thiols terminated with only two ethylene glycol groups, are resistant to protein adsorption [18]. For less organized polymeric biomaterial surfaces, longer chains of PEG must be employed to compensate for a decrease in PEG surface density.

3. OVERVIEW OF METHODS OF CREATING BIOMIMETIC MATERIALS

The creation of biomimetic materials requires methods of attaching cell adhesive peptides and/or non-specific adsorption resistive molecules to polymer chains. In broad terms, there are two methods of achieving this attachment; the application of surface engineering techniques to immobilize peptides on exposed surfaces of fabricated materials or the covalent incorporation of peptides into the bulk polymer structure to form polymer–peptide hybrids.

Surface engineering techniques used to create biomimetic materials utilize either covalent coupling to surface functional groups, non-specific adsorption, coating or entrapment to immobilize peptides. Conformationally favorable presentation of short peptide motifs to cells may not be ideal following simple adsorption, coating or entrapment and, therefore, covalent attachment strategies have been intensively investigated.

For polymers that possess reactive groups in their repeat structure, surface engineering by covalent attachment is relatively simple. However, many materials used in surface engineering lack these groups. For these materials the major challenge of surface engineering is the introduction of reactive groups to the surface. Approaches to this introduction include: the coating of a secondary reactive polymer onto the non-functionalized surfaces [19], the introduction of reactive groups by plasma or chemical modification [20], and the photochemical derivatization of surfaces using phenyl azido chemistry [21]. Methods of surface engineering and surface covalent attachment have been discussed in a number of excellent reviews [4, 20, 22].

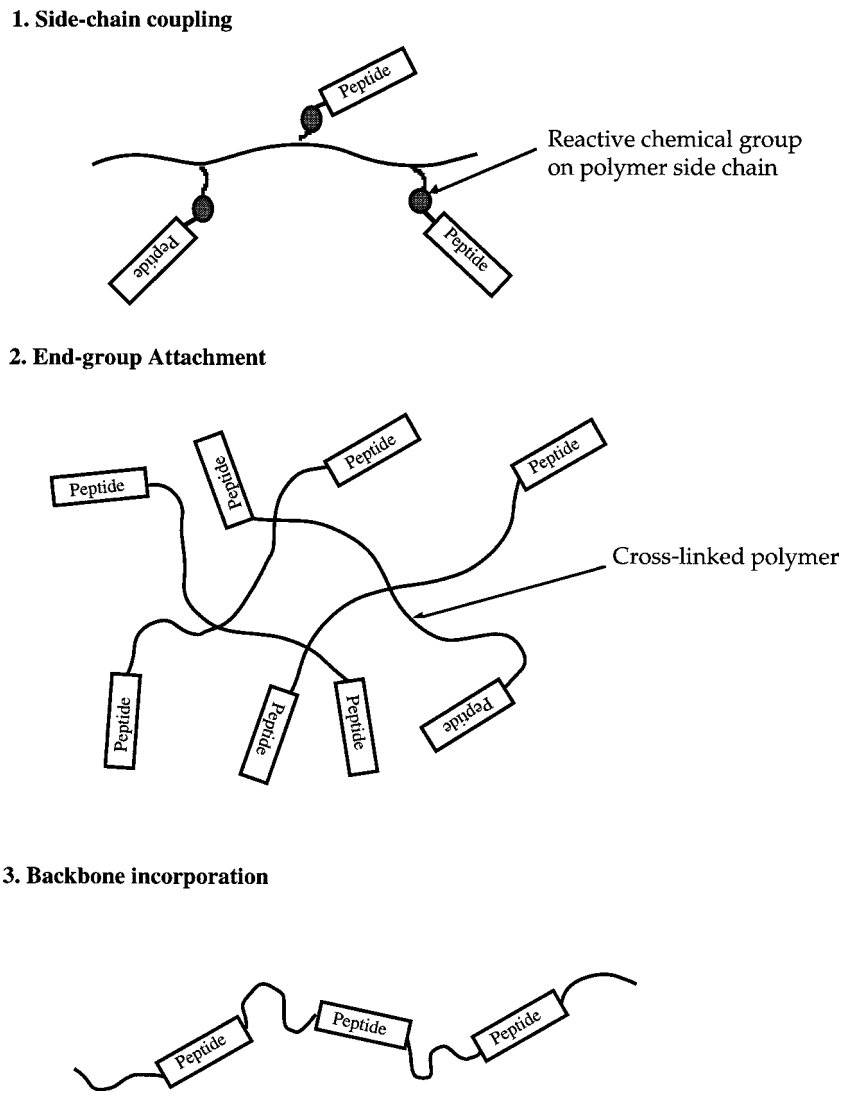

Figure 1. Mechanisms of forming polymer–peptide hybrid molecules.

In this review we will consider in detail the methods of creating biomimetic materials that are based on polymer–peptide hybrid formation. Potential advantages of these materials over the use of surface engineering include improved peptide attachment efficiency and ease of fabrication of tissue engineering templates. In Fig. 1, three approaches to the formation of these molecules are shown schematically. In the first approach, a synthetic polymer is designed to contain reactive chemical groups on its side-chains and these groups are then activated to allow the formation of covalent bonds between the polymer and the peptide. The second approach does not require the polymer backbone to possess side-group reactivity because the inherently reactive polymer end-groups are utilized. In the third approach, new block co-polymers are synthesized that contain peptides as blocks in the in the polymer backbone. Examples of each of these approaches are discussed in the next section.

4. EXAMPLES OF APPROACHES TO POLYMER–PEPTIDE HYBRID FORMATION

4.1. Side-chain coupling

The major obstacle to the use of side-chain coupling is the need for synthetic polymers with reactive side groups. Few polymers used in biomaterial science possess these groups and, therefore, tissue engineering applications have stimulated the design of a number of new biodegradable and non-biodegradable polymers.

4.1.1. Biodegradable polymers. For many tissue engineering applications, the polymer–peptide hybrid is required as an interactive support material only during tissue formation, when cell-to-matrix interactions to a template are required. After this process has occurred the developing tissue can synthesize its own ECM. By employing biodegradable polymers as the template, it is possible for the template to be naturally resorbed after the desired function has been achieved.

Biodegradable polymers based on the poly(α-hydroxyesters) have been used extensively for tissue engineering applications. These polymers are attractive candidate materials for tissue engineering applications due to their relatively long history of *in vivo* biomaterial application in surgical [23] and pharmaceutical fields [24]. This history ensures that a large body of evidence exists of their biocompatibility and low toxicity [25, 26]. In addition, the physicochemical properties of these polymers have been extensively characterized. However, this class of biodegradable polymers lacks the reactive side-groups required for polymer–peptide hybrid formation.

Poly(lactic acid-*co*-lysine) (PLAL) was designed to preserve the beneficial properties of the poly(α-hydroxyesters) whilst incorporating lysine monomer units to introduce primary amines for covalent peptide attachment strategies [27]. The major obstacle to the introduction of lysine units into a poly(α-hydroxyester) sequence was the synthesis of lysine containing monomer that polymerized by the same ring-opening mechanism as the cyclic lactone monomers. Barrera *et al*. overcame this obstacle with the synthesis of 3-(*N*-ε-benzoxycarbonyl-L-lysyl)-6-L-methyl-2,5-morpholinedione, a

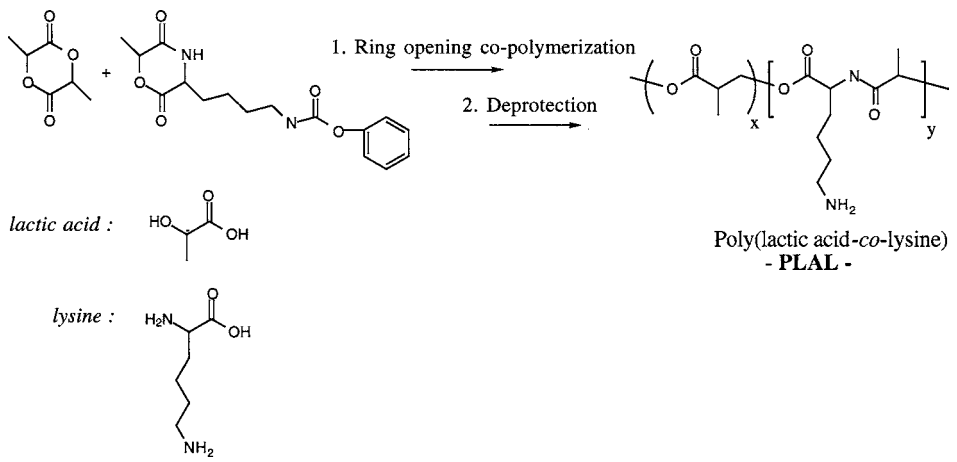

Figure 2. Copolymerization of 3-(*N*-ε-benzoxycarbonyl-L-lysyl)-6-L-methyl-2,5-morpholinedione with L,L-lactide to give PLAL.

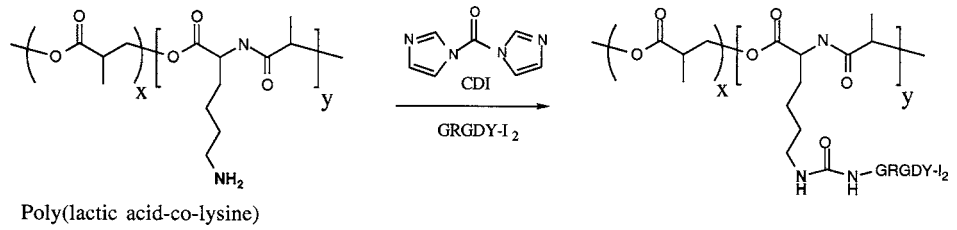

Figure 3. Covalent attachment of RGD to PLAL.

cyclic dimer of L-lactic acid and L-lysine. Copolymerization of this dimer with L,L-lactide generated PLAL as shown in Fig. 2.

PLAL has been used as a foundation for the covalent attachment of RGD-containing peptides using 1,1′-carbonyldiimidazole to activate primary amines presented at the polymer surface (see Fig. 3) [28]. Surface chemistry analysis, by X-ray photoelectron spectroscopy and colorimetric analysis, has been used to quantify the amount of RGD peptide presented at surfaces formed the polymer–peptide hybrid. Cell adhesion studies, using bovine endothelial cells, have proven that this hybrid causes integrin-mediated cell adhesion.

There is evidence that a spacing of less than 140 nm between RGD units on polymer surfaces is required to initiate integrin-mediated cell adhesion [29]. A spacing of 140 nm equates to a low surface coverage of the peptide that can easily be achieved with PLAL. However, if more complex micro-environments are to be created there is a need for high densities of reactive chemical groups along the polymer backbone. The synthetic pathway employed for PLAL was found to permit no more than 2% lysine incorporation into random copolymer structure. Hrkach *et al.* demonstrated that this limit could be exceeded to enable lysine contents in excess of 80% by utilizing the lysine units in the original polymer to initiate a ring opening polymerization

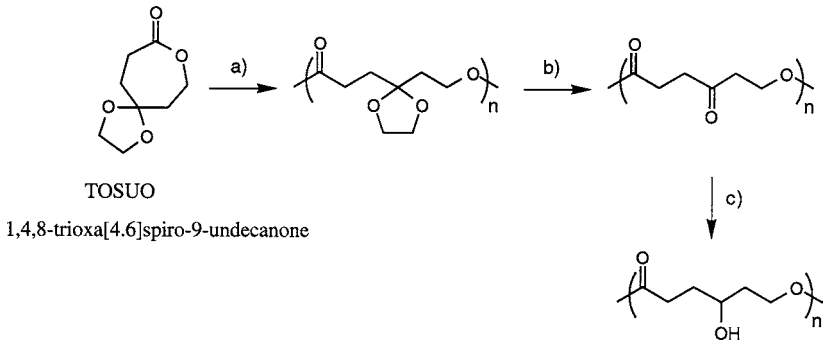

Figure 4. Functional modification to poly(ε-caprolactone); synthesis of polymers based on 1,4,8-trioxa-[4.6]spiro-9-undecanone: (a) $Al(OiPr)_3$, toluene, 25°C; (b) $(C_6H_3)_3CBF_4$, CH_2Cl_2, 25°C, 0.5 h; and (c) NaBH4, CH_2Cl_2/EtOH, 25°C, 0.5 h.

of *N*-ε-(carbobenzoxy)-L-lysine [30]. This ring opening creating comblike grafts of lysine repeat units extending from sites of lysine incorporation in the backbone.

Recently, other functionalized poly(α-hydroxyesters) have been described and employed in tissue engineering. Elisseeff *et al.* have synthesized a aspartic acid containing poly(α-hydroxyesters) using similar synthetic principles to those originated for PLAL [31].

Functionalized poly(α-hydroxyesters) have also been created by Jerome *et al.* who synthesised derivatives of poly(ε-caprolactone) containing pendant hydroxyl functionality (Fig. 4) [32]. Ring opening polymerization based on 1,4,8-trioxa[4,6]spiro-9-undecanone (TOSUO), a modification of the cyclic monomer for poly(ε-caprolactone), gives the poly(α-hydroxyesters) chain bearing an acetal moiety. Subsequent deacetalization to the ketone followed by selective reduction yields the pendent alcohol. The authors report quantitative conversion for these two steps with no scission of the polymer. Further, living polymerization with aluminum isopropoxide as an initiator allowed for the preparation of AB and ABA block copolymers of ε-caprolactone and TOSUO [32].

4.1.2. Non-biodegradable polymers. In a number of tissue engineering application, biodegradation of the polymer–peptide hybrid is not desirable. An important example of such application is the *in vitro* endothelialization of vascular prosthesis, where the attachment of endothelial cells is designed to inhibit surface-induced thrombosis on prosthesis designed for long-term residence in the body [19]. A number of non-biodegradable cell adhesive systems have been investigated [33–40]. However, the majority of these systems are derived from surface modifications and are not polymer–peptide hybrids. Systems which can be defined as a bulk modification of the biological motif with the polymer are presented here.

Polyurethanes are extensively employed as non-biodegradable implants and, therefore, are attractive candidates as components of hybrids. Cooper *et al.* have described a method of covalently attaching RGD-containing peptides to these polymers [41, 42]. The reaction scheme, shown in Fig. 5, involves grafting ethyl carboxylate groups to the urethane nitrogen by reaction of β-propriolactone with sodium azide treated polymer.

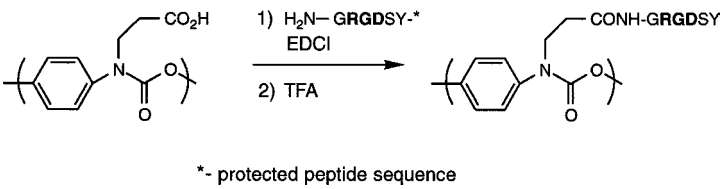

Figure 5. Side-chain coupling of an RGD containing peptide to a polyurethane.

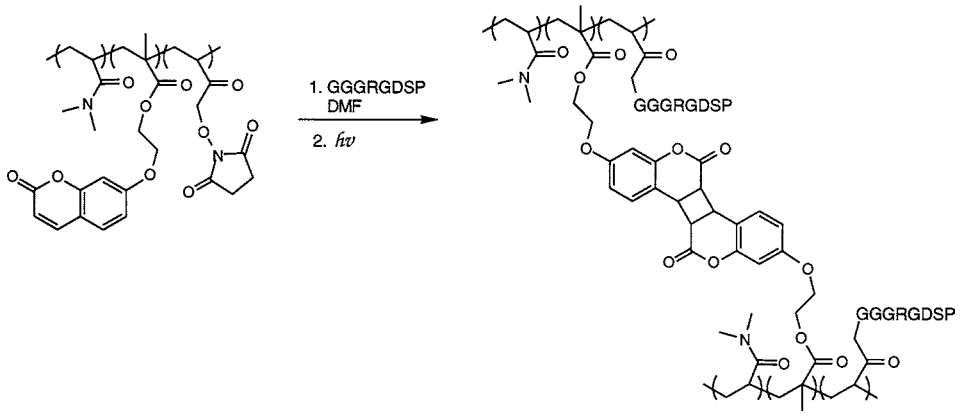

Figure 6. Methacrylic acid/methacrylamide copolymer containing a *N*-acryloxy succinimide repeat unit. Coupling of RGD containing peptide and dimerization.

The formation of a polymer–peptide hybrid molecule offered a significant advantage over the use of a surface engineering method because once formed the hybrid could be fabricated into cell-interactive biomaterials by a simple solvent-casting processes.

Moghaddam and Matsuda have described a further example of a polymer–peptide hybrids forming by a side-chain covalent attachment strategy [43]. Their system is based on a methacrylic acid/methylacrylamide copolymer containing a *N*-acryloxy succinimide repeat unit in the initial polymer structure. This reactive side-chain of this unit provides a site for peptide attachment. The advantage and novelty of this polymer system lies in the ability to photodimerize the methacrylic acid derivatives that contain coumarin. This dimerization process and peptide attachment are shown in Fig. 6. Photodimerization leads to photogelation of the polymer generating three-dimensional hydrogel matrices. The authors demonstrated that photogelation could be induced in a solution of the polymer containing smooth muscle cells. The hydrogel then formed a three-dimensional artificial extracellular matrix around the cells.

4.2. End-group attachment

A number of groups have employed PEG based polymers as the foundation for functionalized synthetic polymers. In these applications, biologically active groups are coupled to PEG end-groups rather than to chemical groups along the polymer backbone. Two advantages of employing PEG for these applications can be identified. Firstly, as discussed above, the protein-resistivity of PEG is a desirable attribute

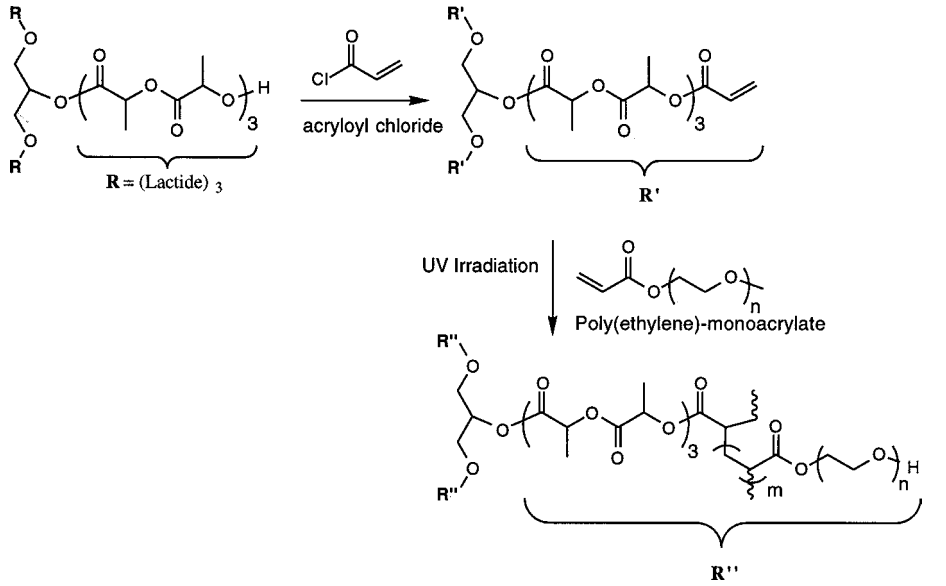

Figure 7. Synthesis of a biodegradable polymer network containing PEG.

because it prevents adsorptive processes blocking the chemical contribution of cell adhesion motifs. Secondly, the freedom of movement of PEG chains within aqueous environments appears to allow PEGs to act as a excellent spacer groups that provides cell adhesion motifs with sufficient mobility to enhance the probability of receptor-ligand interactions.

Hubbell and co-workers have incorporated PEG into highly cross-linked polymers that can immobilize RGD or other cell adhesion motifs. Their first system of this type was a non-degradable material that incorporated PEG diacrylate and acrylic acid in trimethylolpropane triacrylate networks [44]. The acrylic acid groups provide sites for RGD coupling. This approach was extended to generate a biodegradable polymer by polymerizing poly(lactic acid) (PLA) chains from a glycerol core, functionalizing the end groups of the PLA with acryloyl chloride, and cross-linking this material with PEG-monoacrylate (Fig. 7) [45].

Griffith *et al*. have developed a new synthetic polymeric material using PEG incorporated into star molecules [16, 46]. The star molecules consist of divinyl benzene cores from which PEG chains radiate. Cross-linked gels were formed from these star molecules by electron-beam irradiation that generated carbon–carbon interchain bonds. The hydroxyl groups at the end of the PEG chains were modified to present monosaccharide ligands. These ligands caused primary rat hepatocytes to adhere via asialoglycoprotein receptors. The success of this system is based on the use of star molecular architecture combined with the hydrophilicity of the PEG chains. The star architecture generated a high density of monosaccharides and the freedom of movement of the PEG chains enabled the polymer to mimic highly branched oligosaccharide structures.

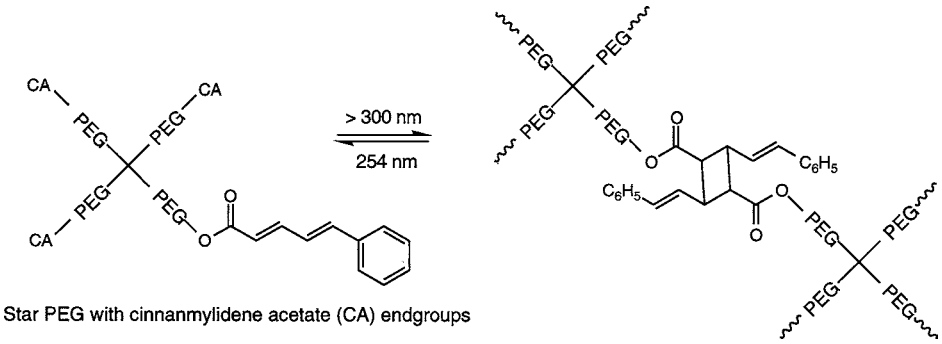

Figure 8. Photopolymerization of cinnanmylidene acetate groups on PEG star polymers.

Andreopoulos *et al.* have also employed star architecture PEG polymers to form functional hydrogel systems [47]. They modified PEG end groups with cinnanyldene acetyl chloride to form photosensitive cinnamylidene acetate end-groups. Under UV irradiation, *cis*-cinnamylidene undergoes photodimerization (Fig. 8). The photopolymerization process is reversible if the hydrogel is irradiated with light at a wavelength of 254 nm. This phenomenon offers the potential to 'de-gel' the hydrogel *in vivo*.

The above examples of end-group functionalized PEGs utilized cross-linking procedures to generate three-dimensional tissue engineering templates. An alternative approach to controlling the three-dimensional architecture of engineered tissue is to employ water soluble bifunctional PEG chains, such as RGD–PEG–RGD and YIGSR–PEG–YIGSR [48]. These bifunctional molecules aggregated fetal rat brain cells cell in solution to generate aggregates with ten times the volume of cell aggregates formed in conventional PEG solution. These cell aggregates displayed enhanced cell viability and differentiated function. This aggregation could form the basis of procedures to create three-dimensional artificial organs because the receptor mediated binding produces cell–cell interactions of the type required to facilitate tissue differentiation. In further studies, Dai and Saltzman demonstrated that their bifunctional PEGs aggregate 3T3 fibroblasts and genetically modified 1N-8A fibroblasts [49]. They found that the size of cell aggregates was dependent on the molecular weight of the PEG employed. PEG (M_w 3400) produced larger aggregates than PEG (M_w 20 000). They proposed that the higher molecular weight GRGDY–PEG–GRGDY molecules were less effective at generating large aggregates due to the increased probability of both GRGDY motifs binding to the same cell and due to increased PEG excluded volume.

4.3. Backbone incorporation

The final method of synthesizing polymer–peptide hybrids is the formation of block copolymers in which one block is the cell adhesive peptide. This strategy has been proposed by Ho and Britton [50]. They described the synthesis of the polyurethane shown in Fig. 9. This synthesis involved substituting varying amounts of ethylene diamine with a diamine terminated peptide sequence (GRGDSG). Solid phase peptide

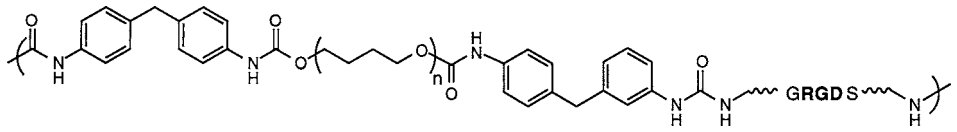

Figure 9. A poly(urethane) polymer incorporating RGD into the polymer backbone.

synthesis side-chain protecting groups were used to protect the R, D, and S residues ensuring the formation of straight-chain polymers.

One potential disadvantage of backbone incorporation as a method of polymer-protein hybrid formation is the constrained positioning of the peptide. A number of studies have indicated that RGD and other cell adhesive motifs require spacer chains to maximize interactions with integrin active centers [51]. In the case of the polyurethanes synthesized by Ho and Britton, cell adhesion studies indicated that the RGD sequence maintained its binding ability.

5. CONCLUSIONS

The interactions that occur between cells and tissue engineering templates must be tightly controlled if functional tissues are to be engineered. The demands placed on the surface properties of these templates are, therefore, highly restrictive. The most promising strategy to ensure that the surface properties of polymers generate suitable cell interactions is to copy the surface properties of the ECM whilst minimizing non-specific interactions between biomolecules and the polymer. This review has presented an overview of the synthetic methods of copying the ECM structure, and has highlighted the current approaches to the formation of polymer–peptide hybrids. However, there are clear signs that as the goals of tissue engineering increase in complexity there is a need to development novel polymer structures.

Acknowledgements

K.M.S. thanks the EPSRC for his Advanced Research Fellowship. S.M.C. would like to thank NIH for a National Research Service Award. RSL acknowledges NSF grant BCS-9202311.

REFERENCES

1. G. K. Michalopoulos and M. C. DeFrances, *Science* **276**, 60 (1997).
2. L. G. Cima and R. Langer, *Chem. Eng. Prog.* **6**, 46 (1993).
3. R. Langer and J. P. Vacanti, *Science* **260**, 920 (1993).
4. J. A. Hubbell, *Bio/technology* **13**, 565 (1995).
5. R. Langer, *Ann. Biomed. Eng.* **23**, 101 (1995).
6. D. L. Elbert and J. A. Hubbell, *Ann. Rev. Mater. Sci.* **26**, 365 (1996).
7. S. M. Moghimi and S. S. Davis, *Crit. Rev. Therapeutic Drug Carrier Systems* **11**, 31 (1994).
8. M. Delcommenne and C. H. Streuli, *J. Biol. Chem.* **270**, 26794 (1995).
9. M. Humphries, *Current Opinion Cell Biol.* **8**, 632 (1996).

10. E. Ruoslahti, *Ann. Rev. Cell. Dev. Biol.* **12**, 697 (1996).
11. M. D. Pierschbacher and E. Ruoslahti, *Nature* **309**, 30 (1984).
12. A. Varki, *Proc. Natl Acad. Sci.* **91**, 7390 (1994).
13. K. M. Yamada, *J. Biol. Chem.* **266**, 12809 (1991).
14. R. Brackenbury, *Ann. Rep. Medicinal Chem.* **25**, 235 (1990).
15. P. M. Novokoff, M. Cammer, L. Tao, H. Oda, R. J. Stockert, A. W. Wolkoff and P. Satir, *J. Cell Sci.* **109**, 21 (1996).
16. S. T. Lopina, G. Wu, E. W. Merrill and L. Griffith-Cima, *Biomaterials* **17**, 559 (1996).
17. A. S. Lea, J. D. Andrade and V. Hlady, *Colloids Surfaces A — Physicochem. Eng. Aspects* **93**, 349 (1994).
18. M. Mrksich and G. M. Whitesides, *Ann. Rev. Biophys. Biomolec. Structure* **25**, 55 (1996).
19. K. P. Walluscheck, G. Steinhoff, S. Kelm and A. Haverich, *Eur. J. Vasc. Endovasc. Surg.* **12**, 321 (1996).
20. B. D. Ratner, in: *Surface Modification of Polymers*, B. D. Ratner and D. G. Gastner (Eds), p. 1. Plenum Press, New York (1996).
21. T. Sugawara and T. Matsuda, *J. Biomed. Mater. Res.* **29**, 1047 (1995).
22. B. D. Ratner, *J. Molec. Recognition* **9**, 617 (1996).
23. A. G. A. Coombes and M. C. Meikle, *Clin. Mater.* **17**, 35 (1994).
24. J. Heller, *Advanced Drug Delivery Rev.* **10**, 163 (1993).
25. A. Park and L. Griffith-Cima, *J. Biomed. Mater. Res.* **31**, 117 (1996).
26. P. Mainil-Varlet, S. Gogolewski and P. Nieuwenhuis, *J. Mater. Sci. Mater. Med.* **7**, 713 (1996).
27. D. A. Barrera, E. Zylstra, P. T. Lansbury and R. Langer, *Macromolecules* **115**, 11010 (1993).
28. A. D. Cook, J. S. Hrkach, N. N. Gao, I. M. Johnson, U. B. Pajvani, S. M. Cannizzaro and R. Langer, *J. Biomed. Mater. Res.* **35**, 513 (1997).
29. S. P. Massia and J. A. Hubbell, *J. Cell Biol.* **114**, 1089 (1991).
30. J. S. Hrkach, J. Ou, N. Lotan and R. Langer, *Macromolecules* **28**, 4736 (1995).
31. J. Elisseeff, K. Anseth, R. Langer and J. S. Hrkach, *Macromolecules* **30**, 2182 (1997).
32. D. Tian, P. Dubois and R. Jerome, *Macromolecules* **30**, 2575 (1997).
33. S. P. Massia and J. A. Hubbell, *J. Cell Biol*. **114**, 1089 (1991) and *J. Biomed. Mater. Res.* **25**, 223 (1991).
34. W. Breuers, D. Klee, H. Hocker and C. J. Mittermayer, *Mater. Sci. Mater. Med.* **2**, 106 (1991).
35. Y. Hirano, T. Hayashi, K. Goto and A. Nakajima, *Polym. Bull.* **26**, 363 (1991).
36. K. Nakajima, Y. Hirano, T. Iida and A. Nakajima, *Polym. J.* **22**, 985 (1990).
37. Y. Ito, M. Kajihara and Y. Imanishi, *J. Biomed. Mater. Res.* **25**, 1325 (1991).
38. B. K. Brandley and R. L. Schnaar, *Anal. Biochem.* **172**, 270 (1988).
39. S. Tobe, Y. Takei, K. Kobayashi and T. Akaike, *Biochem. Biophys. Res*, *Commun.* **184**, 225 (1992).
40. O. A. Weisz and R. L. Schnarr, *J. Cell Biol.* **115**, 485 and 495 (1991).
41. H.-B. Lin, Z.-C. Zhao, C. García-Echeverrica, D. H. Rich and S. L. Cooper, *J. Biomater. Sci. Polymer Edn* **3**, 217 (1992).
42. H.-B. Lin, C. Carcía-Echeverria, S. Asakura, W. Sun, D. F. Mosher and S. L. Cooper, *Biomaterials* **13**, 905 (1992).
43. M. J. Moghaddam and T. Matsuda, *J. Polymer Sci. Part A: Polymer Chem.* **31**, 1589 (1993).
44. P. D. Drumheller and J. A. Hubbell, *Anal. Biochem.* **222**, 380 (1994).
45. D. K. Han and J. A. Hubbell, *Macromolecules* **29**, 5233 (1996).
46. L. G. Cima and S. T. Lopina, *Macromolecules* **28**, 6787 (1995).
47. F. M. Andreopoulos, C. R. Deible, M. T. Stauffer, S. G. Weber, W. R. Wagner, E. J. Beckman and A. J. Russell, *J. Am. Chem. Soc.* **118**, 6235 (1996).
48. W. G. Dai, J. Belt and W. M. Saltzman, *Bio-technology* **12**, 797 (1994).
49. W. G. Dai and W. M. Saltzman, *Biotechnol. Bioeng.* **50**, 349 (1996).
50. S. P. Ho and D. H. O. Britton, *Advanced Mater.* **6**, 130 (1994).
51. J. H. Beer, K. T. Springer and B. S. Coller, *Blood* **79**, 117 (1992).

Section 2

Polymer Modification

This page intentionally left blank

Polymers for Tissue Engineering, pp. 127–143
Molly S. Shoichet and Jeffrey A. Hubbell (Eds)

Enhancing the interaction of central nervous system neurons with poly(tetrafluoroethylene-*co*-hexafluoropropylene) via a novel surface amine-functionalization reaction followed by peptide modification

YEN W. TONG [1] and MOLLY S. SHOICHET [1,2,*]

[1] *Department of Chemical Engineering and Applied Chemistry,*
[2] *Department of Chemistry, University of Toronto, 200 College Street, Toronto, Ontario, M5S 3E5, Canada*

Received 28 October 1997; accepted 27 January 1998

Abstract—Poly(tetrafluoroethylene-*co*-hexafluoropropylene) (FEP) surfaces were modified with cell adhesive peptides, via a novel amination reaction, to enhance the neuron–substrate interaction. Amination of FEP surfaces was achieved by exposing FEP film samples to a UV-activated mercury/ammonia system for either 3 or 24 h, yielding nitrogen compositions of 3.5 and 13.2%, respectively. By labeling the nitrogen functionality with trichlorobenzaldehyde, the surface amine compositions were calculated to be 14 and 4.3% for the 3 and 24 h amination reactions, respectively. Three oligopeptide sequences derived from laminin (GYIGSR, GRGDS, and SIKVAV) were coupled to the aminated FEP (FEP$-NH_2$) surfaces and found to have almost identical surface concentrations as determined by XPS. Using radiolabeled GYIGSR, three coupling agents were compared and the concentration of peptide per surface area was calculated to be 3 and 6 fmol cm^{-2} for surfaces aminated for 3 and 24 h, respectively, regardless of the coupling agent. The interaction of embryonic hippocampal neurons with the modified surfaces was compared to that with the positive poly(L-lysine)/laminin control in terms of number and length of extended neurites. After 1 day incubation, neurite extension on the GYIGSR- and SIKVAV-coupled surfaces was similar to that on the positive control but significantly greater than that on FEP and FEP$-NH_2$ control surfaces. These peptide-coupled fluoropolymer surfaces enhance the neuron–fluoropolymer interaction, similar to that observed with PLL/laminin.

Key words: Fluoropolymer; surface modification; peptides; hippocampal neurons; regeneration; central nervous system.

*To whom correspondence should be addressed. E-mail: molly@ecf.utoronto.ca

INTRODUCTION

Following injury, mature neurons of the central nervous system (CNS) will not regenerate spontaneously, but are capable of regenerating in an environment such as that provided by the peripheral nerve [1–3] or the embryonic CNS [4]. The extracellular matrix (ECM), particularly laminin, mediates axonal elongation during development, providing contact adhesive cues and guidance to axonal growth cones. In an attempt to mimic the ECM found in the peripheral nerve (or during development), a series of laminin adhesive peptides were introduced to the surface of an amine-functionalized fluoropolymer and compared in terms of the response of primary CNS neurons.

Fluoropolymers, such as expanded poly(tetrafluoroethylene) (ePTFE), enjoy widespread use as vascular grafts [5] and dental implants [6]. Fluoropolymers are chemically inert and, consequently, few strategies exist to modify the surface and even fewer methods have been described to introduce nitrogen functionalities. For example, fluoropolymers have been modified by small molecule chemistry [7–9], plasma [10–12], or excimer laser processing [13] to introduce nitrogen functionalities, such as amine [7, 14], hydrazide [15], and nitrile [16]. Recently, it was shown that tertiary fluorocarbons could be aminated using an activated mercury/ammonia system [17]. We take advantage of this mercury/ammonia ('mercat') reaction to introduce amine functionality to the surface of poly(tetrafluoroethylene-*co*-hexafluoropropylene) (FEP) which, unlike ePTFE, has the necessary tertiary carbon for successful amination. The surface amine groups on FEP serve as reactive handles for coupling cell adhesive peptide sequences from laminin, thereby promoting cell interaction with the modified surfaces. The laminin amino acid sequences used to modify FEP-amine surfaces include Arg–Gly–Asp (RGD) [18, 19], Tyr–Iso–Gly–Ser–Arg (YIGSR) [20], and Iso–Lys–Val–Ala–Val (IKVAV) [21]. It has been suggested that the amine functionality alone may act as a cell-adhesion mimic of glycosaminoglycan-binding domains [22, 23]. Previously, FEP that was peptide-modified via a radio frequency glow discharge (RFGD) oxygen functionalization technique [24] required pre-treatment with albumin for an interaction with cell lines to be observed [25]. Herein, the dual effect of amine- and peptide-functionalized surfaces is assessed in terms of the interaction of primary hippocampal neurons in serum-free conditions.

FEP film samples were aminated by vapor phase mercury photosensitization with ammonia [17] for either 3 or 24 h, as shown in Fig. 1. The amine functionality was either quantified by an XPS labeling reaction, using 2,3,5-trichlorobenzaldehyde, or further modified with the laminin adhesive peptides, as shown in Fig. 2. The surfaces were characterized in terms of relative hydrophilicity, atomic composition and chemical functionality. The hippocampal neuron–surface interaction was evaluated qualitatively, in terms of cell adhesion and viability, and quantitatively, in terms of number and length of extended neurites per cell body.

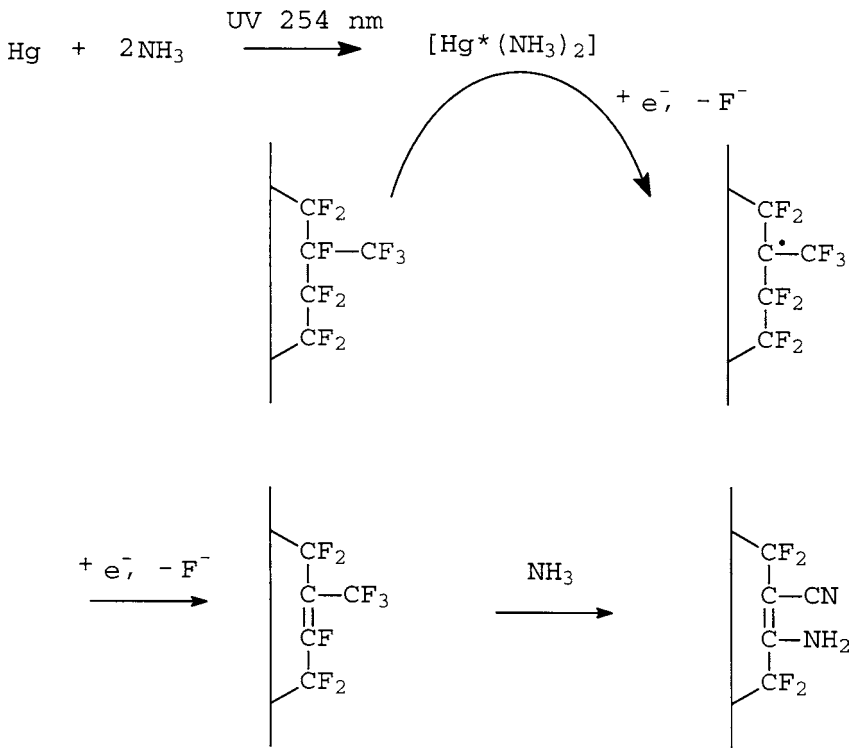

Figure 1. Proposed mechanism for the introduction of amine functional groups to the surface of poly(tetrafluoroethylene-*co*-hexafluoropropylene) (FEP) by a mercury/ammonia UV-photosensitization reaction [17].

EXPERIMENTAL

Materials

All chemicals were purchased from Aldrich (Milwaukee, WI, USA) and used as-received unless otherwise indicated. Tetrahydrofuran (THF, Fisher, Nepean, ON, Canada) was distilled from sodium benzophenone dianion and stored under nitrogen in Schlenk flasks. Hanks balanced salt solution (HBSS), neurobasal medium, B27 supplement and phosphate buffered saline (PBS) were sterile-filtered with 0.22 μm cellulose acetate filters (all from Gibco BRL, Burlington, ON, Canada). All oligopeptides were purchased from Vetrogen, ON, Canada and were used as received. FEP films (5 mm thickness, received from DuPont and cut into 2 $\times$ 2 cm samples) were Soxhlet-extracted in THF for 24 h. All water was deionized and distilled from Millipore Milli-RO 10 Plus and Milli-Q UF Plus (Bedford, MA, USA) systems and used at 18 MΩ resistance.

X-ray photoelectron spectroscopy (XPS) data were collected of film samples within 1 week of modification on a Leybold LH Max 200 using a Mg K_α X-ray source at 15 kV and 20 mA emission current. An aperture size of 13 $\times$ 7 μm

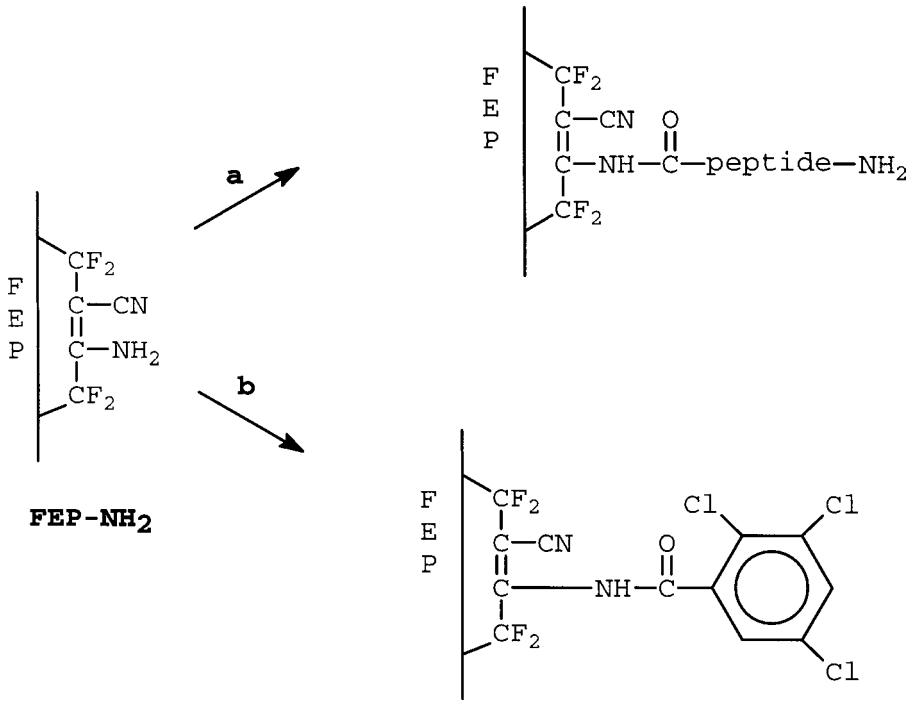

Figure 2. Amine functionalized poly(tetrafluoroethylene-*co*-hexafluoropropylene) (FEP−NH_2) film samples are either (a) coupled with cell adhesive peptides using either tresyl chloride, sulfosuccinimidyl 4-(*N*-maleimidomethyl)cyclohexane-1-carboxylate (SMCC) or *O*-(*N*-succinimidyl)-*N*,*N*,*N*′,*N*′-tetramethyluronium tetrafluoroborate (TSU); or (b) labeled with 2,3,5-trichlorobenzaldehyde.

was used to collect data at takeoff angles of 20 and 90 deg between sample and detector ($n = 3$ samples). Unless otherwise specified, all the data presented were taken at a 20-deg takeoff angle. Advancing and receding water contact angles were obtained on a Ramé−Hart NRL telescopic goniometer. Values reported represent the average and standard deviation of five measurements per sample ($n = 3$ samples). Attenuated total reflectance Fourier transform infrared (ATR-FTIR) spectra of FEP film samples were obtained on a Mattson Galaxy 5400 spectrometer using a germanium crystal (45 deg). Scanning electron microscopy (SEM) micrographs were taken on a Hitachi S4500 field emission microscope at 5 kV acceleration voltage. Iodine-125 radiolabeled tyrosine (Y) of GYIGSR was quantified using a scintillation counter (LKB Wallac 1282-802 Universal γ-Counter) with a 2 × 2 cm sodium iodide detector well of 80% efficiency. Embryonic mouse (CDI Type, Charles River, ON, Canada) hippocampal neurons, that were cultured on all surfaces, were photographed under normal light or filters for fluorescently-stained cells at 20 × magnification under an Axiovert 150 microscope.

Introduction of nitrogen functionality, FEP−NH_2

FEP−NH_2 film samples were prepared using a technique similar to that described by Burdeniuc *et al*. [17]. Briefly, a quartz Schlenk tube, containing FEP film samples and a drop of mercury, was evacuated ($P < 0.01$ mm Hg) and purged with nitrogen (three times). After the fourth evacuation, the tube was re-filled with gaseous ammonia (99.99% purity) to 1 atm pressure and the films were irradiated with eight 15-W mercury lamps (254 nm) in a UV photoreactor (Rayonet) for either 3, 24, or 72 h.

Labeling FEP−NH_2, FEP−NH−CO−$C_6H_2Cl_3$

FEP−NH−CO−$C_6H_2Cl_3$ film samples were prepared by reacting FEP−NH_2 with 20 ml of a 0.012 M 2,3,5-trichlorobenzaldehyde solution in THF for 3 h and then rinsing three times each in THF, methanol, and dichloromethane prior to drying under vacuum. Unmodified FEP film samples were treated identically, thereby, serving as controls.

Peptide coupling to functionalized FEP, FEP−NH−peptide

Three peptides (GYIGSR, SIKVAV, and GRGDS) were coupled to FEP−NH_2 film surfaces using trifluoroethanesulfonyl chloride (tresyl chloride). In addition to tresyl chloride, CGYIGSR was coupled to FEP−NH_2 film surfaces using *O*-(*N*-succinimidyl)-*N*,*N*,*N*′,*N*′-tetramethyluronium tetrafluoroborate (TSU) or sulfo-succinimidyl 4-(*N*-maleimidomethyl)cyclohexane-1-carboxylate (SMCC), as described below. Unmodified FEP film samples were treated identically and used as controls.

FEP−NH_2 film samples were immersed in a solution containing 200 μl of tresyl chloride in 1 ml pyridine/19 ml THF for 20 min at RT in a Schlenk flask under N_2. Film samples were then added to a beaker containing 10 ml of a 0.2 M pH 10 sodium carbonate-buffered solution and 0.1 μg ml^{-1} of peptide (i.e. GYIGSR, GRGDS, or SIKVAV) for 24 h [26]. The film samples were rinsed five times each with the buffer solution, dilute hydrochloric acid, water, and THF prior to drying under vacuum.

FEP−NH_2 film samples were immersed in 20 ml of dimethyl formamide (DMF) containing 1.3 mM TSU and 1.3 mM diisopropylethylamine for 4 h at RT in a Schlenk flask under N_2. Film samples were then added to a beaker containing 10 ml of a 0.2 M pH 10 sodium carbonate-buffered solution containing 0.1 μg ml^{-1} of GYIGSR for 24 h [27]. The film samples were rinsed five times each with the buffer solution, water and THF prior to drying under vacuum.

FEP−NH_2 were immersed in a breaker containing 30 ml of a 0.2 M sodium bicarbonate-buffered solution at pH 10 and containing 2 mg of SMCC. After 4 h, the activated film samples were immersed in a 0.2 M pH 10 buffered sodium bicarbonate solution containing 0.1 μg ml^{-1} of cysteine-terminated CGYIGSR for 24 h at RT [28]. The film samples were rinsed five times each with the buffer solution, dilute hydrochloric acid, water and THF and then dried under vacuum.

Radioactive labeling of tyrosine

Tyrosine (Y) of GYIGSR was labeled as previously described [27] with radioactive iodine ^{125}I. Briefly, 2 mg of CGYIGSR was dissolved in 5 ml of a pH 11 buffer containing 20 mM sodium phosphate and 0.15 M sodium chloride and then reacted with 1 mCi of carrier-free Na^{125}I (ICN, Costa Mesa, CA, USA) in the presence of Iodobeads (Pierce, Rockford, IL, USA) for 15 min. Free iodide was removed by successive passes through columns packed with anion-exchange resin (Dowex 1-X8, Aldrich). The labeled peptides were coupled to FEP$-NH_2$ surfaces as described above. The FEP$-$NH$-$peptide films were also rinsed with 10 mM sodium iodide to desorb any trace ^{125}I before counting by scintillation.

Hippocampal neuron–fluoropolymer interaction

FEP$-$NH$-$peptide films and controls (FEP and FEP$-NH_2$) were immersed in 70% ethanol for 1 h and then rinsed four times with sterile distilled water before air-drying. Positive control surfaces were prepared by coating glass coverslips with 1 ml of an aqueous 1 mg ml^{-1} solution of poly(L-lysine) (PLL, Sigma, M_w = 37 000 g mol^{-1}) for 24 h at 37°C and then with 10 μl of a 1 mg ml^{-1} aqueous solution of laminin (Gibco) for 2 h at 37°C. PLL/laminin-coated glass coverslips were rinsed with sterile, distilled water and then air-dried. Embryonic day 18 (E18) mouse hippocampal neurons were isolated, as previously described [29], by dissociation with papain (Worthington Biochemical Corporation) and DNase (Sigma) for 30 min and mechanical trituration in calcium-free HBSS. 1 ml of a hippocampal neuron suspension was then plated at 1×10^6 cells ml^{-1} (or 2.5×10^5 cells cm^{-2}) in serum-free medium (SFM) on each film sample. The SFM consisted of 2 ml B27 supplement, 100 mg chicken egg albumin (Sigma), 10 mg pyruvic acid (Sigma), 1 ml glutamine (Sigma), and 1 ml penicillin/streptomycin (Gibco, 10 000 U ml^{-1}and 10 000 μg ml^{-1}, respectively) in 100 ml of neurobasal medium. The anti-mitotic agent, fluorodeoxyuridine/uridine (Sigma), was added after 12 h. The cells were incubated at 37°C in 5% CO_2 for 4 days. The cell–material interaction was assessed after 1 and 4 days in terms of the number and relative length of extended neurites per cell body (n = 50 cells). Phase contrast micrographs were taken after 1 and 4 days. To assess cell viability at 4 days, samples were incubated for 30 min at 37°C with 150 μl of stock viability assay solution (20 μl ethidium bromide and 5 μl calcein AM in 10 ml PBS, Molecular Probes, Eugene, OR, USA) and examined under fluorescent filters of the optical microscope.

Statistics

Triplicate experimental data were subjected to statistical analysis using SAS (SAS Institute Inc., Cary, NC, USA) on a SGI Challenge L Unix-based computer system. One way ANOVA analysis assuming a constant variance and a 95% confidence interval was used to determine statistical differences of various data sets. Results are

reported as the mean ± the standard error of the mean and statistically significantly different data sets are labeled with different letters.

RESULTS AND DISCUSSION

Introduction of nitrogen functionality, FEP−NH_2

The exposure of FEP film samples to mercury-activated ammonia (i.e. mercat reaction) resulted in the introduction of amine functional groups (FEP−NH_2) as determined by XPS and contact angle. The surface composition of the top 10–40 Å was measured at a takeoff angle of 20 deg while that of the top 40–100 Å was measured at a takeoff angle of 90 deg. In Table 1, the 20-deg takeoff angle data is summarized. After a 3 h exposure, amination was evidenced by a decreased contact angle (84/31 deg) relative to FEP (120/101 deg) and by the presence of nitrogen in the XPS spectrum ($C_{46.2}F_{46.4}O_{3.9}N_{3.5}$). The increased hydrophilicity of FEP−NH_2 relative to FEP is reflected by the lower contact angles and the XPS composition having a higher nitrogen and oxygen and lower fluorine concentrations. After a 24 h exposure, the contact angle was further decreased (27/22 deg) and the nitrogen concentration further increased ($C_{72.5}F_{3.7}O_{10.6}N_{13.2}$), relative to the 3 h exposure, indicating that the extent of amination can be controlled by exposure time. The reaction was self-limiting as amination did not increase at exposure times greater than 24 h. For example, after 72 h of exposure to the mercat reaction, aminated FEP film samples had similar properties to those aminated for only 24 h. After the 72 h exposure, the water contact angles were 31/20 deg and the atomic composition at a 20-deg takeoff angle was $C_{71.4}F_{4.5}O_{11.1}N_{13.0}$. Scanning electron micrographs of FEP, FEP−NH_2-*24h* and FEP−NH_2-*72h* were identical and smooth, having no topographical features and indicating that surface chemistry was modified independently from surface morphology. Due to the similarities observed between FEP−NH_2-*24h* and FEP−NH_2-*72h*, further studies were conducted on FEP aminated for 3 and 24 h only.

In order to determine the surface selectivity of the amination reaction, angle resolved XPS was performed by comparing the 20- and 90-deg takeoff angle data. For a 3 h exposure, FEP−NH_2-*3h* film samples had more nitrogen and less carbon and fluorine at a 20-deg takeoff angle ($C_{46.2}F_{46.4}O_{3.9}N_{3.5}$) than that at a 90-deg takeoff angle ($C_{41.4}F_{53.3}O_{3.1}N_{2.3}$), indicating the surface selectivity of this reaction. For a 24 h exposure, the FEP−NH_2-*24h* film samples had an equivalent amount of fluorine and less nitrogen at the 20-deg takeoff angle ($C_{72.5}F_{3.7}O_{10.6}N_{13.2}$) than that at the 90-deg takeoff angle ($C_{65.2}F_{3.7}O_{10.8}N_{20.4}$), indicating that reactive ammonia penetrated below the FEP surface. Up to 24 h, the longer the exposure time, the deeper the modification. The increased nitrogen concentration at greater depths for FEP−NH_2-*24h* reflects the solubility of ammonia in FEP. By comparing the 20- and 90-deg takeoff angle XPS data, it is clear that the surface of FEP−NH_2-*24h* is enriched with carbon and depleted in nitrogen which may result

Table 1.
Average contact angle and XPS data of surface modified FEP film samples ($n = 3$ samples). XPS data were taken at a takeoff angle of 20 deg between the sample and detector

Film type	Contact angle (θ_A/θ_R)	XPS atomic composition (%)	Contact angle (θ_A/θ_R)	XPS atomic composition (%)
Clean FEP	$120 \pm 2/101 \pm 2$	$C_{31.1}F_{68.9}$	$120 \pm 2/101 \pm 2$	$C_{31.1}F_{68.9}$
	Amination for 3 h		Amination for 24 h	
FEP—NH_2	$84 \pm 2/31 \pm 2$	$C_{46.2}F_{46.4}O_{3.9}N_{3.5}$	$27 \pm 2/22 \pm 1$	$C_{72.5}F_{3.7}O_{10.6}N_{13.2}$
FEP—NH—CO—$C_6H_2Cl_3$	$86 \pm 2/46 \pm 2$	$C_{42.7}F_{49.0}O_{5.2}N_{2.3}Cl_{0.9}$	$66 \pm 3/20 \pm 1$	$C_{62.8}F_{13.2}O_{12.8}N_{10.0}Cl_{1.3}$
FEP + $C_6H_2Cl_3$—CHO (control for labeling)	$119 \pm 2/101 \pm 2$	$C_{32}F_{68}$	$119 \pm 2/101 \pm 2$	$C_{32}F_{68}$
FEP—NH—GYIGSR	$74 \pm 4/21 \pm 1$	$C_{51.8}F_{36.6}O_{7.7}N_{3.9}$	$56 \pm 2/20 \pm 3$	$C_{70.0}F_{6.5}O_{14.0}N_{9.5}$
FEP—NH—GRGDS	$77 \pm 3/22 \pm 2$	$C_{53.3}F_{35.8}O_{7.2}N_{3.7}$	$59 \pm 2/14 \pm 1$	$C_{71.8}F_{4.2}O_{14.7}N_{9.3}$
FEP—NH—SIKVAV	$71 \pm 1/18 \pm 2$	$C_{52.3}F_{36.8}O_{7.0}N_{3.9}$	$67 \pm 3/13 \pm 1$	$C_{69.7}F_{9.5}O_{12.2}N_{8.6}$

from surface rearrangement of the functional groups to minimize surface free energy. While FEP−NH_2-*24h* films were modified to a greater depth of modification than FEP−NH_2-*3h* films, no peaks, other than those ascribed to unmodified FEP, were evident in the ATR-FTIR spectra of all film samples. This indicates that the mercat reaction was limited to depths of modification significantly less than 1 μm (the sampling depth of ATR-FTIR).

The presence of surface oxygen functionality, although not accounted for by the mechanism in Fig. 1, likely results from air-oxidation of either or both the carbon–carbon double bonds or the nitrile group.

Labeling FEP−NH_2, FEP−NH−CO−$C_6H_2Cl_3$

The labeling reaction of FEP−NH_2 with trichlorobenzaldehyde (FEP−NH−CO−$C_6H_2Cl_3$) was used to estimate the concentration of surface primary and secondary amines that would be available for peptide modification. As shown in Table 1, relative to FEP−NH_2 (3 or 24 h), FEP−NH−CO−$C_6H_2Cl_3$ surfaces were less hydrophilic, as expected, due to the phenyl ring. FEP−NH-*3h*−CO−$C_6H_2Cl_3$ surfaces had an increased receding contact angle whereas FEP−NH-*24h*−CO−$C_6H_2Cl_3$ surfaces had an increased advancing contact angle relative to FEP−NH_2-*3h* or FEP−NH_2-*24h*, respectively. The increased hysteresis between advancing and receding contact angles of FEP−NH_2-*24h*−CO−$C_6H_2Cl_3$ film surfaces reflects their chemical heterogeneity relative to that of FEP−NH_2-*3h*−CO−$C_6H_2Cl_3$ films. Since the control reaction of FEP with trichlorobenzaldehyde resulted in FEP (cf. Table 1 for XPS and contact angle data), we can assume that all of the chlorine results from the reaction of trichlorobenzaldehyde and primary and secondary amine groups of FEP−NH_2. Assuming 100% yield for the amine labeling reaction with trichlorobenzaldehyde, the XPS atomic chlorine to nitrogen ratios can be used to calculate the minimum percentage of nitrogen present as primary and secondary amines. For example, for FEP−NH_2-*3h*−CO−$C_6H_2Cl_3$ films, the surface chlorine concentration was 0.9% indicating that 0.3% of the total 2.3% surface nitrogen concentration exists as primary or secondary amines. Thus 14% of the nitrogen functionality of FEP−NH_2-*3h* is available for further modification with peptides. By a similar analysis, FEP−NH_2-*24h*−CO−$C_6H_2Cl_3$ films had 1.3% chlorine and thus 0.43% of the total 10.0% (or 4.3%) surface nitrogen was available for further modification with laminin adhesive peptide sequences. The greater hysteresis in the contact angle data for FEP−NH_2-*24h*−CO−$C_6H_2Cl_3$ is consistent with the greater chemical heterogeneity observed. The relative number of surface amine groups to FEP repeat units was determined from both the 20-deg XPS fluorine to nitrogen data and the calculated amine concentrations. For FEP−NH_2-*3h*, there was 1 amine group per 23 FEP repeat units and for FEP−NH_2-*24h*, there was 1 amine group per 1.6 FEP repeat units.

Since a low percentage of nitrogen functionality was available for further chemical modification with peptides, methods will be developed to increase both their reactivity and the percent of surface amine groups. For example, based on the

mechanism in Fig. 1, the amine groups will be more reactive after reducing the carbon–carbon double bonds to single bonds. To further increase the number of amine groups, the nitrile group will be reduced to primary amine.

Peptide coupling to functionalized FEP, FEP—NH—peptide

FEP—NH_2 surfaces were modified with three cell adhesive peptides (GYIGSR, GRGDS, SIKVAV) using tresyl activation. For the FEP—NH_2-*3h* films, the contact angles decreased after peptide modification reflecting the increased hydrophilic nature of the peptide group on FEP—NH—peptide relative to FEP—NH_2-*3h* (cf. Table 1). The XPS data confirm the contact angle data: FEP—NH—peptide surfaces have depleted fluorine and increased carbon, oxygen and nitrogen. For FEP—NH_2-*24h*, the advancing contact angles increased while the receding contact angles decreased after peptide modification. The XPS data indicate that similar amounts of the three peptides GYIGSR, GRGDS and SIKVAV were introduced to the FEP—NH_2 film surfaces for each amination time (i.e. 3 and 24 h); however, a greater concentration of peptides were introduced to FEP—NH_2-*24h* than to FEP—NH_2-*3h*. The increased hysteresis observed for FEP—NH_2-*24h*—peptide indicates a chemically heterogeneous surface and likely less peptide per nitrogen than that observed for FEP—NH_2-*3h*—peptide as confirmed by the labeling reaction. The XPS data confirm this observation with a surface enrichment of oxygen and fluorine after peptide modification for FEP—NH_2-*24h*. The increased fluorine concentration may reflect surface rearrangement, facilitated by the use of THF that slightly swells FEP.

To determine which of the three coupling agents, tresyl chloride, SMCC and TSU, could yield the greatest amount of peptide per surface area, ^{125}I radiolabeled tyro-

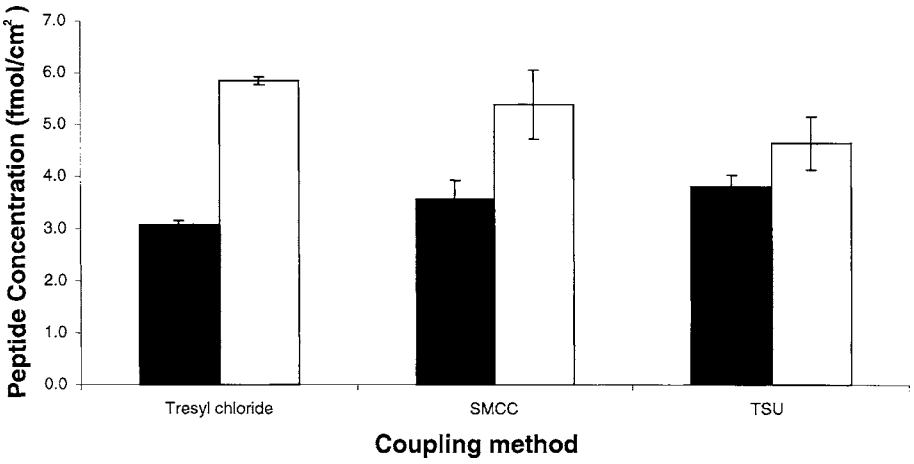

Figure 3. The surface peptide concentrations of FEP—NH—GYIGSR films were determined by counting the γ-radiation of ^{125}I radiolabeled tyrosine (Y) of GYIGSR. The radiolabeled GYIGSR peptide was coupled to FEP—NH_2 using tresyl chloride, SMCC or TSU. The mean with the respective standard error of the mean are plotted for films aminated for 3 (■) and 24 h (□).

sine (Y) of CGYIGSR was coupled to FEP—NH_2 surfaces. As shown in Fig. 3, the amount of peptide that was introduced to FEP—NH_2-*24h* was greater than that introduced to FEP—NH_2-*3h* for all coupling reagents; however, the differences between the three reagents were statistically indistinguishable within 95% confidence. Given the low amount of peptide introduced, the lack of differentiation among the coupling reagents may reflect the low surface concentration of reactive amine groups.

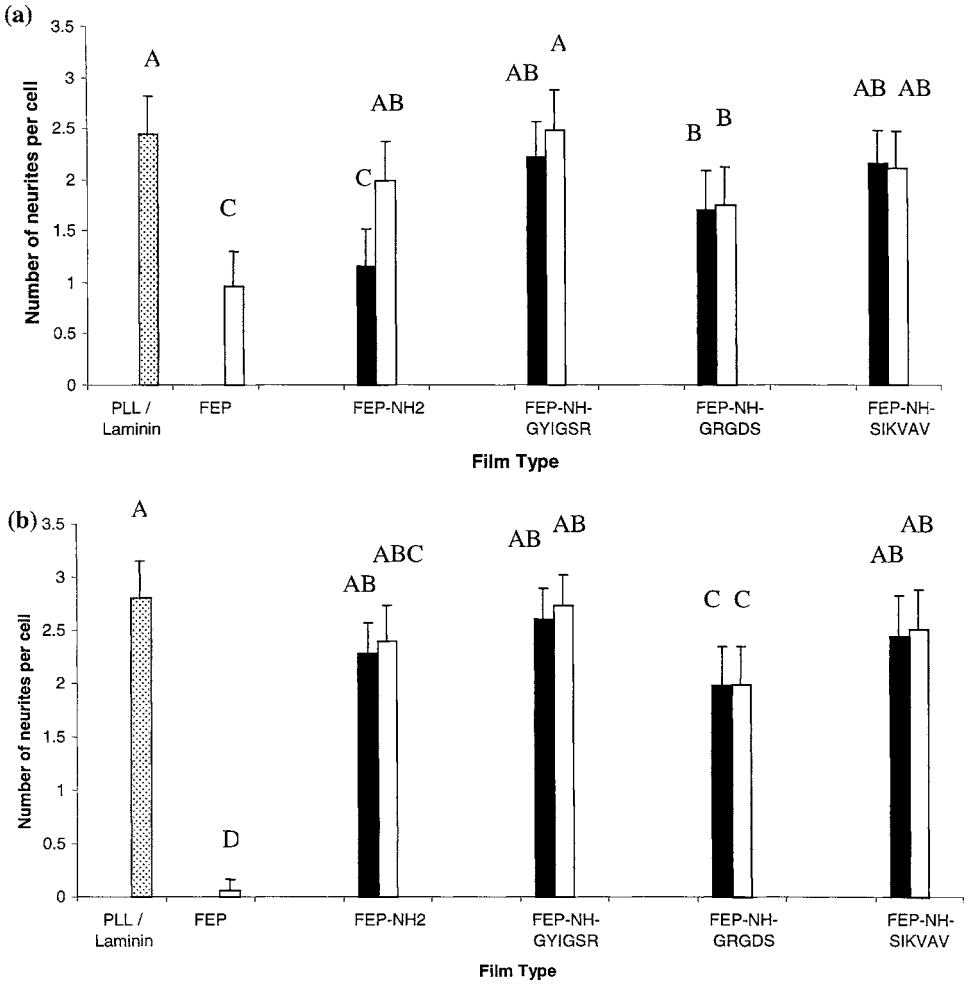

Figure 4. The number of neurites extending per cell (averaged over 50 cells) of embryonic day 18 (E18) hippocampal neurons cultured in serum-free medium on PLL/laminin-coated glass coverslips, FEP and FEP—NH—peptide (peptide = GYIGSR, GRGDS, SIKVAV) surfaces after (a) 1 and (b) 4 days of plating. Surfaces were prepared from FEP—NH_2 for 3 (■) vs 24 h (□). The mean numbers of neurites per cell body with the standard error of the mean are reported for $n = 50$ cells, repeated twice. Data sets with a similar letter are statistically the same whereas those with different letters are statistically different from FEP—NH_2 controls of the same conditions (the data were calculated using one one way ANOVA with $p < 0.05$).

Hippocampal neuron–fluoropolymer interaction

The peptide-functionalized surfaces were compared, in terms of the response of hippocampal neurons, to FEP−NH_2, FEP and a positive control, i.e. glass modified with PLL/laminin. The number of neurites extending per cell body (averaged over 50 cells) is summarized in Fig. 4 after 1 and 4 days of plating. In Fig. 4, statistical differences in the data are designated with different letters. The biggest differences between the surfaces were observed after 1 day of plating. The response observed, from greatest to least, on the FEP−NH_2-*3h* surfaces was FEP−NH-*3h*−GYIGSR ∼ PLL/laminin ∼ FEP−NH-*3h*−SIKVAV > FEP−NH-*3h*−GRGDS > FEP−NH_2-*3h* ∼ FEP. For FEP−NH_2-*24h*, the or-

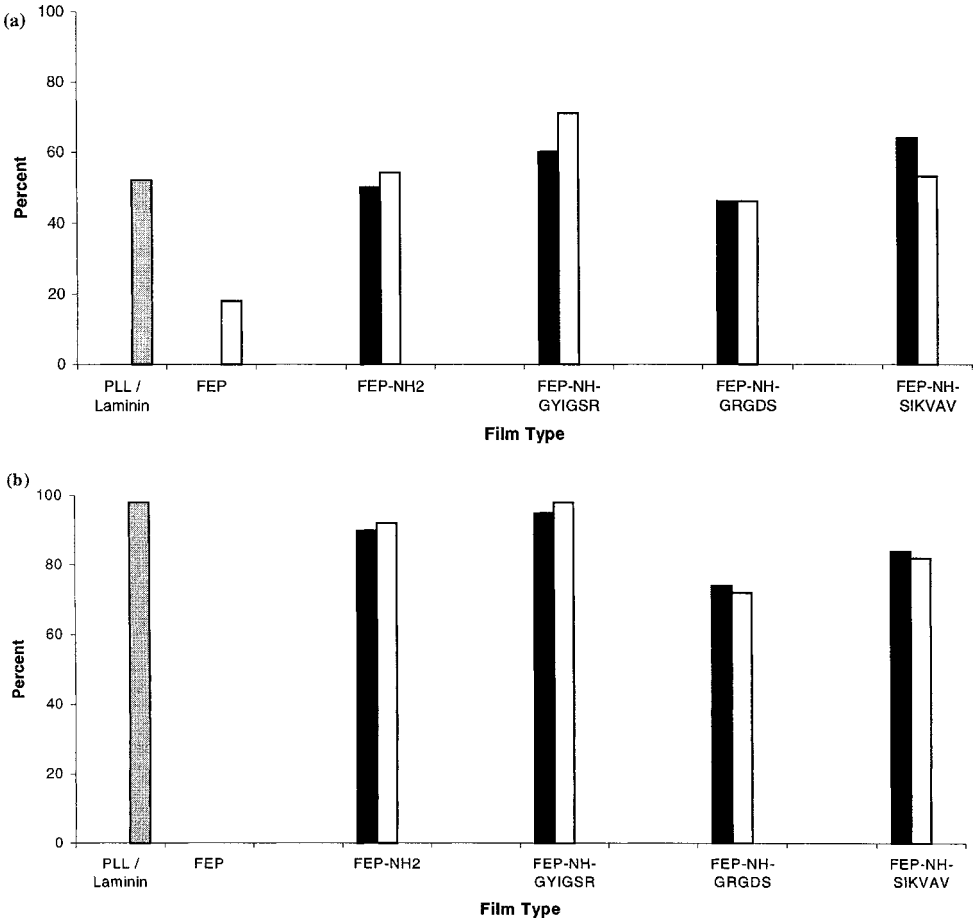

Figure 5. The percentage of cells ($n = 50$ cells, for two film samples) with neurites longer than one cell body length, of embryonic day 18 (E18) hippocampal neurons cultured in serum-free medium, were compared on PLL/laminin-coated glass coverslips, FEP and FEP−NH−peptide (peptide = GYIGSR, GRGDS, SIKVAV) surfaces after (a) 1 and (b) 4 days of plating. Films were aminated for either 3 h (■) or 24 h (□).

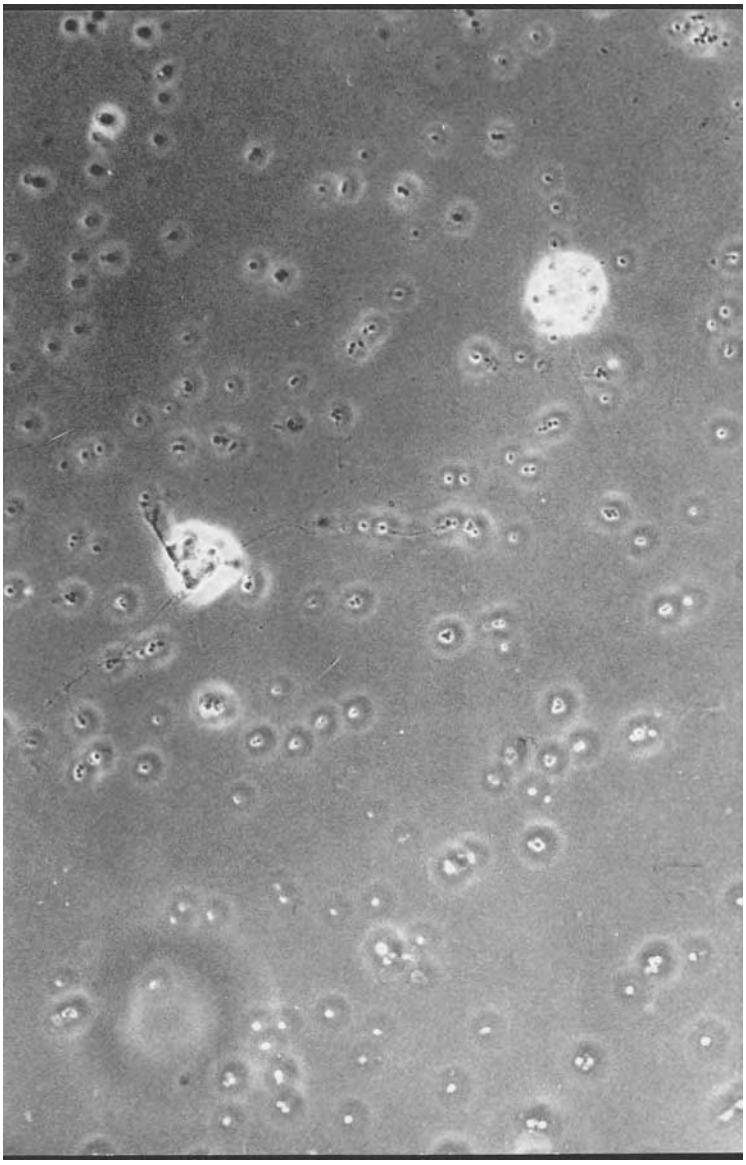

(a)

Figure 6. Phase contrast micrographs of hippocampal neurons plated on different functionalized surfaces after 4 days of incubation demonstrate the enhanced interaction after peptide modification: (a) unmodified FEP, (b) FEP−NH_2-*3h*, (c) FEP−NH−GYIGSR.

der was FEP−NH-*24h*−GYIGSR ∼ PLL/laminin > FEP−NH-*24h*−SIKVAV ∼ FEP−NH-*24h*−GRGDS ∼ FEP−NH_2-*24h* > FEP. After 4 days of plating, the differences among the peptide-functionalized surfaces, FEP−NH_2 and PLL/laminin were difficult to elucidate; however, no cells were supported on FEP. While there was no statistical difference between PLL/laminin controls and GYIGSR- and

(b)

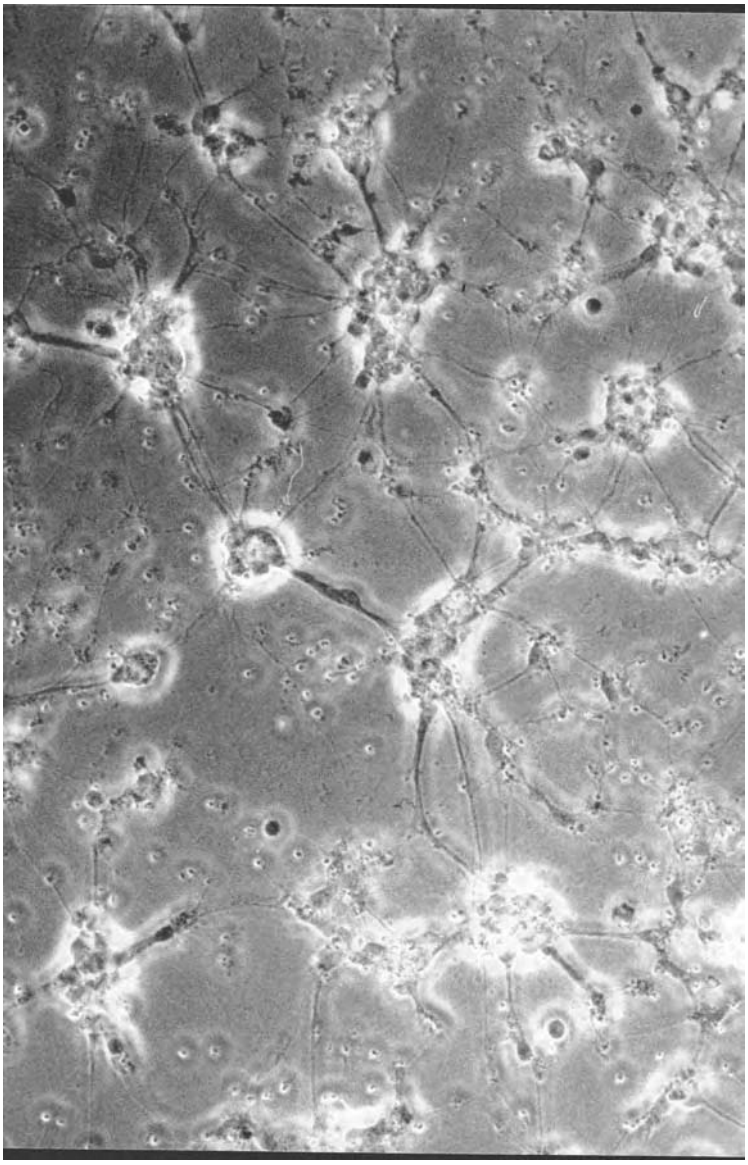

Figure 6. (Continued).

SIKVAV-functionalized surfaces, PLL/laminin supported statistically more axonal interaction than both the GRGDS- and NH_2-functionalized FEP surfaces.

In order to further gauge the cell-material interaction, the relative length of neurites on the modified surfaces was compared by calculating the percentage of cells having one or more neurites greater than the cell body length, as shown in Fig. 5. After 1 day of plating, the response was greatest on FEP—NH—GYIGSR and least on FEP, with the other surfaces showing similar percentages of cells having

(c)

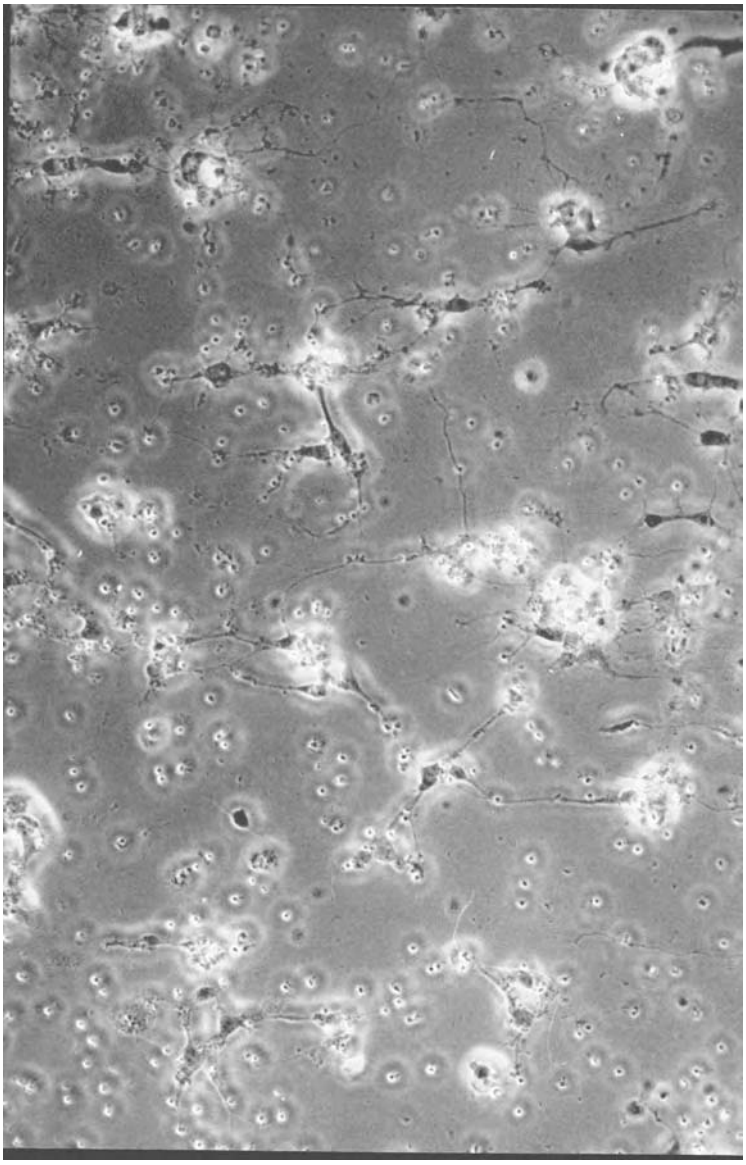

Figure 6. (Continued).

long neurites between these two extremes. After 4 days of plating, all peptide-modified surfaces had similar percentages, with FEP—GRGDS having the lowest response of the peptide surfaces. By using both number and length of neurites as indicators of the cellular response to the modified surfaces, it is clear that, of the three peptides studied, the GYIGSR-functionalized surfaces are the most conducive to cellular interaction while the GRGDS-functionalized surfaces are the least conducive. These results are consistent with other results we have obtained

using different surface chemistry to achieve peptide immobilization [30]. The phase contrast micrographs, included in Fig. 6, represent the range of responses observed between the hippocampal neurons and the FEP surfaces. FEP supported neither cell adhesion nor neurite outgrowth (cf. Fig. 6a). FEP−NH_2 supported both cell adhesion and neurite outgrowth, yet the large cell clusters indicate that the neurons prefer to grow on each other than on the surface (cf. Fig. 6b). FEP−NH−GYIGSR supported both cell adhesion and neurite outgrowth; the enhanced interaction of neurons with this surface is represented by the distribution of cells (cf. Fig. 6c).

CONCLUSIONS

FEP films were surface-modified with amine functional groups after exposure to the mercat reaction for 3 and 24 h, resulting in 14 and 4.3% of reactive amines, respectively. Despite the lower percentage of nitrogen present as amine groups for the modification at 24 h, more nitrogen was present on FEP−NH_2-*24h* than on FEP−NH_2-*3h*. Coupling the oligopeptide CGYIGSR with FEP−NH_2-*3h* and -*24h* surfaces resulted in surface peptide concentrations of 3 and 6 fmol cm^{-2}, respectively, using tresyl chloride, SMCC or TSU. The hippocampal neuron-material interaction was compared on the following surfaces: nitrogen-functionalized FEP, peptide-coupled films, including GYIGSR-, SIKVAV- and GRGDS-functionalized FEP, unmodified FEP (control) and PLL/laminin-coated glass coverslips (positive control). From the neurite extension and neurite length results, we conclude that the peptide-modified surfaces, and in particular FEP−NH−GYIGSR, enhanced the hippocampal neuron interaction and best mimicked the effects of PLL/laminin surfaces *in vitro*. These surface modification methods may impact strategies used to enhance nerve regeneration.

Acknowledgement

The authors are grateful to the Natural Sciences and Engineering Research Council of Canada and the University of Toronto for financial support. The authors thank Professor Peter Pennefather for supplying the hippocampal neurons and for related discussions.

REFERENCES

1. S. David and A. J. Aguayo, *Science* **214**, 931 (1981).
2. H. Cheng, Y. Cao and L. Olson, *Science* **273**, 510 (1996).
3. R. P. Bunge, *J. Neurol.* **242**, S19 (1994).
4. Y. Iwashita, S. Kawaguchi and M. Murata, *Nature* **366**, 167 (1994).
5. B. Boyce, in: *Biologic and Synthetic Vascular Prostheses*, J. C. Stanley (Ed.), p. 553. Grune & Stratton, New York (1982).
6. B. D. Ratner, *J. Biomed. Mater. Res.* **27**, 837 (1993).

7. C. Costello and T. J. McCarthy, *Macromolecules* **17**, 2940 (1984).
8. M. S. Shoichet and T. J. McCarthy, *Macromolecules* **24**, 982 (1991).
9. I. Noh, K. Chittur, S. L. Goodman and J. A. Hubbell, *J. Pol. Sci. A: Polym. Chem.* **35**, 1499 (1997).
10. A. Dekker, K. Reitsma, T. Beugeling, A. Bantjes, J. Feijen and W. G. Van Aken, *Biomaterials* **12**, 130 (1991).
11. J. P. Badey, E. Urbaczewski-Espuche, Y. Jugnet, D. Sage, T. M. Duc and B. Chabert, *Polymer* **35**, 2472 (1994).
12. T. G. Vargo, J. A. Gardella, Jr., A. E. Meyer and R. E. Baier, *J. Pol. Sci.: Part A* **29**, 555 (1991).
13. N. Ichinose and S. Kawanishi, *Macromolecules* **29**, 4155 (1996).
14. H. Niino and A. Yabe, *Appl. Surf. Sci.* **96–98**, 550 (1996).
15. R. C. Bening and T. J. McCarthy, *Macromolecules* **23**, 2648 (1990).
16. J. V. Brennan and T. J. McCarthy, *Polym. Prep.* **29**, 338 (1987).
17. J. Burdeniuc, W. Chupka and R. H. Crabtree, *J. Am. Chem. Soc.* **117**, 10 119 (1995).
18. M. D. Pierschbacher and E. Ruoslahti, *Nature* **309**, 30 (1984).
19. D. S. Grant, K.-I. Tashiro, B. Segui-Real, Y. Yamada, G. R. Martin and H. K. Kleinman, *Cell* **58**, 933 (1989).
20. J. Graft, R. C. Ogle, F. A. Robey, M. Sasaki, G. R. Martin, Y. Yamada and H. K. Kleinman, *Biochemistry* **26**, 6896 (1987).
21. M. Jucker, H. K. Kleinman and D. K. Ingram, *J. Neurosci. Res.* **28**, 507 (1991).
22. S. P. Massia and J. A. Hubbell, *J. Biol. Chem.* **267**, 10133 (1992).
23. P. E. Hockberger, H.-Y. Tseng and J. A. Connor, *J. Neurosci.* **7**, 1370 (1987).
24. T. G. Vargo, E. J. Bekos, Y. S. Kim, J. P. Ranieri, R. Bellamkonda, P. Aebischer, P. E. Margevich, P. M. Thompson, F. V. Bright and J. A. Gardella, Jr., *J. Biomed. Mater. Res.* **29**, 767 (1995).
25. J. P. Ranieri, R. Bellamkonda, E. J. Bekos, T. G. Vargo, J. A. Gardella, Jr. and P. Aebischer, *J. Biomed. Mater. Res.* **29**, 779 (1995).
26. K. Nilsson and K. Mosbach, *Biochem. Biophys. Res. Commun.* **102**, 449 (1981).
27. P. D. Drumheller and J. A. Hubbell, *Anal. Biochem.* **222**, 380 (1994).
28. G. Mattson, E. Conklin, S. Desai, G. Nielander, M. D. Savage and S. Morgensen, *Molecular Biol. Rep.* **17**, 167 (1993).
29. G. J. Brewer, J. R. Torriceilli, E. K. Evege and P. J. Price, *J. Neurosci. Res.* **35**, 1 (1993).
30. Y. W. Tong and M. S. Shoichet, *J. Biomed. Mater. Res.* (1998) (accepted).

This page intentionally left blank

Polymers for Tissue Engineering, pp. 145–164
Molly S. Shoichet and Jeffrey A. Hubbell (Eds)

Chemical modification and photograft polymerization upon expanded poly(tetrafluoroethylene)

INSUP NOH,[1,2] STEVEN L. GOODMAN[3] and JEFFREY A. HUBBELL[2,*]

[1]*Department of Chemical Engineering, University of Texas, Austin, TX 78712, USA*
[2]*Division of Chemistry and Chemical Engineering, California Institute of Technology, Pasadena, CA 91125, USA*
[3]*Center for Biomaterials, University of Connecticut Health Center Farmington, CT 06030, USA*

Received 16 June 1997; accepted 21 October 1997

Abstract—Poly(tetrafluoroethylene) (PTFE) films were surface-modified by employing a reaction solution of benzophenone and sodium hydride in anhydrous dimethylformamide at a temperature of 150°C for 12 h. Electron spectroscopy for chemical analysis (ESCA) showed defluorination, oxygen incorporation, and extensive unsaturation within the treated PTFE surfaces. The suitability of these reduced PTFE films as substrates for graft polymerization was initially assessed via photograft polymerization of the sodium salt of styrenesulfonic acid (SS-Na), which permitted unequivocal surface analysis by the introduction of a new atom, as well as poly(ethylene glycol) monoacrylate (PEG-Ac). All photograft polymerization was performed employing ultraviolet irradiation with 2,2-dimethoxy-2-phenylacetophenone as an initiator. Photograft polymerization of SS-Na was verified by further reduction of fluorine atomic content and the appearance of new sulfur and sodium atomic peaks on ESCA survey spectra, and that of PEG-Ac was verified by further reduction of fluorine atomic content and increase of atomic percent ratio of O/C from ESCA survey spectra as well as appearance of a new ester peak on high resolution ESCA C 1*s* spectra. Dynamic water contact angles on reduced and PEG-Ac photograft polymerized films were measured and showed that the PTFE film surface became more hydrophilic after reduction (from 120 to 89 deg) and the reduced film became more hydrophilic after photograft polymerization with PEG-Ac (from 89 to 36 deg).

Modification of the complete surface of expanded PTFE (ePTFE), i.e. of the lumenal, outside and pore surfaces, was performed by employing the reaction described above, except at 105°C for 1 day, followed by photograft polymerization of PEG-Ac. ESCA was performed on the superficial surfaces (i.e. the lumen and exterior) as well as on cross-sections of the ePTFE to permit analysis of the pore surfaces. This analysis showed that both the initial surface reduction and the subsequent photograft polymerization were successful as indicated from F/C and O/C atomic percent ratios from ESCA survey spectra, from overall peak shapes of high resolution ESCA C 1*s* spectra and from generation of new ester peaks on high resolution ESCA C 1*s* spectra of ePTFE graft polymerized with PEG-Ac, which demonstrated an O/C atomic percent ratio close to that of PEG-Ac homopolymer. Low voltage scanning electron microscopy confirmed minimal morphological damage to the ePTFE microstructure after reduction and graft polymerization. The approach explored thus provides a means for modulation of biological interactions at ePTFE

*To whom correspondence should be addressed at Institute for Biomedical Engineering, Mousson-strasse 18, Swiss Federal Institute of Technology and University of Zürich, CH-8044 Zürich, Switzerland. E-mail: hubbell@biomed.mat.ethz.ch

surfaces with only minimal modification of material morphology, with some surface texture appearing on a length scale of 50–100 nm.

Key words: Pore surface modification; ePTFE; benzophenone; sodium hydride; photograft polymerization; PEG monoacrylate; DCA; ESCA; LV-SEM.

INTRODUCTION

Expanded poly(tetrafluoroethylene) (ePTFE) has many applications in medical devices. In the use of ePTFE in vascular grafts, large caliber vascular grafts (> 5 mm) with high flow rate and low resistance have high patency [1], but small caliber vascular grafts (< 5 mm) in more peripheral locations have met with less success [1, 2]. Complete coverage of endothelial cells (ECs) upon the lumenal surface would presumably improve graft performance by limiting thrombosis and intimal thickening. Morphological studies on explanted vascular grafts, however, showed that EC coverage by healing is typically limited to approximately 10 mm from the anastomoses while the central portion of grafts remained uncovered [3, 4], even though ECs have been shown to grow well throughout the entire graft length in animal models [5, 6]. Instead of complete EC overgrowth, a fibrin coagulum typically occupies the central portion of the graft, leading to ongoing platelet activation and thrombosis [7, 8]. Adherent platelets may release a variety of growth factors, which may then induce excessive migration or proliferation of smooth muscle cells, leading to intimal thickening and graft failure [8]. In an attempt to preform a monolayer coverage of ECs on ePTFE surfaces, seeding of ECs was performed after adsorption of adhesion proteins, e.g. fibronectin, or precloting with whole blood before implantation [9–11]. This approach, although promising, has as yet led to less success than hoped, partly due to EC loss after seeding and to inability to control EC function.

It has been suggested by one of us [12] and others [13, 14] to selectively promote the attachment and proliferation of only specific cells via grafting of synthetic oligopeptides that bind to adhesion receptors on the surface of targeted cells, such as RGD [15], YIGSR [16, 17], or REDV [18–20]. By selecting adhesion ligands to target the cells that are favorable in a healing response, but which do not permit the adhesion of particularly undesirable cell types, it may be possible to guide the graft integration response. For example, the sequence REDV has been shown to support EC attachment but not blood platelet attachment. These chemical signals for cell adhesion have been incorporated by a variety of methods, such as physicochemical adsorption [21, 22], chemical grafting [23] and copolymerization [24]. It is particularly important to us to graft adhesion signals on the entire graft surface, thus guiding rapid cell growth through ePTFE pores. Golden *et al*. demonstrated that ePTFE grafts with a large internodal spacing, 60 μm, healed by transmural, rather than transanastomotic, endothelialization in the baboon [6], however not in the human [3, 4]. Thus, it is our goal to incorporate bioactive signals within the pore and superficial surfaces to attempt to induce this behavior in the human. Furthermore, it is our goal to introduce these signal-grafting sites in a manner that will lead to minimal nonspecific

adhesion, via adsorbing proteins, so that the majority of the biological interactions can be induced by the incorporated signal.

In this paper we report the modification of the entire surface of ePTFE and the subsequent incorporation of PEG chains with numerous terminal hydroxyls for incorporation of biological adhesion signals [12, 15–18]. Cell nonadhesiveness has been explored by incorporating poly(ethylene glycol) (PEG) by numerous laboratories using a variety of methods, e.g. chemical grafting [25, 26], copolymerization [27, 28], graft polymerization [29, 30] and physicochemical adsorption [31, 32]. As no acceptable means for grafting of cell-nonadhesive PEG on ePTFE had been reported, a method of PEG grafting that permits the ability to incorporate biologically active features into the modified superficial and pore surfaces would be useful. Toward this end, formation of functional sites for grafting of PEG onto the entire surface of ePTFE was accomplished by thermal excitation of a reaction solution of benzophenone and sodium hydride in dimethyformamide. Subsequently covalent photograft polymerization of α-hydroxy, ω-acryloyl poly(ethylene glycol) was made with the terminal hydroxyl groups providing functional sites for chemical grafting of bioactive factors such as adhesion-promoting oligopeptides.

EXPERIMENTAL

Materials

PTFE films (disks of 15 mm diameter, 0.4 mm thickness; Small Parts Inc., Miami Lakes, FL, USA) and ePTFE samples (Impra Inc., Tempe, AZ, USA; fibril length of 20–30 μm, wall thickness of 650–750 and 500–630 μm from 4 and 6 mm inside diameter grafts, respectively) were extracted by reflux in tetrahydrofuran (THF) for 2 days and dried in vacuum at 60°C for 1 day. Benzophenone, sodium hydride (dry, 95%), anhydrous dimethylformamide (DMF), anhydrous dichloromethane (DCM), 2,2-dimethoxy-2-phenylacetophenone (benzyl dimethyl ketal, BDMK) and the sodium salt of 4-styrenesulfonic acid (SS-Na) were purchased from Aldrich (Milwaukee, WI, USA). α-Hydroxy, ω-acryloyl poly(ethylene glycol) (PEG-Ac) (200 and 8000 g mol^{-1}) were purchased from Monomer–Polymer & Dajac Laboratories (Feasterville, PA, USA) and used as received.

Surface modification of (e)PTFE

Both PTFE films and ePTFE samples (together abbreviated as (e)PTFE) were modified as follows. Benzophenone (0.86 g) was added into a 100 ml round flask after introduction of 50 ml anhydrous DMF. Sodium hydride (0.4 g) was transferred into the benzophenone solution. After mixing the flask contents with a magnetic stir bar, two PTFE films or three ePTFE samples were added in the reaction solution. All of the above handling was done under an argon atmosphere. The surface modification reaction was performed at a temperature of 150°C for 12 h for PTFE films or 105°C for 1 day for ePTFE samples. The treated ePTFE samples were removed from the

reaction flask, rinsed several times, extracted with deionized water for more than 24 h, and dried in vacuum at 60 °C for 1 day. This material is denoted as reduced PTFE or reduced ePTFE.

Photograft polymerization of acrylates upon reduced (e)PTFE

After extraction and drying, the reduced (e)PTFE samples were treated with a photoinitiator solution for 10 min (0.4 g BDMK in 10 ml anhydrous DCM) to adsorb this compound. An acrylate solution was prepared in a quartz Erlenmeyer reaction vessel with a 24/40 neck and a reflux condenser under argon. Initiator-adsorbed samples were added into the acrylate solution under argon gas. Photograft polymerization was performed under argon for 1 to 1.5 h by long wavelength ultraviolet light irradiation onto the reduced (e)PTFE samples from beneath the reaction vessel with frequent shaking. Long wavelength ultraviolet light was employed from a mercury vapor lamp (medium pressure, 100 W; Ultra-Violet Products Inc., San Gabriel, CA, USA) with a cobalt glass long-pass filter (21.7 mW cm^{-2}, $\lambda_{max} = 366$ nm). The acrylate solution was either SS-Na (0.5 g in 40 ml anhydrous DMF), PEG-Ac 200 (200 g mol^{-1}; 2 ml in 40 ml anhydrous DCM), or comacromonomers of PEG-Ac 200 and PEG-Ac 8000 (2 ml PEG-Ac 200 and 3 g PEG-Ac 8000 in 40 ml anhydrous DCM). Following photograft polymerization, the (e)PTFE samples were rinsed several times with DMF and then extracted with deionized water for 1 day with shaking, followed by drying under vacuum for 1 day.

Electron spectroscopy for chemical analysis (ESCA)

ESCA was performed with an M-Probe Surface Spectrometer (Surface Science Instruments, Mountain View, CA, USA) and analyzed as described elsewhere [33, 34]. Briefly, a monochromatic Al K_α X-ray source was employed and data were collected on three different spots on each (e)PTFE sample at a 55 deg take-off angle, the angle between the sample surface and the spectrometer. Both a flood gun with 6 eV feed and a nickel screen, approximately 1–2 mm above the sample, with a mesh of 70 lines per inch having 90% transmittance (Surface Science Instruments), were employed for charge neutralization of the sample surfaces [35]. Cross-sections of tubular samples were flat on the mounting stub, and three different spots on each cross section were tested. The center of each spot was located at 175, 350, or 525 μm from the lumenal to the outside surface, where the sample thickness was approximately 700 μm. The X-ray beam irradiated was an ellipsoid of 320 × 800 μm, aligned circumferentially. The nickel screen was used on the cross-sectional samples as usual.

Dynamic contact angle measurement (DCA)

Advancing and receding DCAs were measured with a Wilhelmy plate apparatus (Cahn Instruments; Cerritos, CA, USA). Three semi-continuous cycles of advancing and receding DCA measurements were performed with HPLC grade deionized water on dry unmodified, reduced and photograft polymerized PTFE films (1.2 × 1.2 cm^2) at a stage travel speed of 100 μm s^{-1}. The dwell time between each cycle was 5 s, and that between the advancing and receding movements of the travel stage was 60 s.

Low voltage scanning electron microscopy (*LV-SEM*)

Stereo-pair high resolution LV-SEM using a modified Hitachi S-900 (San Jose, CA, USA) was performed to determine the extent of morphological changes to the ePTFE samples caused by the first step of reductive modification and the second step of photograft polymerization. ePTFE samples were ion-beam coated (Ion Tech, Teddington, UK) with a 4–6-nm thickness of gold. Three different surface images, i.e. of the lumen, outside and cross sections, of ePTFE were obtained of the magnification up to 20 000 times at a 1.5 kV accelerating voltage to improve high resolution topographic imaging [36]. Micrographs were obtained from randomly selected regions of ePTFE samples with multiple regions of each ePTFE sample were observed to ensure that images were representative of typical structure.

RESULTS

Reductive modification of PTFE films

As a preliminary test toward ePTFE modification, surface modification of PTFE films was performed by thermal excitation of a reaction solution of benzophenone and sodium hydride in DMF. The unmodified PTFE film showed only the expected characteristic peaks by ESCA: only fluorine and carbon peaks observed in the ESCA survey spectrum (Fig. 1a) with a single fluorocarbon peak at 292.5 eV on the high resolution ESCA C 1*s* spectrum (Fig. 2a). Qualitative surface modification was readily observed by defluorination and oxygen incorporation upon the PTFE surfaces modified at a reaction temperature of 150°C for 12 h (Table 1 and Fig. 2b). ESCA survey spectra of the reduced films showed a reduction of fluorine peak intensity and the appearance of new oxygen peak. The extent of chemical modification was judged from the atomic percent ratios of F/C and O/C, where the atomic percent ratio of F/C reduced from 2.1 in unmodified PTFE to 0.44 after reduction, and that of O/C increased from 0.00 to 0.14. The reduction of fluorocarbon peak intensity in ESCA C 1*s* spectra was accompanied by generation of a new oxygenated hydrocarbon peak which appeared at and higher energy of 285 eV (Fig. 2b). The binding energy difference between

Table 1.
Atomic composition, as demonstrated from ESCA survey spectra, of PTFE film surfaces after thermochemical reduction and photograft polymerization with SS-Na and PEG-Ac 200

PTFE film	C (%)	F (%)	O (%)	S (%)	Na (%)	F/C (%/%)	O/C (%/%)
Control[a]	32	68	0	—	—	2.1	0
Reduced[b]	57	25	18	—	—	0.44	0.14
SS-Na[c]	63	0	26	4.5	6.8	0	0.41
PEG-Ac 200[d]	70	0	30	—	—	0	0.43

[a] Unmodified PTFE film.
[b] PTFE film thermochemically reduced at a reaction temperature of 150°C for 12 h.
[c] Sample of (b) photograft polymerized with the sodium salt of styrenesulfonic acid.
[d] Sample of (b) photograft polymerized with α-hydroxy, ω-acryloyl poly(ethylene glycol) (200 g mol^{-1}).

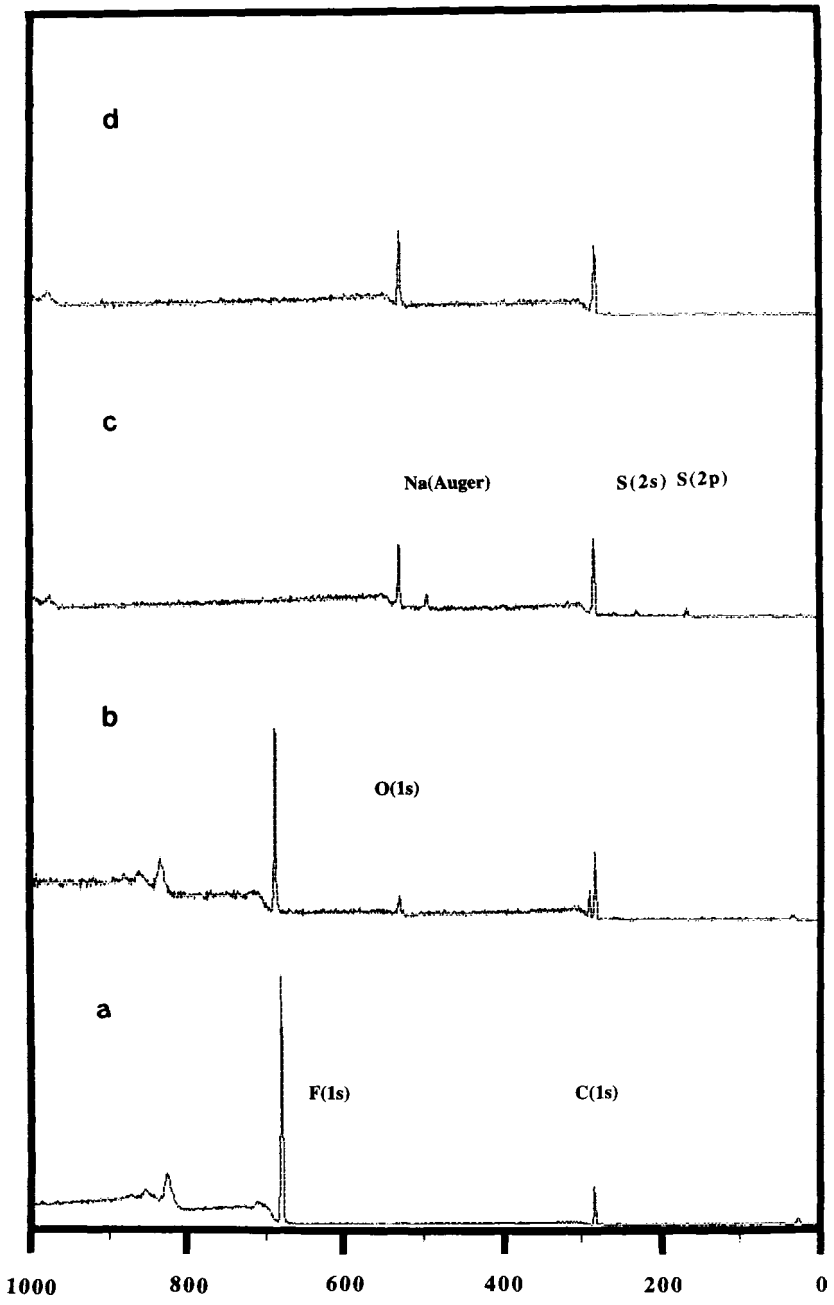

Figure 1. ESCA survey spectra of PTFE films thermochemically reduced and photograft polymerized with SS-Na and PEG-Ac 200: (a) unmodified PTFE film; (b) PTFE film thermochemically reduced at a reaction temperature of 150 °C for 12 h; (c) sample of (b) photograft polymerized with the sodium salt of 4-styrenesulfonic acid by UV light irradiation for 1 h; and (d) sample of (b) photograft polymerized with α-hydroxy, ω-acryloyl poly(ethylene glycol) (PEG-Ac) (200 g mol^{-1}) by UV light irradiation for 1 h.

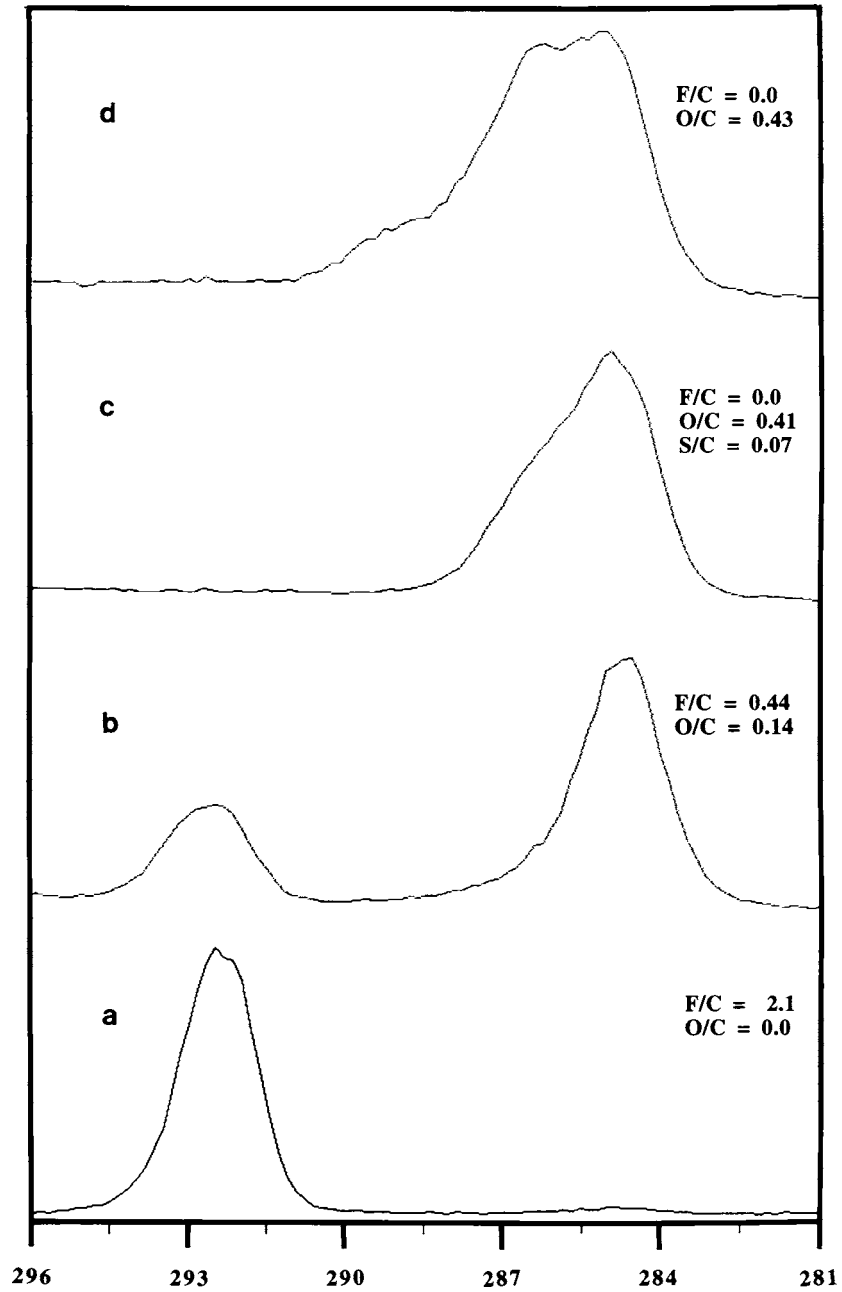

Figure 2. High resolution ESCA C 1*s* spectra of PTFE films thermochemically reduced and photograft polymerized with SS-Na and PEG-Ac 200 by UV light irradiation. Samples are as identified in Fig. 1.

the original fluorocarbon peak and the newly appearing peak was measured to be 7.7–7.9 eV, which is suggestive of the generation of unsaturation upon the reduced PTFE film surface.

Photograft polymerization of SS-Na and PEG-Ac 200 upon reduced PTFE films

SS-Na was photograft polymerized upon the thermally reduced PTFE films as a measure of the ability of the reduced PTFE substrate to serve as a substrate for photograft polymerization; the use of SS-Na permitted unambiguous interpretation of grafting by ESCA because of the introduction of new atoms. Photograft polymerization was clearly observed as shown in the ESCA survey spectrum (Fig. 1c). The ESCA survey spectrum showed no fluorine atom peak, the appearance of new sulfur atom peaks at binding energies of 229 eV ($2s$), 165 eV ($2p$) and 164 eV ($2p$), an oxygen atom peak at binding energy of approximately 532.5 eV and a sodium Auger peak at binding energy of 497 eV. The atomic percent ratios of C/O, C/S, and C/Na were 2.4, 14 and 9.3 (Table 1), whereas the theoretical atomic percent ratios for poly(SS-Na) are 2.7, 8.0, and 8.0. These atomic percent ratios indicate that the acrylate monomer was 92% photograft polymerized on the film surface from the judgment of O/C atomic percent ratio by ESCA to the depth of X-ray signal detection (approximately 57 Å; the method of estimation was described in previous report in detail [33]). The atomic percent ratio of S/Na was observed as 0.7 which is somewhat lower than that of a theoretical atomic percent ratio, 1.0, perhaps due to exchange with protons. High resolution ESCA C 1s spectra also showed evidence of photograft polymerization by complete disappearance of the fluorine atom peak (at 292.5 eV) and the appearance of a new carbon peak at lower binding energy (Fig. 2c). No aromatic C 1s $\pi \rightarrow \pi^*$ satellite was observed.

PEG-Ac 200 macromonomer was photograft polymerized on films that had been reductively modified as described above. The PEG-Ac 200 photograft polymerized films showed complete elimination of surface atomic fluorine, from 25 to 0.0%, and an increase of incorporated oxygen atomic percent from 18 to 30% (Table 1). The resulting atomic percent ratio of F/C decreased from 0.44 to 0.0 and that of O/C increased from 0.14 to 0.43 (Fig. 2d), whereas the theoretical atomic percent ratio of O/C in homopolymer PEG-Ac 200 is 0.54. The high resolution ESCA C 1s spectrum clearly showed a change in peak shape after photograft polymerization, i.e. transition from a relatively sharp peak shape of the reduced film containing unsaturation to a broad peak shape containing an ether carbon from PEG at binding energy of approximately 286.5 eV and ester carbonyl groups from acrylates at binding energy of approximately 289.2 eV. Detailed peak analysis of the PTFE films photograft polymerized with PEG-Ac 200 is not reported here, since its analysis had been described in detail in our previous report employing photochemical, rather than thermochemical, reduction of PTFE films [33]. Although it is not possible to exclude some residual benzophenone in the reduced PTFE sample surface (Fig. 2b), the distinction between photograft polymerization of ether-containing species (Fig. 2d) from possible surface ketone from benzophenone or benzophenone fragments is clear.

Surface energetics was measured on the reduced and photograft polymerized films, as indicated by dynamic water contact angles (Table 2). After surface reduction, the advancing dynamic water contact angle changed from 120 deg on the unmodified substrate to 89 deg. That advancing contact angle further decreased to 36 deg after photograft polymerization with PEG-Ac 200. Reorientation of graft polymerized

Table 2.
Advancing and receding dynamic water contact angles of PTFE films thermochemically reduced and photograft polymerized with PEG-Ac 200

Sample	Advancing DCA			Receding DCA		
	1st	2nd	3rd	1st	2nd	3rd
Control[a]	120	119	120	90	89	90
Reduced[b]	89	54	53	8.6	8.3	8.2
PEG-Ac 200[c]	36	22	24	9.4	8.5	7.4

[a]Unmodified PTFE film.
[b]PTFE film thermochemically reduced at a reaction temperature of 150°C for 12 h.
[c]Sample of (b) photograft polymerized with PEG-Ac 200.

PEG macromers was observed as a decrease of advancing contact angles from the first cycles to the second and third cycles, i.e. the values from the first cycles of the PEG-Ac 200 photograft polymerized films decreased from 36 to 22 deg at the second cycles with no further change in the third cycle. Receding water contact angles were very small (8–9 deg), both after reduction and photograft polymerization of PEG-Ac 200.

Reductive modification of ePTFE

Expanded PTFE was reductively modified under similar conditions as described above for PTFE films, only at a lower reaction temperature (105°C) for a longer duration (1 day). The results described below demonstrate that surface reduction of ePTFE also resulted in extensive defluorination, incorporation of oxygen species and introduction of unsaturation into the entire ePTFE surface, i.e. the lumenal, outside and pore surfaces, in a manner similar to that for PTFE films. ePTFE prior to modification appeared essentially free of contamination, with a F/C atomic percent ratio of 2.1, close to the theoretical value of 2, with no atoms other than C and F apparent. The high resolution ESCA C 1*s* spectra of ePTFE prior to modification (in Fig. 3a) showed only CF_2 at a binding energy of 292.5 eV with no signals at other binding energies. Thus, any reductive modification of the ePTFE surface was interpreted as surface modification of the actual fluorocarbon rather than of contaminant hydrocarbon.

Surface modification of ePTFE by treatment in benzophenone and sodium hydride solution at 105°C for 1 day may be readily observed in Figs 3b and f, showing high resolution ESCA C 1*s* spectra of the lumenal and outside surfaces of an ePTFE graft, respectively. The extent of defluorination of the lumenal surface was similar to that of the outside surface of ePTFE (Table 3), specifically extents of 72 and 74% on the lumen and outside were measured to the depth of measurement of ESCA at the 55-deg take-off angle employed. Defluorination was accompanied by oxygen incorporation. Incorporation of oxygen species on the defluorinated lumenal and outside surface was approximately 14 and 12%, respectively. The similarity of modification on the lumenal and outside surfaces may be seen clearly from the F/C and O/C atomic percent ratios, specifically the decrease of F/C atomic percent ratio from 2.1 to 0.28 on the lumenal surface and 0.26 on the outside surface, and the increase of O/C

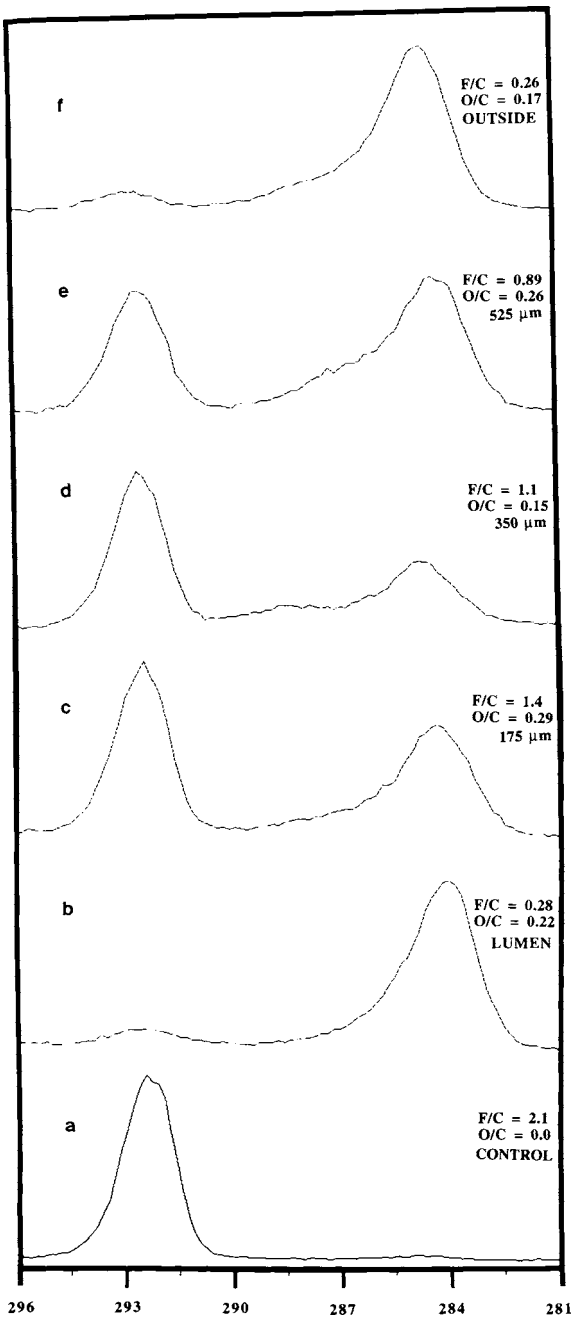

Figure 3. High resolution ESCA C 1*s* spectra of superficial and cross-sectional surfaces of ePTFE samples thermochemically reduced at a reaction temperature of 105 °C for 1 day: (a) unmodified of ePTFE; (b) superficial lumenal surface; (c) cross-section 175 μm from lumenal surface; (d) cross-section 350 μm from lumenal surface; (e) cross-section 525 μm from lumenal surface; and (f) superficial outside surface.

Table 3.
Atomic composition, as demonstrated from ESCA survey spectra, of ePTFE after thermochemical reduction and photograft polymerization with comacromonomers of PEG-Ac 200 and PEG-Ac 8000. Measurements were made on the lumenal and outside superficial surfaces, and also on cross-sections at spots centered at the distances shown from the lumenal surface (wall thickness, 700 μm)

ePTFE[a]	C (%)	F (%)	O (%)	F/C (%/%)	O/C (%/%)
Control	32	68	0	2.1	0
After thermochemical reduction					
Lumen	67	19	14	0.28	0.21
175 μm	38	52	11	1.4	0.29
350 μm	44	50	6.6	1.1	0.15
525 μm	47	42	12	0.89	0.26
Outside	70	18	12	0.26	0.17
After photograft polymerization					
Lumen	66	7.3	27	0.11	0.41
175 μm	44	39	17	0.89	0.39
350 μm	50	27	23	0.54	0.46
525 μm	53	19	28	0.36	0.53
Outside	60	8.0	32	0.13	0.53

[a]Control, lumen and outside measurements were made on superficial surfaces without sectioning, whereas the measurements at the distances shown were performed on cross-sections, thereby exposing new unmodified PTFE by sectioning.

atomic percent ratio from 0.0 to 0.21 on the lumenal surface and to 0.17 on the outside surface (Table 3).

Surface defluorination was accompanied by changes in the nature of carbon and fluorine species present on the modified surface, as may be observed in the high resolution ESCA C 1*s* spectra shown in Fig. 3b (lumenal surface) and f (outside surface). The fluorocarbon peak on high resolution ESCA C 1*s* spectra, initially at 292.5 eV, was observed to broaden during modification, indicating introduction of CF species other than CF_2, with a peak shift to lower binding energy. Moreover, a new oxygenated hydrocarbon peak was observed to emerge during modification. This new peak remained broad, indicating a diversity of oxygenated hydrocarbon species. After the surface was defluorinated, the F 1*s* peak (spectra not shown) was observed to broaden from the initial sharp peak, indicative of an introduction of CF species other than CF_2 on the modified ePTFE surfaces. The binding energy differences between the original fluorocarbon peak and the newly generated oxygenated hydrocarbon peak on high resolution ESCA C 1*s* spectra were measured to be 7.8–8.2 eV, which may indicate the existence of surface unsaturation after modification (Fig. 3b and f).

Modification of the ePTFE pore surfaces was examined by ESCA on cross-sections of the ePTFE tube wall, cut after reductive modification and photograft polymerization. The ESCA was performed on three different spots of the cross sectional surface of the 700 μm graft wall. Table 3 shows atomic compositions obtained from measurements, made roughly in the middle of the cross-section and at one-quarter of the thickness inward from the lumenal and the outer surfaces. These atomic compositions can not be straightforwardly interpreted as quantitative indices of the extent

of defluorination, however, since sectioning through the graft wall exposes fresh unmodified PTFE where ePTFE fibrils and nodes are sectioned. Thus, the measured signal indicates an average of measurement for the modified and the freshly exposed PTFE. Since the morphology of the fibrils and nodes may vary with distance along the wall thickness, understanding what fraction of the signal derive from the surface modified PTFE vs freshly exposed PTFE is not straightforward. For this reason, the results are considered only qualitatively. Defluorination was observed to proceed, as expected, and was accompanied by incorporation of oxygenated hydrocarbon species. Figure 3c–e show high resolution ESCA C 1*s* spectra obtained at the three positions along the wall cross-section. The shapes of the newly appearing C 1*s* peaks were similar internal within the graft wall to those on the lumenal and outer surfaces (normalizing for peaking height as justified above). In addition, the binding energy differences between the original fluorocarbon and newly appearing oxygenated hydrocarbon peaks at the three positions were identical to those values obtained on the lumenal and outside surfaces of ePTFE, i.e. 7.8–8.2 eV. Based on this analysis, albeit qualitative, it would appear that the pore surfaces were indeed reduced in a similar manner to that observed on the superficial lumenal and outside surfaces.

Photograft polymerization of ePTFE with comacromonomers of PEG-Ac 200 and PEG-Ac 8000

Based on the observation of photograft polymerization with SS-Na and PEG-Ac 200 on the reduced PTFE films and based on the observation of thermochemical reduction of ePTFE, photograft polymerization upon thermochemically reduced ePTFE was attempted. Rather than employing PEG-Ac 200 as a macromonomer, PEG-Ac 200 and PEG-Ac 8000 were employed as comacromonomers (at approximately 3.3 mol% PEG-Ac 8000), based on previous observation of greater biocompatibility with surfaces incorporating higher molecular weight PEG [25]. The extent of photograft polymerization on the lumenal and outside surfaces of the modified ePTFE grafts was clearly indicated from surface fluorine and oxygen atomic contents as determined from ESCA survey spectra (Table 3). The F/C atomic percent ratio on the lumenal surfaces decreased from 0.28 to 0.11, while that O/C atomic percent ratio increased from 0.21 to 0.41. For comparison, the theoretical O/C atomic percent ratio for the polymer of the PEG-Ac 200 and PEG-Ac 8000 mixture ranges 0.54–0.50. The outside surface showed evidence of more extensive photograft polymerization, with the O/C atomic percent ratio increasing from 0.17 to 0.53, approaching to the theoretical value for homopolymeric PEG-Ac 200. The high resolution ESCA C 1*s* spectra of the lumenal and outside surfaces of photograft polymerized ePTFE showed clear evidence of the presence of PEG with a peak corresponding to ether bonded carbon at a binding energy of 286.5 eV, accompanied by a shoulder corresponding to ester carbonyl at binding energy of approximately 289 eV (Fig. 4b and f). These changes in surface composition were all very similar to those observed on photograft polymerized PTFE film substrates.

Photograft polymerization of PEG-Ac on the pore surfaces was tested by ESCA of the cross-sections at spots at the same positions as described above, and their atomic

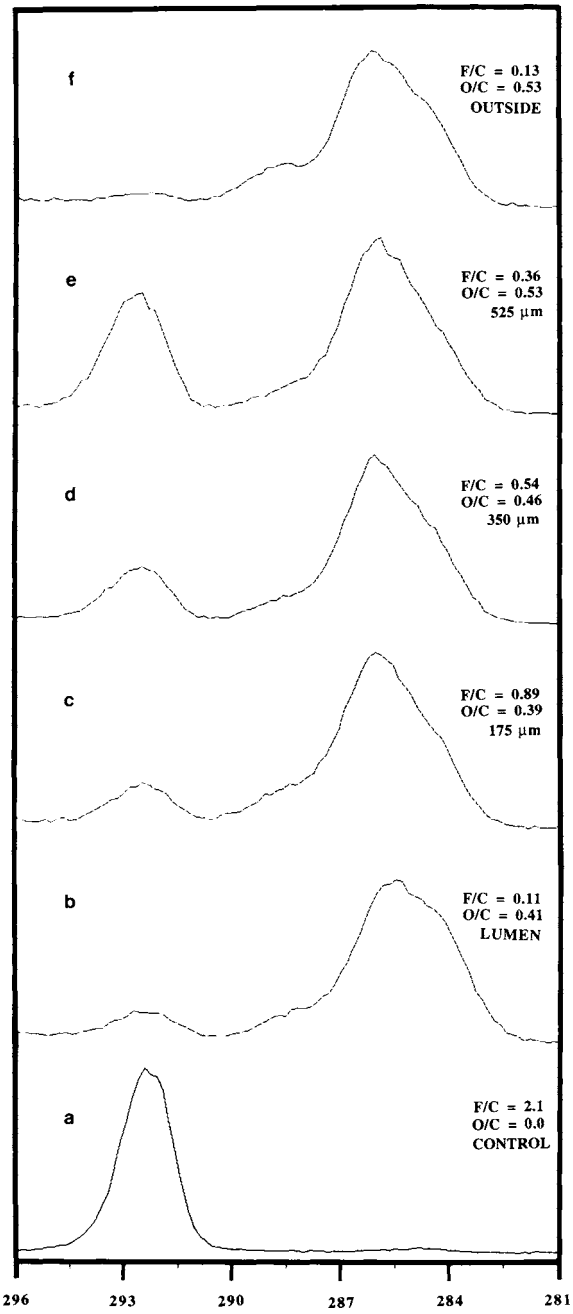

Figure 4. High resolution ESCA C 1*s* spectra of superficial and cross-sectional surfaces of ePTFE samples photograft polymerized with comacromonomers of PEG-Ac 200 and PEG-Ac 8000 by UV light irradiation for 1.5 h on the substrates of Fig. 3. Samples are as identified in Fig. 3.

compositions from ESCA survey spectra are shown in Table 3. As described above, this analysis is only qualitative, due to the exposure of fresh, unmodified PTFE by sectioning, but based on the peak locations and peak shapes it is clear that photograft polymerization proceeded on the pore surfaces in addition to the superficial lumenal and outside surfaces (Fig. 4c–e).

Three different surface images of ePTFE, i.e. of the lumen, outside and the center of cross-section, were observed by LV-SEM at magnifications up to 20 000 times to view surface morphological changes relative to unreduced ePTFE, as shown in Fig. 5. Since the images of the lumenal and outside surface were very similar, the image of the outer surfaces are not presented here. The morphology of the unreduced control ePTFE (Fig. 5a–c) was compared with that of ePTFE thermally reduced at a temperature of 105 °C for 1 day (Fig. 5d–f) and photograft polymerized with a mixture of PEG-Ac 200 and PEG-Ac 8000 (Fig. 5g–i): images of the lumenal superficial surface are shown at low (Fig. 5a, d, and g) and high (Fig. 5b, e, and h) magnification, and images of the cross-section at roughly the middle are shown at low magnification (Fig. 5c, f, and i). The control, unreduced ePTFE showed the typical material morphology of nodes connected by fibrils (Fig. 5a). The nodes were essentially smooth and approximately 10 μm wide (Fig. 5a), and the fibrils were approximately 0.5 μm in diameter and also essentially smooth (Fig. 5b). This structure was seen also within the interstices, as suggested by imaging of cross-sections of the grafts (Fig. 5c). The morphological changes induced by the thermochemical reduction process were minimal: the morphology showed subtle change, that is there was indication of small scale texture on the node surfaces with a characteristic size of 50–100 nm (Fig. 5d and e). There was, however, no breakage of either fibrils or nodes or obvious change in pore morphology (Fig. 5b and c vs Fig. 5e and f). The images of the nodes were suggestive, but certainly not conclusive, of some disconnection of crystalline microstructures from the amorphous microstructures (Fig. 5e), while the fibrils showed no obvious alteration in surface texture. This may indicate that the crystalline microstructure in fibrils and in nodes is more resistant to chemical attack than that in the amorphous domain. The morphology of ePTFE photograft polymerized with PEG-Ac showed no essential difference compared to that of the thermochemically reduced ePTFE: there was a similar extent of morphological fluctuations of the crystalline microstructures on nodes with a size of 50–100 nm in diameter (Fig. 5g and h). No breakage of fibril strands was observed after treatment (Fig. 5f) and there was no blockage of pores by graft polymerization with PEG-Ac (Fig. 5i).

DISCUSSION AND CONCLUSIONS

Thermochemical reduction of PTFE film and ePTFE was accomplished in a reaction solution of benzophenone and sodium hydride in DMF at reaction temperatures of 150 and 105 °C for 12 h and 1 day, respectively. Cooler reaction conditions and shorter durations of modification were necessary to retain ePTFE micromorphology. The results showed extensive defluorination, incorporation of oxygen species and generation of unsaturation in the treated (e)PTFE surfaces. Our previous studies demonstrated

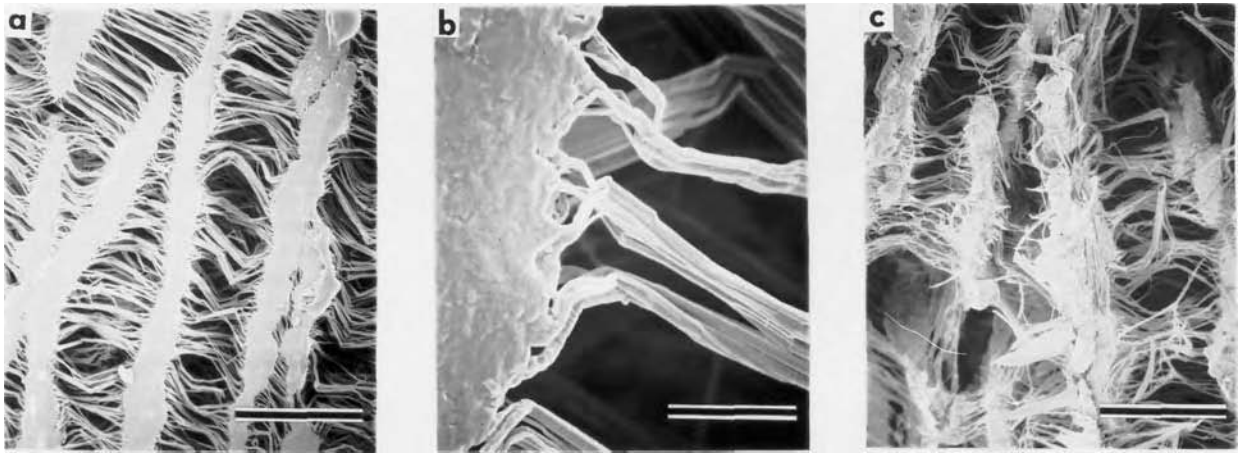

Figure 5. Low voltage scanning electron microscopy of modified ePTFE. Images were collected at the superficial lumenal surfaces at low magnification (a, d, g; 1000 ×, bar = 30 μm) and at high magnification (b, e, h; 20 000 ×, bar = 1.5 μm); and approx. mid-way across the graft wall in cross-sections (c, f, i; 1000 ×, bar = 30 μm). Images at high magnifications were obtained at the center of the lower magnification regions. The outer superficial surface appeared very similar to the lumenal superficial surface and is not shown here. (a, b, c) Control unmodified ePTFE; (d, e, f) ePTFE thermochemically reduced at a reaction temperature of 105 °C for 1 day; and (g, h, i) ePTFE photograft polymerized with comacromonomers of PEG-Ac 200 and PEG-Ac 8000 by UV irradiation for 1.5 h on the thermochemically reduced substrate.

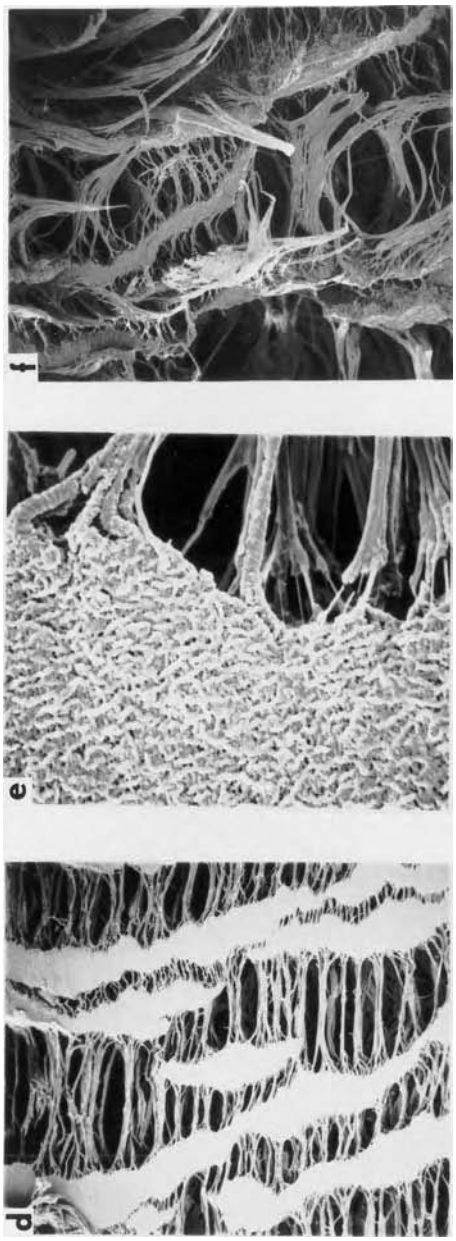

Figure 5. (Continued).

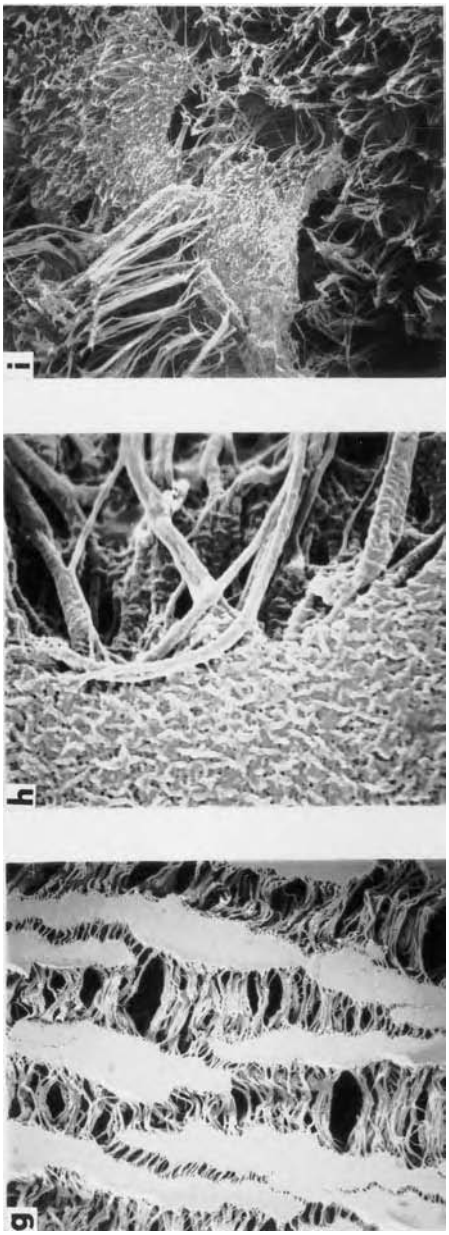

Figure 5. (Continued).

the ability to reductively modify PTFE films by photoexcitation of benzophenone in the presence of sodium hydride in DMF [33, 34]: the same reaction solution was employed but the reaction temperature was higher (105 vs 49 °C) and treatment time was longer (1 day vs 20 min) than that of photochemical treatment. This treatment resulted in extensive surface modification of PTFE films like the results induced by thermochemical reduction. Surface reduction of (e)PTFE likely occurred by similar mechanisms; electron transfer with diphenyl ketyl radical anions formed as intermediates during conversion of benzophenones to final products of benzhydrol anions [34, 37–39]. Surface modification of ePTFE was explored by thermal excitation in these studies since our photochemical treatment demonstrated some difficulty in surface modification of ePTFE pores. This thermochemical surface modification explored here induced a similar extent of surface modification as in the photochemical reduction that we have previously described [33, 34]. Surface fluorine atomic content was reduced by approximately 72% and atomic oxygen was introduced to an O/C ratio of approximately 0.21 in the lumen surface of ePTFE. The presence of surface unsaturation was clearly demonstrated in our previous studies with photochemical excitation of solutions of benzophenone and sodium hydride [33, 34] and the same unsaturation is presumed to be present in these materials subjected to thermal excitation. The reduced (e)PTFE was clearly on adequate substrate for photograft polymerization of PEG-Ac. The fluorine atomic content was reduced to zero, the O/C atomic percent ratio rose to approximately 0.43 in PTFE films, compared to 0.5 for PEG, and the advancing dynamic contact angle fell to 36 deg, compared to 120 deg for the unmodified PTFE films. The thermochemical reduction and subsequent graft polymerization were accomplished with quite modest alteration in the surface morphology of ePTFE, with some surface texture appearing on a length scale of approximately 50–100 nm. The fibrils were not damaged, and the crystalline microstructure in fibrils and in nodes seems to be more resistant to chemical attack than that in the amorphous domains.

ePTFE is an important material in a number of medical applications, including vascular graft implants. In its application to vascular grafts, small inside diameter (< 5 mm) ePTFE shows rapid thrombosis at an initial stage and formation of pseudointima at a latter stage, leading to graft failure. To increase its patency, i.e. to alter its biocompatibility and to control interactions with cells, incorporation of biologically active oligopeptides was suggested [12], leading to a necessity for surface modification of chemically stable ePTFE without inducing morphological damage. The modification described above was readily achieved with minimal alteration of the surface morphology of ePTFE, thus providing a novel approach for improving biocompatibility of this material without the loss of its important engineering properties.

Numerous studies have demonstrated reduction in biological adhesion by PEG chain grafting [25–27]. For this reason, we sought to incorporate PEG chains at high density, exploring graft polymerization as a means to that end. A mixture of PEG-Ac 200 and PEG-Ac 8000 did indeed yield effective graft polymerization: the superficial lumenal and outer surfaces demonstrated a high O/C atomic percent ratio, approaching that of PEG homopolymer. Homophotograft polymerization of PEG-Ac 8000 did not yield effective graft polymerization (not shown), and for this reason we sought to incorporate high molecular weight PEG as a comonomer with the more readily

polymerizable monomer PEG-Ac 200. In both cases, the PEG is linked to the acrylate via an ester; one could improve the hydrolytic stability of this junction, if necessary, by linkage through an amide. Importantly, ESCA of cross-sections of graft segments provided clear evidence of both photograft polymerization on the surfaces of pores within the wall of the graft and LV-SEM of cross-sections demonstrated that the internal pores were not blocked or changed in morphology. Complete and relatively homogenous surface modification of ePTFEs with retention of micromorphology may open a pathway to improved graft healing by reducing nonspecific interactions via PEG grafting followed by coupling of bioactive factors such as adhesion-promoting oligopeptides to the material surface.

Acknowledgements

We thank Alan P. Rice for help with the ESCA sample stage design. The Integrated Microscopy in Madison, Wisconsin (NIH-RR-570) is acknowledged for the use of the Hitachi S-900 Low Voltage-Scanning Electron Microscopy.

REFERENCES

1. R. B. Chard, D. C. Johnson, G. R. Nunn and T. B. Cartmill, *J. Thorac. Cardiovasc. Surg.* **94**, 132 (1987).
2. S. K. Williams, T. Schneider, B. Kapelan and B. E. Jarrell, *J. Electron Microsc. Tech.* **19**, 439 (1991).
3. L. R. Sauvage, K. Berger, S. Wood, S. G. Yates, J. C. Smith and P. B. Mansfield, *Arch. Surg.* **109**, 698 (1974).
4. K. Berger, L. R. Sauvage, A. M. Rao and S. J. Wood, *Ann. Surg.* **175**, 118 (1972).
5. A. W. Clowes, T. R. Kirkman and M. A. Reidy, *Am. J. Pathol.* **123**, 220 (1986).
6. M. A. Golden, S. R. Hanson, T. R. Kirkman and A. W. Clowes, *J. Vasc. Surg.* **11**, 838 (1990).
7. C. O. Esquivel and F. W. Blaisdell, *J. Surg. Res.* **41**, 1 (1986).
8. A. W. Clowes and M. A. Reidy, *J. Vasc. Surg.* **13**, 885 (1991).
9. A. Kusaba, C. R. Fischer, T. J. Matulewski and T. Matsumoto, *Amer. Surgeon* **47**, 347 (1981).
10. M. D. Herring, R. Dilley, R. A. Jersild, L. Boxer, A. Gardner and J. Glover, *Ann. Surg.* **190**, 84 (1979).
11. H. M. Carr, R. Vohra, H. Sharma, J. V. Smith, O. B. Rooney, P. D. Dodd and M. G. Walker, *Ann. Vasc. Surg.* **10**, 469 (1996).
12. J. A. Hubbell, *Bio/Technology* **13**, 565 (1995).
13. N. R. Peppas and R. Langer, *Science* **263**, 1715 (1994).
14. R. Langer and J. P. Vacanti, *Science* **260**, 920 (1993).
15. S. P. Massia and J. A. Hubbell, *J. Cell Biol.* **114**, 1089 (1991).
16. S. P. Massia and J. A. Hubbell, *Anal. Biochem.* **187**, 292 (1990).
17. S. P. Massia, S. S. Rao and J. A. Hubbell, *J. Biol. Chem.* **268**, 8053 (1993).
18. S. P. Massia and J. A. Hubbell, *J. Biol. Chem.* **267**, 14 019 (1992).
19. J. A. Hubbell, S. P. Massia, N. P. Desai and P. D. Drumheller, *Bio/Technology* **9**, 568 (1991).
20. J. A. Hubbell, S. P. Massia and P. D. Drumheller, *Thromb. Haem.* **65**, 789 (1991).
21. E. Ruoslahti and M. D. Pierschbacher, *Nature* (*Lond.*) **309**, 30 (1984).
22. K. P. Walluscheck, G. Steinhoff, S. Kelm and A. Haverich, *Eur. J. Vasc. Endovasc. Surg.* **12**, 321 (1996).
23. P. D. Drumheller and J. A. Hubbell, *Anal. Biochem.* **222**, 380 (1994).
24. B. K. Brandley and R. L. Schnaar, *Anal. Biochem.* **172**, 270 (1988).
25. W. R. Gombotz, W. Guanghui, T. A. Horbett and A. S. Hoffman, *J. Biomed. Mater. Res.* **25**, 1547 (1991).

26. Y. C. Tseng and K. Park, *J. Biomed. Mater. Res.* **26**, 373 (1992).
27. C. P. Pathak, A. S. Sawhney, C. P. Quinn and J. A. Hubbell, *J. Biomater. Sci. Polym. Edn* **6**, 313 (1994).
28. J. H. Lee, P. Kopeckova, J. Kopecek and J. D. Andrade, *Biomaterials* **11**, 455 (1990).
29. K. Fujimoto, H. Tadokoro, Y. Ueda and Y. Ikada, *Biomaterials* **14**, 442 (1993).
30. E. Uchida, Y. Uyama and Y. Ikada, *Langmuir* **10**, 481 (1994).
31. J. X. Zhao and W. Brown, *J. Phy. Chem.* **100**, 5908 (1996).
32. M. Malmsten and J. M. Valalstine, *J. Coll. Interf. Sci.* **177**, 502 (1996).
33. I. Noh and J. A. Hubbell, *J. Polym. Sci. A*, *Polym. Chem. Ed.* (1997) (in press).
34. I. Noh, K. K. Chittur, S. L. Goodman and J. A. Hubbell, *J. Polym. Sci. A*, *Polym. Chem. Ed.* **35**, 1499 (1997).
35. C. E. Bryson III, *Surface Sci.* **189**, 50 (1987).
36. S. L. Goodman, K. S. Tweden and R. M. Albrecht, *Cell Mater.* **5**, 15 (1995).
37. P. Caubère and J. Moreau, *Bull. Soc. Chim.* **9**, 3270 (1971).
38. P. Caubère, *Angew. Chem. Int. Ed. Engl.* **22**, 599 (1983).
39. C. A. Costello and T. J. McCarthy, *Macromolecules* **20**, 2819 (1987).

Polymers for Tissue Engineering, pp. 165–188
Molly S. Shoichet and Jeffrey A. Hubbell (Eds)

Biomolecular modification of p(AAm-*co*-EG/AA) IPNs supports osteoblast adhesion and phenotypic expression

J. P. BEARINGER [1,2], D. G. CASTNER [3] and K. E. HEALY [1,2,*]

[1] *Division of Biological Materials, Northwestern University Dental School. 311 E, Chicago Ave., Ward 10-116, Chicago, IL 60611-3008, USA*

[2] *Department of Biomedical Engineering, McCormick School of Engineering and Applied Science, Northwestern University, Evanston, IL 60201, USA*

[3] *NESAC/Bio, University of Washington, Departments of Chemical Engineering and Bioengineering, Box 351750, Seattle, WA 98195, USA*

Received 21 August 1997; accepted 17 December 1997

Abstract—Interpenetrating polymer networks (IPNs) were designed to resist materials fouling caused by non-specific protein adsorption, and indiscriminate cell or bacterial adhesion. These IPNs were thin adherent films ($\sim$ 20 nm) comprised of acrylamide (AAm), ethylene glycol (EG), and acrylic acid (AA) grafted to either silicon waters or quartz substrates via photoinitiated free radical polymerization. These networks were further modified to promote specific cell adhesion by tethering bioactive groups such as peptides that mimic cell-binding domains found on extracellular matrix molecules. As a specific example of biomolecular surface engineering, peptides from the cell-binding domain of bone sialoprotein were tethered to a p(AAm-*co*-EG/AA) IPN to control cell behavior at the surface. The networks were characterized by contact angle measurements, spectroscopic ellipsometry, and X-ray photoelectron spectroscopy to convey information on IPN wettability, thickness, and chemistry. The surface characterization data supported the theory that the PEG/AA layer formed an IPN with the underlying p(AAm) network, and after graft modification of this IPN with diamino PEG ($PEG(NH_2)_2$), the $PEG(NH_2)_2$ chains were enriched at the surface. Rat calvarial osteoblasts attached to Arg–Gly–Asp (RGD) modified IPNs at levels significantly greater than on clean quartz, Arg–Gly–Glu (RGE) modified, or the $PEG(NH_2)_2$ modified IPN, with or without serum in the media. Cells maintained in media containing 15% fetal bovine serum (FBS) proliferated, exhibited nodule formation, and generated sheets of mineralized extracellular matrix (ECM) with the addition on β-glycerophosphate to the media. Cell adhesion and mineralized ECM formation were specifically dependent on the peptide sequence present at the surface.

Key words: Surface engineering; biomolecular recognition; RGD; mineralization; osteoblasts; interpenetrating polymer network (IPN).

*To whom correspondence should be addressed.

INTRODUCTION

Materials fouling caused by non-specific protein adsorption and subsequent indiscriminate cell or bacterial adhesion is one of the leading causes of service performance failure or product loss in the medical device, pharmaceutical, and biotechnology industries. Engineering the surface chemistry of a material to prevent non-specific protein adsorption and also exploit specific interactions with biological systems can substantially improve performance and cultivate new paradigms in the design of medical devices, bioreactors, biosensors, macromolecular separation and purification systems, rapid DNA analysis and sequencing chips, storage containers, and cell culture substrates [1–4]. Biomolecular surface engineering implies altering a material's performance by covalently coupling to the material's surface a biologically relevant molecule that either proteins or cells exposed to the material recognize through a cellular or biomolecular pathway. Integrins, such as $\alpha_1\beta_1$, $\alpha_3\beta_2$, and $\alpha_v\beta_3$, recognize the peptide sequence Arg–Gly–Asp (RGD) which is present in the cell binding domain of numerous extracellular matrix proteins such as fibronectin (Fn), fibrinogen (Fb), vitronectin (Vn), laminin (Lam), the collagens (Col), osteopontin, and bone sialoprotein (BSP) [5–9]. Coatings and polymers have been designed which incorporate some form of the RGD sequence into substrate materials to elicit specific cell responses. For example, RGD-peptide modification of glycophase glass, polyethylene terepthalate (PET), polytetrafluoroethylene (PTFE), poly(2-hydroxyethyl methacrylate) (PHEMA), polyurethane (PU), poly(vinyl alcohol) (PVA), titanium, quartz, and silicon have been reported [2, 10–14].

The base materials of these systems all support non-specific protein adsorption to some degree, and therefore permit uncontrolled cell behavior. In attempt to eliminate the effects of non-specific protein binding and promote selectivity in cell adhesion, non adhesive substrates have been derivatized with RGD-based peptides. For example, polyacrylamide gel surfaces have been modified with Tyr–Ala–Val–Thr–Gly–Arg–Gly–Asp–Ser (YAVTGRGDS), and an endothelial cell selective adhesion sequence found in fibronectin, Gly–Arg–Glu–Asp–Val–Tyr (GREDVY), was grafted to a surface physical interpenetrating network (SPIN) of poly(ethylene oxide) (PEO) within PET [4, 15]. More recently, Drumheller and Hubbell [3] designed a semi-interpenetrating polymer network (semi-IPN) which was initially resistant to cell adhesion, and was then grafted with Gly–Arg–Gly–Asp–Ser (GRGDS) in order to support adhesion of human foreskin fibroblasts.

In an attempt to build on the work of Drumheller and Hubbell [3], we have functionalized an interpenetrating network (IPN) coating of p(AAm-*co*-EG/AA) with a biomimetic peptide sequence (Cys–Gly–Gly–Asn–Gly–Glu–Pro–**Arg–Gly–Asp**–Thr–Tyr–Arg–Ala–Tyr) from the cell binding domain of BSP. This IPN coating is a departure from previous studies [3, 4, 15], since it is amenable to producing a thin and tenacious conformal coating on either metals, ceramics, or polymers. The choice of the RGD sequence from BSP was based on observations that it supports specific attachment of rat calvaria osteoblasts (RCOs) even in non-serum containing media, and induces mineralization of the synthesized ECM in cell

culture [16, 17]. Furthermore, endogenous proteases of rat osteosarcoma cell lines have enzymatically degraded BSP into fragments (RGD- and non-RGD-containing) which mediated attachment of primary human osteoblast-like cells in culture. The peptide functionalized IPN was characterized via contact angle measurements, spectroscopic ellipsometry (SE), and X-ray photoelectron spectroscopy (XPS) to verify network chemistry and confirm grafting of the peptide. RCO viability and attachment experiments were performed, and cell growth kinetics were analyzed. RCOs inoculated onto RGD modified p(AAm-*co*-EG/AA) attached in significantly greater quantities than on control substrates, and in long term cell cultures grew to confluence, exhibited nodule formation, and demonstrated mineralization of the synthesized ECM *in vitro*.

MATERIALS AND METHODS

Surface modification

Polished silicon wafers (*n* type, ⟨100⟩, International Wafer service, Portola Valley, CA, USA) were used for all studies involving contact angle measurements, spectroscopic ellipsometry, and X-ray photoelectron spectroscopy (XPS). Quartz discs (Quartz Scientific Inc., Fairport Harbor, OH, USA) were used for all cell plating experiments. Substrates were sequentially cleaned ultrasonically for 10 min in ASTM grade I water (ultrapure water), acetone, and hexane[1], and then subjected to a Piranha etch (90% v/v sulfuric acid, 10% v/v hydrogen peroxide) for 15 min and thoroughly rinsed in ultrapure water. Surfaces that were modified with a silane and polymers underwent additional cleaning by an oxygen plasma (March Plasmod, Concord, CA, USA) set at 0.5 Torr O_2 pressure and 150 W power for 5 min.

An unsaturated organosilane, allyltrichlorosilane (ATC) was grafted to silicon and quartz substrates using previously described [18]. Acrylamide (AAm, Polysciences, Warrington, PA, USA) was then grafted onto the ATC in the same concentrations and by the same protocol as previously described [18]. The crosslinked PEG layer was modified from that of the original IPN in order to accommodate the functionalization of the IPN coating by dissolving 0.0200 mg ml^{-1} poly(ethylene glycol) monomethyl ether monomethacrylate (M_W 1000) (PEG, Polysciences), 0.0100 mg ml^{-1} *N*,*N*-methylene-bis-acrylamide (BIS, Polysciences), 0.1620 ml ml^{-1} acrylic acid (AA), and 0.03324 mg ml^{-1} D,L-camphporquinone (CQ, Polysciences) in methanol. The mixture was sonicated to solvate all species and nitrogen was bubbled through the mixture for 15 min to remove residual oxygen. The mixture was adsorbed onto p(AAm) modified substrates in covered glass dishes for 5 min and then the samples were transferred into glass dishes and placed in a Demetron Lab Lite box (Danbury, CT, USA) for photoinitiation using

[1] All chemicals (ACS grade or better) were purchased from Aldrich (Milwaukee, WI, USA) unless otherwise noted, and used as received.

a Heraeus Amersil Z7 indium lightsource that had a predominant emission peak at approximately 470 nm. Exposure to the light (3 min) was limited so that the solvent/monomer mixture did not gel, but was allowed to increase in viscosity. Substrates were removed from the dishes, rinsed, and sonicated in ultrapure water for 30 min to remove unreacted materials. Figure 1A shows a schematic of the reaction scheme for synthesis of the p(AAm-*co*-EG/AA) network.

A PEG-based spacer arm was then covalently grafted to the carboxyl groups on the AA so that biomolecules such as peptides, enzymes, or growth factors could be presented in an accessible manner in aqueous environments. The spacer arm, diamino PEG ($PEG(NH_2)_2$ M_W 3400, Shearwater Polymers, Huntsville, AL, USA) was grafted to the AA moieties by inducing a carbodiimide reaction utilizing 0.200 $g\,ml^{-1}$ $PEG(NH_2)_2$, 0.400 $mg\,ml^{-1}$ 1-ethyl-3-(3-dimethylaminopropyl)carbodiimide (EDC, Pierce, Rockford, IL, USA), and 1.100 $mg\,ml^{-1}$ *N*-hydroxysulfosuccinimide (Sulfo-NHS, Pierce) in 2-(*N*-morpholino)ethanesulfonic acid, 0.100 M, in 0.5 M NaCl conjugation buffer (MES, Pierce) at a pH of 6.0. The reaction was left to proceed for 1 h in a glass dish at room temperature after which samples were again sonicated in ultrapure water to remove unreacted materials. Some samples were set aside at this point to serve as non-adhesive controls in attachment experiments.

On surfaces now containing a free primary amine, due to the diamino PEG spacer arm, a peptide containing a free thiol on a terminal cysteine was covalently linked to demonstrate the usefulness of the approach to create surfaces that exploit biomolecular recognition processes. Sulfosuccinimidyl 4-(*N*-maleimidomethyl)cyclohexane-1-carboxylate (Sulfo-SMCC, Pierce) was used as a heterobifunctional cross-linker at a concentration of 0.500 $mg\,ml^{-1}$ in 0.17 mM sodium borate buffer, pH 7.5, between the terminal amino groups of the $PEG(NH_2)_2$ and the cysteine terminated RGD peptide for the samples that underwent further modification. Samples to be modified were presoaked in buffer solution and then the Sulfo-SMCC was dissolved in buffer and adsorbed onto the samples after the presoak solution had been aspirated off. The solution was left to react the NHS ester with the primary amine of the $PEG(NH_2)_2$ for 30 min. The samples were then sonicated in ultrapure water for 5 min before being immersed in 0.1 mM sodium phosphate buffer, pH 6.6. The final step of peptide conjugation was accomplished by making a 0.300 $mg\,ml^{-1}$ solution of the RGD based peptide in sodium phosphate buffer (pH 6.6) and adsorbing it onto substrates after the presoak solution had been aspirated off. Maleimide terminated surfaces were left to react with the thiol groups in solution for 24 h at 4°C, and then sonicated for 30 min ultrapure water and spun dry. A schematic of the reaction scheme to generate the peptide modified network is shown in Fig. 1B. The peptide sequences used were: Ac–Cys–Gly–Asn–Gly–Glu–Pro–**Arg–Gly–Asp**–Thr–Tyr–Arg–Ala–Tyr–NH_2 (CGGNGEP**RGD**TYRAY) and Ac–Cys–Gly–Asn–Gly–Glu–Pro–**Arg–Gly–Glu**–Thr–Tyr–Arg–Ala–Tyr–NH_2 (CGGNGEP**RGE**TYRAY) (Tana Laboratories, Houston, TX, USA). To reduce the reactivity of the peptides' end groups

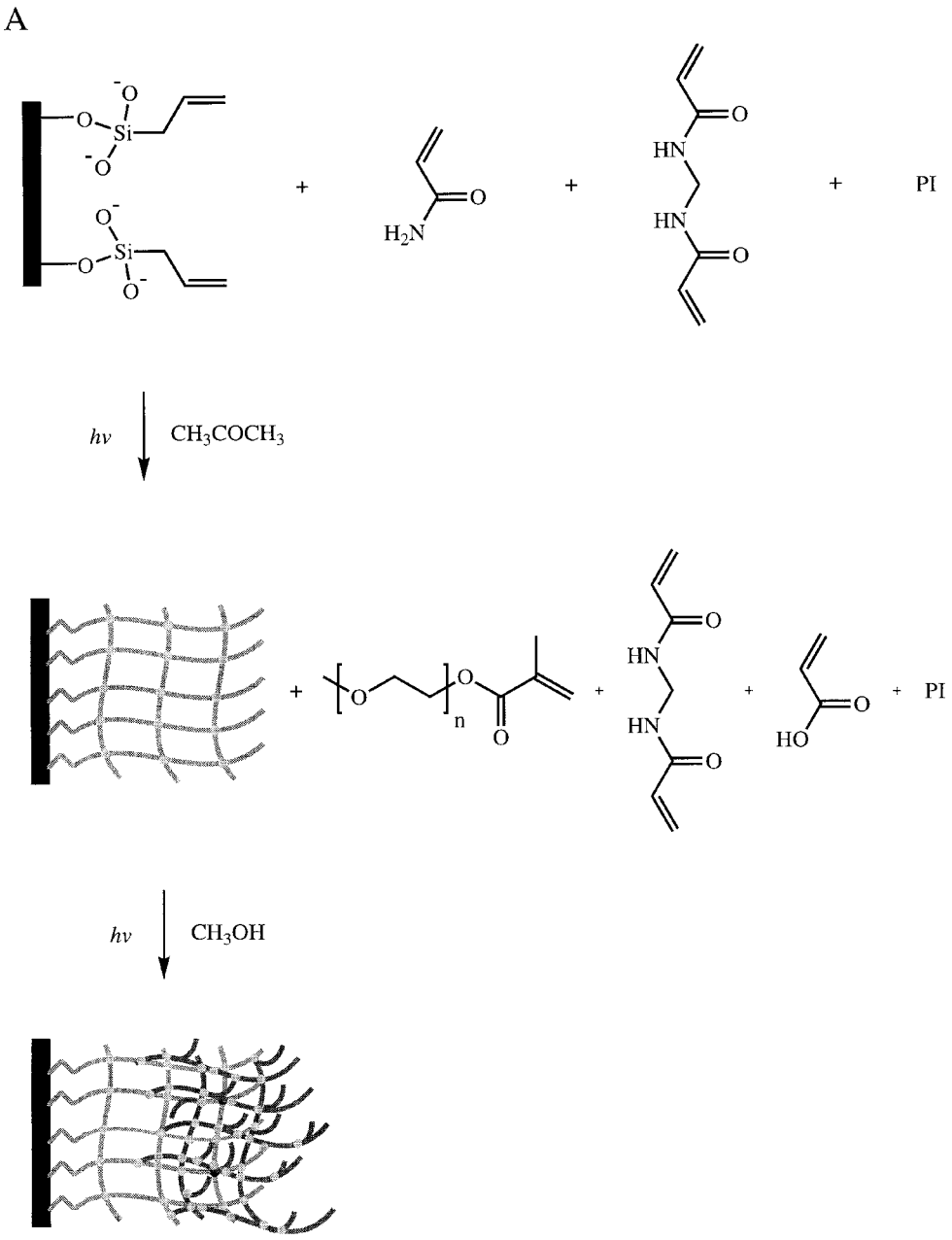

Figure 1. Schematic of the reaction scheme to synthesize the p(AAm-*co*-EG/AA) IPN and modify it with a cysteine-terminated peptide. (a) Synthesis of the p(AAm-*co*-EG/AA) IPN. (b) Grafting the diamino PEG to acrylic acid sites in the IPN, and then coupling the peptide to the free amine on the extended PEG chains. PI: photoinitiator, camphporquinone.

B

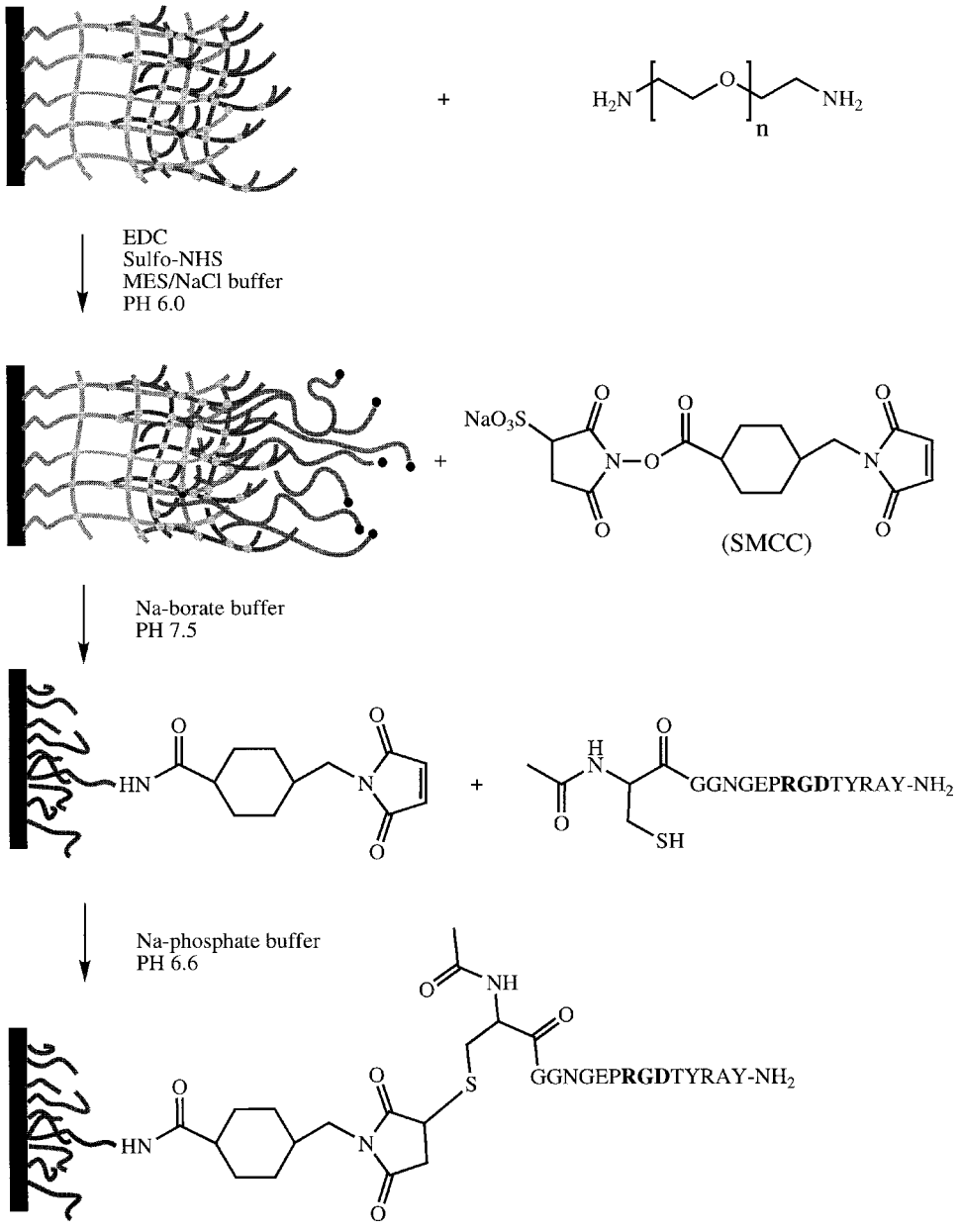

Figure 1. (Continued).

and degradation by exoproteases, the amino and carboxy termini were acetylated (Ac) and amidated (NH_2), respectively. The sequence CGNGEP**RGE**TYRAY was conjugated to SMCC modified samples in a similar manner and served as a control.

Surface characterization

Surfaces were characterized by contact angle measurements, spectroscopic ellipsometry (SE), and X-ray photoelectron spectroscopy (XPS). Contact angle measurements were made using a customized micrometer microscope fitted with a goniometer eyepiece (Gaerther, Chicago, IL, USA). Quasistatic advancing (θ_{adv}) and receding (θ_{rec}) angles were measured as previously described [19]. SE analyses were conducted on a Woollam spectroscopic spectrometer (M44-STD) and XPS analyses were conducted on a Surface Science Instrument (SSI) X-probe spectrometer. Spectroscopic ellipsometry was used to determine the thickness of all layers (oxide through grafted peptide) on silicon wafer samples. All film measurements were taken on samples that had been desiccated overnight. The ellipsometer was equipped with a high-pressure xenon arc lamp (75 W) and was controlled by Wvase32, a data analysis software program supplied with the ellipsometer. Wavelengths from 430 to 720 nm were used in the measurements necessary for determination of thickness. Prior to each measurement, the signal was optimized by focusing the X, Y, and Z settings of the light beam. An offset calibration served to determine the starting analyzer angle, Ψ, and polarizer angle, Δ, with respect to the plane of incidence. The angle of incidence was initially input in the computer at 75 deg and then the actual angle was calculated using a silicon wafer standard with an oxide 24.0 nm thick. The actual angle was usually within 0.5 deg of the set value. Fitting of data was accomplished by methods previously described using a multilayer Cauchy model [14, 18].

In the XPS experiments photoemission was stimulated with a monochromatic Al $K_{\alpha 1,2}$ X-ray source (1486.6 eV). XPS was used to determine percent composition, collect high resolution C 1*s* data, and perform non-destructive depth profiling studies. Briefly, the CH_x peak maximum in the C 1*s* spectrum was set to 285.0 eV to reference binding energy. Survey spectra were collected at a takeoff angle of 55 deg and high resolution C 1*s* spectra were collected at take off angles of 0, 55, and 80 deg[1]. A three layer model by Paynter was used with the standard XPS intensity equation to give percentages of carbon species according to depth [21] and a regularization algorithm developed by Tyler was used to fit the angle-dependent study data from the near surface region of the samples (~ 8 nm) and determine a compositional depth profile (CDP) [22]. The CDP generated in this manner is consistent with, but not necessarily unique to, the experimental angle-dependent XPS data.

[1]Take-off angle (Φ) is defined as the angle between the surface normal and the axis of the analyzer lens system. The solid acceptance angle of the analyzer lens was decreased to 12×30 deg by placing an aperture over the analyzer lens to improve the depth resolution at each takeoff angle [20].

Cell harvest and culture

Rat calvarial osteoblasts (RCOs), were isolated and characterized according to the methods described previously [19]. RCOs were incubated at 37°C in a 5% CO_2, 95% air, 99% relative humidity and were fed a growth media containing Dulbecco's Modified Eagle's Medium (DMEM, Gibco, Grand Island, NY, USA), 15% heat-inactivated fetal bovine serum (FBS), 1% penicillin-streptomycin, 1% fungizone, HEPES buffer (15 mM), sodium pyruvate (1 mM) and ascorbic acid (5 mg ml^{-1}) twice weekly, and used between passages 2 and 3. When cells used in experiments grew to confluence and exhibited nodule formation, the media was changed to mineralization media: DMEM, 15% FBS, 1% penicillin-streptomycin, 1% fungizone, HEPES buffer (15 mM), sodium pyruvate (1 mM), ascorbic acid (50 mg ml^{-1}), calcium (additional 1.2 mM), β-glycerophosphate (10 mM), insulin (2.5 mg ml^{-1}), transferrin (2.5 mg ml^{-1}), and selenium (92.5 mg ml^{-1}).

Cell viability

Cell viability was determined for cultures used in the attachment and proliferation assays. Cells were collected from 75 cm^2 culture flasks upon exposure to 0.5 mM ethylene glycol-bis[β-aminoethyl ether]-N,N,N',N'-tetraacetic acid (EGTA) for 20 min, and then the culture flasks were rinsed with PBS in an attempt to remove 90–95% of the cells. Cell suspensions were then centrifuged for 5 min and the pellet resuspended in growth media or DMEM. Cell viability was examined via trypan blue exclusion: viable cells were impermeable to trypan blue (Sigma), whereas non-viable cells were permeable [23, 24]. A drop of the cell-trypan blue mixture was transferred to a glass slide, a cover slip was placed on top, and viable cells were counted using phase contrast microscopy (10 × objective) at five adjacent, but not overlapping fields. The area examined in each field was 0.0063 cm^2, and at least 100 cells were counted in each field between 30 s and 2 min after mixing. Percent viability was calculated as: nonstained cells/(stained + nonstained cells) × 100. Percent viability was taken into account when reporting results from cell attachment experiments.

Cell attachment

For attachment experiments, cells that had grown out of the bone chips (pass 2) were suspended in serum and serum-free media to see if adhesive interactions occurred independently of proteins in the media. The density of cells in DMEM and growth media was determined with a hemocytometer (cells ml^{-1}) and then related to (cells cm^{-2}) according to the volume of solution plated and the area of the substrates. Cells were plated on either RGD modified p(AAm-*co*-EG/AA), RGE modified p(AAm-*co*-EG/AA), PEG$(NH_2)_2$ modified p(AAm-*co*-EG/AA), or clean quartz substrates at an approximate density of 1.5×10^4 cells ml^{-1}. Plated cells were incubated for 4 h, rinsed three times with phosphate buffered saline (PBS, Gibco,

Grand Island, NY, USA) and then maintained in growth media containing 15% FBS. One set of $PEG(NH_2)_2$ modified p(AAm-*co*-EG/AA) samples was reseeded with cells 2 days after the initial plating to see if the substrates had become more conductive to cells adhering.

Cell attachment to the various surfaces was assessed via digital-based microscopy, acquisition, and analyses. A program was written in Oncor Image (Gaithersburg, MD, USA) to move a XYZ computer controlled stage to ten predetermined positions. Ten images were taken of each group of samples and each group consisted of at least three samples. The images were taken with a Photometrics Sensys CCD (Tucson, AZ, USA) camera that enabled rapid data acquisition for subsequent analysis. The number of cells attached per sample was compared to the number of cells attached to the other samples from the same type of substrate (same group). Next, the number of cells attached was compared for the three samples of each group according to serum or serum-free media conditions. Cell attachment data on four different types of surfaces: RGD modified p(AAm-*co*-EG/AA); RGE modified p(AAm-*co*-EG/AA); $PEG(NH_2)_2$ modified p(AAm-*co*-EG/AA); and clean quartz substrates were compared to each other. Lastly, the average number of cells attached per viewing field per type of sample was calculated as a ratio of the initial plating density to give information on cell attachment as a function of viable cell plating. Image analysis of cells attached to the RGD modified p(AAm-*co*-EG/AA) at 4 h were also used to calculate average cell area according to serum or serum-free media conditions. Average cell area calculations were not performed on RGE modified p(AAm-*co*-EG/AA), $PEG(NH_2)_2$ modified p(AAm-*co*-EG/AA), or clean quartz substrates because of the low number of cells attached to these surfaces.

Cell proliferation kinetics

Multiple sets of RGD modified p(AAm-*co*-EG/AA) modified p(AAm-*co*-EG/AA) substrates samples were prepared for testing cell growth kinetics. Experiments were conducted with bone cells from digest or bone chip outgrowth. Experiments began in an identical manner to that of cell attachment experiments and at similar densities. After the initial 4 h incubation period, samples were thoroughly rinsed three times and then the number of attached cells was calculated as described above. This number represented the first time point for cell surface coverage and cell population doubling data. After 4 h, all cultures were maintained in growth media, so different conditions (serum versus serum-free containing media) were only present during the first 4 h. Cultures were fed every other day and images were taken at least every other day to obtain cell surface coverage and cell population doubling data. Theoretical population doubling times were determined using a nonlinear optimization code (GRG2) in Solver within Excel [25]. Cultures that grew to confluence and exhibited nodule formation, typically after 10–15 days, were changed to mineralization media and still fed every other day.

Phenotypic characterization

Cells that had grown to confluence were subsequently cultured in mineralization media for approximately 10–15 days ($\sim$25 days total), and were characterized by alkaline phosphatase (AP) (Sigma) and Von Kossa assays [26]. $PEG(NH_2)_2$ grafted p(AAm-*co*-EG/AA) IPNs were used as controls. The AP stains for membrane bound alkaline phosphatase which is an early indicator of the osteoblast phenotype. The Von Kossa assay tests for calcium in the presence of phosphate and is therefore a general measure of mineralization of the ECM in both culture and histologic sections.

RESULTS

Surface characterization

The results of the contact angle measurements are reported in Table 1. ATC grafted onto the SiO_2 was relatively hydrophobic and showed a moderate amount of hysteresis attributed to surface heterogeneity. The cross-linked p(AAm) layer was hydrophilic and exhibited negligible hysteresis [$\Delta(\cos\theta)$]. Grafting of PEG/AA led to a significant increase in θ_a, but not in θ_r, with wettability consistent with a mixed layer of EG and AA. Addition of the $PEG(NH_2)_2$ led to a significant increase in θ_r but not in θ_a. Contact angle and hysteresis data for the $PEG(NH_2)_2$ layer was very close to that of oligo(ethylene glycol) terminated self assembled monolayers (SAMs) reported by Pale-Grosdemange *et al*. [27], which indicated that the grafted $PEG(NH_2)_2$ was segregated at the surface and that the density was similar to that of the oligo(ethylene glycol) SAMs. Reaction of SMCC with the amine terminated PEG chains once again increased θ_a more than θ_r, and the final RGD or RGE couple to the maleimide group of SMCC did not significantly change either θ_a or θ_r. Peptide modification of the non-adhesive base layers served to slightly

Table 1.
Advancing (θ_a) and receding (θ_r) water contact angles ($\pm$ SD) and hysteresis data on IPN modified surfaces

Surface	Contact angle (deg)		Hysteresis $\Delta(\cos\theta)$	
	θ_a	θ_r		
Si/SiO_2	< 10	< 10	0.00	$n = 3$
ATC	68.3 ± 2.9	49.8 ± 3.8	0.28	$n = 9$
p(AAm)	13.0 ± 2.9	< 10	0.01	$n = 10$
PEG/AA	33.3 ± 6.7	12.0 ± 3.2	0.14	$n = 6$
$PEG(NH_2)_2$	35.4 ± 1.3	23.5 ± 1.1	0.10	$n = 8$
SMCC	42.4 ± 1.4	25.1 ± 1.7	0.17	$n = 8$
RGE	39.9 ± 3.3	24.5 ± 2.1	0.14	$n = 3$
RGD	43.9 ± 1.4	28.0 ± 1.7	0.16	$n = 8$

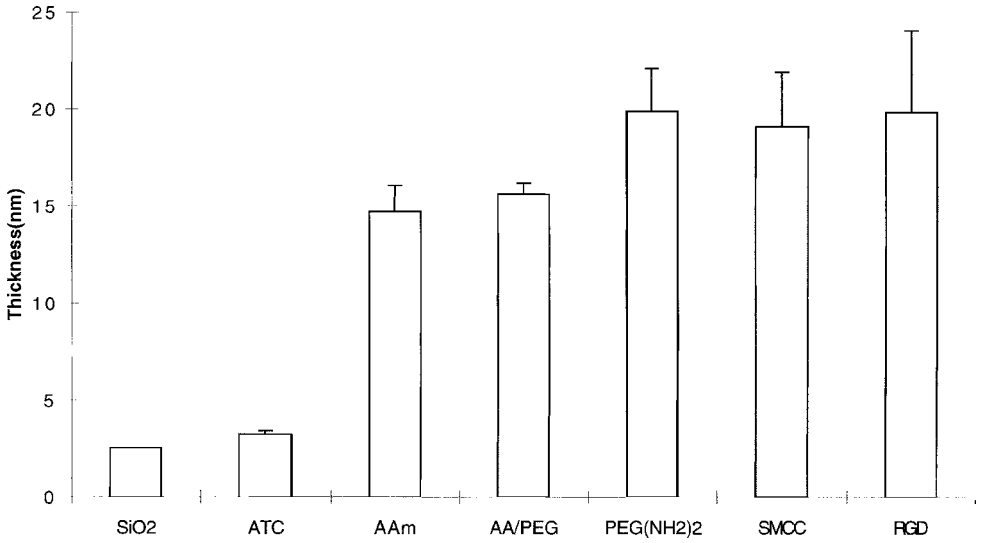

Figure 2. Thickness data during each stage of the synthesis of the peptide modified p(AAm-*co*-EG/AA) IPN. The thickness of each layer was determined by spectroscopic ellipsometry on silicon substrates as described in the text.

increase both the advancing and receding water contact angles to 43.9 ± 1.4 deg and 28.0 ± 1.7 deg, respectively. Hysteresis was equal to 0.16, which indicates that some surface restructuring was probably occurring upon addition and removal of water from the surface. Slight surface heterogeneities may also exist at a nanoscopic level between amine terminated PEG regions and areas modified with RGD.

Figure 2 shows the results of ellipsometry measurements taken on samples at all stages of the grafting scheme. The thickness of the oxide, silane, and p(AAm) layers were similar to values previously reported [18]. Only a slight increase in thickness was observed at the PEG/AA stage of the modification, but then a substantial increase in thickness was observed upon carbodiimide reaction of $PEG(NH_2)_2$ with the carboxyl groups present in the acrylic acid. Layer thickness data for subsequent modification of the $PEG(NH_2)_2$ grafted IPN did not change significantly since the thickness of SMCC/peptide coupling led to only a small increase in overall thickness ($\sim$2 nm), which was within the standard deviation of the thickness values for the IPN.

The XPS data supported the model of an IPN formed between p(AAm) and PEG/AA with a $PEG(NH_2)_2$ overlayer. XPS atomic percent data are shown in Table 2. Carbon content progressively increased as the graft was built up. Oxygen content dropped through the grafting of the PEG/AA materials as the carbon content steadily increased. The polymerization of AAm led to a jump in nitrogen content, but subsequent layering showed a decrease in nitrogen content, until grafting of the peptide. The Si signal steadily decreased throughout all grafting

Table 2.
XPS elemental analysis and elemental ratios of grafted layers on silicon substrates

	XPS (at.%)				
	C	O	N	Si	S
Oxygen plasma	8.9	49.3	0.4	41.4	
ATC	20.9	48.2	0.3	30.6	
p(AAm)	35.6	32.9	6.7	24.9	
PEG/AA	63.0	29.9	5.4	1.7	
$PEG(NH_2)_2$	67.4	31.2	1.1	0.3	
SMCC	67.7	31.1	1.0	0.2	
RGD	67.7	30.0	2.1	0.1	0.1

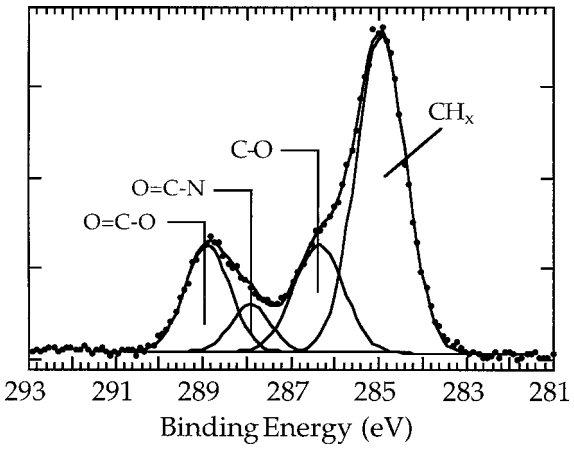

Figure 3. XPS high resolution C 1*s* spectrum taken at a 55 deg take-off angle of the PEG/AA layer grafted into the p(AAm) layer. Photoinitiation of the p(AAm) network was in acetone, and the PEG/AA layer was polymerized in methanol.

steps, indicative of attenuation through the grafted layers. Sulfur content was only detected in the RGD layer, and was present in trace concentrations from the cysteine residue in the peptide.

Figure 3 shows a C 1*s* spectra of samples modified through the PEG/AA stage. Four peaks were determined to be present representing the hydrocarbon, ether, amide, and acid moieties. Table 3 shows C 1*s* percentages of specific carbon species as a function of depth for samples of which the top layer was PEG/AA. A three layer model by Paynter and the standard XPS intensity equation were used to calculate percentages of the carbon species [21]. In addition, Fig. 4 shows a depth profile determined using an algorithm developed by Tyler *et al.*, which corroborated the same compositional trends [20, 22]. The surface of the PEG/AA layer exhibited some PEG chain enrichment, as compared to either amide or acid contribution,

Table 3.
XPS High resolution carbon (C 1*s*) chemical species (hydrocarbon, ether, amide, and ester/acid, respectively) percentages as a function of depth below the surface of the PEG/AA layer grafted to the p(AAm) layer

Carbon species	C 1*s* species percentages by depth		
	0–1.0 nm	1.0–3.0 nm	> 3.0 nm
CH_x	49	62	58
C—O	32	6	16
O=C—NH_2	8	10	14
O=C—O	11	22	12

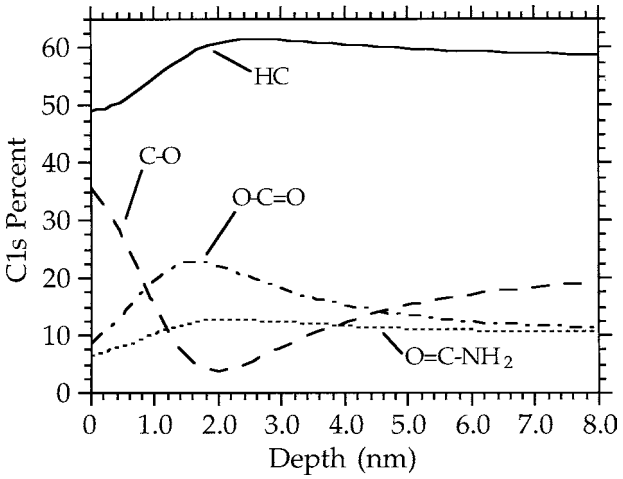

Figure 4. XPS C 1*s* depth profile of the p(AAm) layer polymerized in acetone, and PEG/AA layer in methanol. The origin of the abscissa (0 nm) represents the polymer-ambient interface. The CDP only models penetration up to 8 nm, which is approximately 45% of the total thickness of the p(AAm-*co*-EG/AA) IPN.

and was consistent with the contact angle measurements. Just below the ambient-polymer surface, in the range from 1.0–3.0 nm, the acrylic acid appears to be enriched and the PEG is somewhat depleted. Below 3.0 nm in these samples, there is a rather constant composition of ether, amide, and acid moieties. Using the three layer Paynter model, the calculated C 1*s* percentages of specific carbon species were obtained at 0, 55, and 80 deg. Table 4 lists these calculated as well as experimental results from the peak fitting the C 1*s* spectra. The differences between calculated and experimental values are well within experimental error. Figure 5 shows stacked C 1*s* plots of samples modified from the p(AAm) through the RGD peptide stage. Peaks shift from predominant hydrocarbon and amide peaks to a predominant PEG ether peak; a shoulder is seen on the PEG/AA curve indicative

Table 4.
XPS angle-dependent study of the C 1*s* spectra of RGD modified p(AAm-*co*-EG/AA) at take-off angles of 0, 55, and 80 deg. Various carbon chemical species (hydrocarbon, ether, amide, and ester/acid, respectively) percentages are listed as a function of takeoff angle for the PEG/AA layer grafted to the p(AAm) layer. Calculated as well as experimental values are listed

Carbon species	C 1*s* percentages at each takeoff angle					
	0 deg		55 deg		80 deg	
	Calc.	Exp.	Calc.	Exp.	Calc.	Exp.
CH_x	57.0	57.5	55.8	55.8	51.2	51.1
C—O	16.9	16.9	18.9	18.5	27.8	28.2
O=C—NH_2	11.0	10.6	9.9	10.0	8.4	8.0
O=C—O	15.1	15.0	15.4	15.7	12.8	12.7

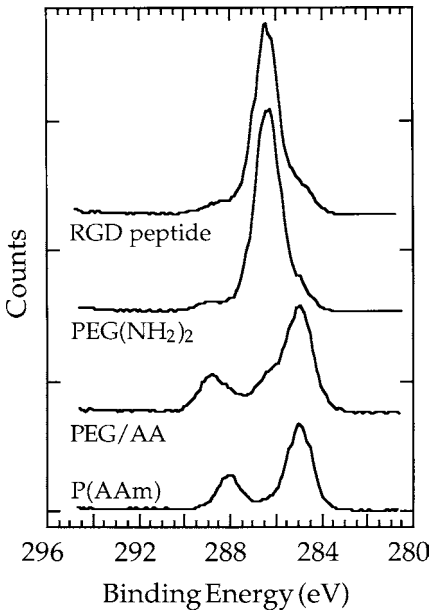

Figure 5. Stacked plot of XPS C 1*s* spectra taken at a 55 deg take-off angle of substrates modified through the p(AAm), p(AAm-*co*-EG/AA) IPN (PEG/AA), diamino PEG grafted IPN ($PEG(NH_2)_2$), and RGD peptide coupling stages of the synthesis.

of the carboxyl moieties. Although the SE results do not report drastic changes in thickness above the p(AAm) layer, the XPS atomic percent data (Table 2) and high resolution C 1*s* spectra (Fig. 5) both confirm that the intended modifications took place.

Cell attachment

The percent of plated cells attached after a 4 h incubation is shown in Table 5. $PEG(NH_2)_2$ reseed represents those samples re-plated with cells 2 days after the initial cell plating. These samples were incubated and exposed to serum containing media up to the reseeding experiment. $PEG(NH_2)_2$ modified p(AAm-*co*-EG/AA), $PEG(NH_2)_2$ modified p(AAm-*co*-EG/AA) reseed, and clean samples did not support cell adhesion or growth. On the $PEG(NH_2)_2$ modified samples (initial and reseeded) less than one percent of plated and viable cells attached under either serum or serum-free conditions. The morphology of the few cells that were attached was spherical, as opposed to spread. Clean substrates supported adhesion of about 2 and 3% of plated cells in serum and serum-free containing media, respectively; and these cells spread to a greater extent on this surface compared to the $PEG(NH_2)_2$ modified networks. RGE modified p(AAm-*co*-EG/AA) supported adhesion of approximately 7% of viable cells with serum, and 1% without serum in the media; spreading was greater on surfaces plated in serum. In contrast, RGD modified p(AAm-*co*-EG/AA) supported adhesion of about 22 and 25% of viable cells plated in the presence or absence of serum in the media. Attachment of cells on RGD modified samples was significantly higher than on clean, $PEG(NH_2)_2$ modified, or RGE modified samples (MANOVA, $p < 0.0002$, *post-hoc* Newmann–Keuls) with or without the addition of serum to the media. Attachment of cells among clean, $PEG(NH_2)_2$ modified samples, and RGE modified p(AAm-*co*-EG/AA) was not significantly different under serum-free conditions, but was significantly different (all groups) with serum (MANOVA, $p < 0.05$, *post-hoc* Newmann–Keuls). Within the same type of group, the only samples that showed a significant difference between serum versus serum-free conditions was the RGE modified p(AAm-*co*-EG/AA) (ANOVA, $p < 0.0002$).

Table 5.
Percent cells attached to $PEG(NH_2)_2$, clean, RGE modified p(AAm-*co*-EG/AA), and RGD modified p(AAm-*co*-EG/AA) networks. Cells were incubated for 4 h with (+) or without serum (−) in the media and were then rinsed three times in PBS before the analysis was performed. The viability of the cell suspensions without serum in the media was 67%, and for serum containing media was 71%

	% Cells attached	
	+ serum	− serum
$PEG(NH_2)_2$	0.09 ± 0.24	0.09 ± 0.19
$PEG(NH_2)_2$ (reseed)	0.34 ± 0.19	
Clean	2.16 ± 1.11	3.07 ± 1.88
RGE	7.14 ± 4.31	1.24 ± 1.11
RGD	21.83 ± 7.25	25.49 ± 9.55

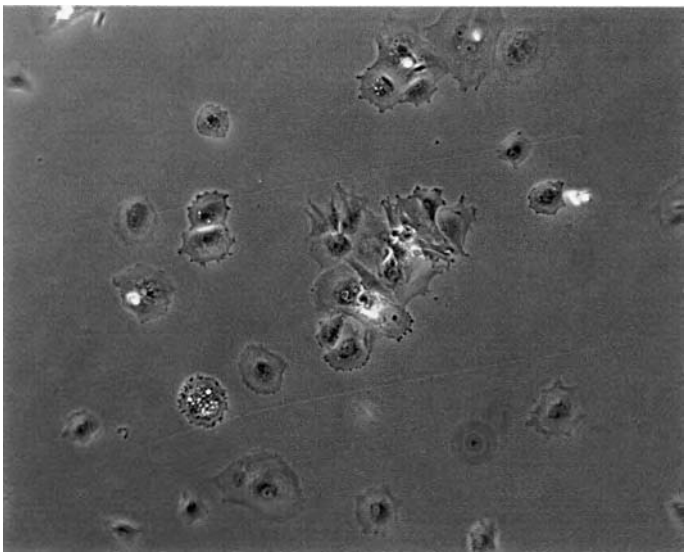

(a)

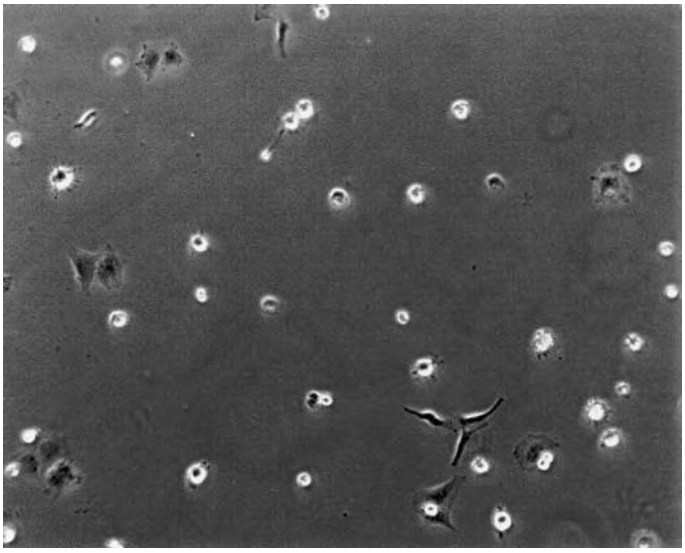

(b)

Figure 6. Cell morphology on RGD modified p(AAm-*co*-EG/AA) networks as a function of serum in the media. (a) Cells incubated for 4 h with serum in the media. (b) Cells incubated for 4 h without serum in the media. All surfaces plated with cells were rinsed three times with PBS before the images were collected.

Although there was no significant difference between level of attachment between serum and no serum media conditions for the RGD modified p(AAm-*co*-EG/AA), there was a significant difference in average cell area per group (ANOVA, $p < 0.0002$, *post-hoc*, Newmann–Keuls). Average cell area of samples incubated for 4 h in serum containing media was $7377.0 \pm 4029.0\ \mu m^2$ and without serum cell area was $3221.4 \pm 1913.8\ \mu m^2$. Figure 6 exemplifies differences in cell morphology between samples initially exposed to serum and those not introduced to serum until after rinsing at 4 h.

Cell proliferation kinetics

Cell proliferation was monitored on RGD modified p(AAm-*co*-EG/AA) IPNs to obtain information on cell growth kinetics, and percent cell coverage as a function of time. Figure 7 shows an exemplary proliferation plot of cells plated with and without serum on RGD modified p(AAm-*co*-EG/AA). These samples were rinsed after the first 4 h of incubation and were then maintained in growth media. It should be noted that Fig. 7 represents the growth kinetics of just one plating experiment and that the standard deviations drawn represent the standard deviation in number of cell cm^{-2} of the different images taken from the same batch of samples from the same plating experiment. Each plating experiment performed revealed slightly different kinetics, and theoretical population doubling times varied from 1.5 to 3.5 days regardless of serum being present during the first 4 h. Figure 8 shows an exemplary plot of cell surface coverage as a function of time. Similarly, these are the results of one plating experiment, and batch to batch differences

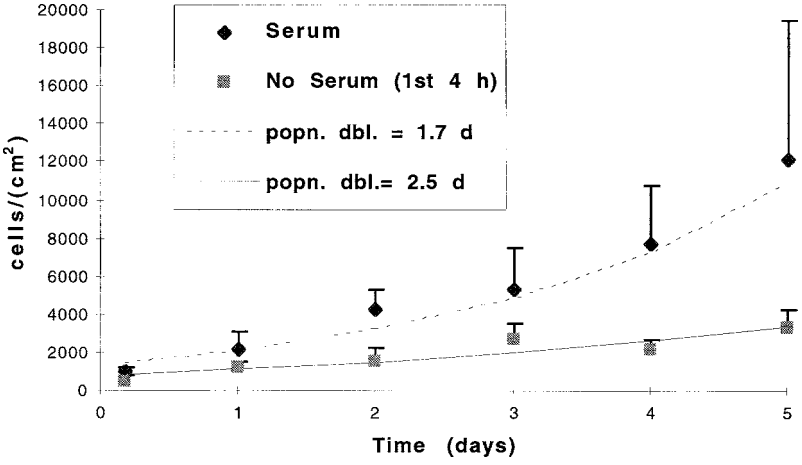

Figure 7. Proliferation of cells on RGD modified p(AAm-*co*-EG/AA) networks. The top curve (◆) is for samples that began in serum containing media, and the bottom curve (■) is for samples that began without serum in the media for the first 4 h, and then were rinsed and changed to serum containing media for the duration of the experiment. Theoretical population doubling curves are included in the figure for samples started under serum and no serum conditions.

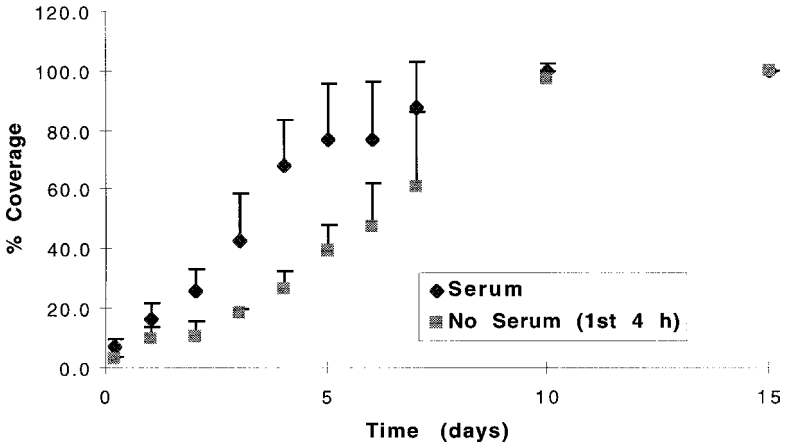

Figure 8. Cell surface coverage as a function of time (first 12 days). The top curve (◆) is the result of an experiment that began in serum containing media (modified surfaces were rinsed after 4 h and pictures were taken for analysis). The bottom curve (■) is the result of an experiment that began without serum in the media for the first 4 h, and then samples were rinsed and changed to serum containing media.

existed. By approximately day ten samples from both groups were confluent and nodule formation was evident. When the media was subsequently changed to mineralization media, evidence of calcification occurred after approximately 10 more days in culture. Figure 9 shows a nodule cluster grown on a RGD modified p(AAm-*co*-EG/AA) sample.

Phenotypic characterization

Cells grown to confluence on RGD-p(AAm-*co*-EG/AA) samples stained positive for membrane bound alkaline phosphatase. In addition, the Von Kossa staining method was used to test for formation of mineralized tissue. The top row of Fig. 10 shows a picture of a positive alkaline phosphatase staining result of cells cultured on RGD modified p(AAm-*co*-EG/AA) for approximately one month (Fig. 10A) next to the staining result of a $PEG(NH_2)_2$ modified p(AAm-*co*-EG/AA) sample that was maintained under the same media conditions (Fig. 10B). The bottom row of Fig. 10 shows a picture of positive Von Kossa staining of cells cultured on RGD modified p(AAm-*co*-EG/AA) for approximately one month (Fig. 10C) next to the staining result of a $PEG(NH_2)_2$ modified p(AAm-*co*-EG/AA) sample that was maintained under the same media conditions (Fig. 10D). The $PEG(NH_2)_2$ modified p(AAm-*co*-EG/AA) was chosen as a control surface on the basis that low molecular weight PEG has been shown to calcify, theoretically through the mechanism of chelating of calcium ions [28]. Calcification of the $PEG(NH_2)_2$ modified p(AAm-*co*-EG/AA) IPN was not significant (Fig. 10D), and is consistent with commonly observed background staining.

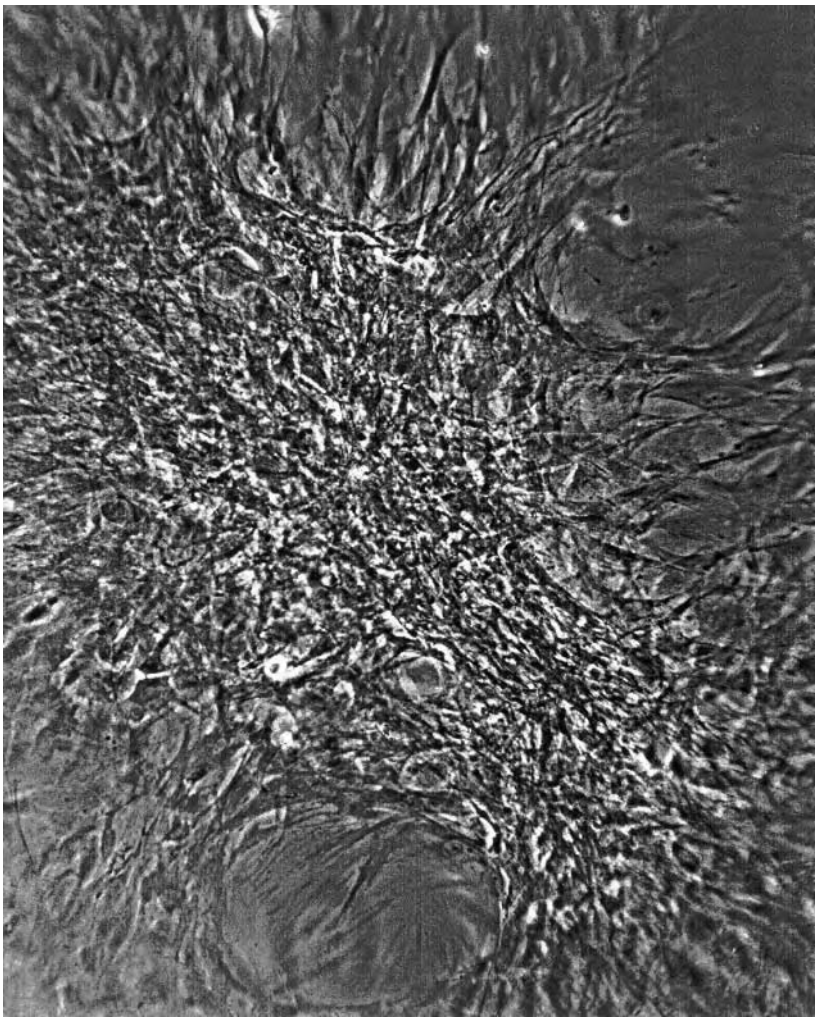

Figure 9. Typical osteoblast nodule cultured *in vitro* (15 days) on a RGD modified p(AAm-*co*-EG/AA) quartz surface.

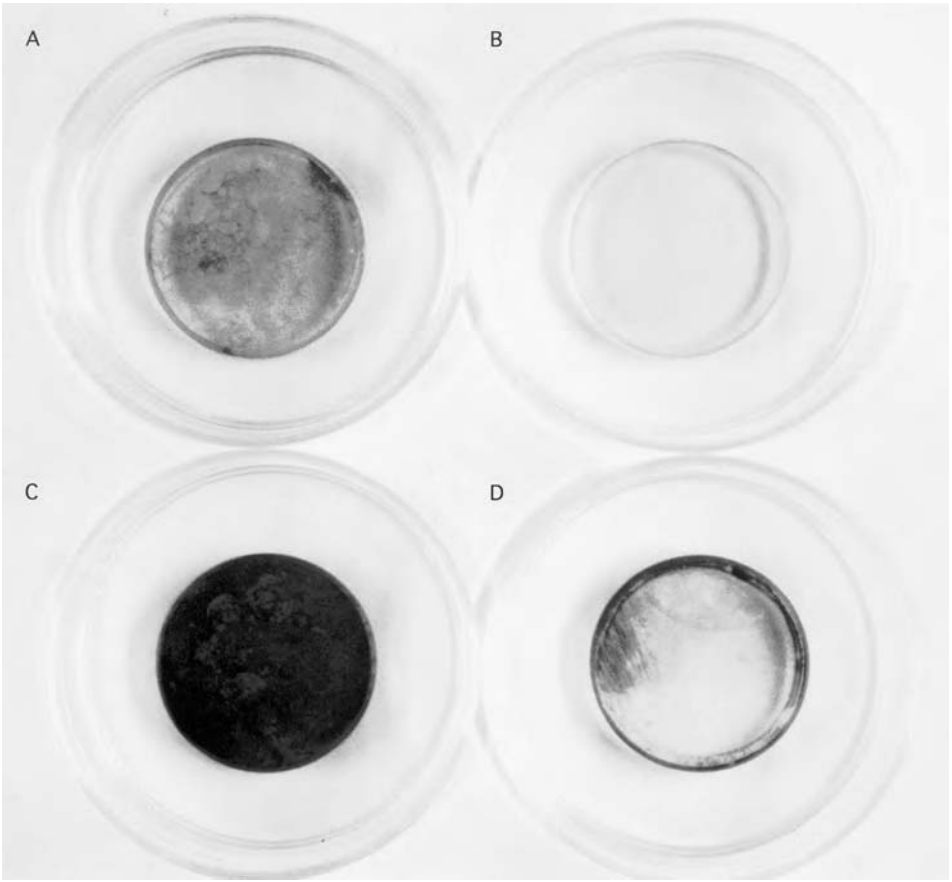

Figure 10. Alkaline phosphatase and Von Kossa staining results of RGD modified p(AAm-*co*-EG/AA) IPNs, and PEG$(NH_2)_2$ grafted p(AAm-*co*-EG) IPNs. Alkaline phosphatase (membrane bound) stained samples are presented in the top row (A and B), and Von Kossa stained samples are present in the bottom row (C and D). The left column contains the RGD modified p(AAm-*co*-EG) quartz samples (A and C), and the right column contains the PEG$(NH_2)_2$ modified p(AAm-*co*-EG) quartz samples (Band D).

DISCUSSION

A nonadhesive IPN of acrylamide, ethylene glycol, and acrylic acid was successfully functionalized with a biomimetic peptide in order to attract and accelerate the adhesion of osteoblasts in the presence or absence of serum proteins. Biomolecular recognition processes were established, while the system retained the ability to minimize non-specific protein binding interactions. This work is relevant to the design of implants contacting bone and is essentially universal in the capacity to couple bioactive molecules to material surfaces. Current ceramic, metallic, and polymer implants can be modified with this coating and a myriad of biological molecules that includes peptides, proteins, growth factors, and DNA can be covalently linked to the PEG$(NH_2)_2$ modified IPN.

The surface characterization data support the theory that the PEG/AA layer formed an IPN with the underlying p(AAm) layer, and after grafting, the $PEG(NH_2)_2$ chains were enriched at the surface. XPS compositional and C 1*s* spectra were used to establish the chemical modification of all layers, and SE was used to determine the coating thickness during each stage of the graft. The PEG/AA layer only increased the thickness of the network by ~ 1 nm when the p(AAm) layer was ~ 12 nm thick (Fig. 2). The Tyler algorithm (used to generate Fig. 4) and the Paynter model (used to for Tables 3 and 4) both indicated that the PEG ether and acrylic acid carboxyl moieties were both present in appreciable quantities well below the polymer ambient interface (to at least 8 nm below the surface according to the Tyler algorithm). The thickness increase of ~ 1 nm and the fit of the data that shows the PEG ether, AA carboxyl, and p(AAm) amide all displayed at least a 10% contribution to the high resolution XPS C 1*s* percentage, suggest that there is an approximate 7 nm layer of interpenetration of the different polymer networks. Although there is a large putative IPN region, it is noted that there is some PEG enrichment and AA depletion at the near surface region (outer 2 nm). It is thought that this is due to diffusional and mass stochastic limitations. The AA is a smaller molecule and is present at a higher concentration than the PEG; it may be that the lower molecular weight AA is able to diffuse into the P(AAm) to a greater extent during the adsorption step which precedes the photoinitiation. Wettability data also supports the claim that the $PEG(NH_2)_2$ chains were preferentially distributed at the surface after grafting to the IPN.

Cell attachment data indicated that both clean and $PEG(NH_2)_2$ modified p(AAm-*co*-EG/AA) surfaces were non cell binding. There was neither cell spreading nor proliferation on $PEG(NH_2)_2$ modified IPN, even when the surfaces were challenged with secondary inoculation. These results imply that protein adsorption was minimized, which limited cell adhesion. If significant protein adsorption had taken place on the $PEG(NH_2)_2$ modified quartz as a result of endogenous protein synthesis, then cells would have attached to the conditioned substrates during the second inoculation. A few cells did attach and spread on clean surfaces; however, no significant proliferation took place, and none of the samples grew to confluence. Other studies have identified that a critical level of cell inoculation or attachment is necessary for substantial cell culture proliferation to occur [29–32].

RCOs specifically interacted with the RGD modified p(AAm-*co*-EG/AA) surfaces. Approximately 25% of viable plated cells attached to the RGD modified IPN regardless of the presence of serum in the media, whereas serum was required for cell adhesion ($\sim 7\%$ of cells) to RGE modified p(AAm-*co*-EG/AA) surfaces. As levels of attachment between RGD modified samples plated with or without serum in the media were not significantly different, it was initially thought that serum proteins were not influencing the system during attachment. Allegedly, binding of cells to the modified surfaces in the absence of serum can only take place through the interaction of the peptide and the integrins within the cell membrane, indicating the specificity of the system. The observation of cell attachment to the RGE surface

in serum containing media may depend on adsorption/conjugation of proteins with the peptide. Thus, the BSP-based RGD peptide was a specific adhesion promoter, and RCO attachment to the RGE modified p(AAm-*co*-EG/AA) surfaces was a non-specific event associated with the peptide.

Spreading of the cells on the RGD modified p(AAm-*co*-EG/AA) surface was significantly different depending on whether or not there were serum proteins present in the media. Projected cell areas were twice as large on average on samples incubated in growth media as opposed to samples incubated in DMEM. This suggested that soluble serum molecules influenced events that drive cell spreading once the cell has accomplished the critical step of attaching to the substrate. Serum containing media has a number of constituents including proteins, growth factors, hormones, lipids, vitamins, and amino acid. Components of serum surrounding and/or contacting the cells may have increased the signal to cells and triggered a cell transduction mechanism that then facilitated spreading. The necessity of serum and growth factors for rapid propagation of cell cultures has been previously addressed by Ozturk and Palsson [33]. It is important to note that cells in either initial media condition spread enough to maintain their phenotype. Osteoblasts are an anchorage-dependent cell type, and need to attach and spread in order to divide and become confluent. This is one of the main reasons why cells struggled to survive on clean and $PEG(NH_2)_2$ modified p(AAm-*co*-EG/AA) surfaces. On RGD modified p(AAm-*co*-EG/AA) surfaces nominal spreading was not a problem and proliferation proceeded rapidly. However, due to the more favorable spreading reaction of cells attached to the RGD modified surface with serum present, cells plated in serum entered the proliferative stage of cell development earlier than the 4 h no serum batch, and cell growth kinetics (proliferation and surface coverage) proceeded more rapidly in general for these cells.

The peptide sequence from BSP seems to be very effective in recruiting the attachment of RCOs. BSP binds Ca^{2+}, is recognized by multiple integrins, and its phosphorylation has been implicated in regulating cell attachment [7, 34]. The efficacy of the BSP-RGD peptide in recruiting the attachment of RCOs most likely aids the whole system by decreasing time to confluence in cultures. This would in turn regulate differentiation of cultures and subsequent calcification of bone-forming cells. Cells that grew to confluence tested positive for membrane bound alkaline phosphatase. Cell cultures that had been incubated in mineralization media after nodule formation also demonstrated positive Von Kossa staining. These combined staining results indicated that in addition to the peptide modified surfaces being able to sustain viable cells and support growth, the cells that proliferated were of the intended phenotype and were able to deposit a mineralized ECM *in vitro*.

Ligand density has been identified as a critical determinant in cell-materials interactions. At this point, the ligand density on the RGD modified p(AAm-*co*-EG/AA) surfaces has not been quantified. Massia and Hubbell determined that a minimum grafted peptide density of 0.01 pmol cm^{-2} was necessary to mediate complete cell spreading [10]. Lauffenberger and Horwitz [35] previously

determined that an optimal ligand density exists for cell migration. The present system must be within the desirable ligand density envelope for cell adhesion and spreading, but the effect of migration with the rat calvaria osteoblasts is not known. Future studies will optimize this coating for cell spreading in order to decrease time for cells to progress to a proliferative state.

The RGD modified IPN has a variety of logical applications for biomedical implants, such as coatings on total joint replacements or dental implants. The coating could accelerate attachment of the desired type of cell, while minimizing competing reactions, such as bacterial fouling or prolapse caused by fibroblast invasion of the wound site. These IPNs also accomplish the goal of providing such desirable qualities to metal oxide surfaces, which impart justifies the synthesis scheme chosen. An additional advantage is evident in dental implant design, or other devices that contact multiple tissues in service, where different areas of the implant could be coated with either the non-adhesive or biologically modified coating to elicit different reactions on different areas of the implant. In essence, epithelial cell downgrowth could be prevented in apical tooth areas, and osteoblast cell attachment could be targeted in bone contacting areas.

CONCLUSION

An IPN coating of RGD modified p(AAm-*co*-EG/AA) was engineered to minimize non-specific interactions, such as protein adsorption, and simultaneously target adhesion of mammalian cells. The IPN is amenable to substrate materials containing either metal oxides or abstractable protons, and therefore has a multitude of potential applications in coating corrosion resistant metal alloys and polymers. RCOs plated on RGD modified p(AAm-*co*-EG/AA) selectively attached and spread in significantly greater quantities than on control surfaces. Under the specified conditions, cell cultures inoculated and grown to confluence on RGD modified p(AAm-*co*-EG/AA) substrates formed mineralized sheets of ECM across the surface.

Acknowledgements

This research was supported by NIH R01 AR43187, NIH/NIDR T32 DE07042, NIH RR01296, and the Whitaker Foundation. A. Rezania and C. H. Thomas are acknowledged for the assistance with image processing. Helpful discussions with Paul Drumheller are also gratefully acknowledged.

REFERENCES

1. P. R. Kuhl, L. G. Griffith-Cima, *Nature Med.* **2**, 1022 (1996).
2. S. P. Massia and J. A. Hubbell, *Biomed. Mater. Res.* **25**, 223 (1991).
3. P. D. Drumheller, D. L. Elbert and J. A. Hubbell, *Biotechnol. Bioeng.* **43**, 772 (1994).

4. D. B. Holt, R. C. Eberhart and M. D. Prager, *ASAIO J.* **40**, M858 (1994).
5. M. D. Pierschbacher, E. G. Hayman and E. Ruoslahti, *Proc. Natl Acad. Sci.* **80**, 1224 (1983).
6. M. D. Pierschbacher and E. Ruoslahti, *Proc. Natl Acad. Sci.* **81**, 5985 (1984).
7. E. Ruoslahti and M. D. Pierschbacher, *Science* **238**, 491 (1987).
8. C. Buck and A. F. Horwitz, *Ann. Rev. Cell Biol.* **3**, 179 (1987).
9. M. J. Humphries, *J. Cell Sci.* **97**, 585 (1990).
10. S. P. Massia and J. A. Hubbell, *J. Cell Biol.* **114**, 1089 (1991).
11. S. P. Massia and J. A. Hubbell, *Ann. NY Acad. Sci.* **589**, 261 (1990).
12. H. B. Lin, Z. C. Zhao, C. Garcia-Esceverria, D. H. Rich and S. L. Cooper, *J. Biomater. Sci. Polymer Edn* **3**, 217 (1992).
13. T. Sugawara and T. Matsuda, *J. Biomed. Mater. Res.* **29**, 1047 (1995).
14. A. Rezania, R. Johnson, D. Kelso, A. R. Lefkow and K. E. Healy, *Langmuir* (1998) (submitted).
15. B. K. Brandley and R. L. Schnaar, *Anal. Biochem.* **172**, 270 (1988).
16. A. Oldberg, A. Franzen and D. Heinegard, *Proc. Natl Acad. Sci.* **83**, 8819 (1986).
17. H. Y. Zhou, H. Takita, R. Fujisawa, M. Mizuno and Y. Kuboki, *Calcif. Tissue* **56**, 403 (1995).
18. J. P. Bearinger, D. G. Castner, S. L. Golledge, S. Hubchak and K. E. Healy, *Langmuir* **13**, 5175 (1997).
19. K. E. Healy, C. H. Thomas, A. Rezania, J. E. Kim, P. J. McKeown, B. Lom and P. E. Hockberger, *Biomaterials* **17**, 195 (1996).
20. B. J. Tyler, D. G. Castner and B. D. Rather, *J. Vac. Sci. Technol.* **A7**, 1646 (1989).
21. R. W. Paynter, *Surf. Interface Anal.* **3**, 186 (1981).
22. B. J. Tyler, D. G. Castner and B. D. Rather, *Surface Interface Anal.* **14**, 443 (1988).
23. R. I. Freshney, *Culture of Animal Cells: A Manual of Basic Technique*. Wiley–Liss, New York (1983).
24. P. F. Kruse and M. K. Patterson, *Tissue Culture: Methods and Applications*. Academic Press, New York (1973).
25. L. Lasdon and A. Waren (Eds), *Generalized Reduced Gradient (GRG2)*. Frontline Systems: Incline Village (1990).
26. G. R. Dickson, *Methods of Calcified Tissue Preparation*. Elsevier, New York (1984).
27. C. Pale-Grosdemange, E. S. Simon, K. L. Prime and G. M. Whitesides, *J. Am. Chem. Soc.* **113**, 12 (1991).
28. S. F. A. Hossainy and J. A. Hubbell, *Biomaterials* **15**, 921 (1994).
29. H. Rubin, *Exp. Cell Res.* **41**, 138 (1966).
30. A. Rein and H. Rubin, *Exp. Cell Res.* **49**, 666 (1968).
31. W. S. Hu, J. Maier and D. I. C. Wang, *Biotech. Bioeng.* **27**, 585 (1985).
32. W. S. Hu and D. I. C. Wang, *Biotech. Bioeng.* **30**, 548 (1987).
33. S. S. Ozturk and B. O. Palsson, *J. Biotech.* **16**, 259 (1990).
34. B. Ecarot-Charrier, R. F. Bouchard and C. Delloye, *J. Biol. Chem.* **244**, 20 049 (1989).
35. D. A. Lauffenburger and A. F. Horwitz, *Cell* **84**, 359 (1996).

Polymers for Tissue Engineering, pp. 189–199
Molly S. Shoichet and Jeffrey A. Hubbell (Eds)

Surface grafting of poly(ethylene glycol) onto poly(acrylamide-co-vinyl amine) cross-linked films under mild conditions

Y. YAMAMOTO and M. V. SEFTON*

Department of Chemical Engineering and Applied Chemistry, and Centre for Biomaterials, University of Toronto, Toronto, Ontario M5S 3E5, Canada

Received 9 June 1997; accepted 20 November 1997

Abstract—Poly(ethylene glycol) (PEG) was grafted onto poly(acrylamide-co-vinyl amine) (poly(AM-co-VA)) film using tresylated PEG (TPEG) at 37 °C in aqueous buffers (pH 7.4) with a view to surface-modifying microencapsulated mammalian cells. Poly(AM-co-VA) film was synthesized by Hofmann degradation of a cross-linked poly(acrylamide) film. Conversion to vinyl amine on the surface of the film was approximately 50%, but bulk conversion was not observed; surface specificity was thought to be the result of cleavage of aminated polymer chains at the surface due to chain scission. Reaction between primary amine and TPEG gave a graft yield of 2 mol% (based on XPS) with respect to available surface amine groups, equivalent to 54 mol% ethylene oxide based on monomer units. Physical adsorption of non-activated polymer was done under identical conditions as a control and the difference in oxygen content was significant compared to TPEG. The type of buffer agent and buffer concentration did not influence graft yields. This graft reaction, which was completed in as little as 2 h was considered to be mild enough to be used for a surface modification of microcapsules containing cells without affecting their viability. Such a surface modification technique may prove to be a useful means of enhancing the biocompatibility of microcapsules (or any tissue engineering construct) even after cell encapsulation or seeding.

Key words: Surface grafting; polyamine; PEO; hydrogel; biomaterials.

INTRODUCTION

Although microcapsulated cells have been studied for many years, there have been few attempts to develop new capsule materials: a poly(phosphazene) [1], and a poly(acrylonitrile) copolymer (AN69) [2] are exceptions. These materials must be processable, mechanically suitable, and biocompatible. The first is especially important since the cells need to tolerate the encapsulation process and is, therefore, limited

*To whom correspondence should be addressed.

in terms of temperature, pH, and solvent. Since new materials differ in chemical properties, each material may need a unique encapsulation process. This is likely the major obstacle that restricts the development of new capsule materials.

To overcome these problems and develop better microcapsules, we are trying to establish a method to surface-modify cell-containing capsules by surface grafting. This would allow to us prepare capsules with a single material and process but would allow us to have different surface chemistries in order to induce a particular tissue response to satisfy specific applications or functions by changing the graft molecule. This would eliminate the need to devise a new encapsulation process for each new material in order to produce different microcapsules. In addition, this may allow us to produce a series of microcapsules that have different surface chemistries but with the same permeability. The central problem in surface-modifying microcapsules is that it has to be done after the cells are encapsulated, so that they are only a few tens of microns away from potentially toxic reactants during the reaction. In the first instance the reaction conditions must be mild enough to permit this.

There are a few reports which indicated that microcapsules containing cells inside can be modified. Hubbell *et al*. photopolymerized onto a microcapsule surface or directly on cell aggregates [4] while Kung *et al*. have used tosyl or cyanuric chloride-activated poly(ethylene glycol) (PEG) and poly(vinyl alcohol) to surface modify poly(L-lysine)−alginate capsules [5]. These reports suggest that 'doing' organic chemistry in the presence of cells is not unfeasible.

Here, we report on the grafting reaction of tresylated PEG (TPEG) onto poly(acrylamide-co-vinyl amine) (poly(AM-co-VA)) film. The reaction is a nucleophilic substitution of the primary amine with a tresyl activated compound (trifluoroethane sulphonate). This is a common reaction for protein modification and enzyme immobilization by reacting amine residues on the proteins with tresylated substrates such as tresylated agarose or tresylated silica [6]. Tresyl-activated PEG has been used for anchoring the PEG to various substrates as well as attaching bioactive molecules to PEG chain ends [7, 8]. Conditions for these reactions were very mild (e.g. 37°C physiological buffers) and it was presumed that encapsulated cells would be able to tolerate this reaction. PEG was chosen as the graft molecule because of its low toxicity and its well known influence on protein adsorption. Its modified surfaces have been extensively studied as biomaterials [9–12]. It was considered that PEG would also be a good model for other water-soluble compounds that could be grafted onto the microcapsule surface. TPEG used in experiments was monofunctional and one chain end was terminated with methoxy group. Non-activated PEG which was used as a control had a similar chemistry: one end with methoxy group and the other end with hydroxyl group.

To model the microcapsule material, we synthesized a cross-linked hydrogel containing primary amine groups: poly(AM-co-VA). A hydrogel was chosen for its high permeability to low molecular weight compounds, where the primary amine group was preferred due to its high reactivity. Linear copolymer hydrogels, poly(AM-co-methyl methacrylate-co-VA), were initially tested [13] but due to their limited solubility and processability, we decided to prepare the cross-linked films. While easier to prepare as a film than the linear polymer, we cannot make microcapsules out of this material.

Hence it must be considered as a model of the capsule wall and the effect of the chemistry on encapsulated cells was examined in a different geometry. The results are reported separately [14].

EXPERIMENTAL

Materials

Acrylamide (Schwarz/Mann Biotech, Cleveland, OH, USA) was purified by recrystallization from water/methanol. *N*,*N*,*N*′,*N*′-tetramethylenediamine ammonium persulphate, methylene bisacrylamide, sodium hypochlorite (all from BDH Laboratory Supplies, Poole, UK), acetonitrile (Aldrich, Milwaukee, WI, USA), PEG5000 (poly(ethylene glycol methyl ether), M_w 5000, Aldrich), TPEG (M_w 5000, Shearwater Polymers, Huntsville, AL, USA) were used as received. DPBS (Dulbecco's phosphate buffered saline) was obtained from the University of Toronto medium preparation facility. Na_2HPO_4 and $NaH_2PO_4 \cdot H_2O$ were obtained from Aldrich and TES (*N*-tris(hydroxymethyl)-2-aminoethane sulfonic acid) was obtained from Sigma Chemical Co., St. Louis, MO, USA.

Poly(acrylamide) film preparation and Hofmann degradation

Poly(acrylamide) film was prepared by mixing acrylamide and bisacrylamide (2.5 or 10 mol% cross-linker with respect to total monomer, 0.6 g) in 3 ml of water followed by degassing. 1.5 μl of tetramethylenediamine and 30 μl of degassed 0.05 g ml^{-1} ammonium persulphate aqueous solution were added to initiate the polymerization which was carried out in a 0.5-mm thick mold at 30°C for 2 h. Cross-linked films were washed in distilled water for 3 days and vacuum-dried.

Water was gently wiped off swollen cross-linked films of known dry weight, and sodium hypochlorite equivalent to 4.8 NaOCl : AM mole ratio, cooled to 0°C, was poured onto the films. After 5 min, 10.5 N NaOH (cooled to 0°C), equivalent to 20.3 NaOH : AM mole ratio, was added. The reaction mixture was kept at 0°C with occasional gentle mixing while the films' integrity was monitored. These reaction conditions were determined in pilot studies and were based on the Hofmann degradation of an acrylamide copolymer [13]. The reaction was terminated by removing the films from the reaction mixture and placing them into deionized distilled water and 2 N HCl was added to neutralize the supernatant. The resulting VA films were extracted in deionized distilled water for several weeks and the conductivity of the supernatant was measured. The films were vacuum dried, rehydrated, and stored in deionized distilled water.

PEG grafting

Cross-linked poly(AM-co-VA) films were soaked in 0.2 M TES buffer (adjusted to pH 7.4 by NaOH) for 2 h prior to the grafting. 0.8 ml of fresh buffer and TPEG were added and grafting was allowed to proceed at 37°C for 2–24 h. After the reaction,

grafted films were washed in deionized distilled water for 3 days and then further washed with acetonitrile using a soxhlet extractor for 24 h. Grafted films were dried in air and then in vacuum. The following buffers were used in a similar manner: PBS (2.7 mM KCl, 1.2 mM KH_2PO_4, 138 mM NaCl, and 8.1 mM $Na_2HPO_4 \cdot 7H_2O$, pH 7.4); 0.2 M phosphate buffer (189 mM Na_2HPO_4 and 11 mM $NaH_2PO_4 \cdot H_2O$, pH 8.0); 0.1 M TES buffer (adjusted to pH 7.4 by NaOH). As a control, PEG5000 or hydrolyzed TPEG was allowed to be adsorbed to the films under identical condition as for TPEG; hydrolyzed TPEG was prepared by dissolving TPEG in buffer for 3 days.

Analysis

Films were analyzed by XPS (LEYBOLD MAX200) using a Mg or Al K_α X-ray source at 90 or 20 deg take off angle (with respect to the surface). Surface elemental compositions were calculated from low resolution spectrums using the sensitivity factors supplied by the manufacturer. Bulk elemental analysis was done by Guelph Chemical Laboratories Ltd. (Guelph, ON, Canada).

RESULTS

Cross-linked polyAM films were flat, opaque, and rubbery. During Hofmann degradation to introduce primary amines, the films were able to maintain their integrity for up to 2 h under the extremely basic conditions; after 4.5 h, the films dissolved completely. The weight loss during 2 h of Hofmann degradation was $28 \pm 2\%$ for both 10 and 2.5 mol% ($n = 4$ and 3, respectively) cross-linked films. There were crevices in the surface of the film. After the reaction, the supernatant contained soluble material which precipitated in organic solvents. There was no significant change in film thickness after Hofmann degradation. The product poly(AM-co-VA) film, was yellow and slightly wrinkled yet still strong enough to hold its shape. It took about 3 weeks to extract most of the water-soluble impurities, as judged by the conductivity of the supernatant becoming constant. Surface elemental compositions (XPS) are shown in Table 1. There was a decrease in oxygen content and O/N ratio after Hofmann degradation. The composition of poly(AM-co-VA) films was consistent from batch to batch. Small amounts (less than 0.8%) of impurities such as fluorine, sulfur, and silicon were found in most of the XPS spectra. In contrast, the bulk O/N ratio after Hofmann degradation did not decrease much and was similar to the theoretical value for polyAM homopolymer (Table 1). High resolution spectra of C 1*s* are shown in Fig. 1 and they show a decrease of the peak at 288 eV assigned to amide carbon.

Surface elemental compositions of grafted films are listed in Tables 2 and 3. The TPEG grafted films had a higher oxygen content and O/N ratio compared to the poly(AM-co-VA) film. Moreover, they were even higher than the films to which PEG was adsorbed; these were made using unreactive PEG5000 or hydrolyzed TPEG (Table 3). In addition to the O/N ratio, PEG-grafted films showed a shift of the O 1*s* peak to a higher binding energy compared to the poly(AM-co-VA) film (Fig. 2). Grafting was done in four different buffers but no significant difference was found

Table 1.
Surface and bulk composition of vinyl amine copolymer films

	Found			Theoretical value
	Surface composition[a]		Bulk composition	PolyAM cross-linked film[e]
	PolyAM cross-linked film[b] (before Hofmann deg.)	Poly(AM-co-VA) film[c] (after Hofmann deg.)	Poly(AM-co-VA) film[d] (after Hofmann deg.)	
C%	67.2 ± 0.9	70 ± 1	59.0	60.7
O%	17.6 ± 0.6	10.6 ± 0.3	19.1	19.6
N%	15 ± 1	19.4 ± 0.7	21.9	19.6
C/N	4.45	3.61	2.69	3.10
O/N	1.17	0.55	0.87	1.00
O/C	0.26	0.15	0.32	0.32

[a]XPS was taken at 90 deg take-off angle for all sample.
[b]Polymerized with 10 mol% bisacrylamide ($n = 2 \pm$ range/2).
[c]Hofmann degradation was carried at 0°C for 2 h using NaOCl : AM = 4.8 (mole ratio) ($n = 3 \pm$ SD samples from two different batches were analyzed).
[d]Hofmann degradation was carried at 0°C for 2 h using NaOCl : AM = 4.8 (mole ratio). Calculated from C, H, N bulk elemental ratios. Hydrogen content (%) was excluded from the calculation.
[e]Calculated for polyAM homopolymer with 10 mol% bisacrylamide.

even though there were differences in their initial pH (for phosphate buffer pH 8.0; PBS and TES buffer, pH 7.4) or because of differences in pH change during the reaction (PBS, decrease of about 3 pH units; phosphate and TES buffers, decrease of less than 1 pH unit). Similarly, there was no difference in elemental composition at the two take off angles, indicating the absence of a significant depth effect. There were only slight increases in O/N ratios by increasing the TPEG feed or reaction time (Table 3).

DISCUSSION

Poly(AM-co-VA) synthesis

XPS analysis of the polyAM film showed a decrease in amine carbon and the surface elemental composition showed a decrease in oxygen content after Hofmann degradation (Fig. 1 and Table 1), showing that the conversion from amide to primary amine was successful. The O/N ratio was expected to decrease from 1 (the theoretical value) by conversion of amide to primary amine. Using the O/N ratio and the theoretical relationship between O/N ratio and vinyl amine content, the amount of vinyl amine in the film surface was calculated to be around 50 mol%. The total number of amide groups which had been converted to primary amine was likely higher since a water soluble portion of the polymer was observed in the supernatant after the reaction. It might have been possible to introduce more amine to the polymer because conversions near 90% have been reported [15, 16], but for our application maintaining the films' integrity was essential hence the reaction was stopped after 2 h.

Table 2.
Effect of buffer on PEG immobilization and adsorption (XPS results)

		0.2 M phosphate buffer (pH 8.0)[c]		0.1 M TES buffer (pH 7.4)[c]		0.2 M TES buffer (pH 7.4)[c]	
		PEG adsorbed	PEG grafted	PEG adsorbed	PEG grafted	PEG adsorbed	PEG grafted
Reaction conditions[a]	Poly(AM-co-VA)[b]	Poly(AM-co-VA) + PEG5000 200 μmol g^{-1} 24 h	Poly(AM-co-VA) + TPEG 200 μmol g^{-1} 24 h	Poly(AM-co-VA) + hydrolyzed TPEG 10 μmol g^{-1} 2 h	Poly(AM-co-VA) + TPEG 10 μmol g^{-1} 2 h	Poly(AM-co-VA) + PEG5000 20 μmol g^{-1} 2 h	Poly(AM-co-VA) + TPEG 20 μmol g^{-1} 2 h
C%	70 ± 1	68 ± 1	65 ± 2	69.9 ± 0.8	68.1 ± 0.5	68.7 ± 0.3	67.9 ± 0.1
O%	10.6 ± 0.3	15.1 ± 0.4	20 ± 1	12.2 ± 0.5	16.1 ± 0.9	12.1 ± 0.5	17.8 ± 0.6
N%	19.4 ± 0.7	17.0 ± 0.7	14.3 ± 0.9	17.5 ± 0.3	15.4 ± 0.8	19.1 ± 0.7	13.5 ± 0.9
C/N	3.61	3.99	4.58	3.99	4.44	3.60	5.04
O/N	0.55	0.89	1.42	0.69	1.05	0.63	1.32
O/C	0.15	0.22	0.31	0.17	0.24	0.18	0.26

[a] Reactions were carried at 37 °C and XPS was taken at 90 deg take-off angle for all sample ($n = 2 \pm$ range/2, unless noticed otherwise).
[b] ($n = 3 \pm$ standard deviation, samples from two different batches were analyzed.)
[c] Significant difference in oxygen % between PEG adsorbed and PEG grafted films based on unpaired t-test ($p < 0.05$).

Table 3.
Effect of reaction conditions and XPS sampling depth on PEG immobilization (XPS results)

	TPEG concentration			Reaction time		Sampling depth		Theoretical value of PEG grafted film[b]
Buffer	0.2 M TES buffer (pH 7.4)			DPBS (pH 7.4)		0.1 M TES buffer (pH 7.4)		
Reaction conditions[a]	Poly(AM-co-VA) + TPEG 2 μmol g^{-1} 2 h	Poly(AM-co-VA) + TPEG 20 μmol g^{-1} 2 h	Poly(AM-co-VA) + TPEG 200 μmol g^{-1} 2 h	Poly(AM-co-VA) + TPEG 200 μmol g^{-1} 2 h	Poly(AM-co-VA) + TPEG 200 μmol g^{-1} 24 h	Poly(AM-co-VA) + TPEG 20 μmol g^{-1} 2 h		
Take-off angle	90 deg	90 deg	90 deg	90 deg	90 deg	90 deg	20 deg	
C%	68.5 ± 1.6	67.9 ± 0.1	66.9 ± 0.5	65.3 ± 0.3	63 ± 2	64.8 ± 0.1	65.8 ± 1.2	64.4
O%	13.2 ± 0.9	17.8 ± 0.6	17.9 ± 0.4	17.0 ± 0.6	19.5 ± 0.4	18.6 ± 0.6	18.4 ± 0.5	22.1
N%	17.3 ± 0.9	13.5 ± 0.9	14.8 ± 0.1	12.9 ± 0.3	12 ± 2	15.8 ± 0.9	15.1 ± 0.6	13.5
C/N	3.97	5.04	4.53	5.06	5.43	4.10	4.35	4.77
O/N	0.76	1.32	1.21	1.31	1.67	1.17	1.22	1.64
O/C	0.19	0.26	0.27	0.26	0.31	0.29	0.28	0.34

[a]Reaction was carried at 37 °C ($n = 2 \pm$ range/2).

[b]Theoretical elemental composition of the grafted film that consists of 1 mol% PEG, 49.5 mol% VA, and 49.5 mol% AM (i.e. 2% graft yield with respect to primary amine, equivalent to 53.5 mol% ethylene oxide based on monomer units). Composition of poly(AM-co-VA) film was considered as 50 mol% AM and 50 mol% VA, and molecular weight of PEG was calculated as 5000 g mol^{-1} (114 repeating units).

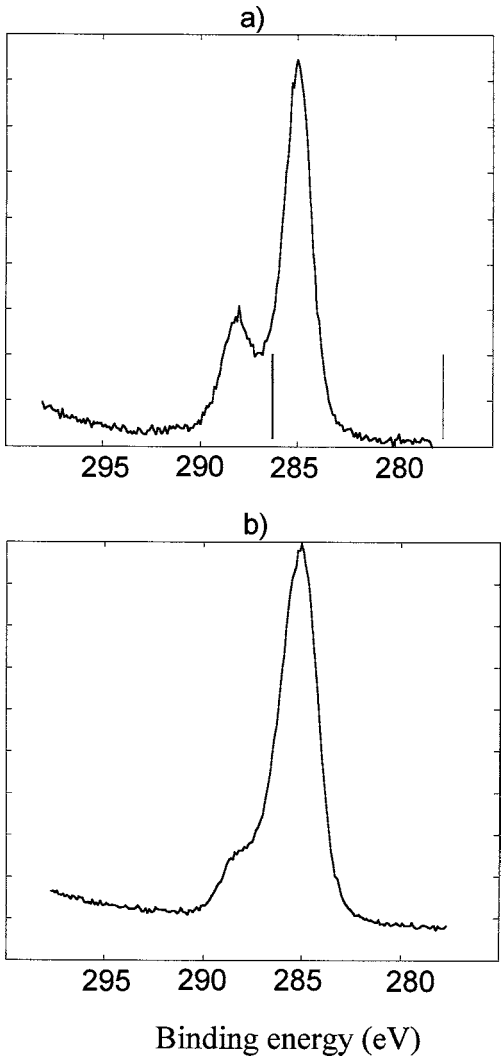

Figure 1. XPS spectra of: (a) cross-linked polyAM film (before Hofmann degradation); and (b) poly(AM-co-VA) film (after Hofmann degradation) (288 eV peak assigned to amide carbon decreased after the Hofmann degradation).

Unlike the surface elemental composition, the bulk composition did not change much after Hofmann degradation (Table 1). The O/N ratio was almost 1 which showed that the introduction of primary amine was somewhat restricted to the surface. Side reactions during Hofmann degradation are well known and the major one is the production of carboxylic acid [15, 16]. We assume that the carboxyl on the surface of the film was minimal because the measured O/C ratio was smaller than the theoretical value for the 50% amine conversion and the C 1*s* spectrum did not show a peak at 289.2 eV (for carboxyl group) [17].

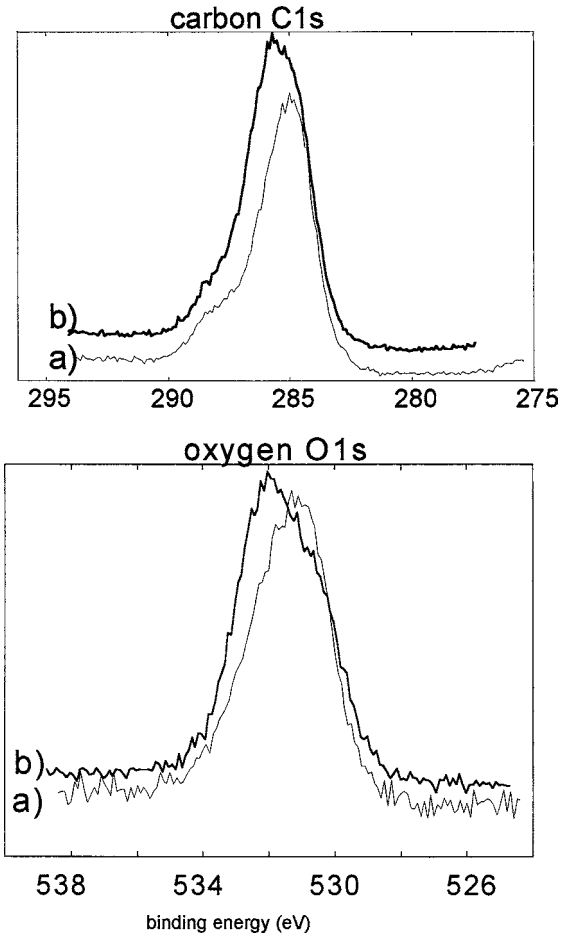

Figure 2. Carbon and oxygen high resolution spectra of: (a) poly(AM-co-VA) film; and (b) PEG-grafted poly(AM-co-VA) film. PEG-grafted film showed peak shifts to higher binding energies due to the addition of ether oxygen.

Grafting of PEG

After treating the poly(AM-co-VA) films with PEG5000, hydrolyzed TPEG, or TPEG, there was a higher oxygen ratio than before, due to the addition of PEG. Since the amount of nitrogen did not change by grafting, it was used to normalize the oxygen content. Films treated with tresylated PEG gave a higher O/N ratio than non-activated PEG5000 or the nonreactive hydrolyzed TPEG. The unpaired t-test ($p < 0.05$) showed that the differences in oxygen percent between TPEG and non-active PEG (PEG5000 or hydrolyzed TPEG) -treated films were significant in all three conditions. This demonstrates that PEG was covalently attached to the surface in addition to the physical adsorption represented by the increase in O/N for films treated with unreactive PEG. Apart from the increase in O/N ratio, the shift of the O 1s peak to a higher energy also demonstrates the presence of ether oxygen (Fig. 2).

The amide oxygen peak was expected to be around 531.5 eV and the ether oxygen peak around 532.8 eV [17]. This peak shift was not apparent for PEG adsorbed films and films with low TPEG feed, since they had less PEG on their surfaces.

The graft yield of PEG was calculated based on 50 mol% primary amine at the surface of the film and the theoretical composition of PEG. The maximum amount of PEG grafted on the film was considered to be around 1 mol% (based on O/N = 1.67, 200 μmol g^{-1} TPEG reacted for 24 h). In other words, 2% of available primary amine on the surface of the film reacted with TPEG which is equivalent to 54 mol% ethylene oxide units on a monomer basis. The elemental compositions and O/C ratio also matched the corresponding theoretical value. Others have reported the grafting of PEG onto aminated poly(ethylene terephtalate) and aminated poly(tetrafluoroethylene) using TPEG in pH 9.0 bicarbonate buffer for 24 h at 40°C [18]; the XPS results did not clearly show the presence of PEG due to the low graft yield. We believe that the higher primary amine content obtained here (approximately 10 mol% nitrogen content due to primary amine) compared to their samples (approximately 2.5 mol% nitrogen content due to primary amine) allowed us to graft more PEG. The absence of the tresyl leaving group did not change the amount of adsorption of the PEG (Table 3). The amount of PEG adsorption was considered to be less than 0.5 mol% relative to the repeating units of poly(AM-co-VA).

There was a small effect of reaction time on the O/N ratio (Table 3). Typical reaction times for protein modification with tresylated supports are from 1 to 24 h [19]. In one report a 70% yield (amount of protein immobilized/amount of protein initially fed) was achieved even for times as short as 1.5 h and only increased to 74% after 15 h [20]. We estimated the hydrolysis rate constant k_H for TPEG as approximately 2×10^{-3} s^{-1} from k_H values of isopropyl tosylate (1.47×10^{-5} s^{-1}) [21], adamantyl tosylate (7.70×10^{-7} s^{-1}), and adamantyl tresylate (8.172×10^{-5} s^{-1}) [22] (all three values were measured in 50% aqueous ethanol at 25°C). Using this k_H and assuming the mechanism to be a S_N1 reaction, the TPEG half life was estimated to be $\sim$ 10 min. This value corresponds to a complete hydrolysis of TPEG after 2 h. Since primary amine is a stronger nucleophile than water, the reaction with poly(AM-co-VA) film is expected to be faster and hence we considered that grafting was completed after 2 h of reaction. A small increase in the O/N ratio for 24 h reaction compared to 2 h (Table 3) was thought to be result of a possible increase in adsorption or absorption of the non reactive PEG.

CONCLUSION

Poly(acrylamide-co-vinyl amine) cross-linked film with a surface composition of approximately 50% acrylamide and 50% vinyl amine was synthesized by Hofmann degradation of poly(acrylamide). The primary amine appeared to be limited to the film surface. Using tresylated PEG, PEG was grafted on the vinyl amine film under very mild conditions with a maximum 2% graft yield with respect to primary amine. Simple adsorption resulted in less than half this amount of PEG on the surface. Under mild reaction conditions PEG was grafted onto an amine containing copolymer. It

remains to be shown that similar conditions are useful for producing surface modified microcapsules in the presence of live animal cells.

Acknowledgements

Helpful discussions with Professor M. A. Winnik and his group are gratefully acknowledged. This research was financially supported by NSERC.

REFERENCES

1. S. Cohen, M. C. Bano, K. B. Visscher, M. Chow, H. R. Allcock and R. Langer, *J. Am. Chem. Soc.* **112**, 7832 (1990).
2. S. Darquy, J. Honiger, M. E. Pueyo, F. Capron, C. Arbet-Engels, G. Reach, C. Collier and E. Muscat, Microencapsulation of islets of Langerhans with hydrogel of AN69, a copolymer of acrylonitrile, for the design of a bioartificial pancreas, Pancreas Transplantation Meeting, Amsterdam, p. 114 (1993).
3. A. S. Sawhney, J. A. Hubbell and C. P. Pathak, *Biomaterials* **14**, 1008 (1993).
4. C. P. Pathak, A. S. Sawhney and J. A. Hubbell, *ACS J.* **114**, 8311 (1992).
5. I. M. Kung, F. F. Wang, Y. C. Chang and Y. J. Wang, *Biomaterials* **16**, 649 (1995).
6. K. Nilsson and K. Mosbach, *Methods Enzymol.* **135**, 65 (1987).
7. L. G. Cima, S. T. Lopina and E. W. Merrill, Hepatocyte responses to PEO-tethered carbohydrates depend on tether conformation, 21st Annual Meeting of the Society for Biomaterials, San Flancisco, CA, p. 147 (1995).
8. L. G. Griffith-Cima and P. R. Kuhl, Tethered growth factors elicit mitrogenic responses in cultured hepatocytes, Fifth World Biomaterials Congress, Toronto, ON, p. 990 (1996).
9. S. Nagaoka, H. Takeuchi, K. Yokota, Y. Mori, H. Tanzawa and T. Kikuchi, *Kobunshi Ronbunshu* **39**, 173 (1983).
10. S. Nagaoka, H. Takeuchi, K. Yokota, Y. Mori, H. Tanzawa and T. Kikuchi, *Kobunshi Ronbunshu* **39**, 165 (1982).
11. K. Berström, K. Holmberg, A. Safranj, A. S. Hoffman, M. J. Edgell, A. Koxlowski, B. A. Hovanes and J. M. Harris, *J. Biomed. Mater. Res.* **26**, 779 (1992).
12. N. P. Desai and J. A. Hubbell, *J. Biomed. Mater. Res.* **25**, 829 (1991).
13. Y. Yamamoto and M. V. Sefton, *J. Appl. Poly. Sci.* **61**, 351 (1996).
14. Y. Yamamoto, PhD Thesis, University of Toronto (1997).
15. H. Tanaka and R. Senju, *Kobunshi Ronbunshu* **33**, 309 (1976).
16. H. Tanaka, *J. Polym. Sci.*, *Polym. Chem. Ed.* **17**, 1239 (1979).
17. G. Beamson and D. Briggs, *High Resolution XPS of Organic Polymer*, *the Scienta ESCA 300 Data Base*. John Wiley, New York (1992).
18. N. P. Desai and J. A. Hubbell, *Proc. PMSE* **62**, 731 (1990).
19. K. Nilsson and K. Mosbach, *Methods Enzymol.* **104**, 56 (1984).
20. K. Nilsson and K. Mosbach, *Biochem. Biophys. Res. Comm.* **102**, 449 (1981).
21. P. V. R. Schleyer, J. L. Fry, L. K. M. Lam and C. J. Lancelot, *J. Am. Chem. Soc.* **92**, 2542 (1970).
22. V. J. Shiner, Jr. and R. D. Fischer, *J. Am. Chem. Soc.* **93**, 2553 (1971).

This page intentionally left blank

Polymers for Tissue Engineering, pp. 201–217
Molly S. Shoichet and Jeffrey A. Hubbell (Eds)

Periodontal ligament cell culture on the hydrophobic substrate coated with proteins of periodontal ligament fibroblast-conditioned medium

YUKIHIKO KINOSHITA,[1,*] TAKEHIRO HIDAKA,[1] SATORU OZONO[2] and TOSHIO KAWASE[3]

[1]*The Second Department of Oral and Maxillofacial Surgery*, [2]*Department of Oral Pathology*, *and* [3]*Department of Dental Bioengineering*, *Kanagawa Dental College*, *82 Inaoka-cho*, *Yokosuka City 238-8580*, *Japan*

Received 24 June 1997; accepted 24 November 1997

Abstract—In regenerating periodontal ligament (PDL) around the root of an artificial tooth, an important role is played by some physiologically active substance that promotes adhesion of the cells to the surface of the tooth root and induces cell proliferation and differentiation. In this study, the supernatant of the conditioned medium (CM) of dog periodontal ligament fibroblast (DPLF) was fractionated using an ion exchange chromatography–diethylaminoethyl (IEC-DEAE) column. DPLFs were cultured on hydrophobic dishes coated with each fraction. Cell proliferative activity and alkaline phosphatase (ALPase) activity, including electron microscopic features of the contact surface between the cells and the dish, were investigated. The DPLF-CM was separated by IEC-DEAE column into six fractions. Each fraction promoted an increase in DNA content and ALPase activity of the cultured DPLF, and especially remarkable were fractions 2 and 3. Fraction 2 at a molecular weight (M_w) of 210, 160, 85, 50 and 22 kD, and fraction 3 at $M_w = 21$ and 23 kD contained the type of proteins not found in other fractions. Electron microscopic analysis revealed that the cells in the coating group were in close contact with the surface of the dishes and that fine fibers protruding from the cell membrane clinged to the dishes. In the control group, a wide gap between the cells and the dishes was observed.

These findings suggest that the DPLF-CM fractions contain specific physiological activating factors that induce proliferation and differentiation as well as cell adhesion of the DPLF cells.

Key words: Periodontal ligament fibroblast; cell culture; conditioned medium; IEC-DEAE; proliferation; differentiation; hydrophobic substrate.

INTRODUCTION

The periodontal ligament (PDL) is a thin connecting tissue with a thickness of only 0.2 or 0.3 mm, which is located between the alveolar bone and the cementum in the

*To whom correspondence should be addressed.

periodontal surface layer. The PDL supports the tooth in the jawbone and provides an excellent stress-breaking ability thanks to the viscoelasticity of its capillary network and to the specific structure and arrangement of the collagen fibers [1]. This makes the PDL capable of withstanding frequent occlusal stress, responding permanently to external mechanical forces, and maintaining structural and physiological homostasis by secreting agents which adjust cellular proliferation and differentiation [2]. The PDL is lost when the natural tooth is lost. Although it is desirable to form a new PDL if dental implants are introduced, this has not yet been successfully accomplished. However, some studies have clarified that a new PDL can only be formed by the progenitor cells which remain in the PDL tissue [3, 4]. Boyko *et al.* [5] reported that new PDL can be formed between the tooth root and the bone by transplanting decalcified canine tooth root together with cultured autologous PDL cells. Also, recent research has clarified that the primary condition for regenerating the PDL is the attachment, proliferation, and differentiation of cells on the periodontal surface [6, 7], and that the PDL cells which are similar in shape to fibroblasts have functionally an osteoblastic property with a high ALPase activity and present a special differentiation ability with controlled calcification [1, 8, 9]. Therefore, to regenerate PDL tissues for dental implants, it is required to assure the existence of a sufficient amount of PDL progenitor cells and also to provide the appropriate surface condition of artificial materials so that cells can proliferate and differentiate into the PDL without losing the properties described above [10].

The present research utilizes a periodontal ligament fibroblast conditioned medium PLF-CM which is a liquid agent produced by cultured PDL cells for the adjustment of cell proliferation and differentiation, and studies the effects of this medium on the proliferation, differentiation, and attachment of PDL cell by coating a hydrophobic substrate with this medium.

MATERIALS AND METHODS

Cell culture of DPLF

In accordance with the institutional Animal Care Committee guidelines of the Kanagawa Dental College, beagles pretreated with propionyl promazine (0.5 $mg\,kg^{-1}$, i.m., Bayer Chemical Co., Osaka, Japan) were anesthetized with sodium pentobarbital (25 $mg\,kg^{-1}$, i.v., Dainippon Pharmachemical Co., Osaka, Japan). The mandibular third and fourth premolars and first molar were extracted. The extracted teeth were washed with Ca^{2+}- and Mg^{2+}-free Dulbecco's phosphate buffered saline: PBS(−) (Nissui Pharmachemical Co., Tokyo, Japan). The periodontal ligaments attached to the middle one-third of the root were removed carefully by scraping with a scalpel, avoiding the contamination of cell-derived gingiva and apical connective tissues, as described by Kawase *et al.* [1] and Brunette *et al.* [11]. The scraped tissue fragment were explanted between the bottom of a well of a 24-multi well plate (Falcon 3047, Becton Dickinson Co., Lincoln Park, NJ, USA) and a 15-mm thermanox cover slip (Lux, Nunc Co., Naperville, IL, USA) in α-minimal essential medium (α-MEM,

Gibco Co., NY, USA) supplemented with 10% fetal bovine serum (FBS, Hyclone Co., Logan, UT, USA), 100 U ml^{-1} penicillin G, 100 $\mu g\,ml^{-1}$ streptomycin, and 2.5 $mg\,ml^{-1}$ amphotericin B.

Cells were grown out of an explant for 10 days until confluent condition in a humidified environment of 5% CO_2 and 95% air at 37°C. The migrated cells were then subcultured by enzymatic digestion using 0.25% trypsin (1/250, Gibco Co., NY, USA) in PBS(−). Cells were inoculated at a cell density of 2×10^4 cells cm^{-2} and maintained on 100-mm dishes (Falcon 3003, Becton Dickinson Co., Naperville, IL, USA). In this study, cells were used the third and fourth passage in culture.

Experimental procedure of conditioned medium of DPLF

DPLF were inoculated into 100-mm dishes at a density of 1.0×10^6 cells per dish. On reaching confluency, the cells were washed twice with PBS(−) and cultured in FBS-free Molecular, Cellular and Developmental Biology 107 (MCDB 107, Kyokuto Chemical Co., Tokyo, Japan) supplemented with ascorbic acid (Vitamin C) containing antibiotics for 24 h. The conditioned medium (DPLF-CM) was subsequently decanted, cleared of cellular debris by centrifugation at 1000 *g* for 5 min, and condensed 100 fold by the ultrafiltration of Diaflow membrane YM-5 (Amicon Co., Beverly, MA, USA).

DPLF-CM was subjected to DEAE ion-exchange chromatography (IEC-DEAE, Jasco Co., Tokyo, Japan) in 20 mM Tris–HCl (pH 8.0) containing 0.1 mM phenylmethylsulfonyl fluoride (PMSF, Sigma Chemical Co., St Lous, MO, USA), eluted with a linear gradient of 0–0.5 M NaCl. The DEAE column was run at a flow rate of 0.5 $ml\,min^{-1}$, and half minute fractions were collected. Protein was detected by absorbance at 280 nm.

Hydrophobic 96-well plates (Sumilon, Sumitomo Bakelite Co., Tokyo, Japan) were coated with fractions separated by IEC-DEAE for 1 h at 37°C, 5% CO_2 in 200 μl PBS(−). Growth phase cells were detached from dishes with 0.25% trypsin and 2.5×10^4 cells were added to each well and cultured for 7 days.

The DNA content of cell layers was measured using diamino benzoic acid (DABA, Aldrich Co., Milwarkee, WI, USA) described by Puzas and Goodman [12], using salmon sperm DNA as a standard. Fluorescence was measured with a microplate fluorometer (MRF-100, Jasco Co., Tokyo, Japan); excitation was 405 nm and emission was 500 nm.

The assay of ALPase activity was performed by the modified method of Puzas and Brand [13]. The cell layers were reacted with 16 mM *p*-nitrophenyl phosphate (*p*-NPP) in 0.25 M 2-amino-2-methyl-1-propanol (AMP, Sigma Chemical Co., St Lous, MO, USA) containing 1 mM $MgCl_2$ at 37°C, for 15 min. The reaction was stopped by adding 1 M NaOH containing 5 mM EDTA. The amount of *p*-nitrophenol (*p*-NP) liberated was determined at 405 nm.

Sodium dodecyl sulfate-acrylamide gel electrophoresis (SDS-PAGE) was performed according to Laemmli [14]. Proteins were mixed with sample buffer before being applied to 5–15% linear gradient polyacrylamide gels under reducing conditions. Proteins were visualized by staining with 0.05% Coomassie Blue.

The statistical significance between the control and the experimental groups were determined by Student's *t*-test.

Morphological analysis

The cells on the plastic dish, coated with or without each fraction, were observed daily using phase-contrast microscopy (Nikon, Tokyo, Japan) until the tenth culture day and photographed. For an electron microscopic examination, the cells cultured on a plastic dish for 7 days were fixed with 2.5% glutaraldehyde, and post-fixed in 1% osmium tetroxide. After dehydration, the specimens were embedded in Spurr's resin and sectioned longitudinally together with a plastic dish. The ultrathin sections were double stained with uranyl acetate and lead citrate, and observed using transmission electron microscope (JEOL-1220, Japan).

RESULTS

Culture of DPLF

After 5 days' culture, fibroblast-like cells were observed migrating from the explants and proliferating (Fig. 1a). These cells grew to confluence with fibroblasts for 10 days. Under phase-contrast microscope, the subcultured DPLF obtained were typical fibroblasts (Fig. 1b).

Fractionation of DPLF-CM

Proteins obtained by an ultrafiltration of DPLF-CM from confluent cells cultured with FBS-free MCDB 107 were separated on IEC-DEAE (Fig. 2). Bound proteins were eluted with a linear NaCl gradient from 0 to 0.5 M. The anion exchange column fractions containing non-bound fraction (F. 0) were analyzed by SDS-PAGE under reducing conditions and protein was visualized by Coomassie staining on 5–15% gel (Fig. 3).

Each fraction contained several bands which can interact with the hydrophobic well. There were different bands between F. 2 and F. 3 proteins. The components of F. 2 were consistently found at an apparent molecular weight of 210, 160, 85, 50, and 22 kD (lane F. 2 in Fig. 3), and those of F. 3 at 23 and 21 kD (lane F. 3 in Fig. 3).

PLF cultured on a hydrophobic well coated with proteins from DPLF-CM

It was studied whether proteins from DPLF-CM caused fibroblasts to attach, spread, and proliferate. DPLF were inoculated and cultured for 7 days on the hydrophobic wells coated with the indicated fractions from the DPLF. Significant numbers of cells had proliferated in the presence of 0.15 M NaCl (F. 2) and 0.19 M NaCl (F. 3) eluted fractions (Fig. 2). In contrast, the exposure of cells to other fractions had a smaller effect on cell growth (Fig. 2 — F. 0, F. 1, F. 4, F. 5, and F. 6). Growth characteristics in cell culture were performed by DNA content which was quantitated fluorimetrically. The growth of DPLF was enhanced approximately 6- and 4.6-fold by F. 2 and F. 3 compared with F. 0, respectively (Table 1).

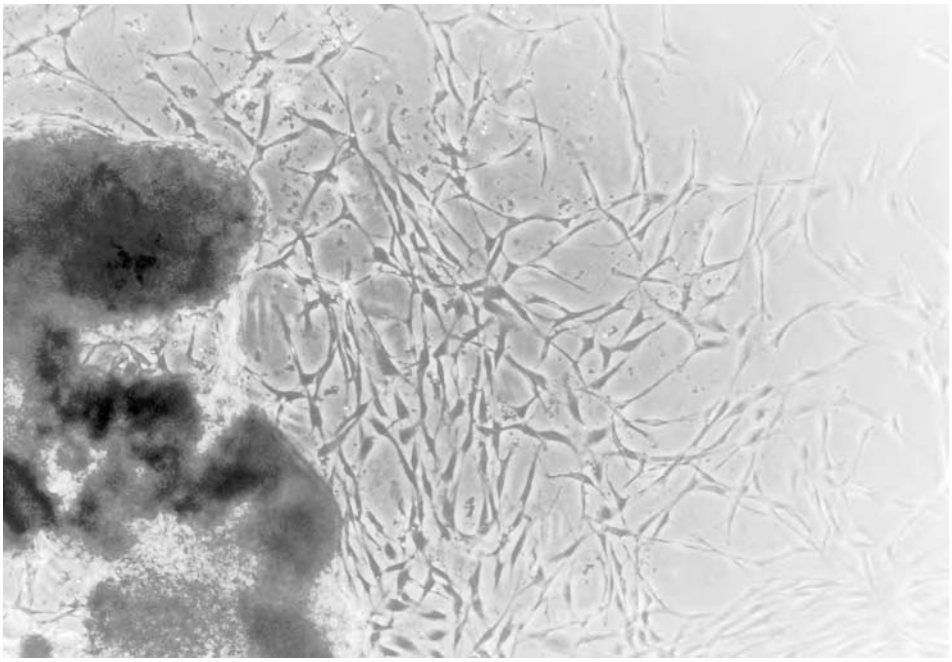

(a)

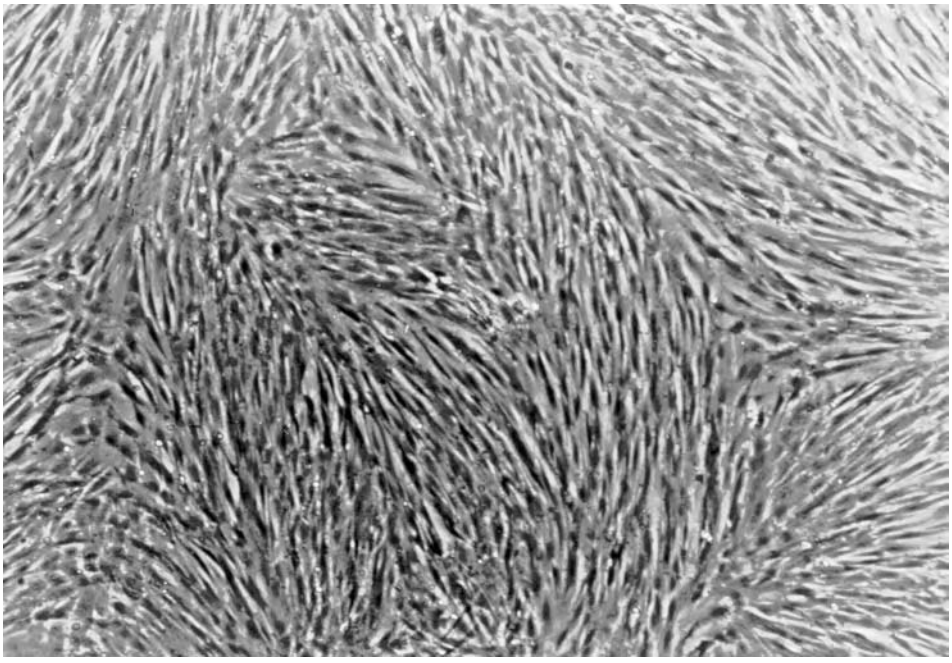

(b)

Figure 1. Dog periodontal ligament fibroblast-like cells migrated from an explanted tissue and cultured. (a) Explanted for 5 days. (b) Subcultured DPLF (confluent cells).

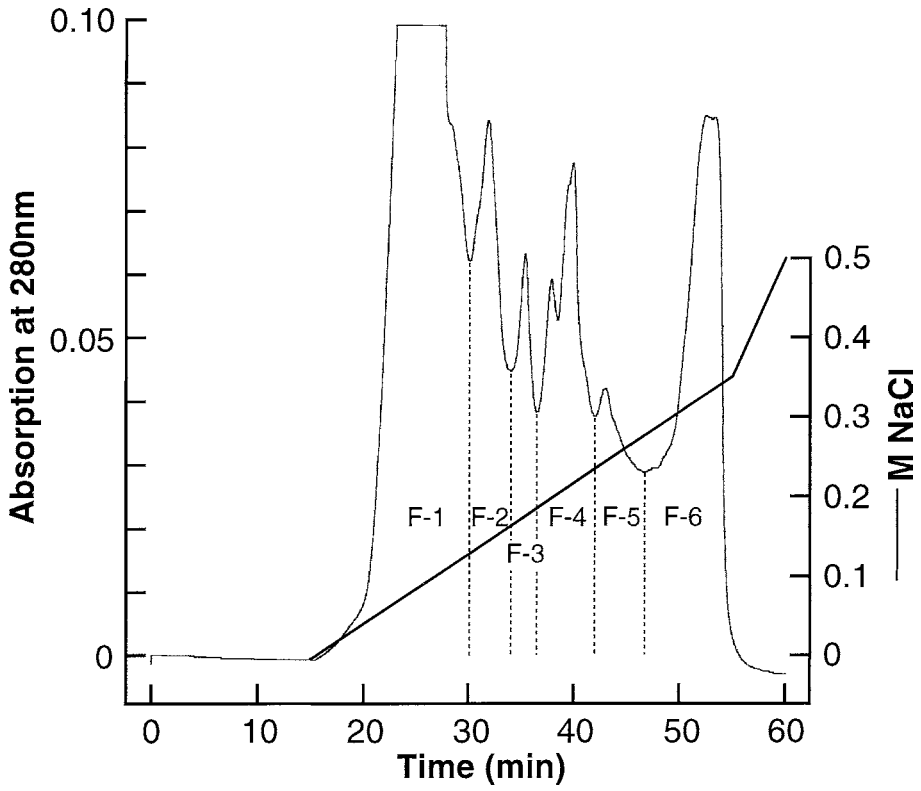

Figure 2. Chromatogram of DPLF-CM separated by ion exchange chromatography (IEC-DEAE).

ALPase activity of cell layers was exhibited a degree of differentiation of osteoblast-like properties. An increase of ALPase levels seems to be one of the earliest known markers for commitment to the osteoblastic phenotype. Treatments of DPLF with F. 2 and F. 3 coated on hydrophobic wells increased ALPase activity by about 4-fold in comparison with F. 0 (Table 2).

Phase contrast microscopic observation of DPLF cultured on a hydrophobic well which coated each fraction of DPLF-CM was performed (Fig. 4). At 7 days' culture, DPLF cultured with F. 2 and F. 3 proteins exhibited almost confluent phase and an elongated shape as well as confluent cells in Fig. 1b.

Ultrastructually, the cultured cells were spindle in shape, and arranged in a band approximately parallel to the plastic dish. The cells cultured on the plastic dish without fraction coating (controls) were composed of a single cell layer, and its cytoplasm contained moderately developed rough-surfaced endoplasmic reticulum, many pinocytotic vesicles, and a more conspicuous filamentous structure. In the fraction-coated groups, the cells increased in number and consisted of two to three layers — the individual layers were separated by collagenous bundles. In the middle or upper part of the layer, the cells had well developed rough-surfaced endoplasmic reticulum with dilated cisternae and numerous free ribosomes. Ultrastructural features of the cells of the dish surface were similar to those of the control groups. However,

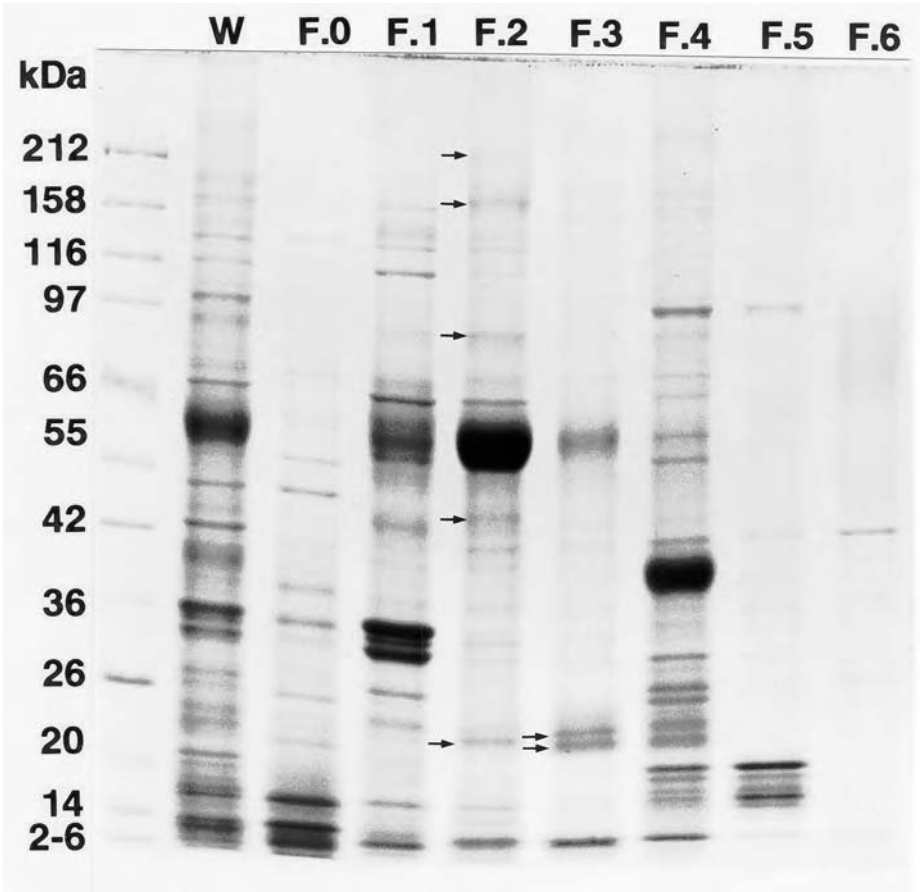

Figure 3. SDS-gel electrophoresis (5–15% gel) of proteins in DPLF-CM separated by IEC-DEAE stained with Coomassie Brilliant Blue. Arrows show characteristic bands in fractions 2 and 3.

in the fraction-coated groups, the gap between the dish surface and cells was narrower than that of the control groups, especially in fraction 2, and it was often bounded by the filament protruding from the cell membrane.

DISCUSSION

Cell proliferation and differentiation activities of DPLF-CM

It is said that the initial reactions of cell proliferation and differentiation occur when cells adhere to the protein constituent of cell adhesion molecules having Arg–Gly–Asp (RGD) sequences, such as collagen and fibronectin [15–17]. In addition, recent research has shown that the conditioned medium obtained from the cell culture supernatant fluid contains a variety of protein constituents and agents which are involved in cell proliferation and differentiation [9]. Kawase *et al.* [1] separated and fractionated a human periodontal ligament fibroblast-conditioned medium (HPLF-CM)

Table 1.
Effect of DPLF-CM separated by IEC-DEAE column on the growth of DPLF

	DNA (μg/well) (mean $\pm$ SE, $n = 4$)		Fx : F0
	Fx	Fx − blank	
Blank	0.42 ± 0.03		
F. 0	1.15 ± 0.12	0.73 ± 0.09	1.00
F. 1	1.90 ± 0.09	1.48 ± 0.13^a	2.03
F. 2	4.80 ± 1.10	4.38 ± 1.05^a	6.00
F. 3	3.74 ± 0.39	3.32 ± 0.42^a	4.35
F. 4	2.84 ± 0.49	2.42 ± 0.45^a	3.32
F. 5	2.21 ± 0.33	1.79 ± 0.30^a	2.45
F. 6	2.02 ± 0.74	1.60 ± 0.60^a	2.19

DPLF were cultured on hydrophobic wells coated with the column-separated fractions.

[a] Significantly different from F. 0 (non-bound fraction) value ($p < 0.01$).

Table 2.
Effect of DPLF-CM separated by IEC-DEAE column on the ALPase activity of DPLF

	ALPase (nmol/well) (mean $\pm$ SE, $n = 4$)		Fx : F0
	Fx	Fx − blank	
Blank	2.35 ± 0.12		
F. 0	4.18 ± 0.02	1.83 ± 0.13	1.00
F. 1	5.70 ± 0.25	3.35 ± 0.23^a	1.83
F. 2	10.06 ± 0.87	7.71 ± 0.77^a	4.21
F. 3	10.65 ± 1.35	8.30 ± 1.13^a	4.54
F. 4	7.52 ± 0.05	5.17 ± 0.27^a	2.83
F. 5	6.15 ± 0.17	3.80 ± 0.22^a	2.08
F. 6	8.06 ± 0.18	5.71 ± 0.32^a	3.12

DPLF were cultured on hydrophobic wells coated with the column-separated fractions.

[a] Significantly different from F. 0 (non-bound fraction) value ($p < 0.01$).

using ion exchange chromatography. They recognized the presence of attachments and spreading agents which are different from collagen, fibronectin, or hydronectin in the fractions which are eluted from the 0.35–0.56 M NaCl salt concentration among the eight fractions. With the present experiment using dog DPL cells, the conditioned medium are divided roughly into six fractions. The diffraction pattern is slightly different from human PDL cells and this may be attributable to the difference in animal species. The fact that remarkable increases in DNA quantity (cell proliferation activity) and ALPase activity were observed with the treated groups in fractions 2 and 3 that are eluted respectively by the 0.15 and 0.19 M NaCl which contain relatively small amounts of protein, indicate that these fractions contain a certain agent

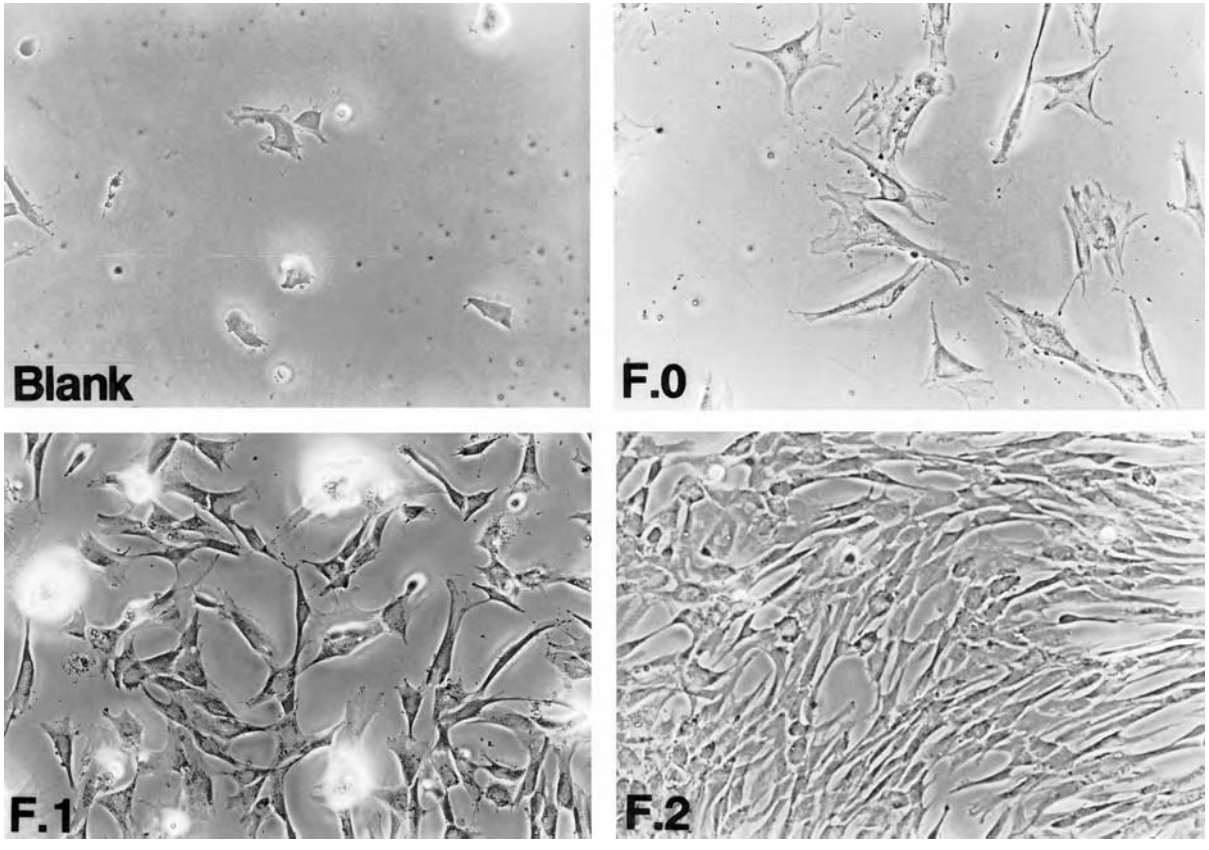

Figure 4. The phase contrast micrograph observation of DPLF growing on the wells coated with fractionated DPLF-CM (F. 1–F. 6) compared with non-bound fraction (F. 0). Cell proliferation was markedly observed in F. 2 and F. 3.

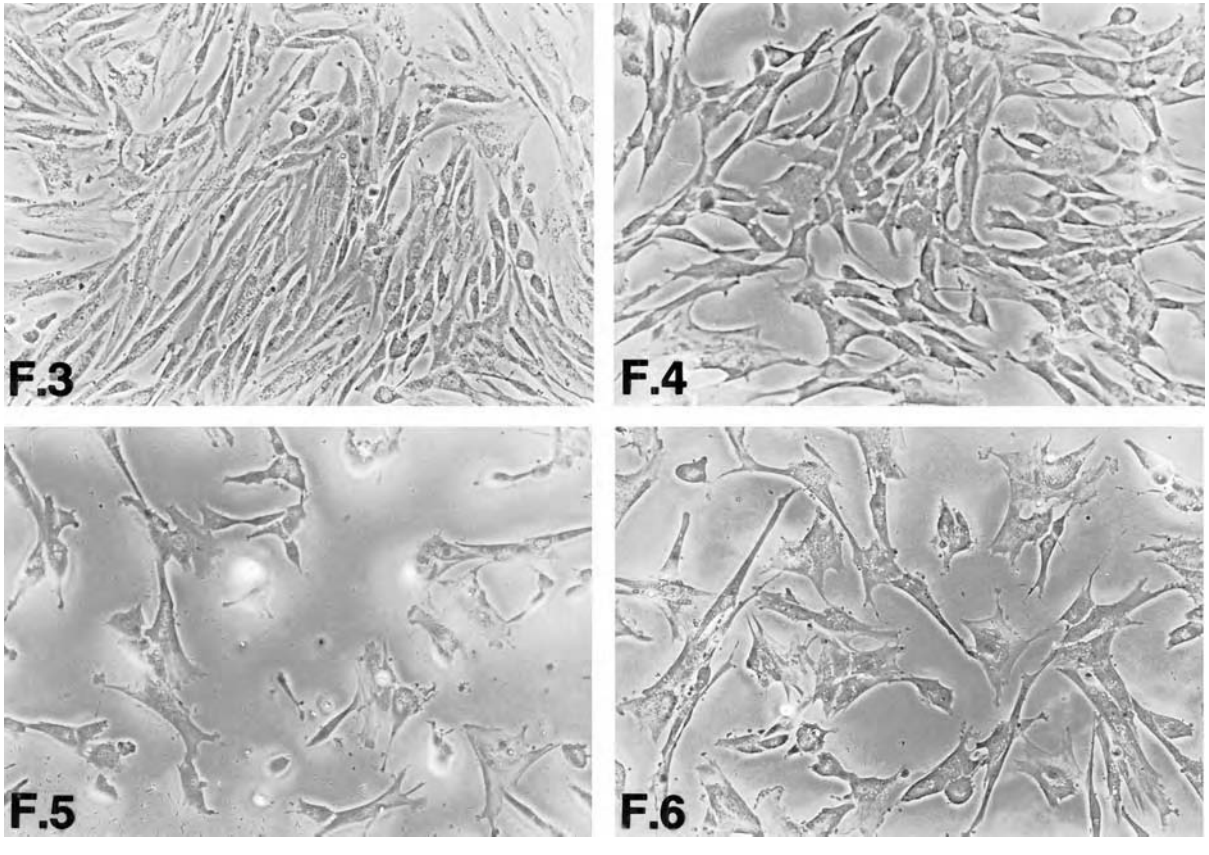

Figure 4. (Continued).

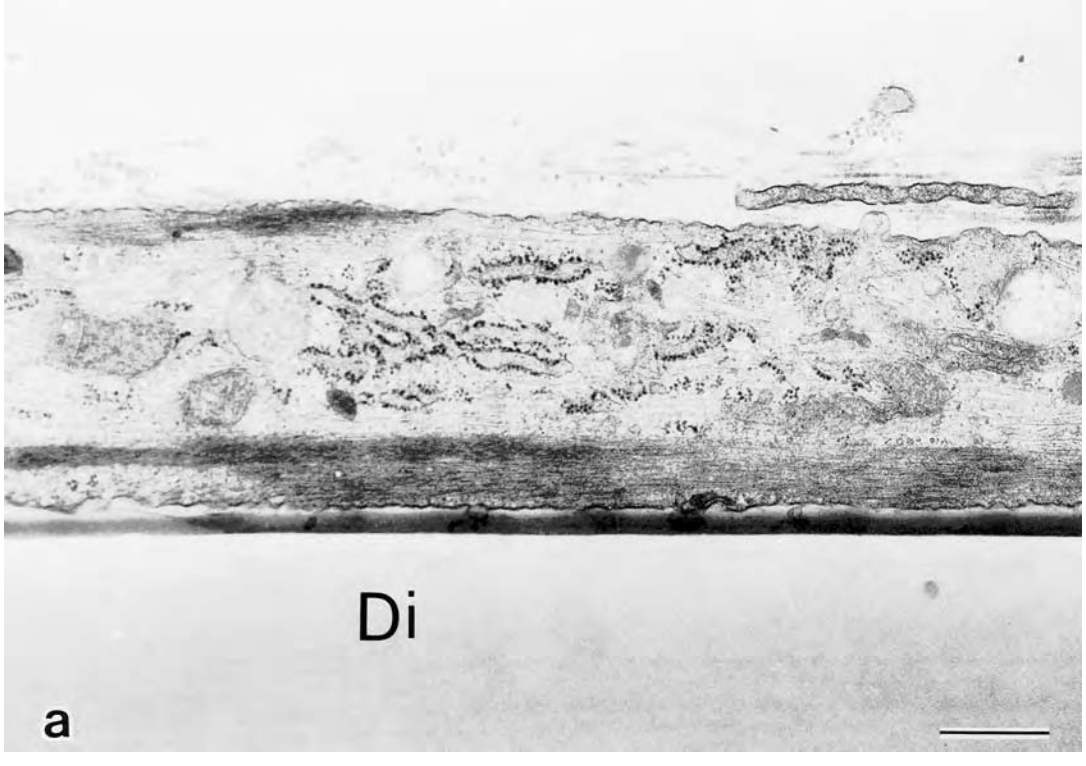

Figure 5. Electron micrograph of the DPLF cells at day 7 of culture. (a) F. 0. It shows only a single cell layer on the dish. Note a more conspicuous filament structure. (b) Culture on the F. 2-coated dish. The cell become many-layered and the individual layers were separated by collagenous bundles. Di; dish. Bar = 0.5 μm for (a) and (b).

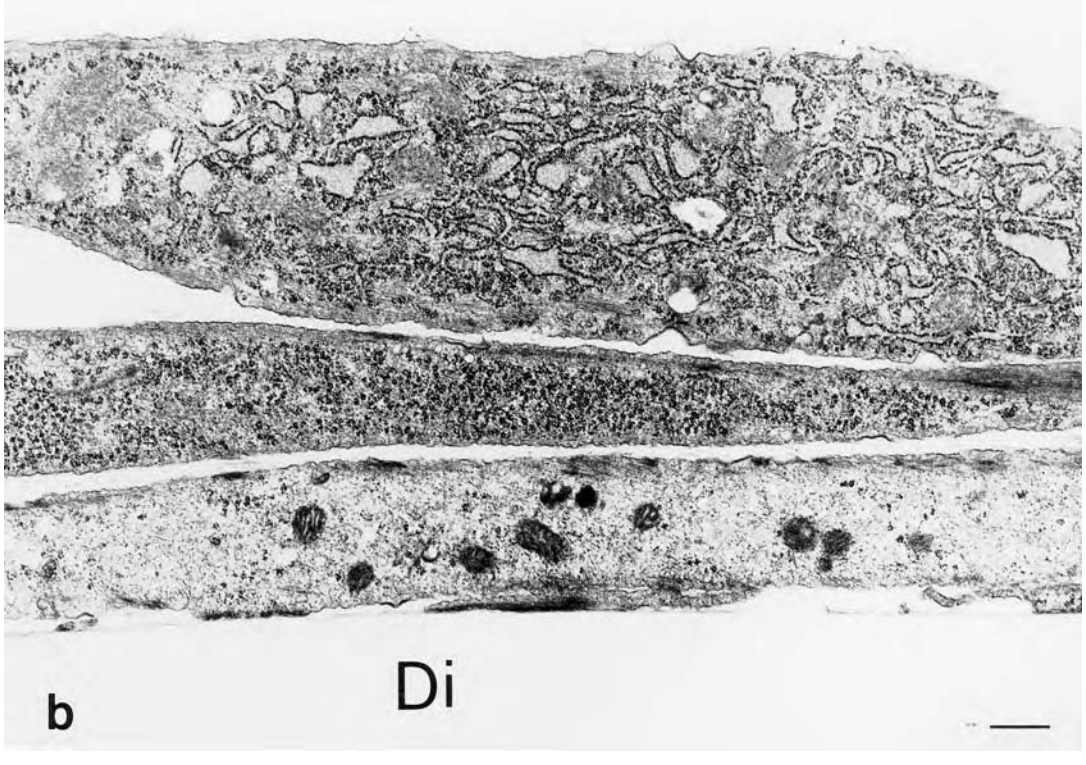

Figure 5. (Continued).

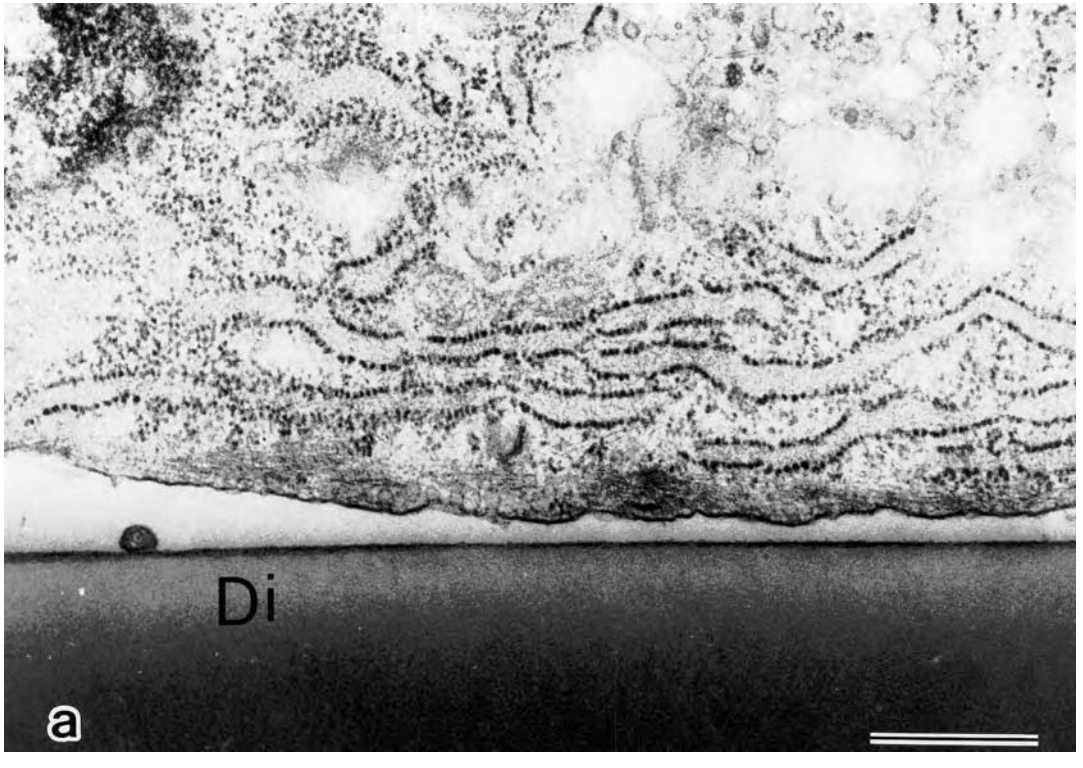

Figure 6. Electron micrograph of the DPLF cells situated the dish surface at day 7 of culture. (a) F. 0. A wide space exists between the dish surface and cell membrane. (b) Culture on the F. 3-coated dish. The gap between the dish surface and cell is narrower than that of the F. 0 culture. Inset; the cell is sticked to the dish by the filaments protruding from cell membrane. Di; dish. Bar = 0.5 μm for (a) and (b), and 0.01 μm for inset.

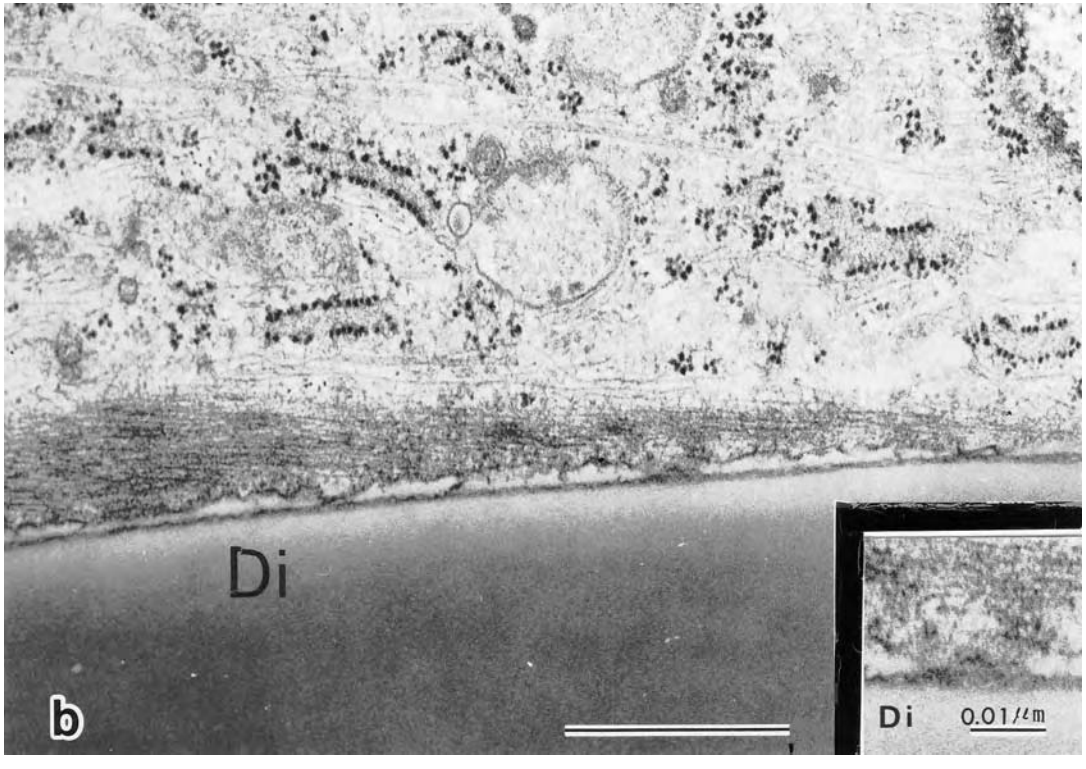

Figure 6. (Continued).

which promotes the proliferation and differentiation of dog PDL cells. In addition, the fact that a high increase in ALPase compared to the increase in the DNA quantity is found with the treated group with fraction 6 indicates the potential for the presence of protein with high cell differentiation activity in this fraction. As these active proteins have affinity with the dish which is a hydrophobic medium and their activity is effective even after the culture period of 7 days, it is suggested that these active proteins may have an amino acid composition with strong hydrophobic bonding or amino acid sequences, as reported by Woldenden *et al*. [18]. On the other hand, McAllister *et al.* [19] reported that they fractionated human cementum protein with ion exchange chromatography and observed a cell attachment and proliferation activity substance which can be eluted with 0.313 M NaCl. Similarly, Somerman *et al*. [20] observed similar cell activity in the substance eluted from cementum with 0.85 M NaCl, and Arzata *et al*. [21] observed a similar cell activity in the substance eluted from cementum with 0.5 M NaCl. These cementum proteins are regarded as being produced originally by cementoblasts, that is, PDL cell-derived cells. Therefore, the result of present research does not conflict with previous reports and also indicates that PDL-derived cells synthesize and secrete a variety of characteristic proteins involved in the attachment, spreading, proliferation, and differentiation of cells.

Pattern analysis of proteins extracted by SDS-PAGE

Kim [22] separated the fractions of a human periodontal ligament fibroblast-conditioned medium (HPLF-CM) by SDS-PAGE-applied silver dyeing and found that each fraction has a specific pattern and consists of a variety of proteins and that specific proteins are involved in the attachment and spreading of cells. Kawase *et al*. [1] analyzed the fraction patterns of HPLF-CM, researched various activation agents, and came to expect to find the presence of cell attachment and active spreading substances at estimated molecular weights of approximately 70, 50, and 10 kD and the presence of chemotactic active substances at an estimated molecular weight of 70 kD. With the present research, bands with almost similar molecular weights are observed in some fractions. Also, single bands which are not observed in other fractions were recognized at estimated molecular weights of approximately 210, 160, 85, 50, and 22 kD in fraction 2 where strong activities in the cell proliferation and differentiation was evident and at estimated molecular weights of 23 and 21 kD in fraction 3. These bands are regarded as being important agents which regulate the proliferation and differentiation of PDL cells. According to their molecular weights, the substances in the high-molecular weight region of fraction 2 are supposed to be adhesive glycoproteins such as collagen and fibronectin or complexes of biglycan which is a non-collagenous protein existing in large amounts in cartilage and bones, and the substance observed in the low-molecular weight region of the fraction 3 is supposed to be one of the phosphoproteins. However, to identify these proteins, it is required to apply immunochemical demonstrations and amino acid sequence analyses in the future.

Fine structure on the cell–dish interface

What is important in regenerating the PDL tissue is to arrange the substrate properties in an environment where cells can be attached and held easily and in one which is advantageous for the phenotypic expression of PDL cells [23]. Ririe *et al*. [24] reported that PDL reattachment and regeneration can be promoted by exposing the collagen in dentin by decalcificating the tooth root surface of a dog with a gingival flap operation. Also, Boyko *et al*. [5], Higashi *et al*. [25], and Ogawa *et al*. [26] recognized that there is an explicit increase in the number of attached PDL cells on a decalcificated tooth root surface compared to a non-decalcificated surface *in vitro*. According to the reports by Tanaka [27] , and Onizuka *et al*. [28], both of them made an electron microscopic search of the attaching ability of cultured cells on a tooth root surface exposed after acid treatment and found that neither microfibrils nor collagen fibrils are observed in the gap between the non-decalcified tooth root surface and cells, but that their fine-fibrous structures are observed in the gaps between decalcified tooth root surface and cells. According to observations in the present research, the gap between the untreated dish surface and the PDL cells is wide, no fibrous structures such as collagen fibrils and microfibrils are observed, and cases of cells being attached to the dish surface were hardly observed. On the other hand, with the coated fractionated constituents, attaching of cell membranes and the connection of the dish and cells by fine-fibrous structures projected from the attached cell membranes were observed in many places. This result resembles the results of observations of the attaching of cultured cells on decalcified tooth root surfaces by Tanaka [27], and Onzuka *et al*. [28], indicating that the protein constituents synthesized by PDL cells play an important role in cell attachment which is indispensable in the initial process of PDL regeneration. The reason why the collagen fibrils reported by Tanaka [27], and Onizuka *et al*. [28] are not observed between the cells and dish in the present research may be attributable to the short culture period which was not enough to form collagen fibrils. The fact that the connection with the dish surface is favorable in the groups treated by fractions 2 and 3 corresponds to the fact that the cell proliferation and differentiation abilities are promoted most in these fractions. In other words, this can be regarded as a morphological demonstration that these fractions contain important protein constituents which promote the adhesion and proliferation of cells in a similar way to the protein constituents of the cementum [24–28].

As a result of the above, it has been suggested that the coating of hydrophobic macromolecular materials with the above mentioned protein constituents function effectively for the attaching, proliferation, and differentiation of PDL cells on the material surface.

In the future, the author of the present research believes that extracting and identifying these proteins will widen the way to PDL regeneration in dental implants.

CONCLUSION

The supernatant of the conditioned medium (CM) of dog periodontal ligament fibroblast (DPLF) was fractionated with the IEC-DEAE column. PDLFs were cultured

on hydrophobic dishes coated with the each fraction. Cell proliferative activity and ALPase activity as well as electron microscopic feature of the contact surface between the cells and the dish were investigated.

The DPLF-CM could be separated by IEC-DEAE column into six fractions. It was suggested that the DPLF-CM fractions contained specific physiological activating factors that induce proliferation and differentiation as well as cell adhesion of the DPLF cells.

REFERENCES

1. T. Sou and M. Kobatashi, *Kanagawashigaku* **28**, 1 (1993).
2. T. Kawase and S. Saito, *Tiss. Cult. Commun.* **14**, 109 (1995).
3. T. Karring, S. Nyman and J. Lindhe, *J. Clin. Periodontol.* **7**, 96 (1980).
4. T. Karring, F. Isidor, S. Nyman and J. Lindhe, *J. Clin. Periodontol.* (1985).
5. G. A. Boyko, D. M. Brunette and A. H. Melcher, *J. Periodont. Res.* **15**, 297 (1980).
6. J. E. Piche, D. L. Carnes and D. T. Graves, *J. Dent. Res.* **68**, 761 (1989).
7. N. Nojima, M. Kobayashi, M. Shinome, N. Takahashi, T. Suda and K. Hasegawa, *J. Periodont. Res.* **25**, 179 (1990).
8. M. J. Somerman, S. Y. Archer, G. M. Imm and R. A. Foster, *J. Dent. Res.* **67**, 66 (1988).
9. M. J. Somerman, R. A. Foster, G. M. Imm, J. J. Sauk and S. Y. Archer, *J. Periodontal.* **60**, 73 (1989).
10. M. Kobayashi, S. Fukuoka and Y. Kinoshita, *Bull. Kanagawa. Dent. Col.* **22**, 169 (1994).
11. D. M. Brunnete, A. H. Mercher and H. K. Moe, *Arch. Oral. Biol.* **21**, 393 (1976).
12. J. E. Puzas and D. B. P. Goodman, *Anal. Biochem.* **86**, 50 (1978).
13. J. E. Puzas and J. S. Brand, *Endocrinology* **116**, 2463 (1985).
14. U. K. Laemmli, *Nature* **227**, 680 (1970).
15. E. Ruoslahti and M. D. Pierschbacher, *Science* **238**, 491 (1987).
16. R. O. Hynes, *Cell* **48**, 549 (1987).
17. K. M. Yamada and D. W. Kennedy, *J. Cell Physiol.* **130**, 21 (1987).
18. R. U. Wolfenden, P. M. Cullis and C. C. F. Southgate, *Science* **206**, 575 (1979).
19. B. McAllister, A. S. Narayanan, Y. Miki and R. C. Page, *J. Periodont. Res.* **25**, 99 (1990).
20. M. J. Somerman, J. J. Sauk, R. A. Foster, K. Norris, K. Dickerson and W. S. Argraves, *J. Periodont. Res.* **26**, 10 (1991).
21. H. Arzate, M. J. Chimal, L. L. Hernandez and L. L. Diaz, *J. Periodont. Res.* **31**, 144 (1996).
22. S. Kim, *Kanagawashigaku* **29** (1997) (in press).
23. U. M. E. Wiskesjo, R. E. Nilveus and K. A. Selvig, *J. Periodontol.* **63**, 158 (1992).
24. C. M. Ririe, M. Crigger and K. A. Selvig, *J. Periodont. Res.* **15**, 314 (1980).
25. T. Higashi, T. Onzuka, G. Satoh, H. Yoshino and H. Okamoto, *J. Periodontol.* **66**, 267 (1995).
26. T. Ogawa, H. Kawaguchi, Y. Fujitani, H. Yoshino, M. F. Liu, J. M. Oliveira, K. Nakanishi, T. Higashi and H. Kurihara, *Oral Med. Pathol.* **1**, 23 (1996).
27. H. Tanaka, *J. Japan. Soc. Peridont.* **31**, 434 (1989).
28. T. Onizuka, T. Higashi, G. Satho, H. Yoshino and H. Okamoto, *J. Japan. Soc. Peridont.* **36**, 420 (1994).

This page intentionally left blank

Section 3

Scaffolds

This page intentionally left blank

Polymers for Tissue Engineering, pp. 221–234
Molly S. Shoichet and Jeffrey A. Hubbell (Eds)

Surface characteristics and biocompatibility of lactide-based poly(ethylene glycol) scaffolds for tissue engineering

DONG KEUN HAN [1], KI DONG PARK [1], JEFFREY A. HUBBELL [2] and YOUNG HA KIM [1,*]

[1] *Biomaterials Research Center, Korea Institute of Science and Technology, P.O. Box 131, Cheongryang, Seoul 130-650, Korea*
[2] *Department of Materials and Institute for Biomedical Engineering, ETH Zürich and University of Zürich, CH-8044 Zürich, Switzerland*

Received 25 August 1997; accepted 17 December 1997

Abstract—Novel lactide-based poly(ethylene glycol) (PEG) polymer networks (GL9-PEGs) were prepared by UV copolymerization of a glycerol-lactide triacrylate (GL9-Ac) with PEG monoacrylate (PEG-Ac) to use as scaffolds in tissue engineering, and the surface properties and biocompatibility of these networks were investigated as a function of PEG molecular weight and content. Analysis by ATR-FTIR and ESCA reveled that PEG was incorporated well within the GL9-PEG polymer networks and was enriched at the surfaces. From the results of SEM, AFM, and contact angle analyses, GL9-PEG networks showed relatively rough and irregular surfaces compared to GL9 network, but the mobile PEG chains coupled at their termini were readily exposed toward the aqueous environment when contacting water such that the surfaces became smoother and more hydrophilic. This reorientation and increase in hydrophilicity were more extensive with increasing PEG molecular weight and content. As compared to GL9 network lacking PEG, protein adsorption as well as platelet and *S. epidermidis* adhesion to GL9-PEG networks were significantly reduced as the molecular weight and content of PEG was increased, indicating that GL9-PEG networks are more biocompatible than the GL9 network due to PEG's passivity. Based on the physical and biological characterization reported, the GL9-PEG materials would appear to be interesting candidates as matrices for tissue engineering.

Key words: Tissue engineering; scaffold; polylactide; PEG; hydrophilicity; biocompatibility.

INTRODUCTION

Biomaterials play an important role in tissue engineering [1, 2]. Polymeric biomaterials in tissue engineering research are being applied in conducting, guiding,

*To whom correspondence should be addressed. E-mail: yhakim@kistmail.kist.re.kr

and inducing tissue formation as well as in blocking tissue interactions [3, 4]. These polymers for structural scaffolds require proper physical and mechanical properties, designable biodegradability, nontoxicity, good biocompatibility, and the ability to interact with specific cells. Scaffolds meeting these requirements may be useful regenerating damaged tissues or organs by combining scaffolds with living cells.

From the perspective of scaffold biocompatibility, one would like to be able to limit protein adsorption and cellular interactions with the scaffold's base material, thus permitting specific cell adhesion to be designed separately via the incorporation of cell adhesion peptides [4]. Moreover, it is desirable that interactions with potentially colonizing bacteria be minimized. A variety of approaches have been taken to accomplish these ends in improving the biocompatibility of polymer surfaces [5, 6]. Surface modification, for example, has been explored by: (1) chemical grafting of a hydrophilic component, such as poly(ethylene glycol) (PEG); (2) incorporating bioactive agents such as anticoagulant (heparin), platelet-passivating prostaglandins (e.g. PGE_1), and fibrinolytic enzymes (tPA); and (3) biological modification using protein adsorption or cell seeding.

PEG is a hydrophilic synthetic polymer and has received much attention because it is highly water soluble compared with other similar polyethers. PEG's passivity to biological responses may be caused by many factors, such as a very low interfacial free energy with water, lack of ionic binding sites, high chain mobility, steric stabilization effects, and molecular conformation in water [7]. These characteristics have led to many investigations on the utilization of PEG as a biocompatible material. It has been reported that PEG-treated biomaterials showed less protein adsorption [8], platelet and cell adhesion [9, 10], and bacteria adhesion [11] due to the characteristics listed above. The antigenicity and immune clearance of therapeutic proteins have also been shown to be reduced by grafting of PEG [12]. PEG has almost been introduced into polymer substrates by physical adsorption [13] and entrapment [14], covalent coupling [15, 16], photoinduced grafting [17], glow discharge treatment [18], and gamma irradiation [7] to improve their biocompatibility. Covalent coupling of PEG to substrates is usually the most effective way to provide stable performance for biomedical applications.

Recently, we have developed novel polymer network scaffolds for use in tissue engineering, which have biodegradable, biocompatible, and ligand-immobilizable characteristics [19, 20]. Lactide-based PEG-containing scaffolds were synthesized by UV copolymerization using two nontoxic precusors, triacrylated lactic acid oligomer emanating from a glycerol center and monoacrylated PEG (PEG-Ac). The obtained cross-linked polymer networks were glassy and transparent. All such networks showed low swelling in water and had no melting endotherms, but displayed a glass transition temperature that was indicative of phase-mixing of the PEG. The mobile PEG chains in the copolymer networks were enriched at the surfaces and made the surfaces more hydrophilic. In addition, PEG-containing networks were highly resistant to fibroblasts adhesion compared to glass as well as network lacking PEG.

In this study we have focused our attention on one particularly favorable triacrylated lactide oligomer macromonomer emanating from a glycerol center, with lactide arms of average degree of polymerization 9 (thus, GL9-Ac). We have performed a detailed analysis of surface character and investigated interactions with proteins, platelets, and bacteria as PEG molecular weight and content were varied.

MATERIALS AND METHODS

Synthesis of GL9-PEG networks

Figure 1 shows the synthetic reactions leading to the formation of GL9-PEG networks. The synthetic methods employed to obtain GL triols, GL triacrylates, and GL-PEG networks have been previously reported in detail elsewhere [19, 20]. Networks were formed from two reactive precursors, a GL9-Ac and α-monoacrylate-ω-monohydroxy PEG (PEG-Ac; M_w = 1000, 1K; 4000, 4K; 8000, 8K; Monomer-Polymer & Dajac).

The typical synthetic procedure is as follows: first, 1.02 g glycerol (G, Aldrich), 43.2 g L-lactide (L, 27 mol per G mol; Aldrich), and 0.61 g stannous octoate (St-Oct, 1/200 of L mol; Sigma) were reacted in melt at 130°C for 6 h under argon. The melt was allowed to cool and was dissolved in chloroform, micro-filtered, precipitated in hexane, and vacuum-dried to yield GL9 triol. Second, 4.77 g acryloyl chloride (AcCl, 6 mol per GL9 triol mol; Aldrich) dissolved in 18 ml of dichloromethane (DCM) was slowly dropped into 35 g GL9 triol and 5.33 g triethylamine (TEA, 1 mol per AcCl mol; Aldrich) dissolved in 315 ml of DCM and reacted at 0°C for 6 h and at room temperature for 42 h. The solution was micro-filtered, precipitated in diethylether, and vacuum-dried to yield triacrylated GL9, GL9-Ac. Finally, a 25% w/v solution of 1 g GL9-Ac, PEG-Ac (10, 20, and 30 wt% of GL9-Ac), and 1% w/w 2,2-dimethoxy-2-phenylacetophenone (benzyl dimethyl ketal, BDMK; Aldrich) dissolved in DCM were copolymerized by a 100-W medium pressure mercury ultraviolet (UV) irradiation (Black-Ray Model B-100A, 365 nm, UV Products) on Petri dishes to obtain GL9-PEG networks. The photocopolymerization was continued until gelation occurred, typically 10 min. The GL9-PEG network films produced were dried under vacuum at 60°C for 1 day, and then extracted with chloroform at room temperature for 1 day to remove unreacted macromers and homopolymers. The films were dried again and used for surface characterization and biocompatibility analysis.

The synthesized networks were denoted as follows: GL9-PEGn*K*-p, where 9 is the total number of dimeric repeats of lactic acid, n (1, 4, and 8) is the molecular weight (K = 1000) of PEG-Ac, and p (10, 20, and 30) is weight % of PEG-Ac per GL9-Ac. In addition, GL9 homonetwork was prepared using only GL9-Ac in the absence of PEG-Ac for comparison.

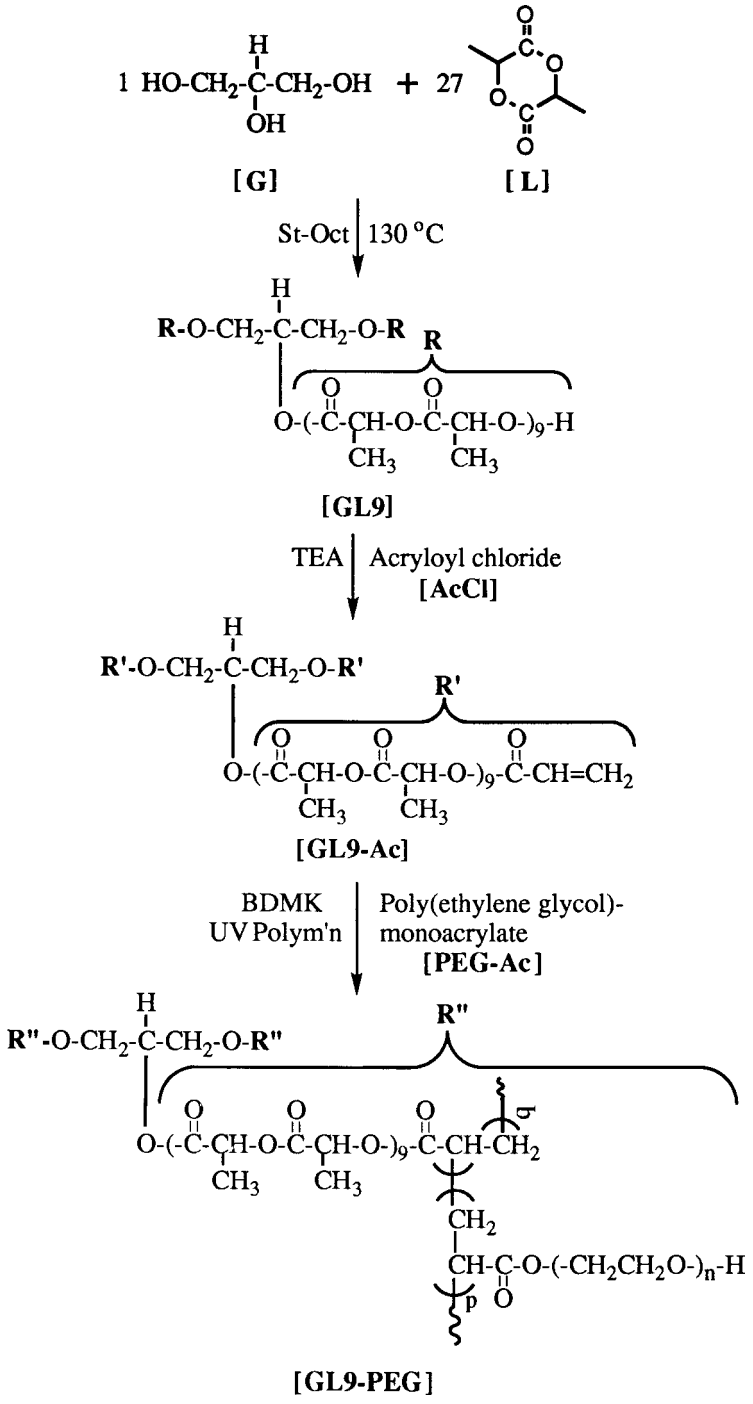

Figure 1. Scheme for synthesis of GL9-PEG networks.

Surface characterization

Attenuated total reflectance–Fourier transform infrared (ATR-FTIR) spectra were obtained from the surfaces of the networks using a Mattson Genesis Series FTIR spectrophotometer. The elemental compositions of the surfaces were determined using an electron spectroscopy for chemical analysis (ESCA) spectrometer (S-Probe Surface Science) at a take-off angle of 55 deg. The subpeaks of C_{1s} were deconvoluted using a curve-fitting method from a series of Gaussian–Lorentzian curves [21].

The surface morphology of networks was examined with a Hitachi S-2460N scanning electron microscopy (SEM) at an accelerating voltage of 19 kV. Samples were mounted and then sputter-coated with gold using an ion coater (Hitachi E-1010). Atomic force microscopy (AFM) in contact mode (DC mode) was performed with an Autoprobe CP system from Park Scientific Instruments (PSI, Sunnyvale, CA, USA). Images were obtained from dry and wet (hydrated in water for 1 day) sample surfaces in air using a 100-μm piezo-scanner and a microfabricated triangular cantilever supporting an integrated pyramidal tip (Ultralever^{TM}, PSI).

Surface wettability was assessed by two methods: static contact angles [22] were measured by the sessile drop method using an Erma Contact Anglemeter G-I, and dynamic contact angles (DCA) [23] were determined by the Wilhelmy plate method using a DCA-315 apparatus (Cahn Instruments) in water.

Biocompatibility

Measurements of protein adsorption were carried out by ESCA. Human plasma (Sigma) was diluted with phosphate-buffered saline (PBS, pH 7.4) to make a 10% solution. The polymer network samples (1×1 cm^2) were placed on 12-well polystyrene plates (Corning) and equilibrated with PBS for 1 h. After removing the PBS solution from the wells by pipetting, the plasma protein solution (4 ml) was added to the wells. After 1 h incubation at 37°C, the samples were washed with PBS, followed by washing with water to remove nonadsorbed proteins. After vacuum drying, the protein-adsorbed sample surfaces were analyzed by ESCA [24]. The N_{1s} peaks from the detailed scan spectra were used as a measure of the amount of proteins adsorbed on the surfaces.

Measurements of platelet adhesion were carried out with human platelet-rich plasma (PRP). Whole blood, anticoagulated with citrate, was centrifuged at 300 *g* for 10 min to obtain PRP. The platelet concentration of PRP was adjusted to 2×10^4 platelets μl^{-1} by adding platelet-por plasma to PRP. Sample films (1×1 cm^2) prehydrated for 24 h in PBS were immersed in the diluted PRP. After 2 h incubation at 37°C, unadhered platelets in the PRP were counted by a hematocytometer. The amount of platelets that adhered upon the film was calculated by subtracting the number of unadhered platelets from the number of diluted platelets that were initially incubated.

S. epidermidis (ATCC no. 12228), a Gram-positive bacterial strain, was used for measurement of bacterial adhesion to the networks. The films (1×1 cm^2) were incubated in human plasma, which had been diluted to 80% with tryptic soy broth (TSB, DIFCO), inoculated with 2×10^6 bacteria ml^{-1} for 24 h at 37°C with constant swirling. After the films were washed with PBS, the bacteria were eluted from the surface using an ultrasonicator. The bacteria eluted in PBS were diluted, incubated on agar plates for 19 h at 37°C, and then counted as single colony-forming unit (CFU).

RESULTS AND DISCUSSION

Synthesis and surface properties

The structure of reaction intermediates, GL9 triol and GL9 triacrylate, was confirmed by elemental analysis, FTIR, and NMR. The obtained GL9 network films were glassy and transparent and the gel content of the networks that were formed by crosslinking was typically 90%. The bulk and some surface characteristics as well as fibroblasts adhesion of these polymer networks have been described in detail elsewhere [20].

Figure 2 shows typical ATR-FTIR spectra of GL9 and GL9-PEG8K-20 surfaces. While three sharp peaks at 1082, 1182, and 1750 cm^{-1} were attributed to C—O, antisymmetric C—O, and C=O stretchings from GL9 network, a strong broad band of C—O stretching in PEG was observed at 1000–1150 cm^{-1} for the GL9-PEG8K-20 network. Although the C—O peaks from lactide in GL9 and from PEG in GL9-PEG networks were overlapped, the composite C—O peak was broader with increasing molecular weight and content of PEG.

Table 1 shows the atomic surface composition of GL9 and GL9-PEG networks analyzed by ESCA. After the incorporation of PEG in the GL9 network, the oxygen atomic percentage of the GL9-PEG networks considerably increased at the expense of a decrease in the carbon atomic percentage. From the results of analysis of the C_{1s} peaks obtained from curve fitting, no PEG ether peak was founded in the

Table 1.
ESCA results for GL9 and GL9-PEG networks

Material	C	O	C—O/C—C[a]
GL9 network	72	28	0
GL9-PEG1K-20	64	36	0.11
GL9-PEG4K-10	64	36	0.16
GL9-PEG4K-20	65	35	0.18
GL9-PEG4K-30	67	33	0.19
GL9-PEG8K-20	67	33	0.21

[a] Ratio of PEG ether (C—O) % (286.5 eV) over GL hydrocarbon (C—C) % (285.0 eV) from C_{1s} high resolution spectra.

GL9 network. As the PEG molecular weight and content in GL9-PEG networks were increased, the oxygen atomic percentage was relatively decreased, but the value of PEG ether percentage over the GL hydrocarbon percentage increased, suggesting that PEG was enriched at the network surfaces. This enrichment was observed both as PEG-Ac molecular weight was increased at constant PEG mass content and as PEG content was increased at constant PEG molecular weight.

The surface morphology of GL9 networks was examined by SEM and AFM. Figure 3 shows typical SEM micrographs of GL9 and GL9-PEG8K-20 surfaces. The GL9 surface was relatively smooth, whereas GL9-PEG surfaces were more rough and irregular, irrespective of the molecular weight and content of PEG incorporated. To study further the irregularities and reorientation of GL9-PEG surfaces in the dried and hydrated states, AFM observation was carried out, as shown in Figs 4 and 5. The GL9 surface in the dry state was considerably smooth and homogeneous, but GL9 in the wet state became relatively rough. In addition, the GL9-PEG surface in the dry state was very rough and heterogeneous, perhaps due to partial coverage by PEG chains on the surface. After hydration in water for 1 day, the GL9-PEG surface became more smooth. This surface roughness of dry GL9-PEG networks increased gradually with increments in PEG molecular weight and content. It was proved from statistical analysis of the roughness measurement that rms roughness of the wetted GL9 surface (47 Å) was increased compared to that of the dried one (28 Å). On the contrary, the wetted GL9-PEG surface (420 Å) showed much less rms roughness than did the dried one (700 Å), suggesting that the flexible PEG chains coupled within the GL9-PEG network were reoriented into the aqueous environment and more completely covered on the surface. Such a phenomenon was also supported from 3D images of network surfaces (Fig. 5). As

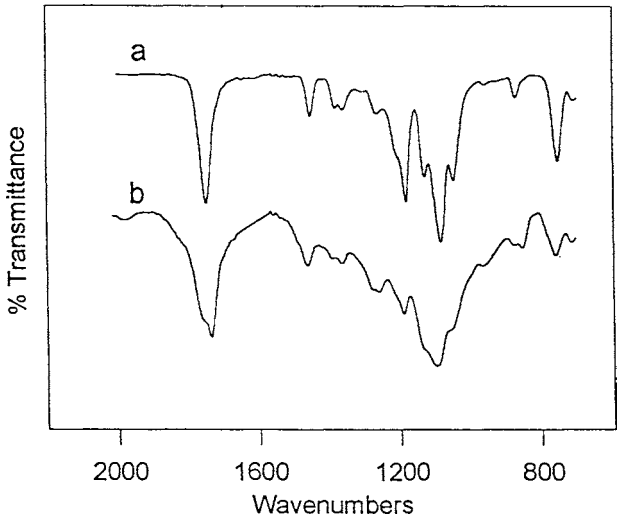

Figure 2. Typical ATR-FTIR spectra of (a) GL9 and (b) GL9-PEG8K-20 surfaces.

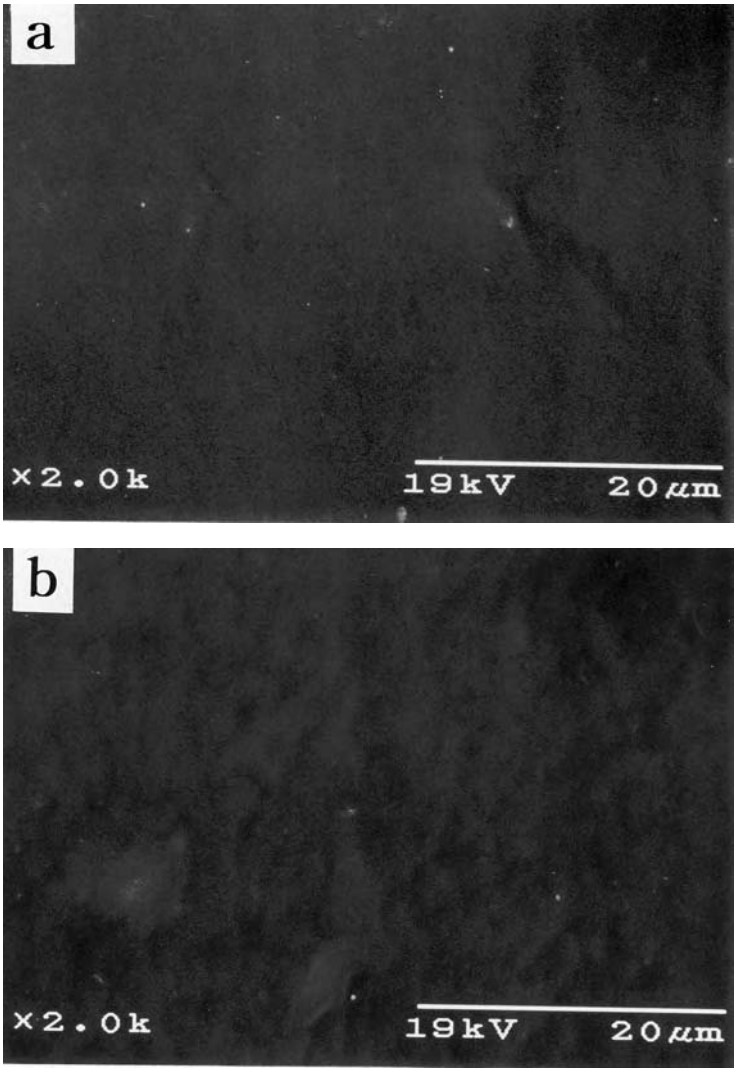

Figure 3. Typical SEM micrographs of (a) GL9 and (b) GL9-PEG8K-20 surfaces.

compared to the dried surfaces, the hydrophilic aspects of the wetted surfaces may have been exposed to the water phase by swelling in the hydrophilic environment.

The hydrophilicity of the network surfaces in the dried and wetted states was evaluated by measuring the static and dynamic contact angles at the air–water interface. Table 2 lists the contact angles obtained for the GL9-containing networks. The GL9 network showed relatively hydrophobic surfaces compared to GL9-PEG networks. The hydrophilicity increased both with increasing PEG molecular weight and content for the GL9-PEG networks, resulting from the introduction of hydrophilic PEG to the GL9 network surface, which was confirmed by ESCA analysis. In addition, after hydration in PBS for 1 day, the hydrophilicity was

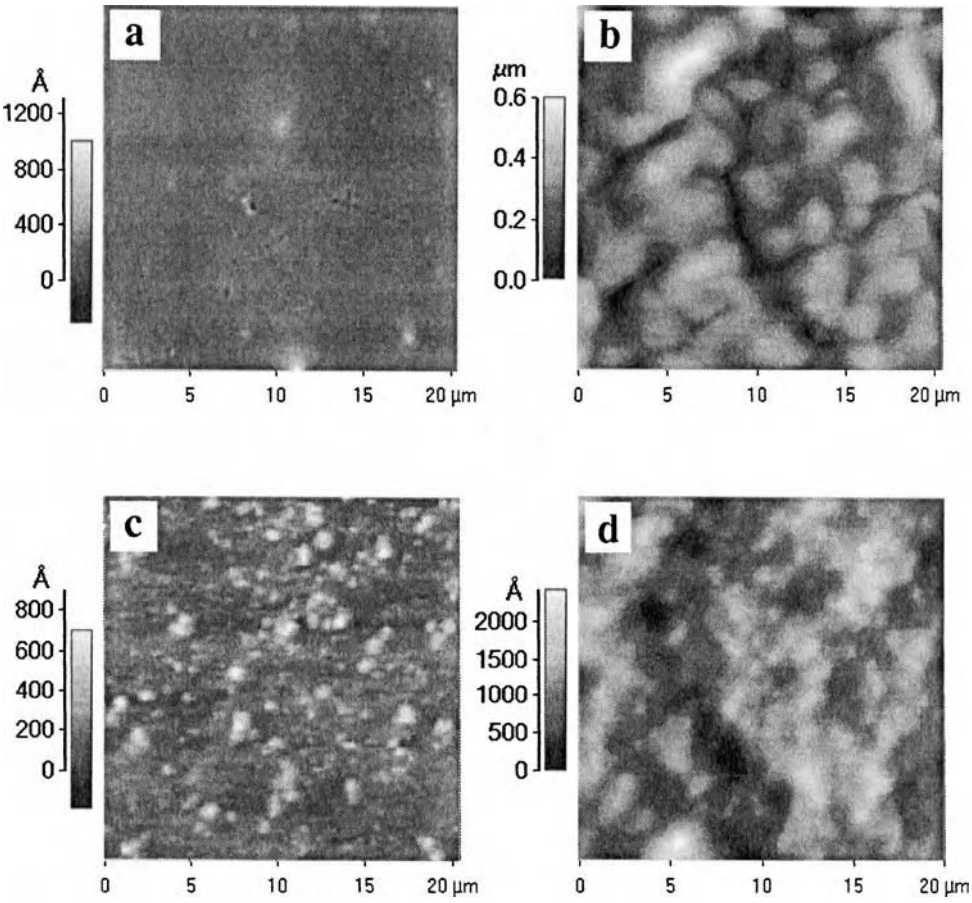

Figure 4. Typical AFM 2D images of GL9 and GL9-PEG surfaces: (a) GL9 network in dried state; (b) GL9-PEG8K-20 network in dried state; (c) GL9 network after hydration for 1 day; and (d) GL9-PEG8K-20 network after hydration for 1 day.

Table 2.
Contact angle results[a] for GL9 and GL9-PEG networks

Material	Static		Dynamic[b]	
	Dry	Wet[c]	θ_{adv}	θ_{rec}
GL9 network	70	65	92	58
GL9-PEG1K-20	50	43	85	55
GL9-PEG4K-10	46	39	78	50
GL9-PEG4K-20	43	35	73	45
GL9-PEG4K-30	40	31	69	42
GL9-PEG8K-20	37	26	67	40

[a] Unit: degree ($n = 3–5$).
[b] θ_{adv}: advancing contact angle; θ_{rec}: receding contact angle.
[c] After hydration in PBS for 24 h.

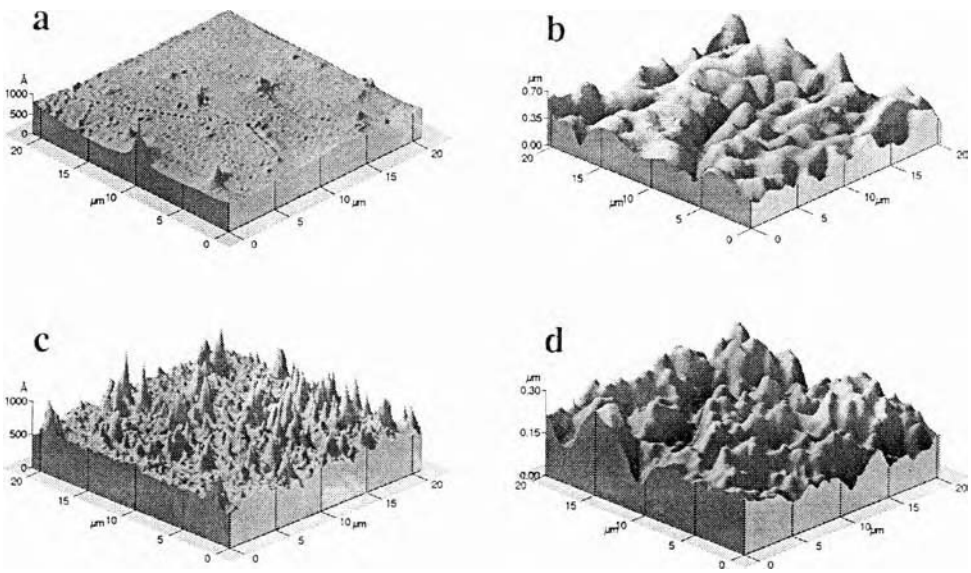

Figure 5. Typical AFM 3D images of GL9 and GL9-PEG surfaces: (a) GL9 network in dried state; (b) GL9-PEG8K-20 network in dried state; (c) GL9 network after hydration for 1 day; and (d) GL9-PEG8K-20 network after hydration for 1 day.

considerably increased in comparison with same samples before such extensive hydration. These results, specifically the observation at constant PEG content, suggest that the surfaces are more hydrophilic because the pendent PEG chains at the surfaces are highly mobile and are capable of rearrangement to minimize their interfacial free energy depending on the environment, such as air or water [25]. This interpretation of the contact angle measurement is consistent with the AFM observations. Accordingly, it seems that such surface properties of GL9-PEG networks might be expected to positively affect their biocompatibility.

Plasma protein adsorption

To quantify the adsorption on plasma proteins to GL9 and GL9-PEG network surfaces, the films were exposed to diluted plasma and the relative amounts of adsorbed proteins on the surfaces were evaluated by ESCA narrow scan spectra (Fig. 6). The nitrogen signal from peptide bonds in proteins was used as an indicator of surface protein adsorption, because all of the used samples have no nitrogen without adsorbed proteins. All GL9 and GL9-PEG surfaces showed lower protein adsorption than glass used as a reference material. The GL9 network lacking PEG exhibited a larger amount of protein adsorption than did the GL9-PEG networks, in which the flexible hydrophilic PEG chains were incorporated. As the PEG molecular weight and content were increased independently, the amount of adsorbed protein on GL9-PEG surfaces decreased. In particular, GL9-PEG8K-20 network showed the lowest protein adsorption of networks studied.

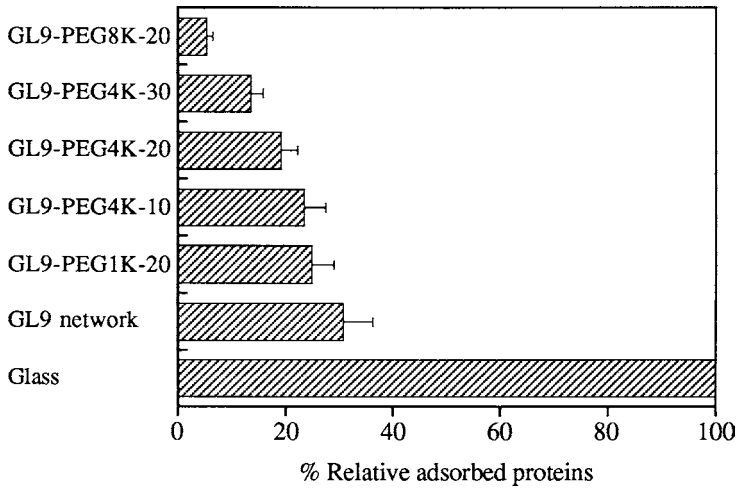

Figure 6. Relative amounts of protein adsorption on GL9 and GL9-PEG surfaces in plasma for 1 h ($n = 3–5$).

Many factors are involved in protein adsorption onto polymer surfaces. Of importance are hydrophobic interactions, electrostatic interactions, and acceptor–donor interactions [26]. It is well agreed that more protein generally adsorbs upon hydrophobic surfaces compared to hydrophilic surfaces, which is mainly attributed to hydrophobic interaction between protein and surface in which the protein acts as a surfactant. In the case of the GL9 network lacking PEG, the hydrophobic interaction of plasma proteins with hydrophobic lactide in the GL9 surface may induce relatively high levels of protein adsorption. It was reported that PEG-grafted polymer surfaces decreased significantly the extent of protein adsorption due to low interfacial free energy, highly dynamic motion and the extended chain conformation of PEG [8, 27, 28].

Platelet adhesion

PRP exposure was used to examine the adhesion behavior of platelets to the GL9 and GL9-PEG network surfaces (Fig. 7). GL9-PEG surfaces displayed relatively lower amounts of platelet adhesion and activation than did GL9 network lacking PEG. This trend was more remarkable when the PEG molecular weight was increased from 1000 to 8000 and its content was increased from 10 to 30%. The lowest amount of platelet adhesion was revealed on GL9-PEG8K-20 surface, that being reduced to 80% of the amount on the GL9 network lacking PEG.

It is highly likely that the reduced adhesion of platelets to GL9-PEG networks relative to GL9 is due to reduced levels of protein adsorption, as described above; adsorbed fibrinogen is known to be critically important in mediating platelet adhesion to materials, via interaction with GPIIb/IIIa receptor. This effect has been observed by others and is attributed to influence protein adsorption via the dynamic movement of the incorporated PEG [5, 9]. The greater the PEG molecular

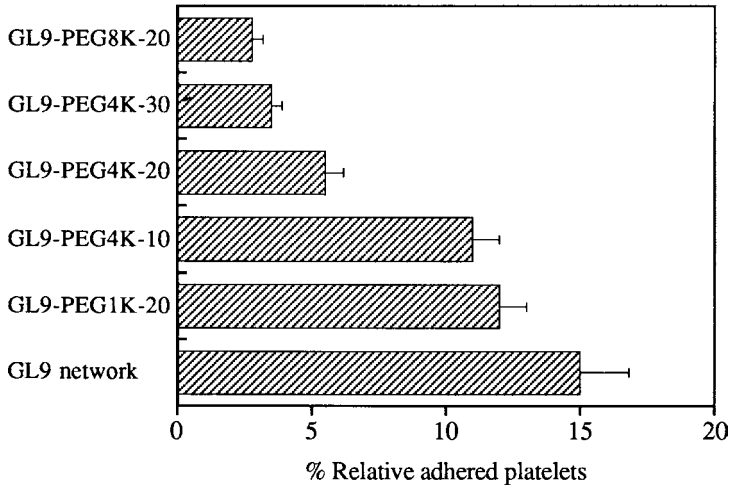

Figure 7. Relative platelet adhesion on GL9 and GL9-PEG surfaces in diluted PRP for 2 h ($n = 3-5$). 100% corresponds to adhesion of 6.7% of the platelets in the plasma sample.

weight is, the greater the expected molecular mobility would be, and thus the lower the adsorption of proteins and the adhesion of platelets. The results, therefore, suggest that longer PEG chain incorporated is more effective to minimize the platelet adhesion, perhaps resulting from both the volume restriction effect and local osmotic pressure effect of long chain molecules [27]. Such a suppressed platelet interaction of GL9-PEG networks may enhance blood compatibility in use as scaffolds in tissue/organ regeneration in the cardiovascular system.

Bacterial adhesion

Bacterial colonization of biomaterial surfaces and subsequent biomaterial-centered infection is known to be an important factor affecting biocompatibility. Bacterial adhesion to GL9 and GL9-PEG networks was evaluated using *S. epidermidis*, one of the bacteria that is commonly implicated in implant-related infections (Fig. 8).

As compared to the GL9 network surface, a significant decrease in bacterial adhesion was observed on GL9-PEG networks. Bacterial adherence on GL9-PEG surfaces was reduced notably with both increasing PEG molecular weight and content. In the case of the GL9 series, GL9-PEG8K-20 as well as GL9-PEG4K-30 showed similar low bacterial adhesion, which were reduced by approximately 90% relative to GL9 network lacking PEG.

The relationship between biomaterial properties and bacterial adhesion has been studied with the goal reducing infection in medical devices and implants. It has been reported that adsorbed plasma proteins such as fibrinogen and high molecular weight kininogen act as important mediators in the adherence of bacteria to biomaterial surfaces. Generally, bacteria adhere more on hydrophobic surfaces than on hydrophilic ones, an effect that is likely related to protein adsorption as described above [29, 30]. Relative to the hydrophobic GL9 surface, the hydrophilic

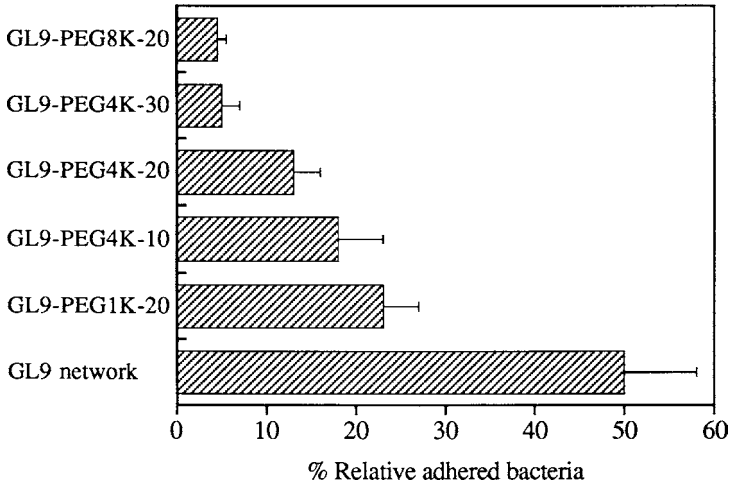

Figure 8. Relative *S. epidermidis* adhesion on GL9 and GL9-PEG surfaces ($n = 3-5$). 100% corresponds to 2.5×10^5 CFU.

GL9-PEG networks exhibited significantly decreased bacterial adhesion, which is consistent with other reports on polymer surfaces containing PEG [11, 31]. In addition, the effects of chain length and content of PEG were consistent with the results of protein adsorption and platelet adhesion presented above.

CONCLUSIONS

Two nontoxic macromers, triacrylated glycerol-lactide and monoacrylated PEG were copolymerized by UV photoinitiation to obtain new lactide-based PEG polymer network scaffolds. These surfaces were observed to be enriched with PEG, especially after the networks were hydrated, suggesting extensive reorganization in the aqueous environment. Such reorientation was correlated by imaging with SEM and AFM. Correlated behavior was consistently observed between an increase in surface hydrophilicity, a decrease in plasma protein adsorption, a decrease in platelet adhesion, and a decrease in *S. epidermidis* adhesion, all as either the PEG molecular weight was increased at constant mass content or as PEG mass content was increased at constant molecular weight. Given that these networks are constructed from nontoxic components and that the networks swell to a limited extent, and thus have good mechanical properties, they may be useful as scaffolds in tissue engineering.

Acknowledgement

This research was supported by Korea MOST grant V00194.

REFERENCES

1. R. Langer and J. P. Vacanti, *Science* **260**, 920 (1993).
2. R. M. Nerem and A. Sambanis, *Tissue Eng.* **1**, 3 (1995).
3. J. A. Hubbell and R. Langer, *Chem. Eng. News* March 13, 42 (1995).
4. J. A. Hubbell, *Bio/Technology* **13**, 565 (1995).
5. J. D. Andrade, S. Nagaoka, S. L. Cooper, T. Okano and S. W. Kim, *Am. Soc. Artif. Intern. Organs J.* **10**, 75 (1987).
6. Y. H. Kim, K. D. Park and D. K. Han, in: *Polymeric Materials Encyclopedia*, J. C. Salamone (Ed.), Vol. 1, p. 825. CRC Press, Boca Raton, FL (1996).
7. M. Amiji and K. Park, *J. Biomater. Sci. Polymer Edn* **4**, 217 (1993).
8. D. K. Han, K. D. Park, G. H. Ryu, U. Y. Kim, B. G. Min and Y. H. Kim, *J. Biomed. Mater. Res.* **30**, 23 (1996).
9. D. K. Han, S. Y. Jeong, Y. H. Kim, B. G. Min and H. I. Cho, *J. Biomed. Mater. Res.* **25**, 561 (1991).
10. A. S. Sawhney, C. P. Pathak and J. A. Hubbell, *Macromolecules* **26**, 581 (1993).
11. N. P. Desai, S. F. A. Hossainy and J. A. Hubbell, *Biomaterials* **13**, 417 (1992).
12. F. Fuerteges and A. Abuchowski, *J. Control. Rel.* **11**, 139 (1990).
13. J. H. Lee, P. Kopeckova, J. Kopecek and J. D. Andrade, *Biomaterials* **11**, 455 (1990).
14. J.-H. Chen and E. R. Stein, *J. Colloid Interface Sci.* **142**, 545 (1991).
15. D. K. Han, S. Y. Jeong and Y. H. Kim, *J. Biomed. Mater. Res.: Appl. Biomater.* **23** (A2), 211 (1989).
16. K. D. Park, W. G. Kim, H. Hacobs, T. Okano and S. W. Kim, *J. Biomed. Mater. Res.* **26**, 739 (1992).
17. Y. C. Tseng and K. Park, *J. Biomed. Mater. Res.* **26**, 373 (1992).
18. M. S. Sheu, A. S. Hoffman, J. G. A. Terlingen and J. Feijen, *Clin. Mater.* **13**, 41 (1993).
19. D. K. Han and J. A. Hubbell, *Macromolecules* **29**, 5233 (1996).
20. D. K. Han and J. A. Hubbell, *Macromolecules* **30**, 6077 (1997).
21. J. D. Andrade, in: *Surface and Interfacial Aspects of Biomedical Polymers*, J. D. Andrade (Ed.), Vol. 1, Chap. 5. Plenum Press, New York (1985).
22. D. K. Han, S. Y. Jeong, Y. H. Kim and B. G. Min, *J. Appl. Polym. Sci.* **47**, 761 (1993).
23. L. Smith, C. Doyle, D. E. Gregonis and J. D. Andrade, *J. Appl. Polym. Sci.* **27**, 1269 (1982).
24. J. H. Lee, B. J. Jeong and H. B. Lee, *J. Biomed. Mater. Res.* **34**, 105 (1997).
25. D. K. Han, S. Y. Jeong, K.-D. Ahn, Y. H. Kim and B. G. Min, *J. Biomater. Sci. Polymer Edn* **4**, 579 (1993).
26. J. D. Andrade and V. Hlady, *Ann. NY Acad. Sci.* **516**, 158 (1987).
27. Y. Mori, S. Nagaoka, H. Takiuchi, N. Kikuchi, N. Noguchi, H. Tanzawa and Y. Noishiki, *Trans. Am. Soc. Artif. Intern. Organs* **28**, 459 (1982).
28. E. W. Merrill and E. W. Salzman, *Am. Soc. Artif. Intern. Organs J.* **6**, 60 (1983).
29. J. Dankert, A. H. Hogt and J. Feijen, *CRC Crit. Rev. Biocompat.* **2**, 219 (1986).
30. S. Nagaoka and H. Kawakami, *Am. Soc. Artif. Intern. Organs J.* **41**, 365 (1995).
31. K. D. Park, Y. S. Kim, D. K. Han, Y. H. Kim, E. H. B. Lee, H. Suh and K. S. Choi, *Biomaterials* (1998) (in press).

Polymers for Tissue Engineering, pp. 235–254
Molly S. Shoichet and Jeffrey A. Hubbell (Eds)

Poly(vinyl alcohol) synthetic polymer foams as scaffolds for cell encapsulation

REBECCA H. LI,* MELISSA WHITE, SCOTT WILLIAMS and TYRONE HAZLETT

CytoTherapeutics, Inc., 701 George Washington Highway, Lincoln, RI 02865, USA

Received 10 June 1997; accepted 29 August 1997

Abstract—Poly(vinyl alcohol) (PVA) foams were used as scaffolds in hollow fiber membrane-based cell encapsulation devices. The surrounding permselective membrane serves as an immunoisolation barrier while allowing metabolites and other small molecules to be freely transported. The internal matrix defines the microenvironment for the encapsulated cells. PC12 cell-containing devices represent one possible strategy for safe transplantation of dopamine-secreting cells for the treatment of dopamine-deficient diseases such as Parkinson's disease. PC12 cells — a dopamine-secreting cell line — were encapsulated with PVA foam as a matrix material in the lumen of these hollow fibers. In this work, we demonstrate the presence of the PVA matrix increased the catecholamine secretion efficiency of the cells as compared to devices containing a chitosan matrix. Devices were implanted *in vivo* into rodent striatum and device output of catecholamines was measured preimplant and post-explant. Evoked stores of dopamine remained constant (preimplant vs explant) for devices encapsulated with the foam matrix and increased with devices encapsulated with chitosan matrix. Cell proliferation within devices was inhibited in the presence of the foam matrix. Cell viability and distribution was significantly improved with the inclusion of the foam matrix in both *in vitro* and *in vivo* studies. In comparison to chitosan — a typical matrix material for PC12 cells — addition of a foam-type matrix altered the encapsulated cell microenvironment and resulted in more efficient secretion of catecholamines and improved distribution within the device resulting in smaller necrotic regions and a lower rate of cell proliferation.

Key words: Parkinson's disease; PVA; scaffold; immobilization matrix; foam; transplant; encapsulation; PC12.

INTRODUCTION

One of the newest approaches to the treatment of Parkinson's disease is neural transplantation. This strategy is based on the idea of replacing dopamine-secreting cells in the brain [1, 2]. Progress has been made in this area by implanting human fetal

*To whom correspondence should be addressed. E-mail: rhli@cyto.com

tissue [3, 4] or adrenal tissue that secretes dopamine [5]. Availability of sufficient quantities of viable tissue, ethical issues concerning the use of fetal tissue, and the necessity of immunosuppressive drugs to prevent graft rejection have proven to be major limitations of this approach. An alternative approach is the transplantation of a dopamine-secreting cell line such as PC12 — an immortalized rat adrenal chromaffin cell line — which when encapsulated with a permselective membrane prevents immune cell contact, overcomes limitations of uniform tissue sourcing, and allows one to retrieve transplanted tissue if desired [6]. The immunological barrier of acute and long-term rejection of xenogeneic transplants may be overcome by utilizing cell encapsulation techniques.

In cell encapsulation therapy, xenogeneic or allogeneic cells are surrounded with a semi-permeable polymer membrane prior to transplantation. This membrane can be fabricated so that it is permeable to small molecules such as metabolites needed to nourish the encapsulated cells; yet, the membrane remains relatively impermeable to large molecules such as components of the hosts' immune system. Using this cell encapsulation technique, cells from one species can be transplanted into a host from a discordant species without immune rejection or the use of immunosuppressive drugs [7–11].

In addition to a surrounding membrane, cell encapsulation devices typically utilize an internal matrix which defines the microenvironment for the cells once they are encapsulated. Once the device is implanted, this microenvironment may be altered by the interaction with soluble molecules from the host. Most mammalian cells are reliant on a natural extracellular matrix structural support to maintain their phenotypic expression. Within a cell encapsulation device, the strategy is generally to reconstruct a 3-dimensional tissue environment that will support cell viability and function. For cell encapsulation devices designed to be transplanted into a living host, additional consideration must be made for biocompatibility and biostability of the matrix material. This matrix or scaffold serves to keep the cells well dispersed within the device and provides them a substrate on which to lay their extracellular matrix if necessary. In the absence of an internal suspending matrix, cell types used in these types of devices may aggregate and adhere to one another. The problem associated with formation of these sometimes large (> 100 μm) cell clusters is that central necrotic regions develop as those cells in the core become starved for nutrients such as oxygen [12].

Traditionally, hydrocolloid or hydrogel-based matrices have been used in cell encapsulation devices to immobilize cells. Collagen, a substantial component of natural extracellular matrix has been widely used for this purpose [13, 14]. The natural polysaccharides agarose and alginate [15] have been used successfully to microencapsulate islet cells for the treatment of diabetes. Alginate has also been used as a matrix in hollow fiber membrane devices to immobilize adrenal chromaffin cells used in the treatment of chronic pain [16]. Water-insoluble polyacrylates have been used to successfully encapsulate mammalian cells and have shown exceptional stability and mechanical durability [17].

A foam scaffold approach has several potential advantages over hydrogel-based materials for proliferating or adherent cell lines in that foam scaffolds: (1) provide a

physical surface onto which the cells can lay their own extracellular matrix; (2) may inhibit cell growth of adherent contact-inhibited cells; (3) provides improved nutrient transport to the center of the device through the porous interconnecting channel network; and (4) may limit cluster size to the pore size of the foam thereby eliminating very large clusters that can potentially develop a necrotic center. Thus for proliferating contact-inhibited cell lines, foam scaffolds can potentially provide a stable cell number once the surface area or pores become confluent with cells. Although hydrogels are highly permeable due their high degree of swelling, once cells proliferate and occupy much of the available space in the hydrogel, transport is inhibited. However, in the foam materials only 60% of the void volume is comprised of cell-permeable pores (generally those pores > 10 μm) and the remaining $\sim 40\%$ of the void volume is comprised of smaller cell-impermeable pores. It is through the interconnections of these smaller pores not occupied by cell mass that much of the transport to the inner regions of the device is hypothesized to occur — thus, a higher cell density may be supported. A stable cell number is a potential benefit for cell encapsulation devices as a more consistent and predictable dose of the active molecule can be released once the devices are implanted. In addition, if cell proliferation can be slowed, the buildup of debris within the device is lessened and the lifetime of the device may be extended. Many cell types used in encapsulated devices are of the adherent type — in the absence of a solid scaffold material, these cells (whether dividing or post-mitotic cells) will aggregate and adhere to one another.

Sponge or foam materials have been used in tissue engineering applications — especially when ingrowth of host tissue, bone regrowth, or organ vascularization is desirable. Poly(vinyl alcohol) (PVA) sponge however has never been used as a matrix in a cell encapsulation device. Synthetic PVA foam (available under the tradename Ivalon®) is biologically stable and has been used as a permanent implant in the past in plastic, reconstructive and cardiovascular surgery for reinforcing body structures and cavities [18]. In recent years PVA has been replaced by biodegradable natural and synthetic polymers that resorb as host tissue is regenerated.

The present work investigates the use of PVA synthetic, macroporous polymeric foam material as a matrix or scaffold within an encapsulation device containing PC12 cells. PC12 cells — natural secretors of L-Dopa and dopamine — have shown efficacy when encapsulated in animal models of Parkinson's disease [8, 19–22]. Previous studies using encapsulated PC12 cells have utilized either no immobilization matrix [8], sodium alginate or precipitated chitosan [23, 24]. Precipitated chitosan is a cationic hydrocolloid naturally derived from the deacetylation of chitin — a main component of shrimp and crab exoskeletons.

In the present study, PC12 cell-loaded devices were encapsulated with either a chitosan matrix or a PVA foam matrix. We first evaluated PC12 encapsulated cells *in vitro* for cell viability, proliferation rate and output of catecholamines. This work was followed by direct transplantation of encapsulated PC12 cell devices into rat striatum for 1 month. These devices were then evaluated for cell viability and output of catecholamines after explant.

MATERIALS AND METHODS

Subjects

Adult Sprague-Dawley rats (approximately 2–3 months old and weighing 300–400 g) were used in the implant studies. The animals were housed in a temperature and humidity controlled colony room maintained on a 12-h light/dark cycle. Food and water were available on an ad libitum basis.

Surgery

Rats were anesthetized with an intramuscular injection of a ketamine, xylazine, and acepromazine mixture (33, 1.7 and 10 mg ml^{-1}) and positioned in a Kopf stereotaxic instrument. A sagittal incision was made in the scalp, and two holes drilled for bilateral placement of the devices into the striatum.

Cell culture and encapsulation procedure

Permselective hollow fiber membranes were prepared via the wet–dry phase inversion spinning technique of Cabasso [25]. The asymmetric hollow fibers were cast from 12.5% polyacrylonitrile–polyvinyl chloride (PAN/VC) copolymer in dimethyl sulfoxide (w/w) (DMSO) solvent. Hollow fiber membranes with a dense permselective skin on the lumenal side and an open trabecular wall structure were produced using this method. The hollow fibers were spun into a non-solvent water bath, soaked in 25% glycerin overnight then dried. Fiber dimensions were 680 ± 60 μm inner diameter with a 90 ± 10 μm wall thickness.

PC12 cells were cultivated in T75 (Falcon®) tissue culture treated flasks with PC-1 media (Hycor, Portland, ME, USA) supplemented with 15% fetal bovine serum at 37 °C in a water-saturated, 5% CO_2 ambient air atmosphere. Cells were harvested by trypsinizing the cells from the bottom of the flasks, washing with HBSS and centrifugating at 800 rpm. Cell viability was assessed prior to the encapsulation procedure by using the trypan exclusion method and found to be 90–95% viable.

PVA sponges (Unipoint Industries, Inc., Thomasville, NC, USA) are water insoluble foams formed by the reaction of aerated PVA solution with formaldehyde vapor as the crosslinker. The hydroxyl groups on the PVA covalently cross-link with the aldehyde to form the cross-linked network. The foams are flexible and elastic when wetted and semi-rigid when dried. Average foam pore size at equilibrium swelling in water is ~ 150 μm (of cell permeable pores). These foam materials also allow the attachment of extracellular matrix materials thus providing specific sites for cell attachment on the solid surfaces. PVA foam rods were coated with TIV human collagen prepared in 1 mg ml^{-1} PBS solution and allowed to dry. Foam rods were cut to desired size by boring through dried foam blocks with a round titanium-coated bore drilling bit. Compressed foam rods were then filled into 1 cm long hollow fiber membrane devices prior to sterilization and cell loading. A septal hub assembly for cell loading was then attached to the foam-filled hollow fiber membrane device. The

devices were then sterilized by ethanol soaking or alternatively by ethylene oxide gas sterilization.

Chitosan is soluble in weakly acidic solutions (below pH 6.3). Above pH 6.3 it precipitates out of solution. Immediately prior to encapsulation, cells in media were mixed in a 2 : 1 (v/v) ratio with chitosan solution. Chitosan matrix devices were then prepared by suspending cells in an isotonic saline solution containing 2% (w/v) of low viscosity chitosan (SEACURE®, chitosan chloride, Protan Biopolymer, Drammen, Norway). In this method the chitosan was precipitated prior to cell contact by mixing with the physiologic buffer. Alternatively, the chitosan may be precipitated post-encapsulation by incubating the capsules in physiologic saline at pH 7.4.

Single cell suspensions of PC12 adherent cells were removed from tissue culture flasks by trypsinization, resuspended in medium and pelleted by centrifugation at 800 rpm for 2 min. The cells were then resuspended in medium to a final concentration of 50 000 or 100 000 cells μl^{-1}. Two μl of cells suspended in media (for PVA foam devices) or cell/chitosan slurry were loaded into each 1 cm long hollow fiber device using a glass 10 μl Hamilton syringe. After cell loading, the scored septum of the loading hub was snapped off and the access port sealed with a light-cured acrylate glue (Luxtrak LCM 24, ICI Resins US, Wilmington, MA, USA). The cell-loaded devices were maintained in Neurobasal medium with B-27 supplement (Gibco, Inc., Grant Island, NY, USA). Devices sectioned immediately post-encapsulation showed uniform cell distribution along the entire 1 cm length and throughout the cross-sectional area using this loading technique.

In vitro *device release kinetics*

The primary catecholamines released by PC12 cells are dopamine and the dopamine precursor L-Dopa. When the cells are depolarized with 55–60 mM potassium they release up to 30–40% of their catecholamine stores in a 15-min incubation period. Basal *in vitro* device catecholamine release kinetics was evaluated by incubating HEPES-buffered saline solution (HBSS) rinsed devices in 250 μl HBSS for 30 min. Stimulated release was evaluated immediately after the basal assay by incubating devices in 250 μl HEPES-buffered saline solution containing 56 mM potassium for 15 min. Analysis of the incubated samples was performed using HPLC with electrochemical detection [26].

In vitro *device metabolic activity measurements*

The cell number within each device was estimated using the alamar Blue® Fluorescence Assay (Accumed International, Sacramento, CA, USA). The alamar Blue® assay incorporates a fluorometric/colorimetric growth indicator which correlates fluorescence signal with cell metabolic activity. The system incorporates an oxidation–reduction indicator which fluoresces and undergoes a color change corresponding to chemical reduction of the growth medium. For the present system, a change in alamar fluorescence signal correlates with a change in metabolic activity of the device. This change in device metabolic activity can be due to either a change in cell number

(resulting from cell proliferation or death) or in the activity level of the encapsulated cells. We performed an alamar calibration analysis for encapsulated cells and found that the activity level of the same number of encapsulated cells did not change significantly with a change in matrix material from chitosan to PVA foam. The correlation between cell number and alamar fluorescence (devices assayed 24 h post-encapsulation) has been shown in calibration experiments to be linear. Based on these calibration results, we assumed that for this particular experimental system, a change in fluorescence correlated approximately with a change in device cell number rather than a change in metabolic activity. The assay was performed by incubating devices in 500 μl of medium with 50 μl alamar Blue reagent at 37 °C for 4 h. The incubated media samples were then removed and alamar Blue fluorescence signal read on a fluorescent plate reader (Labsystems Fluoroskan II) set at 590 nm emission and 540 nm excitation wavelengths. Although this assay requires uptake by the cells, it is not cytotoxic.

Histological analysis

For both *in vitro* maintained devices and explanted devices, histological analysis was performed by fixing devices in 4% paraformaldehyde solution, rinsing in PBS and dehydrating up to 95% ethanol. The devices were then immersed in a 1 : 1 solution of glycol methacrylate (Historesin, Reichert-Jung, Cambridge Instruments) for 1 h. The solution was then replaced with pure infiltration solution and incubated for 2 h. The devices were then rinsed with embedding solution, transferred to molds and embedded in glycol methacrylate for sectioning. Five-μm thick sections were cut (Reichert-Jung, Super cut microtome 2065), mounted on glass slides and stained with hematoxylin and eosin.

EXPERIMENT 1: *IN VITRO* DEVICE MONITORING

The initial experiments evaluated the survival, metabolic activity and output of catecholamines for hollow-fiber encapsulated PC12 cells utilizing either a PVA foam matrix or a precipitated chitosan matrix. For this study, devices with PVA foam matrix ($n = 10$) or precipitated chitosan matrix ($n = 10$) were prepared with the following final cell densities (for 2 μl volume devices): (1) precipitated chitosan matrix with cell densities of 50 000 and 100 000 cells μl^{-1} (for final device cell numbers of 100 000 and 200 000); and (2) PVA foam matrix with cell densities of 50 000, 100 000, and 200 000 cells μl^{-1} (for final device cell numbers of 100 000, 200 000, and 400 000).

The devices were maintained in a 37 °C humidified, 5% CO_2 incubator and cell medium replenished three times per week. Devices were assayed weekly for catecholamine release (basal and potassium evoked release) using HPLC analysis. Cell proliferation rate was monitored weekly with the alamar Blue assay. Two representative devices were fixed, sectioned and stained with hematoxylin and eosin at 2 weeks and 6 weeks.

Results

The measured alamar fluorescence data (Fig. 1) indicates that the cell proliferation in devices with PVA foam matrix has slowed dramatically as compared to the approximate linear increase with time observed in the chitosan matrix devices. The range of linearity of the alamar assay performed under these conditions has been shown in previous experiments to be between 50 and 1500 fluorescence units. From calibration curve data it was estimated that over the duration of the study (35 days), the PVA foam loaded devices increased in cell number ~ 6.6-fold (from 100 000 cells initially loaded to $\sim$ 660 000 cells) whereas the chitosan devices increased their cell number by ~ 32-fold (from 100 000 to $\sim 3.2 \times 10^6$ cells).

The basal L-Dopa release curve as a function of time (Fig. 2) shows that PC12 cells in the PVA foam matrix devices secrete significantly more basal L-Dopa than the chitosan matrix devices at all timepoints up to 35 days. The release increases from day 1–35 post-encapsulation from 50 to 300 pm/device/30 min for the PVA matrix devices and from 10 to 160 pm/device/30 min for the chitosan matrix devices. This basal L-Dopa release data coupled with estimated device cell numbers obtained from alamar correlations indicates that the PC12 cells in the foam devices are more efficient secretors of catecholamines vs cells in the chitosan matrix. By day 35, PVA foam matrix devices (containing an average of $\sim$ 660 000 cells per device) are secreting twice as much L-Dopa as chitosan matrix devices which contain almost a 5-fold greater number of cells.

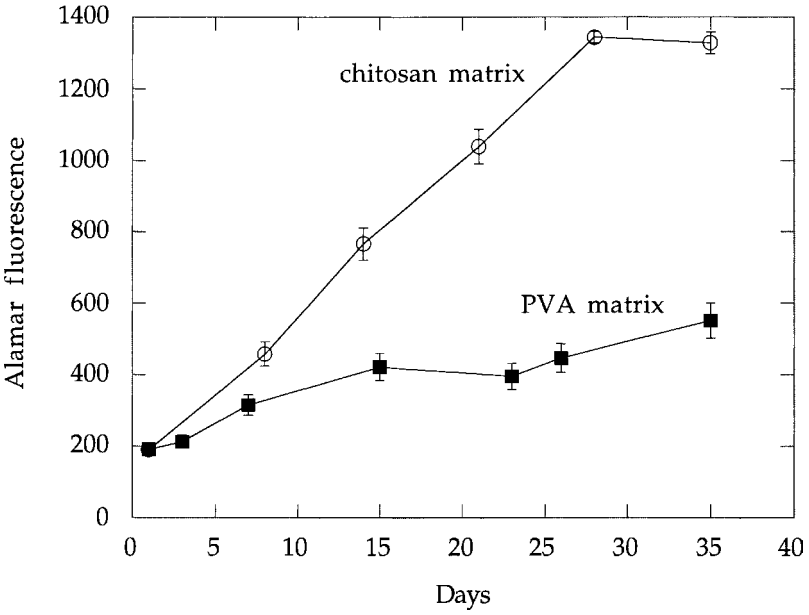

Figure 1. Alamar fluorescence of PC12 loaded devices with chitosan or PVA matrix, initial device cell number = 100 000. Each data point is the average of $n = 10$ devices; error bars are $\pm$ standard errors of the mean.

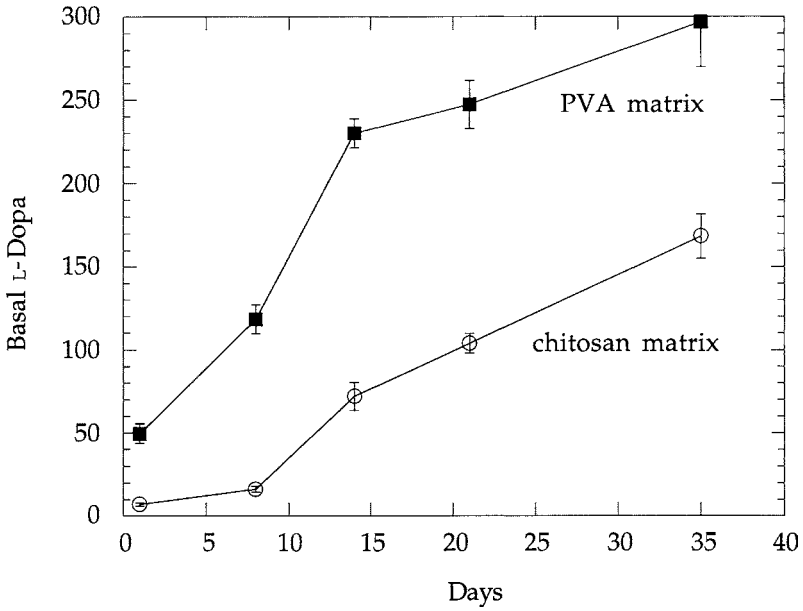

Figure 2. Basal L-Dopa release (in pmol ml^{-1} 30 min^{-1}) from *in vitro* PC12 loaded devices with PVA or chitosan matrix. Each data point is the average of $n = 10$ devices; error bars are $\pm$ standard errors of the mean.

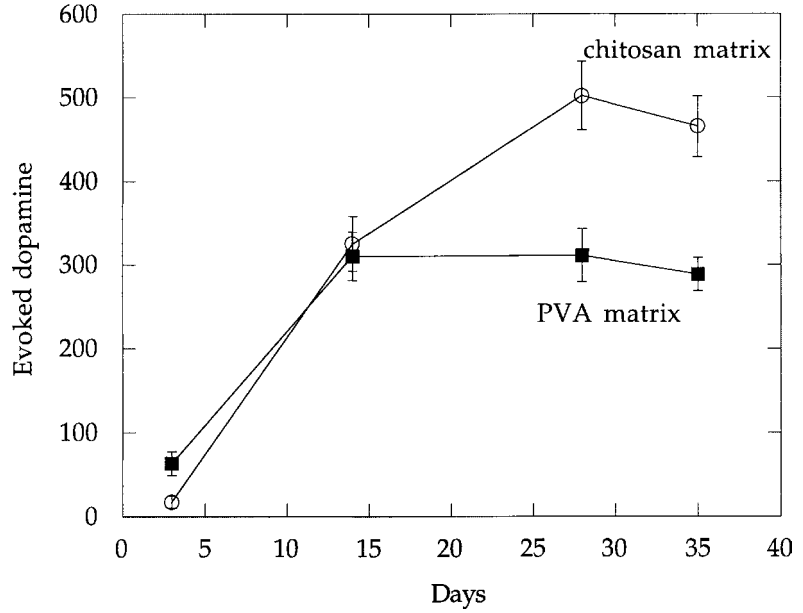

Figure 3. Evoked dopamine release (pmol ml^{-1} 15 min^{-1}) from *in vitro* PC12 loaded devices with PVA or chitosan matrix. Each data point is the average of $n = 10$ devices; error bars are $\pm$ standard errors of the mean.

Cells encapsulated with either precipitated chitosan as the matrix or PVA were stimulated to release vesicular dopamine stores under high potassium depolarizing conditions. Release of K^+ evoked dopamine was similar for the two groups for the first 2 weeks (Fig. 3) after which the PVA matrix devices stabilized in their output whereas the devices with chitosan matrix showed a continued increase in dopamine release out to 4 weeks. The release of evoked dopamine trends similarly with device cell number (as correlated by alamar Blue fluorescence). This is not an unexpected result since these cells are thought to release a fixed percent of their dopamine stores under stimulated conditions. On a per cell basis, the PC12 cells in PVA matrix are releasing more dopamine.

Histology sections taken from devices 2 weeks after encapsulation and held *in vitro* show that PC12 cells encapsulated with PVA foam matrix have a predominantly flattened and perhaps more differentiated morphology whereas PC12 cells in chitosan matrix have a more rounded morphology. The sections show well distributed medium-sized (50–100 μm diameter) clusters of healthy cells in the chitosan matrix devices after 2 weeks *in vitro*; after 6 weeks, these chitosan devices show large cell clusters (200–400 μm diameter) have formed with necrotic cores in the majority of the larger clusters (Figs 4 and 5). Histological analysis of the PVA matrix devices shows after 2 weeks, the cells are primarily flattened in monolayers within the pores of the foam and have excellent distribution throughout the hollow fiber membrane. After 6 weeks, the PVA-containing devices show some small areas of cells containing pyknotic nuclei; however, these areas of necrosis in the foam are not concentrated at the center of the device as in the chitosan-containing devices, but are randomly dispersed throughout. In these foam matrix devices, the pores have completely filled with cells and cell distribution in the device remains excellent (Figs 6–8). Histological analysis was performed on uniformly selected device sections ~ 300 μm from the outer membrane wall (close to the device center) and in the middle of the device longitudinally.

EXPERIMENT 2: IMPLANTED DEVICES

Experiment 1 demonstrated that viability (as estimated from histological sections) and function (as measured by L-Dopa and dopamine output) of the encapsulated PC12 cells in PVA foam matrix was significantly greater than those encapsulated in chitosan matrix. In the follow-up *in vivo* study, the objective was to determine how the device viability and function correlated when implanted into rat striatum. Encapsulated PC-12 cell loaded devices were implanted bilaterally with each rat host receiving one PVA foam matrix device and one chitosan matrix device. Both groups of devices were manufactured with both high and low initial loading density (200 000 cells/device and 100 000 cells/device): chitosan matrix high density devices ($n = 5$), chitosan matrix low density devices ($n = 9$), PVA foam high density devices ($n = 6$), PVA foam low density devices ($n = 10$). The encapsulated cells were tested for basal and K^+ evoked catecholamine release 1 week after encapsulation (pre-implant) and immediately post-explant after 1 month.

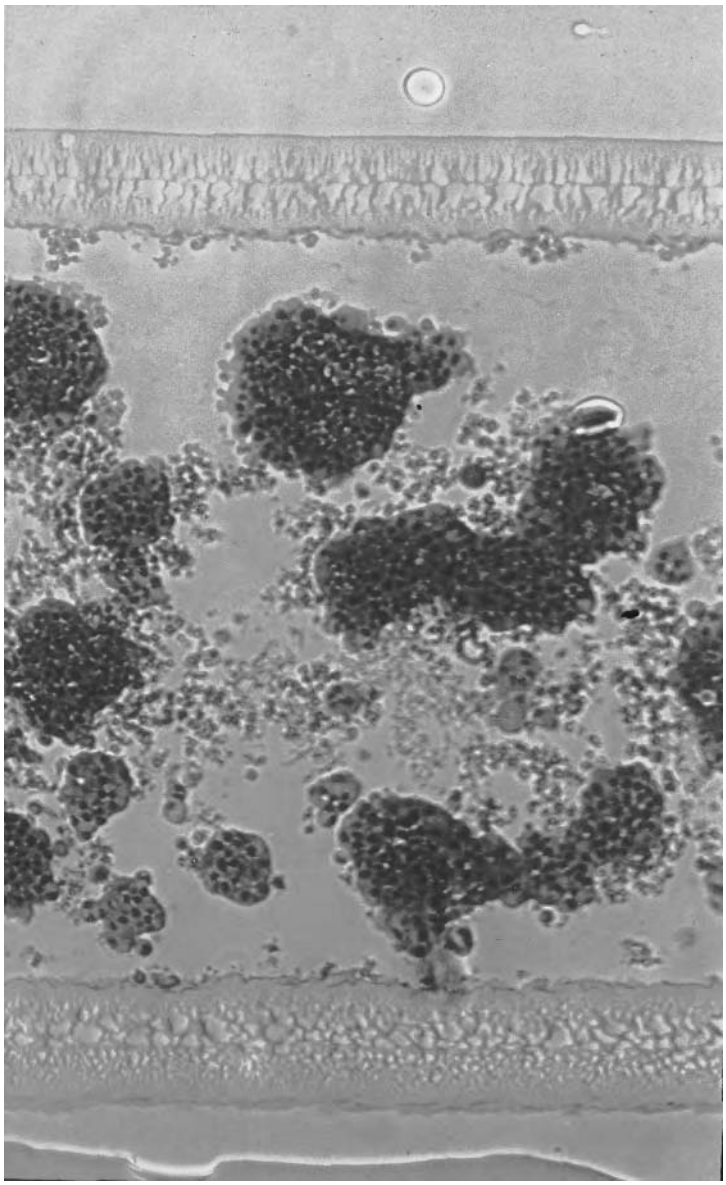

Figure 4. Representative histological section from 2 week post-encapsulation PC12 cell, chitosan matrix device (*in vitro*) (10 ×).

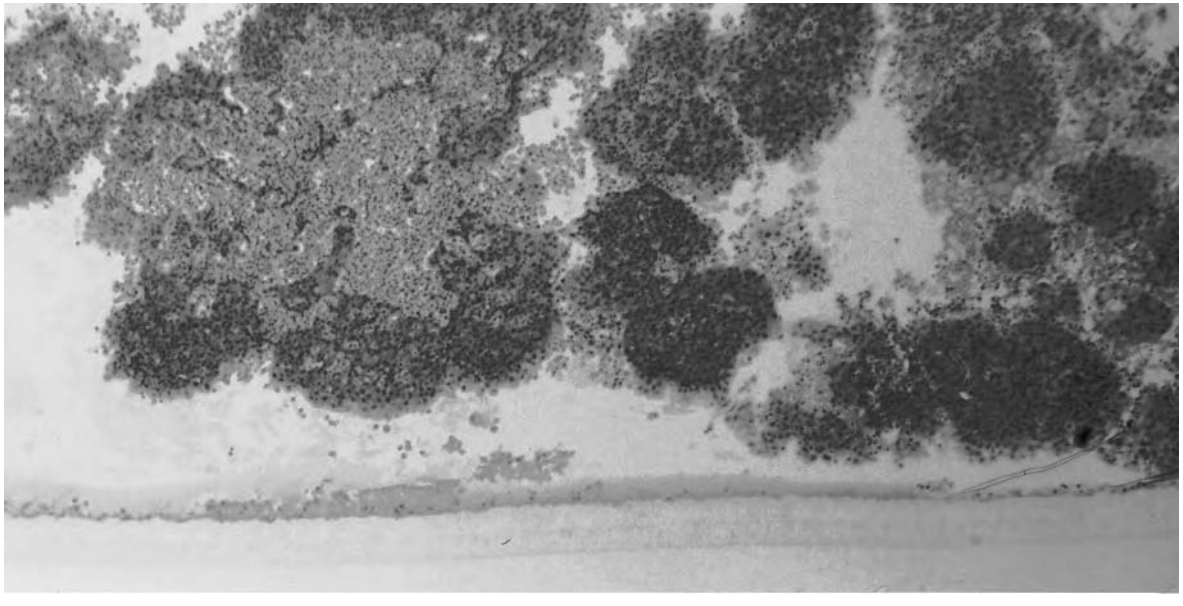

Figure 5. Representative histological section from 6 week post-encapsulation PC12 cell, chitosan matrix device (*in vitro*) (10 ×).

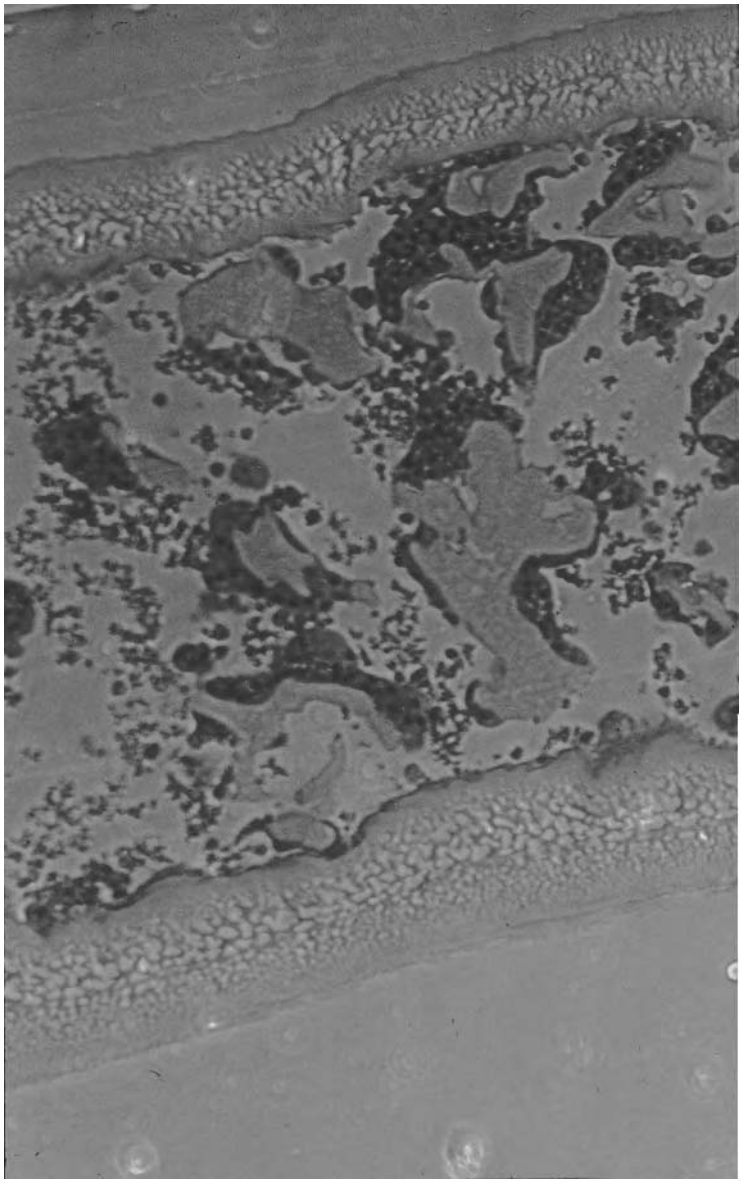

Figure 6. Representative histological section from 2 week post-encapsulation PC12 cell, PVA matrix device (*in vitro*) (10 ×).

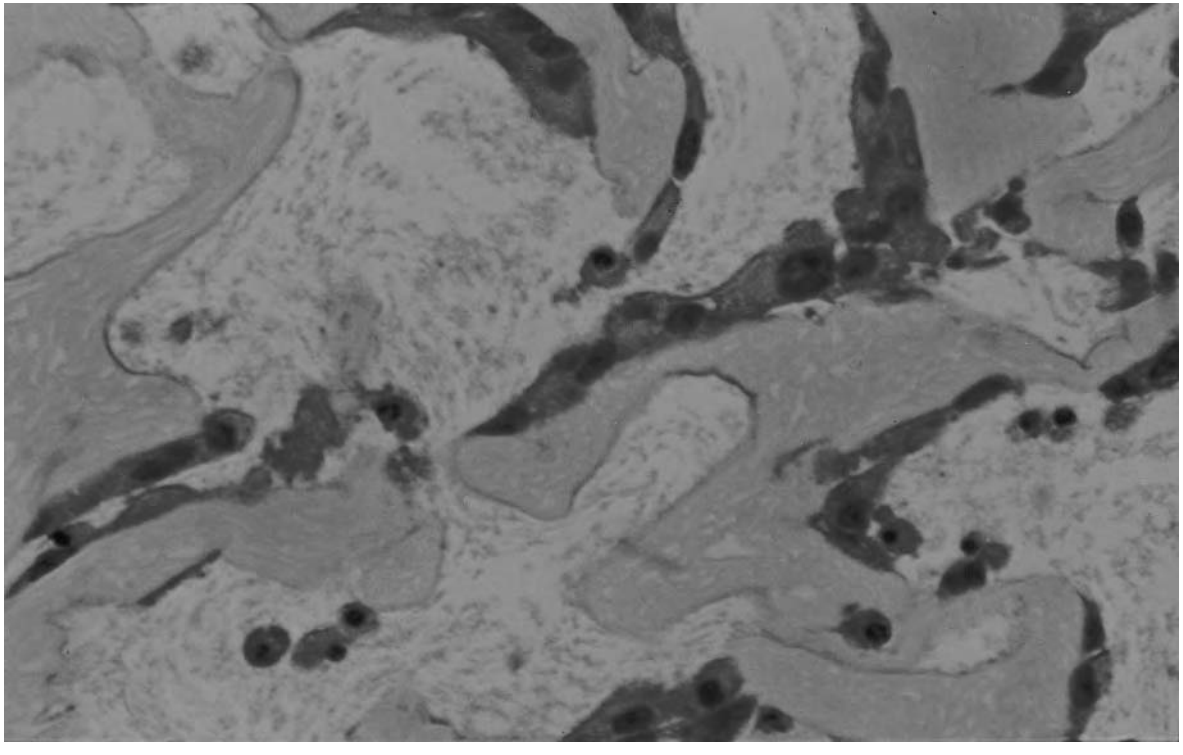

Figure 7. Representative histological section from 2 week post-encapsulation PC12 cell, PVA matrix device (*in vitro*) (40 ×).

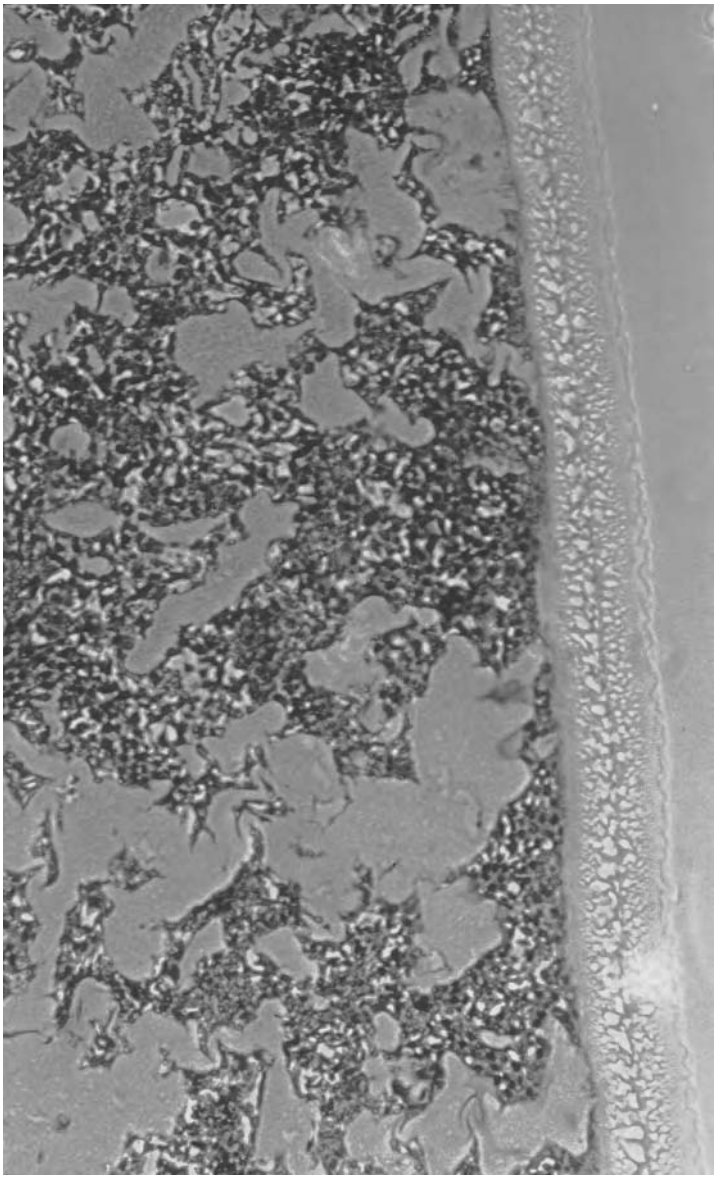

Figure 8. Representative histological section from 6 week post-encapsulation PC12 cell, PVA matrix device (*in vitro*) (10 ×).

Results

The potassium evoked dopamine release appears to have remained relatively constant (preimplant vs explant, Fig. 9) in the PVA foam devices for both high density (100 000 cells μl^{-1}) and low density (50 000 cells μl^{-1}) initial cell loadings. K^+ dopamine secretion in chitosan matrix devices decreased significantly over the 1 month implantation for the high density devices since these devices had most likely grown to their upper limit of cell number they can support within the 1 week hold time prior to implantation — histology sections substantiate this hypothesis by showing corresponding large necrotic areas in these devices. This is a different trend than the K^+ dopamine secretion profile for the chitosan devices obtained *in vitro*. A possible explanation of this disparity is that the encapsulated cells may have altered their metabolic state when in the host environment. From the K^+ dopamine secretion data, it appears the low cell density chitosan devices were still increasing in cell number when explanted. On explant, there was no statistical difference in K^+ evoked dopamine output between devices initially loaded at high or low loading densities. Basal L-Dopa release (Fig. 10) shows an increase over preimplant values

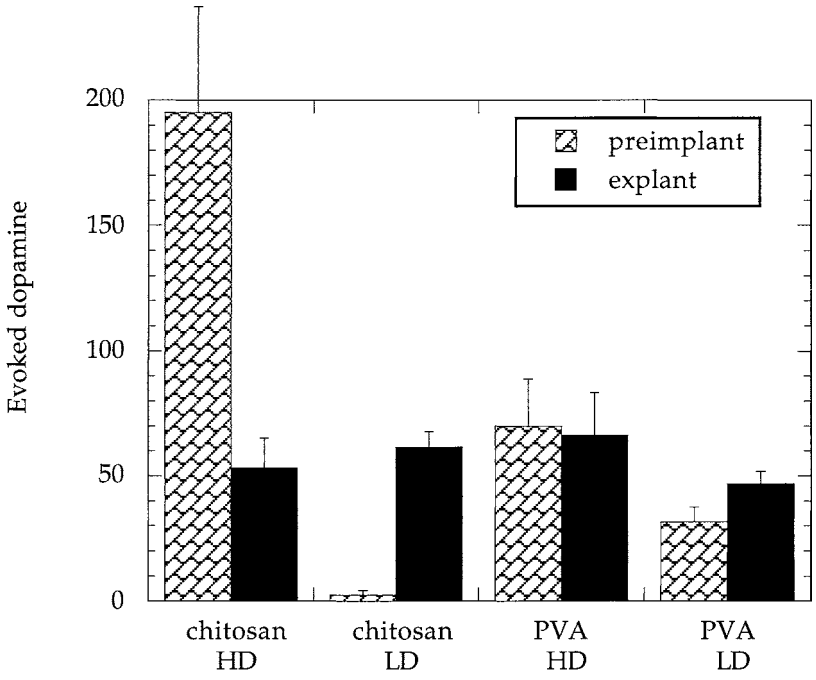

Figure 9. Evoked dopamine release (pmol ml^{-1} 15 min^{-1}) from PC12 loaded devices with PVA or chitosan matrix preimplant and after explant from rodent striatum (1 month). Each data point is the average of $n = 5$ devices (chitosan HD); $n = 9$ (chitosan LD); $n = 6$ (PVA HD); $n = 5$ (PVA LD); error bars are $\pm$ standard errors of the mean.

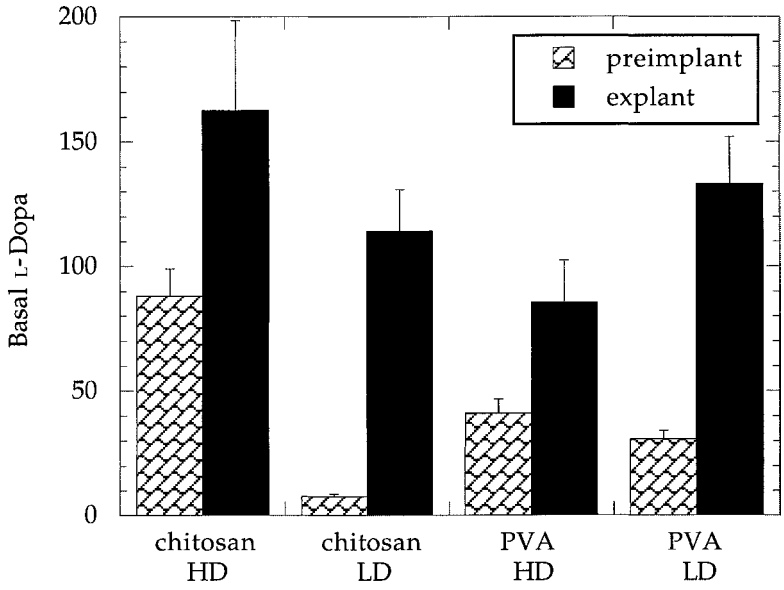

Figure 10. L-Dopa release (pmol ml^{-1} 30 min^{-1}) from PC12 loaded devices with PVA or chitosan matrix preimplant and after explant from rodent striatum (1 month). Each data point is the average of $n = 5$ devices (chitosan HD); $n = 9$ (chitosan LD); $n = 6$ (PVA HD); $n = 5$ (PVA LD); error bars are $\pm$ standard errors of the mean.

for all groups. The PVA matrix low density devices have equivalent output as the chitosan devices; however, the PVA matrix high density devices have a lower output than the chitosan matrix devices.

Histology sections taken post-explant (Figs 11 and 12) show that much of the pore space of the PVA foams have filled with cells. A few pyknotic nuclei are visible but most cells appear healthy and well distributed within the device. The chitosan matrix devices have large clusters (200–300 μm) of cells with viable rims and necrotic centers; in these devices, viable cell distribution is concentrated mostly along the membrane wall. The biocompatibility of the devices at the host interface is excellent and similar to that observed in several other studies with this configuration and membrane material [19, 23]. Similar devices with the equivalent membrane type have also been implanted in humans under a Phase I clinical trial for chronic pain treatment and demonstrated excellent tolerability and safety after over one year of implantation [27].

DISCUSSION

Cell therapy using membrane-based encapsulated devices is a relatively recent approach that has been used successfully to deliver neuroactive molecules to the central

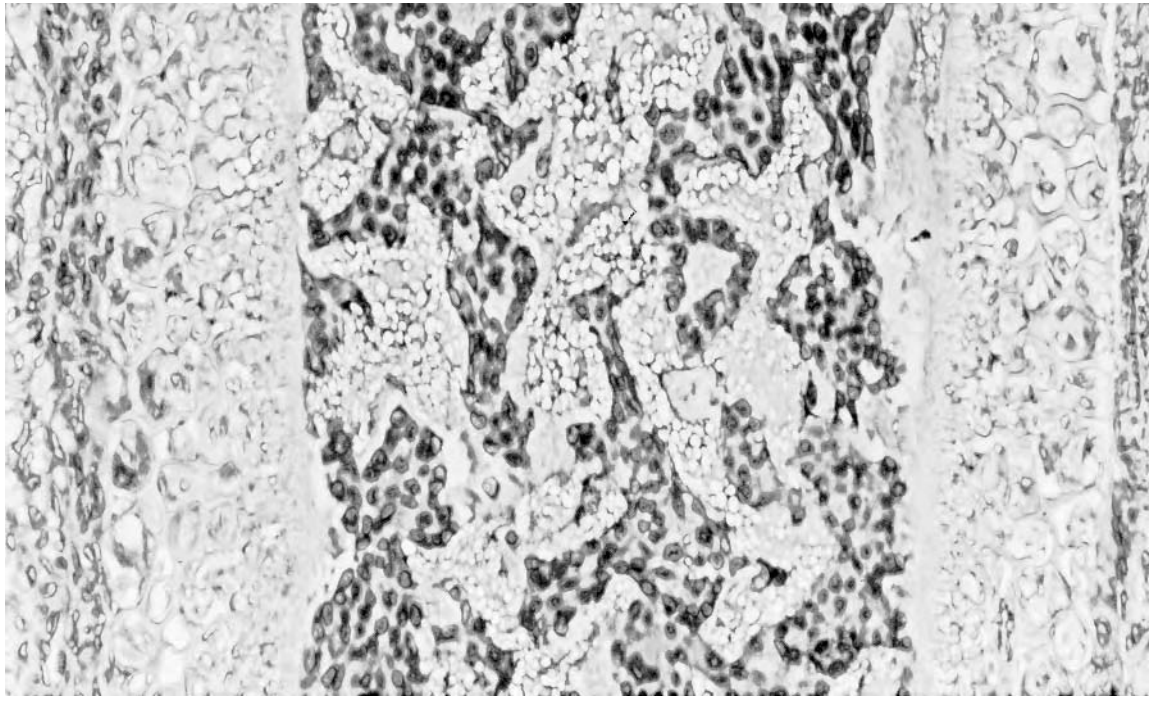

Figure 11. Representative histological section from 1 month implanted PC12 cell, PVA matrix device (rat striatum) (10 ×).

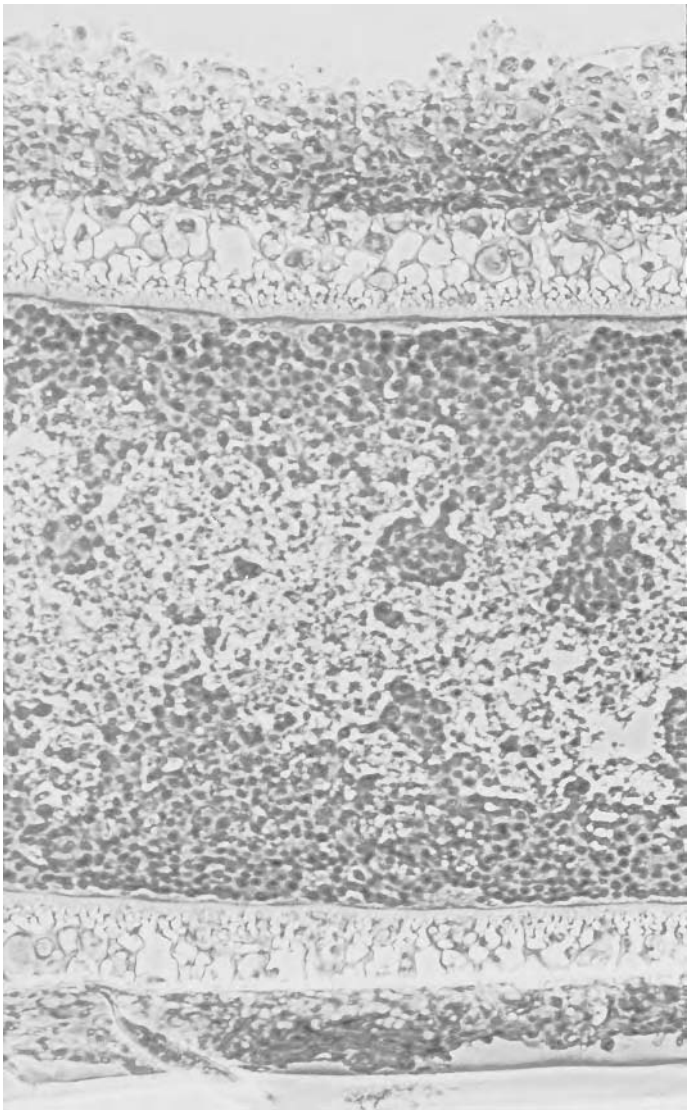

Figure 12. Representative histological section from 1 month implanted PC12 cell, chitosan matrix device (rat striatum) (10 ×).

nervous system. PC12 cells have demonstrated efficacy in alleviating symptoms in Parkinsonian animal models and have been a model cell line used to deliver L-Dopa and dopamine to deficient regions in the brain. For neurodegenerative diseases such as Parkinson's disease, the longevity of the encapsulated device in sustaining its secretory output becomes especially important. The lifetime of such an encapsulated cell device can be optimized by creating the ideal intracapsular microenvironment for the specific cell of interest. PC12 cells in particular tend to have a relatively high proliferation rate *in vitro* and *in vivo*, prefer a solid substrate on which to adhere, and have a relatively high oxygen metabolic rate. In the absence of a solid scaffold or substrate, the cells quickly form large clusters with necrotic centers. The use of a foam scaffold for these cells appears to have significantly controlled the proliferation rate of these cells both *in vivo* and *in vitro* when encapsulated thus leading to less necrosis and buildup of cellular debris. In addition, the cells have increased the efficiency of their secretory output of catecholamines when adhered to a solid scaffold material as compared to chitosan matrix. The duration of the present study was 1 month; longer studies are currently underway to confirm the stability of foam matrix properties over longer implant periods.

These results from the two experiments show that *in vitro* observations simulated the implanted *in vivo* situation for these two matrix materials.

SUMMARY

The results from this work demonstrate that the encapsulated microenvironment can be manipulated to significantly change the secretory behavior of immobilized cells. Significant findings from *in vitro* device studies were that PC12 cells encapsulated with a foam scaffold matrix became up to 10-fold more efficient in their secretion of catecholamines as compared with cells immobilized within a chitosan matrix. Histological analysis of these scaffold matrix devices showed less necrosis in the centers of these devices and a more flattened adherent cell morphology; cell cluster size was also reduced as compared to chitosan matrix devices. When these devices were implanted into rodent striatum, the foam scaffold appeared to control their proliferation rate and maintain higher cell viability as compared to the chitosan matrix; however, secretion rates of catecholamines were not significantly different between groups upon explant.

In summary, these results demonstrate that use of a foam scaffold matrix for encapsulated PC12 cells can significantly impact the secretory efficiency of these cells. In addition, the rate of cell proliferation was controlled using the foam scaffold and resulted in a higher ratio of viable to necrotic cells *in vitro* and when transplanted *in vivo* as an encapsulated cell device.

REFERENCES

1. J. R. J. Sladek and D. M. Gash, *J. Neurosurg.* **68**, 337 (1988).
2. D. M. Yurek and J. R. J. Sladek, *Ann. Rev. Neurosci.* **13**, 415 (1990).
3. A. M. Walters, D. J. Clarke, H. F. Bradford and G. M. Stern, *Neurochem. Res.* **17**, 893 (1992).

4. G. V. Swale, P. M. Bloomfield, A. Bjorklund, D. A. Brooks, P. Brundin, K. L. Leenders, O. Lindvall, C. D. Marsden, S. Rehncrona, H. Widner and R. S. J. Frackowiak, *Ann. Neurol.* **31**, 166 (1992).
5. W. J. Freed, M. Poltorak and J. B. Becker, *Exp. Neurol.* **110**, 139 (1990).
6. L. A. Greene and A. S. Tischler, *Proc. Natl Acad. Sci. USA* **73**, 2424 (1976).
7. L. Christenson, K. E. Dionne and M. J. Lysaght, in: *Fundamentals of Animal Cell Encapsulation and Immobilization*, M. F. A. Goosen (Ed.), p. 7. CRC Press, Boca Raton, FL (1993).
8. P. Aebischer, P. A. Tresco, S. R. Winn, L. A. Greene and C. B. Jaeger, *Exp. Neurol.* **111**, 269 (1991).
9. P. E. Lacy, O. D. Hegre, A. Gerasimidi-Vazeou, F. T. Gentile and K. E. Dionne, *Science* **254**, 1782 (1991).
10. J. Sagen, *ASAIO J.* (1992).
11. P. Aebischer, S. R. Winn and P. M. Galletti, *Brain Res.* **448**, 364 (1988).
12. C. K. Colton, *Cell Transplantation* **4**, 415 (1995).
13. R. Shatford, S. Nyberg, S. Meier, J. White, W. Payane, W. Hu and F. Cerra, *J. Surg. Res.* **53**, 549 (1992).
14. J. C. Y. Dunn, R. G. Tompkins and M. L. Yarmush, *Biotechnol. Prog.* **7**, 234 (1991).
15. H. Yang, H. Iwata, H. Shimizu, T. Takagi, T. Tsuji and F. Ito, *Biomaterials* **15**, 113 (1994).
16. S. R. Winn and P. A. Tresco, *Methods Neurosci.* **21**, 387 (1994).
17. M. V. Sefton, R. M. Dawson and R. L. Broughton, *Biotech. Bioeng.* **29**, 1135 (1987).
18. B. D. Ratner and A. S. Hoffman, in: *ACS Symposium Ser.*, J. D. Andrade (Ed.), Vol. 31, p. 1. Washington, DC (1976).
19. D. Emerich, S. R. Winn and M. D. Lindner, *Cell Transplantation* **5**, 589 (1996).
20. P. A. Tresco, S. R. Winn, C. B. Jaeger, L. A. Greene and P. Aebischer, *Cell Transplantation* **1**, 255 (1992).
21. S. R. Winn, P. A. Tresco, B. Zielinski, L. A. Greene, C. B. Jaeger and P. Aebischer, *Exp. Neurol.* **113**, 322 (1991).
22. M. Goddard, A. P. Signore, R. L. Timpson and P. Aebischer, *Restor. Neurol. Neurosci.* **4**, 169 (1992).
23. D. F. Emerich, B. R. Frydel, T. R. Flanagan, M. Palmatier, S. R. Winn and L. Christenson, *Cell Transplantation* **2**, 241 (1993).
24. B. A. Zielinski and P. Aebischer, *Biomaterials* **15**, 1049 (1994).
25. I. Cabasso, in: *Kirk-Othmer Encyclopedia of Chemical Technology*, 3rd edn, Vol. 12, p. 492. John Wiley, New York (1980).
26. M. P. Lavoie, M. Palmatier, F. T. Gentile, F. A. Kaplan, D. M. Fiore, T. F. Hazlett, W. J. Bell and T. R. Flanagan, *Cell Transplantation* **2**, 163 (1993).
27. E. Buchser, M. Goddard, B. Heyd, J. Joseph, J. Favre, N. de Tribolet, M. Lysaght and P. Aebischer, *Anesthesiology* **85**, 1005 (1996).

Polymers for Tissue Engineering, pp. 255–272
Molly S. Shoichet and Jeffrey A. Hubbell (Eds)

Skeletal myogenesis on elastomeric substrates: implications for tissue engineering

MARY M. MULDER, ROBERT W. HITCHCOCK and PATRICK A. TRESCO *

University of Utah, Department of Bioengineering, Tissue Engineering Laboratory, Salt Lake City, UT 84112, USA

Received 16 July 1998; accepted 28 January 1998

Abstract—Studies geared towards understanding the interaction between skeletal muscle and biomaterials may provide useful information for the development of various emerging technologies, ranging from novel delivery vehicles for genetically modified cells to fully functional skeletal muscle tissue. To determine the utility of elastomeric materials as substrates for such applications, we asked whether skeletal myogenesis would be supported on a commercially available polyurethane, Tecoflex® SG-80A. G8 skeletal myoblasts were cultured on Tecoflex® two-dimensional solid thin films fabricated by a spin-casting method. Myoblasts attached, proliferated, displayed migratory activity and differentiated into multinucleated myotubes which expressed myosin heavy chain on solid thin films indicating that Tecoflex® SG-80A was permissive for skeletal myogenesis. Porous three-dimensional (3-D) cell scaffolds were fabricated in a variety of shapes, thicknesses, and porosities by an immersion precipitation method, and where subsequently characterized with microscopic and mechanical methods. Mechanical analysis revealed that the constructs were elastomeric, recovering their original length following 100% elongation. The 3-D substrates were seeded with muscle precursors to determine if muscle differentiation could be obtained within the porous network of the fabricated constructs. Following several weeks in culture, histological studies revealed the presence of multinucleated myotubes within the elastomeric material. In addition, immunohistochemical analysis indicated that the myotubes expressed the myosin heavy chain protein suggesting that the myotubes had reached a state of terminal differentiation. Together the results of the study suggest that it is indeed feasible to engineer bioartificial systems consisting of skeletal muscle cultivated on a 3-D elastomeric substrate.

Key words: Skeletal muscle; tissue engineering; polyurethane; cell material interaction; migration; differentiation.

INTRODUCTION

A scarcity of donor organs and tissues, coupled with recent advances in material science and cell biology, has sparked the development of tissue engineered con-

*To whom correspondence should be addressed. E-mail: PatrickTresco@m.cc.utah.edu

structs for use as therapeutic agents and basic science tools. Recent studies using a variety of cell types cultivated on porous synthetic three-dimensional (3-D) polymer matrices indicate that it is possible to engineer several tissues including bone, skin, cartilage, tendon, and blood vessels [1–6]. This same strategy, however, has not been used to address tissue engineering applications utilizing skeletal muscle.

Most of the *in vitro* skeletal muscle basic science studies have been limited to two-dimensional (2-D) solid surfaces consisting of tissue culture plastic and elastomeric substrates constructed of silastic, silicone, and polyurethane derivatives [7–14]. Although 3-D substrates such as collagen lattices and microcarriers have been utilized as *in vitro* culture systems, they have not been developed for tissue engineering applications of skeletal muscle tissue [13, 14]. One group has cultured skeletal muscle tissue *in vitro* using a mechanical straining system to align the developing muscle fibers [15]. Their elegant approach which attempts to mimic normal muscle development does not utilize a synthetic growth surface but makes use of the fact that muscle naturally secretes a robust extracellular matrix and displays a tendency for confluent cultured tissue to detach from its substrate. Furthermore, this group demonstrated the utility of the approach to engineer muscle tissue for use as a genetically engineered biologically-based sustained delivery system [16].

Studies geared towards understanding the interaction between skeletal muscle and biomaterials may provide useful information for the development of various emerging technologies that range from novel sustained-delivery devices to the fabrication of fully functional skeletal muscle tissue. The use of a porous three-dimensional elastomeric substrate for culturing muscle may offer several advantages which aid in the development of these emerging technologies. For example, a compliant porous substrate which allows cellular in growth may have utility as a tissue integrating interface between solid implants and host tissue to enhance fixation and device performance. Alternatively, a 3-D elastomeric substrate containing genetically-modified muscle tissue may be useful for anchoring under tension to promote the prolonged expression of the differentiated phenotype [16]. Finally, it may be possible to fabricate scaffolds into a variety of controlled geometries to induce the formation of a variety of biologically-based architectures found *in vivo*. Implicit in all of these applications is the requirement that the seeded muscle precursors differentiate into muscle tissue. Three-dimensional elastomeric materials have not previously been studied as a growth substrate for skeletal muscle tissue. The present study was, therefore, designed to determine if skeletal myogenesis could be obtained on a porous three-dimensional elastomeric substrate, and if so, to determine whether the construct would be useful for tissue engineering applications utilizing skeletal muscle.

MATERIALS AND METHODS

Cell culture

The G8 myoblastic skeletal muscle cell line, originally derived from the hind limb of a Swiss Webster mouse, was obtained from American Type Tissue Culture and maintained as described by Beach *et al*. [17, 18]. The myoblasts were cultured in Dulbecco's Modified Eagle's Medium (DMEM, Sigma) supplemented with 10% bovine calf serum (Hyclone) and 10 U ml^{-1} of both penicillin and streptomycin. The cultures were maintained at 37°C in a humidified 5% CO_2 atmosphere and fed every 3 days. To induce differentiation of the myoblasts into myotubes, fusion medium was added to cultures prior to confluence. The fusion medium contained DMEM supplemented with 0.5% bovine calf serum, 5% equine serum (Hyclone), and 10 U ml^{-1} of both penicillin and streptomycin. All experiments utilized myoblasts which were from passages 23–29 at the time of seeding. Cell suspensions were produced by incubating the attached myoblasts in the log phase of growth with a 0.02% EDTA solution (Sigma) for 15 min at 37°C, triturating with a pipette to separate cells, centrifuging at 200 g for 5 min and resuspending in fresh medium.

Polymer thin film fabrication and characterization

Solid thin films were fabricated from a Tecoflex® (SG-80A, Thermedics) solution by solvent casting onto glass coverslips. Tecoflex®, a medical grade aliphatic thermoplastic polyurethane, contains a methylene bis(cyclohexyl)diisocyanate hard segment, a poly(tetramethylene ether glycol) soft segment and a 1,4-butanediol chain extender (Fig. 1) [19]. The biocompatibility of the polyurethane has been demonstrated in medical applications with no evidence of degradation after 9 months implantation [19–21]. A silane coupling reagent was used to increase the surface hydrophobicity of glass coverslips to promote the attachment of the polymer film. Coverslips, 25 mm diameter (Fisher) for migration studies or 22×22 mm (Corning) for all other studies, were dried for 2 h at 104°C in a vacuum oven then immersed in 0.05% (v/v) dimethyldichlorosilane (DDS) in trichloroethylene for 1 h. Coverslips were subsequently rinsed thoroughly with acetone, blown dry with nitrogen gas and used immediately. The polymer solution, 300 μl of a 3.0% (w/w) solution Tecoflex® in methylene chloride, was pipetted onto the center of a silanized coverslip and spun at 1500 rpm for 5 s on a spin caster (Headway Research, Inc.).

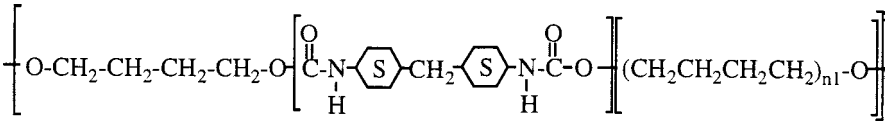

Figure 1. Chemical formulation of Tecoflex®. The thermoplastic, aliphatic polyurethanes are reactions products of poly(tetramethylene ether glycol) (PTMEG), bis(cyclohexyl)diisocyanate (HMDI), and 1,4-butanediol chain extender.

Films were stored in a dessicator overnight to allow the solvent to evaporate. Contact angle measurements were performed on the untreated glass coverslips, silanized coverslips and Tecoflex® thin films. Static contact angles ($n = 6$) were measured by the sessile drop method with distilled water (DI) using a goniometer (Model A-100, Rame-Hart). Prior to cell culture studies, the Tecoflex®-coated coverslips and control surfaces were glued (Master Bond EP21LV) into six-well plates (Becton Dickinson), sterilized for 2 h by immersion in 70% ethanol and rinsed three times with sterile phosphate buffered saline (PBS). All cell assays were performed using a cell density between $3.0–6.0 \times 10^5$ cells ml^{-1}.

Myoblast attachment to solid thin films

Myoblasts were seeded on the Tecoflex®-coated coverslips ($n = 6$) or in a tissue culture polystyrene (TCPS) six-well plate (Becton Dickinson), which served as a control surface. The wells were rinsed twice with sterile PBS after 2 h to remove unattached myoblasts. After 24 h, the wells were rinsed three times with PBS, fixed in 1.25% glutaraldehyde in PBS for 2 h and rinsed an additional three times with PBS. To determine the number of adherent myoblasts, cells which were attached and spread were counted in nine representative fields at 100 × magnification.

Myoblast proliferation on solid thin films

Myoblasts were seeded on the Tecoflex®-coated coverslips ($n = 10$) glued into six-well plates which did not facilitate cell attachment (Ultra-low Attachment, Corning). To determine proliferation, the cell number was quantified at two time points using Resazurin (Sigma), a metabolic indicator of cell viability. After 24 h, five wells were assayed by rinsing three times with PBS, incubating in 100 μl of Resazurin in 1 ml of media for 2 h at 37°C and measuring the fluorescent intensity using a multi-well plate reader (Cytofluor II Reader, PerSeptive Biosystems, Inc.) with excitation wavelength set at 530 nm and an emission wavelength of 590 nm. After an additional 72 h, the remaining five wells were assayed. Proliferation was expressed as the percent increase in cell number.

Myoblast migration on solid thin films

Myoblasts were seeded on the Tecoflex®-coated coverslips in Minimal Essential Media (Hyclone) supplemented with 10 mM Hepes (Sigma), 10% bovine calf serum (Hyclone) and 10 U ml^{-1} of both penicillin and streptomycin and incubated for 2 h at 37°C to allow cell attachment and spreading. Time-lapse videomicroscopy was conducted on a representative region of the film using a micro-incubator (Medical Systems Corp.) [22]. Cell behavior was recorded over 24 h using a time-lapse video recorder (AG-6740, Panasonic). Cell culture temperature was maintained at 37 ± 0.2°C by a temperature controller (TC-102, Medical Systems Corp). The migration of individual myoblasts was analyzed by playback of video recordings

and the rate was quantified using an image processor (Argus-2, Hamamatsu). The migratory activity was recorded over three experiments ($n = 45$ cells).

Myoblast differentiation on solid thin films

Myoblasts were seeded on the Tecoflex®-coated coverslips and cultured in full growth media as described until they reached approximately 70% confluence. Fusion media was then added and the cells were cultured an additional week to allow differentiation into myotubes. To quantify myotube diameters, cultures ($n = 5$) were rinsed three times with PBS, fixed in a 1.25% glutaraldehyde solution in PBS for 2 h and rinsed an additional three times with PBS. The average diameters of thirty myotubes from each thin film were measured with a microscope micrometer at 150 × magnification.

To stain for myosin heavy chain (MHC), cultures on thin films were rinsed three times with PBS, fixed for 8 min in 3% paraformaldehyde in PBS at room temperature, rinsed three times with PBS, permeabilized for 2 min in 0.5% Triton X-100 (Sigma) in PBS at room temperature and rinsed a final three times in PBS. Monoclonal anti-skeletal myosin (Sigma), raised in mouse, was diluted 1 : 100 in PBS and applied for 1 h at room temperature. Following three rinses with PBS, FITC conjugated goat anti-mouse IgG (Sigma) was applied for 30 min at room temperature shielded from light. Prior to observation, the thin films were rinsed three times with PBS and mounted in 90% glycerol/10% PBS with 1mg ml^{-1} *n*-propyl gallate (Sigma).

Three-dimensional substrate fabrication

Porous substrates were fabricated from a Tecoflex® solution by immersion precipitation. Pluronic (10-R5, BASF), a triblock copolymer of poly(ethylene oxide) and poly(propylene oxide), was used as a pore forming agent. A solution of 6.75% (weight percent) Tecoflex® and 32.65% Pluronic was dissolved in 60.61% *N*,*N*-dimethylacetamide (DMAC, Fisher Scientific). The polymer solution was maintained at 47–48°C in a closed system. Two different methods were used to form substrates. Spin-casting was used for forming porous scaffolds of thicknesses up to 500 μm. Two ml of polymer solution were pipetted onto a 4-in. diameter silicone wafer and spun at variable rpm for 2 s. The thin polymer film on the wafer was quickly immersed in 1.25 l of non-solvent, distilled water (DI), at 25°C where it remained for at least 30 min. For thicknesses up to 5 mm, the polymer solution was pipetted into a Teflon mold of various geometries. The mold containing the liquid polymer was quickly immersed in 2 l of DI at 25°C where it remained undisturbed for least 2 h. The non solvent bath was then stirred for an additional hour. The scaffolds were rinsed thoroughly with DI and stored at room temperature until use. To prepare porous Tecoflex® scaffolds for bonding to solid Pellethane® sheets, the scaffolds were frozen in DI and lyophilized (Lyovac GT 2, Leybold-Heraeux). The surface of the polyurethane sheet was solubilized with a gauze pad

soaked in DMAC, the lyophilized scaffold was positioned at the wetted interface, and the composite structure was bonded under a compressive load of 13.7 kPA for 12 h as the solvent evaporated.

Three-dimensional substrate characterization

The morphology of three different substrate thicknesses was analyzed by a scanning electron micrograph (SEM). Substrates were frozen in DI, lyophilized, re-frozen in liquid nitrogen and fractured to expose interior regions of the scaffold. Samples were sputter-coated with gold (Hummer 5 sputter-coated, Technic) and imaged on a Cambridge SEM using an acceleration voltage of 15 kV. Substrate thickness, cross-sectional porosity and pore distribution were determined using NIH Image by averaging representative digital images for each scaffold ($n = 3$). All pores > 2 μm in diameter were included in the porosity analyses.

Substrates were clamped into diffusion chambers with PBS on one side of the scaffold and 2% Blue Dextran M_w 2000 kD (Sigma) in PBS on the other side. The passage of Blue Dextran into the PBS was assayed by sight to determine if the substrate pores provided an interconnected path from one side of the material to the other.

Mechanical analysis of the three-dimensional substrates

Substrates were evaluated for stress-strain characteristics, ultimate tensile strength and elastomeric properties. Briefly, samples were evaluated in both the dry and hydrated state, following 48 h in PBS at 37°C. The samples were approximately 10 mm wide $\times$ 5 mm thick and 50 mm in length. Fiduciary marks were placed on the samples at a gauge length of 25 mm and the samples were suspended from a clamp. A second clamp was weighed and secured to the bottom of each specimen. Weights of 10 g were added sequentially to the bottom clamp until specimen failure. The distance between the fiduciary marks was recorded after the addition of each weight to determine elongation. The data was normalized to each sample's cross-sectional area and standard stress–strain curves were produced. Standard regression analysis, mean and standard error were calculated to determine the modulus of the material, ultimate tensile strength, and the percent elongation to failure. Elastomeric properties were analyzed as described above by applying a load to effect 100% elongation and analyzing recovery following removal of the load.

Cell culture on the three-dimensional substrates

Substrates which were 5 $\times$ 5 mm and of thicknesses ranging from 300 μm to 2 mm were incubated in proliferation medium for 30 min at 37°C. Substrates were subsequently rinsed three times with sterile PBS to remove nonadsorbed protein and placed in fresh twelve plates (Becton Dickinson). Myoblasts were seeded at a density of 10 000 cells per scaffold and incubated for 15 min at 37°C. An additional

3 ml of medium were then added to the wells. Control scaffolds, which were not cultured with myoblasts, were incubated in the same medium for the same periods of time. After 2 weeks, the culture medium was replaced with fusion medium to induce myotube formation. The scaffolds were cultured for an additional 2 weeks. At selected time intervals, cell-containing scaffolds were rinsed three times with PBS, fixed in a 3% paraformaldehyde solution in PBS for 2 h and rinsed an additional three times with PBS. To visualize cell coverage on scaffold surfaces, 1 ml of Acridine Orange (Molecular Probes), a nucleic acid stain, at a concentration of 5 μg ml^{-1} in PBS, was added to the surface of the cell-containing scaffolds and incubated at 37°C for 15 min. The substrates were then rinsed three times with PBS and viewed under fluorescent illumination. Myoblast coverage was qualitatively assessed by the degree of fluorescence on the material. To visualize myoblast infiltration into the cell scaffolds, fixed specimens were prepared for histology dehydrating to 95% ethanol. A 1 : 1 solution of 95% ethanol and infiltration solution (benzol peroxide activated hydroxyethyl methacrylate, Historesin, Reichert-Jung) was then added to the specimens. After 2 h, the solution was replaced with pure infiltration solution. After an additional 2 h, the specimens were transferred to 7 × 10 × 6 mm deep polypropylene molds (Histomold, Leica) and embedded in hydroxyethyl methacrylate hardened with dimethyl sulfoxide (Historesin, Reichert-Jung). Specimens were sectioned 10–14 μm thick using a rotary microtome (Jung 2035 Biocut, Leica), mounted on glass slides and stained with Cresyl Violet Acetate (Sigma) and Sudan Black B. In other cases, fixed specimens were immersed in 20% sucrose in PBS overnight and subsequently frozen in aluminum foil on dry ice. The frozen specimens were fixed to cryostat stubs with O.C.T. Compound (Polysciences) and sectioned at 14 μm with a cryostat at −20°C. Random specimens were selected for immunohistochemical localization of MHC as previously described.

Statistical analysis

The mean and standard deviation of three–forty-five samples were determined for contact angle, attachment, migration, proliferation and myotube diameter studies on solid thin films, and mechanical testing, scaffold porosity, pore distribution and pore area distribution, for characterization studies of the porous 3-D cell scaffolds.

RESULTS

Polymer thin film characterization

The contact angle of the glass coverslips prior to modification was 4 ± 3 deg. Following silanization with DDS, the contact angle was 90 ± 2 deg. Following spin-casting and an overnight solvent evaporation stage, the contact angle of the thin films of Tecoflex® was 69 ± 3 deg.

Myoblast culture on solid thin films

Tecoflex® was permissive to myoblast attachment and spreading. After 24 h of incubation, 932.9 ± 75.8 myoblasts cm^{-2} were attached to the solid thin films (Fig. 2A). This was 62.3% of the cell density (1496.9 ± 210.8 myoblasts cm^{-2}) on the TCPS controls. The morphology of the myoblasts on both surfaces was bipolar. Myoblasts also proliferated on the polyurethane substrate. The number of myoblasts on the solid Tecoflex® thin films increased by 479.1 ± 32.3% after 72 h as demonstrated by the increase in fluorescence measured at the two time points (Fig. 2B). In addition, Tecoflex® was a migration permissive substrate as evidenced by the movement of myoblasts cultured on the thin films during the 24 h recorded time period. Myoblasts migrated at a rate of 47.2 ± 14.9 $\mu m\,h^{-1}$.

Myotubes, recognized in contrast to myoblasts by their increased size and multiple nuclei, developed on the Tecoflex® solid thin films with random orientation following withdrawal of growth factors. The average myotube diameter ranged from 14.0 to 48.8 μm with the majority of the myotubes, approximately 95%, having an average diameter of 14–40 μm (Fig. 2C). Approximately 55% of the cultured area was fused into myotubes at the time of analysis. In addition, the myotubes stained positive for myosin heavy chain (MHC), confirming that differentiation had occurred (Fig. 3A, B). Undifferentiated myoblasts were MHC negative.

Three-dimensional substrate fabrication and characterization

The cell scaffolds shown in Fig. 4A were fabricated from Tecoflex® SG-80A using either spin casting or molding techniques. The scaffolds were molded on a macroscopic scale to obtain a variety of geometries ranging from 100 μm to 5 mm thick. Following the immersion precipitation process, the polymer formed a three-dimensional sponge-like architecture that was permeated by a network of pores created as the solvent and the pore forming agent slowly diffused into the nonsolvent or precipitation bath. Scanning electron micrographs revealed that the pores formed an open-celled foam structure (Fig. 4B). Transport of Dextran Blue across the substrates indicated that pores were part of an interconnected network that extended throughout the bulk of the material. The composite structure shown in Fig. 4C consists of an approximately 3 mm thick molded scaffold which was solvent bonded onto a 1-mm thick solid sheet of Pellethane®. The scaffold remained attached to the polymer sheet following elongation, flexion and torsion.

The pore morphology varied as a function of substrate thickness. The pore size distribution shifted towards larger pores sizes as shown in the pore distribution graphs of representative 317, 684, and 1842 μm thick substrates (Fig. 5A, C, E). Substrate porosity also increased as a function of increasing substrate thickness. The thinnest scaffolds analyzed, 317 μm thick on average, were 42.2 ± 5.1% porous. Scaffolds which were 684 μm thick on average were

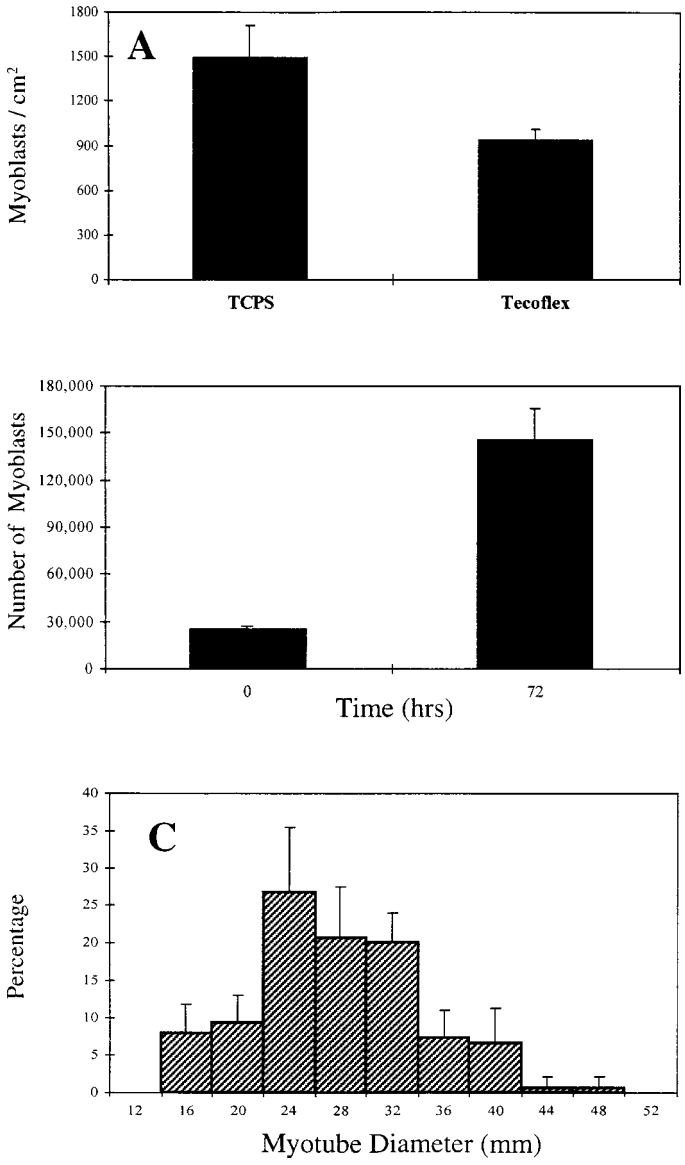

Figure 2. Characterization of G8 myoblast behavior on solid Tecoflex® thin films. (A) Comparison of cell attachment tissue culture polystyrene (TCPS) and Tecoflex® coated glass coverslips in serum containing growth media. (B) Change in number of myoblasts attached to Tecoflex® over a 72-h period in serum containing media. (C) Range of measured diameters of differentiated myotubes after 1 week of culture in fusion media.

49.1 ± 3.1% porous. The thickest scaffolds analyzed, which were 1842 μm thick on average, had a porosity of 57.2 ± 1.5%. There was also an increase in the percentage of the overall pore area that consisted of pores large enough to accommodate myotubes ($\geqslant$14 μm). Approximately 80% of the pore area

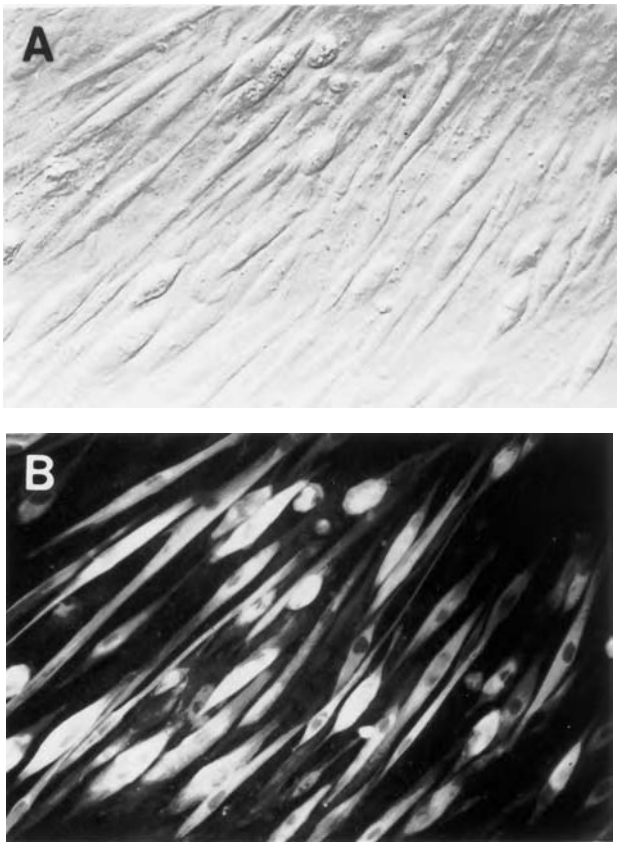

Figure 3. Immunofluorescent staining of myosin heavy chain within differentiated G8 myotubes after 1 week of culture in fusion media on Tecoflex® thin films. A large proportion of cells retained their ability to differentiate when grown on the surface of Tecoflex®. (A) Light photomicrograph taken with Hoffman modulation optics (200 × magnification). (B) Same field showing cells immunoreactive for myosin heavy chain. Note multiple nuclei within the same cells (200 × magnification).

of the 317 μm thick scaffolds was $\geqslant 14$ μm (Fig. 5B), which increased to 97 and 99%, as the average scaffold thickness increased to 684 and 1842 μm (Fig. 5D, F).

A statistical analysis of the results of the mechanical tests by Student's t-test revealed no difference in the mechanical performance of the hydrated and the nonhydrated specimens analyzed. Qualitatively the substrates were supple to the touch, easily deformable by hand, and recovered shape following deformation. The elastic modulus of the dry material was 0.269 ± 0.021 kPa ($n = 6$) compared to 0.227 ± 0.007 kPa ($n = 5$) for the hydrated specimens. The tensile strength of the dry substrates was 46.2 ± 2.8 kPa ($n = 6$) compared to 40.0 ± 4.8 kPa for the hydrated samples. Analysis of recovery following elongation to 100% was 99.2 ± 0.52% for dry samples and 95.3 ± 1.14% for hydrated

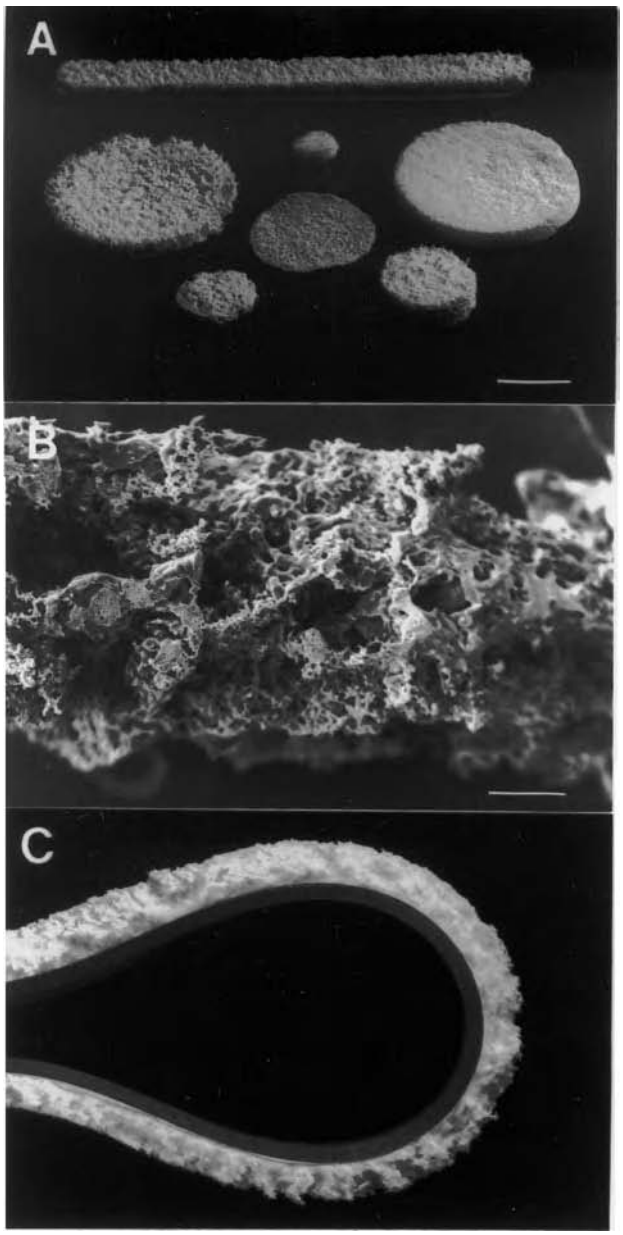

Figure 4. Morphological characterization of a variety of 3-D cell substrates fabricated from Tecoflex® by controlled precipitation. (A) Representative photograph showing various substrate geometries and thicknesses that were fabricated using Teflon molds followed by controlled precipitation (bar = 15 mm). (B) Representative scanning electron photomicrograph of a cross-section through the interior of a Tecoflex® scaffold showing internal pore structure (bar = 200 μm). (C) Photograph showing that the 3-D cell substrate can be solvent bonded to solid Pellethane® sheet and still maintain its compliance.

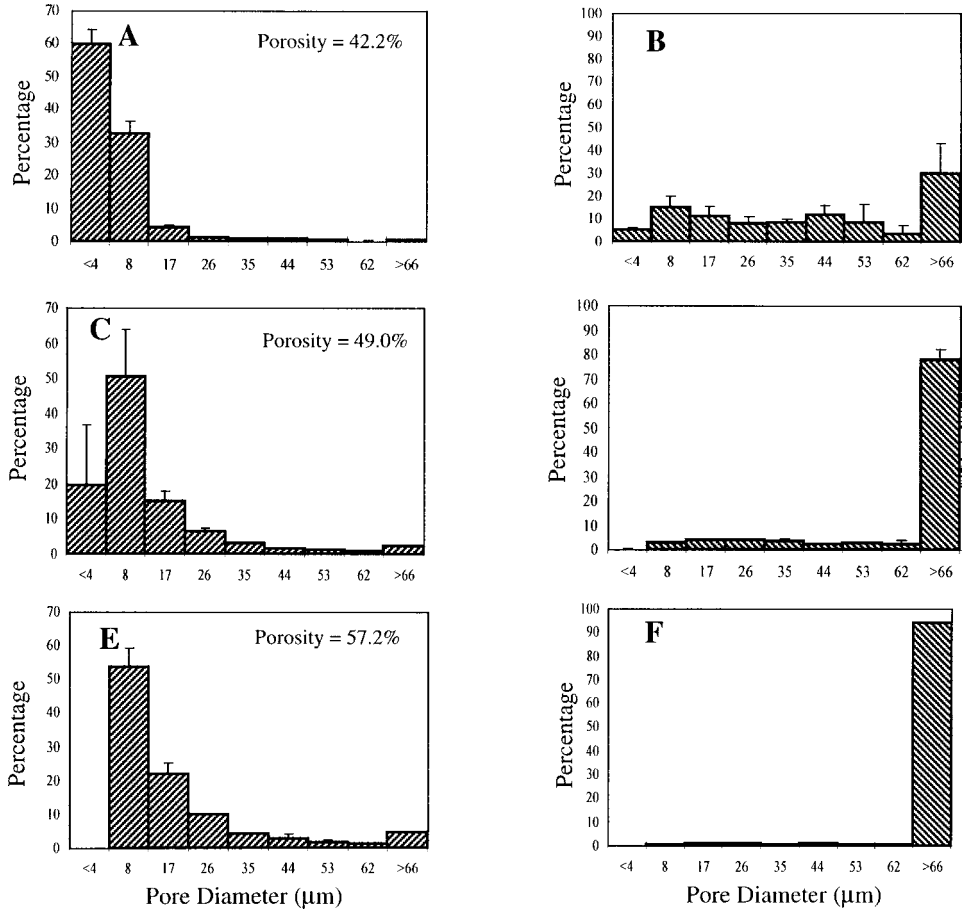

Figure 5. Pore distribution data taken from digital SEM images of cross-sections of 3-D Tecoflex® substrates of various thicknesses. (A, C, E) Comparison of pore size distribution of three scaffold thicknesses; 317, 684, and 1842 μm, respectively. (B, D, E) Comparison of pore area distribution comparing the same scaffold thicknesses.

samples, respectively. The elongation to break was approximately 180% for each group.

Cell culture on elastomeric three-dimensional substrates

Skeletal myoblasts attached to the porous three-dimensional Tecoflex® scaffolds as revealed by fluorescent labeling one week after the cells were cultured on substrates ranging from 300 μm to 2 mm thick (data not shown). Myoblasts, stained with Acradine Orange, were randomly distributed throughout the bulk of the material. At later time periods, the intensity or fluorescent labeling increased indicating that cell proliferation had occurred. When the cell-seeded substrates were viewed at higher magnification, the presence of multiple nuclei could be

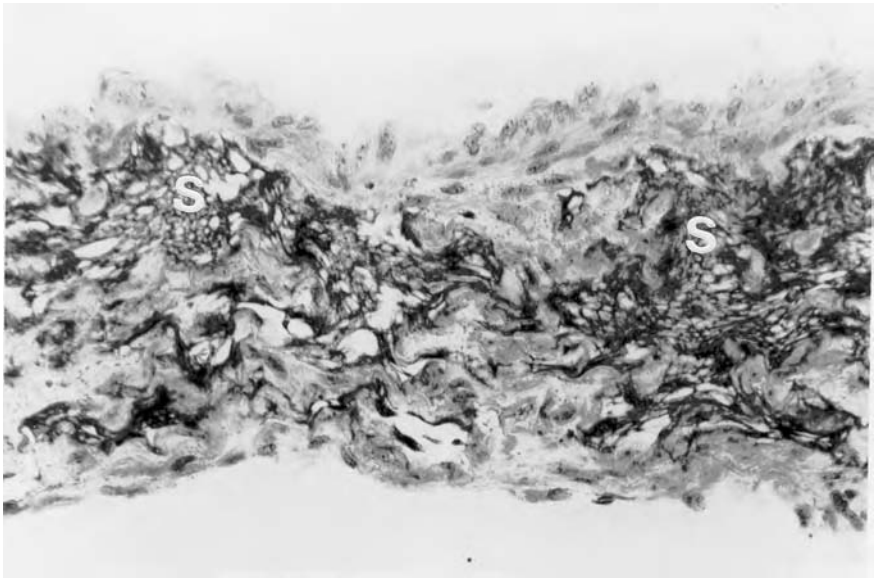

Figure 6. Light photomicrograph of histological cross-section of Cresyl Violet stained G8 myoblasts seeded on a 350-μm thick Tecoflex® scaffold following long-term culture in fusion media. Note presence of myotubes on both surfaces and within the porous interior. The 3-D substrate (s), stained with Sudan Black, is the darker structure in the micrograph (200 × magnification).

readily observed within the same cell indicating that myoblasts had fused to create myotubes.

The presence of cells on the interior of polymer scaffolds in histological cross-sections indicated that the myoblasts could gain access top the inner portions of scaffolds ranging in thickness from 300 μm to 2 mm. A representative histological section shown in Fig. 6 was taken from a scaffold which was seeded with myoblasts and maintained in culture for 4 weeks. Myotubes were observed both on the surface and within the interior of the substrates. The histological analysis revealed multiple nuclei stained with Cresyl Violet within the same cell in single histological sections. In addition, multiple nuclei could be detected in adjacent serial sections within the same cell. Pores less than 10 μm excluded the cells and could be clearly observed in sections that were countered stained with Sudan Black which bound to the hydrophobic substrate. Larger pores were typically infiltrated by myoblasts which were observed within the interior portions of substrates up to 2 mm in thickness. The majority of cells were viable even in the thickest substrates. There was little evidence of cell debris or cell death although some areas of the thicker substrates were devoid of cells. After several weeks in culture, the initially flat scaffolds gradually buckled and curled. Control scaffolds, which did not contain myoblasts, retained their flat geometry. Immunohistochemical analysis of cryostat sections revealed positive staining for MHC expression indicating that differentiation of the multinucleated muscle cells had taken place within the porous elastomeric substrate.

DISCUSSION

The results of this study indicate that skeletal myogenesis can be achieved on substrates of Tecoflex® SG-80A, most noteworthy, throughout the porous three-dimensional network of an elastomeric substrate made of the same material. Myogenesis, or the development of skeletal muscle, was confirmed by the formation of multinucleated myofibers that expressed myosin heavy chain, a specific indicator of muscle differentiation [14, 27–29]. Together, the results of our study suggest that it is indeed feasible to engineer bioartificial systems consisting of skeletal muscle cultivated on a 3-D elastomeric substrate.

The assessment of a substrate's utility in tissue engineering applications should rely upon a wide range of cell–material interactions. The strategy in this study was to initially quantify cellular responses on 2-D solid thin films in order to determine if studies utilizing 3-D substrates were warranted. The ability of cells to attach to a substrate is clearly a requirement for such applications, but the efficiency of attachment and the subsequent behavior of the attached cells also needs to be considered. For applications utilizing skeletal muscle, one must consider that skeletal myoblasts can be harvested from adult hosts, whether animal or man, and expanded *in vitro*. For example, one study suggests that a muscle biopsy of 1 g of human rectus femoris can yield up to 12.5 billion myoblasts after 20 days in culture [26]. Consequently, a high attachment efficiency may not be critical in certain applications that utilize cell types of high proliferative capacity. The morphology of the G8 myoblasts cultured on Tecoflex® was similar to that observed by investigators studying G8 behavior on TCPS and type I collagen-coated polystyrene [31–33].

Dynamic indices of cell interaction are arguably more indicative of the potential utility of a material in tissue engineering applications. Proliferation of the seeded cells on the substrate is typically necessary although the proliferation requirements may vary between applications. A better indicator may be the combination of attachment efficiency and proliferation rate on the substrate. For example in the present study, 62% of the number of myoblasts which attached to TCPS attached to Tecoflex® (Fig. 2A). However, based on the proliferation rate, the number is recovered within the first 28 h of culture on Tecoflex®. The ability of cells to migrate on a substrate, another dynamic index, may enhance colonization of interior regions of the scaffold. The migration rate of another skeletal myoblast cell line on laminin coated TCPS is very similar to the rate determined here for G8 myoblasts on Tecoflex® thin films coated with serum proteins [7]. Although cells tend to migrate in random directions when a chemotactant is not present, the migration rate of myoblasts on Tecoflex® would theoretically allow them to travel from the surface of a 2-mm thick cell scaffold to the center within 1 day. The presence of areas lacking cell colonization within the thicker substrates may be related to the unique properties of muscle precursors which alter cell signaling events following physical contact with cells of their own kind. G8 myoblasts, similar to other cells, are known to synthesize their own extracellular matrix proteins in culture [22]. As

these cells migrate, it is reasonable to expect that they will modify the surface with secreted proteins, thereby potentially creating a more biomimetic surface which will allow appropriate phenotypic expression and differentiation of myoblasts which subsequently colonize the region.

Differentiation on a substrate is critical, particularly in applications utilizing precursor cells such as myoblasts. The formation of myotubes on Tecoflex® solid thin films and their subsequent expression of MHC indicates that the cells retain the ability to differentiate following several weeks of interaction with the material in culture. Confirmation of skeletal myogenesis on the solid thin films provided the rationale to extend the studies to porous 3-D scaffolds. Similar to the results on thin films, porous 3-D scaffolds supported G8 myoblast attachment, proliferation, and differentiation into myotubes that expressed MHC.

Given the substrate's elastomeric nature, ability to be bonded to solid sheets of polyurethane, and its support of cellular ingrowth, the material may be useful as an interface between muscle and solid implant materials. One such application is the adherence of the latissimus dorsi to a flexible blood pump to create a skeletal muscle ventricle [30]. In this technique, the skeletal muscle is wrapped around a polyurethane blood pump near the physiologic site of the muscle. The ultimate effectiveness of power transmission from the muscle depends upon the coupling between the muscle and blood pump. Another potential application of the substrate used in this study is the permanent fixation of electrodes to skeletal muscle used for functional electrical stimulation. In both cases, skeletal myoblasts could be harvested from the host and expanded *in vitro*. The scaffold, molded in the appropriate 3-D configuration, could be attached to the material portion of the junction using techniques such as solvent bonding utilized in this study. The expanded myoblast culture could be seeded on the scaffold and the entire construct could be returned to the host where proliferation of the myoblasts and fusion with the host muscle would ensure firm attachment. Studies would be required to answer questions regarding the potential for vascularization of the interface and the scaffold thickness which supports viable tissue within the transition region. The base material for such applications would not be limited to Tecoflex®. Also, the use of a compliant porous scaffold as a cellular interface would not be limited to the culture of muscle but could be utilized in any application where cellular ingrowth or fixation was desired. Such a construct could provide an interface of graded modulus for force dampening and may minimize reactivity at the host implant interface. Furthermore, a compliant material may provide additional benefits through increased patient comfort.

Based on the scaffold's ability to support skeletal myogenesis, it may be a useful vehicle for a variety of gene therapy applications especially in cases were genetically engineered muscle tissue is used as a biologically-based sustained delivery device. Myoblasts represent a promising delivery vehicle because they can be readily isolated from muscle biopsies, can be transfected *in vitro*, are capable of synthesizing large quantities of recombinant proteins and are capable

of sustaining gene expression *in vivo* [35, 36]. In this application the myoblasts could be seeded on the scaffold, allowed to proliferate and differentiate *in vitro* and then be implanted subcutaneously or intramuscularly using the elastomeric substrate as a suturing anchor. The polyurethane scaffold can be strained to the necessary degree during implantation in order to maintain tension on the implant for long-term maintenance of the terminally differentiated phenotype [20].

The 3-D geometry and porosity of the substrate are important variables to consider if it is to be used to guide muscle formation in the development of a skeletal muscle tissue equivalent [33–36]. Although myoblasts were observed to infiltrate the porous scaffolds (Fig. 6), the phase inversion method employed in this study provided little control over the pore orientation or alignment of the pore structure. Of the three scaffold thicknesses analyzed for pore distribution, only 3–27% of the total pore size distribution was comprised of pores between 14 and 40 μm in diameter. This size represents the diameter of 95% of the myotubes and therefore is the diameter which would be necessary to accommodate single muscle fibers within individual pores. Our results indicate, however, that multiple myofibers form within the larger pores suggesting that a one-to-one relationship between myotube diameter and pore size may not be a necessary specification for a scaffold for culturing skeletal muscle. A more critical limitation of the present scaffold is the lack of control over pore orientation and alignment. Even though approximately 80–98% of the cross-sectional pore area was comprised of pores greater or equal to 14 μm in diameter, the size necessary to accommodate myotubes, the interconnected pores had a random orientation within the bulk of the substrate. Therefore, there is little possibility of achieving organized contraction or directed work from a tissue equivalent using scaffolds fabricated with methods employed in this study other than by possibly changing the volume of a sphere or tube. However, now that it has been demonstrated that skeletal myogenesis can be obtained within a porous elastomeric substrate and the potential feasibility of obtaining a bioartificial skeletal muscle tissue equivalent has been established, further efforts directed towards fabricating a growth substrate with aligned pores are warranted.

In summary, this study geared towards understanding the interaction between G8 myoblasts and elastomeric substrates has yielded results which suggest that it is indeed feasible to utilize tissue engineering approaches to design novel biohybrid systems that incorporate differentiated muscle tissue. The porous substrate used in this study may have utility both as a compliant tissue integrating interface positioned between host tissue and medical implants, as well as, a cell delivery vehicle for transplanting genetically-modified muscle tissue.

Acknowledgements

The authors gratefully acknowledge a fellowship for MMM from the Whitaker Foundation under the Biobased Engineering Program administered by the Department of Bioengineering, University of Utah, and funding for BWH from the Huntsman Cancer Institute.

REFERENCES

1. M. Casser-Bette and A. B. Murray, *Calcif. Tissue Int.* **46**, 46 (1990).
2. J. Hansbrough, C. Dore and W. Hansbrough, *J. Burn Care Rehabil.* **13**, 519 (1992).
3. L. Freed, J. Marquis, A. Nohria, J. Emmanual, A. Mikos and R. Langer, *J. Biomed. Mater. Res.* **27**, 11 (1993).
4. Y. Cao, J. Vacanti, X. Ma, K. Paige, J. Upton, Z. Chowanski, B. Schloo, R. Langer and C. Vacanti, *Transplant. Proc.* **26**, 3390 (1994).
5. L. Graham, T. Brothers, C. Vincent, W. Burkel and J. Stanley, *J. Biomed. Mater. Res.* **25**, 525 (1991).
6. S. K. Williams, T. Carter, P. K. Park, D. G. Rose, T. Schneider and B. E. Jarrell, *J. Biomed. Mater. Res.* **26**, 103 (1992).
7. S. Goodman, G. Risse and K. von der Mark, *J. Cell Biol.* **109**, 799 (1989).
8. J. E. Anderson, R. S. Carvalho, E. Yen and J. E. Scott, In Vitro *Cell Dev. Biol.* **29A**, 183 (1993).
9. K. A. Barbee, E. J. Macarak and L. E. Thibault, *Ann. Biomed. Eng.* **22**, 14 (1994).
10. S. Swasdison and R. Mayane, *J. Cell Sci.* **102**, 643 (1992).
11. S. Hatfaludy, J. Shansky and H. H. Vandenburgh, *Am. J. Physiol.* **256**, c175 (1989).
12. J. L. Samuel and H. H. Vandenburgh, In Vitro *Cell Dev. Biol.* **26**, 905 (1990).
13. C. Perrone, D. Fenwick-Smith and H. Vandenburgh, *J. Biol. Chem.* **270**, 2099 (1995).
14. A. Shahar, in: *Methods in Neuroscience*, Vol. 2, p. 195. Academic Press, New York (1990).
15. H. Vandenburgh, S. Swasdison and P. Karlisch, *FASEB J.* **5**, 2860 (1991).
16. H. Vandenburgh, M. Tatto, J. Shansky, J. Lemaire, A. Chang, F. Payumo, P. Lee, A. Goodyear and L. Raven, *Human Gene Ther.* **7**, 2195 (1996).
17. C. Christian, P. Nelson, J. Peacock and M. Nirenberg, *Science* **196**, 995 (1977).
18. R. Beach, W. Burton, W. Hendricks and B. Festoff, *J. Biol. Chem.* **257**, 11 437 (1982).
19. D. E. Sakas, K. Charnvises, L. F. Borges and N. T. Zervas, *J. Neurosurg.* **73**, 936 (1990).
20. Y. Marois, A. Akoum, M. King, R. Guidoin, W. von Maltzahn, R. Kowligi, R. C. Eberhart, F. J. Teijeira and J. Verreault, *J. Invest. Surg.* **6**, 273 (1993).
21. T. L. Lambert, V. Dev, E. Rechavia, J. S. Forrester, F. Litvack and N. L. Eigler, *Circulation* **90**, 1003 (1994).
22. C. Ince, D. L. Ypey, M. M. C. Diesselhoff-Den Dulk, J. A. M. Visser and R. Van Furth, *J. Immun. Meth.* **60**, 269 (1983).
23. M. Kiess, R. M. Gill and P. A. Hamel, *Oncogene* **10**, 159 (1995).
24. J. M. Wells and S. Strickland, *Development* **120**, 3639 (1994).
25. M. L. Pearson, in: *The Molecular Genetics of Development*, T. Leighton and W. F. Loomis (Eds), p. 361. Academic Press, New York (1980).
26. P. Law, *Myoblast Transfer: The Therapy for Muscular Dystrophy*. RG Landes, Austin (1994).
27. E. Hu, P. Tontonoz and B. M. Spiegelman, *Proc. Natl Acad. Sci. USA* **92**, 9856 (1995).
28. S. E. Moore, J. Thompson, V. Kirkness, J. G. Dickson and F. S. Walsh, *J. Cell Biol.* **105**, 1377 (1987).
29. K. Romstedt, R. L. Beach and B. W. Festoff, *Muscle Nerve* **6**, 283 (1983).
30. J. Wilde, J. Van Loon, N. Bishop, A. Shelton, C. Marten, W. Kolff, L. Stephenson, F. Bacieqicz, H. Nakajiima, G. Thomas and B. Hammond, *Artif. Organs* **18**, 230 (1994).
31. E. Barr and J. M. Leiden, *Science* **254**, 1507 (1991).
32. J. Dhawan, L. C. Pan, G. K. Pavlath, M. A. Travis, A. M. Lanctot and H. M. Blau, *Science* **254**, 1509 (1991).
33. S. Cohen, M. C. Bano, L. G. Cima, H. R. Allcock, J. P. Vacanti, C. A. Vacanti and R. Langer, *Clinical Materials* **13**, 3 (1993).

34. A. Mikos, G. Sarakinos, S. Leite, J. Vacanti and R. Langer, *Biomaterials* **14**, 323 (1993).
35. M. C. Wake, C. W. Patrick and A. G. Mikos, *Cell Transplant.* **3**, 339 (1994).
36. A. J. Putnam and D. J. Mooney, *Nature Medicine* **2**, 824 (1996).

Polymers for Tissue Engineering, pp. 273–286
Molly S. Shoichet and Jeffrey A. Hubbell (Eds)

Formation of a spherical multicellular aggregate (spheroid) of animal cells in the pores of polyurethane foam as a cell culture substratum and its application to a hybrid artificial liver

HIROYUKI IJIMA, KOHJI NAKAZAWA, HIROSHI MIZUMOTO, TAKU MATSUSHITA and KAZUMORI FUNATSU *

Chemical Engineering Group, Graduate School of Engineering, Kyushu University, 6-10-1 Hakozaki, Higashi-ku, Fukuoka 812-81, Japan

Received 29 July 1997; accepted 28 January 1998

Abstract—Monkey kidney cells (Vero), human embryonic kidney cells (293), human liver cells (PLC/PRF/5), and primary rat, dog, and porcine hepatocytes formed spherical multicellular aggregates (spheroids) in the pores of polyurethane foam which was used as a cell culture substratum. These spheroids of various cell types express high cell activity for a long period.

A practical hybrid artificial liver support system composed of a multi-capillary polyurethane foam packed-bed type cell culture module including primary hepatocyte spheroids was developed. The success of the system is indicated by an 80% recovery rate in hepatic failure rats which died in control experiments.

Key words: Polyurethane foam; artificial liver; spheroid; mammalian cell; primary hepatocyte; packed-bed bioreactor; animal experiment.

INTRODUCTION

Many polymers including those coated by extracellular matrices are used as cell culture substrates for anchorage-dependent mammalian cells [1–5]. Koide *et al*. reported that using proteoglycan-derived reticulin fibers from liver-coated polystyrene cell culture, primary rat hepatocytes formed spherical tissue-like organoids (spheroids) and expressed a high level of albumin secretion activity which was maintained for a long period [6].

In a previous paper, primary rat hepatocytes formed spherical multicellular aggregates (spheroids) in the pores of polyurethane foam (PUF) as a cell culture

*To whom correspondence should be addressed.

substratum without coating the extracellular matrices on its surface [7]. In this paper, we report the spheroid formation of established mammalian cell lines in the pores of PUF. Some kinds of primary hepatocytes rapidly formed spheroids by changing the characteristics of the PUF. We also tried to develop a hybrid artificial liver using PUF/hepatocyte spheroid culture.

MATERIALS AND METHODS

This experiment was reviewed by the Committee of the Ethics on Animal Experiments in Kyushu University and was carried out under the control of the Guideline for Animal Experiments at Kyushu University.

Cells

We used three kinds of established cell lines and three kinds of primary hepatocytes. Monkey kidney cell (Vero cell), human embryonic kidney cell (293 cell) and human liver cell (PLC/PRF/5) were used as the cell lines.

Animals were purchased from Kyudo (Kumamoto, Japan). Primary rat, dog, and porcine hepatocytes were prepared by a two-step collagenase perfusion method [8, 9]. Cell viability of primary hepatocytes was more than 85%, evaluated by the trypan blue dye exclusion method.

Polyurethane foam

Polyurethane foam was kindly donated by Inoac (Nagoya, Japan). It has a sponge-like macroporous structure with each pore made up of smooth thin films and thick skeletons, as reported previously [10]. The characteristics of each PUF are indicated in Figs 1 and 2 and Table 1.

The block of PUF was cut into flat plates ($1.0 \times 25 \times 25$ mm). Before use, the PUF plates were submerged in distilled water and autoclaved in order to sterilize them and remove any chemical contaminants. The PUF plates were then washed with the culture medium and soaked again in the medium prior to cell inoculation.

Three kinds of PUF films were made to measure the contact angles of each PUF. These films were obtained by pressing at 20 kg 900 cm^{-2} during the foaming process of the PUF.

Culture media and cell inoculation

Culture media for all cells are shown in Table 2. These media were based on previous papers [7, 11–13] with minor modifications. Each PUF plate was put into a tissue culture dish (35 mm, Iwaki Glass, Japan), and cell suspension was uniformly dropped on the PUF plate. Four hours after cell inoculation, the PUF plate was transferred to a new tissue culture dish. Then, the culture medium was exchanged at 2-day intervals. The volume of medium in each dish was 2 ml.

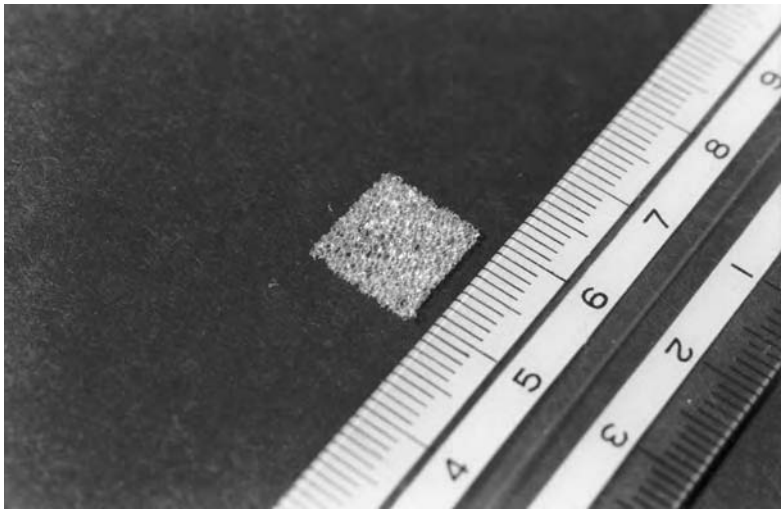

Figure 1. Appearance of a PUF plate. Unit of the scale is cm.

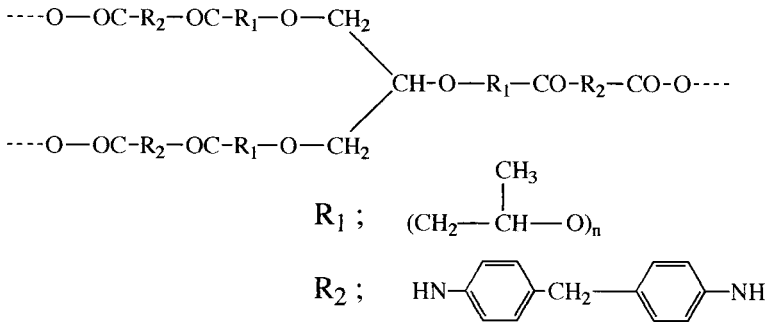

Figure 2. Chemical structure of R-1 PUF.

Table 1.
Characteristics of each PUF

PUF type	R-1	R-4	W-1
Type	Polyether rigid PUF	Polyether rigid PUF	Polyether rigid PUF
Polyol/Isocyanate (wt%)	40/60	40/60	51/49
Pore size (μm)	500	250	250
Bulk density (g cm^{-3})	0.012	0.019	0.018

Artificial liver

A multi-capillary PUF packed-bed (MC-PUF) including primary hepatocyte spheroids was used as an artificial liver module. A characteristic of MC-PUF is simple geometry, i.e. a cylindrical block of PUF has many capillaries for medium flow [14]. These capillaries are opened by drill in a triangle arrangement for uniform medium

Table 2.
Culture medium composition

Cell type	Established cell lines	Rat hepatocyte	Dog and porcine hepatocyte
Basal medium	BME (Vero) MEM (293) WE (PLC/PRF/5)	Williams' medium E (WE)	Williams' medium E (WE)
Fetal bovine serum	10% (Vero) 2 (293) 2 (PLC/PRF/5)	—	—
Epidermal growth factor	—	50 $\mu g\,l^{-1}$	25 $\mu g\,l^{-1}$
Insulin	—	10 $mg\,l^{-1}$	7.3 $mg\,l^{-1}$
Copper ($CuSO_4{\cdot}5H_2O$)	—	0.1 μM	0.1 μM
Selenium (H_2SeO_3)	—	3 $\mu g\,l^{-1}$	0.39 $\mu g\,l^{-1}$
Zinc ($ZnSO_4{\cdot}7H_2O$)	—	50 pM	50 pM
Linoleic acid	—	50 $\mu g\,l^{-1}$	50 $\mu g\,l^{-1}$
Penicillin	58.5 $mg\,l^{-1}$	58.5 $mg\,l^{-1}$	—
Streptomycin	100 $mg\,l^{-1}$	100 $mg\,l^{-1}$	—
Gentamycine	—	—	50 $mg\,l^{-1}$
Chloramphenicol	—	—	50 $mg\,l^{-1}$
Amphotericin B	—	—	1 $mg\,l^{-1}$
$NaHCO_3$	1.05 $g\,l^{-1}$	1.05 $g\,l^{-1}$	1.05 $g\,l^{-1}$
HEPES	1.19 $g\,l^{-1}$	1.19 $g\,l^{-1}$	1.19 $g\,l^{-1}$
Dexamethasone	—	—	1 μM
Transferrin	—	—	6.25 $mg\,l^{-1}$
Albumin	—	—	500 $mg\,l^{-1}$
Glucagone	—	—	4 $\mu g\,l^{-1}$
Liver growth factor	—	—	20 $\mu g\,l^{-1}$

flow. Good mass transfer between the culture medium in the capillaries and the cells in the pores of the PUF was achieved, due to the absence of membranes in the capillaries as a hollow fiber culture module.

The volume of this MC-PUF module is 5.65 cm^3 and the PUF packing ratio is 79%. Immobilized cell density is 7.9×10^6 cells cm^{-3}-PUF, which was decided as the optimum cell density of primary rat hepatocytes previously evaluated in a MC-PUF module [14].

The hybrid artificial liver support system is shown in Fig. 3. This system was composed of a blood circulation line (0.5 ml min^{-1}) connected with the left carotid artery and right jugular vein of a hepatic failure rat, and a plasma circulation line (3.0 ml min^{-1}) including an artificial liver module. These two circulation lines were connected by a plasma separator and bypass line (0.1 ml min^{-1}) as shown in Fig. 3. The blood circulation line had a blood pressure monitoring system (Dyne Scope DS-503, AU-513: Fukuda Denshi, Japan), port of sampling, and transfusion auto supplying line. The volume of the plasma and blood circulation lines containing plasma separator were 12 and 1.4 ml, respectively. The hybrid artificial liver support system filled with normal rat plasma before use.

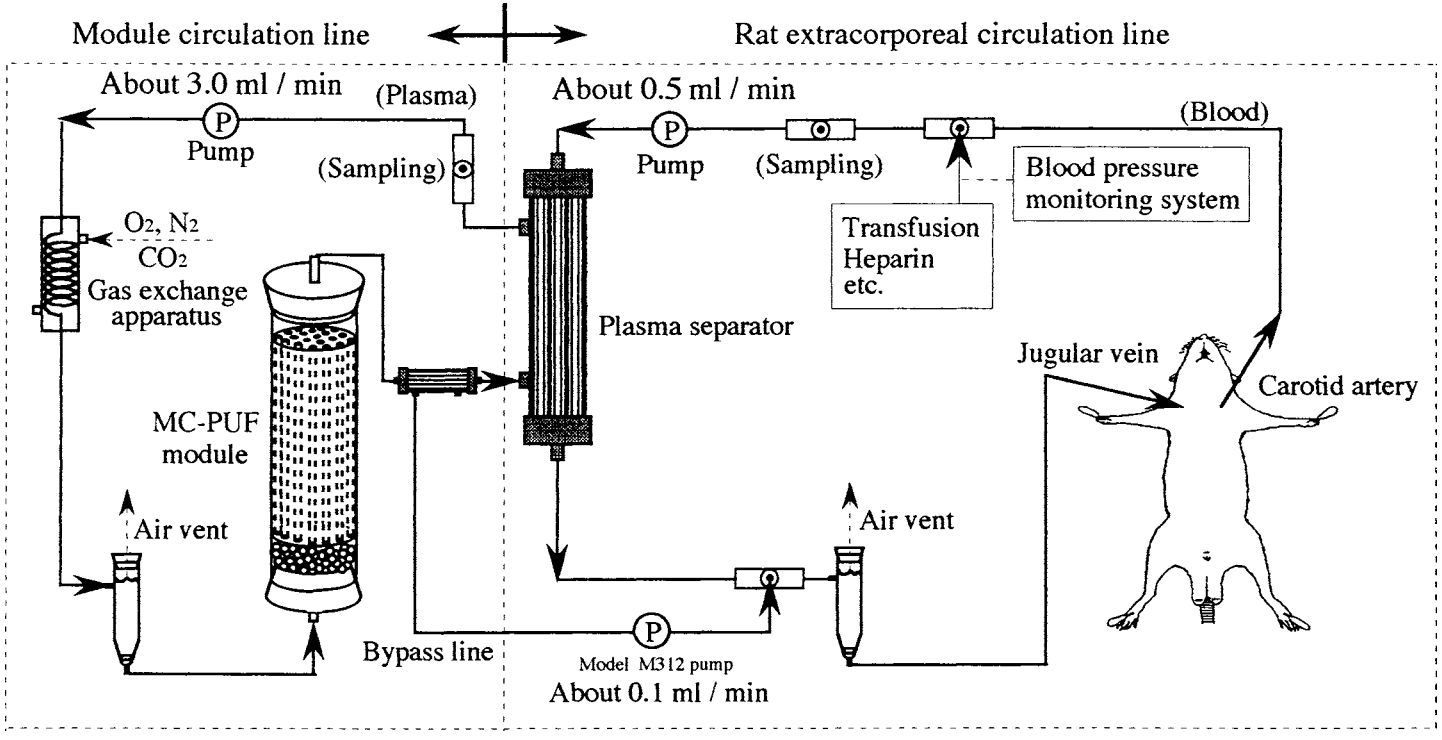

Figure 3. Hybrid artificial liver support system.

Hepatic failure in the rat was caused by intraperitoneal injection of D-galactosamine (0.5 or 0.6 g galactosamine per kg rat body weight) which was left for 24 h. The performance of the system was evaluated by measurement of the blood composition during and after extracorporeal circulation with an artificial liver module including hepatocyte spheroids. Liver function support by extracorporeal circulation with the system was performed for 3 h. An artificial liver module without hepatocytes was used as a control experiment.

RESULTS

Established cell line

Microscopic photographs of three kinds of established mammalian cell lines are shown in Fig. 4. Vero cells formed dome-like cell aggregates. 293 cells and PLC/PRF/5 cells formed spheroids. These 293 cells attached and spread on the internal surface of the PUF pores and formed a monolayer, then grouped and formed spheroids in the pores of the PUF, which were observed by microscope equipped with a time lapse video (AG-6720, Panasonic, Japan) during the culture period.

Tissue plasminogen activator (t-PA) productivity of the 293 cells is shown in Fig. 5. The 293 cells in PUF/spheroid culture maintained high t-PA productivity for more than 6 weeks. For the 293 cells in usual monolayer culture, the highest activity in the late logarithmic growth phase was almost the same as that in PUF/spheroid culture, but the activity rapidly decreased in the stationary phase. From the above, the efficiency of PUF/spheroid culture for the maintenance of the cell specific function is indicated.

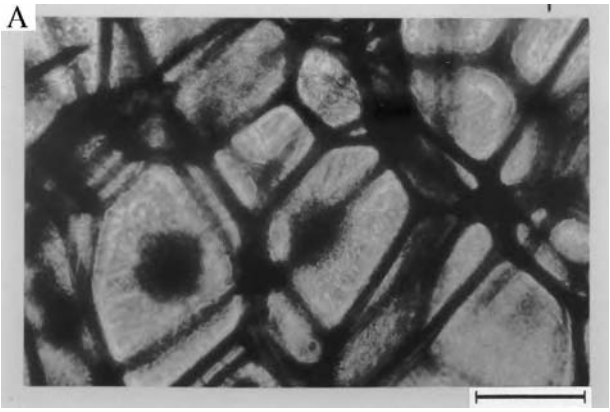

Figure 4. Appearance of various cell lines in the pores of PUF. (A) Vero cell, (B) and (C) 293 cell, (D) PLC/PRF/5 cell, (B) monolayer state (logarithmic growth phase), (C) spheroid state (stationary phase), bar: 200 μm.

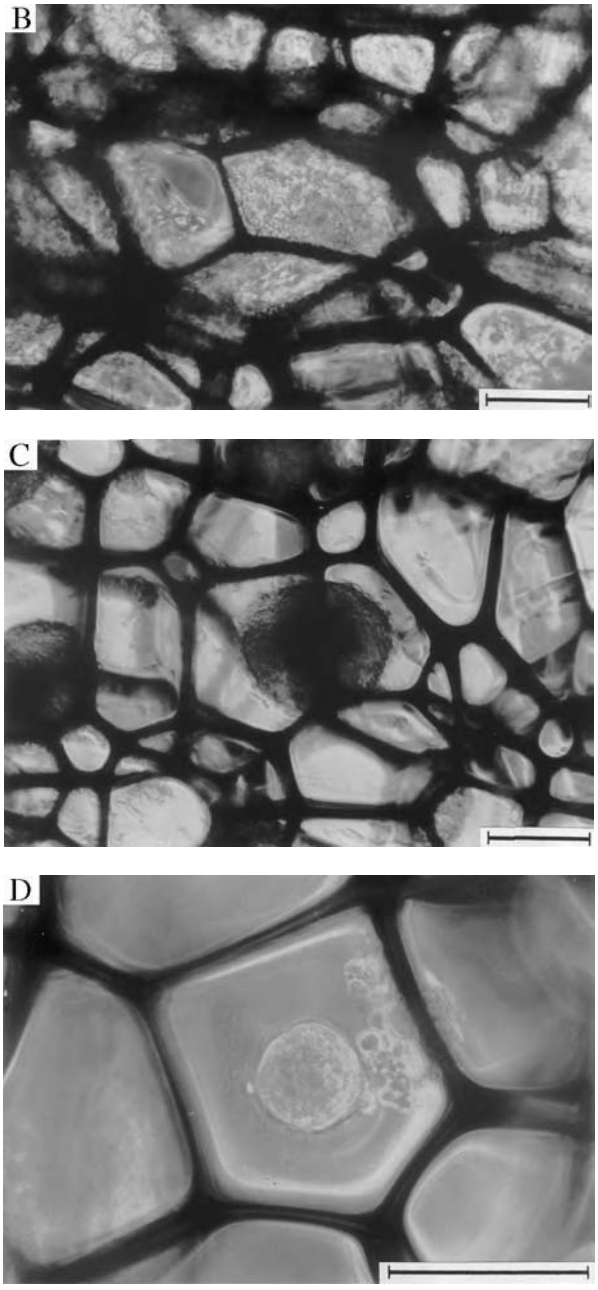

Figure 4. (Continued).

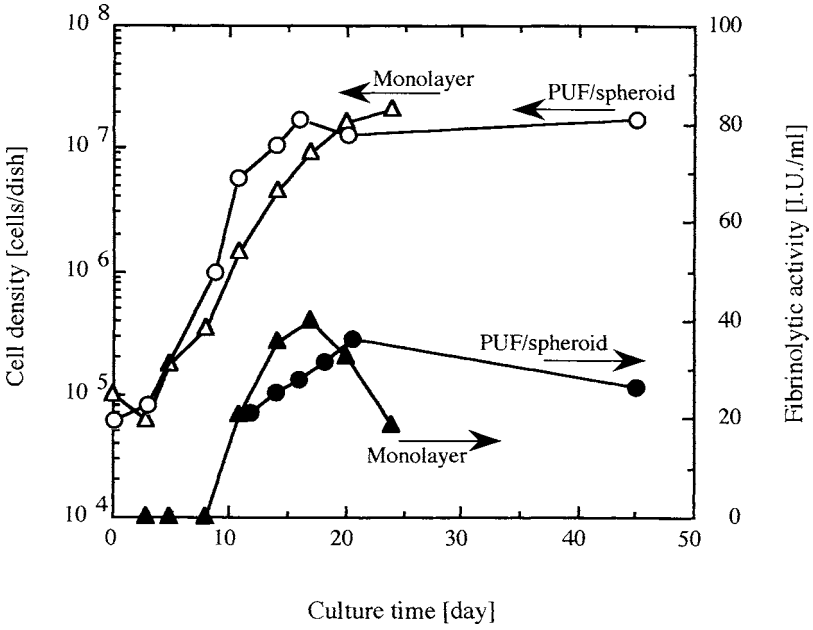

Figure 5. Tissue plasminogen activator (t-PA) productivity of 293 cell. (○) and (●): PUF/spheroid culture, (△) and (▲): monolayer culture, (○) and (△): cell density, (●) and (▲): fibrinolytic activity.

Table 3.
Contact angles of each PUF

PUF type	Contact angle (deg)
R-1	80.6 ± 5.1
R-4	85.2 ± 2.3
W-1	47.8 ± 4.5

Values shown means ± SD in 10 experiments.

Primary hepatocyte

Contact angles of three kinds of PUF were evaluated using distilled water and are shown in Table 3. The contact angles of R-1 and R-4 type PUF are almost the same, and indicate hydrophobic surface characteristics. However, the contact angle of W-1 PUF is much smaller than that of R-1 and R-4 PUF, and indicates relatively hydrophilic characteristics of the W type PUF.

The morphologies of primary hepatocytes cultured for 3 days in three kinds of PUF are indicated in Fig. 6. Primary rat hepatocytes formed spheroids in all types of PUF. Primary dog and porcine hepatocytes formed cell aggregates, but could not form a spheroid. On the contrary, all types of hepatocytes formed spheroids when using W-1 PUF.

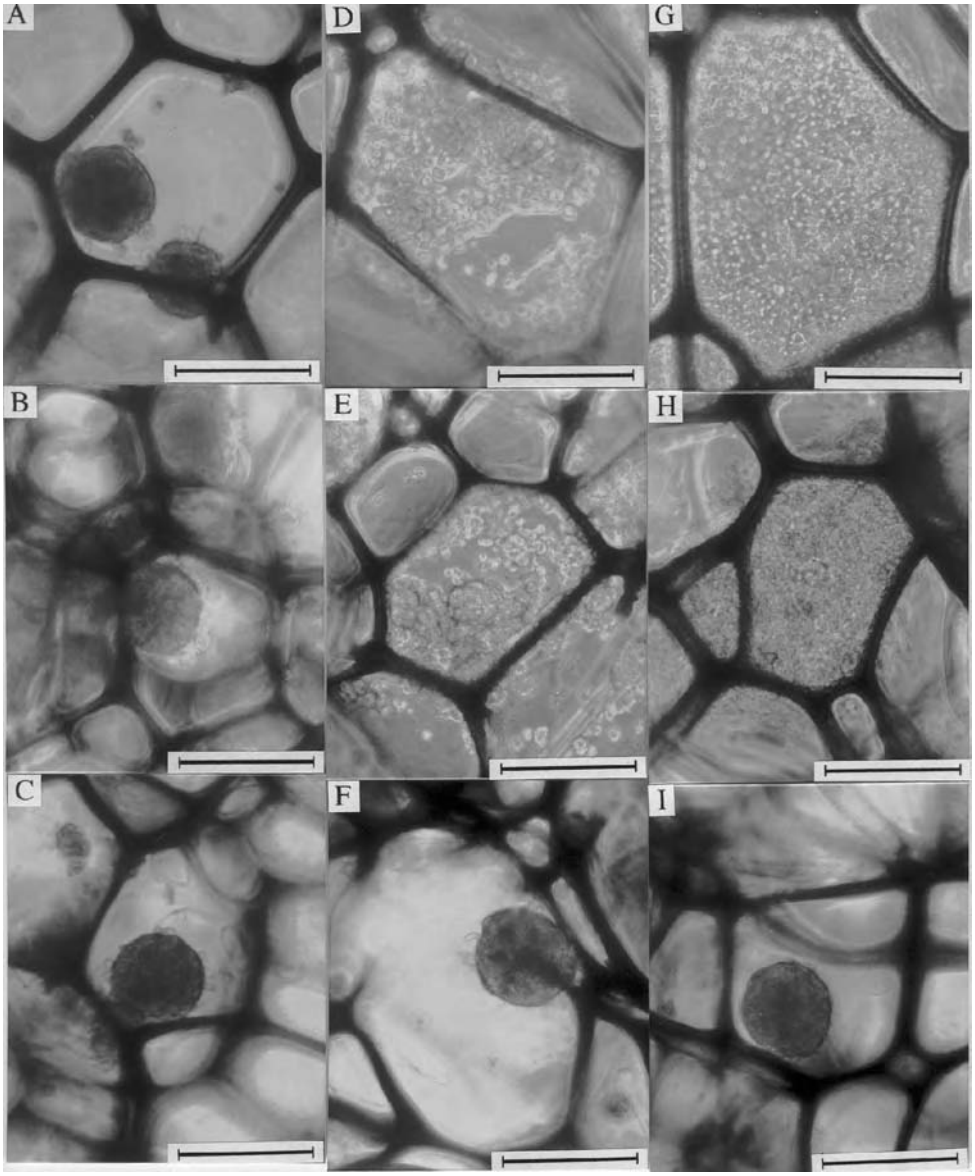

Figure 6. Morphologies of primary hepatocytes in various PUF pores in three days of culture. (A, B, and C): rat hepatocytes; (D, E, and F): dog hepatocytes; (G, H, and I): porcine hepatocytes. (A, D, and G): R-1 PUF; (B, E, and H): R-4 PUF; (C, F, and I): W-1 PUF (bar: 200 μm).

The morphologies of primary hepatocytes cultured for 7 days in three kinds of PUF are indicated in Fig. 7. Primary rat and dog hepatocytes in all types of PUF, and primary porcine hepatocytes in W-1 PUF maintained a spheroid structure. On the other hand, primary porcine hepatocytes in R-1 and R-4 PUF could not form a spherical structure.

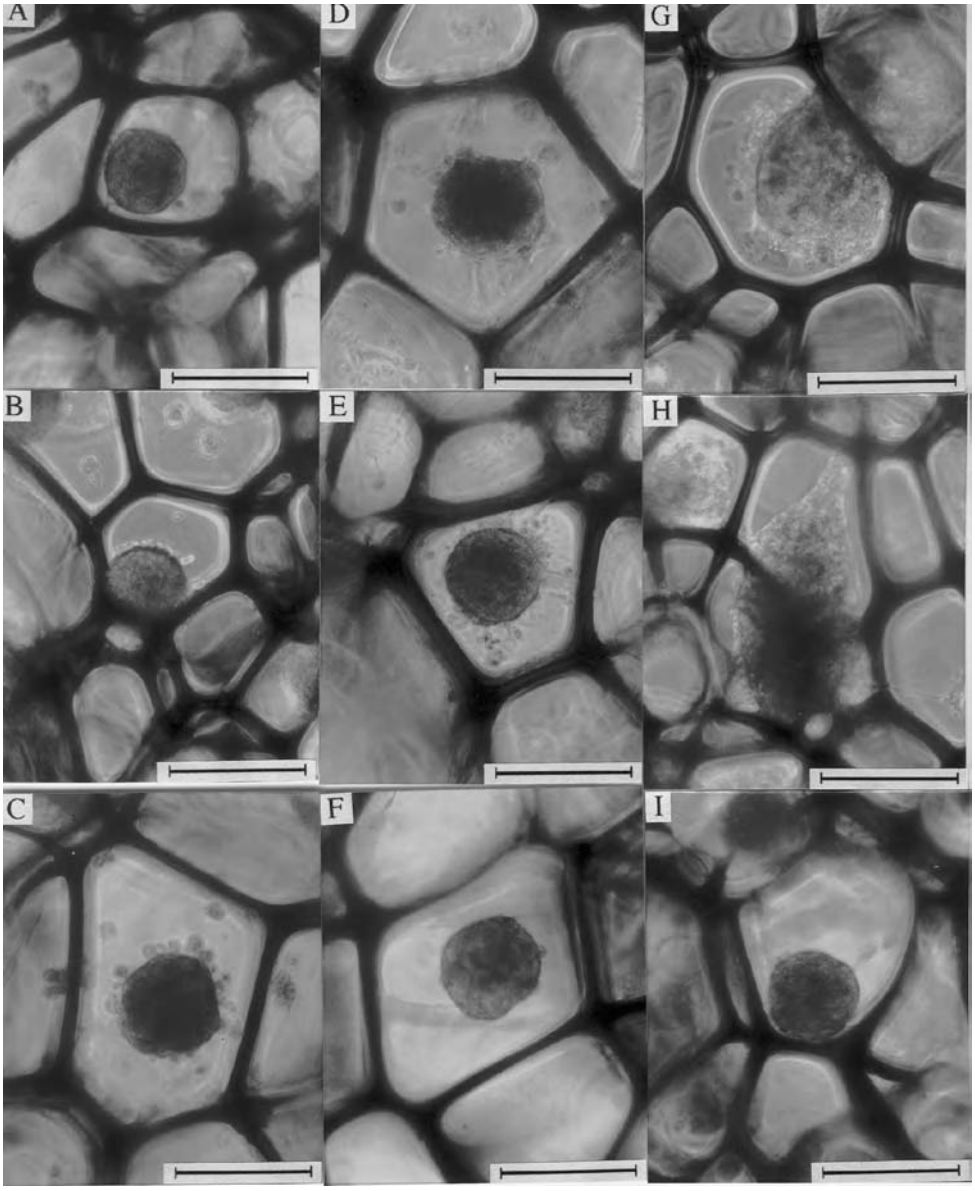

Figure 7. Morphologies of primary hepatocytes in various PUF pores in seven days of culture. (A, B, and C): rat hepatocytes, (D, E, and F): dog hepatocytes, (G, H, and I): porcine hepatocytes. (A, D, and G): R-1 PUF, (B, E, and H): R-4 PUF, (C, F, and I): W-1 PUF (bar: 200 μm).

Part of the hepatocytes spheroid were attached to the internal surface of the PUF and immobilized in its pores. The average diameter of the spheroids was 100–150 μm, and the structure was maintained for more than 3 weeks.

Primary rat hepatocytes in the spheroid were almost viable estimated by haematoxylin-eosin stain of thin section of the spheroid [7]. The hepatocytes spheroid in the

pores of the PUF expressed high albumin secretion and urea synthesis and so on for more than 3 weeks in the *in vitro* experiment [7, 15].

Artificial liver

Artificial liver experiments in five rats and control experiments for three rats were performed. Hepatic failure in the rat was induced by injecting D-galactosamine and leaving alone for 1 day as shown in Fig. 8. Prothrombin times of the artificial liver applying group and control group were 33.1 ± 5.7 and 31.0 ± 4.7 s, respectively, which indicated that the hepatic failure levels of these two groups of rats were almost the same. Prothrombin time recovered to a normal level in 24 h on the artificial liver support system. Furthermore, blood ammonia was well metabolized and recovered to the normal level 17 h after extracorporeal circulation by applying the artificial liver support system indicated in Fig. 9. However, the blood ammonia concentration dramatically increased in control experiments and the rats died over 3 h of extracorporeal circulation. GOT, GPT, total bile acid, total bilirubin, etc. indicated the same phenomena (data is not shown) as Prothrombin time and blood ammonia. Eighty percent of hepatic failure rats which died in the control experiments were recovered by applying an artificial liver support system as shown in Table 4.

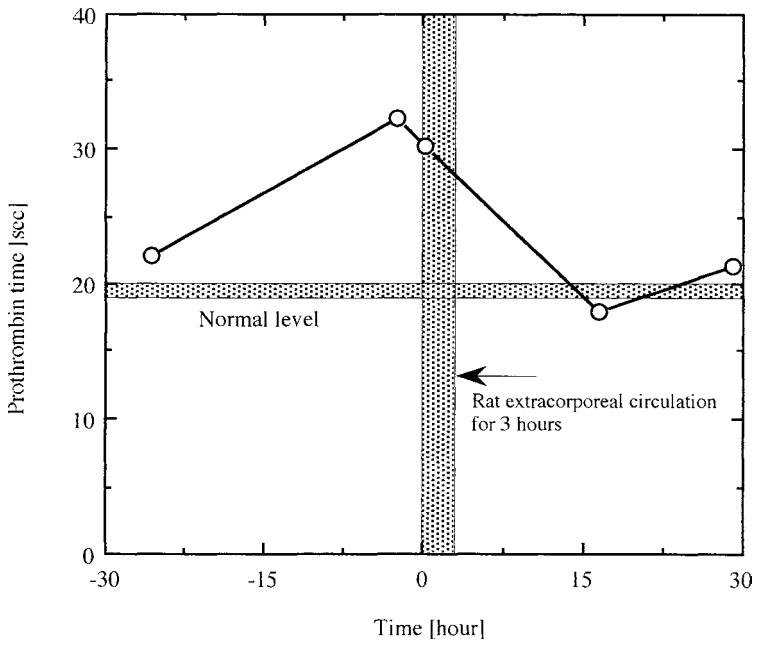

Figure 8. Prothrombin time of hepatic failure animals treated by an artificial liver support system.

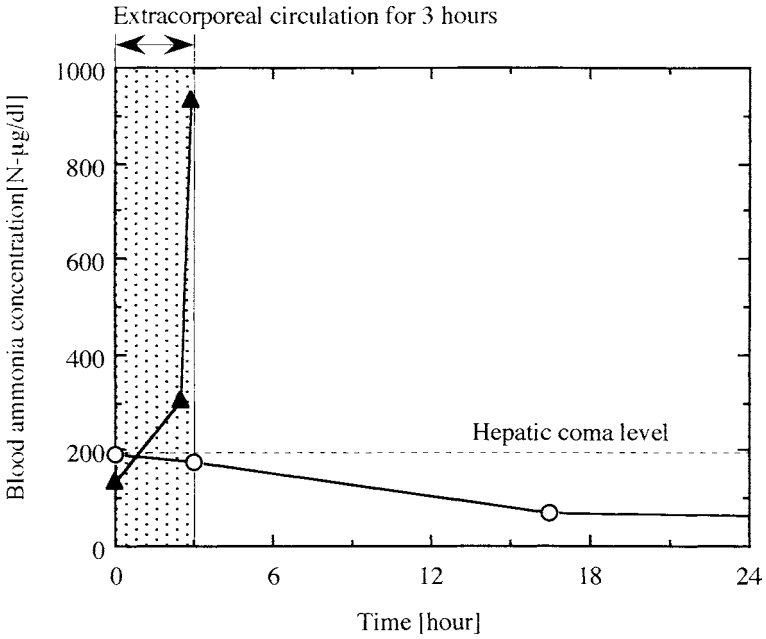

Figure 9. Change of ammonia concentrations in blood of hepatic failure rats. (○): artificial liver, (▲): control. Prothrombin times are 32.3 (○) and 31.2 (▲) s.

Table 4.
Recovery rate of hepatic failure animals. Prothrombin time is 32.3 s

	Prothrombin time (s)	Experimental number	Recovery number	Recovery rate (%)
Control	31.0 ± 4.7	3	0	0
Artificial liver	33.1 ± 5.7	5	4	80

DISCUSSION

Various kinds of mammalian cells (established cell lines and primary hepatocytes) formed spheroids in the pores of the PUF which was used as a cell culture substratum and expressed high cell activity for a long period [7]. Therefore, we can consider PUF as a suitable cell culture substratum for spheroid formation. In the primary hepatocyte culture experiments, spheroid formation is affected by cell type and PUF characteristics. This phenomenon may be caused by the strength of the attachment force between the PUF surface and cells because the spheroid formation follows a peeling off of the hepatocyte, which is in a monolayer state, from the PUF surface. Furthermore, we confirmed the proteoglycan accumulation on the internal surface of the PUF (data not shown), and therefore, the affinity of PUF characteristics and extracellular matrices (proteoglycan, etc.) may also affect the spheroid formation.

Recently, some researchers have tried to develop an artificial liver by using hepatocyte spheroid culture [16–18]. However, hepatocytes spheroids in their reports are formed by agitation culture or extracellular matrix-coated dish culture. They have to be reinoculated to a suitable cell culture substrate or entrapped in gels because they are floating spheroids. On the other hand, hepatocytes spontaneously form spheroids in the pores of PUF, and part of the spheroid is not detached. So, by using our PUF/hepatocyte spheroid culture system we eliminate the immobilization step. Therefore, this culture system is a suitable method for developing a packed-bed type bioreactor.

We successfully developed an effective artificial liver support system composed of a multi-capillary PUF packed-bed type artificial liver module and rat extracorporeal circulation line. By developing this system, we were able to evaluate the performance of an artificial liver using small hepatic failure animals such as rats. The number of the animal experiments is not great but the difference of the treatment results between the artificial liver applying group and the control group is clear.

Rozga *et al*. and Gerlach *et al*. already clinically apply their artificial liver support systems to hepatic failure patients, and have succeeded in using their systems as a 'bridge use' to a liver transplantation for about 2 days [19, 20]. In their *ex vivo* experiments before clinical application, they used warm ischemic liver failure dog and healthy pig [1, 20]. It is not possible to recover from hepatic failure in the warm ischemic liver failure dog model. However, we were able to demonstrate the efficiency of recovery from hepatic failure by using a D-galactosamine induced hepatic failure rat model. Therefore, we can expect our hybrid artificial liver support system to be a practical system for recovery from hepatic failure in clinical use since hepatic failure rats recovered.

Acknowledgement

We thank Professor T. Kajiyama and Associate Professor A. Takahara of Kyushu University for their technical assistance in measurement of contact angles of PUF.

REFERENCES

1. J. Rozga, F. Williams, M. S. Ro, D. F. Neuzil, T. D. Giorgio, G. Backfisch, A. D. Moscioni, R. Hakim and A. A. Demetriou, *Hepatology* **17**, 258 (1993).
2. S. Tobe, Y. Takei, T. Akaike, K. Takeshita and M. Komada, *Jpn. J. Artif. Org.* **21**, 1045 (1992).
3. J. Uchino, T. Tsuburaya, T. Kon, F. Kumagai, T. Hase, T. Hamada, T. Komai, A. Funatsu, E. Hashimura and K. Nakamura, *ASAIO Trans.* **34**, 972 (1988).
4. K. Yanagi, H. Miyoshi, H. Fukuda and N. Ohshima, *Appl. Microbiol. Biotechnol.* **37**, 316 (1992).
5. J. C. Gerlach, J. Enke, O. Hole, C. Muller, J. M. Courtney and P. Neuhaus, *Int. J. Artif. Org.* **17**, 301 (1994).
6. N. Koide, K. Sakaguchi, Y. Koide, K. Asano, M. Kawaguchi, H. Matsushima, T. Takenami, T. Shinji, M. Mori and T. Tsuji, *Exp. Cell Res.* **186**, 227 (1990).
7. T. Matsushita, H. Ijima, N. Koide and K. Funatsu, *Appl. Microbiol. Biotechnol.* **36**, 324 (1991).

8. P. O. Seglen, in: *Methods Cell Biol. 13*, D. M. Prescott (Ed.), p. 29. Academic Press, New York (1976).
9. J. C. Gerlach, J. Brombacher, K. Kloppel, N. Schnoy and P. Neuhaus, *Transplantation* **57**, 1318 (1994).
10. T. Matsushita, M. Ketayama, K. Kamihata and K. Funatsu, *Appl. Microbiol. Biotechnol.* **33**, 287 (1990).
11. R. Enat, D. M. Jefferson, N. Ruiz-Opazo, Z. Gatmaitan, L. A. Leinwand and L. M. Reid, *Proc. Natl Acad. Sci. USA* **81**, 1411 (1984).
12. T. Matsushita, T. Ishii, Y. Kawakubo and K. Funatsu, *Ann. NY Acad. Sci.* **613**, 760 (1990).
13. Y. Kawakubo, T. Matsushita and K. Funatsu, *Appl. Microbiol. Biotechnol.* **41**, 413 (1994).
14. H. Ijima, T. Matsushita and K. Funatsu, *Jpn. J. Artif. Organs* **23**, 463 (1994).
15. T. Matsushita, H. Ijima and K. Funatsu, *Jpn. J. Artif. Organs* **21**, 1050 (1992).
16. H. Takabatake, N. Koide, S. Sasaki, M. Matsushima, T. Takenami, R. Ono, K. Sakaguchi, K. Funatsu and T. Tsuji, *Jpn. J. Artif. Organs* **20**, 139 (1991).
17. F. J. Wu, J. R. Friend, C. C. Hsiao, M. Z. Zilliox, W. J. Co, F. B. Cerra and W. S. Hu, *Biotechnol. Bioeng.* **52**, 34 (1996).
18. K. Naruse, Y. Sakai, I. Nagashima, G. X. Jiang, M. Suzuki and T. Muto, *Int. J. Artif. Organs* **19**, 347 (1996).
19. J. Rozga, E. Morsiani, E. Le Page, A. D. Moscioni, T. Giorgio and A. A. Demetriou, *Biotechnol. Bioeng.* **43**, 645 (1994).
20. J. C. Gerlach, *Int. J. Artif. Organs* **19**, 645 (1996).

Polymers for Tissue Engineering, pp. 287–297
Molly S. Shoichet and Jeffrey A. Hubbell (Eds)

Hepatocyte culture utilizing porous polyvinyl formal resin maintains long-term stable albumin secretion activity

HIROTOSHI MIYOSHI, KEIKO OOKAWA and NORIO OHSHIMA*

Department of Biomedical Engineering, Institute of Basic Medical Sciences, University of Tsukuba, 1-1-1 Tennoudai, Tsukuba City, Ibaraki 305, Japan

Received 9 June 1997; accepted 19 August 1997

Abstract—To investigate the effects of culture conditions on the maintenance of metabolic functions of cultured hepatocytes, long-term hepatocyte culture lasting 20 days was performed under two different culture conditions, i.e. stationary cultures utilizing porous polymer (polyvinyl formal (PVF) resin) as a substratum and conventional monolayer dish cultures without PVF. Metabolic activities specific to hepatocytes were evaluated in terms of ammonia metabolism, urea synthesis, and albumin secretion. Concerning ammonia metabolic and urea synthetic activities, no significant differences in maintenance of these activities were found between the two culture conditions, and these activities rapidly decreased with the elapse of the culture period, especially during the early stage of the experiments. However, after day 10, these activities in the stationary cultures were maintained at a slightly more favorable level than in the monolayer cultures. On the other hand, compared with ammonia metabolism and urea synthesis, stable and well-maintained albumin secretion of hepatocytes (60% of the activity in day 1) was exhibited in the stationary culture experiments, despite that this particular activity under the monolayer culture condition gradually reduced to a very low level (5.7% of that on day 1) at the end of the culture. From the morphological observations, hepatocytes immobilized in the PVF resin revealed individual spherical shapes without forming multicellular aggregation, and it was suggested that this characteristic structure contributed to good albumin secretion of hepatocytes. In conclusion, the advantages of the hepatocyte culture technique utilizing PVF resin over the conventional dish culture in maintaining some representative metabolic function specific to hepatocytes were clarified.

Key words: Hepatocytes; artificial liver; long-term culture; ammonia; urea; albumin; porous polymer.

INTRODUCTION

Even with current advanced medical technology, the average mortality of patients suffering from severe liver insufficiency remains over 60% [1]. To treat such patients, the development of an artificial liver support system (ALSS) is urgently needed. To develop a hybrid-type ALSS that can be applied clinically, the attainment of a high

*To whom correspondence should be addressed.

density culture of hepatocytes is a fundamental requirement for reducing the size of the module [2, 3]. It is also required that metabolic functions of hepatocytes to be cultured in the modules should be kept as long as possible. One of the difficulties facing the development of ALSS is that hepatocytes scarcely proliferate under *in vitro* environments unless their culture density is maintained low enough and growth factors or hormones are supplied abundantly [4–8]. Furthermore, attainment of a large-scale and high density culture of hepatocytes and maintaining their metabolic functions in *in vitro* cultures are far more difficult tasks even with advanced culture techniques. These difficulties should be overcome to realize a feasible ALSS for clinical use. Toward such an ultimate goal, we have attempted to develop a new type of hepatocyte culture system utilizing reticulated polyvinyl formal (polyvinyl alcohol formal; PVF) resin as cell-supporting materials [9–12]. Since this resin has a high specific surface area, it is expected that the highly porous structure of this material provide a scaffold for cellular attachment, thereby enabling the high density culture of hepatocytes as well as other types of animal cells of clinical or industrial importance.

In our previous study, we have demonstrated that a packed-bed type reactor using cubic PVF resins could attain a high density culture of hepatocytes at a cell density as high as 1×10^7 cells cm^{-3} of PVF [10], and that the metabolic performances of the reactor were maintained satisfactorily throughout a relatively long culture period of up to 1 week [11, 12]. This value of the highest hepatocyte density means that a volume of a few liters of the supporting material is sufficient to replace liver functions in adult patients, if scaling-up of the module is properly designed. Thus, it is strongly suggested that the packed-bed type reactor utilizing PVF resin is suited for a realizable module for an artificial liver support. We have also shown that the degree of deterioration of metabolic functions of the cultured hepatocytes using this resin with the elapse of culture period differed considerably between different culture conditions, i.e. monolayer or perfusion cultures, and also between the types of specific metabolic functions to be tested [11, 12].

In the present study, therefore, we intended to examine whether a few representative metabolic functions of the hepatocytes immobilized into the PVF resin could be maintained for a longer culture period over 20 days. Metabolic functions of the hepatocytes on the PVF resins were compared with those of the hepatocytes cultured in the conventional monolayer cultures.

MATERIALS AND METHODS

Cells and culture medium

Hepatocytes were isolated from male Wistar rats weighing 150–250 g by the collagenase perfusion technique [10]. In all culture experiments, serum-containing medium composed of Williams' medium E (ICN Biomedicals Inc., Costa Mesa, CA, USA), hormones (dexamethasone, 0.1 μM; insulin, 0.1 μM; aprotinin, 5000 KIU l^{-1} (Sigma Chemical Co., St. Louis, MO, USA)), antibiotics (penicillin G, 20 000 IU l^{-1}; streptomycin, 20 mg l^{-1}; amphotericin B, 50 μg l^{-1} (Gibco BRL, Grand Island, NY, USA)), and 10% fetal bovine serum (HyClone Laboratories, Logan, UT, USA) was used.

Substrate material

Highly porous and reticulated PVF resin (Kanebo Kasei Co., Osaka, Japan) was used as a substratum of hepatocytes in the same way as in our previous studies [9–12]. The skeletal structure of PVF is synthesized by reacting polyvinyl alcohol with formaldehyde, and the characteristic three-dimensionally reticulated structure with continuous interconnecting pores within its matrix is formed by extracting pre-soaked pore-forming agent. This resin has a substantially high porosity of about 90% and a pore size ranging from 5 to 1000 μm. Based on the results of previous studies, the resins having a mean pore size of 250 μm were selected. The resins were cut into plates ($20 \times 20 \times 2$ mm) and used for hepatocyte-supporting materials.

Procedure of culture experiments

Stationary culture experiments utilizing the PVF resin and monolayer culture experiments on petri dishes chosen as controls were simultaneously performed.

In the stationary culture experiments, the plate-shaped PVF resins were autoclaved, placed in the 35-mm petri dishes (Falcon 1008, Becton Dickinson Labware, Lincoln Park, NJ, USA), and washed with phosphate buffered saline (PBS) and culture medium, successively. Hepatocytes were inoculated by irrigating 1 ml of the culture medium containing 2.5×10^6 cells from the top layer of PVF resins, immediately followed by the addition of 1.5 ml of fresh medium. Thereafter, the hepatocytes immobilized into the PVF plates were cultured in 2.5 ml medium. In the monolayer culture experiments, 1×10^6 hepatocytes were inoculated onto 35-mm petri dishes coated with type I collagen (Koken, Tokyo, Japan), and cultured in 2 ml medium.

Stationary culture experiments using PVF resin plates on conventional dish cultures were simultaneously performed at 37°C under humidified air containing 5% CO_2. In both culture conditions, the culture medium was changed 3 h after the cell inoculation to remove any unattached cells, and later the medium was changed everyday. On day 1, day 3 and every three days thereafter, the culture medium containing 1 mM ammonium chloride, i.e. ammonia-containing medium, was supplied to determine the activities of ammonia metabolism and urea synthesis of the cultured hepatocytes. When ammonia-containing medium was used, the culture medium was sampled at 0 and 6 h after medium exchange, and ammonium metabolic rates and urea-*N* synthetic rates were evaluated from the measured values of differences in concentrations of the test solutes between the sampling points. The spent media were sampled everyday and centrifuged, and albumin concentration of the supernatant were measured.

Both the stationary and monolayer culture experiments were simultaneously performed three times, and activities of the cultured hepatocytes were assessed in terms of ammonium metabolic activity, urea-*N* synthetic activity, and albumin secretion activity as mentioned above. In each experimental run, the metabolic activities were expressed as an averaged value of the three dishes for both culture conditions.

Biochemical assays and scanning electron photomicroscopy (SEM) observation

Ammonium and urea-*N* concentration in the media were measured by colorimetric methods using test kits, i.e. the Wako Ammonium Test (indophenol method) and the

Wako Urea-*N* Test (diacetyl monoxime method), respectively (Wako Pure Chemical Industries, Osaka, Japan). The amounts of secreted albumin to the culture media were measured by sandwich enzyme-linked immunosorbent assay (ELISA) method using goat IgG anti-rat albumin antibody and peroxidase-conjugated sheep IgG anti-rat albumin antibody (Organon Teknika, West Chester, PA, USA).

When the culture experiments were terminated, hepatocytes immobilized in the PVF resin plates were fixed in a buffer containing paraformaldehyde and glutaraldehyde, and later fixed with osmic acid. The PVF plates were subsequently dehydrated, dried, and coated with gold/palladium. The obtained samples were examined by SEM (s-450, Hitachi, Tokyo, Japan). The detailed procedures were reported previously [10].

RESULTS

Ammonium metabolic activity

Time-course changes in ammonium metabolic activities in all culture experiments are illustrated in Fig. 1. Ammonium metabolic activities which were estimated from the balance of ammonium concentrations measured at 0 and 6 h after medium exchange were normalized by the corresponding values of the activities measured on day 1 (0.133 mM h^{-1} for the monolayer cultures and 0.0994 mM h^{-1} for the stationary cultures).

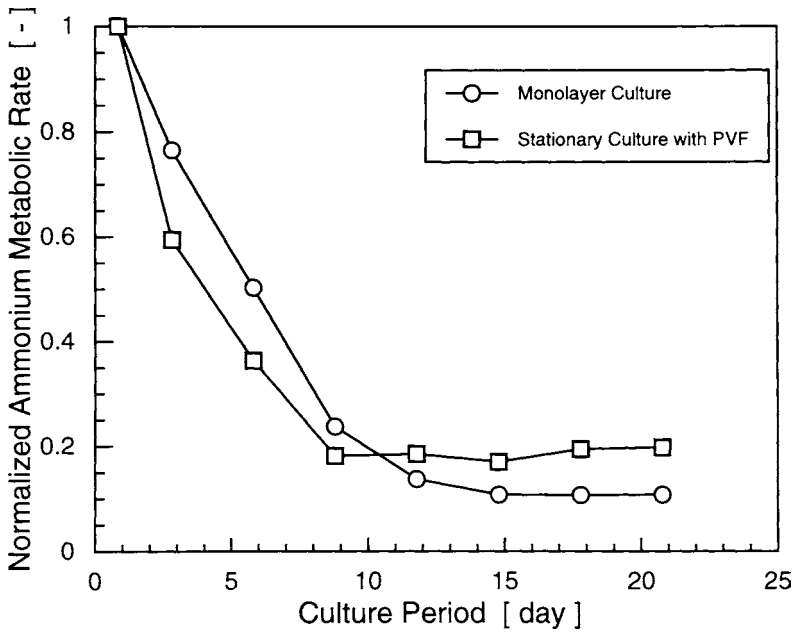

Figure 1. Time-course changes in normalized ammonium metabolic rates in the monolayer and stationary cultures. Ammonium metabolic rates measured on day 1 were 0.133 mM h^{-1} (monolayer cultures (○)) and 0.099 mM h^{-1} (stationary cultures (□)).

From Fig. 1, a similar tendency of the decay of the metabolic activity over time is clearly seen in both culture conditions. Namely, both in the monolayer and stationary cultures, ammonium metabolic activities were considerably reduced in the first 10 days of the culture experiments, and were thereafter relatively stable. It is also noted that no remarkable reduction of ammonium metabolism were observed in the stationary cultures with PVF after day 9. At the end of the culture experiments, ammonium metabolic activity obtained in the stationary cultures with PVF (*c*. 20%) was about twice that in the monolayer cultures (*c*. 11%), despite the fact that ammonium metabolic activity in the stationary cultures with PVF during the earlier period showed the more rapid decay.

Urea-N *synthetic activity*

Figure 2 shows the time course of urea-*N* synthetic rates. These activities were also normalized by the values of the corresponding activities on day 1 (0.220 mM h^{-1} for the monolayer cultures and 0.146 mM h^{-1} for the stationary cultures). The tendency of the decay of urea-*N* synthetic activities in both culture conditions were similar to those of ammonium metabolism showing a more rapid reduction in the stationary cultures than in the monolayer cultures during the first 9 days. Later on, however, the activities in the stationary cultures were kept more stable than those in the monolayer cultures in a similar way to ammonium metabolism. The fact that the time-course change in ammonium metabolism is similar to that of urea-*N* synthesis is regarded as evidence of the accuracy of the measurements of the ammonium metabolic activities.

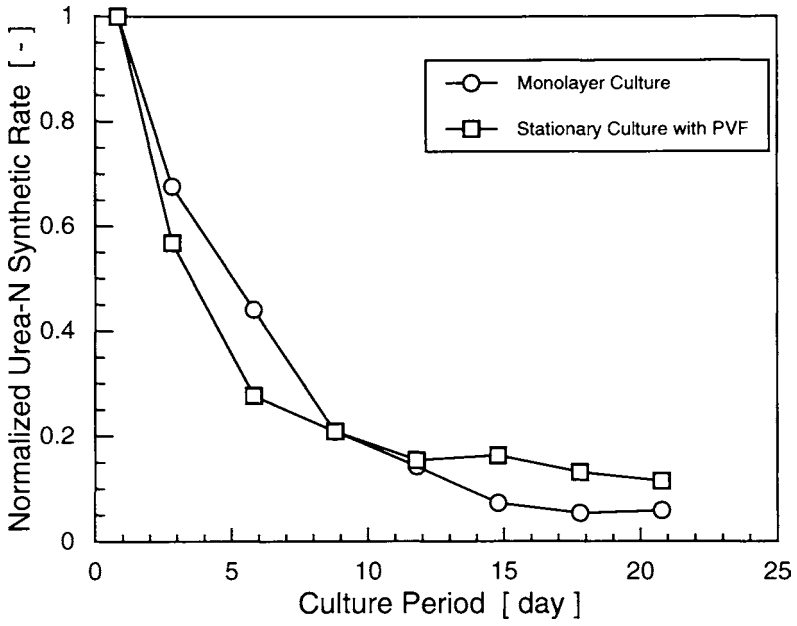

Figure 2. Time-course changes in normalized urea-*N* synthetic rates in the monolayer and stationary cultures. Urea-*N* synthetic rates measured on day 1 were 0.220 mM h^{-1} (monolayer cultures (○)) and 0.146 mM h^{-1} (stationary cultures (□)).

Albumin secretion activity

As shown in Fig. 3, the time course of albumin secretion activities in the two culture conditions showed considerably different tendencies from the results of ammonium metabolism and urea synthesis already presented. The initial albumin secretion rates measured on day 1 were 3.37 $\mu g\,h^{-1}$ per dish for the monolayer cultures and 1.82 $\mu g\,h^{-1}$ per dish for the stationary cultures, and albumin secretion rates obtained throughout the culture period were normalized by these values. In the monolayer culture experiments, albumin secretion rates were precipitously decreased in an earlier culture period up to day 5. These metabolic rates then showed a gradual decrease with the elapse of the culture period, and at the end of the culture experiments only 5.7% of the albumin secretion activities measured on day 1 were preserved.

In the stationary cultures using PVF plates, albumin secretion rates decreased more rapidly than those in the monolayer cultures until day 3, similarly as for the cases of ammonium metabolism and urea-*N* synthesis. After day 3, however, albumin secretion activities were satisfactorily well maintained, and roughly 60% of the albumin secretion rates measured on day 1 were preserved up to the end of the culture experiments. All these facts strongly suggest the advantage of our culture method using PVF resins in maintaining some metabolic functions of hepatocytes.

SEM observation

A representative SEM image of the hepatocytes immobilized in the inner pores of PVF plates observed at the end of culture experiments (on day 22) is illustrated in Fig. 4.

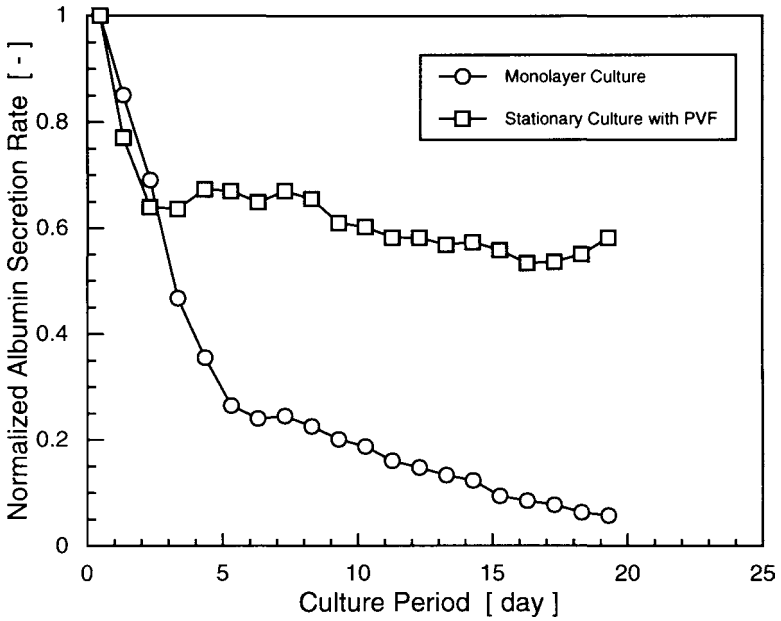

Figure 3. Time-course changes in normalized albumin secretion rates in the monolayer and stationary cultures. Albumin secretion rates measured on day 1 were 3.37 $\mu g\,h^{-1}$ per dish (monolayer cultures (○)) and 1.82 $\mu g\,h^{-1}$ per dish (stationary cultures (□)).

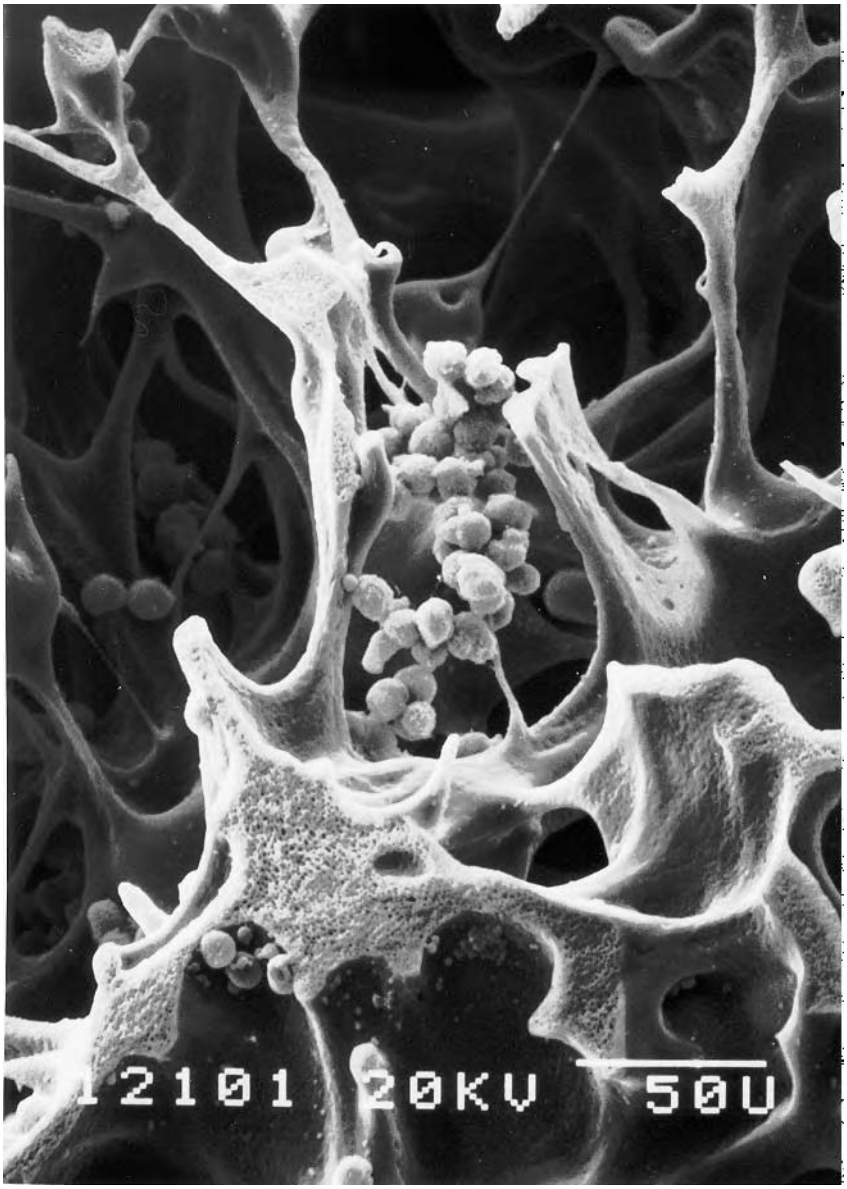

Figure 4. Scanning electron photomicrograph of hepatocytes immobilized in the PVF resin in the stationary culture (day 22).

In case of the monolayer cultures using conventionally used collagen-coated dishes, hepatocytes commonly revealed a flat and spread configuration (figure not shown). As shown in Fig. 4, however, in the stationary cultures hepatocytes immobilized in the PVF resin showed a considerably different appearance to those in the monolayer cultures — individual hepatocytes retaining three-dimensional spherical configuration. No apparent multicellular hepatocyte aggregation such as a spheroid was observed.

DISCUSSION

For several years, we have applied reticulated PVF resin as a supporting material of hepatocyte culture [9–12]. In our previous studies, we have shown that a packed-bed type reactor using PVF resins exhibited more advantageous characteristics over other types of hepatocyte culture methods for the purpose of attaining a high density culture. From short-term culture experiments lasting for 26 h, it was shown that the immobilized cell densities increased in proportion to the numbers of inoculated cells with the maximum hepatocyte density immobilized 1 day after cell inoculation being approximately 1.2×10^7 cells cm^{-3} of PVF [10]. This hepatocyte density is regarded as among the highest ever reported [2, 13, 14]. We have also shown that metabolic performances of the packed-bed reactor, in particular albumin secretion ability, were satisfactorily maintained over 1 week [11, 12]. In the present study, we attempted to investigate the feasibility of maintaining metabolic functions of the cultured hepatocytes immobilized within the PVF resin for a longer period of over 20 days. A simple culture technique using a small-scale dish culture was intentionally adopted in the present study, considering a possibility that the present results might be compared with the future studies in the light of detailed biological functions of the hepatocytes. In the present study, metabolic activities of ammonium metabolism and urea-*N* synthesis of the cultured hepatocytes are shown to decrease considerably within 10 days of the culture both in the monolayer and stationary cultures. However, albumin secretion activities in the stationary cultures were proved to be sufficiently well preserved throughout the culture periods.

Various attempts have thus far been made to improve culture conditions for the purpose of obtaining well-maintained metabolic functions of the cultured hepatocytes. Among such attempts, strategies adopted to maintain satisfactory albumin secretion activities of the hepatocytes for a relatively long culture period of over 20 days are classified as follows: (a) modification of the culture media, for instance, by the addition of hormones [6] or dimethyl sulfoxide [15]; (b) formation of hepatocyte aggregates by modifying medium compositions or surface conditions of the culture substrate [16–18]; (c) use of extracellular matrices including biomatrix isolated from the liver [19], laminin-rich EHS (Engelbreth–Holm–Swarm) gel [20], crude liver membrane fractions [21] or collagen gel [22, 23]; and (d) use of coculture system with liver epithelial cells [24] or liver sinusoidal cells [25]. Some of these attempts have succeeded in obtaining long-term stable ability of albumin secretion lasting for over 20 days. The present study also succeeded in revealing that albumin secretion could be maintained in the stationary cultures using PVF resin to a similar level as in previous studies, merely by utilizing highly porous substrate material.

From the SEM observations as shown in Fig. 4, it was confirmed that the immobilized hepatocytes revealed an individual spherical shape and no spheroids were observed in contrast to the findings of several investigators. When hepatocytes were immobilized in the PVF resin at high densities as in our previous experiments [11, 12], a few multicellular spheroids were observed, although almost all hepatocytes also exhibited a similar spherical shape as in the stationary culture of the present experiments. Thus, it might be possible that as more hepatocytes are immobilized,

multicellular spheroids form easier. Interestingly enough, no special techniques, used in the above mentioned research, aimed to bring about some biological effects on hepatocyte metabolic functions were employed in the present study, except that untreated porous PVF polymer was used. Moreover, it is presumable that the cell–cell or cell–substratum interactions did not contribute in maintaining metabolic functions of the hepatocytes under conditions adopted in the present study, in view of the fact that: (a) no multicellular aggregation of hepatocytes was observed; (b) no extracellular matrices such as collagen was used; and (c) hepatocytes immobilized in the PVF resin retained a spherical shape. Thus, it is suggested that the mechanism by which stable albumin secretion of the hepatocytes was achieved in this study might be related to the formation of a spherical structure of individual hepatocytes, and not the formation of spheroids. The significance of hepatocyte configuration in regulating their growth and liver-specific functions were also suggested by some investigators [7, 26]. However in these studies, spheroid formation were confirmed or extracellular matrix was used to facilitate cell–substratum interactions. Therefore, the effect of hepatocyte configuration on maintaining metabolic functions was not clarified independently so far. Many investigators have postulated that the cell–cell interaction, as found in a spheroidal configuration, or cell–matrix interaction are important to maintain hepatocyte functions. There have been no previous reports showing that hepatocytes could retain their spherical shape individually without forming multicellular aggregation-like spheroids or without the use of extracellular matrices. Thus, a further study to elucidate the effects of cell shape on liver specific functions is required.

At the earlier period of the culture experiments, all metabolic activities of cultured hepatocytes in the stationary cultures decreased faster than those in the monolayer cultures. Such deteriorated functions seem to be attributable to the loss of viable cells in the stationary cultures, since hepatocyte–PVF attachment is considered not so tight as to avoid inevitable cell loss compared with the cellular attachment on collagen. However, as actually was evidenced in the present study by the well-maintained stable metabolic functions during the later culture period, hepatocytes could maintain stable metabolic functions once they were immobilized on the substrata.

Ammonia metabolism is naturally regarded as one of the fundamental hepatic functions. In this study, this particular activity was measured by adding 1 mM ammonium, which value of concentration is almost the same as in the blood of patients suffering from acute hepatitis. In our previous study, ammonium metabolic and urea synthetic activities of the hepatocytes cultured in the packed-bed reactor using the same PVF resin as was used in the present experiments were roughly 40% (30–50%) of the activities on day 1 even at the end of culture experiments lasting over a week (7–9 days) [11]. Compared with these results, observed activities of ammonium metabolism and urea synthesis in the present study seem somewhat unsatisfactory. These inefficiencies were probably due to insufficient supply of nutrients or oxygen under conditions of the stationary, i.e. not perfused culture conditions, since nutrients or oxygen were to be supplied to the cultured hepatocytes merely by diffusion from the free surface. However, a relatively satisfactory level of metabolic activities, as found in the present study, confirmed expectation of the feasibility of our simple culture

techniques. Compared with rather well-maintained albumin secretion ability, ammonium metabolic and urea synthetic activities of cultured hepatocytes showed faster deterioration. The reasons for these differences are still unclear. However, similar tendencies were observed in our previous studies [11, 12]. Thus, further experiments to confirm the mechanisms by which different degree of metabolic functions were maintained among some hepatocyte functions should be required.

In conclusion, the PVF resin have advantageous features to attain high density culture of hepatocytes. Moreover, it is considered that a packed-bed type reactor utilizing PVF resin is a promising means to replace at least a part of the deteriorated liver functions. Apart from the use for ALSS, the stationary culture method using PVF resin is also expected to serve as a useful experimental model to study biochemical, biological, and physiological functions of the hepatocytes. Some other means of modifying hepatocyte viability and functions, such as employment of the coculture system, are worthy of investigation.

Acknowledgements

This work was partly supported by a Grant for 'Research for the Future' Program (JSPS-RFTF96I00202) from the Japan Society for the Promotion of Science (JSPS), by a Grant-in-Aid from the Japanese Ministry of Education, Science and Culture, and by a Grant for Project Research of the University of Tsukuba.

One of the authors (H. M.) would like to thank Dr. Kennichi Yanagi for introducing the experimental techniques.

REFERENCES

1. G. H. de Groot, S. W. Schalm, T. Fick, C. B. Reuvers, A. L. Boks and O. T. Terpstra, *J. Gastroenterol. Hepatol.* **4**, 283 (1989).
2. J. Uchino, T. Tsuburaya, F. Kumagai, T. Hase, T. Hamada, T. Komai, A. Funatsu, E. Hashimura, K. Nakamura and T. Kon, *Trans. Am. Soc. Artif. Intern. Organs* **34**, 972 (1988).
3. J. Rozga, M. D. Holzman, M.-S. Ro, D. W. Griffin, D. F. Neuzil, T. Giorgio, A. D. Moscioni and A. A. Demetriou, *Ann. Surg.* **217**, 502 (1993).
4. T. Nakamura, K. Yoshimoto, Y. Nakayama, Y. Tomita and A. Ichihara, *Proc. Natl Acad. Sci. USA* **80**, 7229 (1983).
5. R. Enat, D. M. Jefferson, N. Ruiz-Opazo, Z. Gatmaitan, L. A. Leinwand and L. M. Reid, *Proc. Natl Acad. Sci. USA* **81**, 1411 (1984).
6. J. Dich, C. Vind and N. Grunnet, *Hepatology* **8**, 39 (1988).
7. A. Ben-Ze'ev, G. S. Robinson, N. L. R. Bucher and S. R. Farmer, *Proc. Natl Acad. Sci. USA* **85**, 2161 (1988).
8. L. Conti-Devirgiliis, M. Massimi, G. Bruscalupi, A. Felici and L. Dini, *Exp. Cell Res.* **210**, 123 (1994).
9. K. Yanagi, S. Mizuno and N. Ohshima, *Trans. Am. Soc. Artif. Intern. Organs* **36**, M727 (1990).
10. K. Yanagi, H. Miyoshi, H. Fukuda and N. Ohshima, *Appl. Microbiol. Biotechnol.* **37**, 316 (1992).
11. H. Miyoshi, K. Yanagi, H. Fukuda and N. Ohshima, *Biotechnol. Bioeng.* **43**, 635 (1994).
12. H. Miyoshi, K. Yanagi, H. Fukuda and N. Ohshima, *Artif. Organs* **20**, 803 (1996).
13. L. Agius, C. Battersby and K. G. M. M. Alberti, In Vitro *Cell. Dev. Biol.* **21**, 254 (1985).
14. A. Shnyra, A. Bocharov, N. Bochkova and V. Spirov, *Artif. Organs* **15**, 189 (1991).
15. H. C. Isom, T. Secott, I. Georgoff, C. Woodworth and J. Mummaw, *Proc. Natl Acad. Sci. USA* **82**, 3252 (1985).

16. J. Z. Tong, O. Bernard and F. Alvarez, *Exp. Cell Res.* **189**, 87 (1990).
17. J. Landry, D. Bernier, C. Ouellet, R. Goyette and N. Marceau, *J. Cell Biol.* **101**, 914 (1985).
18. N. Koide, T. Shinji, T. Tanabe, K. Asano, M. Kawaguchi, K. Sakaguchi, Y. Koide, M. Mori and T. Tsuji, *Biochem. Biophys. Res. Comm.* **161**, 385 (1989).
19. M. Rojkind, Z. Gatmaitan, S. Mackensen, M.-A. Giambrone, P. Ponce and L. M. Reid, *J. Cell Biol.* **87**, 255 (1980).
20. D. M. Bissell, D. M. Arenson, J. J. Maher and F. J. Roll, *J. Clin. Invest.* **79**, 801 (1987).
21. B. Saad, H. Schawalder and P. Maier, In Vitro *Cell. Dev. Biol.* **29A**, 32 (1993).
22. J. C. Y. Dunn, M. L. Yarmush, H. G. Koebe and R. G. Tompkins, *FASEB J.* **3**, 174 (1989).
23. S. L. Nyberg, R. A. Shatford, M. V. Peshwa, J. G. White, F. B. Cerra and W.-S. Hu, *Biotechnol. Bioeng.* **41**, 194 (1993).
24. C. Guguen-Guillouzo, B. Clément, G. Baffet, C. Beaumont, E. Morel-Chany, D. Glaise and A. Guillouzo, *Exp. Cell Res.* **143**, 47 (1983).
25. O. Morin and C. Normand, *J. Cell. Physiol.* **129**, 103 (1986).
26. C. Yuasa, Y. Tomita, M. Shono, K. Ishimura and A. Ichihara, *J. Cell. Physiol.* **156**, 522 (1993).

This page intentionally left blank

Polymers for Tissue Engineering, pp. 299–314
Molly S. Shoichet and Jeffrey A. Hubbell (Eds)

Role of synthetic extracellular matrix in development of engineered dental pulp

KRISTYN S. BOHL [1], JOHN SHON [1], BRUCE RUTHERFORD [3] and DAVID J. MOONEY [1,2,*]

[1] *Department of Chemical Engineering, University of Michigan, Ann Arbor, MI 48109, USA*
[2] *Department of Biologic and Materials Sciences, University of Michigan, Ann Arbor, MI 48109, USA*
[3] *Department of Cardiology, General Dentistry and Endodontics, University of Michigan, Ann Arbor, MI 48109, USA*

Received 1 August 1997; accepted 6 January 1998

Abstract—In cases of damaged oral tissues, traditional therapies, such as a root canal, replace the injured tissue with a synthetic material. However, while the materials currently used can offer structural replacement of the lost tissue, they are incapable of completely replacing the function of the original tissue, and often fail over time. This report describes a tissue engineering approach to dental pulp tissue replacement utilizing cultured cells seeded upon synthetic extracellular matrices. Human pulp fibroblasts were obtained and multiplied in culture. These cells were then seeded onto three different synthetic matrices: scaffolds fabricated from polyglycolic acid (PGA) fibers, a type I collagen hydrogel, and alginate in an effort to examine which matrix is most suitable for dental pulp tissue formation. In addition, methods previously developed for seeding and culturing pulp cells on PGA were optimized. Culturing cells on PGA resulted in a very high cell density tissue with significant collagen deposition. No cell proliferation was observed on alginate, and the growth of cells in collagen gels after 45 days was only moderate. These studies indicate dental pulp-like tissues can be engineered, and this may provide the first step to engineering a complete tooth.

Key words: Polyglycolic acid; dentistry; biodegradable polymer; teeth.

INTRODUCTION

The effects of various oral diseases and injuries often necessitate the replacement of the affected dental tissue. While synthetic materials have been successfully utilized as restorative dental materials [1], they are incapable of replacing the normal structure and function of the lost tissue. Engineering oral tissues using cultured cells may provide an alternative to the traditional therapy, allowing the patient to

*To whom correspondence should be addressed. E-mail: mooneyd@umich.edu

retain the functionality of the natural oral tissue. This report describes how this new approach leads to the development of new dental pulp through the growth of cultured cells on synthetic matrices.

Dental pulp is a loose connective tissue that provides dentinogenic, nutritive, sensory, and defensive functions to the tooth [2]. Dentin, a hard avascular connective tissue that forms the bulk of the tooth structure, is supported by the pulp and is formed by odontoblasts, which reside in dental pulp. These odontoblasts can initiate reparative dentinogenesis subsequent to dentin loss during cavity preparation [3]. Dental pulp may be capable of regenerating following injury, but the specific mechanisms underlying pulp regeneration and dentinogenesis have not been identified. For 15 million patients in the US each year, injury to pulp tissue results in root canal therapy, which involves replacement of the pulp with a non-viable synthetic material. However, such treatment is clearly not capable of replacing the biological functions of the pulp tissue, potentially resulting in failure and, ultimately, tooth loss.

A treatment that may lead to dentinogenesis and ultimately provide an alternative to root canal therapy is the replacement of injured dental pulp with new pulp tissue engineered from cultured cells. This tissue engineering approach involves the isolation of healthy cells from the patient and multiplying them in culture on a three dimensional synthetic matrix to form a new tissue [4]. The matrix material may potentially be fabricated from naturally-derived (e.g. collagen) or synthetic materials (e.g. synthetic polymers). Synthetic, biodegradable polymers such as polyglycolic acid (PGA) meshes are often used as scaffold materials due to their reproducible properties and structures [5]. The polymer degrades over time, eventually leaving only a natural tissue, with no permanent foreign body. While it has already been demonstrated that PGA is an effective synthetic matrix for *in vitro* generation of dental pulp tissue [6], the process of tissue development was not optimized and other possible matrices have not been investigated.

This report compares the ability of PGA matrices, type I collagen, and alginate to promote dental pulp tissue formation *in vitro*, and also suggests an optimized method for seeding and culturing pulp cells on PGA. PGA was utilized in these studies due to previous success in engineering dental pulp-like tissues with this synthetic polymer [6]. Type I collagen was studied as an alternative to PGA as it has been widely utilized to engineer a variety of tissue types [5] due to its ability to promote cell adhesion and allow for cell-based remodelling. Alginate hydrogels were also used in these studies as many tissue engineering applications [5] have utilized this polysaccharide.

MATERIALS AND METHODS

Cell seeding

Cells were explanted and propagated from adult human dental pulp as previously described [7]. In brief, cells were obtained by mincing dental pulp obtained from

adult human molars, and explanting the resulting tissue fragments onto tissue culture flasks to allow cell outgrowth. Migration and expansion of cells led to the formation of confluent cell layers, which were subsequently passaged with standard tissue culture techniques. Cells were cultured in DMEM (Gibco; Grand Island, NY, USA) supplemented with penicillin/streptomycin (Gibco), and 10% fetal calf serum (Gibco) at all times. Cells between passages 8 and 11 were used in all experiments.

Cells were seeded onto non-woven matrices (thickness = 3 mm) fabricated from PGA fibers (12 μm in diameter) utilizing a dynamic cell seeding protocol previously described to introduce cells within the polymer matrix [8]. PGA matrices purchased from Albany Intl (PGA i.v. = 1.25 $\mathrm{dl\,g^{-1}}$; crystallinity = 56.5%; Taunton, MA, USA) and provided as a gift from Davis and Geck (Danbury, CT, USA) were used in these studies. In brief, cells cultured on tissue culture flasks were trypsinized, pooled, and concentrated to 2×10^7 cells $\mathrm{ml^{-1}}$ in tissue culture medium. Each PGA scaffold (5 × 5 mm square) was placed in a 50-ml tube with 0.2 ml of the cell suspension and agitated for 24 h at 100 rpm using an orbital shaker (Bellco Glass, Inc.). Matrices were removed from the tubes and subsequently cultured in standard tissue culture flasks for time periods ranging from 1 to 90 days (5 ml medium was added to each flask per matrix contained in the flask).

Cells were seeded in collagen gel matrices by first preparing a solution of collagen [9 parts type I collagen (2.9 $\mathrm{mg\,ml^{-1}}$; Collagen Corp.), 1 part 10X PBS, 1 part cell suspension (2.9×10^6 cells $\mathrm{ml^{-1}}$)]. In each 1.5 cm diameter well of a 24-well dish, 0.35 ml of the collagen solution was deposited, and then gelled by warming to 37°C for 1 h, after which 0.5 ml of cell growth medium was added. It was not necessary with collagen gels to perform the agitated seeding procedure described above as the cells placed in the collagen solution become entrapped within the gel as it hardens. In contrast, cells must be introduced into the preformed PGA matrix. The method used for forming the collagen matrices is preferred since if the collagen gels were formed first, and then seeded, the cells would not likely penetrate and evenly distribute within the collagen gel. Samples of the cell-seeded collagen matrices were taken for analysis between 1 and 46 days. As controls, cells were also cultured on standard tissue culture plastic surfaces alone (Becton Dickinson; Franklin Lakes, NJ, USA) and coated with an adsorbed layer of type I collagen, both at a density of 1×10^5 cells per well. Type I collagen was adsorbed onto tissue culture dishes at a concentration of 1 $\mu\mathrm{g\,cm^{-2}}$ in a buffer solution of 15 mM sodium carbonate and 35 mM sodium bicarbonate as previously described [9].

Cell seeding on alginate discs involved preparation of a 2% alginate (Pronova Biopolymer; Portsmouth, NH, USA) solution which was gelled with a 1.2 M $CaSO_4$ solution. Alginate discs 1.5 cm in diameter were cut out, placed in wells of a 24-well tissue culture dish, and seeded with cells at a density of 1×10^5 cells per well.

Tissue analysis

Gross measurements were made of the cell–polymer constructs using calipers at each time point to determine tissue volume. Samples were prepared for

visualization with a scanning electron microscope by fixing with a 1% solution of glutaraldehyde for 30 min, dehydrating in ethanol, and sputter coating (Desk II; Denton Vacuum, Cherry Hill, NJ, USA) with gold. Photomicrographs were taken on Polaroid 55 film. Samples were prepared for sectioning and staining by fixing with a solution of 3.7% formalin in phosphate buffered saline, and embedding in paraffin. Thin sections (5 μm) were cut and stained with hematoxylin and eosin using standard techniques. Certain sections were stained with Masson's Trichrome in order to visualize deposited collagen. Photomicrographs were taken with Kodak Elite color slide film.

The cell content in PGA constructs was determined using a variation of a DNA dye binding assay previously described [8], which involves use of a fluorimeter (DyNA Quant 2000; Hoefer Sci. Inst.; San Francisco, CA, USA) to assay the binding of the dye Hoechst 33258 to DNA. A calibration curve was constructed for this assay using known numbers of cultured cells. Cell densities were determined by dividing the number of cells in each construct (determined with DNA assay) by the volume of the tissue (determined with gross measurement). Cells cultured in the collagen gel were removed for quantification by incubating the gels with 0.5 ml of a 3 mg ml^{-1} solution of type I collagenase (Sigma) in PBS for 45 min. A cell count was then obtained using a Coulter counter. This method was utilized as collagenous matrices, unlike PGA matrices, could be readily digested to release the cells for direct counting. Cells cultured on the control surfaces (tissue culture plastic and adsorbed collagen coating) were removed with trypsin and counted with the Coulter counter.

To assess cell metabolic activity, cells were exposed to (3-[4,5-dimethylthiazol-zyl]-2,5-diphenyl tetrazolium bromide) or MTT (Sigma) at time points of 3 and 11 days. A stock solution of 5 mg ml^{-1} MTT in PBS was prepared, and 0.1 ml of this stock solution was added to each milliliter of cell culture media and incubated at 37°C. After 3 h, photomicrographs were taken with Kodak Elite color slide film. Metabolically active cells convert MTT to an insoluble blue product which builds up within the cells.

RESULTS

Pulp derived fibroblasts seeded on and in alginate or within collagen hydrogels did not form new tissues with a high cell density. The cell density on and within alginate-seeded matrices remained constant for the 18 days of the experiment (not shown), while only a modest increase in cell density (to approximately 5×10^5 cells ml^{-1}) was observed over 46 days when a collagen gel matrix was utilized (Fig. 1). Cell growth within the collagen gel was accompanied by contraction of the gel, as it pulled away from the well walls and assumed a size after 42 days that was approximately half its original diameter. Cells on alginate matrices rapidly lost metabolic activity (as indicated by MTT incorporation), while cells in collagen retained high metabolic activity (Fig. 2). Histological examination of cell–collagen

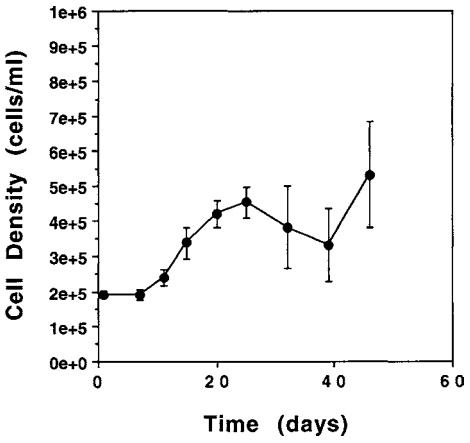

Figure 1. Cell density of tissues developed within a collagen gel. Values represent the mean and standard deviation calculated from three to four samples at each time point.

constructs at 42 days revealed a tissue with a low cellularity (Fig. 3). Cells formed a monolayer on the exterior of the collagen matrix, and very few cells were visible in the interior of the matrix. However, the failure of cells to multiply extensively in collagen matrices was not caused by a general inability of these cells to interact with collagen, as cells cultured on petri dishes coated with type I collagen proliferated rapidly (Fig. 4).

Previous studies with PGA matrices demonstrated that new pulp-like tissues could be engineered with these matrices [6]. The starting cell density in those studies was similar to that utilized with collagen matrices in the present study, but high density tissues (approximately 10^8 cells ml^{-1}) resulted after 30–60 days in culture. To determine if the process of tissue development could be accelerated on PGA matrices by increasing the initial cell density, pulp-derived fibroblasts were seeded onto PGA matrices utilizing a dynamic seeding method which has been previously demonstrated to greatly enhance cellular adhesion to PGA matrices with other cell types [8]. Scanning electron microscopic observation of matrices following seeding revealed numerous cells adherent to individual polymer fibers (Fig. 5a). The cells were generally aggregated into large cell masses, although individual cells could be observed on fibers. The adherent cells subsequently proliferated on the fibers and began to span the space between adjacent fibers by day 7 (Fig. 5b). Cellular proliferation and matrix contraction led to a confluent layer of cells on the exterior of the polymer matrices by 21 days, although polymer fibers were still visible at this time (Fig. 5c). However, by 35 days, no polymer fibers were visible on the exterior of the forming tissue, and a multilayered cell mass was observed at this time (Fig. 5d). Quantitation of the number of cells on the PGA matrices indicated that approximately 85% of the cells in the seeding solution adhered to the polymer matrix following seeding. This resulted in an initial cell density on the matrices of 5×10^7 cells ml^{-1}. This initial cell density was approximately two orders of

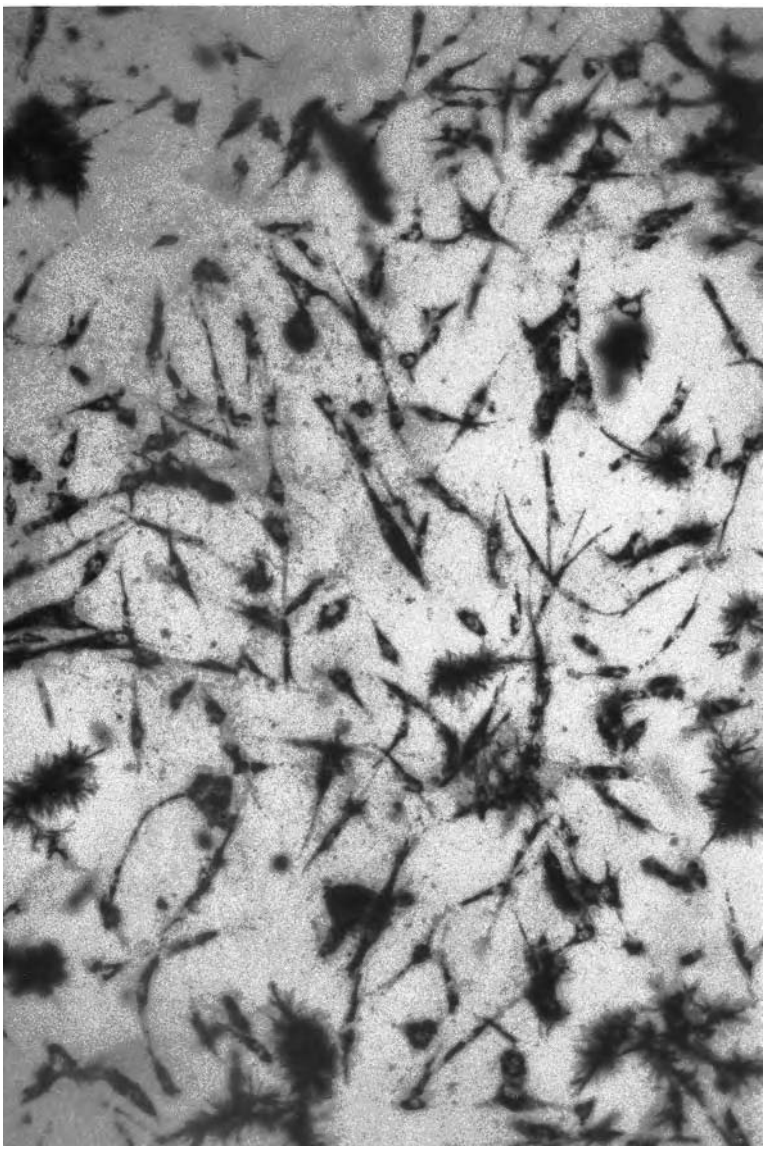

Figure 2. Photomicrograph of cells cultured for 3 days within collagen gels, following staining with MTT (original magnification of photomicrograph was 10×).

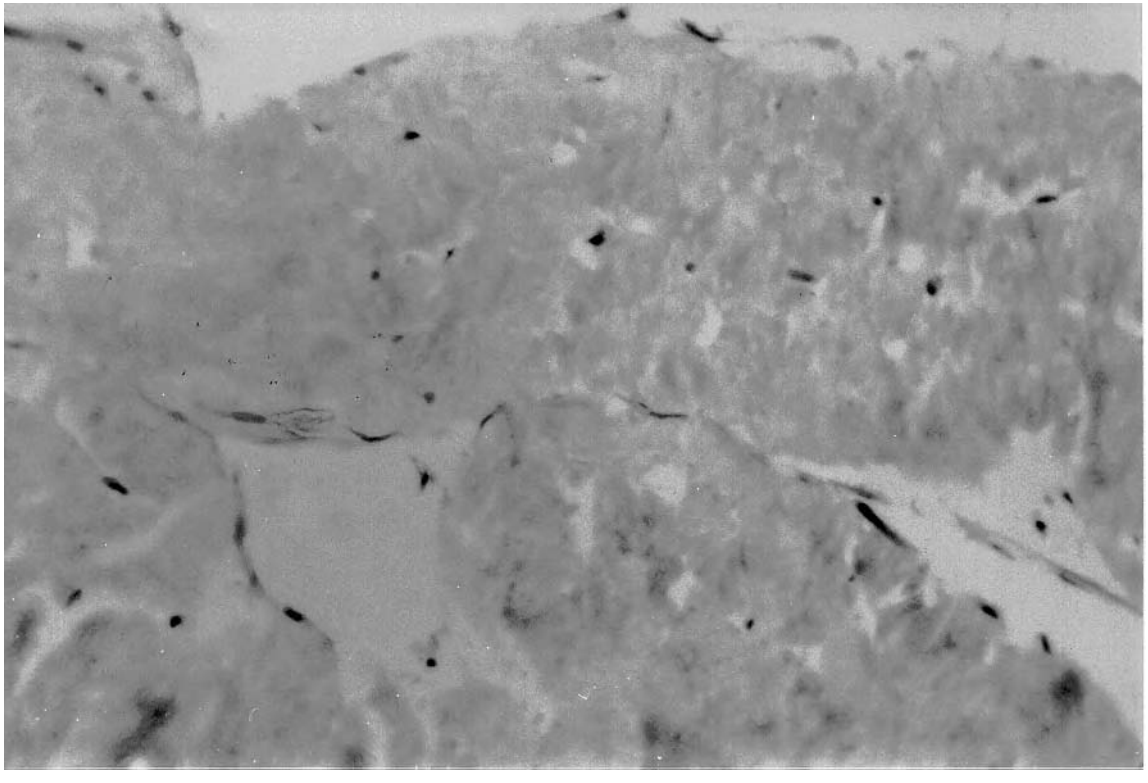

Figure 3. Photomicrograph of histological section of new tissue formed in a collagen gel after 42 days. The section was stained with hematoxylin and eosin.

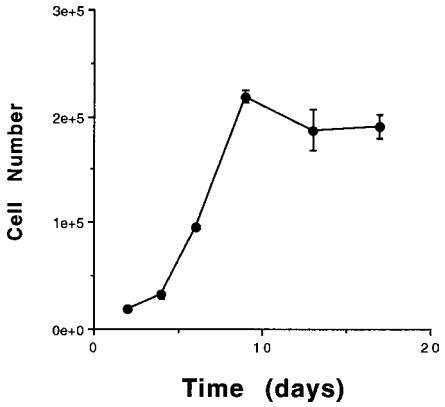

Figure 4. Proliferation of fibroblasts over time on tissue culture dishes coated with an adsorbed lay of type I collagen. Values represent mean and standard deviation ($n = 4$).

magnitude higher than that obtained previously with a static seeding method [6]. The cell density increased after this time, and a tissue density of 10^8 cells ml^{-1} was obtained between days 7 and 21 of culture (Fig. 6). The cells within the PGA matrices remained metabolically active, as indicated by MTT incorporation (Fig. 7). The cell density continued to increase after this time to reach a value of approximately 5×10^8 cells ml^{-1} by day 90 (Fig. 6). However, the increases in cell density after day 21 were largely due to a decreased volume of the tissues. They contracted from day 21 through 90 to volumes ranging from 1 to 5% of the initial tissue volume. Histological examination of cell-PGA constructs cultured for extended time periods revealed tissues comprised of cells distributed evenly throughout a new matrix with little polymer remaining (Fig. 8a). Collagen was present in the matrix surrounding the cells, as indicated by Masson's Trichrome staining (Fig. 8b).

DISCUSSION

New dental pulp-derived tissues can be engineered *in vitro* by culturing pulp-derived human fibroblasts on synthetic ECM. The use of collagen gels or alginate did not lead to the development of new tissues which resembled native pulp, while matrices fabricated from fibers of PGA did lead to the development of a high cell density tissue with a high collagen content. Enhancing the cell seeding and culture techniques resulted in a more efficient method of developing engineering pulp tissue on PGA matrices than previously described [6].

Cells adhered and proliferated in the collagen gel, but the cell density in the matrix after 45 days was still quite low (5×10^5 cells ml^{-1}). This result contrasts with the tissues developed on PGA matrices, where tissues with a much higher cell density were obtained. The optimized seeding technique utilized for PGA matrices resulted in a higher initial cell density than that obtained on collagen

(a)

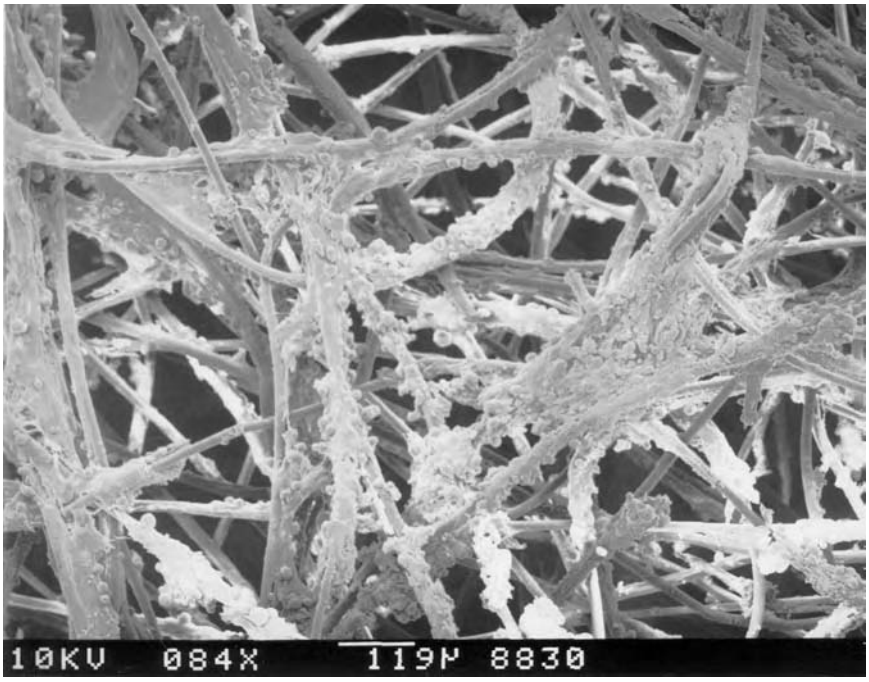

(b)

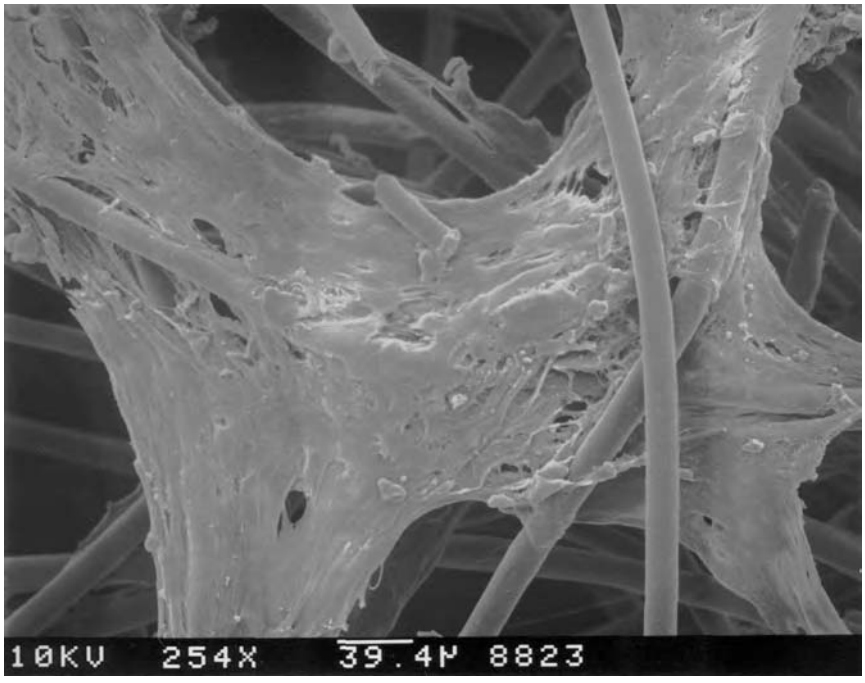

Figure 5. Photomicrographs of pulp-derived fibroblasts adherent to PGA matrices after (a) 1, (b) 7, (c) 21, and (d) 35 days of culture. Size bars are shown on the photomicrographs.

(c)

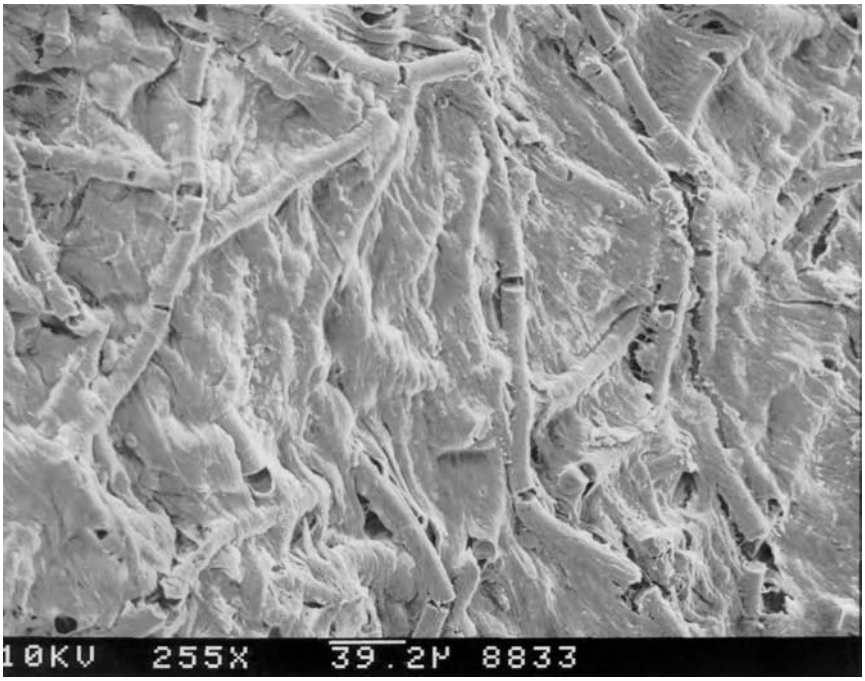

(d)

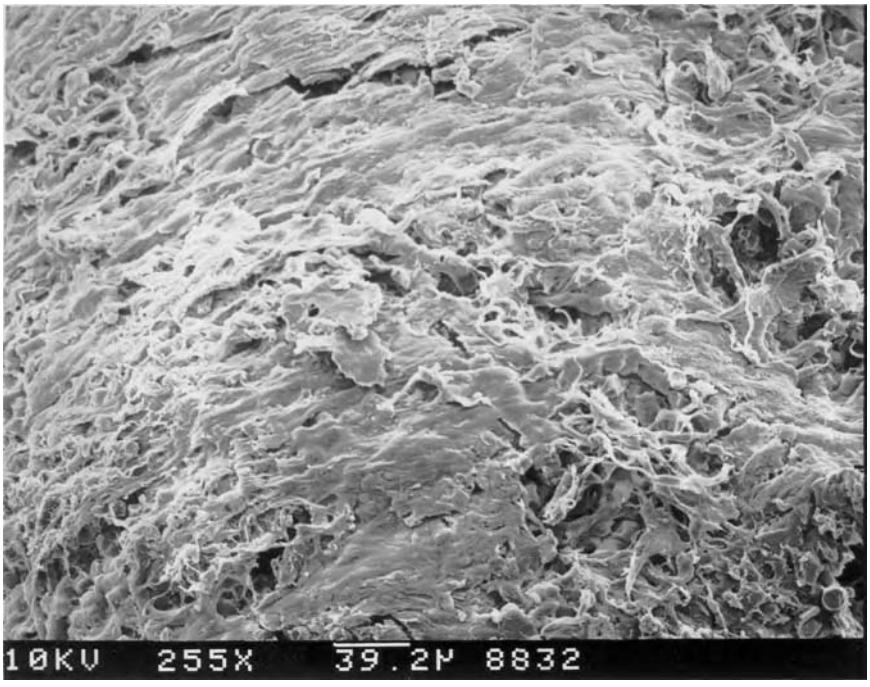

Figure 5. (Continued).

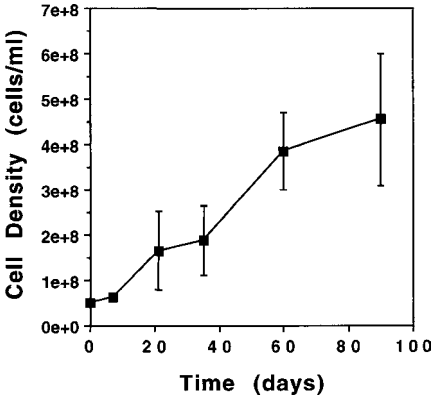

Figure 6. Cell density of tissues developed on PGA matrices. Values represent the mean and standard deviation calculated from three to four samples at each time point.

gels. However, this difference in starting cell densities does not explain the long-term low cell density noted in the collagen matrices. Earlier studies with PGA matrices also were performed with a low initial cell density, but a high density tissue (similar to that obtained in this study) resulted over time in culture [6]. The cells were also not evenly distributed in the collagen gel matrices following 40 days in culture. It is not clear if this is the result of migration of cells from the interior to the surface, or a differential survival and/or growth of cells in the interior versus surface of the collagen gel. It is important to note that cells on an adsorbed layer of collagen exhibited rapid growth, proliferating at a rate comparable to that of the control cells on tissue culture polystyrene. This observation suggests that collagen may be a suitable material for cell proliferation, but the manner in which the matrix is presented is critical. In the form of a gel, the collagen may not provide the correct environment for cell proliferation and pulp tissue development.

The use of alginate as a synthetic matrix for dental pulp tissue did not lead to the formation of a new tissue. This is likely due to the inability of alginate to allow for cell adhesion. Cells can directly adhere to specific amino acid sequences on molecules such as collagen via cell surface receptors [10], but alginate lacks this cell binding function. While cells also do not directly adhere to synthetic polymers such as PGA, they adhere to proteins absorbed onto these hydrophobic polymers [11]. Alginate hydrogels promote minimal protein absorption due to their hydrophilic nature [12], and thus even indirect cell interaction is minimized.

Optimization of the method for seeding cells on PGA led to an increase in initial cell density of approximately two order of magnitude as compared to a previously described static seeding method [6]. The higher initial cell density led to a more rapid development of a high density tissue, and could potentially lead to a quicker return of the engineered tissue to the patient. The efficiency of cell seeding with this new method was also very high (85%), and allows optimal use of the limited cell supply. The phenotype of the cells in the engineered tissues

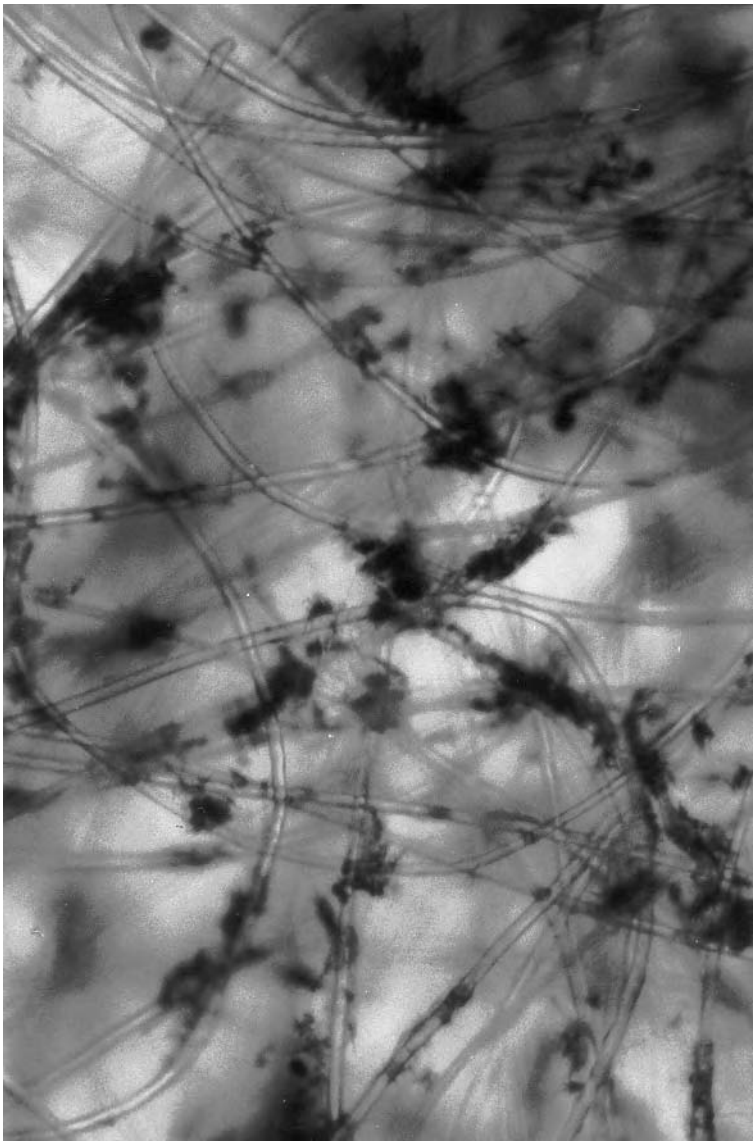

Figure 7. Photomicrograph of cells cultured for 3 days on PGA matrices, following staining with MTT (original magnification of photomicrograph was 10×).

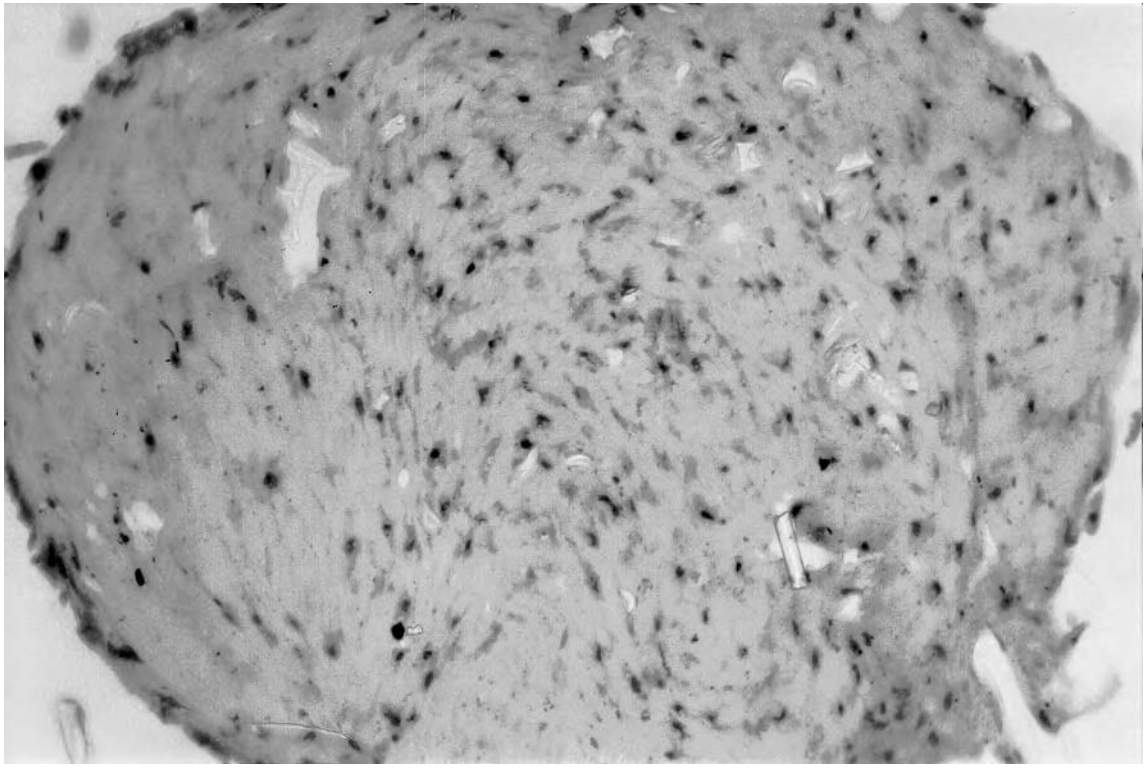

(a)

Figure 8. Photomicrographs of histological sections of new tissues formed on PGA for 90 days following staining with (a) hematoxylin and eosin, or with (b) Trichrome staining. Trichrome stained sections were not counterstained, and all color resulted from the specific staining of collagen.

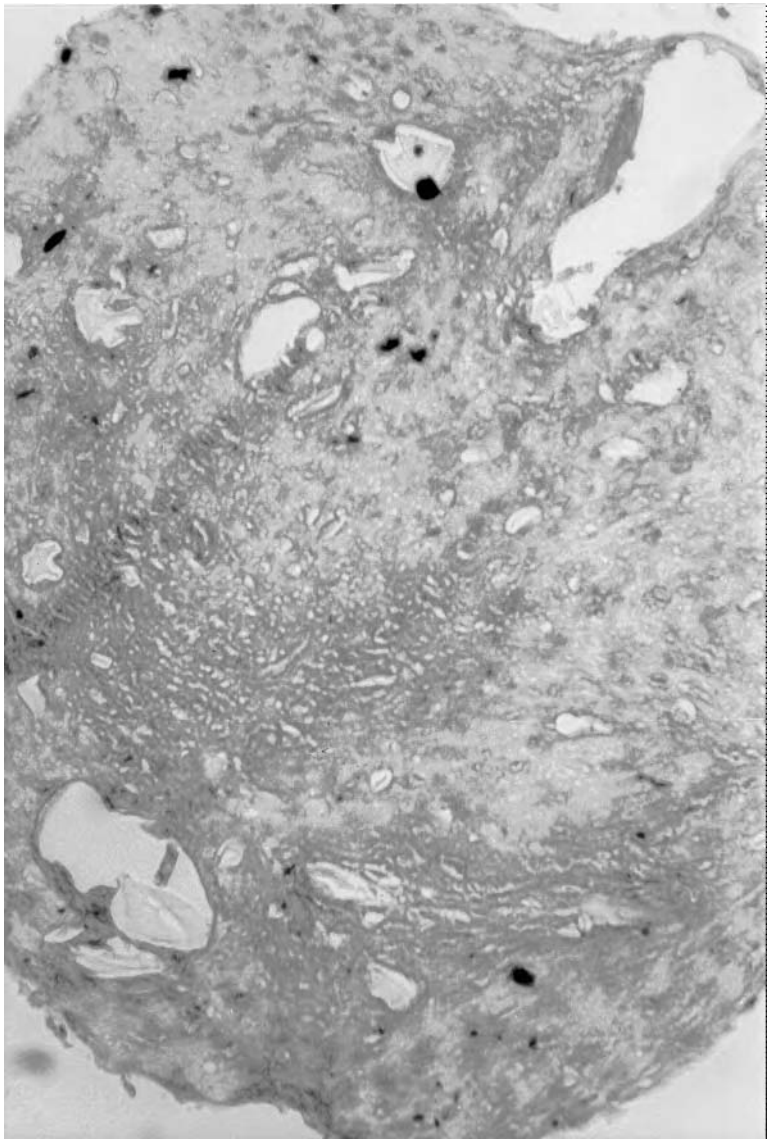

(b)

Figure 8. (Continued).

was not extensively characterized in these studies. However, the cells synthesize and deposit a collagenous matrix, as one would expect from differentiated pulp fibroblasts. In addition, the gene expression of the cells in these tissues has been studied in parallel using reverse transcription-polymerase chain reaction [13]. These studies demonstrated that the cells in these tissues express mRNA for BMP-2, -4, and -7, and type I receptors ActRI, BMPR-IA and -IB, the type II receptor BMPR-II, and type I collagen.

These engineered pulp tissues may ultimately find clinical application as a novel approach to repair and/or regenerate dental pulp, and they may also provide a useful system to assess the biocompatibility of chemicals utilized in dental practice which come in contact with native pulp. The differentiation of odontoblasts to form dentin, a process termed dentinogenesis [3], is still not fully understood. It is possible that engineered dental pulp tissue will provide a model system in which reparative dentinogenesis can be studied. This work may also provide the first step to engineer an entire tooth. Exposing pulp tissue to bone morphogenic proteins may promote reparative dentinogenesis via the formation of odontoblasts, which in turn form dentin [14]. However, further studies are needed in order to understand the role of the synthetic matrix in dental pulp tissue engineering. The results of the current study suggest both the matrix and process of forming cell–polymer constructs are capable of regulating tissue development.

Acknowledgements

Financial support for these studies has been provided by the National Science Foundation (BES-9501376), Reprogenesis, and the Marian Sarah Parker Scholar Program (KSB).

REFERENCES

1. R. G. Craig, *Restorative Dental Materials*, 8th edn. Mosby Co. (1989).
2. D. J. Chiego, in: *Oral Development and Histology*, J. K. Avery (Ed.), p. 262 (1994).
3. H. Lesot, C. Begue-Kirin, M. D. Kubler, J. M. Meyer, A. J. Smith, N. Cassidy and J. V. Ruch, *Cell Mater.* **3**, 201 (1993).
4. R. Langer and J. P. Vacanti, *Science* **260**, 920 (1993).
5. D. J. Mooney and J. A. Rowley, in: *Controlled Drug Delivery*, K. Park (Ed.). ACS Books (1996).
6. D. J. Mooney, C. Powell, J. Piana and B. Rutherford, *Biotechnol. Prog.* **12**, 865 (1996).
7. R. B. Rutherford, M. D. TrailSmith, M. E. Ryan and M. F. Charette, *Arch. Oral Biol.* **37**, 139 (1992).
8. B. S. Kim, A. J. Putnam, T. J. Kuluk and D. J. Mooney, *Biotech. Bioeng.* **57**, 46 (1998).
9. D. J. Mooney, L. Hansen, J. Vacanti, R. Langer, S. Farmer and D. Ingber, *J. Cell. Phys.* **151**, 497 (1992).
10. R. O. Hynes, *Cell* **69**, 11 (1992).
11. J. A. Chin, in: *The Biomedical Engineering Handbook*, Bronzino (Ed.), p. 1597. CRC Press, Boca Raton, FL (1995).

12. K. Smentana, *Biomaterials* **14**, 1046 (1993).
13. B. Buurma, K. Gu, K. Bohl, D. Mooney and B. Rutherford (submitted).
14. R. B. Rutherford, J. Wahle, M. Tucker, D. Rueger and M. F. Charette, *Arch. Oral Biol.* **38**, 571 (1993).

Polymers for Tissue Engineering, pp. 315–327
Molly S. Shoichet and Jeffrey A. Hubbell (Eds)

Comparative study of the use of poly(glycolic acid), calcium alginate and pluronics in the engineering of autologous porcine cartilage

YILIN CAO,[1,*] ANGELA RODRIGUEZ,[1] MARTIN VACANTI,[1,2] CLEMENTE IBARRA,[1] CARLOS AREVALO[1] and CHARLES A. VACANTI[1]

[1]*Department of Anesthesia, the Laboratory for Tissue Engineering, University of Massachusetts Medical Center, 55 Lake Avenue North, Worcester, MA 01655, USA*
[2]*Department of Pathology, Massachusetts General Hospital and Harvard Medical School, Cambridge, MA 00000, USA*

Received 9 June 1997; accepted 28 October 1997

Abstract—New cartilage formation has been successfully achieved by a technology referred to as tissue engineering. Polymers and hydrogels such as poly(glycolic acid), calcium alginate, and poly(ethylene) and poly(propylene) hydrogels have been used as cell carriers to regenerate cartilage in the nude mouse model. The next step toward human applications of engineered cartilage is to demonstrate their potential in immunocompetent animal models. This study compared the suitability of three polymers for generating tissue engineered elastic cartilage using autologous cells in an immuno-competent porcine animal model. Auricular cartilage was obtained from pigs. Chondrocytes were isolated and seeded onto fiber based poly(glycolic acid) (PGA) scaffolds or suspended in calcium alginate or pluronic F127 gel at constant concentrations. Chondrocyte–polymer constructs were either implanted (PGA) or injected (calcium alginate and pluronic) as autologous implants subcutaneously into the pigs from which the cells had been isolated. Specimens were harvested and analyzed grossly and histologically after 6 weeks *in vivo*. All explants demonstrated cartilage formation to a variable degree. When using PGA or calcium alginate, the overall histological appearance of the tissue formed is that of fibrocartilage with thick bundles of collagen dispersed in the tissue. When using pluronics as scaffold, histologic features resemble those of native elastic cartilage, showing a more organized arrangement of the cells, which seems to correlate to functional properties as elastin presence in the tissue engineered cartilage. Elastic cartilage engineered in an immunocompetent animal model varies with the type of polymer used. The behavior of the cell–polymer constructs is not fully understood and outcome seems to be related to several factors, including inflammatory reaction. Further studies with similar models are needed to determine the feasibility of engineering tissue generated from different cell–polymer constructs prior to human application.

Key words: Tissue engineering; chondrocyte; cartilage; autologous; hydrogel; poly(glycolic acid); calcium alginate; pluronic.

*To whom correspondence should be addressed.

INTRODUCTION

Although medical technology has made great advances, tissue loss and organ failure remain challenging problems in health care. Techniques for reconstruction or transplantation often rely on the use of allografts, synthetic implantation devices, or autografts. These treatment alternatives present several specific problems. Allografts are limited in supply and often trigger immunological rejection. Synthetic prosthetic materials present increased susceptibility to infection, long term and sometimes unpredictable immunological interaction with the recipient, or rejection. Autologous cartilage has many ideal characteristics as a graft material, including low absorption rate, lifetime biocompatibility, ability to retain bulk and a low requirement for direct vascular supply. Availability is a major limitation for its use in reconstructive surgery.

To overcome these difficulties, a technology has been developed which combines cells with biodegradable polymers to produce an implant able to generate new tissue [1]. The use of polymers as scaffolds to transplant cells and form new tissue may be helpful in the treatment of tissue loss and organ failure. Polymer scaffolds serve as a guide for three-dimensional tissue regeneration. Biodegradable polymers are absorbed after fulfilling the purpose of a temporary support so that a natural tissue or organ replacement can be achieved [2].

Several experiments have shown cartilage regeneration using cells seeded *in vitro* onto a variety of polymer materials in the nude mouse model. A variety of new tissue equivalents including cartilage structures in the shape of a human ear [3], a hollow tube similar to a trachea [4], osteocyte implants for bone reconstruction [5], and tenocyte implants for tendon reconstruction have been engineered [6, 7].

Several polymers including polyesters of glycolic and L-lactic acid [1, 8], alginic acid [9, 10] and *co*-polymer gels of ethylene and propylene oxide (pluronic F127) [11] have been used successfully to engineer new cartilage in the nude mouse. Polymers have also been used to engineer cartilage *in vitro* and in other animal models [8, 12, 13], but little is known about the use of autologous cells in an immunocompetent animal model. Studying these techniques in such models is essential toward the development of human autologous grafts. Autologous tissue engineered implants theoretically should avoid problems related to rejection, specific polymer properties might trigger the immune system and non-specific inflammatory reactions resulting in destruction of cells as 'innocent bystanders'. These factors make it necessary to study the concepts previously tested in the nude mouse in a larger immunocompetent animal model.

This study was directed to analyze the *in vivo* generation of tissue with potential use in plastic and reconstructive surgery. Therefore, due to its accessibility and mechanical properties such as flexibility, auricular elastic cartilage was studied to compare different polymers as cell carriers for engineering new cartilage.

We compared the suitability of autologous pig ear chondrocytes for regenerating new cartilage using three different matrices: poly(glycolic acid) (PGA), calcium alginate, and pluronic F127 gel.

MATERIALS AND METHODS

Chondrocyte isolation

Three male Yorkshire pigs ranging in ages between 8 and 10 weeks and weighing between 18 and 20 kg were anesthetized with intramuscular xylazine (2 mg kg^{-1}), ketamine (20 mg kg^{-1}), and the inhalation agent isoflurane. Cartilage from the external ear was dissected from the overlying perichondrium. Cartilage was minced, washed in phosphate buffered saline (PBS) with antibiotics, and digested with 3% collagenase II (Worthington Biochemical Corp., Freehold, NJ, USA) at 37°C for 8–12 h. The resulting cell suspension was passed through a sterile 250-μm polypropylene mesh filter, then centrifuged and the resulting pellet washed twice with PBS (phosphate-buffered saline) and suspended in Ham's F-12 plating medium (Gibco, Grand Island, NY, USA) with L-glutamine, 50 mg l^{-1} L-ascorbic acid, 100 u l^{-1} of penicillin, 100 μg l^{-1} of streptomycin, 0.25 μg l^{-1} of amphotericin, and supplemented with 10% fetal bovine serum (Sigma Chemical, St. Louis, MO, USA). Cell number and viability were determined using a hemocytometer and trypan blue vital dye. Chondrocyte preparations having cell viabilities in excess of 85% were used. Chondrocyte suspensions were concentrated to a cellular density of 5×10^7 cell ml^{-1} and were then either seeded onto poly(glycolic acid) fibers or suspended in one of the hydrogels, that is calcium alginate or a *co*-polymer gel of ethylene and propylene oxide (pluronic F127).

Chondrocyte–polymer constructs

Chondrocyte–PGA. A synthetic non-woven mesh of PGA with interfiber spaces of 75–100 μm was cut into 1 cm^2 pieces. 200-μl aliquots of the chondrocyte suspension (1×10^7 cells total) were seeded onto each polymer scaffold and allowed to attach for 4 h at 37°C. After seeding, the thickness of the polymer devices was 0.8–1 mm. Ham's F-12 tissue culture medium (as above) was added and then the constructs were allowed to incubate *in vitro* at 37°C for an additional week in 5% CO_2. The media was replaced every 3–4 days. A total of five constructs were implanted in five non-communicating subcutaneous pockets on the ventral surface of the corresponding pig.

Chondrocyte–calcium alginate gel. An aliquot of the isolated chondrocyte suspension was mixed with a sterile sodium alginate (Pronova, Portsmouth, NH, USA) solution (0.1 M K_2HPO_4, 0.135 M NaCl, pH 7.4) in a cellular concentration of 5×10^7 ml^{-1} in a 1.0% alginate solution. The chondrocyte–sodium alginate suspension was stored on ice at 4°C until use. Immediately prior to injection, 0.2 g of sterilized $CaSO_4$ powder was added to each ml of cold chondrocyte–alginate solution. A total of five aliquots containing 200 μl of the admixture were injected under the subcutaneous space of the ventral surface of the pig from which cells had been isolated.

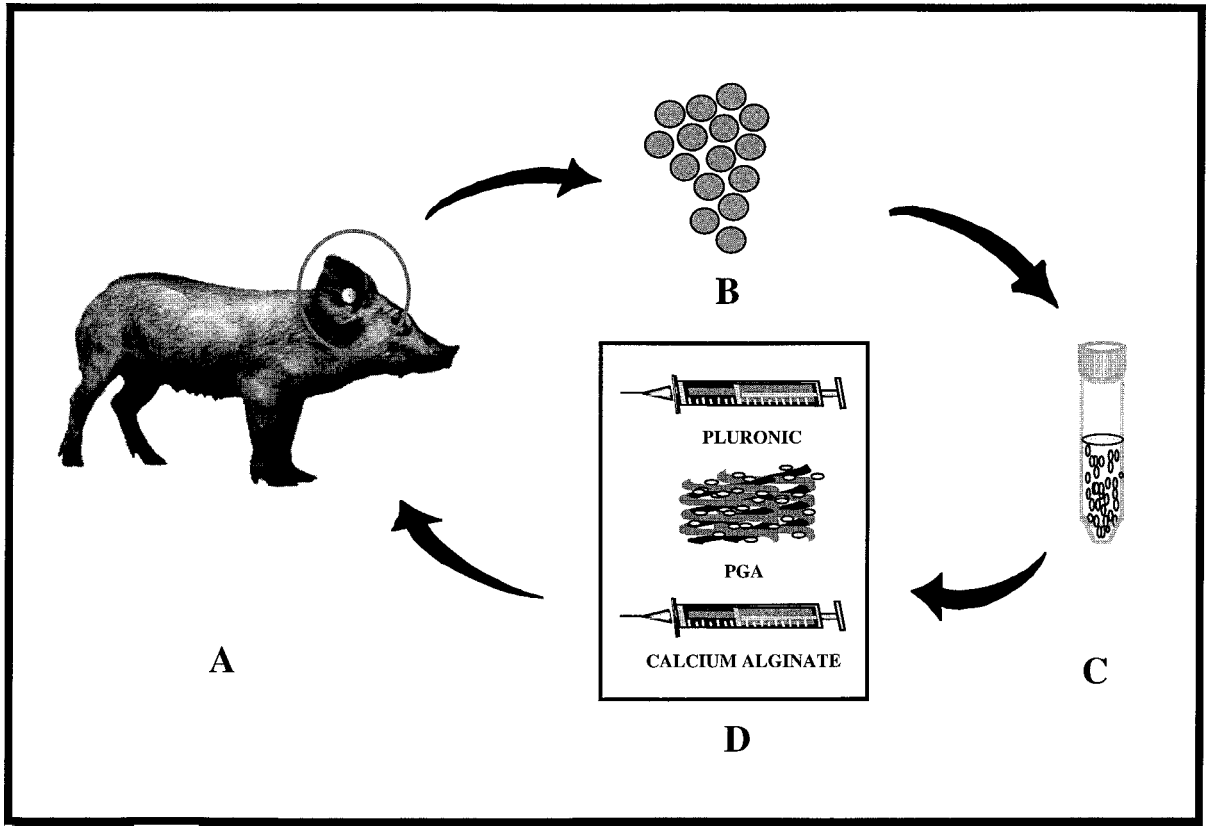

Figure 1. Schematic representation of the protocol used to create pig chondrocyte–PGA or chondrocyte–hydrogel constructs. Starting in the left side and proceeding clockwise; pig ear cartilage is harvested (a), cells isolated via digestion of the cartilage matrix (b), cells are then washed and prepared for seeding, (c) and (d) cells are seeded in either PGA polymer, pluronic or calcium alginate hydrogels.

Chondrocyte–pluronic F127 gel. An aliquot of the chondrocyte suspension was mixed with a 30% (w/v) solution of *co*-polymer gel of ethylene and propylene oxide (pluronic F127) at a cellular concentration of 5×10^7 cells ml^{-1}. Aliquots containing 200 μl of the above mixture were injected subcutaneously using a 22-gauge needle at five sites on the ventral surface of the pig from which the cells had been isolated (autologous implants) (see Fig. 1).

After 6 weeks *in vivo*, the pigs were anesthetized and constructs carefully dissected free of surrounding soft tissue. Specimens were examined grossly and palpated with forceps to assess rigidity. They were then fixed in 10% phosphate-buffered formalin (Fisher Scientific, Fair Lawn, NJ, USA) for histologic analysis.

Once fixed for at least 24 h, specimens were embedded in paraffin and sectioned. By using standard histochemical techniques, slide sections were stained with hematoxylin and eosin, safranin O, Masson's trichrome, and Verhoeff's solution.

RESULTS

Chondrocyte–PGA constructs

At 6 weeks after implantation, five areas of increased firmness could be palpated underneath the pig's skin. Excised specimens were found as a mass of tissue encased within thick fibrous tissue. Transverse sections showed specimens to be composed of a thick outer layer of white tissue with a yellowish central portion.

When analyzed by histology (H&E), all specimens showed broad areas of fibrous tissue containing several nodules of cartilage (Fig. 2). On average, only 40% of each specimen was cartilage. Also seen was a small amount of adipose tissue and occasional small blood vessels. Focally in the fibrous tissue, collections of lymphohistiocytic cells, some of which showed plasmacytoid differentiation were identified. Fragments of foreign body material, seen in the areas of inflammation that were highlighted under polarized light, were being ingested by histiocytes, resulting in foreign body giant cells (Fig. 3). These small areas of cartilage contained numerous evenly spaced triangular lacunae containing single chondrocytes. Occasional bicellular chondrocytes were seen. The matrix was deeply basophilic, with the borders between the islets of cartilage and fibrous tissue being ill-defined. A trichrome stain highlighted the intertwining bands of collagen at the periphery of the cartilage. Cartilage fragments were strongly and evenly positive for safranin O which demonstrated matrix proteoglycans. An elastin Verhoeff's stain showed occasional small bands of positivity.

Chondrocyte–calcium alginate constructs

At 6 weeks after implantation, five chondrocyte–calcium alginate constructs could be easily identified by palpation underneath the pig's skin. At the time of harvesting, they were found as distinct masses of tissue, each surrounded by a thin fibrous tissue capsule with a vascular network with minimal fibrotic and inflammatory reaction. After removal of the soft tissue capsule specimens had the gross appearance of cartilage.

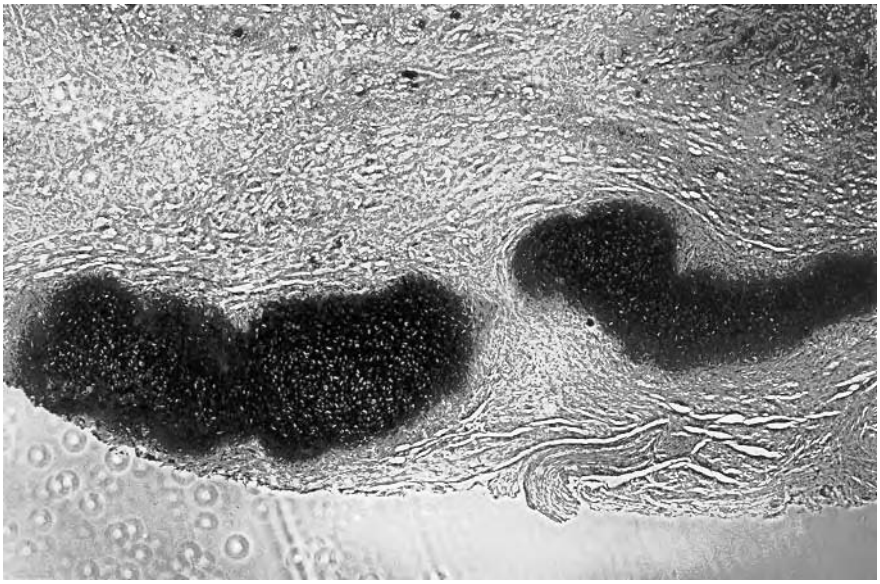

Figure 2. Microscopic view (5 ×) of tissue obtained with cell–PGA construct showing predominately fibrous tissue with two small fragments of cartilage comprised of single chondrocytes surrounded by lacunae in a basophilic matrix.

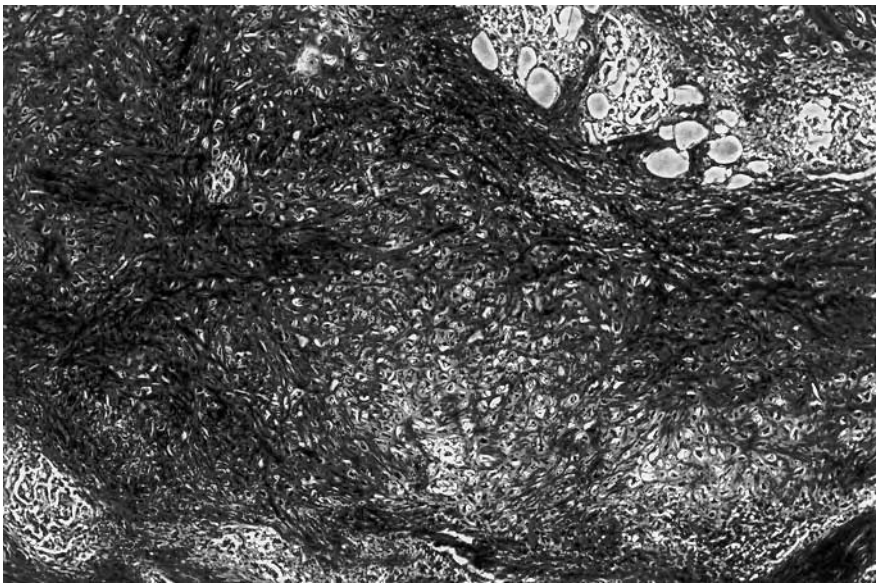

Figure 3. Microscopic view (10 ×) of tissue obtained with cell–PGA construct showing cartilage admixed with fibrous tissue. Chronic inflammation and foreign body giant cell reaction can be observed. The lacunae are triangular in shape and contain single chondrocytes. Interlacing bands of collagen-appearing fibers are seen surrounding the lacunae.

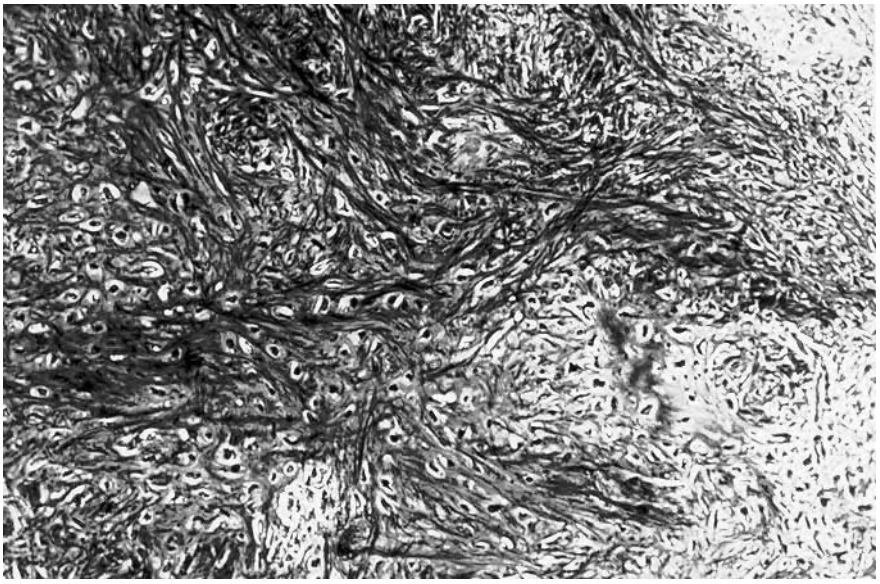

Figure 4. Microscopic view (20 ×) of a section of tissue obtained with a cell–calcium alginate construct showing lacunae with chondrocytes in a basophilic matrix admixed with interlacing bands of collagen-appearing fibers in a histologic pattern reminiscent of fibrocartilage.

Microscopic sections of the five constructs had similar histology that showed broad areas of fibrous tissue containing blood vessels and adipose tissue. Only 30–40% of each specimen was cartilage (Fig. 4). Many lymphohistiocytic cells infiltrated the fibrous areas. There was occasionally foreign body giant cell formation.

Scattered throughout were ill-defined islands of cartilage containing triangular shaped lacunae with single chondrocytes in an even pattern. Trichrome stain highlighted wavy bands of collagen that extended into the cartilage matrix. The safranin O stain was strongly positive in the cartilage matrix indicating presence of proteoglycan. An elastin stain showed occasional strands of positivity.

Chondrocyte–pluronic constructs

At 6 weeks after implantation, five chondrocyte–pluronic constructs could be easily identified by palpation underneath the animal's skin. At the time of harvesting, they were found as distinct masses of tissue surrounded by a thin fibrous tissue capsule with vascular network, but only minimal fibrotic reaction. After removal of the soft tissue capsule, all specimens had the gross appearance of cartilage.

All five constructs had similar histology. Microscopic sections revealed large confluent nodules of cartilage. The entire structure was composed of cartilage rimmed by fibrous tissue suggestive of a perichondrium (Fig. 5). This feature was highlighted by a trichrome stain. Rare focal chronic inflammation was seen in fibrous tissue away from cartilage. The fibrous tissue around the cartilage was not associated with inflammation. Foreign body giant cells were not seen. The lacunae were round to oval and contained single chondrocytes. Occasional bicellular chondrocytes were seen.

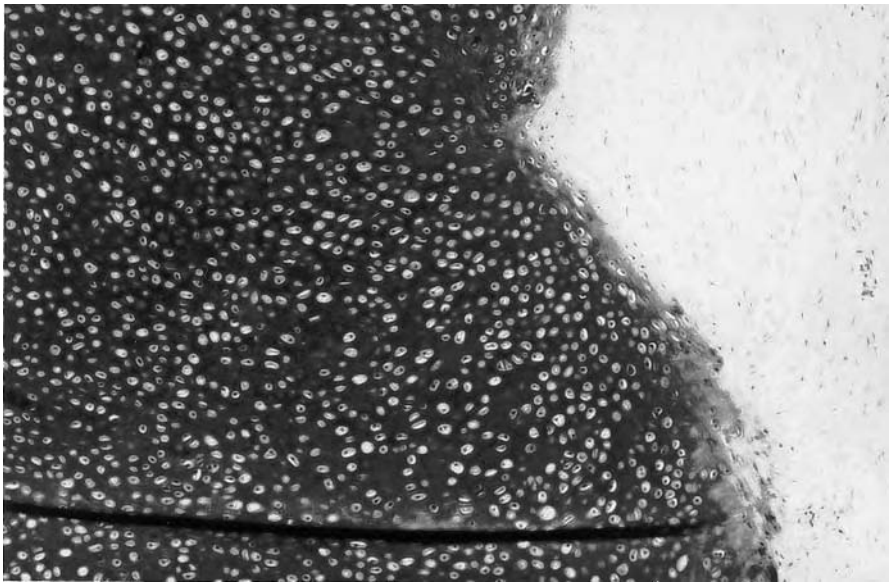

Figure 5. Microscopic view (20 ×) of a section of tissue obtained with a cell–pluronic construct showing cartilage with single chondrocytes in evenly shaped round-to-oval lacunae in a basophilic matrix. A rim of fibrous tissue can be observed at the periphery. No signs of inflammation can be appreciated.

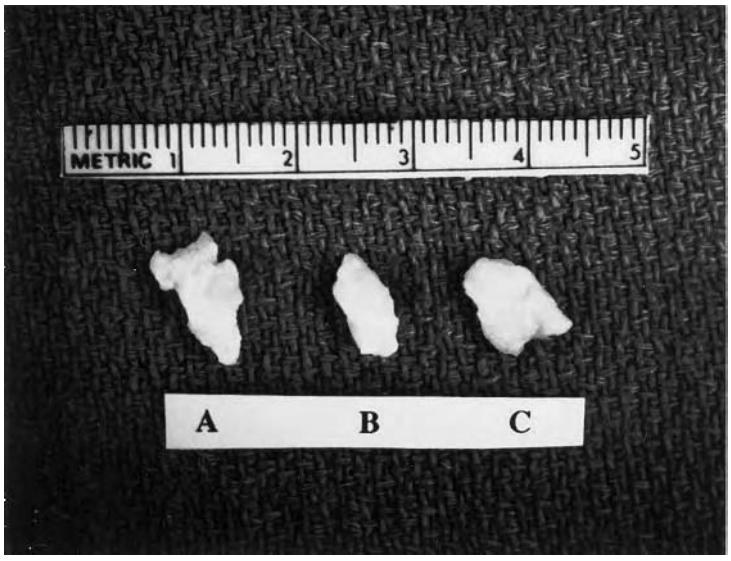

Figure 6. Gross morphology of three specimens after harvest from the subcutaneous space of the mice and removal of the fibrous capsule. From left to right: explant resulting from a chondrocyte–PGA construct (A), explant resulting from a chondrocyte–calcium alginate construct (B), and (C) explant resulting from a chondrocyte–pluronic construct.

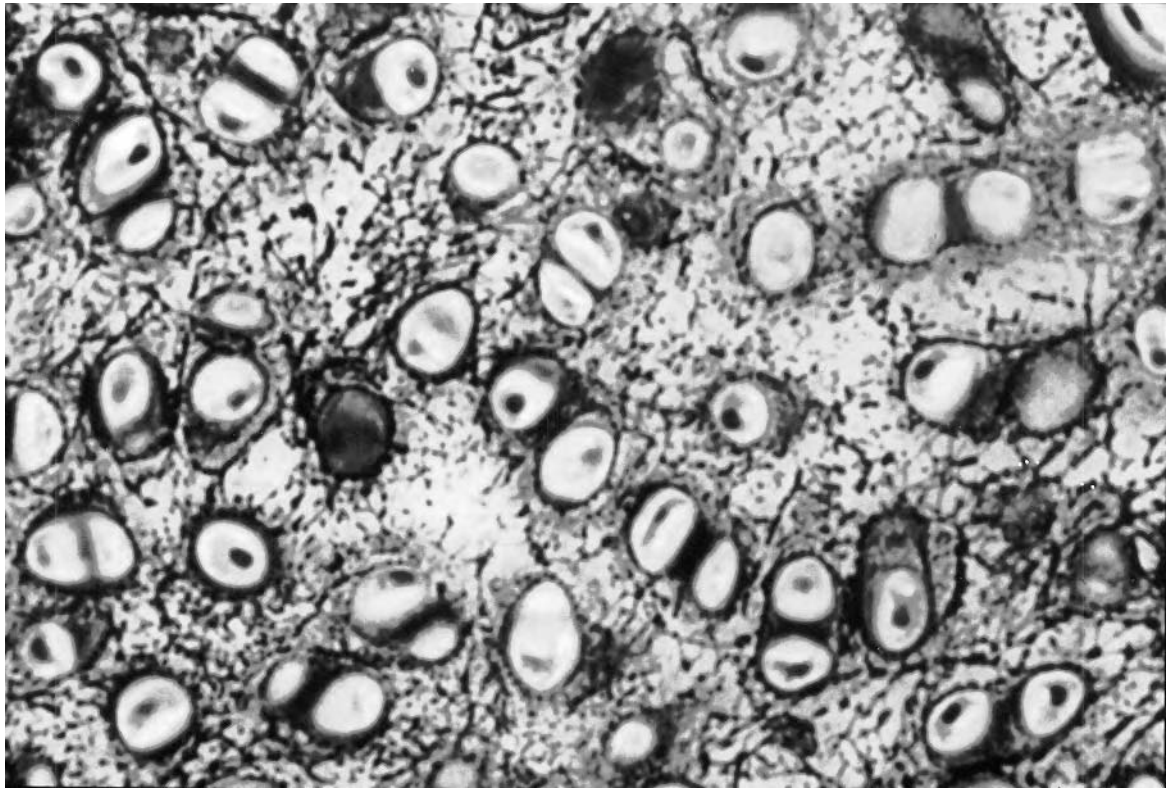

(a)

Figure 7. Microscopic views (40 ×) with elastic stain (Verhoeff's) comparing pig's ear elastic cartilage (a) to cell pluronic construct (b) generated from the same pig. These show essentially the same histology with more cellularity and much lighter staining of matrix elastic fibers (black) in Fig. 6.

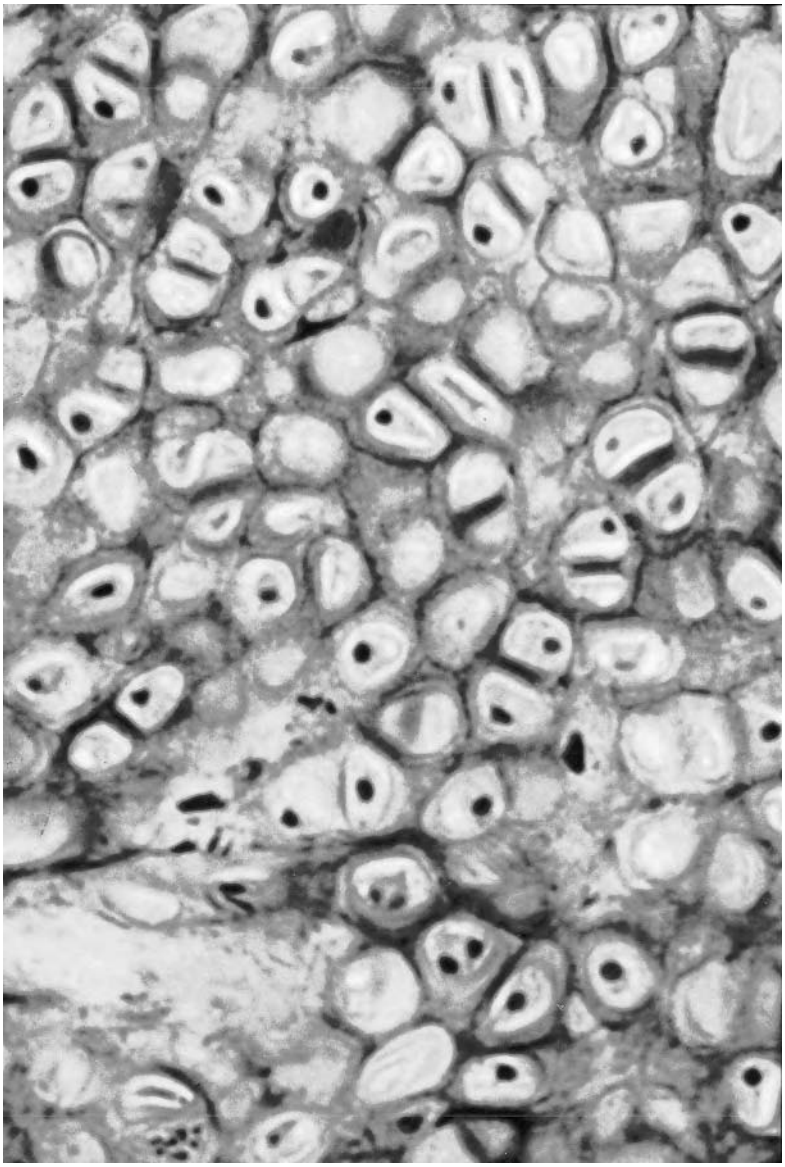

(b)

Figure 7. (Continued).

Table 1.
Histologic characteristics of tissue constructs generated comparing scaffolding material under light microscopy (+ = present with normal distribution; ± = present with abnormal distribution)

	Poly(glycolic acid)	Calcium alginate	Pluronics
Chondrocytes in lacunae	+	+	+
Proteoglycan in matrix	+	+	+
Collagen fibers in matrix	+	+	
Elastic fibers in matrix	±	±	+
Perichondrium-like tissue in periphery			+

A safranin O stain was strongly and evenly positive demonstrating proteoglycan content of the matrix. The matrix of the cartilage was heterogeneous in staining characteristics suggestive of maturation. Verhoeff's solution showed light matrix positivity in a delicate reticular pattern characteristic of elastin.

DISCUSSION

Several studies have shown that chondrocytes seeded onto three-dimensional scaffolds or encapsulated in gels result in cartilage formation after implantation or injection into the subcutaneous space of the nude mouse [8–10].

Cartilage is a specialized type of supporting tissue consisting of cartilage cells (chondrocytes) individually surrounded by spaces (lacunae) that are embedded in an intercellular substance (matrix) that consist of fibers and ground substance. The fiber type will determine the flexibility of the cartilage, e.g. elastic fibers in elastic cartilage and collagen fibers in fibrocartilage. The predominate collagen type in cartilage is type II. The ground substance is composed chiefly of proteoglycans (chondroitin sulfate) and glycoproteins. Cartilage is enveloped by a fibrous connective tissue membrane called a perichondrium from which it receives its blood supply. Distinct classification of cartilage is arbitrary with a continuous spectrum of cartilage type frequently seen [15].

This study has demonstrated that pig elastic cartilage can be engineered in an immunocompetent animal model using autologous chondrocytes seeded onto PGA scaffolds or encapsulated in gels. The newly engineered tissue demonstrated gross and histological qualities of cartilage in variable degrees depending on the polymer used for engraftment. The association between the polymer used and the resultant tissue has not been previously described in an autologous immunocompetent model, although it is of critical importance if tissue engineered cartilage is to be developed for use in humans.

This study demonstrated that cartilage can be engineered in an immunocompetent animal model when employing various polymers to deliver cells. Although chondrocyte–PGA constructs demonstrated cartilage formation, a significant local non specific inflammatory and foreign body giant cell reaction were noticed which we believed resulted in excess formation of fibrous tissue and lead the constructs

to extend beyond the limits of their confines. These results differed from those in nude mice, which consistently showed cartilage formation in a predictable size and shape when chondrocyte–PGA constructs were implanted [14]. While the use of poly(glycolic acid) sutures is common in surgery, it is known that the mild local inflammation elicited by the material is not deleterious to tissue healing. However, the initial stages of cartilage formation seem to be adversely affected by any degree of inflammation in immunocompetent animals.

On the other hand, autologous chondrocytes have been shown to elicit lymphocyte proliferation and migration *in vitro*. This may play a role in triggering a rejection-like cellular response with possible local release of cytokines and other mediators of inflammation. The lack of lymphocytic response to chondrocytes that were seeded onto a scaffolding material and allowed to form an encapsulating extracellular matrix prior to exposure suggests a possible immuno-protective role of the extracellular matrix to chondrocyte surface antigens. In this study, calcium alginate and pluronic gels encapsulated the chondrocytes in a similar fashion to extracellular matrix at the time of implantation. Both gels lead chondrocytes to cartilage formation. Calcium alginate seems to protect the chondrocytes until new matrix is formed, however its long degradation time (remains in the site of implantation even after 6 months of implantation, according to previous studies) can inhibit cartilage formation to some degree. Our experiments show specimens with a moderate non-specific inflammatory response, and non-confluent islets of cartilage corresponding to about 30–40% of the total size of the specimen.

By gross and histologic examination, chondrocyte–pluronics constructs demonstrated consistent cartilage generation. The lacunae of the generated cartilage specimens contained single chondrocytes occasionally arranged in bicellular groups. In addition, the matrix had a heterogeneous staining pattern on H&E, and a positive delicate reticular pattern with an elastic stain. All these histologic features are characteristic of elastic cartilage. The safranin O stain was intensely and evenly positive, demonstrating cartilage matrix proteoglycan production. No pathologic features such as significant inflammation nor foreign body giant cell reaction were seen.

In contrast, tissue generated using PGA and calcium alginate as scaffolds was predominantly fibrous tissue containing ill-defined nodules of cartilage. There was significant chronic inflammation with foreign body giant cell formation in both of these constructs. The elastic stain showed focal positivity in a non-specific pattern. Cartilage matrix proteoglycan presence was demonstrated with a safranin O stain. The calcium alginate specimen had matrix collagen deposition more reminiscent of fibrocartilage.

CONCLUSION

Tissue specimens created from autologous chondrocytes isolated from pig ear elastic cartilage using pluronics as scaffolding material successfully developed into elastic cartilage both grossly and histologically without significant pathology. The tissue constructs created using PGA and calcium alginate both showed significant inflammatory

response and foreign body cell reaction, forming essentially fibrous tissue with only ill-defined nodules of cartilage.

REFERENCES

1. C. Vacanti, R. Langer, B. Schloo and J. P. Vacanti, *Plast. Reconstr. Surg.* **87**, 753 (1991).
2. R. Langer and J. P. Vacanti, *Science* **260**, 920 (1993).
3. Y. L. Cao, J. P. Vacanti, K. T. Paige, J. Upton and C. A. Vacanti, *Plast. Reconstr. Surg.* **100**, 1 (1997).
4. C. A. Vacanti, K. T. Paige, W. S. Kim, J. Sakata, J. Upton and J. P. Vacanti, *J. Pediatr. Surg.* **29**, 201 (1994).
5. C. A. Vacanti, W. S. Kim, J. Upton, M. P. Vacanti, D. Mooney, B. Schloo and J. P. Vacanti, *Transplant Proc.* **25**, 1019 (1993).
6. Y. L. Cao, J. P. Vacanti, P. X. Ma, K. T. Paige, J. Upton, Z. Chowanski, B. Schloo, R. Langer and C. A. Vacanti, *Transplant Proc.* **26**, 3390 (1994).
7. Y. L. Cao, J. P. Vacanti, P. X. Ma, C. Ibarra, K. T. Paige, J. Upton, B. Schloo, R. Langer and C. A. Vacanti, *Mater. Res. Soc. Symp. Proc.* **394**, 83 (1995).
8. L. E. Freed, J. C. Marquis, A. Nohria, J. Emmanual, A. G. Mikos and R. Langer, *J. Biomed. Mater. Res.* **27**, 11 (1993).
9. K. T. Paige, L. G. Cima, M. J. Yaremchuk, J. P. Vacanti and C. A. Vacanti, *Plast. Reconstr. Surg.* **96**, 1390 (1995).
10. Y. L. Cao, J. X. Wang and C. A. Vacanti, 42nd Annual Meeting of Orthopedic Research Society, Atlanta, GA, February 18–22 (1996).
11. Y. L. Cao, C. Peetz, K. Tran and C. A. Vacanti, Inaugural Meeting of the Tissue Engineering Society, Abstract 17 (1996).
12. M. M. Ruusskanen, M. K. Virtanen, H. Tuominen, P. Tormala and T. Waris, *Scand. J. Plast. Reconstr. Hand. Surg.* **28**, 81 (1994).
13. M. Sittinger, J. Bujia, W. W. Minuth, C. Hammer and G. R. Burmester, *Biomaterials* **15**, 451 (1994).
14. W. S. Kim, J. P. Vacanti, L. Cima, D. Mooney, J. Upton, W. C. Peulacher and C. A. Vacanti, *Plast. Reconstr. Surg.* **94**, 223 (1994).
15. *Atlas of Histology*, T. S. Leesoh, C. R. Leesoh and A. A. Paparo (Eds). W. B. Saunders Co. (1988).

This page intentionally left blank

Polymers for Tissue Engineering, pp. 329–340
Molly S. Shoichet and Jeffrey A. Hubbell (Eds)

Cultivation of fibroblast cells on keratin-coated substrata

KIYOSHI YAMAUCHI,* MASASHI MANIWA and TAKESHI MORI

Department of Bioapplied Chemistry, Faculty of Engineering, Osaka City University, Sumiyoshi-ku, Osaka 558, Japan

Received 16 March 1997; accepted 2 September 1997

Abstract—By means of a cell culture method, the attachment and growth of mouse L929 fibroblast cells were studied on matrices of the (−SDS)- and (+SDS)-keratins, which were extracted from wool in the absence and presence of sodium dodecyl sulfate, respectively. The (+SDS)-keratin showed some toxic effect on the cell growth, but upon washing with a pH 7/phosphate buffer, the protein behaved similarly to a substratum of the (−SDS)-keratin. The comparative culture assay on the keratins, collagen (type I), and glass revealed that the keratins were more adhesive to the cells and more supportive for cell proliferation than the collagen and glass. The results were explained by an enhanced initial adsorption of mediator proteins from fetal bovine serum onto the keratin substrata.

Key words: Keratin; fibroblast cell; cell-substratum; cell attachment; biomaterial.

INTRODUCTION

Keratins are fibrous proteins specialized for hair, wool, feathers, nail, and other epitherical coverings [1]. At a molecular level, the keratins are distinguished from collagen, silk fibroin, and other structural proteins by the half-cystine residue amounting to as much as 7–20 mol% of all amino acid residues. The component 8c-1 of wool keratin microfibrils was studied in detail for the primary structure to show that most half-cystine residues are localized in both amino- and carboxylic acid-terminal regions [2, 3]. The keratin fibrils may thus be undertaken as the polymers which are formed by an intra- and intermolecular oxidative S−S bindings of the cysteine residues between the monomeric keratins (40–60 kD).

In a preceding paper we showed that the keratin monomers were prepared as a stable aqueous solution upon extracting human hair and wool by an aqueous mixture of urea, mercaptanol, and sodium dodecyl sulfate (SDS) [4]. Casting the aqueous solution under air resulted in the formation of a film which was no more soluble in water and most organic solvents including dimethyl formamide and dimethyl sulfoxide.

*To whom correspondence should be addressed. E-mail: yamauchi@bioa.eng.osaka-cu.ac.jp

In this paper we wish to describe cultivation of L929 cells from mouse connective tissue on the wool keratin proteins coated on glass and polystyrene. The results were compared with cultivation on collagen-type I and poly(vinyl alcohol) (PVA).

MATERIALS AND METHODS

The keratins were extracted by two methods from Corridale wool as mentioned below. Aqueous atelocollagen from bovine dermal, type I, 0.3 wt% (code name: Cellgen IP-C), a sterilized product, was obtained from Koken, Tokyo, Fibroblast, NCTC clone 929 (Connective tissue, mouse) and Eagle's minimum essential medium (MEM-E) were purchased from Flow Laboratories. Fetal bovine serum (FBS) was obtained from ICN Biochemicals (No. 29-177-49). PVA (average molecular weight 88 kD; saponification extent, 99.5%) of Kurare Chemical Co. was dissolved in water to give a 5 wt% solution. Cultivation was conducted chiefly using polystyrene test dishes for microbiological use (No. SH90-20), culture dishes (No. 25102FK25S) from Iwaki Glass Co. and the optical microscopy-cover glass, which was cleaned by immersing in ethanol.

Preparation of aqueous keratin suspensions with and without the use of SDS

(+*SDS*)-*keratin* [4]. A mixture of wool (Corriedale; 10 g), 7 M urea (180 ml) and 2-mercaptoethanol (15 ml) and SDS (6 g) in a sealed 300 ml-round bottom flask was shaken at 50°C for 12 h, then filtered through a stainless steel mesh. The filtrate was subsequently dialyzed using cellophane tubing (Union Carbide, 30/32; molecular weight cut-off of about 10 kD) against degassed water (3 × 3 l) containing 0.2 wt% of 2-mercaptoethanol overnight. The inner solution (230 ml) was very stable to remain almost clear without giving precipitates for at least 1 year. The protein concentration was 2.5 wt% based on Lowry's microanalysis kit (Sigma Chemical Co., product No. 690-A), and the weight of the keratin powder obtained by freeze-drying. An amino acid analysis of the freeze-dried powder is displayed in Table 1 giving about 11 mol% as a combined content of the cysteine and half-cystine residues. A SDS-polyacrylamide gel electrophoresis (SDS-PAGE) indicated that the solution had microfibril proteins of 40–60 kD as major bands in addition to interfilamental matrix proteins of 15–20 kD as miner bands [5, 6] (Fig. 1, column **R**). An elemental analysis (CHN) suggested that the aqueous keratin solution contained SDS with the amount corresponding to 11 ± 6 wt% of the keratins.

(−*SDS*)-*keratin*. A mixture of wool (5 g), 7 M urea (90 ml) and 2-mercaptoethanol (8 ml) was shaken in a sealed glass bottle at 50°C for 24 h, then filtered through a stainless steel mesh. The filtrate was dialyzed using the aforementioned cellophane tubing against external distilled water (3 l) containing the mercaptoethanol (6 ml) overnight. The dialysis was repeated twice against degassed water containing 0.2 wt% of 2-mercaptoethanol (2 × 3 l) to afford a turbid solution (120 ml). The yield of the extracted keratins was estimated to be 42% by weighing the freeze-dried material.

Table 1.
The amino acid analysis of (−SDS)- and (+SDS)-keratins. The proteins were treated by iodoacetic acid to convert the cysteine residues into *S*-carboxymethylcysteine (cmCys) residues, hydrolyzed by concentrated hydrochloric acid at 110°C for 24 h, then applied to an amino acid analyzer (Hitachi model 835)

Amino acid	Residues per 1000[a]	
	(−SDS)-keratin	(+SDS)-keratin
Aspartic acid	39	56
Threonine	82	65
Serine	131	113
Glutamic acid	97	104
Proline	140	73
Glycine	91	90
Alanine	32	44
Cysteine (cmCys)	45	79
Half-cystine	70	33
Valine	44	53
Methionine	2	5
Isoleucine	22	27
Leucine	49	67
Tyrosine	55	44
Phenylalanine	26	30
Lysine	7	21
Histidine	10	24
Arginine	58	67

[a] Experimental error ± 6%.

An amino acid analysis of the freeze-dried keratin is shown in Table 1, suggesting 12 mol% as a combined content of the cysteine and half-cystine residues. The SDS-PAGE of the keratin is displayed in Fig. 1, column **M**.

Preparation of keratin-, collagen-, and PVA-coated substrata

Method 1. The aqueous solution of (+SDS)-keratin was filtered (through 0.2 μm Millipore filter) prior to use. The sterilized collagen solution was used as received. These protein solutions were poured onto the sterilized microbiological test dished and culture dishes; here, the solution volume was adjusted to load various amounts of the substrata per cm^2 of the surface, air-dried and irradiated for 30 min with the two 10-W UV lights which were placed by 30 cm apart from the surface. The lowest dose was 0.2 mg cm^{-2} (about 2–3 μm in thickness); c.f., thinner coatings with homogeneous thickness was technically difficult in the present coating method because of a subtle warp in the dishes. Immersion into 90% aqueous ethanol of the protein-coated substrata was often effective to fix the film on the glass and dish surfaces. The sterilized Dulbeco's phosphate buffer without Ma^{2+} and Ca^{2+} [PBS(−)] was then added to the protein-coated dishes with the depth of about 0.7 cm, allowed

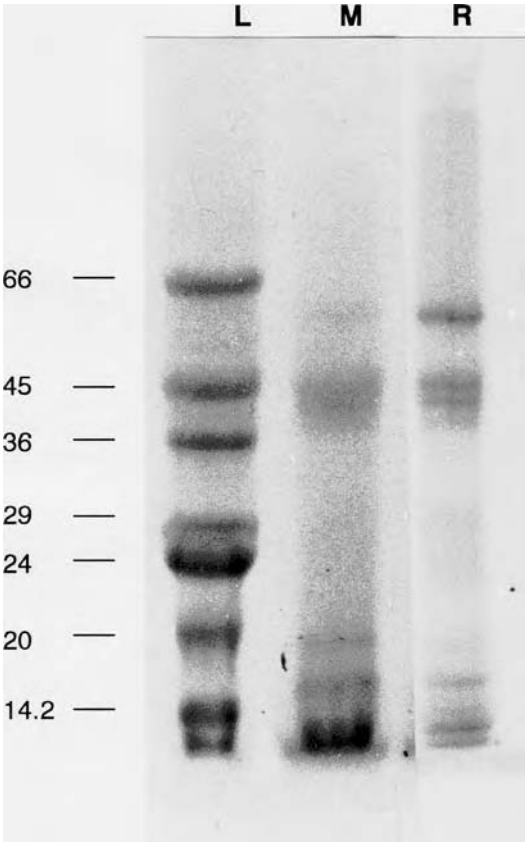

Figure 1. SDS-PAGE (10–15% gradient polyacrylamide gel; Pharmacia PhastGel; code 17-0517-01; pH 8.1/Tris-alanine). **L**: molecular weight markers (kD); **M**: (−SDS)-keratin; **R**: (+SDS)-keratin.

to stand at ambient temperature for 1 h and discarded. This washing process was repeated three times.

Method 2. The aqueous solutions of (+SDS)-keratin, (−SDS)-keratin, collagen and PVA were placed in 1 cm^2 on the cover glasses for optical microscopy (1.8 cm $\times$ 1.8 cm) and dried at 50°C. The (−SDS)-keratin gave a frosted glass-like coating while others afforded clear transparent coatings. The amount of the polymers per area was adjusted properly by loading calculated volume of the solutions on the glasses. The resulting coated glasses were immersed into 90% aqueous ethanol, then washed with PBS for 3 h followed by fresh PBS for 0, 24, and 48 h (designated as 3 h, 3 h + 24 h, and 3 h + 48 h in the text, respectively) and irradiated with the UV light in the manner similar to that mentioned above.

Cell culture

The fibroblast cells were routinely grown in MEM-E containing kanamycin (50 mg l^{-1}) and 10% fetal bovine serum (FBS; ICN Biochemicals) in 50 ml-plastic culture flasks

(Flow Laboratories). The cells were subcultured on about 7-day intervals and used within three- to five cycles of subculture.

Cultivation: cell adhesion and growth

A 1 : 9 v/v mixture of FBS and MEM-E medium was filtered and placed in (protein- and PVA-) uncoated and -coated substrata. The fibroblasts were detached from the culture flasks by 0.2% trypsin–0.02% EDTA at 37°C for 3–5 min, washed twice in a medium containing 10% FBS, collected by centrifugation at 100 rpm for 1 min, and 1.0×10^4 or 1.0×10^5 L929-cells/(cm^2 of the growth area) in 10% FBS were loaded to the dishes and maintained at 37°C in a humidified atmosphere of 5% CO_2 and 95% air. During cultivation, the cell proliferation was checked under a phase contrast microscope (Olympus, CK2, Japan). Some typical results are demonstrated in Fig. 2. After incubation for a certain period, the substrata were dip-rinsed twice in PBS(−) to remove the unadhered cells. The number of cells was counted in a chamber with Neubauer rulings and by assaying lactate dehydrogenase (LDH) activity, which was calibrated by the rulings, in the cells [7]. The representative growth curves on (+SDS)-keratin-coating and collagen-coating (both: 0.2 mg cm^{-2}, 3-h washing with PBS) are shown in Fig. 3. Figures 4a and b and 6a and b plot the cell numbers on various substrata relative to the cell number on glass (= reference substratum), where the cell-number on glass (without coating) was 1.4×10^4 and 3.1×10^4 at an incubation period of 1 and 24 h, respectively; c.f., we did not use commercially available tissue culture polystyrene as a reference because the plastic surface was specially and differently treated by each of the producers. Therefore, the actual cell-numbers on any substrata are given with the ratio $\times 1.4 \times 10^4$ or 3.1×10^4. Results of three to four runs were averaged; experimental error: $\pm 10\%$ in Figs 3, 4b and 6b and $\pm 25\%$ in Figs 4a, 5 and 6a.

RESULTS AND DISCUSSION

The L929 fibroblast cells did not grow on the bare polystyrene surface of the test dishes (for microbiological use); viz., they, despite in the presence of FBS, did not adhere to the dish but remained spherical to float in the culture medium. The cells grew neither on the cell-culture dish nor on the dish coated by the (−SDS)- and (+SDS)-keratins if the culture media did not contain FBS. By contrast, the cells could grow smoothly on the keratin-coated dishes in bipolar and sometimes multipod elongation in the presence of FBS. Any morphological abnormalities were not observed microscopically. Figure 2a and b displays typically the cultivation on the polystyrene dishes without and with the (+SDS)-keratin coating, respectively. It is most likely that some mediator proteins in FBS including those for cell-adhesion and growth overlayered first the protein-coating, enabling the seeded fibroblast cells for scaffolding and proliferating, presumably through interactions between fibroblast receptors and the corresponding ligands of the mediator. The similar phenomenon has often been observed on various protein-coated dishes [8–13]. A doubling rate on the keratin- and collagen-coating

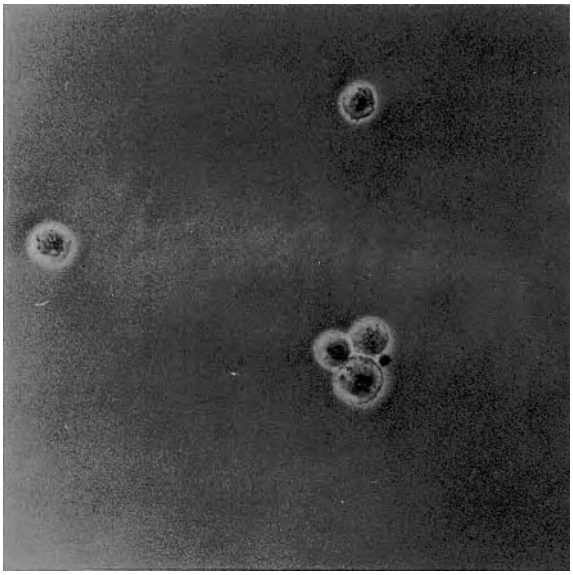

(a)

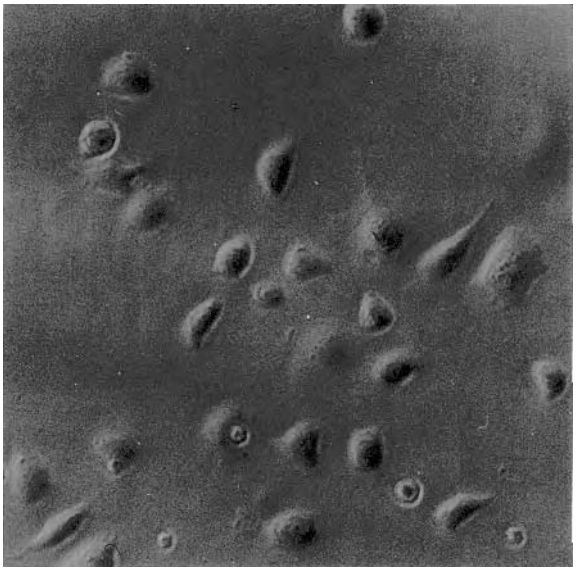

(b)

Figure 2. Phase-contrast micrographs of mouse fibroblast (L929) on various substrata at 37 °C with MEM containing 10% FBS. A number of the cells seeded initially were 1.0×10^4 cell cm^{-2} for (a) and (b) and 1.0×10^5 cell cm^{-2} for (c) and (d). (a) 24 h on the bare polystyrene-dish; (b) 6 h on (+SDS)-keratin-coated polystyrene dish (0.2 mg cm^{-2}; 3-h washing with PBS); (c) 24 h on (−SDS)-keratin-coated glass (0.8 mg cm^{-2}); and (d) 24 h on (+SDS)-keratin-coated glass (1.0 mg cm^{-2}; 3-h washing with PBS).

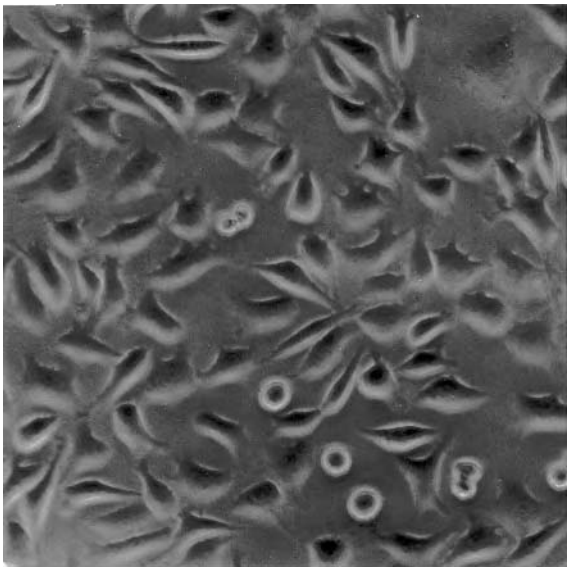

(c)

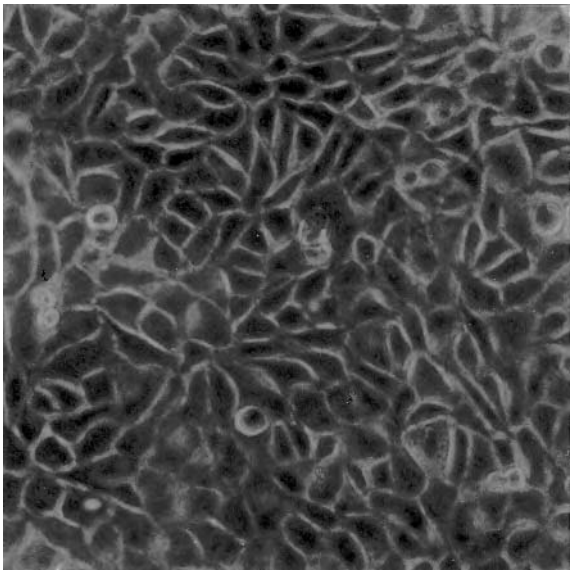

(d)

Figure 2. (Continued).

was about 23–25 h as seen in Fig. 3. With these aspects in mind, the cultivation of the L929 cells was studied on the matrices of the (−SDS)- and (+SDS)-keratins, collagen and PVA, which were coated on glass. The cells adhered and proliferated

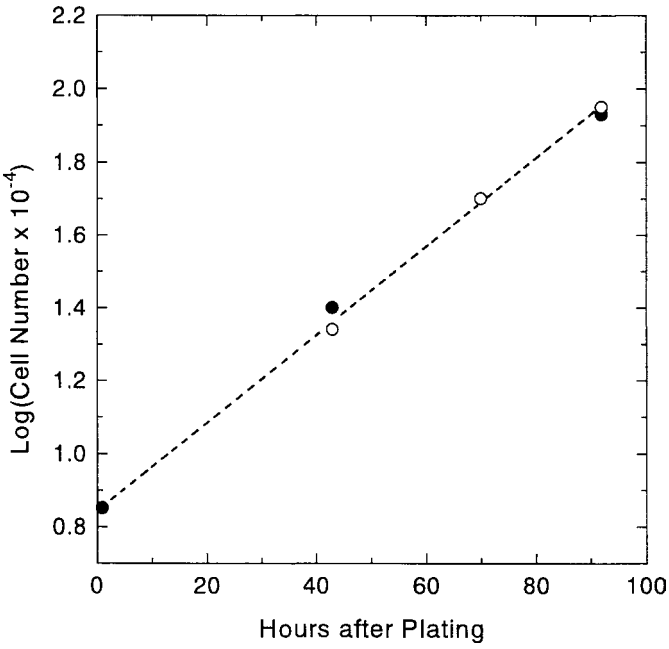

Figure 3. Growth curve on the glass coated by (+SDS)-keratins (0.2 mg cm^{-2}; washing with PBS for 3 h) (●) and collagen (0.2 mg cm^{-2}) (○). Mouse fibroblast cells (L929) were incubated at 37 °C using 1.0×10^4 cell cm^{-2} initially with MEM containing 10% FBS.

on the substrata were counted during incubation (chiefly at a period of 1 and 24 h after plating), and a cell-number ratio (on substrata/on glass) and a cell-number as a function of time were examined for the culture-specificity of the substrata. It has also been well established that glass itself was effective as a substratum perhaps due to adsorption of the mediator proteins onto the polar hydrophilic surface.

Now, the cell growth was virtually independent on an amount of the keratins loaded per area. Namely, the (−SDS)-keratin-coating of 0–1.0 mg cm^{-2} (= 0–*c*. 10 μm and 0–*c*. 14 μm in thickness when dry and wet, respectively) supported the cells to adhere and proliferate similarly as shown in Figs 2c, 4a and 4b (line (○)). Here, Fig. 4a may be considered to express the adhesiveness of the cells on various substrata at 1 h after plating (the culture assay data on *glass* at the condition of each spot was used as reference); or, there is better attachment on the keratin than on glass (control), collagen and PVA. Figure 4b, on the other hand, may be taken to display the proliferation specificity of the substrata after a culture period of 24 h (= approximately doubling time). It appeared that the keratin-coating (to about 1 mg cm^{-2}) was more effective than glass itself, the collagen- and PVA-coatings; Fig. 4b (line (○) vs lines (■) and (□)). No lag time for proliferation were observed for the keratin-immobilized surfaces. By contrast, the collagen surface, on the other hand, did not adhere the cells at least for 1 h after plating as shown in Fig. 4a (line (■)) though the time lag was much shorter than the lag (10–30 h) reported on artificial polymers such as poly(ethyleneterephthalate) and polyfluorocarbons [11].

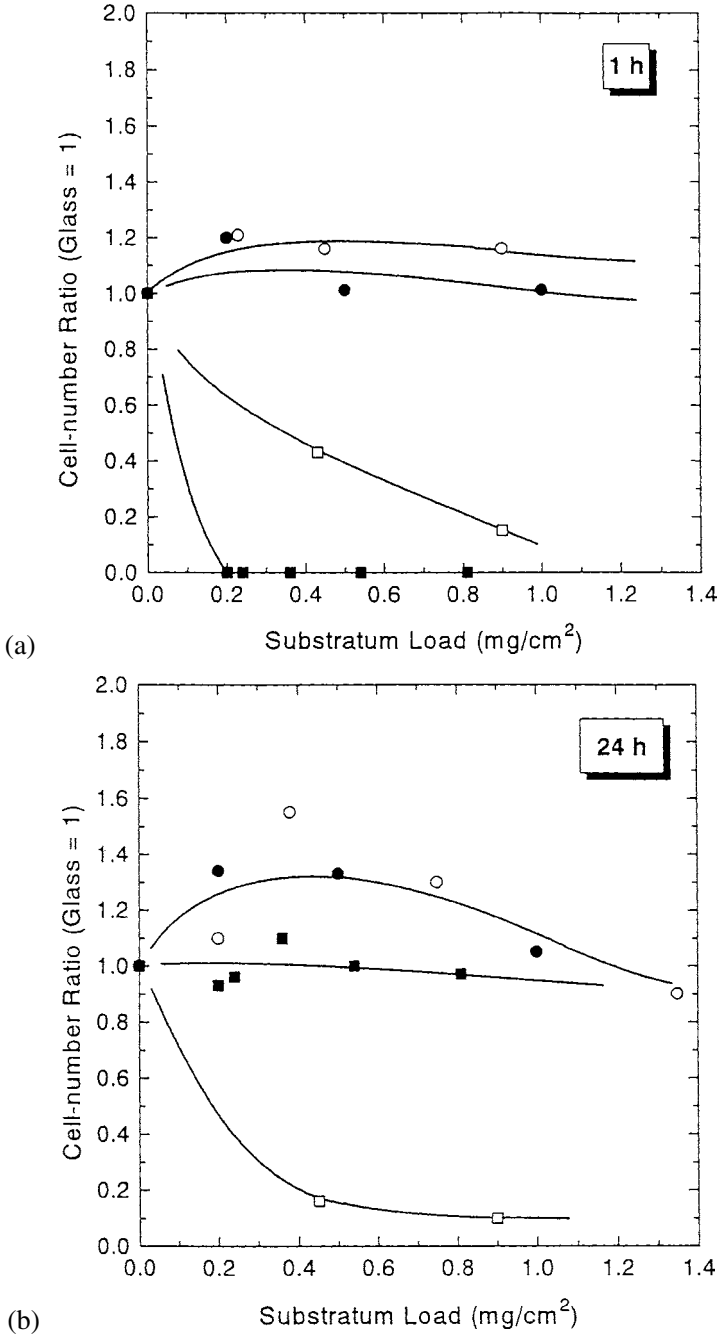

Figure 4. Relationship between the quantity of the substrata coated on glass with the cell number-ratios (= the number of cells on the substratum/the number of cells on the glass). Conditions: 1.0×10^5 cell cm^{-2} were plated at 37 °C in MEM containing 10% FBS. (○), (−SDS)-keratins; (●), (+SDS)-keratins (washing for 3 + 48 h); (■), collagen; (□), PVA. Panel (a) and (b): culture period of 1 and 24 h, respectively. The numbers of the cells found on glass over 1- and 24-h period was 1.4×10^4 and 3.0×10^4, respectively.

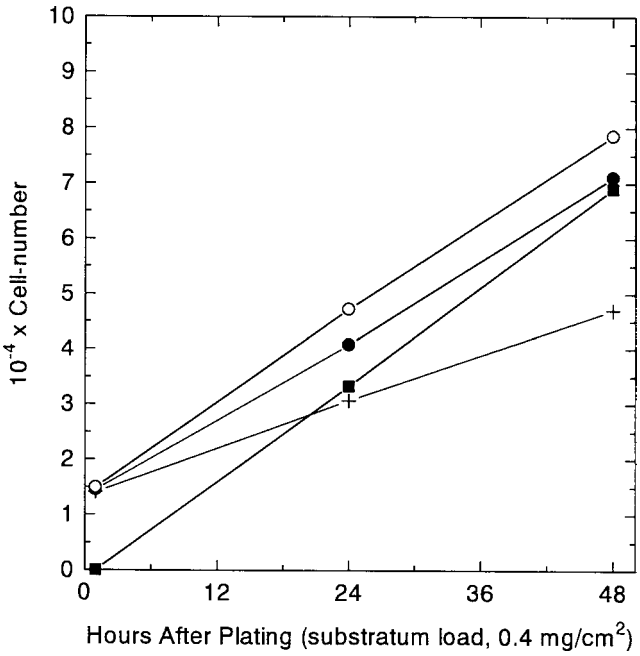

Figure 5. Growth curve on representative substratum surface (0.4 mg cm^{-2}) for fibroblast incubated at 37°C plating 1×10^5 cell cm^{-2} in MEM containing 10% FBS. (○), (−SDS)-keratins; (●), (+SDS)-keratins (washing for 3 h + 48 h); (■), collagen; (×), glass (reference).

The (+SDS)-keratin-coating, on the other hand, suppressed the proliferation of the cells, particularly significantly when the coating was thick and washing with PBS was brief (Fig. 6b, line (×) for 3-h washing). Most cells were spherical when the cell-number ratio (the ordinate in the graph) was less than about 0.5. Such observations may be ascribed to the toxicity of the residual SDS on the keratin coating [14]. Indeed, the cell growth and morphology were recovered to the levels of the (−SDS)-keratin after repeated washing with PBS; for instance, Fig. 6b: lines (○) and (●) for 3 h + 24 h and 3 h + 48 h washing, respectively. By contrast, the cell attachment on (+SDS)-keratin was not affected significantly by washing with PBS (Fig. 6a), being similar to that of (−SDS)-keratin (Fig. 4a, lines (○) and (●)).

The (−SDS)- and (+SDS)-keratins are not identical in SDS-PAGE and amino acid analysis (Fig. 1 and Table 1). Nonetheless, above results indicate that they are virtually indistinguishable in cell culture assay. The attachment and proliferation of the L929 cells on the keratin-coatings, which often exceeded those on collagen-coating, has not been understood. The keratins however, might be covered fast by mediator proteins from FBS to result in enhancing the cell attachment because the proteins consisted of a wide variety of amino acids and have many polar amino acids (Arg + Lys + His + Asp + Glu = about 27 mol%) in comparison with collagen (about 19%); c.f., Table 1. In addition, the recent study on the microfibril of wool keratins (8c-1 component) revealed the presence of an Arg^{328}–Gly–Asp sequence in the 2B region [3]. It has

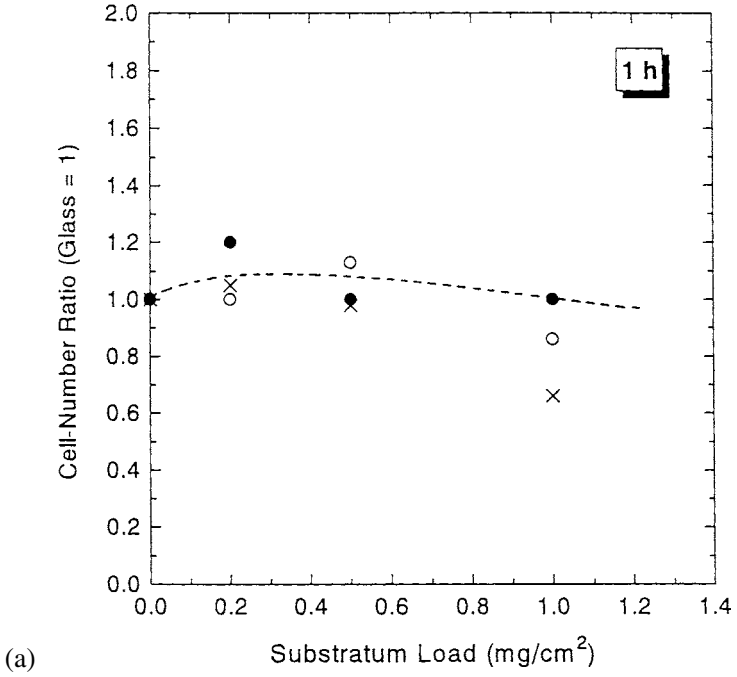

(a)

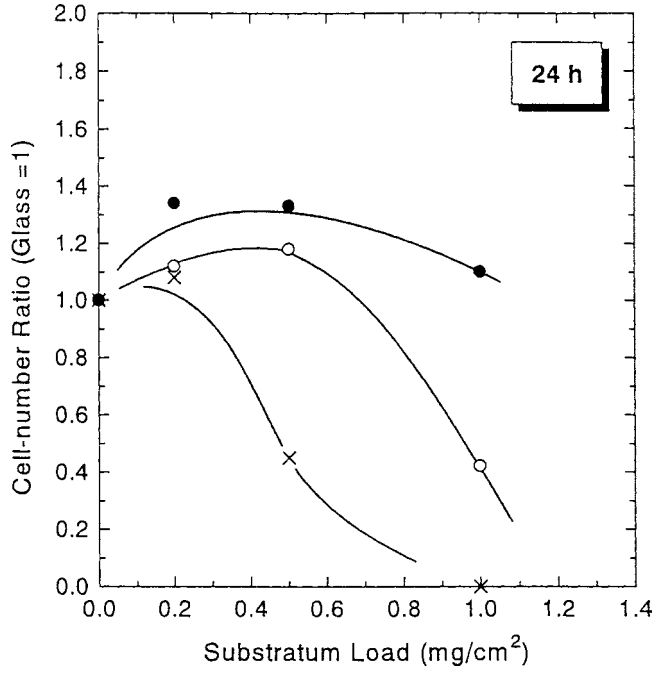

(b)

Figure 6. Effect of washing with PBS on the adhesion and growth of L929 cells. The abscissa and the ordinate are defined similarly as in the Fig. 4; (×), (○) and (●) for washing for 3 h, 3 h + 24 h and 3 h + 48 h, respectively. Panel (a) and (b): incubation period of 1 and 24 h, respectively. The numbers of the cells found after 1 and 24 h on glass are mentioned in the caption of Fig. 4.

been shown that the tripeptide sequence in fibrinogen, fibronectin, vitronectin, von Willebrand factor, silk fibroin is referred to the cell-binding site [15–18].

Before ending this section it would be worth noting that the keratin was extracted readily from wool, hair, etc. and could be polymerized readily by air oxidation into the membranes, films and sponges which were no longer soluble in aqueous media and organic solvents. These products were much higher in tensile strength and slower *in vitro* and *in vivo* biodegradation than those made of collagen and other proteinous materials [4]. From the present cell cultivation results and the unique physicochemical properties, the keratins may be considered as one of potential biomaterials.

REFERENCES

1. M. Feughelman, in: *Encyclopedia of Polymer Science and Engineering*, J. I. Kroschwitz (Ed.), Vol. 8, p. 566. Wiley, New York (1985).
2. W. G. Crewther, L. M. Dowling, P. M. Steinert and D. A. D. Parry, *Int. J. Biol. Macromol.* **5**, 267 (1983).
3. L. M. Dowling, W. G. Crewther and D. A. D. Parry, *Biochem. J.* **236**, 705 (1986).
4. K. Yamauchi, A. Yamauchi, T. Kusunoki, A. Khoda and Y. Konishi, *J. Biomed. Mater. Res.* **31**, 439 (1996).
5. H. Thomas, A. Conrads, K.-H. Phan, M. van de Löcht and H. Zahn, *Int. J. Biol. Macromol.* **8**, 258 (1986).
6. H. W. Heid, E. Werner and W. W. Franke, *Differentiation* **32**, 101 (1986).
7. K. Rubin, L. Kjellén and B. Öbrink, *Exp. Cell Res.* **109**, 413 (1977).
8. F. Grinnell, *Int. Rev. Cytol.* **53**, 65 (1978).
9. Y. Tamada and Y. Ikada, in: *Polymer in Medicine II*, E. Chiellini, P. Giusti, C. Migliaresi and L. Nicolais (Eds), p. 101. Plenum, London (1986).
10. Y. Yamada and Y. Ikada, *J. Colloid Interface Sci.* **155**, 334 (1993).
11. Y. Tamada and Y. Ikada, *J. Biomed. Mater. Res.* **28**, 783 (1994).
12. S. H. Albelda and C. A. Buck, *FASEB J.* **4**, 2868 (1990).
13. I.-K. Kang, Y. Ito, M. Shishido and Y. Imanishi, *J. Biomed. Mater. Res.* **23**, 223 (1989).
14. Ch. Gloxhuber, *Arch. Toxicol.* **32**, 245 (1974).
15. R. O. Hynes, *Scientific American* **254** (6), 32 (1986).
16. M. D. Pierschbacher and E. Ruoslahti, *Proc. Natl Acad. Sci. USA* **81**, 5985 (1984).
17. E. Ruoslahti and M. D. Pierschbacher, *Science* **238**, 491 (1987).
18. N. Minoura, S. Aiba, M. Higuchi, Y. Gotoh, M. Tsukuda and Y. Imai, *Biochem. Biophys. Res. Commun.* **208**, 511 (1995).

Section 4

Hydrogels

This page intentionally left blank

Polymers for Tissue Engineering, pp. 343–373
Molly S. Shoichet and Jeffrey A. Hubbell (Eds)

Heterogeneous PHPMA hydrogels for tissue repair and axonal regeneration in the injured spinal cord

S. WOERLY [1,*], E. PINET [1], L. DE ROBERTIS [1], M. BOUSMINA [2], G. LAROCHE [3], T. ROITBACK [4], L. VARGOVÁ [4] and E. SYKOVÁ [4]

[1] *Organogel Canada Ltd, 1400 Blvd. du Parc Technologique, Quebec City (Quebec), G1P 4R7 Canada*
[2] *Department of Chemical Engineering, Laval University, Quebec City (Quebec), G1K 7P4 Canada*
[3] *Quebec Biomaterial Institute, Quebec City (Quebec), G1L 3L5 Canada*
[4] *Department of Neuroscience, 2nd Medical Faculty, Charles University, and Institute of Experimental Medicine, Academy of Sciences of the Czech Republic, Prague, Czech Republic*

Received 12 June 1997; accepted 14 January 1998

Abstract—A biocompatible heterogeneous hydrogel of poly[*N*-(2-hydroxypropyl) methacrylamide] (PHPMA) showing an open porous structure, viscoelastic properties similar to the neural tissue and a large surface area available for cell interaction, was evaluated for its ability to promote tissue repair and axonal regeneration in the transected rat spinal cord. After implantation, the polymer hydrogel could correctly bridge the tissue defect, form a permissive interface with the host tissue to favour cell ingrowth, angiogenesis and axonal growth occurred within the microstructure of the network. Within 3 months the polymer implant was invaded by host derived tissue, glial cells, blood vessels and axons penetrated the hydrogel implant. Such polymer hydrogel matrices which show neuroinductive and neuroconductive properties have the potential to repair tissue defects in the central nervous system by promoting the formation of a tissue matrix and axonal growth by replacing the lost of tissue.

Key words: Hydrogel; rheology; porosimetry; infrared spectroscopy; scanning electron microscopy; neural tissue; immunocytochemistry; spinal cord; regeneration.

INTRODUCTION

Tissue destruction or tissue loss of the central nervous system (CNS), resulting from elective surgery such as oncological surgery or resection of scarring or necrotic tissue, is associated with interruption of axonal pathways and clinical functional deficits. For example, severe injury of the spinal cord results in the formation of complex scar tissue that prevents regenerating axons to traverse the lesion, resulting

*To whom correspondence should be addressed. E-mail: woerlyst@organogel.com

in paraplegia and tetraplegia [1], and inducing axon of spinal tracts to regenerate requires first to remove the scarring tissue. Reconstruction of damaged parts of the CNS would therefore require methods to be developed to reform a tissue structure into an integrated tissue-to-organ with the various CNS cell constituents that include glia cells, mesenchymal cells, blood vessels, extracellular matrix components, and regenerated nerve fibres. This is because in most vertebrates including human, the capacity for regeneration in the CNS is very limited [2], and restoration of a tissue framework and axonal pathways of the white and grey matter at the end-point cannot be achieved [3, 4]. To overcome this problem, cell and tissue grafts have been investigated for more than a century to replace tissue in the lesioned CNS, both at the experimental and clinical level [5, 6]. Thus, syngenic autograft or homograft, allograft or xenograft, such as foetal neural tissue [7] Schwann cells and sensory neurones [8] and immature astrocytes [9] have been transplanted into the lesioned CNS. A new approach is being developed for restoration of lost cells in the CNS which use isolated precursors of neural tissue cells [10], genetically modified donor cells [11], and immortalized cell lines [12]. Peripheral nerve segments including cultured non-neuronal cells [13] or embryonic neural tissue cells [14] have also been grafted. Natural polymer matrices have shown to be useful in the reconstructive approach of the CNS tissue, such as collagen matrices [15, 16] containing neuroactive agents [17, 18], or including neural grafts [19], Schwann cells [20], or composite collagen matrices [21]. More recently, synthetic biomaterials have been used as an attempt to induce cell and tissue growth in the injured CNS, including nitocellulose membranes [22], tubes of poly(acrylonitrile–vinylchloride), alone [23] or modified with poly(ethylene oxide) [24], tubes of polycarbonate [25, 26] or of nitrocellulose [27] and biodegradable polylactide implants [28].

An entirely new approach to promote tissue repair in the CNS involves the use of synthetic polymer hydrogels as support matrices to help regenerate tissue structure from the cellular post-injury response [29–32]. Hence, in contrast to current cell and tissue grafting technology, this approach is based on tissue repair by manipulating the healing process of the wound in such a way as to promote the formation of a new tissue structure within the polymer matrix. Hydrogels are water-swollen networks of hydrophilic homopolymers or copolymers and are currently utilized for a variety of biomedical applications [33]. Properties of hydrogels such as permeability to small molecules, viscoelastic behavior, low interfacial tension with biological fluids and stability make these materials suitable for implantation in soft tissue [34]. In addition, the design of macromolecular structures with physical properties needed for establishing a permissive interface, mobilizing the host's tissue cells, and stimulating tissue remodelling without mechanical injury at the host tissue interface are required when hydrogels are being contemplated for tissue replacement. Thus, a large specific surface areas available for cell interactions, a high fractional porosity of hydrogels and mechanical properties that match those of the host tissue are favourable characteristics for promoting tissue ingrowth into the hydrogel structure. In addition, pore size distribution and communication between

pores are important structural properties for cell loading and tissue expansion within the polymer matrix. These structural properties are controlled by the polymerisation process of the molecular subunits [35, 36].

This paper presents results of a heterogeneous poly[*N*-(2-hydroxypropyl)methacrylamide] (PHPMA) hydrogel with defined porosity and mechanical properties for promoting tissue repair and axonal regeneration in the CNS. The PHPMA hydrogel was characterized for its porous structure, diffusion and mechanical properties, and network topology. This polymer hydrogel was evaluated in the transected spinal cord for its capacity to bridge between the cut ends of transected spinal cord, and to provide a substrate for tissue ingrowth, angiogenesis, and axonal regeneration. Our results show that the PHPMA hydrogels can correctly bridge the tissue defect created in the spinal cord, initiate tissue formation and axonal regeneration without the addition of exogenous neuroactive factors, resulting in improvement of locomotor functional recovery in some animals.

METHODS

Preparation of PHPMA hydrogels

Macroporous hydrogels were prepared from *N*-(2-hydroxypropyl)methacrylamide (HPMA) (synthesis of HPMA was previously described, see ref. [37]) by heterophase separation using radical polymerization in a pore-forming solvent with a divinyl cross-linking agent. The reaction was carried out in sealed nitrogen atmosphere ampoules. After polymerization, the xerogels were removed from the ampoules and were allowed to swell in ethanol. The white spongy hydrogels were washed with distilled water. The eluates leached out of the gels were exchanged for fresh water every day for 2 weeks. All procedures were carried out in a flow cabinet. The eluates were concentrated by vacuum evaporation at 60°C and separated by HPLC on a Waters LCM1 + system using NovaPack-C18 (Waters) analytical reverse phase column with methanol/water 25/75 at 1 ml min^{-1} with an absorption detection at $\lambda = 210$ nm. The decrease of the monomer leached out of the gels was quantified from the chromatogram peak area using HPMA standard samples.

Characterisation of PHPMA hydrogels

Equilibrium water content (EWC). Gel disks were equilibrated in deionized water at room temperature for 1 week. The gels were blotted with laboratory tissue (to remove surface water), weighed, dried under vacuum at room temperature, and weighed again. The swelling capacity was determined as the mass ratio of water to swollen gel according to the equation:

$$\frac{W_s - W_d}{W_s} \times 100,$$

where W_s is the weight of the swollen gel and W_d the weight of the dried gel. Swelling was calculated as the mean of at least five measurements of different gel samples.

Scanning electron microscopy. The structure of the gel was examined by scanning electron microscopy after drying the gel using 1,1,1,3,3,3-hexamethyldisilazane (HMDS) [38]. The swollen gel was dehydrated through a graded series of ethanol solutions of 70, 85, 95, and 100% for 30 min each. The gel was then immersed in HMDS and air dried in a flow cabinet at room temperature. The dried gel was fractured using an razor blade and was mounted on stubs with colloidal graphite and sputter-coated with gold to an approximate thickness of 200 Å. The surface and the bulk of gels were examined with a Jeol T 300 scanning electron microscope using an accelerating voltage of 15 kV.

Mercury porosimetry. The porosity (pore size distribution and cumulative intruded pore volume) and surface area were determined by mercury porosimetry using a PoreSizer 9329 (Micromeritics) both with a low-pressure and a high-pressure regime. The porosity was measured on freeze-dried samples and the pore diameter, D, was calculated using the Washburn equation [39]:

$$\mathrm{D} = -\frac{4\gamma \cos\theta}{P}, \tag{1}$$

where P is the applied pressure, θ the contact angle (130 deg) and γ the surface tension (485 dyn cm^{-1}) of mercury. The intrusion volume was recorded for pressure ranging from 0 to 30 000 psia. The intrusion is the ratio of the injected mercury volume to the volume of the gel. Cumulative intrusion and pore size (log differential intrusion) distribution were plotted on semilogarithmic co-ordinates. Porosity was calculated using the equation:

$$\frac{d_s - d_b}{d_s} \times 100,$$

where d_s is the skeletal density of the dried gel (derived from gel volume with exclusion of the volume of the samples's pore structure) and d_b is the bulk density of the dried gel (derived from gel volume that includes the volume of the sample's pore structure).

Surface area (i.e. pore wall surface) was computed on the basis of the applied pressure vs intruded volume of mercury using the following equation [40]:

$$A = -\frac{\int_0^{V_{\max}} P \, \mathrm{d}V}{\gamma \cos\theta}. \tag{2}$$

In order to determine the pore distribution domains of the hydrogel, the critical pressure P_c, i.e. the minimum pressure required to intrude the largest pore, was

determined using the following equation [41]:

$$\ln\big[V(\infty) - V(P)\big] = \ln\big[V(\infty) - V(P_c)\big] - m\big[\ln(P) - \ln(P_c)\big], \qquad (3)$$

where $V(\infty)$ is the volume of intruded mercury at the maximum intrusion pressure and $V(P)$ the volume of intruded mercury at pressure P, and m is the slope of the graph.

Rheological measurement. Mechanical properties were measured for both the PHPMA hydrogel and recently sliced rat brain samples. Due to their weak mechanical properties (low modulus) and their sensitive structure, the materials were tested in a dynamic regime at small amplitudes of deformation.

Small-amplitude oscillatory shear measurements were carried out on a Bohlin-CVO constant stress rheometer in parallel-plate geometry. A special cylindrical cell with a serrated bottom plate was designed to run measurements in a liquid environment. The sample (hydrogel or neural tissue) was cut into disks of 15 mm in diameter and 1.3 mm in thickness and then introduced in the cylindrical cell and slightly compressed by the upper serrated plate to create a fixed gap. A gap of 1.1 mm was chosen to compare the mechanical properties of the gel and the rat brain. In addition, successive oscillatory shear measurements were carried out on the gel subjected to compression and decompression cycles. Starting at 1.1 mm, the gel was smoothly compressed to 1.05, 1.0, 0.95, and 0.9 mm and was subjected to oscillatory shear for each gap. After each compression the sample was left for 5–15 min to ensure osmotic equilibrium between the solution and the gel prior to testing. The cell was filled with a saline solution (0.9% NaCl) prior to testing and all experiments were conducted at 37°C. To avoid evaporation of the solution the cylinder was isolated with a Teflon cover. The frequency was varied from 0.01 to 100 rad s^{-1}. Stress sweep measurements were first conducted to delimit the region of linear viscoelasticity, that is the stress, τ^*, is proportional to the strain, γ^*. Depending on the frequency range, the stress was adjusted so that the rheological behavior was linear viscoelastic. Care was taken to impose adequate stresses so that the resulting strains were small enough and did not break the structure of the gel. Oscillatory shear tests were carried out from higher to lower frequencies, and the sample stability was verified by reproducing higher frequency measurements. Each measurement was repeated three times and the accuracy of the reported data is believed to be within $\pm 5\%$. Under small harmonic strains, the ratio of the stress to the strain is independent of the imposed strain [42].

$$G^*(\omega) = \frac{\tau^*(t)}{\gamma^*(t)} = G'(\omega) + iG''(\omega), \qquad (4)$$

which means that the stress is a linear function of strain (domain of linear viscoelasticity). $G^*(\omega)$ is the complex shear modulus; $G'(\omega)$ is called the storage

modulus and represents the elastic contribution and $G''(\omega)$ the loss modulus and represents the viscous contribution to the viscoelastic behavior of the material. The complex dynamic viscosity is obtained by the ratio:

$$\eta^*(\omega) = \frac{G^*(\omega)}{i\omega}. \tag{5}$$

Tetramethylammonium (TMA^+) diffusion measurements. TMA^+-selective microelectrodes were used to measure diffusion properties in the hydrogel. The ion-selective microelectrodes for TMA^+ were made from double-barrel tubing as described elsewhere [43]. The ion-exchanger was a Corning 477317, and the ion-sensing barrel was back-filled with 100 mM TMA chloride while the reference barrel contained 150 mM NaCl. Electrodes were calibrated using the fixed-interference method in a sequence of flowing solutions. Calibration data were fitted with the Nikolsky equation to determine electrode slope and interference. The shank of the iontophoresis pipette was bent, so that it could be aligned parallel to that of the ISM. Electrode arrays were made by gluing together an iontophoresis pipette and a TMA^+-selective microelectrode with a tip separation of 140–200 mm. Iontophoresis parameters were a +20 nA bias current (continuously applied to maintain a constant electrode transport number) and a +100 nA current step of 60 s duration to generate a TMA^+ diffusion curve.

TMA^+ diffusion curves were recorded with a PC-based Pentium computer and analysed by fitting the data to a solution of the diffusion equation [44]. TMA^+ concentration vs time curves were first recorded in 0.3% agar gel (Agar Noble, Difco, Detroit, MI, USA) made up in 150 mM NaCl, 3 mM KCl and 1 mM TMA^+. The diffusion curves in agar were used to determine the electrode transport number, n, and free TMA^+ diffusion coefficient, D ($cm^2\,s^{-1}$). Diffusion curves were then recorded in a non-implanted hydrogel or in the brain and analysed to yield a value of α, the TMA^+ apparent diffusion coefficient in gel, ADC_{TMA} ($cm^2\,s^{-1}$), λ and non-specific TMA^+ uptake, k' (s^{-1}). Volume fraction (α) is the restricted volume of the tissue or hydrogel which is available for diffusion. Tortuosity is the effective path length for diffusion of particles between two points due to various obstacles in the tissue or hydrogel which slow down the diffusion of molecules. It is a geometrical factor calculated as $= (D/ADC_{TMA})^{0.5}$. These parameters were extracted by a nonlinear curve-fitting simplex algorithm operating on the diffusion curve described by Eq. (6), which represents the behavior of TMA^+, assuming that it spreads out with spherical symmetry, when the iontophoresis current is applied for duration S [44]. In this expression, C is the concentration of TMA^+ at time t and distance r. The equation governing diffusion is:

$$\begin{aligned} C &= G(t) && t < S \text{ for the rising phase of the curve,} \\ C &= G(t) - G(t-S) && t > S \text{ for the falling phase of the curve.} \end{aligned}$$

The function $G(u)$ is evaluated by substituting t or $t - S$ for u in the following equation:

$$G(u) = \left(Q\lambda^2/8\pi D\alpha r\right)\left\{ \exp\left[r\lambda(k'/D)^{1/2}\right]\mathrm{erfc}\left[r\lambda/2(Du)^{1/2} + (k'u)^{1/2}\right] + \exp\left[- r\lambda(k'/D)^{1/2}\right]\mathrm{erfc}\left[r\lambda/2(Du)^{1/2} - (k'u)^{1/2}\right]\right\}. \quad (6)$$

The quantity of TMA^+ delivered per second is $Q = In/zF$, where I is the step increase in current applied to the iontophoresis electrode, n is the transport number, z is the number of charges associated with substance iontophoresed (+1 here) and F is Faraday's electrochemical equivalent. The function 'efrc' is the complementary error function. When the experimental medium is agar, by definition, $\alpha = 1 = \lambda$ and $k' = 0$, and the parameters n and D are extracted by curve fitting. Knowing n and D, the parameters α, λ (D free solution/ D in hydrogel) and k' can be obtained.

Implantation study

The hydrated polymer gels were sterilized in boiling water. Twenty Sprague Dawley rats (200–250 g) were used. The animals were anesthesized by an intraperitoneal injection of ketamine hydrochloride (87 mg ml^{-1}) and xylazine (13 mg ml^{-1}). Using aseptic surgical techniques, the animals underwent a laminectomy at the thoracic level T9 as previously described [15]. The exposed spinal cord was thoroughly irrigated with a cold saline solution prior to transection. A cordotomy was performed using microscisors, and a 2-mm spinal tissue segment was removed. Following spontaneous hemostasis, excess clot was washed from the cavity with a chilled saline solution. The hydrogel implant was sized to adapt to the dimension and shape of the cavity and was inserted into the lesion cavity ensuring a complete apposition of the polymer surface with the surfaces of the spinal stumps (this was verified under the surgical microscope at high magnification). The muscles were sutured and the skin closed with wound clips. After surgery the rats received an intramuscular injection of penicillin G (10 000 U) and a subcutaneous injection of an antalgic (buprenorphine, 0.05 mg kg^{-1}). Bladder expression was performed twice a day until recovery of sphincter control. During the first week, the rats were given tetracycline in drinking water to prevent urinary tract infection. The animals were observed daily for spontaneous recovery of locomotor activity and postural functions of their hindlimbs during overground locomotion.

Tissue processing

The animals were allowed to survive from 3 days to 20 weeks (Table 1). The animals were anaesthetised and perfused through the heart with a phosphate buffer saline (PBS) containing heparin followed with paraformaldehyde (4% solution in 0.1 M PBS). The spinal cords were removed and transferred to PBS–sucrose 30% for 24 h. After rincage in PBS, 1 cm tissue blocks including the gel implant were embedded in egg yolk that was allowed to harden with formalin vapour. The blocks were cut into 40-μm thick frozen horizontal sections for immunostaining with the following

Table 1.
Numbers of animals at the different survival times

Survival	No.	Experimental groups
3 days	1	Hydrogel implant
1 week	5	Hydrogel implant[a]
5 weeks	2	Hydrogel implant
5 weeks	2	Control transection
12 weeks	6	Hydrogel implant[a]
12 weeks	2	Control transection
20 weeks	5	Hydrogel implant[a]
Total	23	

[a] Animals were lost which were not used for morphological studies.

antibodies: Glial Fibrillary Acidic Protein (GFAP, Dako, 1 : 100), neurofilaments 200 (Sigma, 1 : 75), and fibronectin (1 : 100). The sections were washed 3 × 10 min in Dulbecco's phosphate buffered saline (DPBS) containing 0.1% bovine serum albumin (BSA, Sigma) and 0.2% Triton, then pre-incubated at room temperature for 30 min with 1% swine serum (Laval University) or 1% rabbit serum (Sigma). Sections were incubated with the appropriate antibodies diluted in DPBS-BSA-Triton, and after washing in DPBS (3 × 10 min), sections were further incubated with anti-rabbit TRITC (1 : 30) or anti-mouse TRITC (1 : 30) at room temperature for 3 h. The sections were washed again in DPBS (3 × 10 min) and mounted onto subbed slides and coverslipped using Citifluor. Additional sections were processed for silver impregnation using the Holmes technique.

Image analysis

The implantation site was characterized quantitatively. Eleven horizontal tissue sections were selected to be examined with a 10 × objective through the largest transverse diameter of the cord of spinal cords ($n = 6$) to visualize in bright field the entire implantation site, using a CCD video camera attached to a Nikon microscope and a high resolution Trinitron monitor. The images were digitized and image analysis measurements were performed at constant microscope settings with a Bioquant System. The total area of implant, the perimeter of the polymer that interfaces with the host tissue were determined.

Scanning electron microscopy

Three-month explanted hydrogels were viewed under scanning electron microscopy. The spinal cord containing the gel implants were fixed in 2.5% glutaraldehyde, washed and postfixed in osmium tetroxide (1%) for 2 h, and dehydrated through a graded series of ethanol. The samples were dried using HMDS and processed for scanning microscopy as described above.

Attenuated total reflection–Fourier transform infrared (ATR-FTIR) spectroscopy

Three month-explanted hydrogels, fixed spinal cord tissue and non implanted hydrogels (control) were analysed by ATR-FTIR. Infrared (IR) spectra were recorded with a Nicolet Magna-550 Fourier transform infrared spectrometer with a DTGS detector and a germanium coated KBr beamsplitter. Two hundred and fifty scans were acquired with an optical retardation of 0.25 cm, triangularly apodized and Fourier transformed to yield a 4-cm^{-1} resolution. The attenuated total reflectance (ATR) mode was used for recording the infrared spectra of the hydrogel samples with a Split Pea attachment (Harrick Scientific Corporation) equipped with a Si hemispherical, 3 mm diameter internal reflection element (IRE). The IRE is bevelled on the edge of its flat surface to provide a sampling area slightly larger than the 150–200 μm diameter hot spot on the crystal.

RESULTS

Hydrogel characteristics

The hydrogels were opaque and the water fraction represented 95.66% of the swollen weight of the hydrogel. The high water content and the high fractional porosity of the PHPMA hydrogel were also confirmed by thermogravimetry (not shown) and porosimetry (*vide infra*). Under scanning electron microscopy the PHPMA gels demonstrate a macrophase separated structure. The bulk of the gel constituted a colloidal-type structure forming a three-dimensional network of microspheres of 3–5 μm in loosely-packed contact (Fig. 1A). The limit of the pore system was represented by the contiguity of the surface of the spheres, while the effective surface area of the hydrogel was a function of the mesopores present at the surface of the spheres (Fig. 1B). The voids constituted an extensive open interconnected pore system corresponding to non-circular macropores delimited by the surface of the spheres, while the geometry and the topology of the pore space was represented by the spatial arrangement of the sphere network.

Diffusion measurements showed that TMA^+ diffusion parameters — volume fraction α and tortuosity λ — in hydrogels differ from those in diluted agar gel where there is a free diffusion and, therefore, $\alpha = 1 = \lambda$ and $k' = 0$. In polymer hydrogels the mean values (mean $\pm$ SEM, $n = 14$, at 20°C) were: $\alpha = 0.80 \pm 0.013$ ($p_2 < 0.0001$), $\lambda = 1.13 \pm 0.008$ ($p_2 < 0.0001$) and $k' = 8.48 \times 10^{-6}$ $cm^2\,s^{-1}$. It is, therefore, evident that the diffusion of a rather small molecule such as TMA^+ (molecular mass of 74 Da) is more hindered in polymer hydrogels than in diluted agar. The diffusion of small molecules is however much less hindered than in nervous tissue where typical values of $\alpha = 0.20$ and of $\lambda = 1.5$ [45].

Figure 2 shows the rate of release of HPMA compounds from a xerogel–hydrogel system in ethanol and in water. Most of the low molecular weight compounds were washed out within 5 days. After 3 days, 98% of total unreacted HPMA and oligomers were removed as well as unreacted and decomposition products of

(A)

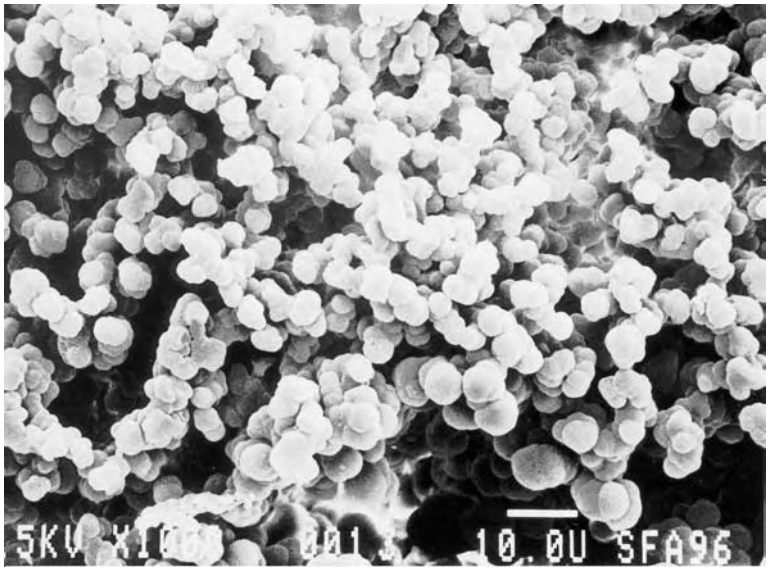

(B)

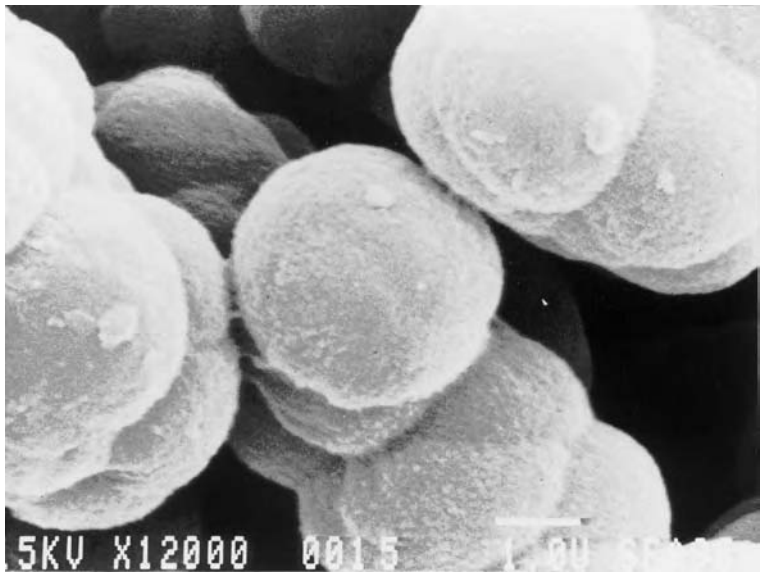

Figure 1. (A) Scanning electron microscopy micrograph of a cross-section of a PHPMA hydrogel showing the structure of the macromolecular network constituted by cross-linked polymer microspheres of 3–5 μm in diameter and the associated porous structure. (B) High power scanning electron microscopy of the PHPMA hydrogel showing the 'orange peel' aspect of the surface of the microspheres, corresponding to the mesopore scale.

initiator. After 2 weeks no trace of HPMA compounds could be detected by UV absorption during the HPLC separation. The hydrogels were thus considered free of low molecular weight compounds for implantation.

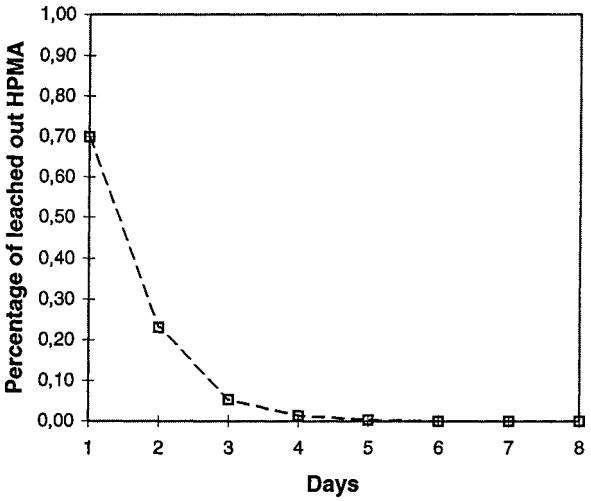

Figure 2. Kinetics of the release of HPMA products from the xerogel–hydrogel system during washing.

Table 2.
Characteristics of the porous structure of the PHPMA hydrogel

	Pore diameter (μm)		
	1–10	10–50	50–300
Pore volume (%)	8.77	78.70	11.47

Pore structure characterization of the PHPMA heterogeneous hydrogels by mercury porosimetry revealed a large void volume (cumulative intruded volume of mercury to the volume of the gel) corresponding to a fractional porosity of $89 \pm 2\%$ ($n = 46$) and a median pore diameter of 22 ± 3 μm ($n = 46$). The largest fraction of the total pore volume of the gel is occupied by a pore regime of 10–50 μm (Table 2). The pore structure of the hydrogel was defined by the surface of the polymer microspheres, forming an open interconnected porous system. The intrusion curve of mercury (Fig. 3A) shows that the hydrogel was hyperporous from 23 μm (fractional porosity for pores larger than 23 μm and which occupy at least 50% of the gel volume) and macroporous with pores extending up to 300 μm. The sigmoid shape of the intrusion curve indicated that the internal pore structure of the PHPMA gel was fairly homogeneous in macro and mesopore domains, corresponding to a log-normal distribution (Gaussian distribution of the logarithm of diameter) (Fig. 3B). Mercury extrusion from pores upon reduction of pressure indicated the existence of a hysteresis between the intrusion and retraction curves due to the entrapment of mercury within the network (Fig. 3A). Pore wall surface area in the range of macropores and mesopores, up to 0.006 μm, shows a value of 40 ± 8 $m^2\,g^{-1}$ ($n = 46$) (Fig. 3C). There was no significant surface detectable above 30 μm. Figure 3C

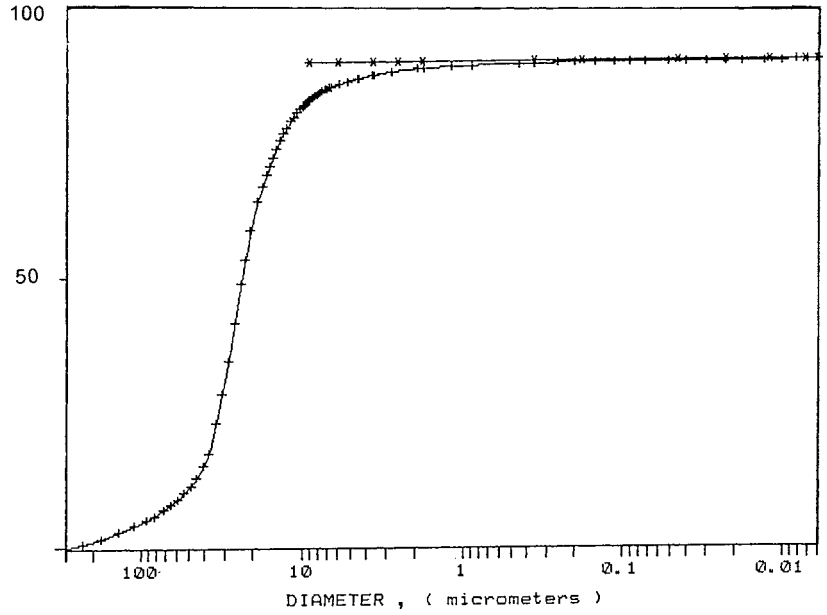

(A)

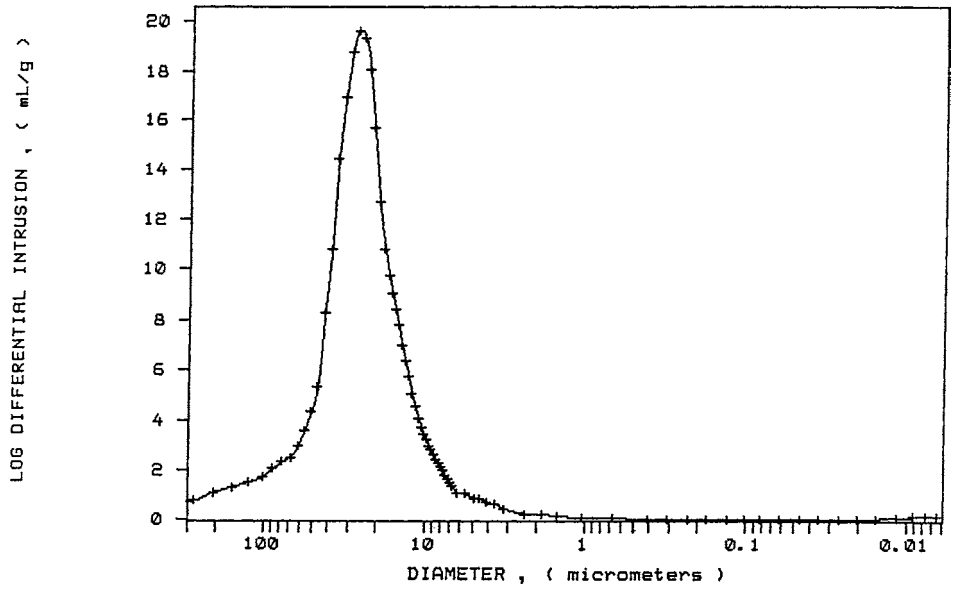

(B)

Figure 3. (A) Mercury porosimetry intrusion–extrusion plots of a PHPMA hydrogel, expressed as a percentage of the intruded–extruded volume of mercury against pore diameter. (B) Plot of pore size distribution (log differential intrusion) against diameter of PHPMA hydrogel. (C) Plot of the cumulative surface pore area of a PHPMA hydrogel against pore diameter. (D) Corrected volume log–log volume plot of a PHPMA gel from intrusion parameters.

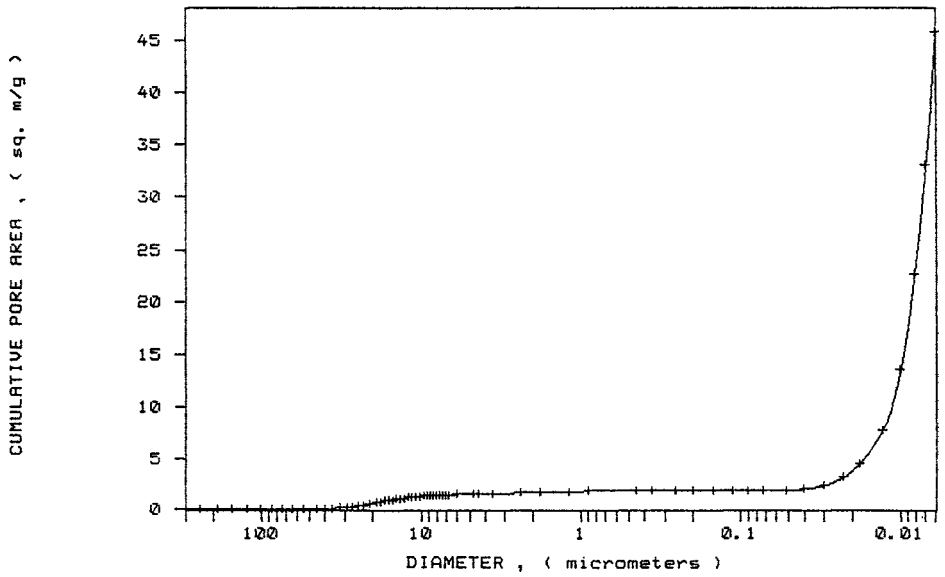

(C)

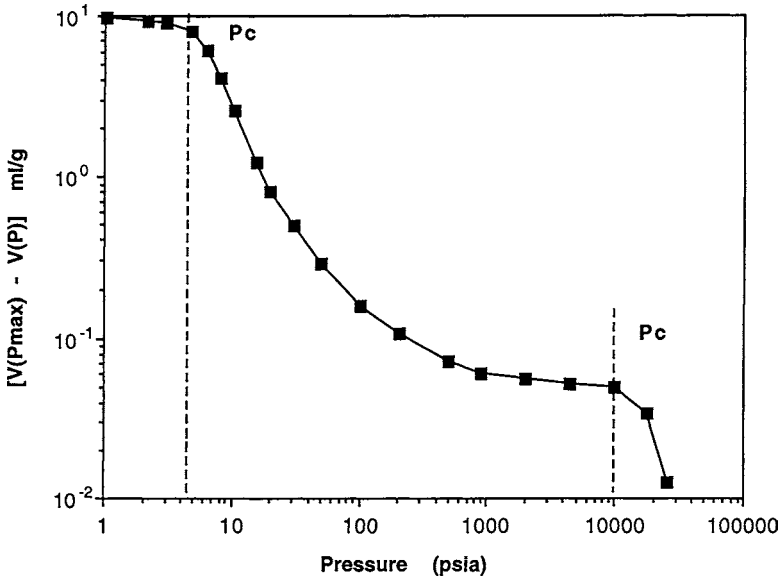

(D)

Figure 3. (Continued).

shows two discontinuities corresponding to an increase of the pore area; at 20 μm and at the upper mesopores (20 nm). The sharp increase of the surface area observed at upper mesopores represented 85% of the total surface of pore area within the range of pores intruded. These results are substantiated in Fig. 3D which shows

the two corresponding critical breakthrough pressures at 5 and 10 000 psia with a sharp decrease in the intrusion slope. This indicates that the hydrogel has two porous domains with two distinct pore distributions; between 5 and 1000 psia and pores intruded between 10 000 and 30 000 psia.

Rheological measurements aimed at characterizing the mechanical behavior of the gel with respect to the CNS tissue, and the intrinsic mechanical properties of the swollen gel network subjected to compression and decompression cycles. The dynamic moduli G' and G'' of the gel are shown in Fig. 4A. The figure shows that the gel typically exhibits a solid-like behavior $G' \gg G''$ [46] with constant elastic modulus ($G' \approx 2600$ Pa). Figure 4B shows the linear viscoelastic functions G^* and η^* of the gel and of the rat brain. This figure shows that the gel and the brain tissue have similar behaviors, that is a constant G^* and an increasing η^* as the frequency is decreasing. Since G^* is constant over the whole frequency range, η^* varies linearly as a function of ω with a slope -1 for both materials (see Eq. 5). A difference in absolute values of G^* and η^* are however observed.

The results of the experiments shown in the previous figures were carried out using the same gap of the gel and the brain in equilibrium with the 0.9% NaCl solution. The question then arises to what extent the solution in contact with the gel may affect its rheological behavior. To clarify this point, successive oscillatory shear measurements were carried out on the same gel at different gaps and the results for the compression/decompression process are shown in Fig. 4C. This figure shows that G^* clearly increases as the gap decreases. This can be explained by the fact that the solution entrapped in the gel slips out by the squeezing flow generated by compression. This for small gaps, the proportion of the solid phase in the swollen network increases, yielding to an increase of the mechanical properties of the gel. The process seems to be reversible. In fact decompression from 0.9 to 1.1 mm by 0.1 mm steps gave similar results as those obtained during compression as evidenced by Fig. 4C. This suggests that the structure of the gel was not disturbed, at least at the sensitivity of the rheometer's transducer, by compression and decompression cycles. Then it is reasonable to assume that the total complex modulus, G^*, of the swollen gel can be written as a function of the complex moduli of the two contributions, G^*_s and G^*_{dg}, as follows:

$$G^* = \varphi G^*_s + (1 - \varphi) G^*_{dg}. \tag{7}$$

G^*_s and G^*_{dg} are the complex moduli of the solution and the dry gel, respectively, φ is the volume fraction of the solution entrapped in the gel and is directly proportional to the gap h ($\varphi = ah, a$ being the constant of proportionality). Equation (7) can then be written in the following form:

$$G^* = ah(G^*_s - G^*_{dg}) + G^*_{dg}. \tag{8}$$

The plot of G^* as a function of the gap, h, shown in Fig. 4D confirms that the complex modulus is a linear function of the gap. Thus, extrapolation of $G^*(h)$ at

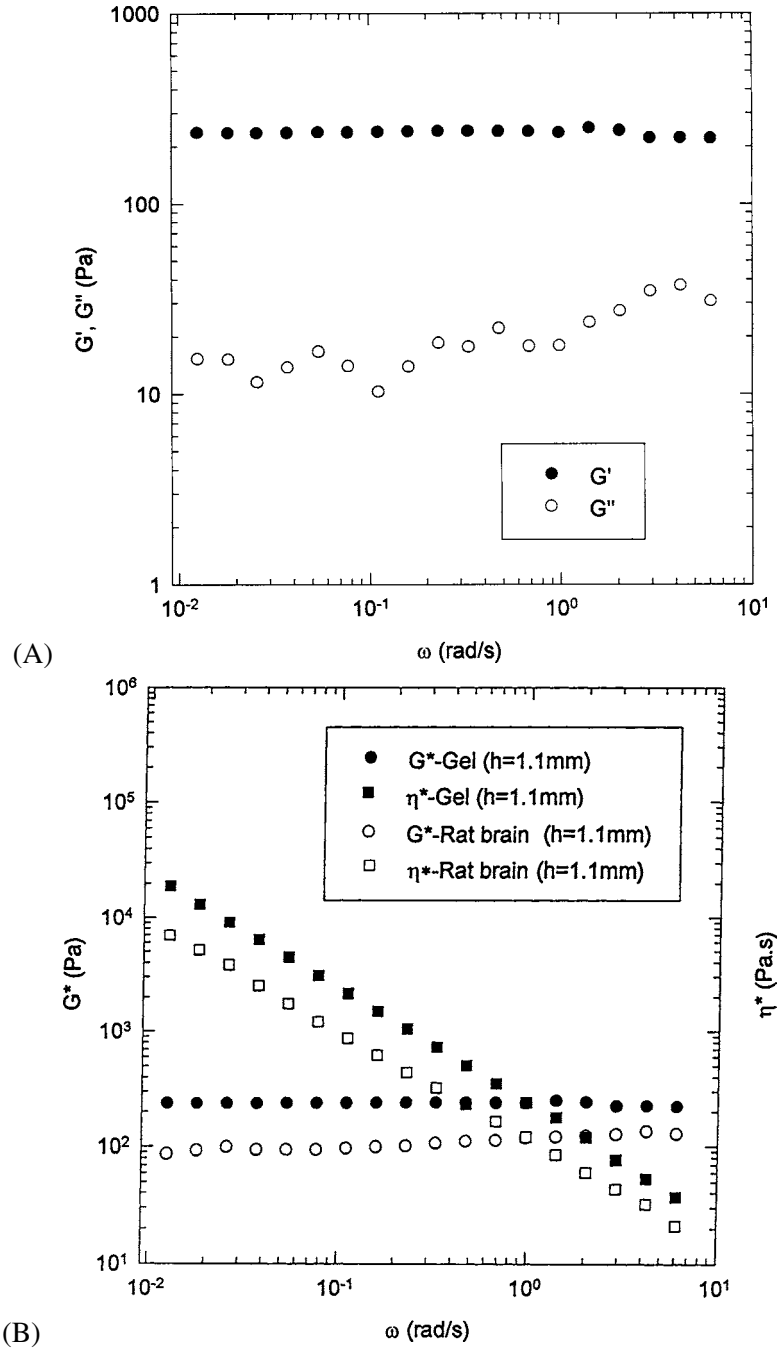

Figure 4. (A) Dynamic moduli, G' and G'', as function of frequency for the PHPMA hydrogel at 37°C. (B) Comparison of linear material functions, G^* and η^*, of the rat brain and the PHPMA hydrogel at 37°C. (C) Complex shear modulus, G^*, of the hydrogel as a function of frequency at different gaps after compression and decompression. (D) Variation of the complex modulus, G^*, of the hydrogel as a function of the gap.

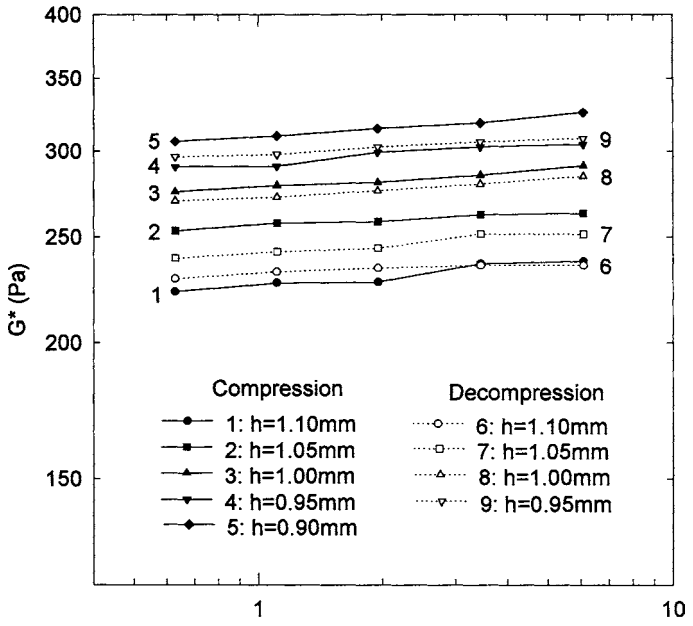

(C)

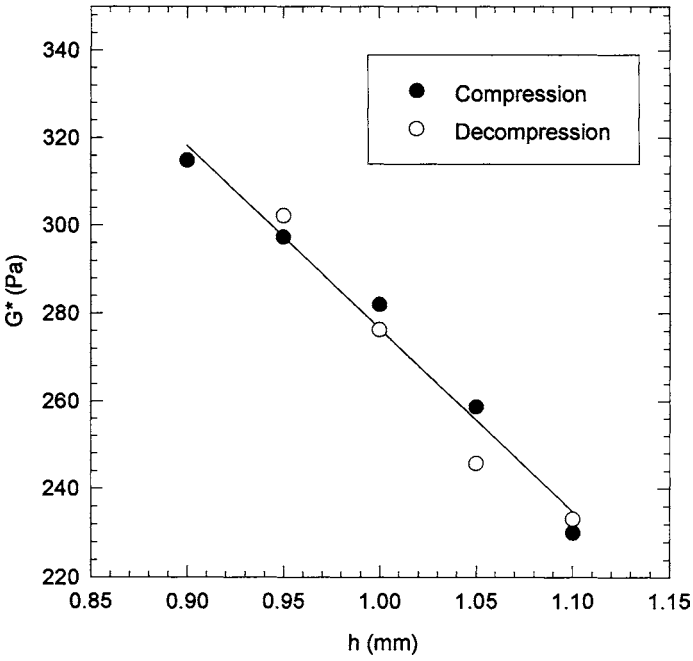

(D)

Figure 4. (Continued).

vanishingly small gaps gives an estimation of the complex modulus of the dry gel which in the present case shows an asymptotic value of 735 Pa. It, however, should be mentioned that extrapolation is an idealization of actual geometry of flow since for completely dry samples, the gap will given by the amount of the dry gel between the two parallel plate fixtures.

PHPMA hydrogel implantation

The transection of the spinal cord severs all elements of the neural tissue, including myelinated axons, neural and glial elements and blood vessels (dorsal and ventral spinal arteries), producing a permanent paraplegia in the rats. The cavity was made after complete transection of the cord at two levels separated by 2 mm and by removing the spinal tissue segment. Clean and straight-line sections of the spinal tissue was facilitated by cooling the spinal cord before lesioning. For each animal, completeness of the lesion was verified visually under the surgical microscope and after control of the hemostasis. A representative sample of the size and shape of the lesion for the implantation of the hydrogel is shown in Table 3. As early as 3 days after surgery, macroscopic examination of the spinal cord showed that the hydrogel implants were found within the spinal cord and formed a complete bridge between the distal and proximal spinal segments (Fig. 5A). Five weeks later, the appearance of the hydrogel had changed and it was difficult to clearly distinguish a sharp interface between the polymer implant and the host tissue as result of the gel integration into the host (Fig. 5B). There was no discontinuity between the polymer surface and the tissue, and the total available surface of the hydrogel merged with the cut surface of the spinal tissue as shown on consecutive adjacent sections. Optimal surgical techniques and an adequate gel placement in the transection site yielded excellent integration of the gel and the absence of cyst formation in the adjacent spinal tissue. The polymer matrices showed a strong bioadhesiveness and this was noticed during the placement of the polymer between the two severed spinal segments; the polymer gel stuck very rapidly and strongly to the cut spinal cord as evidenced by the difficulty of retrieving it after a few seconds without damaging the spinal stump. In contrast, transected spinal cords without gel implantation showed typical pathological changes with massive tissue destruction, microcyst formation and the development of dense scar tissue filling the transection cavity (Fig. 5C). Observations of cross-sectional areas of the water-saturated hydrogels on histological sections as well as a gross examination of the implantation site did

Table 3.
Morphometrics characteristics of the implantation site containing the polymer gel implant ($n = 6$)

Area (mm^2)	Perimeter (mm)	Shape factor[a]
2.86 ± 0.12	8.21 ± 0.16	0.54 ± 0.03

[a] Shape factor: 1 for circle and 0 for line.

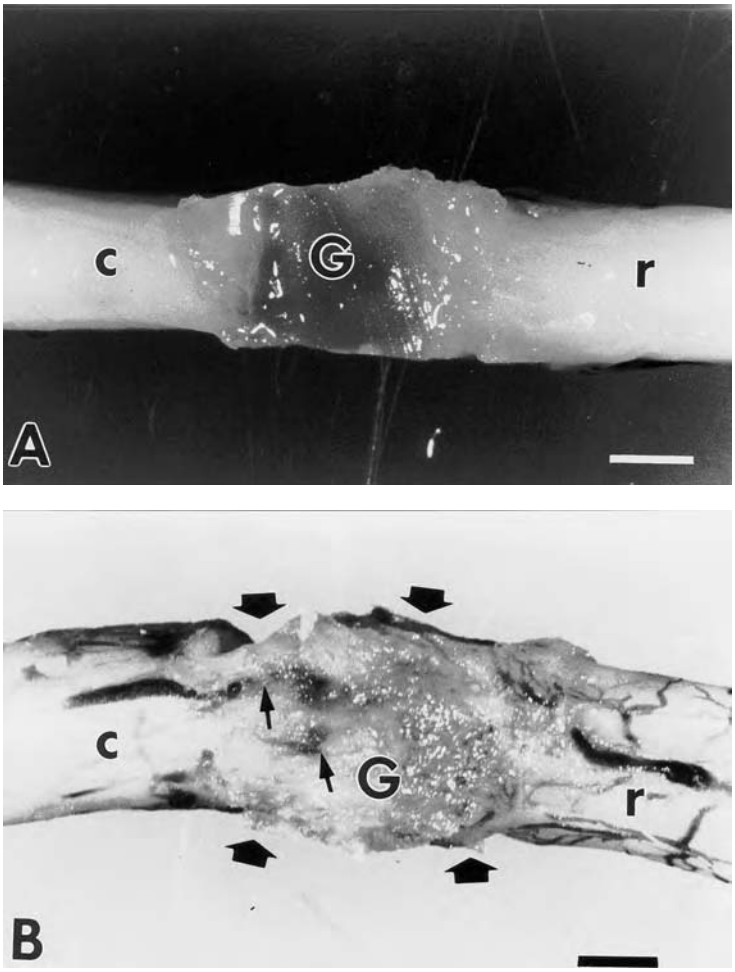

Figure 5. Representative macrophotographs showing the appearance of the transected rat spinal cord grafted with the PHPMA hydrogel after 3 days (A) and 5 weeks (B). Note the fusion of the polymer gel (G) to the rostral (r) and caudal (c) cut end of the cord (arrows) and the restoration of the continuity of the spinal cord (B). (B): note the growth of blood vessels from the cut dorsal spinal artery at the level of the rostral (r) and caudal (c) spinal segments into the polymer gel (small arrows). (C): control spinal cord that did not receive the gel implant, showing degenerative changes of the spinal cord stumps and the fibrous tissue filling the defect (asterix) 5 weeks after transection. Scale bars: (A, B) 1.5 mm; (C) 750 μm.

not reveal any signs of polymer degradation or mechanical disruption as seen under Normansky optics (Fig. 6) and was confirmed by scanning electron microscopy of 5 month-explanted gels (Fig. 7). There was no sign of toxicity, inflammatory or distortion in the surrounding neural tissue.

GFAP immunocytochemistry studies showed that after 3 months of implantation, the gliosis that had developed at the proximal and distal spinal stumps infiltrated the porous structure of the hydrogel and sent processes into the gel implant (Fig. 8).

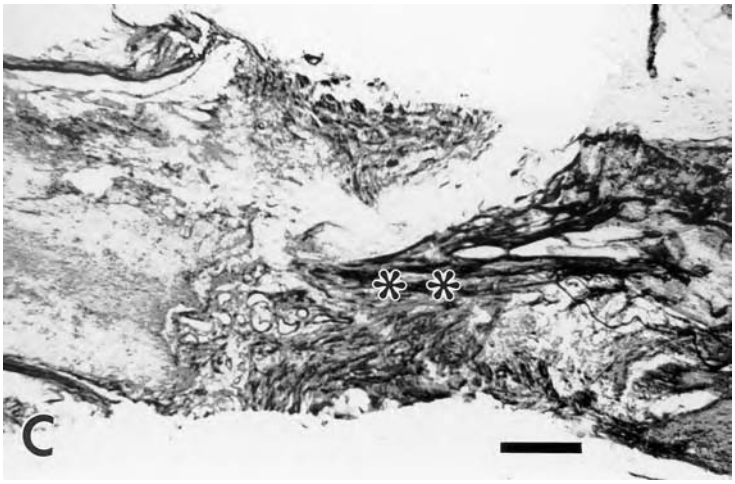

Figure 5. (Continued).

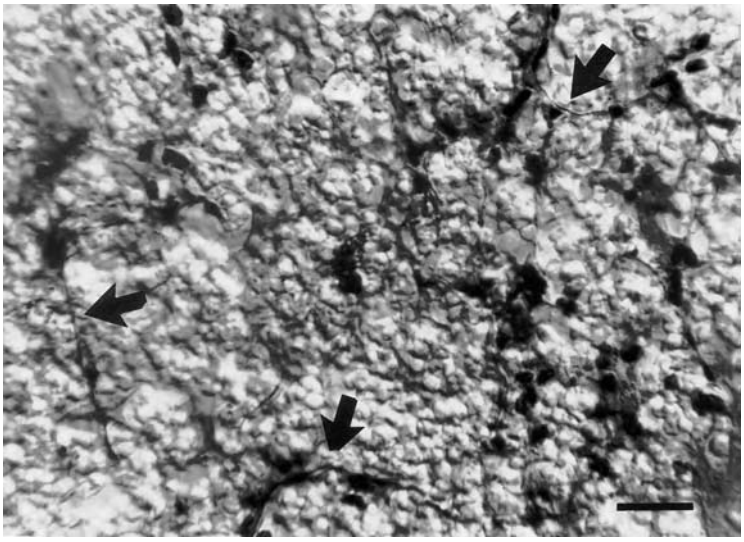

Figure 6. Silver impregnation (Holmes technique) of a section through the hydrogel implant viewed under Normansky optics showing the structure of the gel and nerve fibres between the polymer microspheres (some of them are shown by arrow heads). Scale bar = 15 μm.

This tissue reaction was noticed at the proximal and distal interface and was more pronounced after 20 weeks. Immunostaining with anti-neurofilament antibodies showed intensely stained axons that had crossed the interface and penetrated the gel matrix from the white and gray matter regions of the host (Fig. 9A and B). Twenty weeks after gel implantation, a significant amount of reorganization appeared in the immunoreactive axons at the interface and within the gel matrix. Usually, axons growing within the hydrogel matrices were found in areas which contained astrocytes which have established a network of GFAP-positive processes and blood

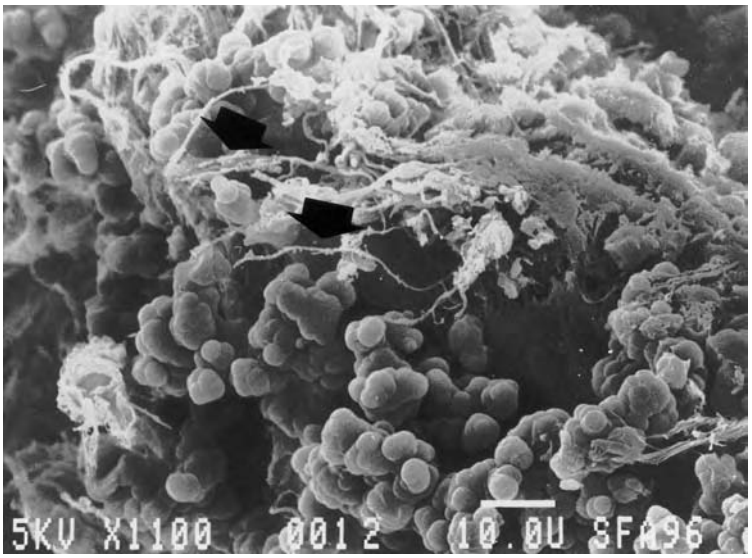

Figure 7. Scanning electron microscopy of the cross-section of a PHPMA gel after 5 months implantation, showing the tissue that has grown within the interstice of the gel and on the surface of the microspheres. Note the structures resembling nerve fibres (arrows).

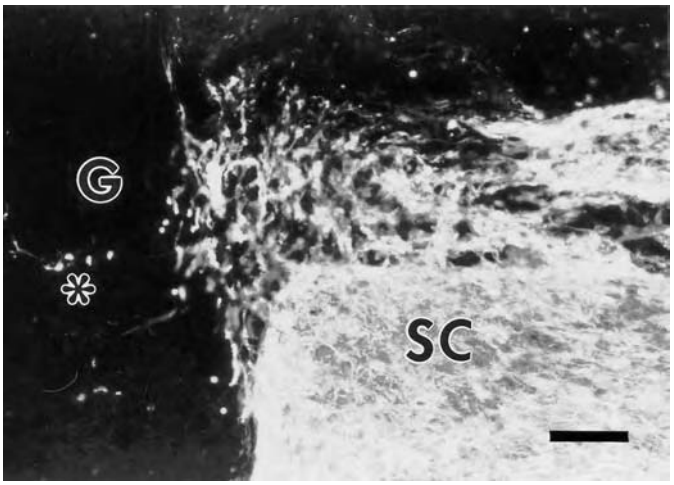

Figure 8. Fluorescent photomicrograph of a longitudinal spinal cord (SC) tissue section (3 months post-implantation) immunostained for glial fibrillary acidic protein (GFAP) showing the gel−tissue interface from the rostral segment of the spinal cord. Astrogliosis occured at the interface and at the level of the spinal stump, while GFAP-positive astrocytes and their processes have spread out into the gel (G). Note the few individual GFAP-positive cells that have detached from the interface and have migrated into the gel (asterix). Scale bar: 100 μm.

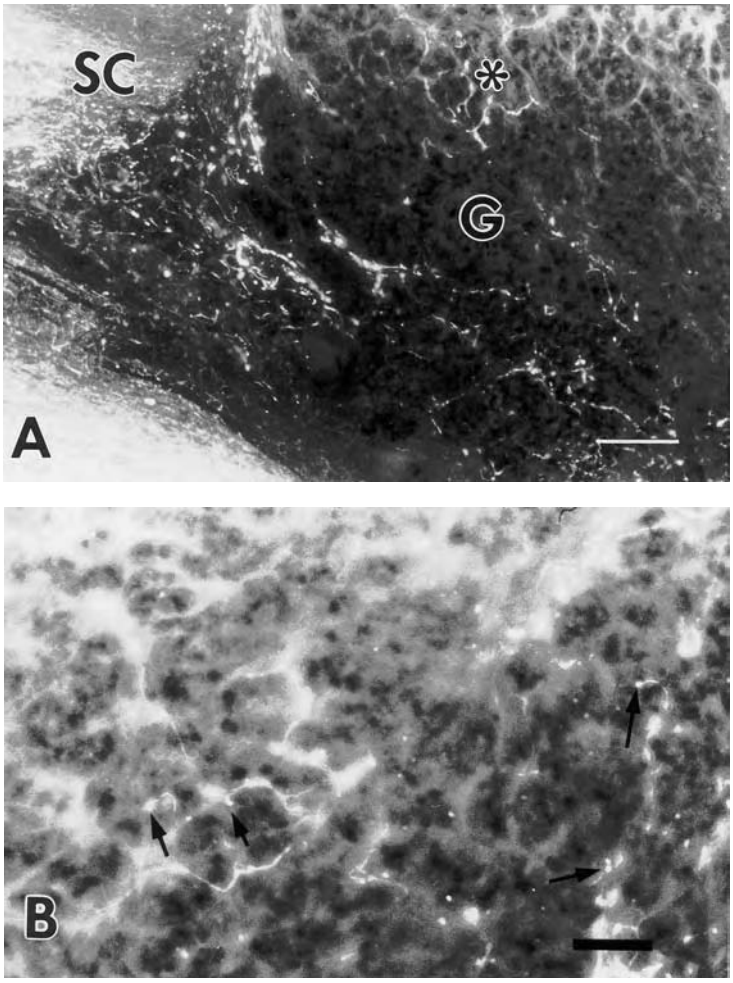

Figure 9. (A) Fluorescent photomicrographs of a longitudinal spinal cord (SC) section (3 months post-implantation) immunostained for neurofilaments showing immunoreactive axons of the white and grey matter of the rostral cut end of the spinal cord. Regenerating fibers have crossed the interface and sprouted (small arrows) within the gel (G) along the trabecular network of the polymer, showing a predominant orientation along the longitudinal axis of the spinal cord. (B) Higher magnification of the area shown by asterix in (A). Very fine diameter axons have grown along different tortuous paths through the porous structure of the gel matrix, mainly as individual fibres displaying ramifications and small terminal varicosities (small arrows). Scale bars: (A) 250 μm; (B) 25 μm.

vessels. Capillary sprouts were constantly observed within the hydrogels (Fig. 10). Immunostaining for fibronectin showed a marked and uniform immunoreactivity of the hydrogel implant and the adjacent tissue (Fig. 11A), and at higher magnification, this immunostaining pattern delineated the microgeometry of the polymer network as a bright and punctuated fluorescence at the surface of the polymer particles (Fig. 11B).

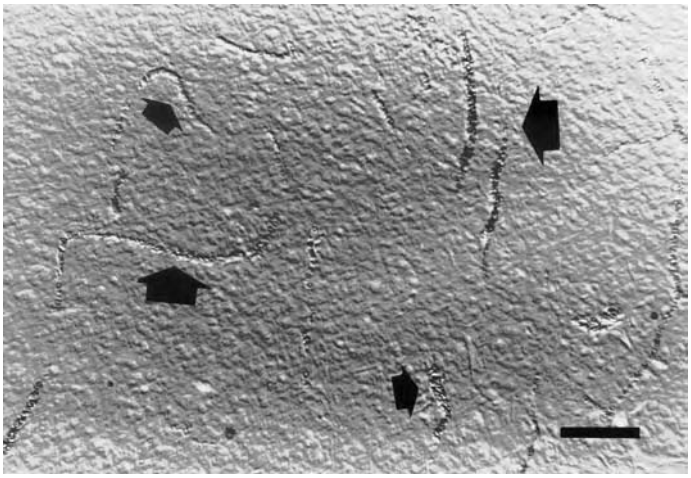

Figure 10. Cross-section through a hydrogel 3 months after implantation into the spinal cord and viewed under Hoffman optics to show capillaries that have grown within the polymer gel (some of them are shown by arrow heads). Scale bar = 20 μm.

Spinal cord sectioning resulted in a loss of reflex and sensory-motor functions below the level of injury. Spontaneous locomotor performance was observed when the rats were allowed to use their hindlimbs during overground locomotion. The differences in locomotor behavior between rats and groups were best seen when the animals were motivated to perform (e.g. stimulation with food). In control groups, the rats were able only to drag their hindlimbs and in some instances were able to perform slight hindlimb joint movements. At 5 weeks post-implantation, the rats grafted with the gel showed significant behavioral improvement compared to the control group with, for instance, extensive movement of all joints of the hindlimbs. However after 5 weeks, improvement was more consistent as all rats regained the ability to take weight-supported steps at least occasionaly during overground locomotion. After 12 weeks post-implantation, six rats stepped consistenly with frequent forelimb-hindlimb coordination and occasional plantar stepping of their hindlimbs, while other rats showed intermediate levels of recovery. No significant improvement was noted for the remaining rats which survived up to 20 weeks.

Figure 12 shows the IR spectra of the hydrated PHPMA control hydrogel and the control (intact) spinal cord, respectively. The IR spectrum of the hydrogel (Fig. 12A) essentially exhibits IR features characteristic of the stretching mode vibration of methylene groups (between 2700 and 3000 cm^{-1}) and of the amide vibrational modes near 1650 (amide I), 1550 (amide II) and 1250 (amide III) cm^{-1}. However, the IR spectrum of the intact spinal tissue (Fig. 12C) shows, despite significant IR absorption due to the presence of water, IR peaks characteristic of proteins as observed by the presence of the amide I (strongly overlapped with the water bending mode feature), amide II and amide III bands. Weak IR peaks are also observed between 2700 and 3000 cm^{-1}, most likely due to the amino acids

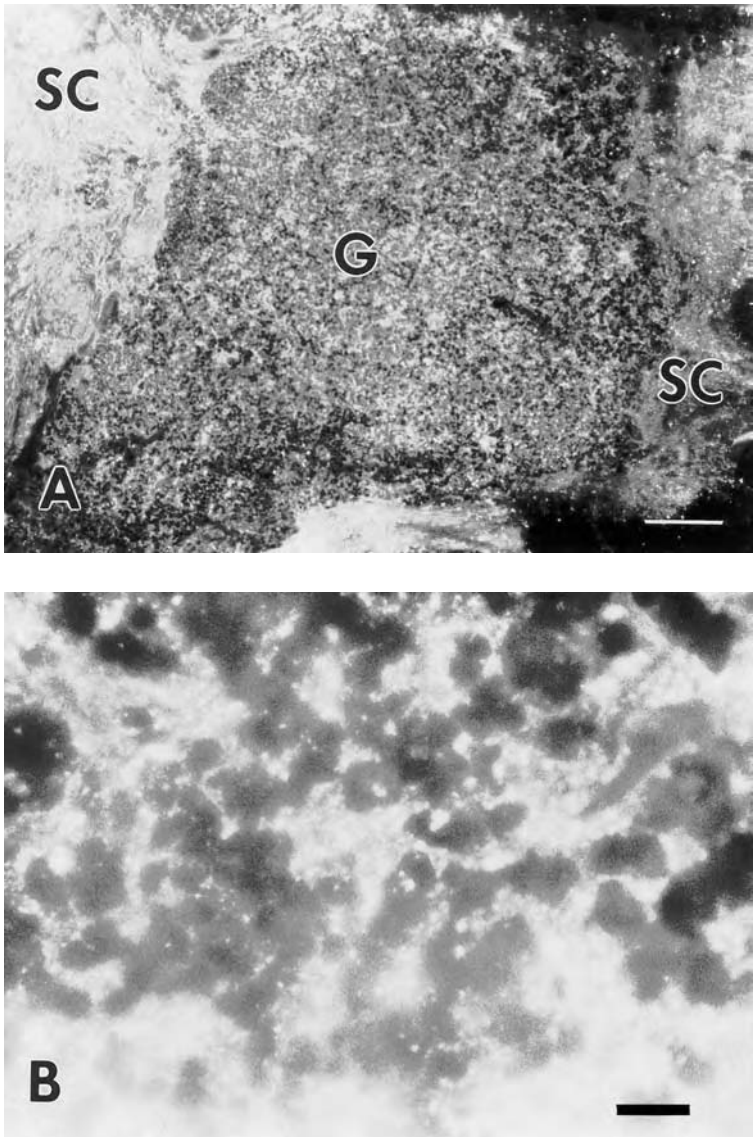

Figure 11. (A) Fluorescent photomicrographs of a longitudinal spinal cord (SC) tissue section (5 months post-implantation) through the implantation site immunostained for fibronectine. (A) At low magnification, the whole hydrogel implant (G) is intensely immunostained and the staining pattern depicts the microgeometry of the gel structure. (B) Higher magnification of the gel showing the punctuated fibronectine staining pattern around the polymer particles. Scale bars: (A) 400 μm; (B) 20 μm.

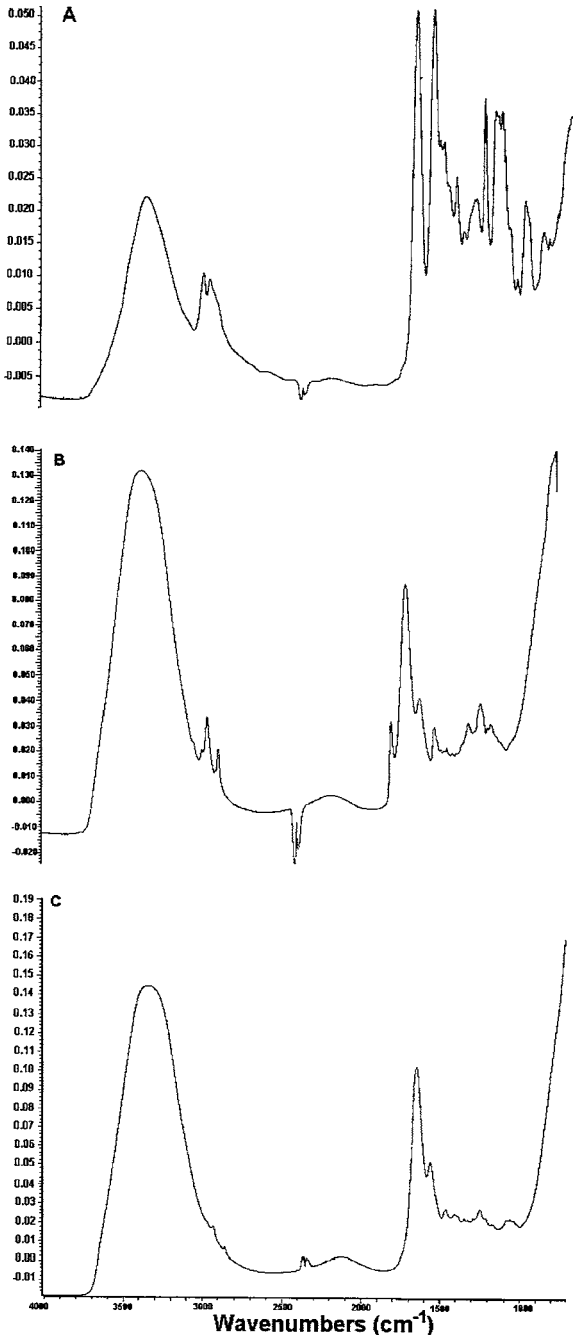

Figure 12. ATR-FTI spectra of a control PHPMA hydrogel (A), a hydrogel explanted after 3 months of implantation in the spinal cord (B), and the intact spinal tissue (C).

side chains. Finally, Figure 12B shows the IR spectra of the explanted PHPMA hydrogel. Interestingly, the low frequency part of the spectrum clearly showed that the hydrogel has been, at least partly, replaced by IR features characteristic of lipids; methyl and methylene stretching mode vibrations between 2700 and 3000 cm^{-1} and ester carbonyl stretching mode vibrations at 1740 cm^{-1} and proteins as similarly observed through the amide bands described above for spinal tissue.

DISCUSSION

The primary goal of this study was to assess the potential of a heterogeneous hydrogel for promoting tissue repair and axonal regeneration in the lesion site of the transected spinal cord. The results show that the hydrogel can correctly bridge the tissue defect, induce glial cell infiltration, angiogenesis and axonal regeneration by recruiting host tissue cells and axons. This study clearly shows differences between the appearance of the spinal cord grafted with the hydrogel and the transected spinal cord without the gel implant. Following severe trauma of the spinal cord, pathological changes occur which are responsible for the progressive necrotizing processes in the spinal stumps [47]. Although the secondary pathological changes may vary considerably according to the severity of the trauma, they include the formation of microcysts and cavitation, formation of a gliomesenchymal scar and tissue necrosis of the gray and white matter in a caudo-rostral extent. In contrast, the spinal cord grafted with the PHPMA hydrogel did not show any such pathological changes. The spinal cord continuity was re-established and, at the microscopic level, the hydrogel was integrated well with the host tissue; on longitudinal sections, fusion of the gel to the host was 100% of the available surface of the polymer implant. Immunocytochemical studies revealed that a major finding of this study was that regeneration of axons within the structure of the polymer hydrogel occurred. The source of regenerating fibers may include: (1) regenerating central axons, either terminal regrowth or collateral sprouting; (2) heterotopic peripheral nerve fibers; (3) proliferating perivascular nerve fibres; (4) regenerating nerve roots [48]. Although intramedullary sprouts from spinal nerve roots, either the posterior root ganglia or the nerve roots themselves, have been reported to be an important source of regenerating fibres [49], it is most likely that axonal regeneration observed through the polymer bridge originates from central axons. This is suggested by the immunocytochemical labbelling patterns which demonstrated that immunoreactive axons originated from the gray and white matter of the proximal and distal spinal segments. In addition, the fact that animals showed some degree of recovery of locomotion and postural functions of the hindlimbs, suggest that timely axonal regeneration occurred when considering that 5–10% of regeneration induce significant functional recovery [50].

Correlation between the performance and the physical characteristics of the hydrogel suggests three levels of control on host tissue response. First, at the macroscopic level (millimetre scale), the high swelling behavior and the viscoelastic

properties of the hydrogel enables the complete sealing of the tissue defect in volume and shape as shown by histopathological studies. Second, on the scale of pore size distribution (micrometric scale and microgeometry), the polymer network control tissue ingrowth as shown by histochemical data and scanning electron microscopy. Finally, at the surface level of the hydrogel (mesoscopic scale), the surface is the site of protein and lipid adsorption as shown by infrared spectroscopy on the explanted hydrogel.

A major issue in tissue engineering using porous polymer devices is the pore size distribution and the communication between pores [51, 52]. In the present study mercury porosimetry and α measurement shows that the PHPMA hydrogel provides a large void volume and an extensive network of interconnected open pores for cell infiltration and tissue growth. Indeed, the intrusion of mercury occurs only within interconnected network of pores which are readily accessible to mercury at increasingly higher pressures [40]. According to porosimetry data and derived equations, the PHPMA hydrogel exhibits a bimodal pore distribution, one in the macropore domain and one in the mesopore domain. It is likely that these domains are occupied by pores with different shapes since the pressure (P) required to intrude a pore volume is inversely proportional to the pore diameter (D) and directly proportional to the shape of the pore (F_s) according to the equation: $P = F_s/\mathrm{D}$ [53]. The presence of the two pore regimes is also consistent with scanning electron microscopy which shows the presence of mesopores at the surface of the microspheres ('orange peel' appearance), while the macropores are formed by the interstices between the polymer aggregates. In addition, the macropore domain of the gel encompasses the dimension of the range of biological structures of the spinal tissue that includes capillaries and axons and tissue expansion in the higher limits of the pore size distribution curve. Regarding the topology of the pore network, the gel is formed by a network of pores of variable size with an average diameter $\mathrm{D_c}$, interconnected throughout pore constrictions with an average diameter D_t, since the existence of a hysteresis between the intrusion and retraction curve depends on $\mathrm{D_c}/\mathrm{D_t}$ [54, 55]. Extrusion data also indicated that pores may trap mercury due to pore irregularities (tortuousness of the network). The large surface area of the polymer network is also a characteristic that promotes tissue formation since cell attachment on a substrate is the initial process in building tissue structure. The value of the surface area of porosimetry data is the area that mercury can reach. However, in this study, this value is underestimated because there is no contribution of the finer mesopores (below 6 mm) and any micropores due to the limit of the pressure range used. However, nitrogen adsorption isotherms have shown a specific surface area of 700 $\mathrm{m^2\,g^{-1}}$ for the range of mesopores and micropores of the PHPMA hydrogels (unpublished data).

The high swelling capacity of the gel is a desirable characteristic because it allows transport of nutrient and fluids through the network and modulates the biological processes by controlling diffusion or sequestration of growth factors and cytokines that are secreted after injury [65]. In addition, the gel shows adequate mechanical

integrity (seen upon implantation and rheology) which is important for tissue organization upon the time scale required for tissue morphogenesis, organization and axonal regeneration.

The main results obtained in the rheology study is that the gel exhibits similar mechanical behavior as found in the rat brain. This property is important because it enables the hydrogel to integrate into the neural tissue without mechanical pressure. The fact that G'' does not vanish at low frequencies [56] suggests that the three-dimensional polymer network is not completely cross-linked and local frictions of strands exist in the network. However, the gel was washed several times before rheological measurements, and therefore the friction could only be due to pendant PHPMA chains within the network. In contrast, the elastic modulus G' which is associated with the long scale three-dimensional network response does not show any change in magnitude as expected. Compression and decompression of the gel network is relatively stable whenever submitted to external stresses of the same magnitude as those imposed during the compression/decompression solicitations. Such a property is important when the gel is intended to be subjected to mechanical constraints within the neural tissue.

Since the mechanical properties of soft tissue are related to its structure, it is tempting to speculate on the resemblance between the PHPMA hydrogel and the developing neural tissue which has relatively large extracellular spaces, representing a significant volume fraction [57]. In early postnatal days the TMA^+ diffusion parameters in a rat cortex and corpus callosum are significantly different from those in adults. The extracellular space volume fraction α in a newborn rat is more than twice as large (about 0.45) than it is in the case in an adult rat brain (about 0.20) [57] and the tortuosity during early postnatal days is significantly lower [58]. Recently, the similar decrease in α and increase in λ were demonstrated in the developing rat spinal cord gray and white matter [60]. For instance, the neural tissue and the PHPMA hydrogel both can be viewed as composed of a deformable porous matrix saturated by interstitial fluids. In the case of the neural tissue, the solid phase is made up of extracellular matrices and the vascular network, and the fluid phase, of the extra- and intracellular fluids. The hydrogel after implantation, can, nevertheless, be viewed as composed of a solid elastic phase, the polymer matrix, and a fluid phase; the biological fluid as described with the poroelastic model [60, 61].

The hydrogel upon implantation interactes closely with the host tissue as evidence by scanning electron microscopy and infrared spectroscopy, showing clearly that the PHPMA hydrogel is invaded by tissue cells, while lipids and protein molecules are adsorbed on the polymer surface. Lipids adsorption may be residual myelin debris or newly formed myelinated axons that have grown on polymer surfaces (however, further immunocytochemical analysis is needed). Adsorption could have been favored by the amide functionality of the PHPMA which confers stability and polarity of the network [62]. Adsorption of extracellular matrix proteins onto polymer surfaces is substantiated by immunocytochemistry of fibronectin that showed a very fine fluorescent signal depicting the microgeometry of the polymer

matrix. This very likely contributes to the attachment and the growth of cells onto the polymer surface as shown in other studies (e.g. [63]).

The present study also shows the importance of the surgical technique used to implant the hydrogel into the lesion cavity. For instance, proximal and distal interfaces free of mesenchymal debris and blood are conditions for apposition of the hydrogel to the traumatic spinal surfaces. Indeed, the quality of the two surfaces (biologic vs synthetic) that come into contact is important for the fate of the integration process of the hydrogel and tissue induction. Indeed, formation of cysts and scarring tissue occur after excessive manipulation of the spinal tissue that results in the failure of the hydrogel function in tissue restoration.

As early as 1990, tissue repair using synthetic polymer hydrogel was suggested as a new strategy for brain tissue repair [29, 30]. Homogeneous transparent hydrogels of glyceryl methacrylate or hydroxyethyl methacrylate have been studied as polymer matrices for tissue replacement in the CNS but were less effective to integrate the neural tissue than the heterogeneous hydrogel in the present study. The neuroinductive property of the PHPMA hydrogel is a function of the water content of the network which facilitates the diffusion of biological fluids and growth factors secreted by cells, the mechanical compliance and adequate integrity to host tissue, the large specific surface area available for tissue interaction and organization, and the porous structure with a median pore diameter compatible with cell infiltration. Other polymer systems that have been used to promote tissue regeneration are different from the hydrogel of this study because they form tubes without three-dimensional tissue structure [23] or are synthesized from biodegradable polymer [28]. Biodegradable materials present disadvantages because their side products released into the systemic circulation may cause, over the long term, organ failure by accumulation into the tissue. In contrast of the present study, heterogeneous hydrogels of poly(2-hydroxyethyl methacrylate) combined with collagen and Schwann cells were tested in the rat brain, showing some degree of tissue ingrowth [32].

Following trauma of the spinal cord, healing of the lesion and the surrounding tissue is the result of two apparently independent processes of tissue necrosis and tissue repair [64]. The aim of neural tissue engineering using polymer hydrogels is to regulate the dynamic balance between these two processes by providing the appropriate substrate to promote the naturally occurring reparative events which may overwhelm the wound healing. These reparative events include the development of a cellular matrix, the secretion of extracellular matrices, axonal sprouting and delivery of growth and angiogenic factors. The ultimate goal is not to recreate a replica of the lost tissue with its original anatomical organization including minute structural features, topographic cell distribution and specific arrangement of dendritic and axonal processes, but to restore the lost tissue with the host cell elements arranged collectively into a level of structural organization that promotes axonal regeneration and the establishment of new neural connections.

In this respect, reactive astrocytes by producing growth-promoting proteins and neurotrophic factors can be beneficial for axonal regeneration [65].

Tissue engineering of the nervous system is a relatively new field of research compared to other organs but, with advanced knowledge in the molecular biology of CNS development and regeneration, materials tailored for reconstituting the CNS tissue will be manufactured. For instance, one of the future challenges will be to control topologically the modification of polymer matrices with bioactive functional groups chemically grafted to the polymer [66, 67]. Another approach that is being developed is the association of hydrogels with developing cells that may further expand within the porous polymer network [68–71] to construct biohybrid implants for tissue replacement.

CONCLUSION

The present finding shows that a biocompatible macroporous polymer hydrogel with defined pore structure and topology that are potentially available for tissue development, and associated tissue-compatible mechanical properties have the capacity to induce and support neural tissue ingrowth and axon regeneration. Engineering the neural tissue based on hydrogel technology has future applications in microreconstruction neurosurgery in the restoration of defective tissue (gliotic scar resection), tissue destruction (trauma) or dysfunctional tissue (spina bifida).

Acknowledgements

We express our thanks to Mrs. Suzanne Bourassa for technical assistance and Dr. R. Guidoin (Quebec Biomaterial Institute) for the use of the scanning electron microscope.

REFERENCES

1. B. A. Kakulas and J. R. Taylor, in: *Handbook of Clinical Neurology*, H. L. Frankel (Ed.), p. 21. Elsevier Science (1992).
2. A. Larner, A. R. Johnson and R. J. Keynes, *Biol. Rev.* **70**, 597 (1995).
3. A. Logan, J. Oliver and M. Berry, in: *Progress in Growth Factor Research*, Vol. 5, p. 379. Elsevier Science, Oxford (1995).
4. J. S. Rudge, G. M. Smith and J. Silver, *Exp. Neurol.* **103**, 1 (1989).
5. E. L. Zager and McL. P. Black, *Surg. Neurol.* **29**, 350 (1988).
6. O. Lindvall, *J. Neurol. Neurosurg. Psychiatry*, supp., 39 (1989).
7. B. S. Bregman, *Dev. Brain Res.* **34**, 265 (1987).
8. K. R. Kuhlengel, M. B. Bunge, R. P. Bunge and H. Burton, *J. Comp. Neurol.* **293**, 74 (1990).
9. J. J. Bernstein and W. J. Goldberg, *Rest. Neurol. Neurosci.* **2**, 261 (1991).
10. O. Brustle and R. D. McKay, *Curr. Op. Neurobiol.* **6**, 688 (1996).
11. C. N. Svendsen, M. A. Cadwell, J. Shen, M. G. Borg, A. E. Rosser, P. Tyers, S. Karmiol and S. B. Dunnett, *Exp. Neurol.* **148**, 135 (1997).
12. A. Martinez-Serrano and A. Bjorklund, *Trends Neurosci.* **20**, 530 (1997).

13. J. R. Wrathall, D. D. Rigamonti, M. R. Bradford and C. C. Kao, *Acta Neuropathol.* **57**, 59 (1982).
14. J.-C. Horvat, C. Baillet-Derbin, J. H. Ye, F. Rhrich and F. Affane, *Rest. Neurol. Neurosci.* **2**, 289 (1991).
15. R. Marchand and S. Woerly, *Neuroscience* **36**, 45 (1990).
16. E. A. Joosten, P. R. Bar and W. H. Gispen, *J. Neurosci. Res.* **41**, 481 (1995).
17. H. S. Goldsmith and J. C. de la Torre, *Brain Res.* **589**, 217 (1992).
18. Y. Hiraizumi, E. Fujimaki, E. E. Transfeld, N. Kawahara, V. D. Fiegel, D. Knighton and J. H. Sung, *Spinal Cord* **34**, 394 (1996).
19. J. J. Bernstein and W. J. Goldberg, *Brain Res.* **377**, 403 (1986).
20. C. L. Paino, C. Fernandez-Valle, M. L. Bates and M. B. Bunge, *J. Neurocytol.* **23**, 433 (1994).
21. M. H. Spilker, I. V. Yannas, H.-P. Hsu, T. V. Norregaard, S. K. Kostyk and M. Spector, *Tissue Eng.* **3**, 309 (1997).
22. D. J. Schreyer and E. G. Jones, *Dev. Brain Res.* **35**, 291 (1987).
23. X. M. Xu, V. Guénard, N. Kleitman and M. B. Bunge, *J. Comp. Neurol.* **351**, 145 (1995).
24. M. S. Shoichet, S. R. Winn, S. Athavale, J. M. Harris and F. T. Gentile, *Biotechnol. Bioeng.* **43**, 563 (1994).
25. C. T. Montgomery, E. A. Tenaglia and J. A. Robson, *Exp. Neurol.* **137**, 277 (1996).
26. A. R. Harvey, M. Chen, G. W. Plant and S. E. Dyson, *Rest. Neurol. Neurosci.* **6**, 221 (1994).
27. A. R. Harvey, A. M. Connor and M. W. Beilharz, *Int. J. Dev. Neurosci.* **11**, 569 (1993).
28. C. Shugens, C. Grandfils, R. Jerome, P. Teyssie, P. Delree, D. Martin, B. Malgrange and G. Moonen, *J. Biomed. Mater. Res.* **29**, 1349 (1995).
29. S. Woerly, C. Lavallée and R. Marchand, *Biomaterials* **11**, 97 (1990).
30. S. Woerly, K. Ulbrich, V. Chytry, K. Smetana, P. Petrovicky, B. Rihova and D. J. Morassutti, *Cell Transplant* **2**, 229 (1993).
31. S. Woerly, *Biomaterials* **14**, 1056 (1993).
32. G. W. Plant, A. R. Harvey and T. V. Chirila, *Brain Res.* **671**, 119 (1995).
33. N. A. Peppas (Ed.), *Hydrogels in Medicine and Pharmacy*. CRC Press, Boca Raton, FL (1987).
34. J. D. Andrade (Ed.), *Hydrogels for Medical and Related Applications,* ACS Symp. Ser. 31. ACS, Washington, DC (1976).
35. K. Dusek, *J. Polym. Sci. B* **3**, 209 (1965).
36. J. Seidl, J. Malinsky, K. Dusek and W. Heitz, *Adv. Polym. Sci.* **5**, 113 (1967).
37. J. Strohalm and J. Kopecek, *Angew. Makromol. Chem.* **70**, 109 (1978).
38. J. L. Nation, *Stain Technol.* **58**, 347 (1983).
39. E. W. Washburn, *Proc. Natl Acad. Sci. USA* **7**, 115 (1921).
40. S. J. Gregg and K. S. W. Sing (Eds), *Adsorption, Surface Area and Porosity*. Academic Press, London (1982).
41. M. Shively, *J. Pharmaceutical Sci.* **80**, 376 (1991).
42. Bird, R. C. Armstrong and O. Hassager, *Dynamic of Polymeric Liquids*. J. Wiley, New York (1987).
43. E. Sykova, J. Svobova, J. Polak and A. Chvatal, *J. Cereb. Blood Flow Metab.* **14**, 301 (1994).
44. C. Nicholson and J. M. Phillips, *J. Physiol.* **321**, 225 (1981).
45. E. Sykova, *The Neuroscientist* **3**, 28 (1997).
46. M. Bousmina and R. Muller, *Rheol. Acta* **35**, 369 (1996).
47. D. Balentine, *Lab. Invest.* **39**, 236 (1978).
48. L. Wolman, *Paraplegia* **4**, 175 (1966).
49. J. Komon, M. Van Meter, S. Salzman and W. Young, *Exp. Neurol.* **148**, 453 (1997).
50. A. R. Blight, *Neuroscience* **10**, 521 (1983).
51. E. Wintermantel, J. Mayer, K. L. Eckert, P. Lüscher and M. Mathey, *Biomaterials* **17**, 83 (1996).
52. R. C. Thomson, M. C. Wake, M. J. Yaszemski and A. G. Mikos, *Adv. Polymer Sci.* **122**, 245 (1995).
53. O. Z. Cebeci, *J. Colloid Interface Sci.* **78**, 383 (1980).

54. C. D. Tsakiroglou and A. C. Payatakes, *J. Colloid Interface Sci.* **137**, 315 (1990).
55. F. A. Dullien and G. K. Dhawan, *J. Colloid Interface Sci.* **47**, 337 (1974).
56. W. M. Abbot and R. P. Cambria, in: *Biological and Synthetic Vascular Prostheses*, J. C. Stanley *et al*. (Eds), p. 189. Grune & Stratton, New York (1989).
57. A. Lehmenkühler, E. Sykova, J. Svoboda, K. Zilles and C. Nicholson, *Neuroscience* **55**, 339 (1993).
58. I. Vorisek and E. Sykova, *J. Cereb. Blood Flow Metab.* **17**, 191 (1997).
59. S. Prokopova, L. Vargova and E. Sykova, *Neuroreport* **8**, 3527 (1997).
60. T. Nagashima, N. Tamaki, S. Matsumoto, B. Horwitz and Y. Seguchi, *Neurosurgery* **21**, 898 (1987).
61. S. Hakim, *Acta Neurol. Latinoam.* **17**, 169 (1971).
62. S. Dumitriu and C. Dumitriu-Medvichi, in: *Polymeric Biomaterials*, S. Dumitriu (Ed.), p. 3. Marcel Dekker, New York (1993).
63. S. T. Carbonetto, M. M. Gruver and D. C. Turner, *Science* **216**, 897 (1982).
64. Z. Zhang, C. J. Krebs and L. Guth, *Exp. Neurol.* **143**, 141 (1997).
65. H. W. Muller, U. Junghans and J. Kappler, *Pharmacol. Ther.* **65**, 1 (1995).
66. G. W. Plant, S. Woerly and A. R. Harvey, *Exp. Neurol.* **143**, 287 (1997).
67. S. Woerly, G. Laroche, R. Marchand, J. Pato, V. Subr and K. Ulbrich, *J. Neural Transpl. Plast.* **5**, 245 (1995).
68. S. Woerly, G. W. Plant and A. R. Harvey, *Neurosci. Lett.* **205**, 197 (1996).
69. S. Woerly, G. W. Plant and A. R. Harvey, *Biomaterials* **17**, 301 (1996).
70. C. E. Krewson, S. W. Chung, W. Dai and W. M. Saltzman, *Biotechnol. Bioeng.* **43**, 555 (1994).
71. A. C. Jen, M. C. Wake and A. G. Mikos, *Biotechnol. Bioeng.* **50**, 357 (1996).

This page intentionally left blank

Polymers for Tissue Engineering, pp. 375–395
Molly S. Shoichet and Jeffrey A. Hubbell (Eds)

The influence of physical structure and charge on neurite extension in a 3D hydrogel scaffold

GEORGE P. DILLON [1], XIAOJUN YU [1], ANIRUDH SRIDHARAN [1], JOHN P. RANIERI [2] and RAVI V. BELLAMKONDA [1,*]

[1] *Biomaterials, Cell and Tissue Engineering Laboratory, Department of Biomedical Engineering, Case Western Reserve University, Wickenden Bldg. #504, 10900 Euclid Avenue, Cleveland, OH 44106-7207, USA*
[2] *Sulzer-Carbomedics, 1300 B East Anderson Lane, Austin, TX 78752, USA*

Received 9 December 1997; accepted 13 May 1998

Abstract—Understanding neural cell differentiation and neurite extension in three-dimensional scaffolds is critical for neural tissue engineering. This study explores the structure–function relationship between a 3D hydrogel scaffold and neural cell process extension and examines the role of ambient charge on neurite extension in 3D scaffolds. A range of agarose hydrogel concentrations was used to generate varied gel physical structures and the corresponding neurite extension was examined. Agarose gel concentration and the corresponding pore radius are important physical properties that influence neural cell function. The average pore radii of the gels were determined while the gel was in the hydrated state and in two different dehydrated states. As the gel concentration was increased, the average pore radius decreased exponentially. Similarly, the length of neurites extended by E9 chick DRGs cultured in agarose gels depends on gel concentration. The polycationic polysaccharide chitosan and the polyanionic polysaccharide alginate were used to incorporate charge into the 3D hydrogel scaffold, and neural cell response to charge was studied. Chitosan and alginate were covalently bound to the agarose hydrogel backbone using the bi-functional coupling agent 1,1′-carbonyldiimidazole. DRGs cultured in chitosan-coupled agarose gel exhibited a significant increase in neurite length compared to the unmodified agarose control. Conversely, the alginate-coupled agarose gels significantly inhibited neurite extension. This study demonstrates a strong, correlation between the ability of sensory ganglia to extend neurites in 3D gels and the hydrogel pore radius. In addition, our results demonstrate that charged biopolymers influence neurite extension in a polarity dependent manner.

Key words: ECM; agarose; tissue engineering; nerve; regeneration; chitosan; alginate.

*To whom correspondence should be addressed.

1. INTRODUCTION

Neural tissue engineering focuses on developing new therapeutic systems that may be used for the repair of nerve injury as well as for the treatment of neurodegenerative disorders such as ALS, Parkinson's disease, and Huntington's chorea. A three-dimensional (3D) extracellular matrix (ECM) equivalent is critical for the successful engineering of neural tissue for enhanced and guided neurite extension *in vitro* and nerve regeneration *in vivo*. During fetal development and in response to nerve injury, the ECM plays a vital role in determining the spatial architecture, differentiation, and cytoskeletal organization of neural cells [1–3]. In the developing embryonic nervous system, the migratory pathways of pioneer neurons consist of a 3D ECM organized into a network of fibrils and granules [4]. The ECM influences neural cell function by diverse mechanisms including mechanical or adhesive interactions [5, 6], charge interactions via electrically charged ECM components [6–9], and specific receptor mediated cell surface receptor-ECM component interactions [4, 5].

Biomaterials may be used to generate controlled cellular environments and influence neural cell function *in vitro* and *in vivo*. Although flat, two-dimensional (2D), biomaterial substrates have been extensively used to influence neural cell function, 3D biomaterials may provide a more relevant emulation of the *in vivo* ECM environment than their 2D counterparts. The differentiated phenotype of cells *in vitro* is regulated by the biochemical composition and the mechanical properties of the substrate [10, 11]. Furthermore, the physical microstructure [12, 13] and charge [6, 9] of the neural cell culture environment have been shown to influence cell function on 2D substrates, but the influence of these parameters on neural cell function in 3D scaffolds is not currently understood. This study explores the structure–function relationship between a 3D hydrogel scaffold and corresponding neural cell neurite extension. In addition, the role of ambient charge on neurite extension in 3D scaffolds is investigated.

The physiochemical characteristics of 2D substrates influence neuronal cell attachment and differentiation [12–15]. Physical microgrooves mimicking the topography of the aligned fibrillar extracellular matrix prompt aligned and microgroove-depth dependent elongation from baby hamster kidney (BHK) cells and Madin Darby canine kidney (MDCK) cells [12, 13]. However, the relationship between the physical properties of 3D scaffolds and corresponding neural cell function is not well understood. This study uses a range of agarose hydrogel concentrations to generate varied gel physical structures and examines the corresponding neurite extension from primary sensory ganglia.

The influence of biologically based electrical charge on neural process extension remains unclear. Piezoelectric polymers such as polyvinylidene fluoride (PVDF) that generate transient surface charges under mechanical strain presented significantly increased differentiation and neurite outgrowth from cultured neuroblastoma cells [9]. Also, significantly higher levels of neuroblastoma neurite outgrowth are observed when cultured on positively charged fluorinated ethylene-

propylene (FEP) films compared to negatively charged and uncharged substrates of identical surface chemistry [16]. However, new standardized systems are required to elucidate the effect of ambient charge on neural cell function in 3D scaffolds.

The polycationic polysaccharide chitosan [17, 18] and the polyanionic polysaccharide alginate [17, 19] were used to incorporate charge of opposite polarities in 3D hydrogel scaffolds. Neither chitosan nor alginate has any known receptor-mediated interaction with dorsal root ganglia (DRG). Thus, the influence of charge on DRG neurite extension in 3D was investigated in a controlled manner.

2. MATERIALS AND METHODS

2.1. Characterization of agarose gel physical properties

2.1.1. Generation of a range of physical structures by varying agarose gel concentration. Agarose is a clear, thermoreversible hydrogel composed of alternating copolymers of 1,4-linked 3,6-anhydro-α-L-galactose and 1,3-linked β-D-galactose polysaccharides derived from red algae. The mechanism for gelation of agarose involves a shift from a random coil of the polysaccharide in solution to an intermediate double helix form in early gelation ultimately to bundles of double helices in final gelation [20, 21]. Water soluble SeaPrep® agarose (FMC Bioproducts, Rockland, ME, USA), used in this study, is a hydroxyethylated agarose that gels at 8–17°C and remains stable unless reliquified by heating to 50°C. When used for cell culture, the agarose was dissolved in pH 7.4 phosphate buffered saline (PBS, Dulbecco's Phosphate Buffered Saline, Gibco, Grand Island, NY, USA) before sterilization by filtration through a 0.2 μm syringe filter (Nalgene® Syringe Filters, Nalge Company, Rochester, NY, USA). After preparation, the solutions were gelled at 4°C and stored in a refrigerator. SeaPrep® agarose gels will be referred to as 'unmodified' agarose gel. A range of 0.75, 1.0, 1.25, 1.5, 1.75, and 2.0% w/v agarose gel concentrations was chosen to characterize the physical structure of unmodified agarose gel by the methods described below.

In order to avoid any possible interference from PBS during the characterization of their physical properties, agarose gels were prepared by dissolving agarose powder in deionized water (Millipore Corporation, Bedford, MA, USA). Unpublished research in our laboratory indicates that there is not a statistically significant difference in the pore radius of agarose gels made in PBS or water as determined by hydraulic permeability. The average pore radii of the gels were determined while the gel was in the hydrated state and in the dehydrated state as described below.

2.1.2. Computation of agarose gel pore radius in the hydrated state using hydraulic permeability testing. Hydraulic permeability of the different agarose gel concentrations was determined using a custom-built water column (see Fig. 1 for schematic). Each 3 ml gel sample was subjected to a known hydraulic

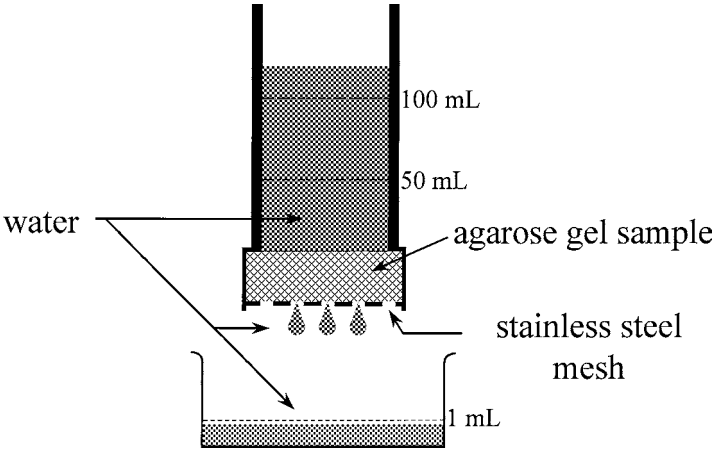

Figure 1. Schematic of custom-built hydraulic permeability quantification apparatus for computation of agarose gel average pore radius in the hydrated state.

pressure, typically a water column generating a pressure of 19 340 dyn cm^{-2}. The hydraulic permeability coefficient for a given hydraulic pressure was measured by quantifying volume of water passed through the gel per unit time for the various gel concentrations. The calculated average pore radius of the gel sample depends on the measured hydraulic permeability and was determined according to previously published methods [22, 23]. For each gel concentration, the mean of at least four independent pore radius calculations was taken to be the average pore radius of the gel.

2.1.3. Computation of agarose gel pore radius in the dehydrated state using scanning electron microscopy (SEM). The agarose gels were prepared for visualization with a scanning electron microscope using two methods: lyophilization (freeze-drying) and critical-point drying. SEM provided access to pore radius measurement after dehydration of gels as well as insight into the morphology of the agarose gels.

2.1.3.1. Agarose gel sample preparation by lyophilization. Lyophilization is commonly used to freeze-dry samples in preparation for electron microscopy. The range of agarose gels mentioned above was frozen to −50°C and dehydrated by lyophilization (Shell Freezer and FreeZone® 4.5 Freeze Dry System, Labconco Corp., Kansas City, MO, USA). The dry gel was submerged in liquid nitrogen for 5–6 min before fracture with a pre-cooled razor blade.

2.1.3.2. Agarose gel sample preparation by critical-point drying (CPD). A different set of agarose gels in the concentration range previously described was prepared for critical-point drying. Each gel sample was submerged in a 25% glycerol solution, a cryo-protectant, for 3 h under gentle agitation. The gels were then fractured while submerged in liquid nitrogen. The fractured gels were thoroughly

washed with increasing concentrations of ethanol, concluding with three 200-proof ethanol washes. The gels were then critical-point dried (CPD 020, Balzers, Hudson, NH, USA) and slowly returned to atmospheric pressure overnight.

Both the lyophilized and the CPD samples were mounted on aluminum stubs and sputter coated (RMC IB-3 Ion Coater, Research and Manufacturing Co., Inc., Tuscon, AZ, USA) at 6 mA for a total of 4 min yielding an approximately 200 Å thick AuPd layer before being analyzed under a JEOL, JSM-840A scanning electron microscope at 10 kV. Scanning electron micrographs of representative sections of the gels were obtained at several different magnifications for analysis of gel morphology and the pore radius was quantified using an image analysis system as described later.

2.2. Culture of embryonic dorsal root ganglia in various agarose gel concentrations–physical structures

Dorsal root ganglia were dissected from embryonic day 9 (E9) chick embryos and cultured in a range of agarose gel concentrations (0.75–2.0% w/v) using a modification of previously published methods [24]. Each full DRG was further dissected into two or three smaller 'DRG pieces.' Briefly, the bottom of one well of a 24-well tissue culture dish (Costar Corporation, Cambridge, MA, USA) was coated with 200 μl of the agarose solution at room temperature. The dish was then placed at 4°C for approximately 15 min to allow the agarose to gel. Typically, 4 DRG pieces were added to another 200 μl of the agarose solution in a 1 ml syringe at room temperature. The liquid agarose solution and the DRGs were carefully mixed by manually pumping the syringe plunger. The entire contents of the syringe were added to the well containing the previously gelled agarose. The dishes were then placed at 4°C and the solution gelled, trapping the DRG pieces in the 3D scaffold. One milliliter of Dulbecco's Modified Eagle's Medium (DMEM, Gibco, Grand Island, NY, USA) supplemented with 10% fetal bovine serum (Gibco), 1% penicillin-streptomycin (Gibco) and 50 ng ml^{-1} nerve growth factor (mNGF 2.5S, M_w: ~26 kDa, Alomone Labs, Jerusalem, Israel) was added to the top of the gels and the dishes stored at 37°C in 5% CO_2 and 95% humidity. The cell-culture medium was changed every 48 h.

2.3. Introduction of charged biopolymers into 3D agarose scaffolds

Polycationic chitosan and polyanionic alginate were used to introduce ambient charge into agarose gels by covalent coupling. Chitosan is a linear cationic polysaccharide consisting of β-(1–4)-linked 2-acetamido-2-deoxy-β-D-glucopyranose and 2-amino-2-deoxy-β-D-glucopyranose. The degree of deacetylation influences both the structure and the physical properties of chitosan [18, 25]. The chitosan used in this study, PROTOSAN^{TM} CL 210 (M_w: 130–160 kDa, Pronova Biopolymer, Oslo, Norway), has approximately 0.85 degree of deacetylation and is soluble in water. The anionic polysaccharide, alginate, is a linear polymer of (1–4)-linked

α-L-guluronic acid (M) and β-D-mannuronic acid (G). Along the alginate molecule, there are both homopolymeric (GG and MM) and heteropolymeric (MG) regions [19, 26, 27]. PRONOVA^{TM} LVG Sodium Alginate (M_w: 150–180 kDa, Pronova Biopolymer, Oslo, Norway) has a relatively high G/M ratio and low viscosity. Both the chitosan and alginate were the generous gift of Dr. Øyvind Skaugrud, Pronova Biopolymer, Oslo, Norway.

2.3.1. Covalent coupling of charged biopolymers to agarose hydrogels. The polycationic polysaccharide chitosan and the polyanionic polysaccharide alginate were covalently coupled to the hydroxyl backbone of agarose to facilitate the probing of the influence of charge on 3D neurite extension. Agarose gels were modified with 1,1′-carbonyldiimidazole (CDI, Aldrich Chemical Co., Inc., Milwaukee, WI, USA) using a modification of the protocol described by M. T. L. Hern [28] (see Fig. 2 for schematic). A 4 ml gel sample of 1.5% agarose was dehydrated by repeated washes in increasing concentrations of acetone followed by dry acetone (dried under 4 Å molecular sieves, Sigma Chemical Co., St. Louis, MO, USA). A CDI solution prepared in dry acetone (30 mg ml^{-1}) was added to the acetone-washed agarose gel. The activation reaction was allowed to proceed for 1 h with gentle agitation. The gel was then washed with dry acetone three times while being shaken vigorously for 5 min per wash to remove unbound CDI. The activated gel was then rehydrated in 3 ml of 100 mM sodium bicarbonate buffer solution (pH = 8.5). Approximately 0.435 μM of either chitosan or alginate was dissolved in deionized water, and the solution was added to the activated gel. The coupling reaction was allowed to proceed overnight under gentle agitation. The chitosan- or alginate-coupled agarose solution was gelled at 4°C. The modified gel was quenched in the sodium bicarbonate buffer overnight to hydrolize unreacted CDI groups and washed five times with deionized water, lyophilized, and reconstituted in PBS to the desired gel concentration of 1.0% w/v. Agarose gels covalently coupled with either chitosan or alginate will be referred to as 'coupled' or 'modified' agarose gels.

Hydraulic permeability testing was performed on 1.0% w/v chitosan-coupled agarose gels and 1.0% w/v alginate-coupled agarose gels following the procedures described earlier. E9 chick DRGs were cultured in 1.0% w/v chitosan-coupled agarose gels and 1.0% w/v alginate-coupled agarose gels following protocols described earlier and neurite extension quantified as described later.

2.3.2. Analytical verification of coupling chemistry. Infrared spectroscopy was used to verify the coupling of chitosan and alginate to agarose. Modified agarose gel samples were dehydrated by lyophilization, to rule out −OH interference and mixed with KBr in powder form. The resulting mixture was pressed into films and analyzed by FTIR spectrometer (Biorad FTS-40, Bio-Rad Laboratories, Digilab Div., Cambridge, MA, USA). In addition to the modified gels, unmodified agarose gels were analyzed as control samples.

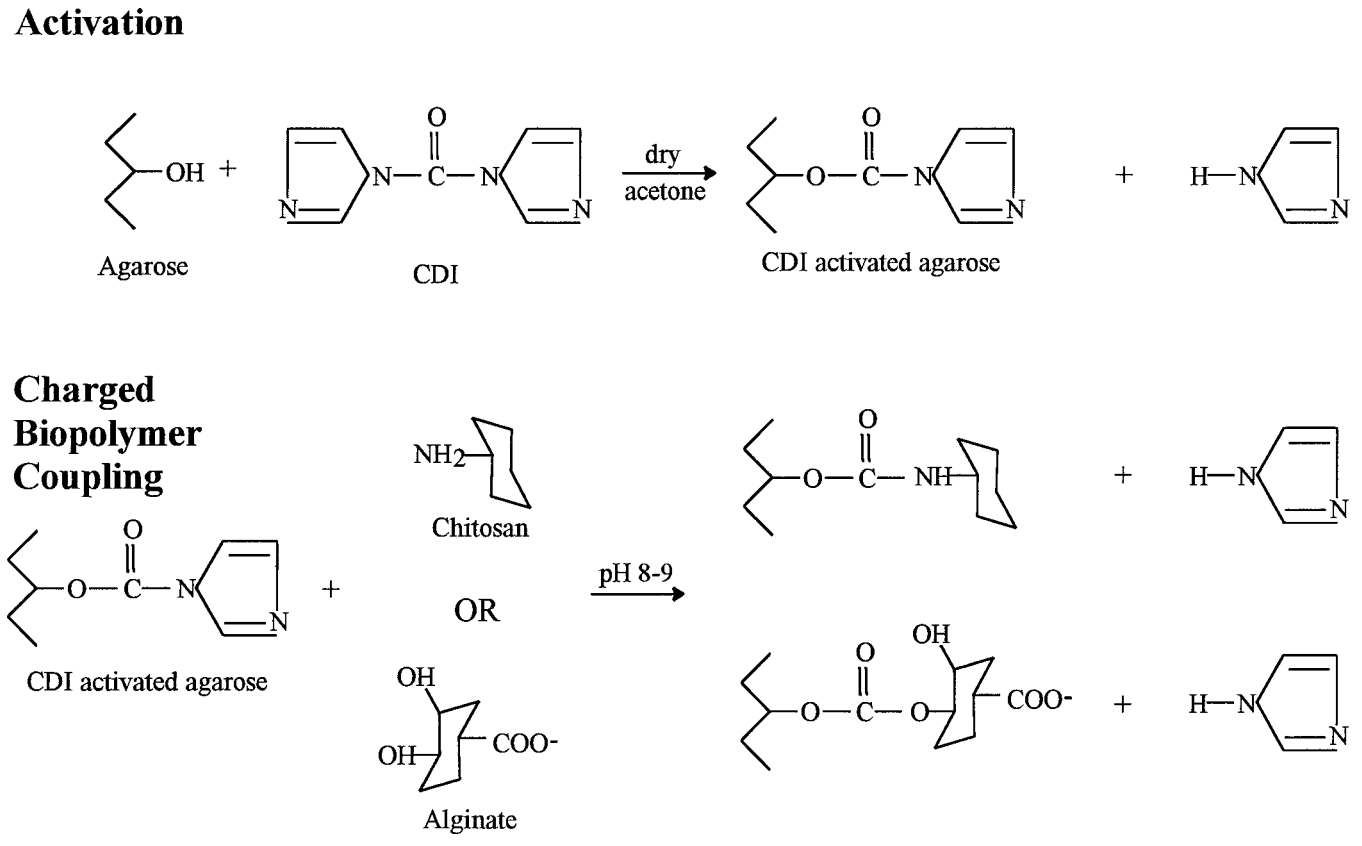

Figure 2. Schematic of 1,1′-carbonyldiimidazole coupling chemistry used to link the charged biopolymers, chitosan and alginate, to agarose gels.

2.4. Analysis and quantification of pore radius and neurite extension

2.4.1. Pore radius of dehydrated gel samples measured via SEM. The electron micrographs obtained during the SEM study were analyzed on a Power Macintosh® 7200 computer (Apple Computer, Inc., Cupertino, CA, USA) running the public domain NIH Image program (developed at the U.S. National Institutes of Health and available on the Internet at http://rsb.info.nih.gov/nih-image/). Two different regions of each gel sample at two different magnifications were analyzed for each agarose gel concentration. The circumference of each completely visible pore within the field of view was manually traced using NIH Image. The pore radius was computed assuming a circular cross section. At least twenty pores were measured at each gel concentration. The average pore radius was taken to be the mean of every pore radius measured at a given concentration.

2.4.2. Quantification of dorsal root ganglia neurite extension. In vitro analysis and quantification of neurite extension in the unmodified and modified agarose gel scaffolds were performed at four days of culture using a digital image analysis system consisting of a Nikon Eclipse TE 300 inverted microscope (Nikon Corporation, Tokyo, Japan), a monochrome CCD camera (Javelin JE7862, Javelin Electronics, Japan), and a Power Macintosh® equipped with the LG-3-PCI frame grabber (Scion Corporation, Frederick, MD, USA) and running the NIH Image software package [29]. Light microscope images of a DRG piece in 3D culture were captured and the eight longest neurites were traced and their length quantified using NIH Image. This process was repeated for at least three more DRGs before the average neurite length for the sample was calculated. The measured neurite lengths were normalized with respect to the 1.0% w/v unmodified agarose control common to all experiments conducted in this study. The length of neurites that DRGs would extend in unmodified agarose gel concentrations other than those experimentally investigated was estimated by using the plot of neurite length versus agarose gel concentration as a standard curve. Two-tailed Student t-tests were performed, and a P-value less than 0.05 was considered to be statistically significant.

3. RESULTS

3.1. Dependence of agarose gel physical properties on gel concentration

3.1.1. Hydraulic permeability. The average pore radius, calculated from the hydraulic permeability measurements of the various agarose gel concentrations, decreased exponentially ($R^2 = 0.938$) as the gel concentration increased (Fig. 3a). With the exception of the 1.5–1.75% w/v values, there is a statistically significant ($P < 0.05$) decrease in average pore radii between consecutive (i.e. 0.75% compared with 1.00%, 1.00% compared with 1.25%, etc.) agarose gel concentrations.

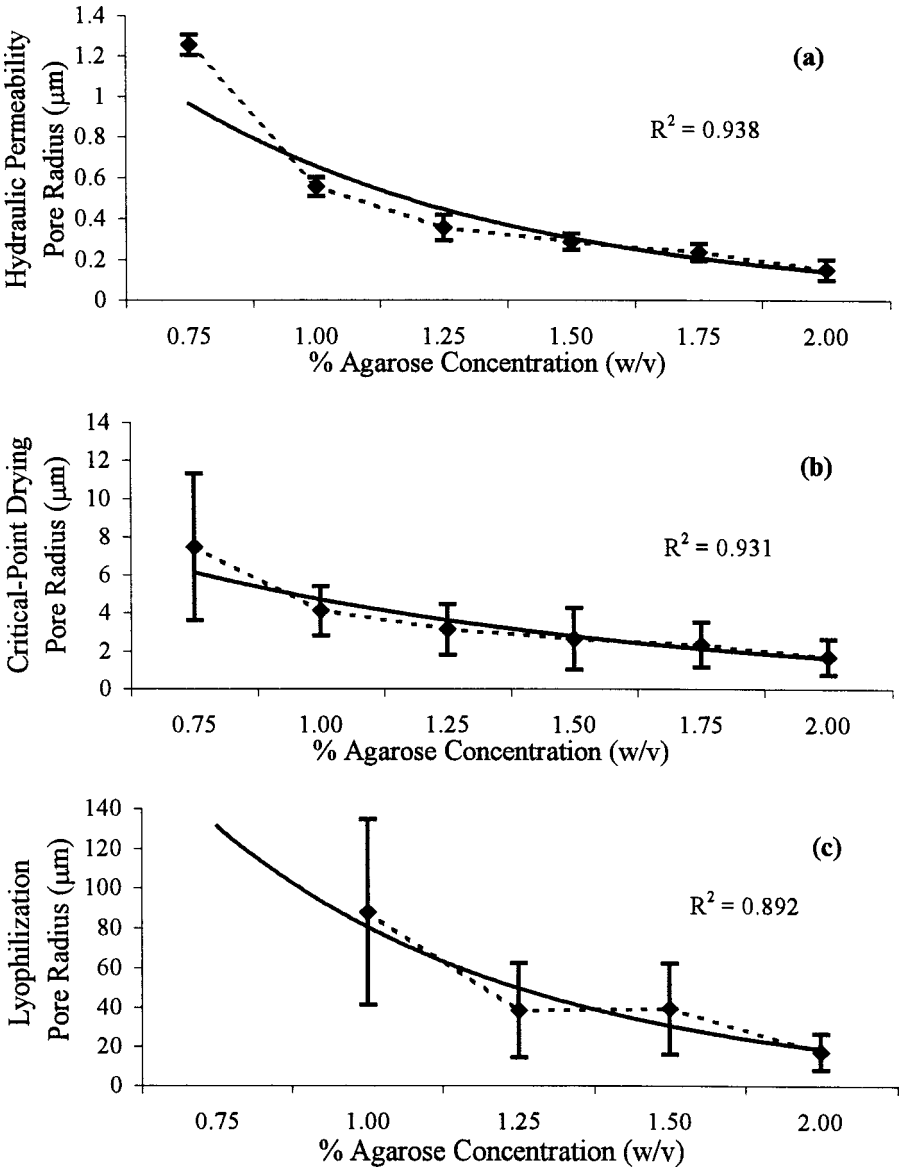

Figure 3. The influence of agarose gel concentration on average pore radius (mean ± SD) — three sample preparation methods. (a) Average wet pore radius calculated by hydraulic permeability. (b) Average dry pore radius measured by analysis of scanning electron micrographs from critical-point dried samples. (c) Average dry pore radius measured by analysis of scanning electron micrographs from lyophilized samples. Note the order of magnitude difference in average pore radius between each of the measurement methods. Solid line through pore radii data points is the exponential fit.

(a)

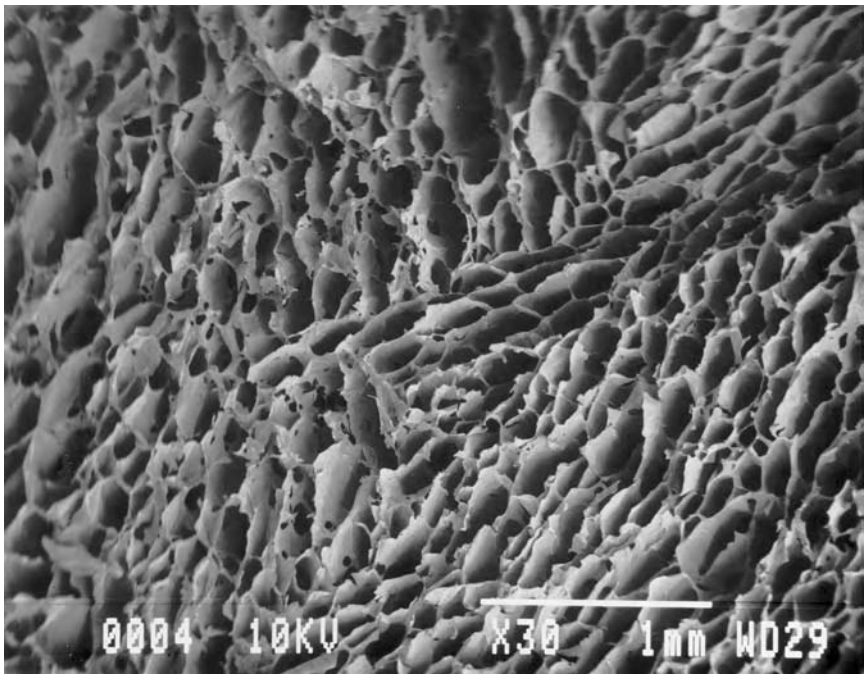

(b)

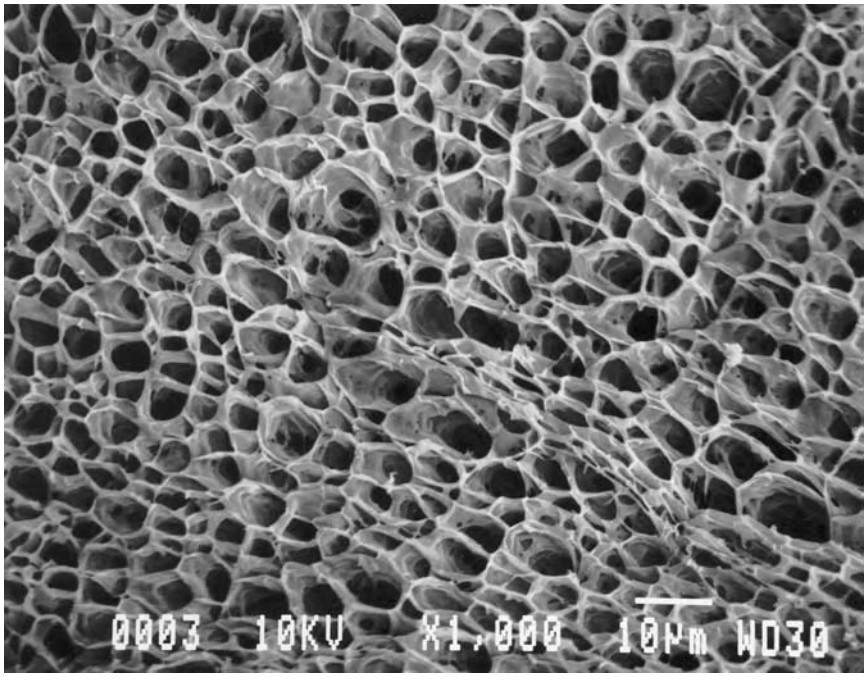

Figure 4. Scanning electron micrographs of 1.0% w/v agarose gels. (a) Lyophilized 1.0% agarose gel at $\times$ 30; scale bar = 1 mm. (b) Critical-point dried 1.0% agarose gel at $\times$ 1000; scale bar = 10 μm. Note the effect of the preparation method on the gel morphology.

3.1.2. SEM. Scanning electron micrographs of different concentrations of agarose gels showed the effect of the preparation method on the morphology of the agarose gel structure (Fig. 4a, b). The lyophilized 0.75% w/v agarose gel concentration sample was not analyzed because the dehydrated gel was too fragile. Both the CPD and lyophilized samples exhibit an open-cell morphology at observed concentrations and an exponential decrease ($R^2 = 0.931$, $R^2 = 0.892$, respectively) in pore radius as agarose gel concentration increased (Fig. 3b, CPD samples; Fig. 3c, lyophilized samples). There is a statistically significant ($P < 0.05$) decrease in average pore radii between each consecutive agarose gel concentration prepared by critical-point drying. At each gel concentration observed, the average pore radius of the lyophilized samples was an order of magnitude greater than that of the CPD samples.

3.2. DRG neurite growth in various agarose gel concentrations

The entire range of agarose gels tested supported neurite outgrowth from cultured DRGs in a concentration-dependent manner. After a statistically significant increase ($P < 0.05$) in neurite length between 0.75 and 1.0% w/v, the length of the neurites extended from the DRGs decreased exponentially ($R^2 = 0.981$) as the gel concentration increased (Fig. 5). The decrease in neurite length is statistically significant ($P < 0.05$) between 1.0–1.25% w/v and 1.25–1.5% w/v agarose gel concentrations.

3.3. Effect of charged biopolymers on DRG function in 3D gels

3.3.1. Confirming covalent coupling of charged biopolymers to agarose gel. After normalization, the FTIR spectrum of the unmodified agarose spectrum was

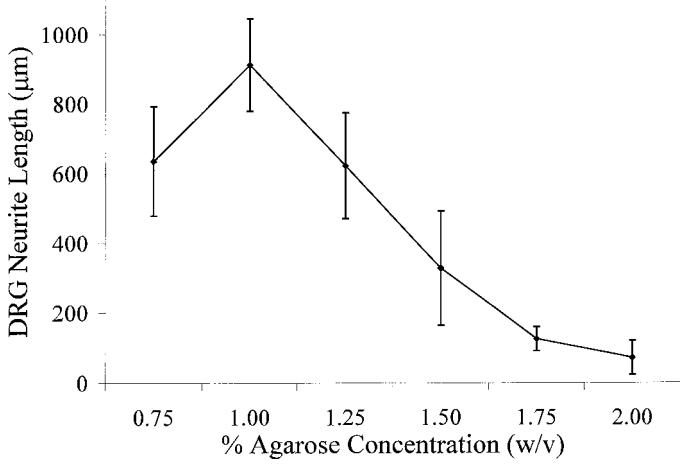

Figure 5. The influence of agarose gel concentration on neurite extension from E9 chick DRGs after 4 days in culture (mean ± SD).

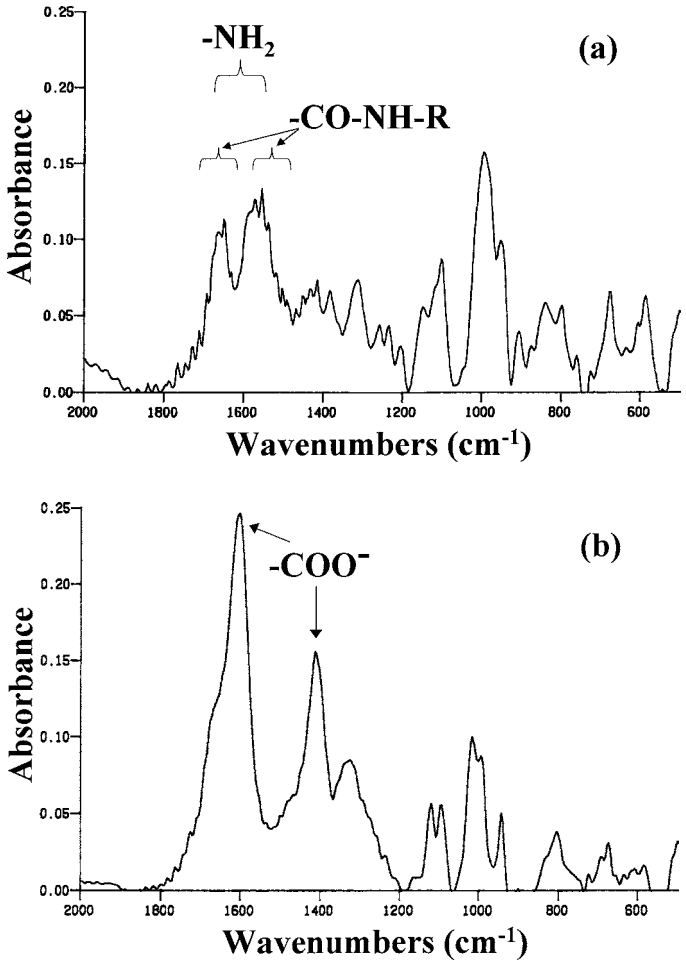

Figure 6. FTIR spectra confirming the presence of charged polysaccharides in CDI modified gels. The unmodified agarose control spectrum has been subtracted from each curve to facilitate peak identification. (a) The presence of coupled chitosan was indicated by the monosubstituted amide, $-CO-NH-R$, peaks. Primary amines, $-NH_2$ groups, may also contribute to the increased absorbance. (b) The labeled peaks are a result of the $-COO^-$ of alginate. SeaPrep® agarose has neither $-CO-NH-R$, $-NH_2$ nor $-COO^-$ groups on its backbone so the groups detected are due to chitosan and alginate, respectively.

subtracted from the modified agarose spectra to highlight the differences in the IR spectra (Fig. 6a, b). The peaks near 1650 and 1560 cm^{-1} are typical of the monosubstituted amides $-CO-NH-R$ present in chitosan-coupled agarose gels [30, 31]. The presence of unreacted $-NH_2$ groups on coupled chitosan also contributes to the increased absorbance near 1650 cm^{-1} [30, 31]. Increased absorbance near 1600 and 1400 cm^{-1} (Fig. 6b) is indicative of the carboxyl ion $-COO^-$ of alginate in the alginate-coupled agarose gels [25, 30, 31].

3.3.2. Hydraulic permeability of charged biopolymer-coupled agarose gels. The average pore radius of 1.0% w/v chitosan-coupled agarose gel determined by hydraulic permeability testing decreased by 35.1% ($P < 0.001$) compared to the pore radius of the unmodified 1.0% w/v agarose gel control. Similarly, the pore radius of 1.0% w/v alginate-coupled agarose gel decreased 25.9% ($P < 0.001$) compared to the same control.

Unmodified agarose gel concentration equivalents to the 1.0% modified gels were estimated by comparing the average pore radii of the modified gels determined by hydraulic permeability to the plot of the average pore radii of various concentration of unmodified agarose gel (Fig. 3a). The chitosan-coupled gel's average pore radius, 0.360 μm, was approximated to be equivalent to the expected pore radius of 1.24% w/v unmodified agarose gel. On the other hand, the alginate-coupled gel's average pore radius, 0.411 μm, was approximately equivalent to the estimated pore radius of 1.17% w/v unmodified agarose gel.

3.3.3. DRG neurite growth in charged biopolymer-coupled agarose gels. E9 chick DRGs suspended in the 1.0% w/v unmodified agarose control (Fig. 7a, c), 1.0% w/v chitosan (Fig. 7b) and 1.0% w/v alginate (Fig. 7d) modified gels extended neurites. Neurite extension was quantified at the fourth day of culture. DRGs entrapped in the chitosan coupled agarose gel exhibited neurites that were 41% longer than the unmodified agarose control (Fig. 8). However, the alginate coupled agarose gel inhibited the neurite extension by 41% (Fig. 8) as determined by the image analysis system described earlier.

4. DISCUSSION

Hydrogels are ideal biomaterial scaffolds for soft-tissue reconstruction due to their low interfacial tension, high molecular and oxygen permeability, high water content, and soft rubbery mechanical properties resembling those of physiological soft tissues [32, 33]. Previous studies have demonstrated that agarose hydrogels have the necessary physiochemical structure to support 3D neurite extension from anchorage-dependent primary neural cells [24, 34]. Agarose gel concentration can be easily modified to yield gels of varying pore radii [34]. These prior results [34] suggest that agarose gel concentration and the corresponding pore radius are important physical properties that influence neural cell function. Since primary chick dorsal root ganglia have no known receptors for agarose, neural cell response to purely physical changes in the scaffold can be isolated and studied *in vitro*. The structure–function relationship between agarose and DRG neurite extension can be explored *in vitro* and, in future studies, will aid the optimization of the agarose gel structure for maximal neurite extension. In this study, the relationship between agarose gel concentration and average pore radius was determined by several different methods. Also, the effects of varied gel concentrations on neurite extension from embryonic day 9 chick dorsal root ganglia were thoroughly examined.

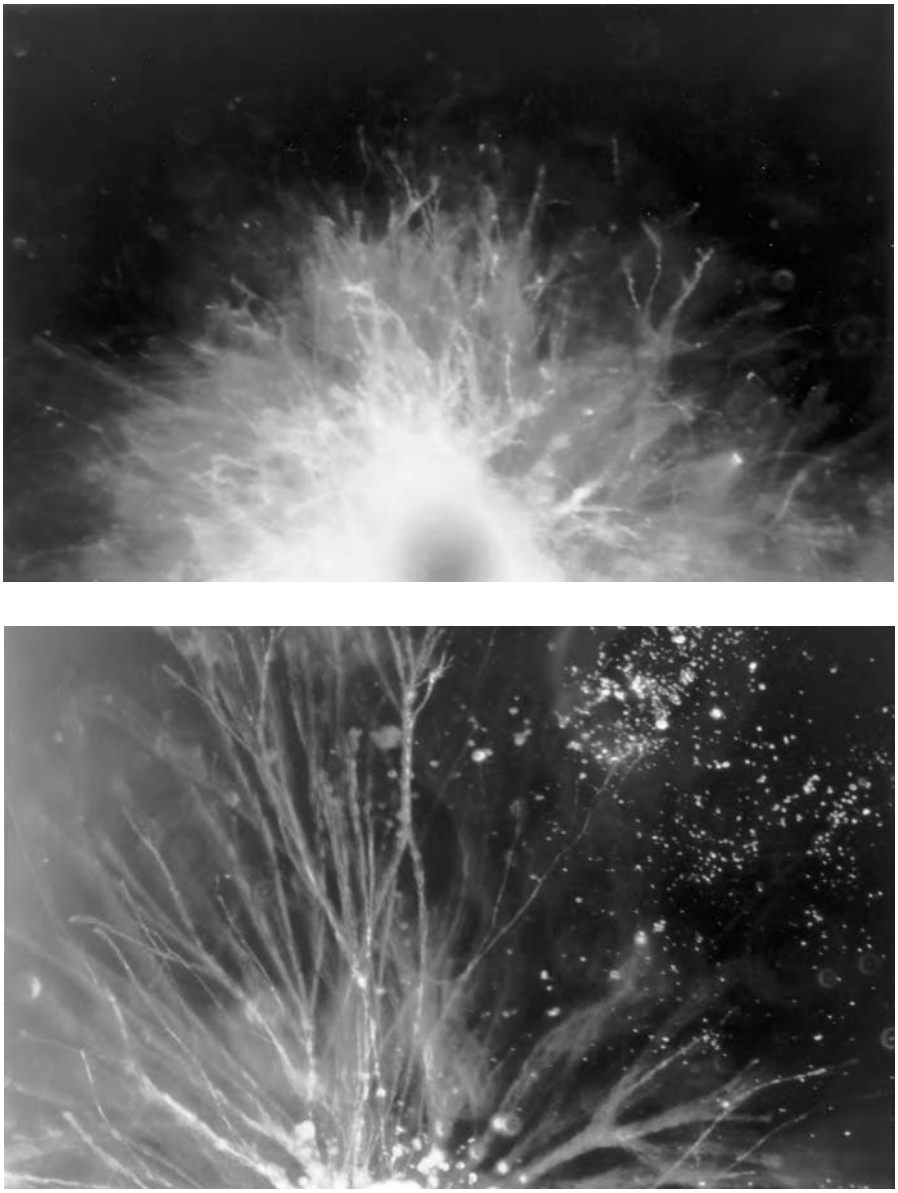

(a)

(b)

Figure 7. Light micrographs of E9 chick DRGs extending neurites in charged polysaccharide coupled and unmodified agarose gels after four days in culture. The 1.0% w/v agarose control is presented at two magnifications to facilitate visual comparison of neurite extension. (a) 1.0% w/v agarose control (magnification $= \times 80$); (b) 1.0% w/v chitosan coupled agarose gel (magnification $= \times 80$); (c) 1.0% w/v agarose control (magnification $= \times 100$); (d) 1.0% w/v alginate coupled agarose gel (magnification $= \times 100$).

(c)

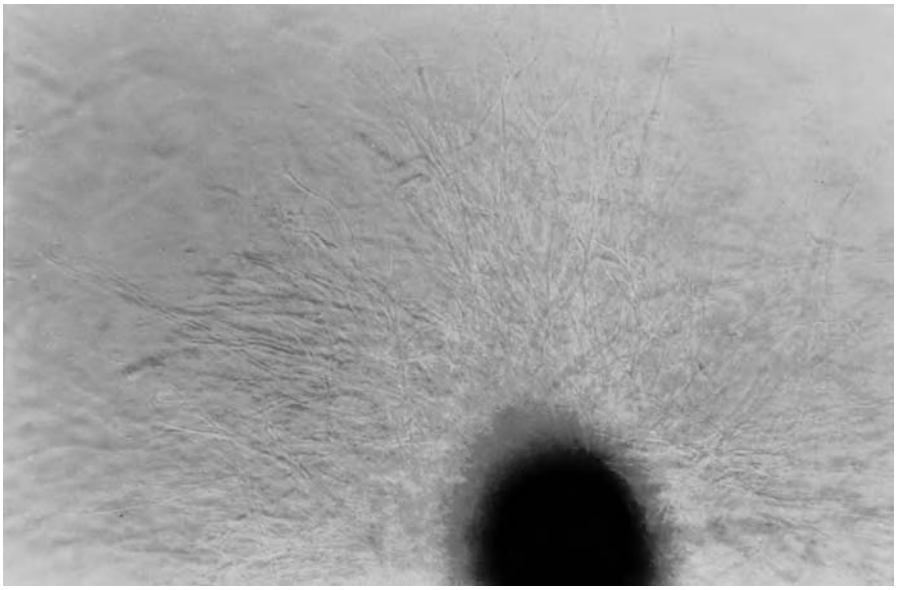

(d)

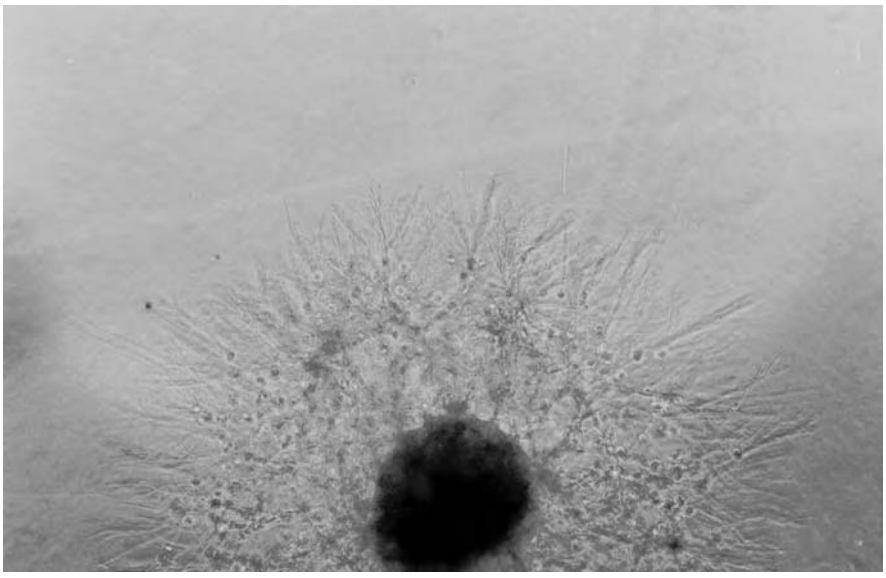

Figure 7. (Continued.)

Agarose gel concentration and average pore radius were taken to be characteristic parameters representing the physical properties of agarose gel that are relevant to neurite extension in three-dimensions. Average pore radius of each of the gel concentrations studied was calculated by three different methods in order to investigate the effects of preparation technique on agarose gel physical structure. Hydraulic permeability measurements allowed the calculation of average pore radius of hydrated agarose gels. As the gel concentration increased, the average

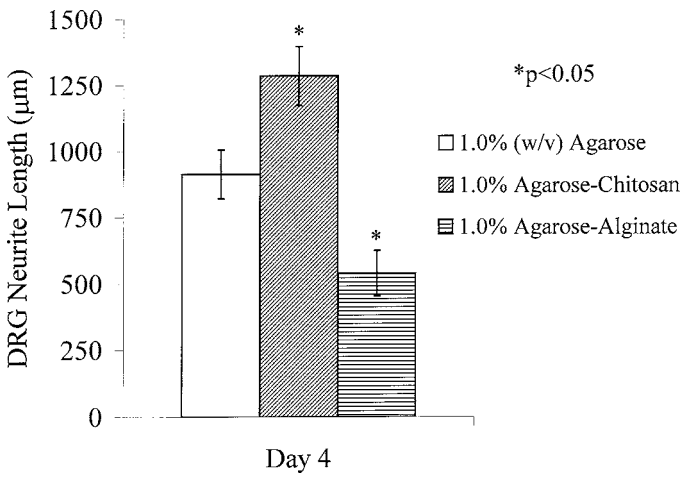

Figure 8. Histogram comparing E9 chick DRG neurite extension in charged polysaccharide coupled and unmodified agarose gels after 4 days in culture. Statistical significance is with respect to the unmodified 1.0% w/v agarose control (mean ± SD).

pore radius decreased exponentially (Fig. 3a). The average pore radii calculated by hydraulic permeability was comparable to the values obtained by Bellamkonda *et al.* using similar techniques [34].

The scanning electron microscopic study was conducted in order to gain insight into the agarose gel morphology. Two dehydration protocols were employed to prepare the range of unmodified agarose gels for visualization by SEM. The routinely employed SEM sample-preparation techniques, lyophilization and critical-point drying allowed for comparison of the effects of the two dehydration processes on gel morphology in their dehydrated states. The micrographs obtained from each preparation technique revealed an open-cell morphology (Fig. 4a, b). Also, consistent with the average pore radii of the hydrated agarose gel samples determined by hydraulic permeability testing, the measured average dry pore radii determined by two different drying techniques decreased exponentially as the agarose gel concentration was increased (Fig. 3b, c). Between consecutive agarose gel concentrations (i.e. 0.75% compared with 1.0%, 1.0% compared with 1.25%, etc.) there is a statistically significant ($P < 0.05$) difference in the average pore radius as determined by hydraulic permeability testing and critical-point drying. The only exception being the 1.5–1.75% average pore radius values determined by hydraulic permeability ($P < 0.065$). This lack of statistical significance could be due to an intrinsic property of agarose gel formation in this concentration range or the nature of the hydraulic permeability test. That is, while many individual pores were directly measured by the SEM methods in order to calculate a single average pore radius at a given concentration, the hydraulic permeability test provides only an estimate of the average pore radius for each sample tested.

The CPD average pore radii were an order of magnitude greater than the values attained by the hydraulic permeability measurement. Similarly, the average pore

radii of lyophilized agarose gels were an order of magnitude greater than the CPD values, and two orders of magnitude greater than the values obtained by hydraulic permeability testing. The relatively rapid freeze and fracture in liquid nitrogen before critical-point drying resulted in an order of magnitude increase in the average pore radii. However, the morphological change of the agarose gel observed using the critical-point drying protocol was not as dramatic as the two orders of magnitude increase observed in the slower freeze to $-50\,^{\circ}C$ before lyophilization. This study indicates that the rate of freezing has a profound effect on the physical structure. Neither of these two SEM preparation methods accurately represents the pore radius of hydrated agarose gels as determined by hydraulic permeability. The three distinct ranges of average pore radii measured by these different methods illustrate that: (a) pore radius varies with gel concentration; and (b) the pore radius measured is dependent on sample preparation. These results confirm the hypothesis proposed by Bellamkonda *et al*. [34] that the dehydration and freeze-dry processing of agarose gels contributes to the increase in average pore radius compared to the pore radii determined in the hydrated state by hydraulic permeability. These results suggest that analytical techniques using high vacuum environments may be of limited value in the characterization of highly hydrated 3D hydrogel physical structure because of the structural changes associated with sample dehydration. When the agarose hydrogel is dried, the hydrophilic agarose chains may be collapsed due to the high surface tension of water [35]. Therefore, the dried hydrogel becomes more compact in size [35] and, as demonstrated here, the pore radius increases. Although the values of the absolute pore radii are perhaps not accurately determined by SEM analysis, the exponential decay in pore radius with increasing agarose gel concentration was confirmed.

The length of neurites extended by DRGs cultured in unmodified agarose gel depends on agarose gel concentration. At concentrations greater than 1.0% w/v, the neurite length decreased as the agarose gel concentration increased. As previously reported [34], when the agarose gel concentration increases from 1.0 to 2.0% w/v, the electrophoretic mobility of insulin (M_w: 5700) and albumin (M_w: 66 000) falls only by 5.7 and 2.9%, respectively. Therefore the decrease in neurite extension is not due to impediments in neuronal cell nutrition, since most of the known cell nutrient, and nerve growth factor (M_w: $\sim$26 kDa) have a molecular weight lower than albumin [34]. Between consecutive agarose gel concentrations below 1.5% w/v, there is a statistically significant ($P < 0.05$) difference in the length of neurites extended. At concentrations greater than 1.5%, the decrease in extended neurite length is no longer statistically significant. The similar trends of the pore radius (Fig. 3a) and neurite length (Fig. 5) vs agarose gel concentration curves indicate a relationship between the physical structure characteristic (i.e. pore radius) and the neural cell function (i.e. neurite extension) being investigated. Due to the decrease in extended neurite length in agarose gel concentrations above and below 1.0%, it is our conclusion that, among the range of concentrations investigated, the physical properties of 1.0% agarose gel are best suited to support neurite extension from E9

chick dorsal root ganglia. Other agarose gel physical parameters, such as stiffness, may have a similar relationship with neurite extension or other neural cell functions. Further investigations are underway to determine the precise mechanisms of the structure–function dependency of neural cell function on agarose gel pore radius and other physical characteristics.

During the covalent coupling of chitosan or alginate to the agarose gel (Section 2.3.1), it is assumed that the CDI-coupled agarose and the charged biopolymer solution (i.e. chitosan or alginate dissolved in deionized water) are uniformly mixed. Although chitosan may begin to precipitate at this pH (pH $\cong$ 8), the solution is vigorously agitated during the coupling reaction. After the coupling reaction, the modified agarose solution is allowed to gel and any chitosan or alginate that is not covalently coupled to the gel, including any chitosan that may have precipitated, is washed away during the sodium bicarbonate quench procedure and the deionized water washes. The modified agarose gel is lyophilized and reconstituted in PBS as a liquid for DRG culture, further ensuring a uniform dispersion of the covalently coupled biopolymer throughout the modified agarose gels. Our hypothesis of uniform dispersion of the charged biopolymer through the modified gel is confirmed by the absence of an observable difference in the length of neurites extended from DRGs cultured in different regions of the modified agarose gels.

Furthermore, unpublished preliminary experiments demonstrated that simply mixing chitosan with agarose gel does not provide a suitable substrate for E9 chick DRG neurite extension. In the chitosan–agarose mixes investigated, there was either no neurite extension or greatly inhibited neurite extension as opposed to the enhanced neurite extension observed in the covalently coupled chitosan–agarose gels. These results imply that any chitosan that was not covalently coupled to the agarose gel would have actually inhibited rather than enhanced neurite extension.

Polycationic chitosan and polyanionic alginate were successfully covalently coupled to an agarose gel as confirmed by FTIR spectroscopy. The significant increase in neurite length in the chitosan-coupled agarose gels is more notable when the average pore radius of the modified agarose gels is taken into consideration. The average pore radius of the 1.0% w/v chitosan-coupled gel is equivalent to that of 1.24% w/v unmodified agarose gel. Compared to DRGs cultured in 1.0% w/v unmodified agarose (control), we would expect DRGs in 1.24% w/v unmodified agarose gel to have approximately a 31% decrease in neurite length at day 4. However, DRGs cultured in the 1.0% w/v chitosan-coupled gel exhibited a 41% increase in neurite length compared to the control. On the other hand, while we would expect DRGs in 1.17% unmodified agarose — the alginate-coupled gel pore radius equivalent — to extend 19% shorter neurites, the length of neurites extended was inhibited by 41%.

Unpublished experiments from our lab demonstrate no statistically significant difference in the neurite length of E9 DRGs cultured in 1.0% (w/v) CDI activated agarose gels (i.e. acetone washed and CDI coupling performed but no bioactive polymer covalently coupled to the gel) compared to 1.0% (w/v) SeaPrep® agarose

control. Since the decrease in pore size has been accounted for and no neural cell receptor interactions with the modified agarose gels are known, we reason that the effect on neurite extension is a result of the charge associated with the biopolymer-coupled agarose gels. These results suggest that charged biopolymers and the polarity of charge can significantly influence neurite extension in 3D hydrogel scaffold.

During fetal development, negatively charged molecules such as chondroitin sulfate proteoglycans repel axons and inhibit neural cell adhesion [36, 37]. Many mechanisms have been proposed to describe the inhibitory and excitatory functions of sulfated proteoglycans. One proposed mechanism implicates the glycosaminoglycan (GAG) chains themselves as the inhibitors of neurite outgrowth [36]. The variations in the inhibitory effect between proteoglycans may be due to differences in the length and/or conformation of the GAG chains or differences in the degree or pattern of sulfation of the GAG chains [36], or their ability to localize growth factors [38, 39]. Although neither chondroitin sulfate proteoglycan (CSPG) nor the chondroitin sulfate sugars alone (CS) are used in this study, the hypothesized influence of the negatively charged sulfated side groups may provide a physiological relevance for the inhibitory effects of ambient negative charge observed in the alginate coupled-agarose substrate.

We believe that a precise understanding of the correlation and the mechanisms responsible for the correlation between 3D scaffolds and corresponding neural cell differentiation in 3D is critical for effective neural tissue engineering. Investigations are underway in our laboratory to further understand, characterize and optimize neurite extension in 3D hydrogel scaffolds. These scaffolds may potentially find application as 3D synthetic bridges for bridging lesioned nerve gaps.

5. CONCLUSIONS

Agarose hydrogels are a suitable model system that can be used to investigate the structure–function relationship between polymer scaffolds and 3D neurite extension. Proper characterization of agarose gel pore radius and corresponding neurite extension is necessary to gain further insight into the structure–function relationship. The introduction of charged biopolymers into the agarose hydrogel backbone influences 3D neurite extension in a polarity dependent manner. Covalently coupling a positively charged biopolymer, chitosan, to the agarose hydrogel significantly enhances neurite extension while covalently coupling a negatively charged biopolymer, alginate, significantly inhibits neurite extension compared to the neurite extension observed in unmodified agarose gel.

Acknowledgements

This research was partially funded by the Elmer L. Lindseth Endowment and The Whitaker Foundation. We would like to thank Dr. Øyvind Skaugrud of Pronova

Biopolymer, Oslo, Norway for the generous gift of both the chitosan and alginate. We would like to thank Mr. Brian Keener for technical assistance and Mr. Khalid Kader for useful discussions.

REFERENCES

1. J. R. Sanes, *Ann. Rev. Neurosci.* **12**, 491 (1989).
2. L. Ettinger and F. Doljanski, *Biol. Rev. Cambridge Phil. Soc.* **67**, 459 (1992).
3. K. A. Venstrom and L. F. Reichardt, *FASEB J.* **7**, 996 (1993).
4. E. D. Hay, *Cell Biology of Extracellular Matrix*. New York, Plenum Press (1991).
5. P. C. Letourneau, M. L. Condic and D. M. Snow, *J. Neurosci.* **14**, 915 (1994).
6. P. C. Letourneau, *Molecular Basis of Neuronal Development*. John Wiley & Sons, New York (1985).
7. C. T. Brighton, J. Black and S. R. Pollack (Eds), *Electrical Properties of Bone and Cartilage*. Grune and Stratton, New York (1979).
8. K. J. McLeod, R. C. Lee and H. P. Ehrlich, *Science* **236**, 1465 (1987).
9. R. F. Valentini, T. G. Vargo, J. A. Gardella and P. Aebischer, *Biomaterials* **13**, 183 (1992).
10. M. Opas, *Developmental Biol.* **131**, 281 (1989).
11. J. C. Geesin, L. J. Brown, J. S. Gordon and R. A. Berg, *Exp. Cell Res.* **206**, 283 (1993).
12. P. Clark, P. Connolly, A. S. Curtis, J. A. Dow and C. D. Wilkinson, *Development* **108**, 635 (1990).
13. P. Clark, P. Connolly, A. S. G. Curtis, J. A. T. Dow and C. D. W. Wilkinson, *J. Cell Sci.* **99**, 73 (1991).
14. S. T. Carbonetto, M. M. Gruver and D. C. Turner, *Science* **216**, 897 (1982).
15. D. Kleinfeld, K. H. Kahler and P. E. Hockberger, *J. Neurosci.* **8**, 4098 (1988).
16. S. A. Makohliso, R. F. Valentini and P. Aebischer, *J. Biomed. Mater. Res.* **27**, 1075 (1993).
17. T. Matsumoto, M. Kawai and T. Masuda, *Biorheol.* **30**, 435 (1993).
18. M. W. Anthonsen, Ph.D. Thesis, Norwegian Institute of Technology, Trondheim (1993).
19. A. Martinsen, Ph.D. Thesis, Norwegian Institute of Technology, Trondheim (1990).
20. D. A. Rees, *Biochem. J.* **126**, 257 (1972).
21. S. Arnott, *J. Mol. Biol.* **90**, 269 (1974).
22. M. L. White, *J. Phys. Chem.* **64**, 1563 (1960).
23. M. F. Refojo, *J. Appl. Polymer Sci.* **9**, 3161 (1965).
24. R. V. Bellamkonda, J. P. Ranieri and P. Aebischer, *J. Neurosci. Res.* **41**, 501 (1995).
25. T. Matsumoto, M. Kawai and T. Masuda, *Biopolym.* **31**, 1721 (1991).
26. A. Martinsen, G. Skjal-Braek and O. Smidsrod, *Biotechnol. Bioeng.* **33**, 79 (1989).
27. A. Haug, B. Larsen and O. Smidsrod, *Acta Chem. Scand.* **20**, 183 (1966).
28. M. T. W. Hearn, *Methods Enzymol.* **135**, 102 (1987).
29. S. Shaw, E. D. Salmon and R. S. Quatrano, *Biotechniques* **19**, 946 (1995).
30. J. F. Rabek, *Experimental Methods in Polymer Chemistry: Physical Principles and Applications*. John Wiley & Sons, New York (1980).
31. D. Lin-Vien, N. B. Colthup, W. G. Fateley and J. G. Grasselli, *The Handbook of Infrared and Raman Characteristic Frequencies of Organic Molecules*. Academic Press, Boston, MA (1991).
32. J. D. Andrade (Ed.), *Hydrogels for Medical and Related Applications*. ACS Symp. Ser. **31**, 1–36 (1976).
33. N. A. Peppas (Ed.), in: *Hydrogels in Medicine and Pharmacy*, Vol. III, pp. 53–82. CRC Press, Boca Raton, FL (1987).
34. R. V. Bellamkonda, J. P. Ranieri, N. Bouche and P. Aebischer, *J. Biomed. Mater. Res.* **29**, 663 (1995).

35. H. Park and K. Park, in: *Hydrogels and Biodegradable Polymers for Bioapplications*, R. M. Ottenbrite, S. J. Huang and K. Park (Eds), Ch. 1, p. 1. American Chemical Society, Washington, DC (1996).
36. D. M. Snow, V. Lemmon, D. A. Carrino, A. I. Caplan and J. Silver, *Exp. Neurol.* **109**, 111 (1990).
37. D. M. Snow and P. C. Letourneau, *J. Neurobiol.* **23**, 322 (1992).
38. R. Roberts, J. Gallagher, E. Spooncer, T. D. Allen, F. Bloomfield and T. M. Dexter, *Nature* **332**, 376 (1988).
39. E. Ruoslahti and Y. Yamaguchi, *Cell* **64**, 867 (1991).

This page intentionally left blank

Polymers for Tissue Engineering, pp. 397–411
Molly S. Shoichet and Jeffrey A. Hubbell (Eds)

Complexation of basic fibroblast growth factor with gelatin

Md. MUNIRUZZAMAN, YASUHIKO TABATA and YOSHITO IKADA*

Research Center for Biomedical Engineering, *Kyoto University*, *53 Kawahara-cho Shogoin*, *Sakyo-ku*, *Kyoto 606*, *Japan*

Received 9 September 1997; accepted 17 November 1997

Abstract—Polyion complexation between basic fibroblast growth factor (bFGF) and gelatin was studied by the turbidity change of mixed solution, heparin high performance liquid affinity chromatography (HPLAC), and isoeletric eletrophoresis. When an aqueous solution of acidic gelatin with an isoelectric point (IEP) of 5.0 was mixed with that of bFGF, the turbidity of the mixed solution increased with time, whereas basic gelatin with an IEP of 9.0 did not cause any solution turbidity. A maximum turbidy of the mixed bFGF and acidic gelatin solution was observed around a bFGF/gelatin molar ratio of 1.0, irrespective of the gelatin concentration and solution temperature. The solution turbidity decreased with an increase in the ionic strength of the mixed solution. Complexation of bFGF with acidic gelatin was slower than that with poly(acrylic acid) probably because of the lower density of gelatin negative charge than that of poly(acrylic acid). HPLAC study revealed that complexation of bFGF with the acidic gelatin reduced the affinity of bFGF for heparin, in contrast to the basic gelatin, although the extent became smaller with the increasing ionic strength of the solution. An electrophoretic experiment showed that the IEP of bFGF shifted to a lower value after its gelatin complexation. These findings indicate that an electrostatic interaction is the main driving force for the complexation between acidic gelatin and basic bFGF.

Key words: Gelatin; basic fibroblast growth factor; polyion complex; turbidimetric titration; heparin HPLAC; isoelectric electrophoresis.

INTRODUCTION

Since the advent of tissue engineering, continuous efforts have been made to design various scaffolds for reconstruction of lost or damaged tissues and organs. Various biodegradable scaffolds have been explored to demonstrate the *in vivo* efficacy in promoting cell proliferation and tissue regeneration [1]. In addition, it has been recognized that cell growth factors are very effective in accelerating tissue regeneration [2]. However, tissue regeneration by use of growth factors has not always succeeded due to several reasons. One of them is too short half-life periods of growth factors in the body to expect the sustained biological activities when the factors are injected

*To whom correspondence should be addressed. E-mail: yyikada@medeng.kyoto-u.ac.jp

without any pharmaceutical modification. One possible way for enhancing the *in vivo* efficacy of growth factors is to facilitate their sustained release over an extended time period by their incorporation into a polymer carrier. If this carrier is biodegraded in harmonization with tissue growth, it will function as a scaffold for tissue regeneration in addition to the carrier for growth factor release. It is well known that some of the functions of basic fibroblast growth factor (bFGF) include being a potent mitogen for mesenchymal cells, inducing neovascularization [3, 4], osteogenesis [5–17], and accelerating nerve regeneration [18, 19]. Therefore, bFGF seems to be a key factor applicable to tissue engineering. If bFGF is effectively released in the body for a required period of time, it will be highly likely to promote body tissue regeneration.

As is widely recognized, bFGF molecules have a strong affinity for acidic glycosaminoglycans, such as heparin and heparan sulfate, probably resulting in protection of bFGF from denaturation and enzymatic degradation *in vivo* [3, 4, 20]. A promising means to release bFGF in the body is to take advantage of this *in vivo* polyion complexation of basic bFGF molecules. We have predicted that a biodegradable hydrogel prepared from acidic gelatin may form a polyion complex with bFGF, which will be released *in vivo* as a result of hydrogel degradation [21]. The scheme for bFGF release is illustrated in Fig. 1. Indeed, acidic gelatin hydrogels incorporating bFGF were found to enhance its *in vivo* vascularization [22] and osteogenesis effects [23] in contrast to the bFGF injected in the solution form, indicating a high *in vivo* efficacy of bFGF–gelatin polyion complexes in potentiating the biological activities of bFGF.

The objective of this study is to get a deep insight into the polyion complexation between gelatin and bFGF. After mixing gelatin and bFGF in an aqueous solution, the complexation process was investigated based on turbidity, heparin HPLAC, and isoelectric electrophoresis, and the results compared with those observed for polyion complexes between bFGF and heparin or synthetic polyanions. In addition, we studied the influence of the temperature and ionic strength of the mixed solution on the polyion complexation.

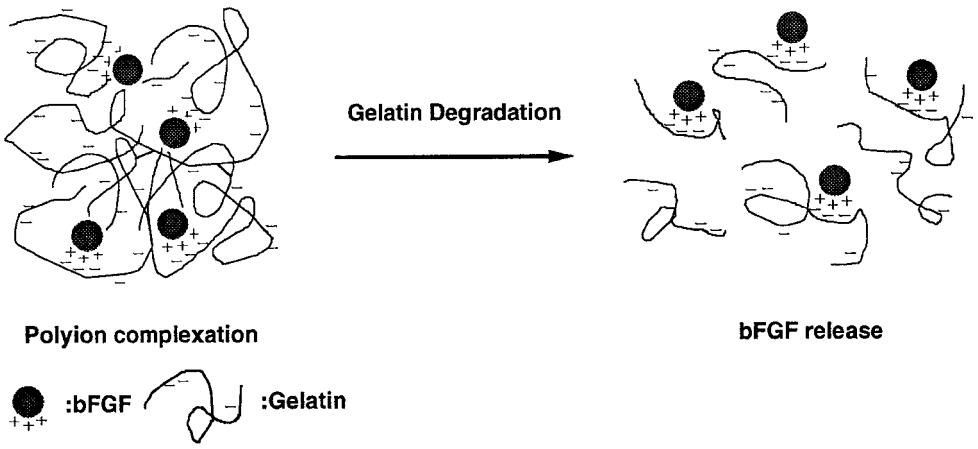

Figure 1. Scheme of bFGF release from biodegradable gelatin hydrogel.

MATERIALS AND METHODS

Materials

Human recombinant bFGF (M_w = 17 000, IEP = 9.6) was kindly supplied from Kaken Pharmaceutical Co., Tokyo, Japan. Gelatin samples with IEPs of 5.0 and 9.0 (M_w = 99 000 and 99 000) were obtained from Nitta Gelatine Co., Osaka, Japan, and are named here as acidic and basic gelatin because of their acidic and the basic features, respectively. Heparin sodium salt (M_w = 20 000), poly(vinyl sulfuric acid) potassium salt (PVS, M_w = 243 300, degree of substitution = 98.8%), and poly(acrylic acid) (PAAc, M_w = 450 000) were purchased from Nacalai Tesque, Inc., Kyoto, Japan and Polysciences Inc., Warrington, PA, USA, respectively. Other chemicals were purchased from Wako Pure Chemical, Ltd., Osaka, Japan, and used without further purification.

Turbidity measurements

The turbidity of bFGF solution appeared upon its mixing with gelatin and bFGF at 4, 25, and 37°C in 1/15 M phosphate-buffered solution (PB, pH 7.0) containing various concentrations of sodium chloride. PB solution containing different concentrations of acidic or basic gelatin (100 μl) was added to each of a 96-well culture plate (Nunc, Kamstrup, Roskilde, Denmark), followed by addition of different concentrations of bFGF solution in PB (100 μl). At different time intervals, the turbidity of the mixed bFGF and gelatin aqueous solution was measured on a UV_{max} Kinetic Plate Reader (Molecular Devices Corp., Menlo Park, CA, USA) at a wavelength of 541 nm. The solution turbidity was expressed by the absorbance at 541 nm. Turbidity change was also measured in PB solutions of different pHs ranging from 4.8 to 7.5 to evaluate the effect of solution pH on the complexation between bFGF and acidic gelatin. PB solutions containing different concentrations of heparin, PAAc, and PVS were added to the PB solution of bFGF at a concentration of 0.313 mg ml^{-1} and the solution absorbance was measured at 37°C. Every experiment was done in triplicate and the absorbance was expressed as means ± standard error (SE).

Chromatographic study

PB solution (200 μl) containing 3.6 mg ml^{-1} of acidic or basic gelatin was mixed with PB solution of various bFGF concentrations (200 μl) in the presence or absence of various concentrations of NaCl. Following incubation at 37°C for different periods of time, the mixed bFGF and gelatin aqueous solution was subjected to chromatographic measurements by HPLAC equipped with a heparin affinity column (HPLAC, Toyo Soda Co., Tokyo, Japan) to evaluate the change in heparin affinity of bFGF accompanied with complexation. Since the intact bFGF and its complex with gelatin were separately eluted at different retention times on the HPLAC chromatogram, we could estimate the time profile of the area change in both HPLAC peaks after mixing bFGF with gelatin.

Isoelectric electrophoresis

Electrophoresis was performed for acidic gelatin, bFGF, and mixtures of bFGF and acidic gelatin after 10 min, 1, 3, 6, and 12 h of mixing at 37°C using a 4% polyacrylamide gel kit (pI 3–10), TEFCO Corp., Tokyo, Japan. The sample solution (15 μl) diluted twice with 20% sucrose aqueous solution was added to 15 μl of 1% cyclohexylaminoethane sulfonic acid aqueous solution, and the solution mixture applied to each sample well of electrophoresis gel. Anolyte and catholyte reservoirs were filled with 500 ml of 0.01 M H_3PO_4 and 200 ml of 0.05 M NaOH aqueous solutions, respectively. Voltage was applied in the following stepup manner; 100 V for 30 min, 200 V for 30 min, and 500 V for 60 min. The electrophoresed gel was fixed with aqueous solution of 17% trichloroacetic acid and 3.2% sulphosalicylic acid for 60 min. After washing with a mixture of methanol : acetic acid : water (500 : 100 : 400), the gel was stained with 0.1% Coomassie Brilliant Blue aqueous solution. Then, the gel was rinsed with the mixed methanol–acetic acid aqueous solution to view the migration of each sample band relative to standard proteins with different IEPs.

RESULTS

Turbidity appearing after mixing bFGF with gelatin

Figure 2 shows the turbidity change with time at 37°C for the mixed solutions prepared from various concentrations of bFGF and 1.8 mg ml^{-1} of acidic or basic gelatin in PB solution. When the acidic gelatin was mixed with bFGF, no solution turbidity was observed until 3 h after mixing, irrespective of the bFGF concentration. However, thereafter the turbidity of the mixed bFGF and gelatin solution appeared and a maximum turbidity was observed at a bFGF concentration of 0.313 mg ml^{-1}, irrespective of the complexation time (Fig. 2A). A similar trend on the time and bFGF concentration profiles of complexation was noticed at a gelatin concentration of 0.18 mg ml^{-1}. On the contrary, it is apparent that the basic gelatin could not elicit any turbidity in the mixed solution, irrespective of the bFGF concentration and complexation time. The turbidity for bFGF in PB solution containing acidic gelatin at 4 and 25°C is given in Fig. 3. The turbidity dependence of the mixed bFGF and gelatin solution on the bFGF concentration at these low temperatures was similar to that at 37°C. The solution turbidity increased with the complexation time and exhibited a maximum at both 4 and 25°C when the bFGF concentration was 0.313 mg ml^{-1}.

Table 1 summarizes the optimal molar ratio of bFGF to gelatin in their polyion complexes, where the maximum solution turbidity was observed, together with that of bFGF to heparin, PAAc, and PVS. The optimal bFGF/gelatin molar ratio was around 1.0, irrespective of the solution temperature and gelatin concentration. For other bFGF/polyanion combinations, higher ratios than 1.0 were observed. The optimal bFGF/polyanion ratio increased in the order PVS $>$ PAAC $\gg$ heparin. The number of repeated residues being complexed with one bFGF molecule increased in the reverse order. The molar ratio of bFGF to PVS was higher than that of PAAc.

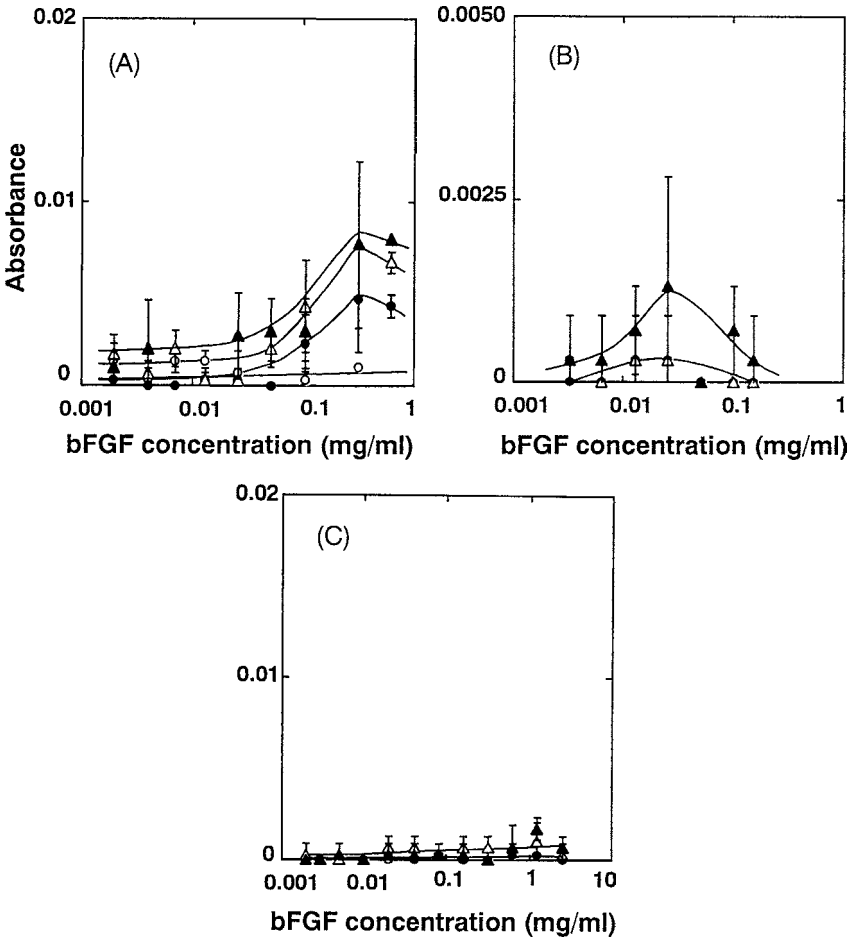

Figure 2. Absorbance change of gelatin solutions mixed with various concentrations of bFGF in 1/15 M phosphate-buffered solution (pH 7.0) with time: (○) 3; (●) 12; (△) 24; and (▲) 48 h after mixing of gelatin with bFGF at 37°C. (A) acidic gelatin (1.8 mg ml^{-1}) with IEP of 5.0, (B) acidic gelatin (0.18 mg ml^{-1}) with IEP of 5.0, and (C) basic gelatin (1.8 mg ml^{-1}) with IEP of 9.0.

Figure 4 shows the time course of complexation between bFGF and acidic or basic gelatin at 4, 25, and 37°C. The turbidity of the mixed bFGF and gelatin solution increased with the complexation time. No significant difference in the time profile of solution turbidity was observed, irrespective of the solution temperature, although a slower increase in the solution turbidity for the initial 5 h was observed at 4°C. For comparison, the time course of complexation between bFGF and PAAc at 37°C is also shown in Fig. 4A. It is apparent that the bFGF was complexed with a synthetic polyanion, PAAc, at a higher rate than with the acidic gelatin. The turbidity of bFGF/PAAc solution increased much more steeply than that of bFGF/gelatin solution for the initial 1 h and gradually levelled off after about 24 h. The solution turbidity increased in a similar time profile, independent of the solution temperature (data not shown).

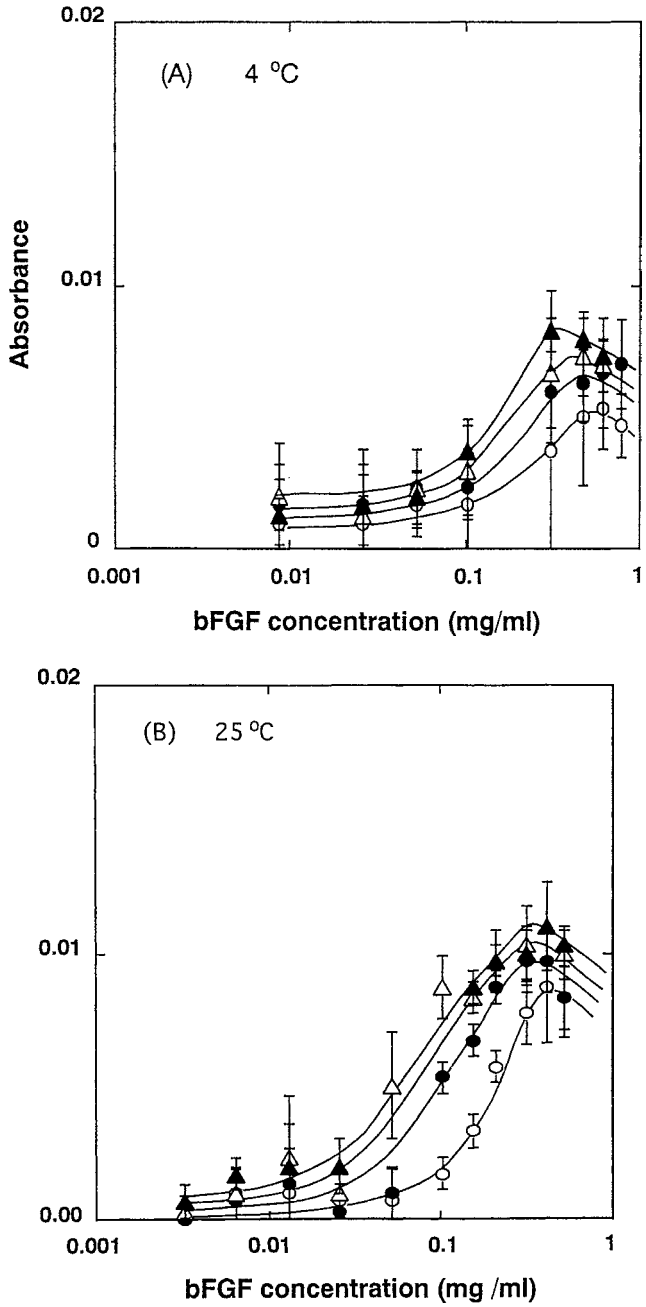

Figure 3. Absorbance change of acidic gelatin solutions (1.8 mg ml^{-1}) mixed with various concentrations of bFGF in 1/15 M phosphate-buffered solution (pH 7.0) with time: (○) 12; (●) 24; (△) 48; and (▲) 72 h after mixing of acidic gelatin with bFGF at (A) 4 and (B) 25 °C.

Table 1.
The optimal molecular ratio of bFGF to various polyanions in their polyion complexes

Polyanion		bFGF concentration ($mg\,ml^{-1}$)	Solution temperature (°C)	Optimal bFGF/polyanion[b] molar ratio
Type	Concentration[a] ($mg\,ml^{-1}$)			
Acidic gelatin	1.8	0.313	4	1.0
Acidic gelatin	1.8	0.313	25	1.0
Acidic gelatin	1.8	0.313	37	1.0
Acidic gelatin	0.18	0.0313	37	1.0
Heparin	0.23	0.313	37	60 (6.3)[c]
PAAc	1.8×10^{-2}	0.313	37	1000 (45.0)
PVS	4.0×10^{-3}	0.313	37	1870 (12.6)

[a]The polyanion concentration where maximum turbidity of mixed solution was observed.
[b]The molar ratio of bFGF to the polyanion for complex formation with a maximum turbidity.
[c]The number of repeated residues complexed per bFGF molecule.

The effect of solution pH on the turbidity of mixed bFGF and gelatin aqueous solution at 37°C is shown in Fig. 5. The solution turbidity tended to increase with the complexation time, irrespective of the solution pH, showing a maximum at pH 5.8. In this study, the solution pH was fixed at the physiological pH 7.0, although such a maximum solution turbidity was not obtained at this pH.

Figure 6 gives the effect of solution ionic strength on the turbidity change of mixed bFGF and acidic gelatin solutions. The complexation experiment was performed in PB solution containing different concentrations of NaCl at 37°C. The turbidity of the solution increased with time, irrespective of the solution ionic strength, but the higher the ionic strength of the mixed solution, the less significantly the turbidity increased. When the ionic strength of solution was higher than 0.5, the increase in solution turbidity was less significant than that at lower ionic strength.

HPLAC evaluation for complexation between bFGF and gelatin

HPLAC chromatograms of bFGF after different time periods of mixing with acidic or basic gelatin in PB solution at 37°C are shown in Fig. 7. When the acidic gelatin was added to the PB solution of bFGF, the HLPAC peak area corresponding to the intact bFGF decreased with the complexation time without any change in the retention time. On the other hand, a new peak attributed to bFGF–gelatin complexes appeared at a shorter retention time than that of intact bFGF, and the peak area increased with the complexation time. After 24 h of complexation, only the complex peak was detected on the HPLAC chromatogram while the bFGF peak disappeared. However, it is apparent from Fig. 7B that no new peak was observed upon mixing of bFGF with the basic gelatin over the time period studied. The peak area of intact bFGF seemed to decrease with complexation.

Figure 8 shows the time course of peak area ratio of the intact bFGF and the peak area of its complex on the HPLAC chromatogram after mixing bFGF with the acidic gelatin in PB solution at 37°C. The peak area ratio of the intact bFGF was defined as the peak area ratio of the intact bFGF after mixing with acidic gelatin to that before

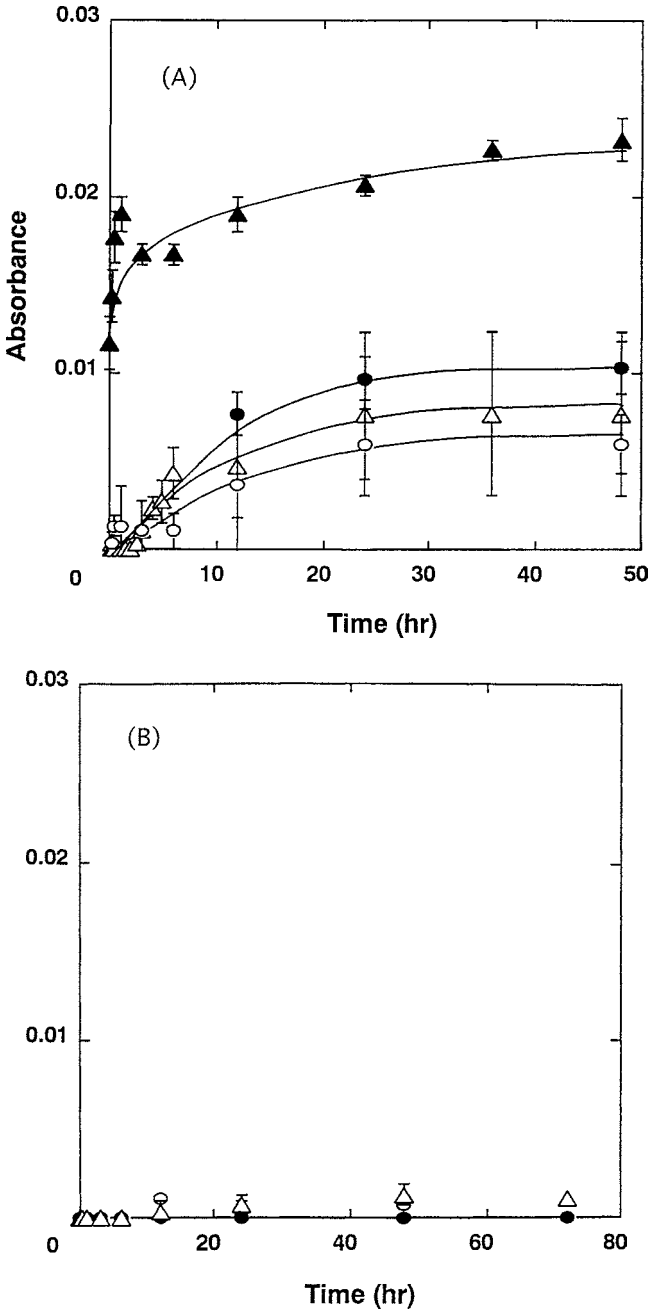

Figure 4. The temperature effect on the absorbance of gelatin and PAAc solutions mixed with 0.313 mg ml^{-1} of bFGF in 1/15 M phosphate-buffered solution (pH 7.0) at: (○) 4; (●) 25; and (△) 37 °C. (A) Acidic gelatin with IEP of 5.0 and PAAc (0.006 mg ml^{-1}) at 37 °C (▲) and (B) basic gelatin with IEP of 9.0.

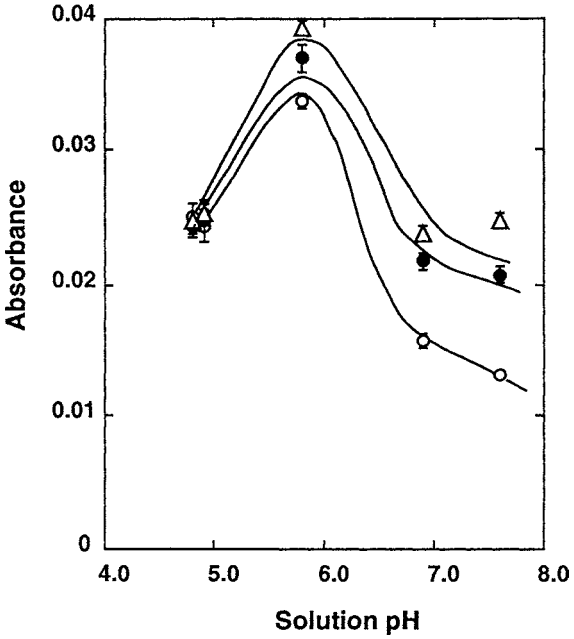

Figure 5. The effect of the solution pH on the turbidimetric titrations of 0.313 mg ml^{-1} of bFGF in 1.8 mg ml^{-1} of acidic gelatin with IEP of 5.0 in 1/15 M phosphate-buffered solution: (○) 24; (●) 48; and (△) 72 h after mixing of gelatin with bFGF at 37°C.

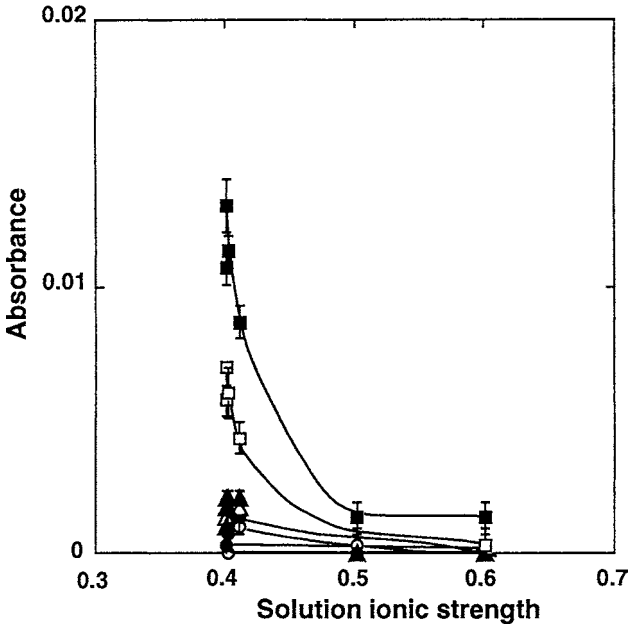

Figure 6. The effect of solution ionic strength on the absorbance of acidic gelatin solution (1.8 mg ml^{-1}) mixed with 0.313 mg ml^{-1} of bFGF in 1/15 M phosphate-buffered solution (pH 7.0): (○) 10 min, (●) 1; (△) 3; (▲) 6; (□) 12; and (■) 24 h after mixing of gelatin (5.0 IEP) with bFGF at 37°C.

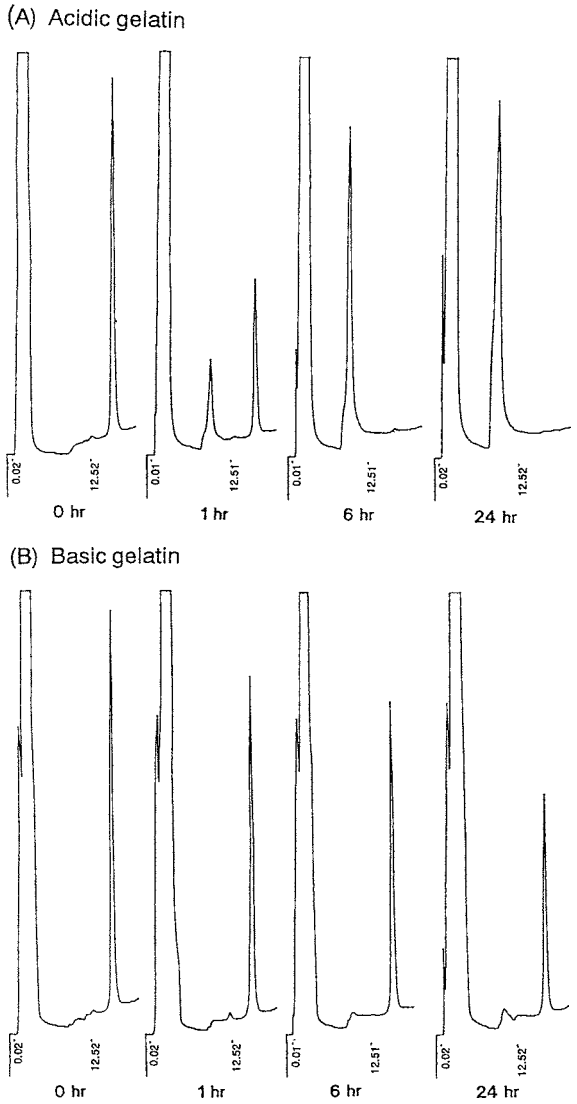

Figure 7. Heparin HPLAC chromatograms of bFGF (0.313 mg ml^{-1}) after mixing with gelatin (1.8 mg ml^{-1}) in 1/15 M phosphate-buffered solution (pH 7.0) at 37°C. (A) Acidic gelatin with IEP of 5.0 and (B) basic gelatin with IEP of 9.0.

mixing. The peak area ratio of bFGF decreased with complexation. Oppositely, the peak area of the bFGF–gelatin complex increased up to 12 h, and then levelled off.

The effect of solution ionic strength on the peak area ratio of intact bFGF and the peak area of its complex with the acidic gelatin after 24 h of solution mixing is shown in Fig. 9. The peak area ratio of the intact bFGF decreased with a decrease in the ionic strength of the mixed bFGF and gelatin solution and became zero when double-distilled water was used for complexation study. On the other hand, the peak area of the bFGF–acidic gelatin complex in turn increased with decreasing solution ionic

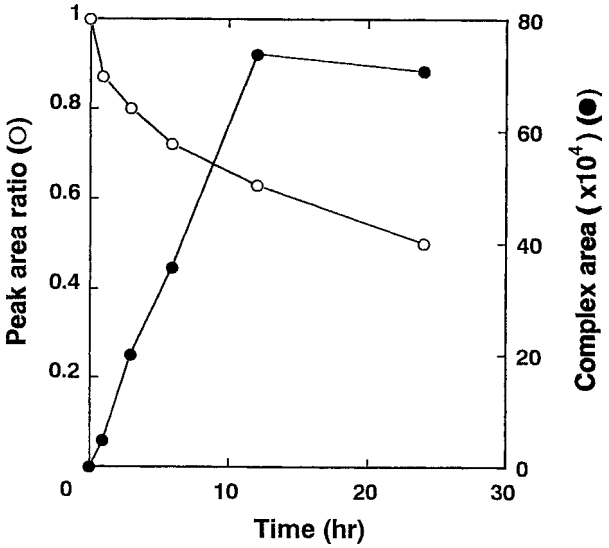

Figure 8. The time course of the HPLAC peak area of bFGF and its complex with acidic gelatin after mixing of gelatin (1.8 mg ml^{-1}) with bFGF (0.313 mg ml^{-1}) in 1/15 M phosphate-buffered solution (pH 7.0) at 37°C.

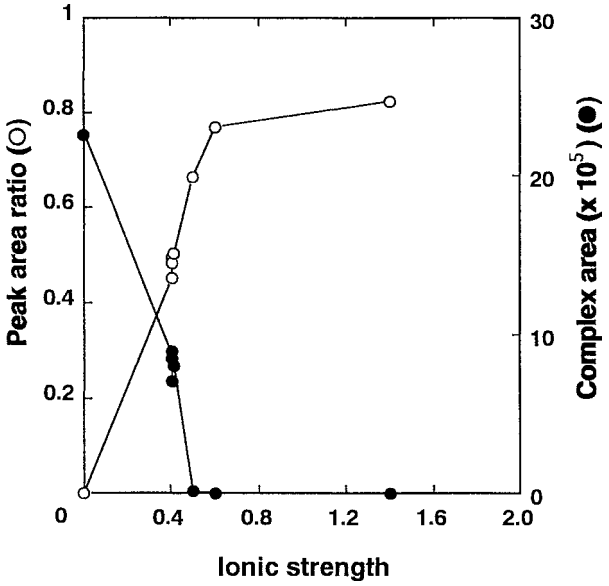

Figure 9. The effect of the solution ionic strength on the HPLAC peak area of bFGF and its complex with the acidic gelatin 24 h after mixing of gelatin (1.8 mg ml^{-1}) with bFGF (0.313 mg ml^{-1}) in 1/15 M phosphate-buffered solution (pH 7.0) at 37°C.

strength. It is apparent that the change in the peak profile of HPLAC chromatogram became more significant with the increase in ionic strength of the mixed solution and the complex peak was not seen at the solution ionic strength of $\geqslant 0.5$ at all.

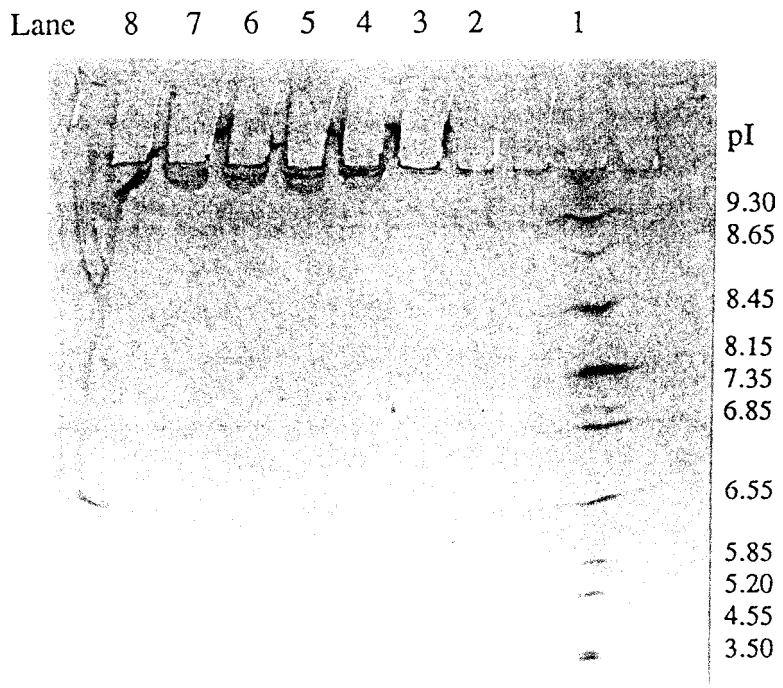

Figure 10. Isoelectric electrophoresis of bFGF (1 mg ml^{-1}) before and after polyion complexation with acidic gelatin (5.75 mg ml^{-1}) in 1/15 M phosphate-buffered solution (pH 7.0) at 37 °C. Lane 1: marker proteins; Lane 2: gelatin; Lane 3: bFGF; and Lanes 4–8: bFGF–gelatin complexes. The complexation times are 10 min (Lane 4), 1 (Lane 5), 3 (Lane 6), 6 (Lane 7), and 12 h (Lane 8).

Isoelectric electrophoresis of bFGF complexed with gelatin

A representative result of isoelectric electrophoresis of bFGF before and after complexation with the acidic gelatin at 37 °C is given in Fig. 10. As is seen in Lane 3, the intact bFGF did not migrate because of its IEP of 9.6. while the acidic gelatin had migrated around the position of marker protein with IEP 5.20 although the band was not clear because of the poor stainability of gelatin. However, bFGF was electrophoresed to the direction of lower IEP through the gelatin complexation. The extent of band migration tended to become larger with complexation time.

DISCUSSION

It is well known in polymer science that a positively or negatively charged polyelectrolyte interacts with the oppositely charged one to form a polyion complex [24, 25]. The present study has demonstrated that polyion complexation is formed between basic bFGF and acidic gelatin, which have positive and negative charges at the physiological pH of 7.0, respectively. On the contrary, the basic gelatin with an IEP of 9.0 could not form a polyion complex with bFGF because of no ionic interaction. Figures 2 and 3 revealed that bFGF formed a polyion complex with the acidic gelatin

in a similar complexation profile, irrespective of the solution temperature. Less occurrence of the initial complexation was observed at 4 °C although the time profile of solution turbidity was similar, irrespective of the solution temperature (Fig. 4). This may be ascribed to the intermolecular interaction of gelatin which more significantly takes place at lower temperature. It is possible that the intermolecular aggregation of gelatin molecules reduced the number of charged groups which could interact with bFGF for polyion complexation, resulting in poor complexation in the initial stage.

Complexation between bFGF and gelatin was suppressed, as the NaCl concentration of the solution increased (Fig. 6). The HPLAC study revealed that the higher the ionic strength of the mixed bFGF and gelatin solution, the less the peak area of the intact bFGF decreased. It is well recognized that an addition of salts decreases the electrostatic interaction among polyelectrolytes due to a charge shielding effect [26]. It is reported that this shielding effect emerges at a solution ionic strength higher than 0.7–1.0 [27]. These findings indicate that the electrostatic interaction is responsible for the bFGF–gelatin complexation.

As is well recognized, stoichiometric polyelectrolyte complexes are formed as a result of charge neutralization, in other words, the optimal ratio between the oppositely charged groups in the complex is 1 : 1 [28, 29]. These complexed compounds are insoluble in water, leading to a maximum turbidity. In the present study, a maximum turbidity of the mixed bFGF and polyanion was observed, irrespective of the polyanion type. Faham *et al*. reported that bFGF ionically complexed with heparin at a complexation ratio of one bFGF molecule per 6.0 repeated residues of heparin [30]. This ratio is in good accordance with that observed in the present study. The optimal ratios for PAAc and PVS were about two and seven times as high as the ratio of heparin, respectively. Such a difference in the ratio may be ascribed to different conformations of polymer chains and acidity of the anionic groups. Since it is likely that the polymer chain of heparin composed of hexose rings possesses more extended conformation than that of PAAc and PVS composed of vinyl chains, bFGF molecules will interact with heparin more readily than with other polyanions, resulting in a smaller number of repeated residues for complexation with one bFGF molecule. As the acidity of sulfonic groups is higher than that of carboxyl groups, this acidity difference will result in a smaller number of VS residues per bFGF molecule. It is known that the content of carboxyl groups in one gelatin molecule is approximately 17% of the total amino acids [31]. These carboxyl groups mainly contribute to the complexation of gelatin with bFGF. The clear dependence of bFGF–gelatin complexation on the solution pH (Fig. 5) suggests that an ionic interaction takes place between the weak acid and base. The optimal molar ratio of bFGF/gelatin was much lower than that of bFGF/PAAc, although both polymers have carboxylic groups. This can be explained in terms of the density and distribution of the charged group. Gelatin is a copolymer of different amino acids with anionic, cationic, and non-charged groups, leading to a low density of negative charges and poor localization of anionic groups along the gelatin molecule. Therefore, it will be more difficult for gelatin to electrically interact with bFGF than for PAAc which is composed of only carboxylic groups although gelatin is totally charged negatively at the physiological pH.

The lower complexation rate of bFGF with acidic gelatin than that of bFGF with PAAc (Fig. 4) may be also ascribed to the lower charged density of gelatin. It follows that gelatin must interact more weakly with bFGF than PAAc, resulting in slower complexation.

HPLAC experiments revealed that complexation with the acidic gelatin affected the chromatographic profile of bFGF in contrast to the basic gelatin. The significant dependence of the chromatographic peak area on the solution ionic strength (Figs 8 and 9) again indicates that the ionic interaction is responsible for the complexation between the acidic gelatin with bFGF. If bFGF molecules are covered with ionically complexed gelatin, the heparin affinity of bFGF will reduce and shorten its retention time. The slightly lowered IEP of bFGF by polyion complexation, as shown in Fig. 10, may be also explained from the viewpoint of ionic interaction. It is reasonable that partial neutralization of the electric charge of bFGF through polyion complexation with the acidic gelatin lowered the IEP of bFGF. However, it was much less than that expected based on complexation. The reason is not clear at present.

CONCLUSIONS

The growth factor, bFGF, could form a polyion complex with acidic gelatin at a bFGF/gelatin molar ratio of 1/1 in contrast to basic gelatin. The complexation extent was reduced with an increase in the ionic strength of the mixed solution, indicating that the main contribution to complexation is electrostatic interaction. The complexation rate was much lower than that between bFGF and PAAc because of its lower density and poor localization of charged groups. The affinity of bFGF for heparin was reduced and the IEP of bFGF was lowered when polyion complextion took place between bFGF and the acidic gelatin. These phenomena seem to be due to the surface covering of bFGF molecules with gelatin through ionic interaction.

Acknowledgements

This work was supported by a grant of 'Research for the Future' Program from the Japan Society for the Promotion of Science (JSPS-RFTF96I00203).

REFERENCES

1. A. Atala and D. J. Mooney, *Synthetic Biodegradable Schaffolds*. Brikhäuser, Boston (1997).
2. W. M. Saltzman, *MRS Bull.* **21**, 62 (1996).
3. D. Gospodarowizc, N. Ferrara, L. Schweigerer and G. Neufeld, *Endocrinol. Rev.* **8**, 95 (1987).
4. D. B. Rifkin and D. Moscatlli, *J. Cell Biol.* **109**, 1 (1989).
5. P. V. Hauschka, A. E. Maurakos, M. D. Ifrati, S. E. Doleman and M. Klagbrun, *J. Biol. Chem.* **261**, 12 665 (1986).
6. R. K. Globus, P. Palouet and D. Gospodarowizc, *Endocrinology* **124**, 1539 (1989).
7. R. K. Globus, P. Patterson-Buckendahl and D. Gospodarowizc, *Endrocrinology* **123**, 98 (1988).
8. S. B. Rodan, G. Wesolowski, K. A. Thomas, K. Yoon and G. A. Rodan, *Connect. Tissue Res.* **20**, 283 (1989).
9. P. Cuevas, J. Burgos and A. Baird, *Biochem. Biophys. Res. Commun.* **156**, 611 (1988).

10. B. Froger-Gaillard, M. Carrier, S. Thenet, X. Ronot and M. Adolphe, *Exp. Cell Res.* **183**, 388 (1989).
11. E. Canalis, M. Centrella and T. McCarthy, *J. Clin. Invest.* **81**, 1572 (1988).
12. H. Kawaguchi, T. Kurokawa, K. Hanada, Y. Hiyama, M. Tamura, E. Ogawa and T. Matsumoto, *Endocrinology* **135**, 774 (1994).
13. T. Nakamura, K. Hanada, M. Tamura, T. Shibanushi, H. Nigi, M. Tagawa, S. Fukumoto and T. Matsumoto, *Endocrinology* **136**, 1276 (1995).
14. H. Schiephake, F. W. Neukam, A. Löhr and D. Hutmacher, *Int. J. Oral Maxillofac. Surg.* **24**, 181 (1995).
15. J.-S. Wang, *Acta Orthop. Scand.* (*Suppl. 269*) **67**, 1 (1996).
16. G. Wellmitz, E. Petzold, K. D. Jentzch, G. Heder and P. Buntrock, *Exp. Pathol.* **18**, 282 (1980).
17. S. B. Trippel, *J. Rheumatol.* (*Suppl. 43*) **22**, 129 (1995).
18. P. Aebischer, A. N. Salessiontis and S. R. Winn, *J. Neurosci. Res.* **23**, 282 (1989).
19. A. Laquerriere, P. Peulve, O. Jin, J. Tiollier, M. Tardy, H. Vaudry, J. Hemet and M. Tadie, *Microsurgery* **15**, 203 (1994).
20. J. Taipale and J. Keski-Oja, *FASEB* **11**, 51 (1997).
21. Y. Tabata and Y. Ikada, *Adv. Drug Delivery Rev.* (1997) (in press).
22. Y. Tabata, S. Hijikata and Y. Ikada, *J. Control. Rel.* **31**, 189 (1994).
23. K. Yamada, Y. Tabata, K. Yamamoto, S. Miyamoto, I. Nagata, H. Hikuchi and Y. Ikada, *J. Neuorosurg.* **86**, 871 (1997).
24. M. Hara (Ed.), *Polyelectrolytes*. Marcel Dekker, New York (1993).
25. P. Dubin, J. Bock, R. M. Davies, D. N. Schulz and C. Thies (Eds), *Macromolecular Complexes in Chemistry and Biology*. Springer Verlag, Berlin (1994).
26. P. C. Hiemenz, *Principles of Colloid and Surface Chemistry*. Marcel Dekker, New York (1996).
27. K. Abe, H. Phno and E. Tsuchida, *Makromol. Chem.* **178**, 2285 (1979).
28. V. A. Kabanov and A. B. Zezin, *Makromol. Chem. Suppl.* **6**, 259 (1984).
29. V. A. Kabanov, *Pure Appl. Chem.* (*Macromol. Chem.*) **8**, 121 (1973).
30. S. Faham, R. E. Hileman, J. R. Fromm, R. J. Linhardt and D. C. Rees, *Science* **271**, 1116 (1996).
31. A. Veis, *The Macromolecular Chemistry of Gelatin*. Academic Press, New York (1964).

This page intentionally left blank

Polymers for Tissue Engineering, pp. 413–432
Molly S. Shoichet and Jeffrey A. Hubbell (Eds)

Ectopic bone formation induced by biodegradable hydrogels incorporating bone morphogenetic protein

MASAYA YAMAMOTO, YASUHIKO TABATA and YOSHITO IKADA*

Research Center for Biomedical Engineering, Kyoto University, 53 Kawahara-cho Shogoin, Sakyo-ku, Kyoto 606, Japan

Received 24 June 1997; accepted 21 October 1997

Abstract—Biodegradable hydrogels were prepared from gelatin by glutaraldehyde cross-linking for release matrix of recombinant human bone morphogenetic protein-2 (BMP-2). BMP-2 solution was impregnated into the dried hydrogels to prepare BMP-2-incorporating gelatin hydrogels. In the *in vitro* study, enhanced retention of BMP-2 was observed from the BMP-2-incorporating gelatin hydrogels after an initial burst of BMP-2 incorporated initially in the hydrogel. Following subcutaneous implantation of ^{125}I-labeled BMP-2-incorporating gelatin hydrogels in the back of mice, the radioactivity remaining in the hydrogels was measured to estimate the *in vivo* release profile of BMP-2. It was found that BMP-2 was retained in the hydrogels for longer than 30 days, whereas 99% of BMP-2 injected in the solution form was cleared from the injected site within one day, completely disappearing within 3 days. Ectopic bone formation studies demonstrated that BMP-2-incorporating gelatin hydrogels exhibited a more potent ability for bone induction than solution injection of BMP-2. This finding indicates that enhanced retention of BMP-2 is promotes its ability to induce ectopic bone formation.

Key words: Recombinant human BMP-2; gelatin; biodegradable hydrogel; ectopic bone formation; release matrix.

INTRODUCTION

Bone regeneration has attracted much attention in the field of tissue engineering because of its high clinical requirement. A promising way to induce regeneration of autogeneous osseous tissues in bone defect is to make use of bone-related growth factors, such as bone morphogenetic protein (BMP) [1–6], transforming growth factor-β1 [27–31], and basic fibroblast growth factor (bFGF) [32–34]. Combinations of these growth factors with various carriers have been found to be effective in bone regeneration, similar to auto- and allo-bone grafts.

BMP was originally characterized by Urist *et al*. as a bone inductive material at an ectopic site [7]. Currently, at least seven distinct human BMPs are isolated, identified,

*To whom correspondence should be addressed. E-mail: yyikada@medeng.kyoto-u.ac.jp

and cloned [8, 9]. In addition, some of them are found to stimulate mesenchymal cells and myoblasts to differentiate into cells of osteoblast lineage [3, 5, 9]. However, one cannot always expect expression of its biological function if BMP is injected into the body without any release matrices, since the BMP diffuses quickly from the implantation site. Therefore, various materials, including fibrin glues [10, 11], glycolide–lactide copolymers [12–20], and calcium phosphates [21–24] have been employed as carrier matrices of BMP for its sustained release. All these studies demonstrated high efficacy of the carrier matrices for bone induction. Although a significant relationship between the release profile of BMP and bone induction has been discussed in some reports, few papers have studied this relationship in detail.

Bone formation is normally evaluated by use of an animal model with a bone defect, but it is often difficult to distinguish the newly formed bone from the intact one, thereby making it difficult to analyze the osteogenic effect of the growth factor-carrier composite. On the contrary, the *in vivo* efficacy of bone-related growth factors will be readily apparent if bone is ectopically formed in nonosseous tissues. It is well recognized that BMP is the only growth factor that can induce bone formation in muscle and subcutaneous tissues [7, 8, 10, 11, 13, 17, 19, 21, 25, 26].

Gelatin is biodegradable and used extensively for pharmaceutical and medical purposes. Biosafety of gelatin has been proven through its long clinical application [35]. Other advantages of gelatin are its high chemical reactivity and commercial availability of electrically different gelatin samples. We have prepared biodegradable hydrogels from acidic gelatin with an isoelectric point (IEP) of 5.0 and succeeded in sustained release of biologically active bFGF with significant angiogenetic [36] and osteogenetic effects [34], which were not observed when free bFGF was administered.

The objective of the present study is to incorporate recombinant human BMP-2 in hydrogels of gelatin with the IEPs of 5.0 and 9.0 and compare the ectopic bone formation induced by this BMP-2-incorporating hydrogel with that induced by simple BMP-2 aqueous solution. *In vitro* and *in vivo* BMP-2 release from the BMP-2-incorporating hydrogel were examined to assess the efficacy of this hydrogel as the release matrix of BMP-2. Following the subcutaneous implantation of BMP-2-incorporating hydrogel in the back of mice, we investigated the effect of BMP-2 release on ectopic bone formation.

MATERIALS AND METHODS

Materials

Human recombinant BMP-2 (BMP-2) with an IEP of 8.5 was supplied from Yamanouchi Pharmaceutical Co., Tokyo, Japan. Gelatin samples with IEPs of 5.0 and 9.0 were isolated from the bovine bone through the alkaline process and the pig skin through the acid process (Nitta Gelatin Co., Osaka, Japan) and are described as acidic and basic gelatin, respectively, because of their electric features. It is known that the alkaline process through hydrolysis of amide groups of collagen yields gelatin having a higher amount of carboxyl groups, resulting in a reduced IEP of gelatin, whereas the

acid process dose not affect the collagen IEP [37]. Other chemical were obtained from Wako Pure Chemical Industries, Osaka, Japan and used without further purification. $Na^{125}I$, 740 MBq ml^{-1} in 0.1 N NaOH aqueous solution, and an anion-exchange resin, Dowex 1-8X, were purchased from NEN Research Products, Du Pont, Wilmington, DE, USA and Dow Chemicals Co., Ltd., Midland, MI, USA, respectively.

Radioiodination of BMP-2

BMP-2 was radioiodinated according to the method of Greenwood *et al*. [38]. Briefly, 4 μl of $Na^{125}I$ and 100 μl of 0.5 M potassium phosphate-buffered solution (KPB, pH 7.5) were added to the mixture of 40 μl of 0.5 mg ml^{-1} BMP-2 solution in 5 mM glutamic acid, 2.5 wt% glycine, 0.5 wt% sucrose, and 0.01 wt% Tween 80 (pH 4.5). Then, 100 μl of chloramine-T in 0.05 M KPB solution (pH 7.2) at 0.2 mg ml^{-1} was added to the solution mixture. After agitation at room temperature for 2 min, 100 μl of double-distilled water (DDW) containing 0.4 mg of sodium metabisulfate was added to the mixed solution to stop the radioiodination. The reaction mixture was passed through a column of an anionic-exchange Dowex to remove the uncoupled, free ^{125}I molecules from the ^{125}I-labeled BMP-2.

Preparation of BMP-2-incorporating hydrogels

Hydrogels were prepared through cross-linking of aqueous gelatin solutions with glutaraldehyde according to the method described elsewhere [34]. Briefly, 5 wt% aqueous solution of acidic or basic gelatin containing 0.05 or 0.9 wt% glutaraldehyde, respectively, was cast into a Teflon mold of 2 mm depth. Following the cross-linking reaction at 4°C for 12 h, cross-linked hydrogels were punched out to produce discs of 5 mm diameter. The hydrogels were immersed in 100 mM aqueous glycine solution at 37°C for 1.0 h to block residual aldehyde groups of glutaraldehyde, followed by washing with DDW. Following immersion in 70 vol% ethanol to sterilize, they were thoroughly rinsed with autoclaved DDW and aseptically freeze-dried. Their weight was determined before and after swelling at 37°C in phosphate-buffered saline solution (PBS, pH 7.4) to calculate the water content, which was defined by the weight percentage of water in the wet hydrogel [36]. The water content of acidic and basic gelatin hydrogels used in this study was both approximately 95 wt%.

To impregnate BMP-2 into hydrogels, 20 μl of aqueous solution containing 0.01, 0.05, 0.1, 0.5, 1.0, and 5.0 μg of BMP-2 or 0.5 μg of ^{125}I-labeled BMP-2 was dropped onto the freeze-dried hydrogel, and left in a culture dish of 60 mm diameter sealed with parafilm at 4°C overnight. BMP-2-incorporating gelatin hydrogel was used without washing. Since the volume of BMP-2 aqueous solution is much less than that theoretically impregnated into each hydrogel, the BMP-2 dose incorporated into the hydrogel is equal to the amount impregnated initially. Thus, in this study, the dose was indicated as the initial impregnation amount. The size of hydrogel disc was 5 mm in diameter and 2 mm in thickness and its dry weight was 7 mg.

In vitro *evaluation of BMP-2 release*

Gelatin hydrogels incorporating 0.5 μg of ^{125}I-labeled BMP-2 were incubated in 1 ml of PBS at 37 °C under shaking. At different time intervals, the supernatant PBS was taken out to measure the radioactivity on a gamma counter (ARC-301B, Aloka Co., Ltd., Tokyo, Japan), while fresh PBS was added and release test was continued.

In vivo *evaluation of BMP-2 release*

^{125}I-labeled BMP-2-incorporating hydrogels were implanted into the back subcutis of 6 week-age female ddY mice. As a control, 100 μl of aqueous solution of ^{125}I-labeled BMP-2 was subcutaneously injected into the mouse back at the central position 15 mm away from their tail root. The dose of ^{125}I-labeled BMP-2 was 0.5 μg for both cases. At different time intervals, mice were sacrificed according to the institutional guidelines of Kyoto University on animal experimentation. The skin on the back of mice around the implanted or injected site of BMP-2 was cut into a strip of 3×5 cm^2 and the corresponding facia was thoroughly wiped off with a filter paper to absorb ^{125}I-labeled BMP-2. The radioactivity of gelatin hydrogel remaining, excised skin, and filter paper was measured on the gamma counter to assess the time profile of BMP-2 retention. Measurement of the radioactivity in the other parts of body, such as blood, heart, lung, thymus, thyroid, liver, spleen, gastrointestine, kidney, and carcass, was made to reveal no accumulation of BMP-2 in any specific organ. Gelatin hydrogels and 100 μl aqueous solution containing 0.5 μg of ^{125}I-labeled BMP-2 were kept at a room temperature as a standard. Measurement of the radioactivity of the standard was made together with experimental samples at each sampling time. The *in vivo* release profile was assessed based on the radioactivity ratio of samples to the standard.

Evaluation of ectopic bone induction

Acidic and basic gelatin hydrogels incorporating 0.01, 0.05, 0.1, 0.5, 1.0, and 5.0 μg of BMP-2 were implanted into the back subcutis of ddY mice, while 100 μl of aqueous BMP-2 solution at concentrations of 1×10^{-4}, 5×10^{-4}, 1×10^{-3}, 5×10^{-3}, 1×10^{-2}, and 5×10^{-2} μg μl^{-1} was injected subcutaneously into mice, as described above. The experimental group was composed of four to eight mice. Acidic and basic gelatin hydrogels incorporating PBS(−) and aqueous PBS(−) solution were implanted as a control.

After 1, 2, and 3 weeks, the implanted site of BMP-2-incorporating hydrogels and the injected site of aqueous BMP-2 solutions were radiographically examined by soft X-rays (Hitex HX-100, Hitachi, Japan) at 54 kVp and 2.5 mA for 20 s. When the radiopaque area on the X-ray film was larger by 1 mm^2 than that of PBS(−)-treated groups, ectopic bone formation was defined as positive. The skin tissue was taken out together with the hydrogel implant or injected site, fixed with 10 vol% neutral formalin solution, dehydrated with ethanol, and embedded in paraffin. The fixed skin tissues were cross-sectioned to 10 μm thickness with a microtome and stained with Mayer's haematoxylin–eosin (H-E) solution. In addition, von Kossa staining was done to clarify calcium deposition in the specimens. The histological sections were viewed with an optical microscope.

RESULTS

In vitro *BMP-2 release profile*

Figure 1 shows the *in vitro* release profiles of BMP-2 from BMP-2-incorporating hydrogels prepared from acidic and basic gelatins. The initial BMP-2 dose was 0.5 μg per hydrogel. As can been seen, BMP-2 was gradually released with time from both gelatin hydrogels, after approximately 60–75% of BMP-2, which amount to 300–375 ng of BMP-2, incorporated in the hydrogels was released within 24 min. No significant difference was observed in BMP-2 release profile between acidic and basic gelatin hydrogels, while a little higher retention of BMP-2 was observed in basic gelatin hydrogel than acidic one. The BMP-2 dose had little influence on the release from acidic and basic gelatin hydrogels.

In vivo *BMP-2 release profile*

Figure 2 shows the *in vivo* decrement patterns of BMP-2 from the implanted site of BMP-2-incorporating hydrogels or the injected site of aqueous BMP-2 solutions. The initial BMP-2 dose was 0.5 μg and almost 100% of radioactivity initially applied was recovered. It is apparent that incorporation of BMP-2 into gelatin hydrogels prolonged *in vivo* BMP-2 retention, irrespective of the gelatin type. For example, 44 ng of BMP-2 were still retained in the vicinity of acidic gelatin hydrogels after 1 day of implantation. The amount of BMP-2 remaining for acidic gelatin hydrogel decreased to about 15 and 3 ng after 1 week and 1 month of implantation. In the case of basic gelatin hydrogels, 67 ng of BMP-2 were retained in the vicinity of hydrogels

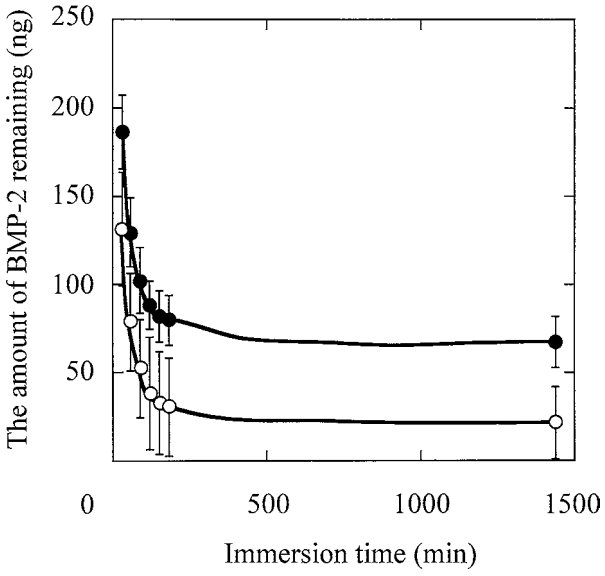

Figure 1. Release profile of BMP-2 *in vitro* from BMP-2-incorporating hydrogels prepared from acidic (○) and basic gelatin (●). The initial BMP-2 dose is 0.5 μg.

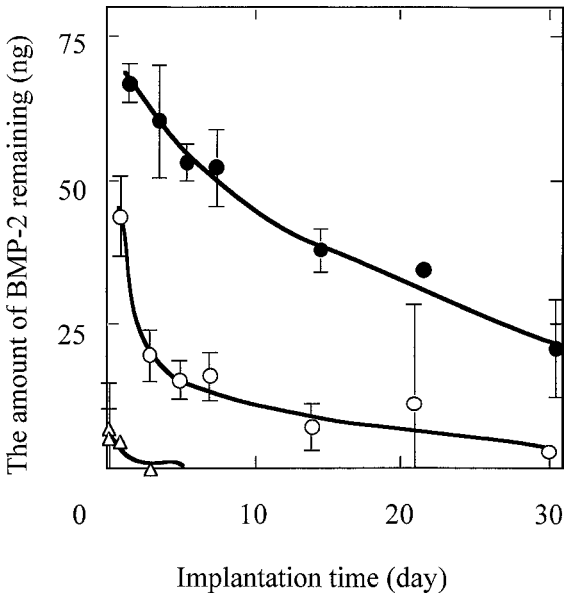

Figure 2. Radioactivity decrement patterns in the back subcutis of mice following subcutaneous implantation of ^{125}I-labeled BMP-2-incorporating hydrogels prepared from acidic (○) and basic gelatin (●) and subcutaneous injection of ^{125}I-labeled BMP-2 in aqueous solution (△). The initial BMP-2 dose is 0.5 μg.

after 1 day of implantation and the amount of BMP-2 remaining decreased to about 50 and 20 ng after 1 week and 1 month of implantation. This finding indicates that gelatin hydrogels allow BMP-2 to release over a 1-month period; BMP-2 retention being longer for the basic gelatin hydrogel than the acidic one. During the experiment period, no significant radioactivity accumulation was detected in any organ (data not shown).

On the contrary, approximately 99% of BMP-2 injected, which amounts to 495 ng of BMP-2, disappeared from the injected site within the first day, and no trace of BMP-2 remained around the injection site 3 days after injection. Approximately 5.0% and 3.5% of BMP-2 injected were found in the gastrointestinal tract and other organs within 5 h of BMP-2 injection. No accumulation of BMP-2 in any specific organ was observed and most of BMP-2 radioactivity was excreted into the urine within first day, suggesting the urinary excretion of BMP-2. A very low radioactivity was detected in the thyroid gland for every experimental group over the time range studied, indicating no release of free radioactive iodine from ^{125}I-labeled BMP-2.

Ectopic bone formation

Figure 3 shows soft X-ray photographs of the mice subcutis after 2 weeks of administration of BMP-2 and PBS(−) in different dosage forms. Apparently, the edge of implants and the subcutaneous tissue became radiopaque strongly on the X-ray film when BMP-2 dose was 5 μg per mouse, irrespective of the dosage form, whereas the weak radiopaque area was found at the gelatin hydrogels and skin when implanted

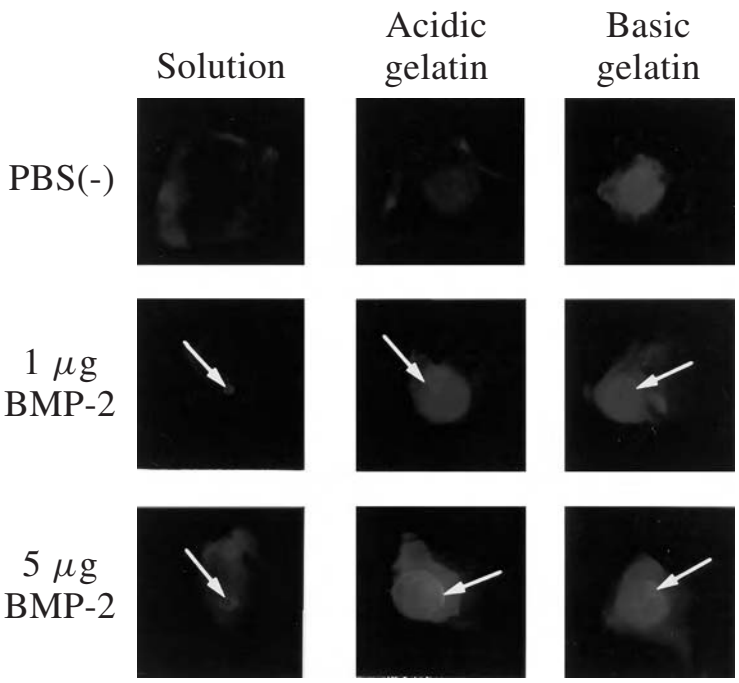

Figure 3. Soft X-ray photographs of ectopically formed bone after 2 weeks of implantation of BMP-2 and PBS(−) in the different dosage forms. Arrows indicate the newly formed bone.

Table 1.
Soft X-ray evaluation of ectopic bone formation induced by 5 μg of BMP-2 in different dosage forms

Implantation time (week)	Dosage form		
	Solution	Hydrogel	
		Acidic gelatin	Basic gelatin
1	0/6	1/6	1/6
2	2/8	5/8	3/5
3	4/5	5/5	3/4

PBS(−) in different dosage form. It seems that the radiopaque area was larger for BMP-2-incorporating hydrogels than for aqueous BMP-2 solutions. The BMP-2 dose effect on the radiopaque area and radiopacity was remarkable when compared with BMP-2 dose of 1.0 μg per mouse. In addition, BMP-2-incorporating hydrogels rendered the implanted site radiopaque, irrespective of the gelatin type, while injection of aqueous BMP-2 solution was not so effective in enhancing the radiopacity.

Table 1 summarizes the implantation schedule and result of soft X-ray evaluation of ectopic bone formation induced by BMP-2-incorporating hydrogels and aqueous BMP-2 solutions. The number of bone induction was estimated by the use of the criterion described above. The rate of bone formation at the implanted site of BMP-2-

Table 2.
Soft X-ray evaluation of ectopic bone formation induced by various amounts of BMP-2 in different dosage forms after 2 weeks of implantation

Amounts of BMP-2 (μg)	Dosage forms	
	Solution	Acidic gelatin hydrogel
0.01	0/4	0/4
0.05	0/4	0/4
0.1	0/4	0/4
0.5	0/4	0/4
1	1/6	1/5
5	2/8	5/8

incorporating gelatin hydrogels was larger than that of at injected site of free BMP-2 solution 1 and 2 weeks after implantation. However, the difference between BMP-2-incorporating gelatin hydrogels and aqueous BMP-2 solutions in the rate of bone formation was not found after 3 weeks of implantation. No significant influence of gelatin IEP was found on the rate of bone formation and no bone induction was detected on the X-ray film after 1 week of BMP-2 solution injection.

The BMP-2 dose effect on the ectopic bone induction by BMP-2-incorporating acidic gelatin hydrogels and BMP-2 solutions is given in Table 2 after 2 weeks of BMP-2 administration. The extent of bone induction was expressed by the number of bone formation at the implanted site of BMP-2-incorporating gelatin hydrogels and aqueous BMP-2 solution injection against the number of treated mice. The number of bone induction was counted on the X-ray film by the use of the criterion described above. The extent of bone induction increased with the increasing BMP-2 dose in both the dosage forms. BMP-2-incorporating hydrogels exhibited stronger induction than BMP-2 solutions.

Histological observation on the subcutaneous tissues after 2 weeks of administration is shown in Figs 4–6. As is apparent in Fig. 4, von Kossa staining demonstrated that both the hydrogels and solutions of BMP-2 induced bone formation in the subcutaneous tissue. Ectopic bone formation was observed only at the injected site of BMP-2 solutions, and bone was formed only along the implanted hydrogel contour, not in the inner portion of the hydrogel. It is seen that the calcium-deposited area was larger at the BMP-2 concentration of 5 μg per mouse than at 1 μg per mouse, indicating that ectopic bone induction was stronger with an increase in the BMP-2 dose.

Figure 5 shows H-E stained cross-sections of the subcutaneous tissues after 2 weeks of treatments. Newly formed bone was observed at 1 and 5 μg of BMP-2 treated site, irrespective of the dosage form. Partially calcified woven bone was found at the acidic gelatin hydrogel containing 1 and 5 μg of BMP-2. At the higher magnification, active cuboidal osteoblasts were found at the 5 μg of BMP-2 administrated site, irrespective of the dosage form.

On the contrary, no bone formation was observed at the PBS(−) implanted site, irrespective of the dosage form, as shown in Fig. 6. The gelatin hydrogels still remained at the implanted site and encapsulated with fibrous tissues. A little inflammatory cell accumulation and a little cell infiltration into gelatin hydrogels was observed.

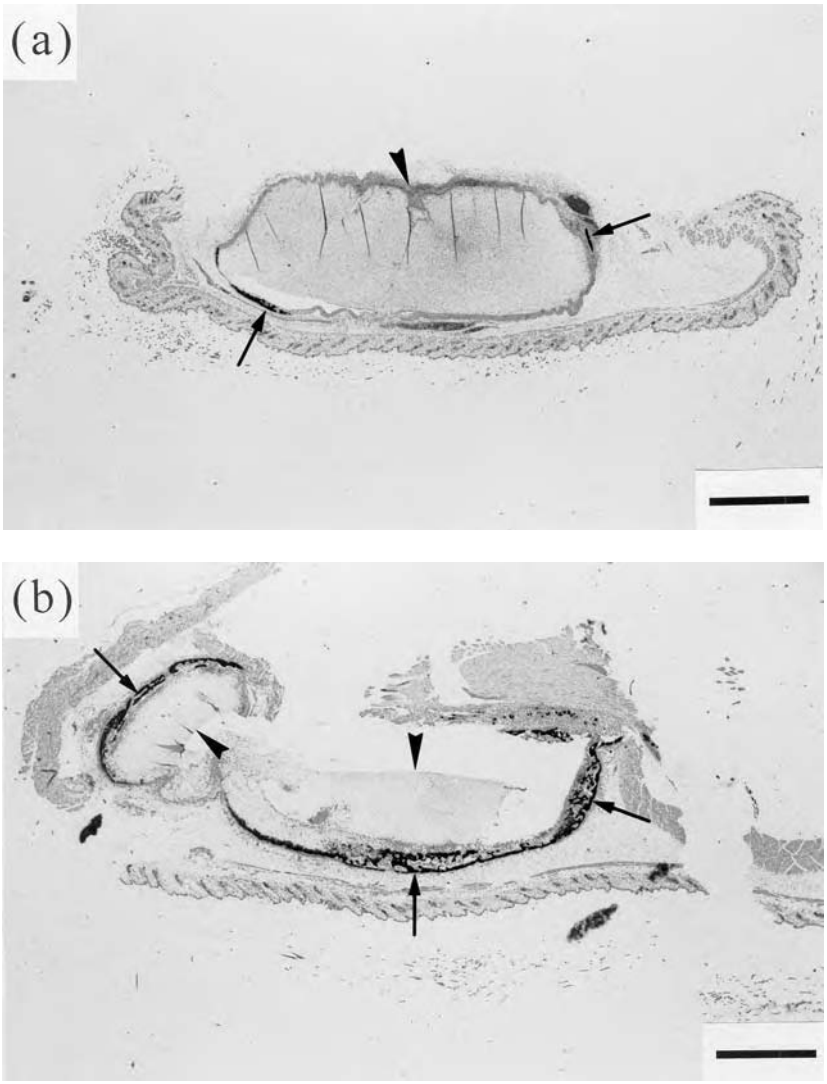

Figure 4. Histological cross-sections of ectopically formed bone after 2 weeks of implantation of BMP-2-incorporating hydrogels prepared from acidic (a, b) and basic (c, d) gelatin and injection of BMP-2 in solutions (e, f): (a, c, e) 1 μg BMP-2/mouse and (b, d, f) 5 μg BMP-2/mouse. Each specimen was subjected to von Kossa staining to identify calcium deposition to the extracellular matrix. Arrows and arrow heads indicate the newly formed bone with calcium deposition and the residual gelatin hydrogel, respectively. Bars correspond to 1 mm.

DISCUSSION

Various delivery systems have been explored for BMP by combining it with biodegradable polymers and ceramics [1–6, 10–26]. These investigations have evaluated the efficacy of the delivery systems in enhancing bone formation in terms of histological examination, calcium deposition, phenotype of bone cells, and gene expression of

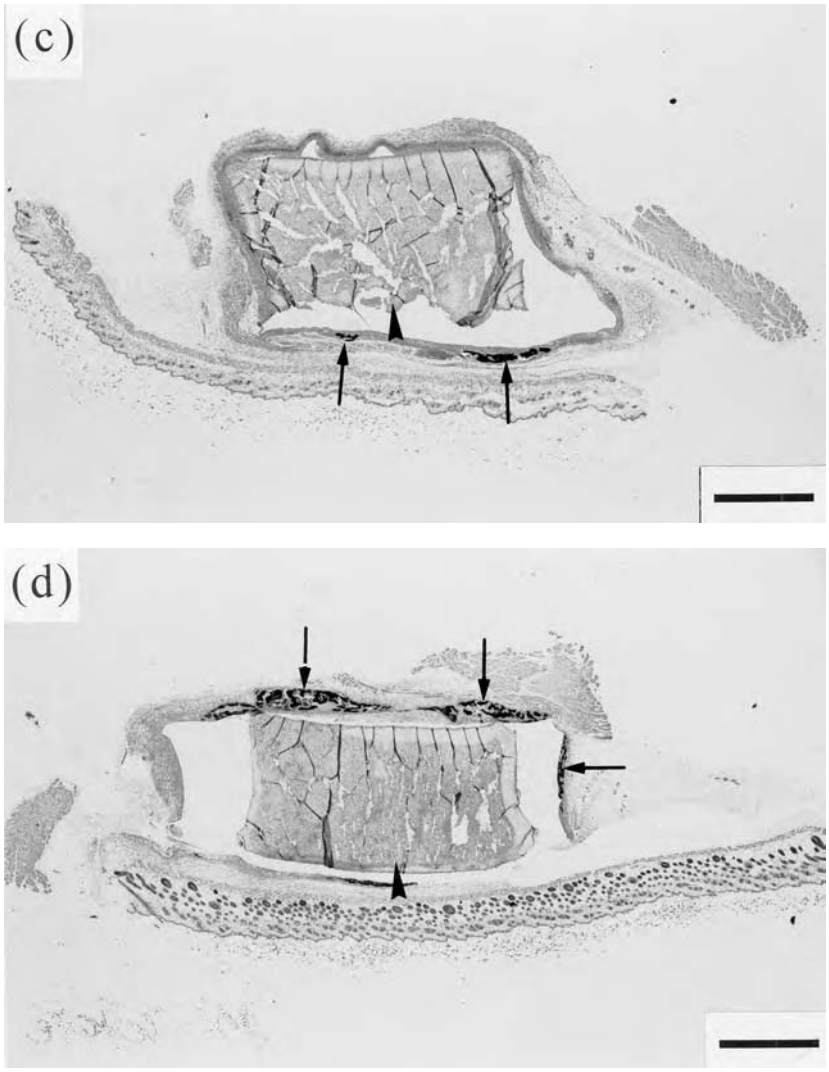

Figure 4. (Continued).

bone specific proteins. However, the body fate of BMP-2 introduced into the body was not studied at all in these reports although this is very important. Therefore, the present work focused on the effect of *in vivo* retention of BMP-2 on its activity of bone induction.

Comparison of the *in vivo* profile of BMP-2 retention in the mouse subcutis with ectopic bone induction by BMP-2 demonstrated that prolonged retention of BMP-2 in the body in addition to the initial burst release enhanced BMP-2-induced ectopic bone formation. As is apparent from Fig. 2, about 10% of BMP-2 initially incorporated in the acidic gelatin hydrogel, that is 500 ng, remained in the hydrogel, even if another 90% was quickly released within 1 day. The amount of BMP-2 remaining in the basic

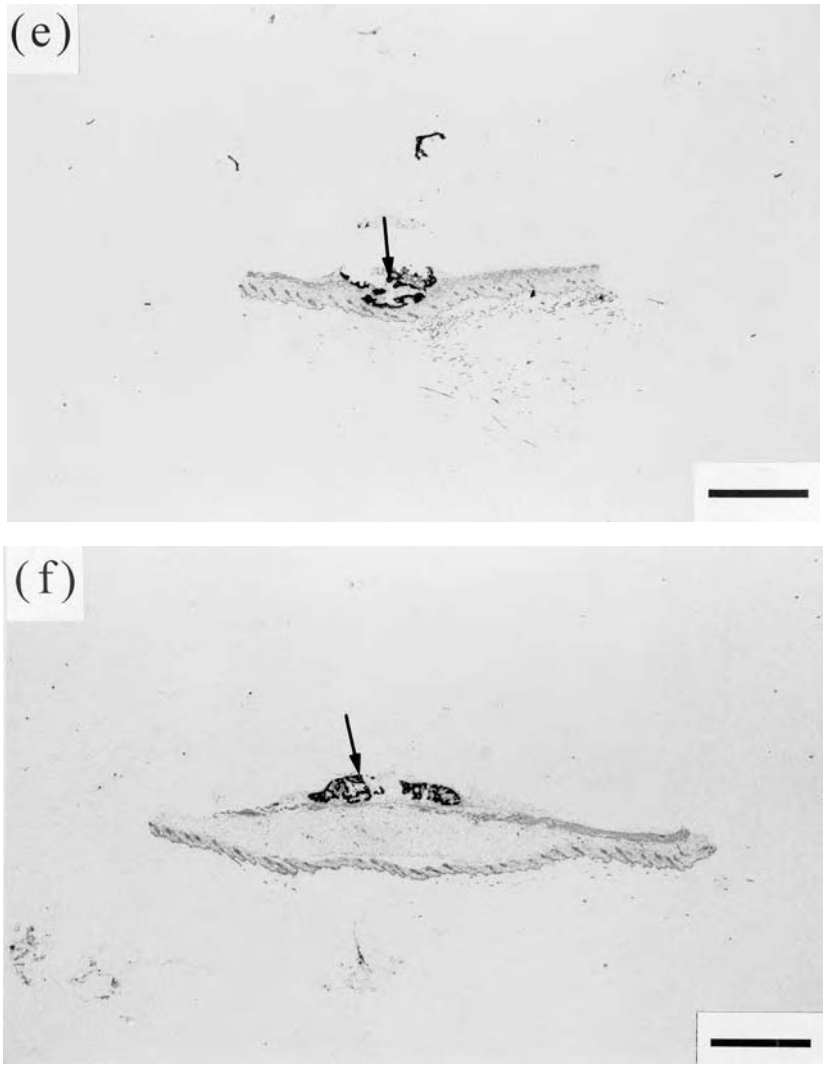

Figure 4. (Continued).

gelatin hydrogel seems to be higher than that in the acidic one. However, the reason for different retention profiles of BMP-2 between the two types of gelatin hydrogels is unclear at present. On the contrary, 99% of BMP-2 injected in the solution form was cleared from the injected site within the first day. This indicates that incorporation in hydrogels was effective in prolonging the *in vivo* retention of BMP-2. However, injection of BMP-2 solution also ectopically induced bone formation although the extent was lower than that induced by BMP-2-incorporating hydrogels. This phenomenon may be explained in terms of high potentiality of BMP-2 for bone induction. In other words, it is likely that an extremely low dose of BMP-2 is enough to enhance bone induction if BMP-2 is appropriately delivered to the site of action. Similar ectopic bone

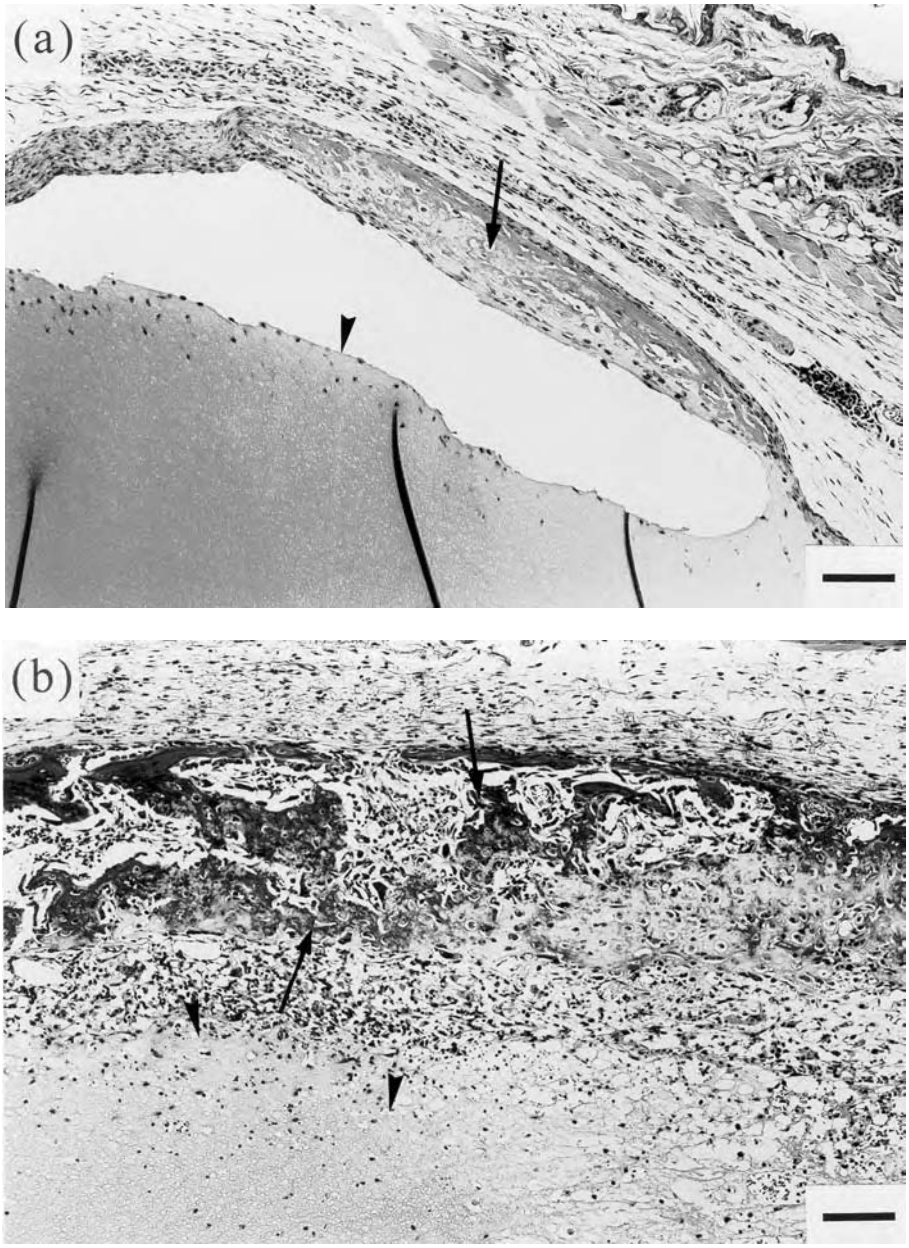

Figure 5. Histological cross-sections of ectopically formed bone after 2 weeks of implantation of BMP-2-incorporating hydrogels prepared from acidic (a, b) and basic (c, d) gelatin and injection of BMP-2 in solutions (e, f): (a, c, e) 1 μg BMP-2/mouse and (b, d, f) 5 μg BMP-2/mouse. Each specimen was subjected to H-E staining. Arrows and arrow heads indicate the newly formed bone and the residual gelatin hydrogel, respectively. Bars correspond to 100 μm. At the higher magnification, active cuboidal osteoblasts (solid arrows) were found at the newly formed bone induced by 5 μg of BMP-2-incorporating hydrogels of acidic and basic gelatin (g, h) and 5 μg of BMP-2 solution (i). Bars correspond to 50 μm.

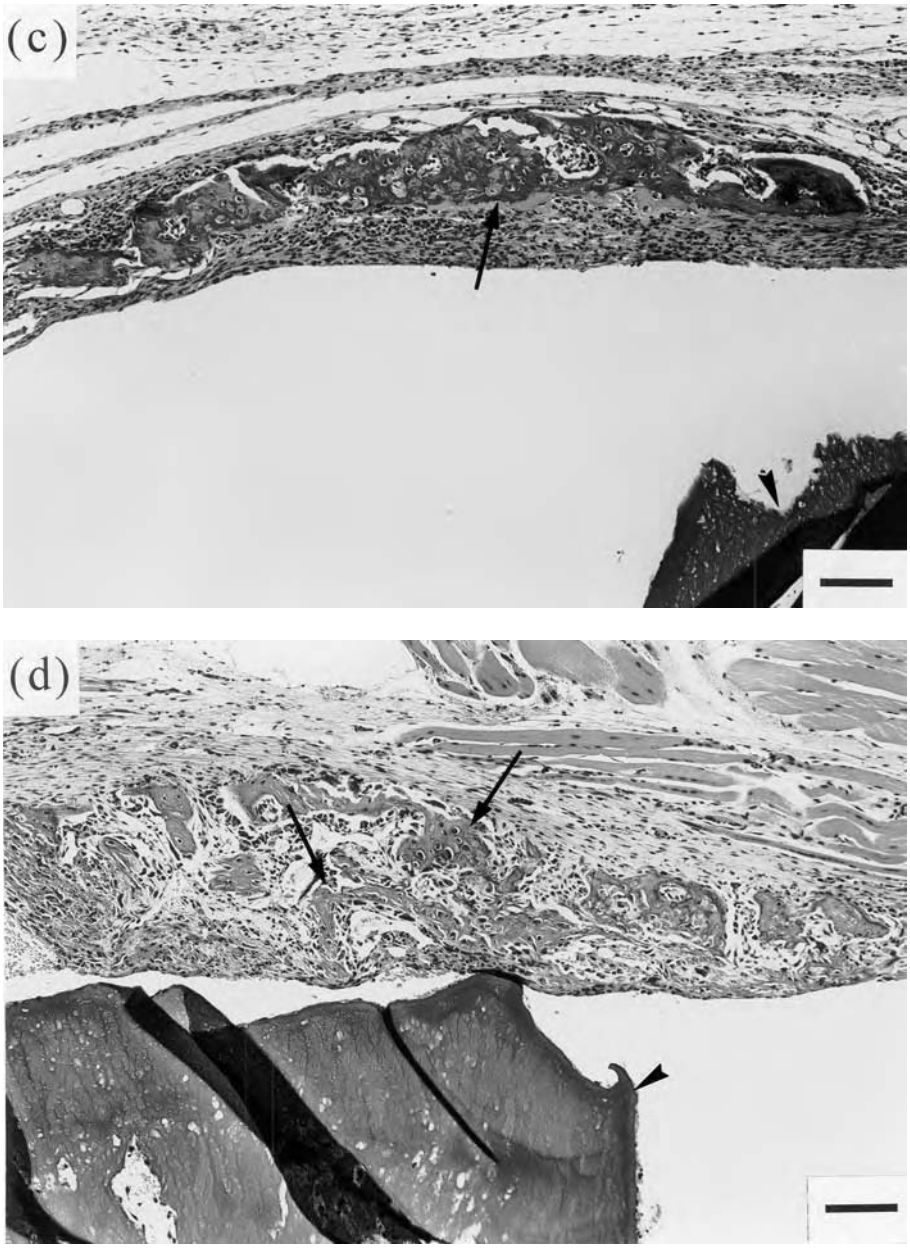

Figure 5. (Continued).

formation was observed for mice treated with BMP-2-incorporating acidic and basic gelatin hydrogels, although the retention profile of BMP-2 was different between the two hydrogels. This finding also suggests that the retention amount of BMP-2 must be high enough compared with that to induce ectopic bone formation. The rate of bone

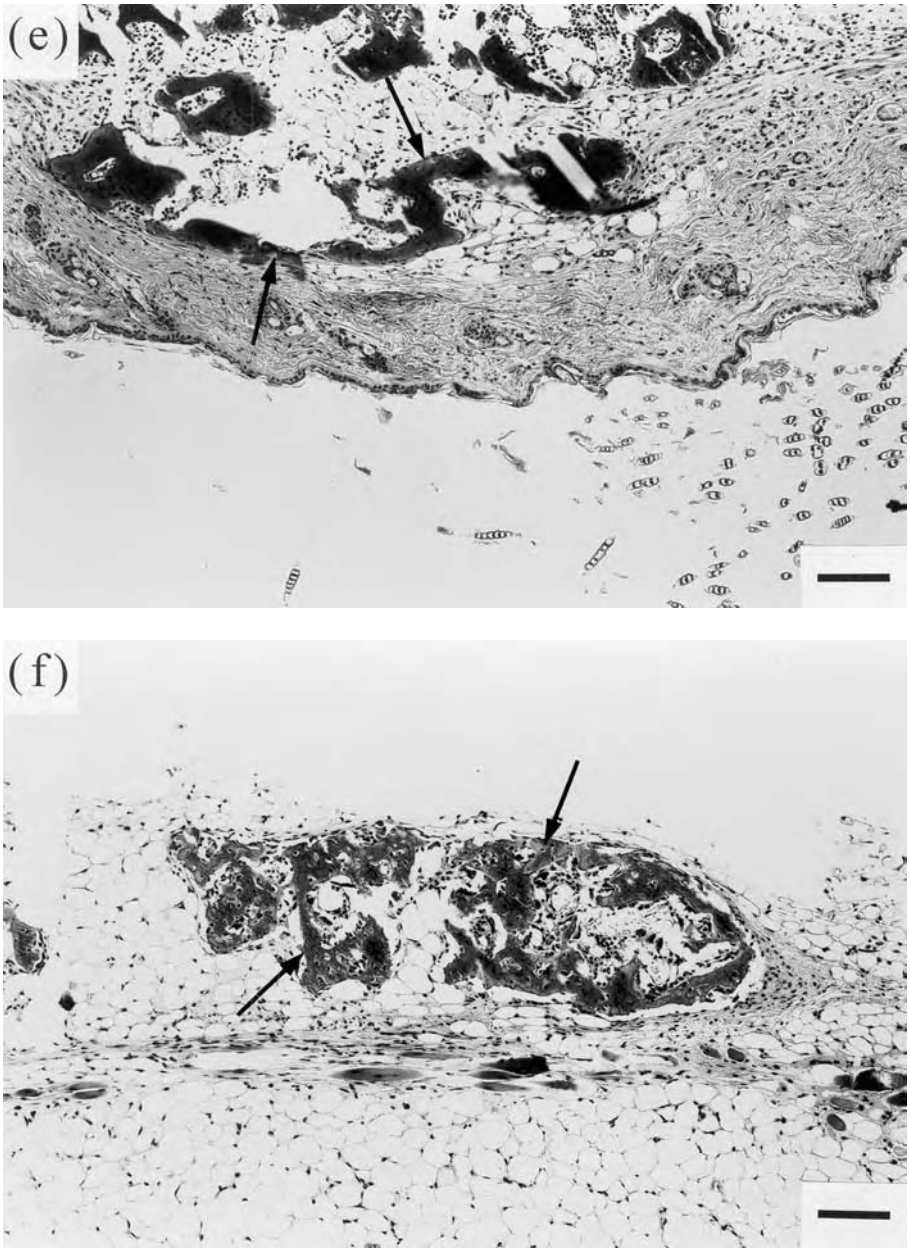

Figure 5. (Continued).

induction by BMP-2 solution injection was similar to that by BMP-2-incorporating hydrogels implantation after 3 weeks of BMP-2 treatment, although the radiopaque area was small at BMP-2 solution injection site, as is seen in Figs 4 and 5. Such a stronger bone induction by BMP-2-incorporating hydrogels than by BMP-2 solution

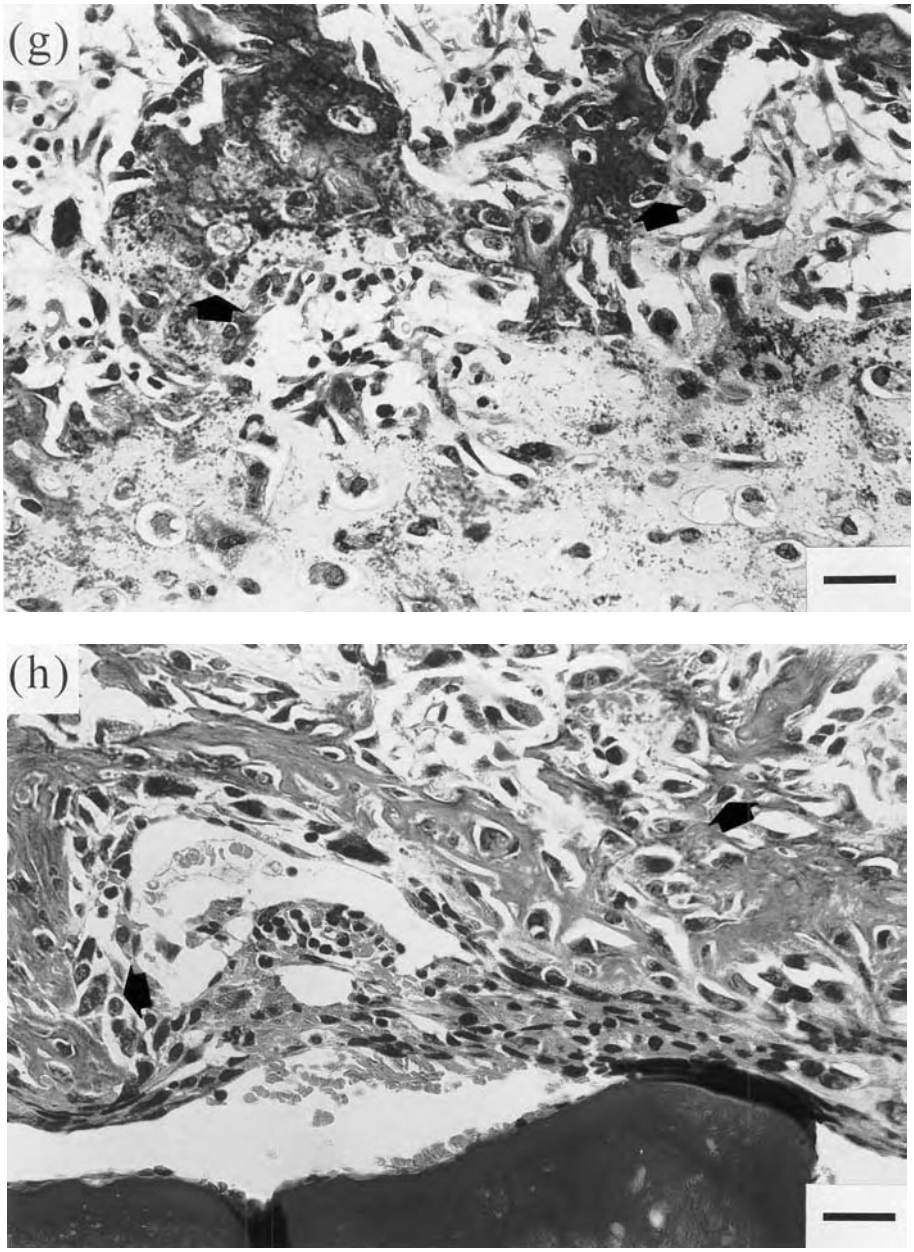

Figure 5. (Continued).

can be ascribed to enhanced retention BMP-2 by gelatin hydrogels. It is possible that retention of BMP-2 in the body continues stimulating differentiation and proliferation of osteoprogenitor cells for a longer time, resulting an enhanced bone formation. It was reported that when BMP-2 was combined with the rat collagenous matrix, the

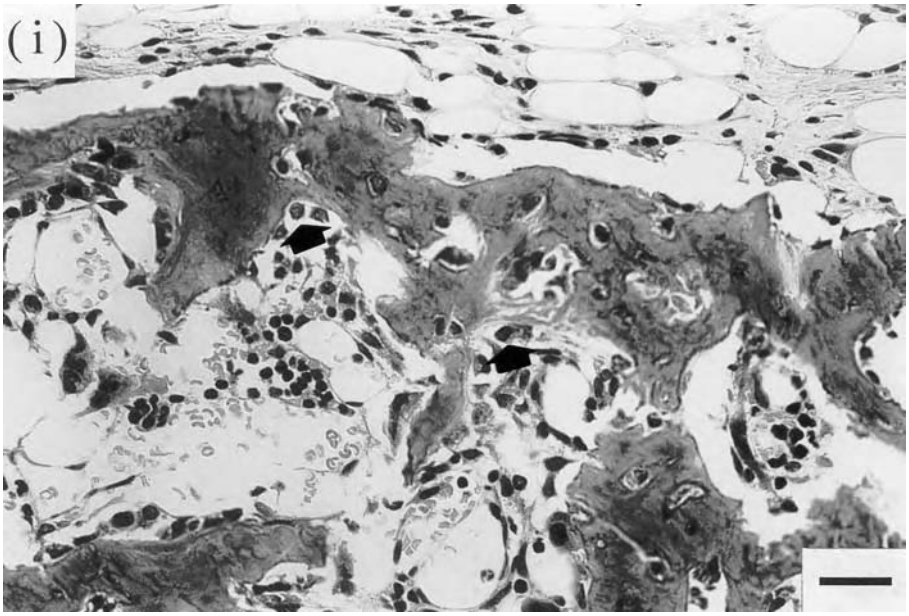

Figure 5. (Continued).

initially given dose required to consistently induce cartilage and bone formation was about 600 ng but 100–200 μg of BMP-2 was required if no matrix was used for rat ectopic bone regeneration [25]. It is safe to say that prolonged retention of BMP-2 *in vivo* is a promising way to efficiently enhance its osteogenetic actions.

It is interesting to point out that the location of calcium deposition was affected by the dosage form of BMP-2, as demonstrated in Fig. 4. When BMP-2 was injected in the solution form, bone formation was induced only at the injected site, while bone was ectopically induced along the periphery of BMP-2-incorporating gelatin hydrogels remaining at the implanted site even at 2 weeks after implantation. When the gelatin hydrogel with a water content of 95 wt% is swollen, the hydrogel pore is occupied with water. It is likely that this water presence did not allow cells to infiltrate into the interior of hydrogel unless it is remarkably degraded (Figs 4–6) [26]. As a result, ectopic bone formation must be induced around at the periphery of hydrogels, because only the osteoprogenetor cells recruited around hydrogels will be most strongly stimulated to differentiate into osteoblasts by BMP-2 released from the hydrogels.

We have demonstrated that bFGF molecules with the IEP of 9.6 ionically interacted with hydrogels of the acidic gelatin with an IEP of 5.0, resulting in sustained release of bFGF accompanied with hydrogel biodegradation [36]. Thus, we expected polyion complexation between BMP-2 and the acidic gelatin, similar to the bFGF–acidic gelatin complex, because of the high IEP of BMP-2 (8.5). However, the expected polyionic complex between BMP-2 and acidic gelatin was not formed and the *in vitro* release profile of BMP-2 from the acidic gelatin hydrogel was similar to that from the basic gelatin hydrogel (Fig. 1). This unexpected result seems to be due to a

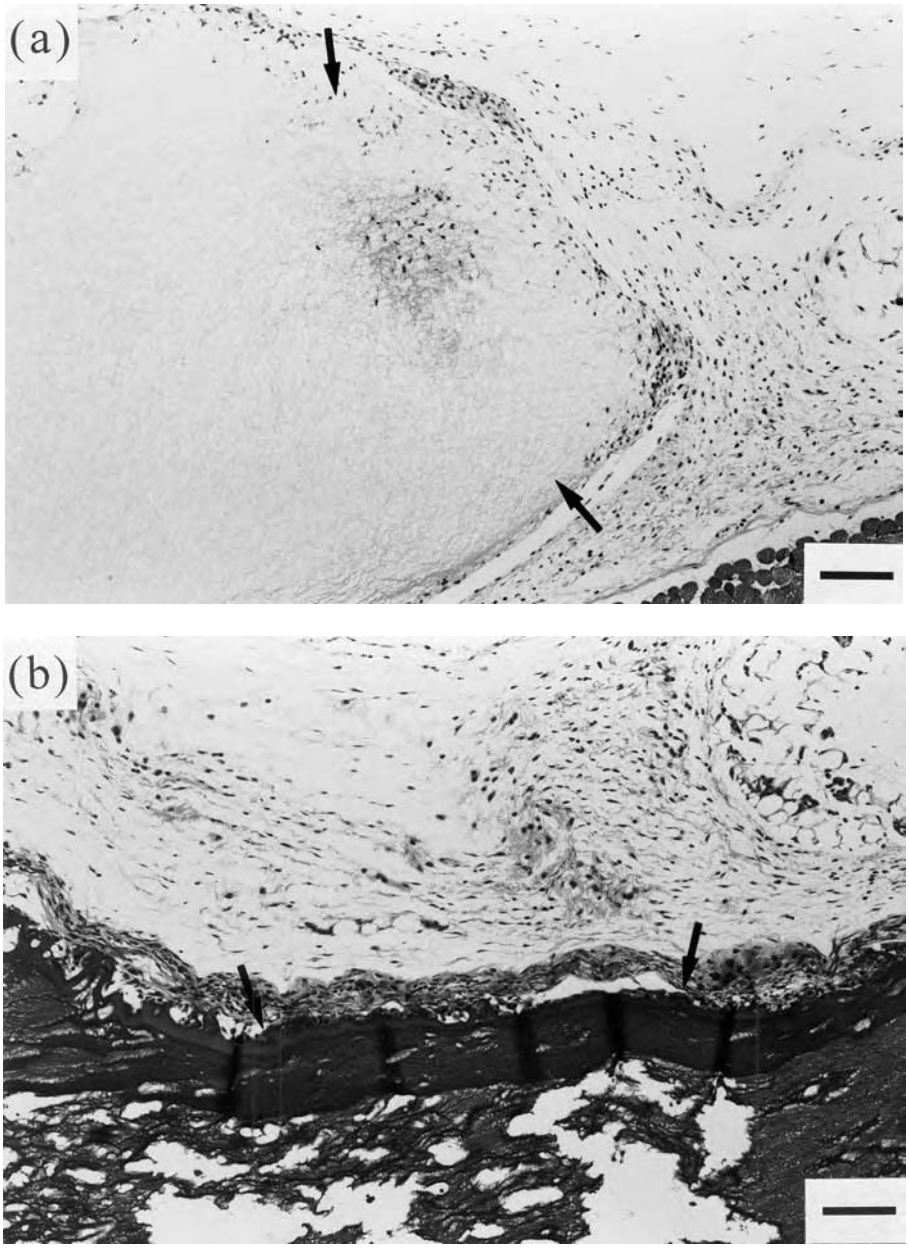

Figure 6. Histological cross-sections of subcutaneous tissues after 2 weeks of implantation of PBS(−)-incorporating hydrogels prepared from acidic (a) and basic (b) gelatin and injection of PBS(−) in solutions (c). Arrows indicate the residual gelatin hydrogels. Bars correspond to 100 μm.

difference in biochemical nature between BMP-2 and bFGF. Unlike bFGF, BMP-2 is a glycoprotein [39] and requires a surfactant to make it water-soluble at high concentrations. Although lysozyme and avidin are both basic proteins with a similar

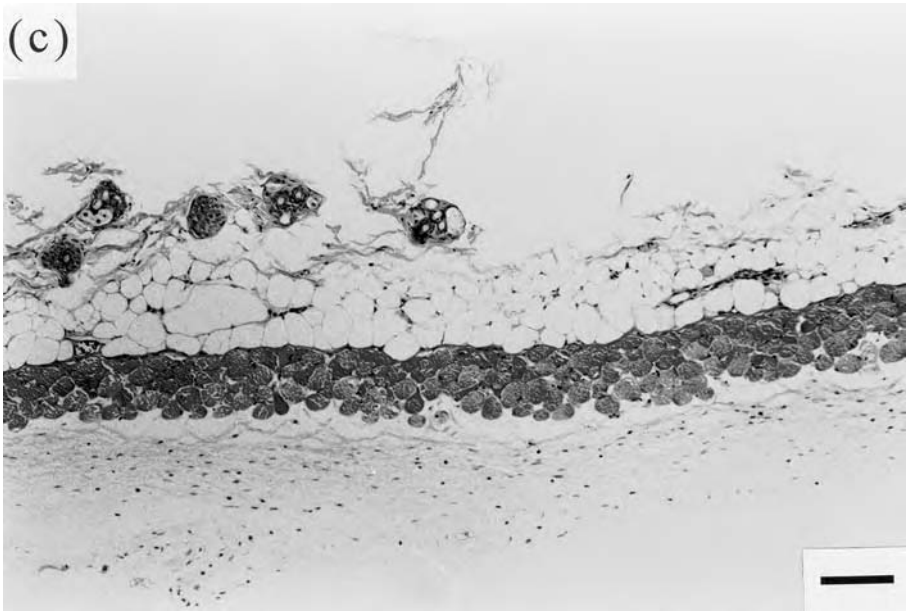

Figure 6. (Continued).

IEP, the glycoprotein avidin was sorbed to the acidic gelatin hydrogel to a lesser extent than the non-glycoprotein lysozyme. In addition, a small amount of avidin was sorbed to the basic gelatin hydrogel, whereas no lysozyme sorption to the basic gelatin hydrogel was observed (data not shown). This finding suggests that the positively charged site on the avidin molecule may be covered with sugar moieties, preventing avidin both from forming a polyion complex with acidic gelatin and from repelling basic gelatin. It is possible that the presence of sugar moieties and surfactant also prevents BMP from ionically interacting with acidic gelatin, resulting in no difference in the release profile of BMP-2 between acidic and basic gelatin hydrogels. Protein was permeated through gelatin hydrogels, although the permeation rate was influenced by their water content [40]. In addition, a similar *in vitro* release profile of BMP-2 was observed for gelatin hydrogels with different water contents, irrespective of their IEP (data not shown). Probably, BMP-2 molecules are small enough to permeate through acidic and basic gelatin hydrogels with the water content around 95%, although the cross-linking extents are different among the two hydrogels. This indicates that there is no structural difference between acidic and basic gelatin hydrogels affecting the release profile of BMP-2. It is conceivable that difference in the BMP-2 retention in hydrogels may be caused by intermolecular interaction between BMP-2 and gelatin, such as an electrostatic interaction and hydrophobic interactions. This interaction will result in different profiles of BMP-2 retention between the two gelatin hydrogels.

Differences in the time profile of BMP-2 retention between *in vitro* and *in vivo* systems may be explained in terms of biological substances presence in the body. This suggests that an initial burst from BMP-2-incorporating gelatin hydrogels *in vivo* is similar to that *in vitro*. When gelatin hydrogels are implanted in the subcutis,

biological substances originally present in the body, such as proteins, will interact both with gelatin and BMP-2 molecules. It is possible that this interaction reinforced the affinity of BMP-2 for the hydrogels, resulting in prolonged retention of BMP-2 *in vivo*. Moreover, many cells infiltrated around the hydrogels will modify the *in vivo* BMP-2 retention. These events will result in a delayed *in vivo* release of BMP-2 compared with that *in vitro*.

In conclusion, incorporation into gelatin hydrogels prolonged the *in vivo* retention of BMP-2 and enhanced ectopic bone formation. Injection of free BMP-2 also formed ectopic bone only at the injected site, although the extent and the induction area were less prominent than that of BMP-2-incorporating hydrogels. Such a stronger bone induction of the hydrogels can be ascribed to their property to prolong *in vivo* BMP-2.

REFERENCES

1. C. J. Damien and J. R. Parsons, *J. Appl. Biomater.* **2**, 187 (1991).
2. T. S. Lindholm and T. J. Gao, *Ann. Chir. Gynaecol.* **82**, 3 (1993).
3. R. A. Kenley, K. Yim, J. Abrams, E. Ron, T. Turek, L. J. Mardden and J. O. Hollinger, *Pharm. Res.* **10**, 1393 (1993).
4. J. Yaszemski, R. G. Payne, W. C. Hayes, R. Langer and A. G. Mikos, *Biomaterials* **17**, 175 (1996).
5. T. S. Lindholm (Ed.), *Bone Morphogenetic Proteins: Biology*, *Biochemistry and Reconstructive Surgery*. R. G. Landes Co. and Academic Press, Inc., Texas (1996).
6. U. Ripamonti and N. Duneas, *MRS Bull.* **21**, 36 (1996).
7. M. R. Urist, A. Mikulski and A. Lietze, *Proc. Natl Acad. Sci. USA* **76**, 1828 (1978).
8. J. M. Wozney, V. Rosen, A. J. Celeste, L. M. Mitsock, M. J. Whitters, R. W. Kriz, R. M. Hewick and E. A. Wang, *Science* **242**, 1528 (1988).
9. J. M. Wozney, *J. Periodontol.* **66**, 506 (1995).
10. M. Kawamura and M. R. Urist, *Clin. Orthop. Rel. Res.* **235**, 302 (1987).
11. N. Schwarz, H. Redl, L. Zeng, G. Schlag, H. P. Dinges and J. Eschberger, *Clin. Orthop. Rel. Res.* **293**, 353 (1993).
12. M. C. Meikle, S. Papaioannou, T. J. Ratledge, P. M. Speight, S. R. Watt-Smith, P. A. Hill and J. J. Reynolds, *Biomaterials* **15**, 513 (1994).
13. S. Miyamoto, K. Takaoka, T. Okada, H. Yoshikawa, J. Hashimoto, S. Suzuki and K. Ono, *Clin. Orthop. Rel. Res.* **294**, 333 (1993).
14. S. C. Lee, M. Shea, M. A. Battle, K. Kozitza, E. Ron, T. Turek, R. G. Schaub and W. C. Hayes, *J. Biomed. Mater. Res.* **28**, 1149 (1994).
15. T. J. Sigurdsson, M. B. Lee, K. Kubota, T. J. Turek, J. M. Wozney and U. M. E. Wikesjö, *J. Periodontol.* **66**, 131 (1995).
16. J. L. Smith, L. Jin, T. Parsons, T. Turek, E. Ron, C. M. Philbrook, R. A. Kenley, L. Marden, J. Hollinger, M. P. G. Bostrom, E. Tomin and J. M. Lane, *J. Control. Rel.* **36**, 183 (1995).
17. Y. Yamazaki, S. Oida, K. Ishihara and N. Nakabayashi, *J. Biomed. Mater. Res.* **30**, 1 (1996).
18. J. O. Hollinger and K. Leong, *Biomaterials* **17**, 187 (1996).
19. M. Isobe, Y. Yamazaki, S. Oida, K. Ishihara, N. Nakabayashi and T. Amagasa, *J. Biomed. Mater. Res.* **32**, 433 (1996).
20. G. Zellin and A. Linde, *J. Biomed. Mater. Res.* **35**, 181 (1997).
21. M. R. Urist, A. Lietze and E. Dawson, *Clin. Orthop. Rel. Res.* **187**, 277 (1984).
22. Y. Horisaka, Y. Okamoto, N. Matsumoto, Y. Yoshimura, J. Kawada, K. Yamashita and T. Takagi, *Clin. Orthop. Rel. Res.* **268**, 303 (1991).
23. T. Sato, M. Kawamura, K. Sato, H. Iwata and T. Miura, *Clin. Orthop. Rel. Res.* **263**, 254 (1988).

24. I. Ono, T. Ohura, M. Murata, H. Yamaguchi, Y. Ohnuma and Y. Kuboki, *Plast. Reconstr. Surg.* **90**, 870 (1991).
25. E. A. Wang, V. Rosen, J. S. D'Alessandro, M. Bauduy, P. Cordes, T. Harada, D. I. Israel, R. M. Hewick, K. M. Kerns, P. Lapan, D. P. Luxenberg, D. McQuaid, I. K. Moutsatsos, J. Nove and J. M. Wozney, *Proc. Natl Acad. Sci. USA* **87**, 2220 (1990).
26. M. Yamamoto, K. Kato and Y. Ikada, *Tissue Eng.* **2**, 315 (1996).
27. L. S. Beck, E. P. Amento, Y. Xu, L. Deguzman, W. P. Lee, T. Nguyen and N. A. Gillett, *J. Bone Mineral Res.* **8**, 753 (1993).
28. T. Tanaka, Y. Taniguchi, K. Gotoh, R. Satoh, M. Inazu and H. Ozawa, *Bone* **14**, 117 (1993).
29. W. R. Gombotz, S. C. Pankey, L. S. Bouchard, D. H. Phan and P. Puolakkainen, *J. Appl. Biomater.* **5**, 141 (1994).
30. D. R. Sumner, T. M. Turner, A. F. Purchio, W. R. Gombotz and J. O. Galante, *J. Bone Joint Surg.* **77A**, 1135 (1995).
31. U. Ripamonti, C. Bosch, B. V. D. Heever, N. Duneas, B. Melsen and R. Ebner, *J. Bone Miner. Res.* **11**, 938 (1996).
32. T. Nakamura, K. Hanada, M. Tamura, T. Shibanushi, H. Nigi, M. Tagawa, S. Fukumoto and T. Matsumoto, *Endocrinology* **136**, 1276 (1995).
33. J. S. Wang, *Acta Orthop. Scand.* (*Suppl. 269*) **67**, 1 (1996).
34. K. Yamada, Y. Tabata, K. Yamamoto, S. Miyamoto, I. Nagata, H. Kikuchi and Y. Ikada, *J. Neurosurg.* **86**, 871 (1997).
35. D. Zekorn, *Bibl. Haematol.* **33**, 30 (1969).
36. Y. Tabata, S. Hijikata and Y. Ikada, *J. Control. Rel.* **31**, 189 (1994).
37. A. Veis, *The Macromolecular Chemistry of Gelatin*. Academic Press, New York (1964).
38. F. C. Greenwood, W. M. Hunter and T. C. Gglover, *Biochem. J.* **89**, 114 (1963).
39. K. Yim, J. Abrams and A. Hsu, *J. Chromatogr.* **A716**, 401 (1995).
40. Md. Muniruzzaman, Y. Tabata and Y. Ikada, *J. Biomater. Sci. Polym. Edn* (1997) (in press).

Polymers for Tissue Engineering, pp. 433–434
Molly S. Shoichet and Jeffrey A. Hubbell (Eds)

Subject index